frontiers | Research Topics

Water-related natural disasters in mountainous area, volume II

Edited by
Jia-wen Zhou, Jie Dou, Xiekang Wang, Xudong Fu, Qihua Ran and Biswajeet Pradhan

Published in
Frontiers in Earth Science

ISSN 1664-8714
ISBN 978-2-8325-4607-9
DOI 10.3389/978-2-8325-4607-9

About Frontiers

Frontiers is more than just an open access publisher of scholarly articles: it is a pioneering approach to the world of academia, radically improving the way scholarly research is managed. The grand vision of Frontiers is a world where all people have an equal opportunity to seek, share and generate knowledge. Frontiers provides immediate and permanent online open access to all its publications, but this alone is not enough to realize our grand goals.

Frontiers journal series

The Frontiers journal series is a multi-tier and interdisciplinary set of open-access, online journals, promising a paradigm shift from the current review, selection and dissemination processes in academic publishing. All Frontiers journals are driven by researchers for researchers; therefore, they constitute a service to the scholarly community. At the same time, the *Frontiers journal series* operates on a revolutionary invention, the tiered publishing system, initially addressing specific communities of scholars, and gradually climbing up to broader public understanding, thus serving the interests of the lay society, too.

Dedication to quality

Each Frontiers article is a landmark of the highest quality, thanks to genuinely collaborative interactions between authors and review editors, who include some of the world's best academicians. Research must be certified by peers before entering a stream of knowledge that may eventually reach the public - and shape society; therefore, Frontiers only applies the most rigorous and unbiased reviews. Frontiers revolutionizes research publishing by freely delivering the most outstanding research, evaluated with no bias from both the academic and social point of view. By applying the most advanced information technologies, Frontiers is catapulting scholarly publishing into a new generation.

What are Frontiers Research Topics?

Frontiers Research Topics are very popular trademarks of the *Frontiers journals series*: they are collections of at least ten articles, all centered on a particular subject. With their unique mix of varied contributions from Original Research to Review Articles, Frontiers Research Topics unify the most influential researchers, the latest key findings and historical advances in a hot research area.

Find out more on how to host your own Frontiers Research Topic or contribute to one as an author by contacting the Frontiers editorial office: frontiersin.org/about/contact

Water-related natural disasters in mountainous area, volume II

Topic editors

Jia-wen Zhou — Sichuan University, China
Jie Dou — China University of Geosciences Wuhan, China
Xiekang Wang — Sichuan University, China
Xudong Fu — Tsinghua University, China
Qihua Ran — Hohai University, China
Biswajeet Pradhan — University of Technology Sydney, Australia

Citation

Zhou, J.-w., Dou, J., Wang, X., Fu, X., Ran, Q., Pradhan, B., eds. (2024). *Water-related natural disasters in mountainous area, volume II*. Lausanne: Frontiers Media SA.
doi: 10.3389/978-2-8325-4607-9

Table of contents

frontiers | Frontiers in Earth Science

TYPE Original Research
PUBLISHED 16 September 2022
DOI 10.3389/feart.2022.992842

OPEN ACCESS

EDITED BY
Biswajeet Pradhan,
University of Technology Sydney, Australia

REVIEWED BY
Supattra Puttinaovarat,
Prince of Songkla University, Thailand
Paramate Horkaew,
Suranaree University of Technology, Thailand

*CORRESPONDENCE
Jianrong Fan,
fjrong@imde.ac.cn

†These authors have contributed equally to this work

SPECIALTY SECTION
This article was submitted to Geohazards and Georisks, a section of the journal Frontiers in Earth Science

RECEIVED 13 July 2022
ACCEPTED 23 August 2022
PUBLISHED 16 September 2022

CITATION
Fan J, Xu F, Zhang X, Zhang X and Liang B (2022), Evaluating the sensitivity and influential factors of freeze-thaw erosion in Tibet, China.
Front. Earth Sci. 10:992842.
doi: 10.3389/feart.2022.992842

Evaluating the sensitivity and influential factors of freeze-thaw erosion in Tibet, China

Jianrong Fan[1*†], Fubao Xu[1,2†], Xiyu Zhang[1], Xiaoxue Zhang[3] and Bo Liang[3]

[1]Research Center for Digital Mountain and Remote Sensing Application, Institute of Mountain Hazards and Environment, Chinese Academy of Sciences, Chengdu, China, [2]University of Chinese Academy of Sciences, Beijing, China, [3]Soil and Water Conservation Bureau of Tibet Autonomous Region, Lhasa, China

Freeze–thaw (FT) erosion has gradually become more severe due to climate warming, and concerns about FT erosion in ecologically fragile areas (e.g., high-altitude and high-latitude areas) continues to grow. Tibet, located at the Third Pole of Earth, is also in a substantial part underlain with seasonally frozen soil and subject to FT erosion. Evaluating the sensitivity and influential factors of FT erosion in Tibet is warranted to manage the ecological environment and human production activities. In this study, we investigated the sensitivity and spatial distribution characteristics of FT erosion in Tibet based on advanced remote sensing and geographic information system (GIS) technologies. To further explore the influence of each factor on FT erosion, we analyzed the sensitivity of FT erosion under each factor condition. Our results showed that the annual temperature range is the most influential factor on FT erosion among temperature, precipitation, topography and vegetation. In addition, we introduced the coefficient of variation (CV) to represent the stability of temperature and then used CMIP5 simulation data to estimate the susceptibility of FT erosion in Tibet over the next 30 years. The CVs in central and western Tibet were higher than those in other areas and thus need more attention to FT erosion in central and western Tibet in the future.

KEYWORDS

FT erosion, sensitivity assessment, GIS, remote sensing, Tibet

Introduction

Freeze-thaw caused by frequent changes of temperature is one of the most crucial characteristics of the land surface in high latitudes, which leads to the change of water volume in soil parent material pores or rock cracks (Gao et al., 2018). One of the serious hazards caused by Freeze-thaw changes is Freeze-thaw erosion. Freeze-thaw (FT) erosion refers to soil erosion resulting from FT alteration in slopes, trench walls, riverbeds, and canals in permafrost (Zhang et al., 2007; Hu et al., 2019). It mostly occurs at high latitudes and altitudes during late winter and early spring periods. It directly affects the hydrological process of frozen soil, changes soil water conductivity and soil water capacity, and threatens vegetation growth (Dong et al., 2000; Li et al., 2015). In

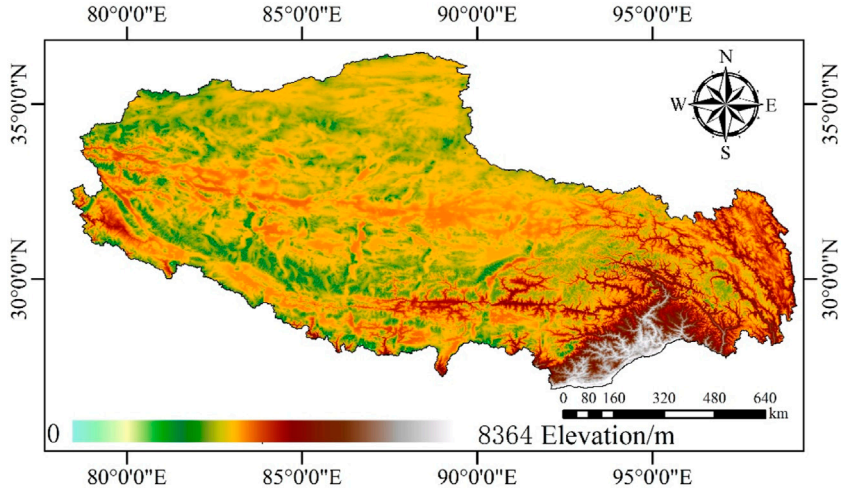

FIGURE 1
Map of study area.

TABLE 1 Overview of the dataset used in this paper.

Dataset	Variables	Spatial resolution	Year	Temporal resolution
SRTM DEM	slope, aspect	30 m	—	—
TRMM	precipitation	0.25°	2016–2018	3 h
MOD13/MYD13	NDVI	250 m	2016–2018	16 days
CRU	surface temperature	0.5°	2016–2018	Daily
CMIP5	surface temperature	1.125o	2019–2,100	Monthly

TABLE 2 Sensitivity of the evaluation factors.

Evaluation factor	Sensitivity				
	Insensitive	Mild	Moderate	High	Extremely high
Annual range of temperature (°C)	≤18	18–20	20–22	22–24	>24
Annual precipitation (mm)	≤100	100–200	200–300	300–400	>400
Slope (°)	0–3	3–8	8–15	15–25	>25
Aspect (°)	0–45, 315–360	45–90, 270–315	90–135	225–270	135–225
Vegetation coverage (%)	≥80	60–80	40–60	20–40	<20
Grading assignment	1	3	5	7	9

addition, FT erosion has become the primary form of erosion in cold regions and therefore is a substantial threat to the environment. In recent years, global warming has exerted a significant impact on terrestrial ecosystems (Reichstein et al., 2013; Wang et al., 2020), and FT erosion processes have been exacerbated due to rising temperatures (Wang et al., 2020). The Intergovernmental Panel on Climate Change (IPCC) fifth assessment report shows that the global average temperature increased by 0.85°C between 1880 and 2012 (Field et al., 2014). Therefore, increased attention to the prevention and treatment of FT erosion is important (Guo et al., 2017). In China, the freeze-thaw erosion covers an area of 1,269,800 km^2, which accounts for

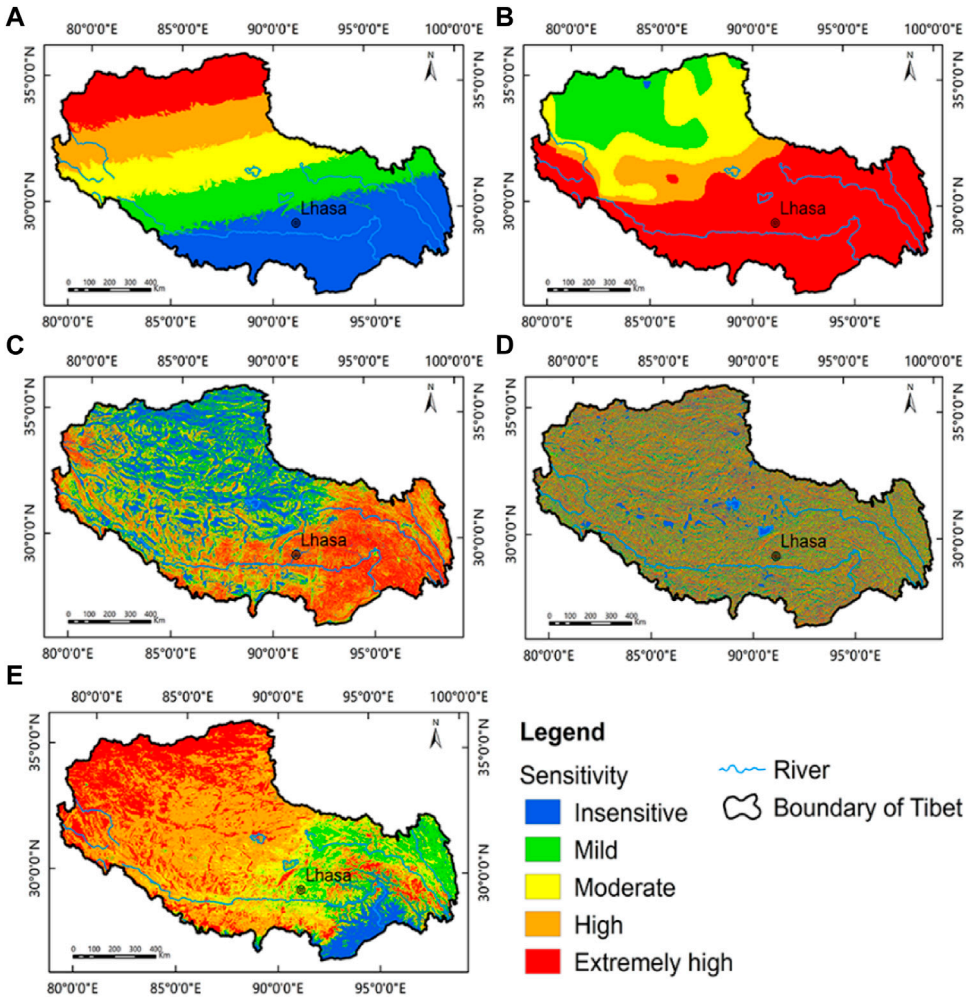

FIGURE 2
Spatial distributions of FT erosion sensitivity factors in Tibet: **(A)** annual temperature range, **(B)** annual precipitation, **(C)** slope, **(D)** aspect and **(E)** vegetation coverage.

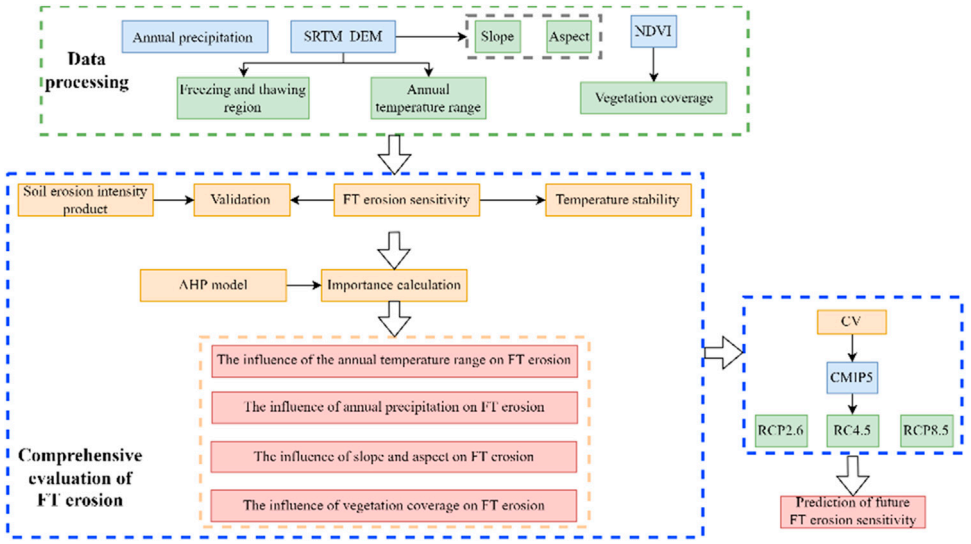

FIGURE 3
Flow chart of evaluating the FT erosion sensitivity in Tibet.

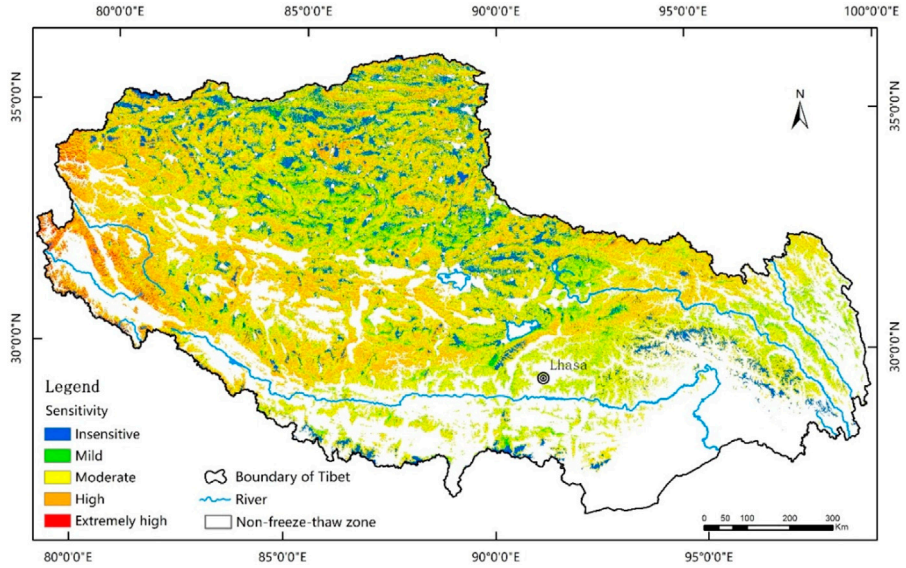

FIGURE 4
Sensitivity of FT erosion.

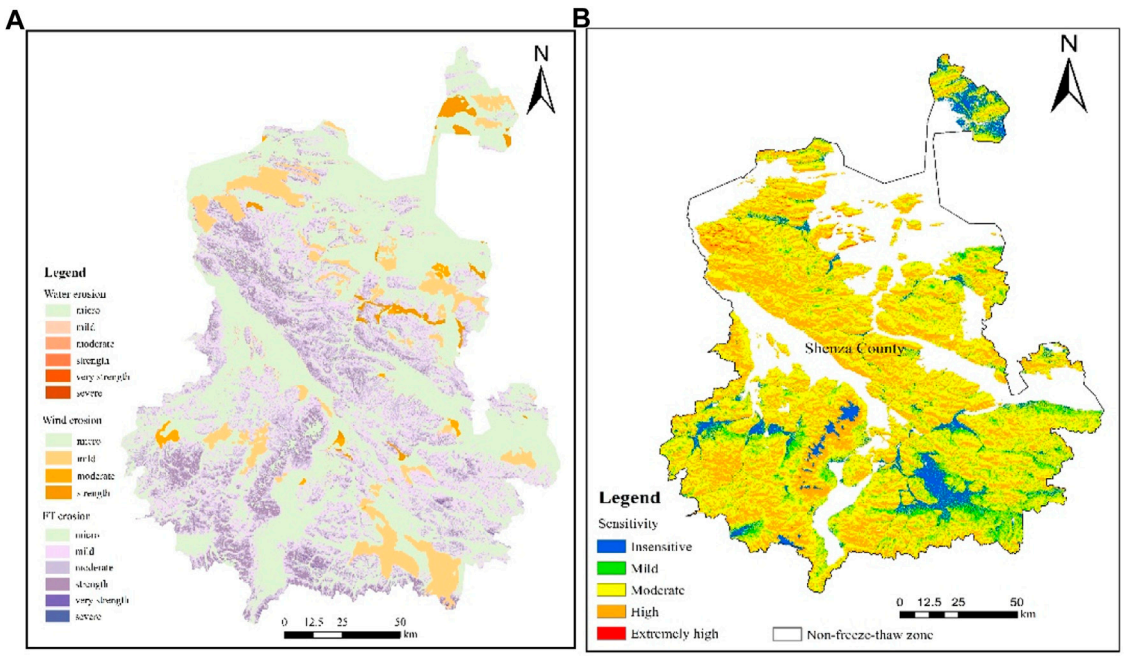

FIGURE 5
Comparison of FT erosion (Shenza County). **(A)** The result of soil erosion intensity product. **(B)** The result of FT erosion sensitivity.

13.36% of the total land area (Wei et al., 2012; Lu et al., 2021). Tibet appears to be particularly vulnerable to climate change and has become one of the most degraded ecosystems in the world (Teng et al., 2018). Moreover, FT erosion is widespread and has a great influence on engineering construction and agricultural activities in Tibet (Li et al., 2008; Zhang and Liu, 2018).

Sensitivity evaluation of FT erosion, particularly at the regional scale, could provide important insights into the prevention and treatment of FT erosion. However, FT erosion is affected by many factors, such as topography, precipitation, temperature, and vegetation, making its sensitivity complicated to evaluate. In recent years, numerous studies have focused on evaluating the sensitivity of soil erosion. Ferrick and Gatto. (2005) quantified FT erosion through laboratory experiments and demonstrated that FT is a primary process contributing to soil erosion in cold climates. Guo and Jiang. (2017) used eight typical factors to establish an evaluation method of FT erosion for the three-river source region in the Qinghai-Tibetan Plateau. Li et al. (2014) used a numerical moisture-heat-mechanics model to explore the FT damage mechanism. Eigenbrod (1996) obtained a linear relationship between the net volume changes after freezing and thawing. Lu et al. (2021) selected seven evaluation factors to analyze the temporal and spatial characteristics of freeze-

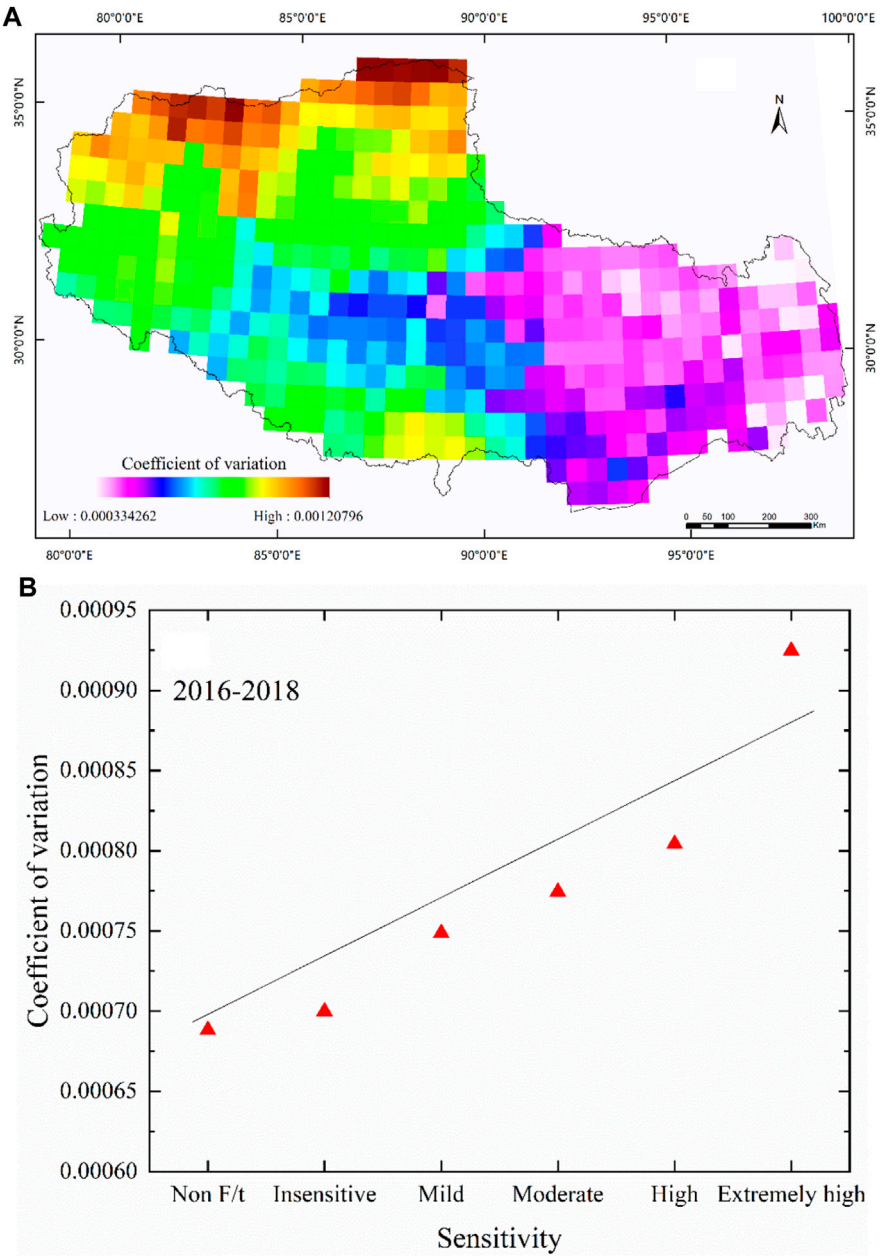

FIGURE 6
(A) Spatial distribution of CV from 2016 to 2018 in Tibet; **(B)** The mean CV in Tibet under different sensitivities.

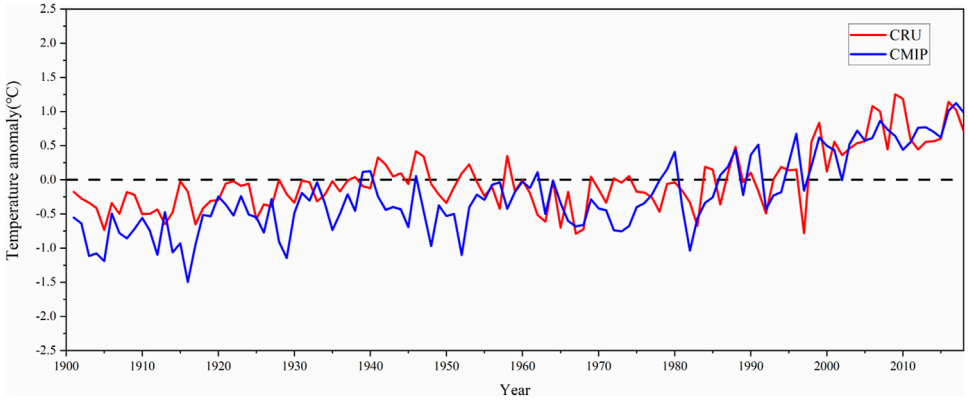

FIGURE 7
Time series of annual mean surface air temperature anomalies with respect to the 1981–2000 mean from CMIP5 and CRU during 1901–2018 over Tibet.

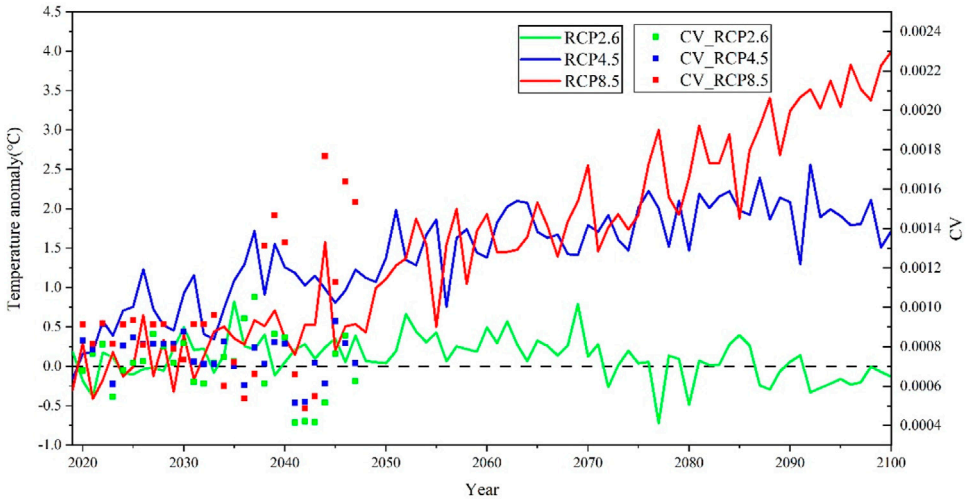

FIGURE 8
Temporal changes in annual mean surface air temperature anomalies with respect to 2019–2020 from different CMIP5 experiments during 2019–2,100 over Tibet.

thaw erosion in the source regions of the Chin-Sha, Ya-Lung and Lantsang Rivers. Guo et al. (2015) established an estimation model of FT erosion by introducing microwave remote sensing techniques. Shi et al. (2012) used the normalized method and evaluation model of freeze-thaw erosion with graded weight, the precipitation, annual temperature difference, vegetation index, slope and solar radiation to carry quantitative research and analysis in the three rivers source area. Additionally, many researchers have assessed the sensitivity of FT erosion and its impact on the environment (Liu et al., 2006; Zhang et al., 2007; Zhang et al., 2009; Kong and Yu, 2013; Liu et al., 2013).

FT erosion sensitivity is used to identify regions that are prone to freeze–thaw erosion and provide a scientific basis for human production and life (Wang et al., 2017). The objective of this study is to assess current FT erosion sensitivity levels in Tibet and evaluate the influence of different factors on FT erosion. Additionally, we evaluated the distribution of FT erosion probability with temperature from the CMIP5 model in the 21st century. In detail, we selected temperature, precipitation, slope, aspect and vegetation coverage as major factors to assess current FT erosion sensitivity based on a comprehensive analysis. The erosion intensity was classified as mild, moderate, high or extremely

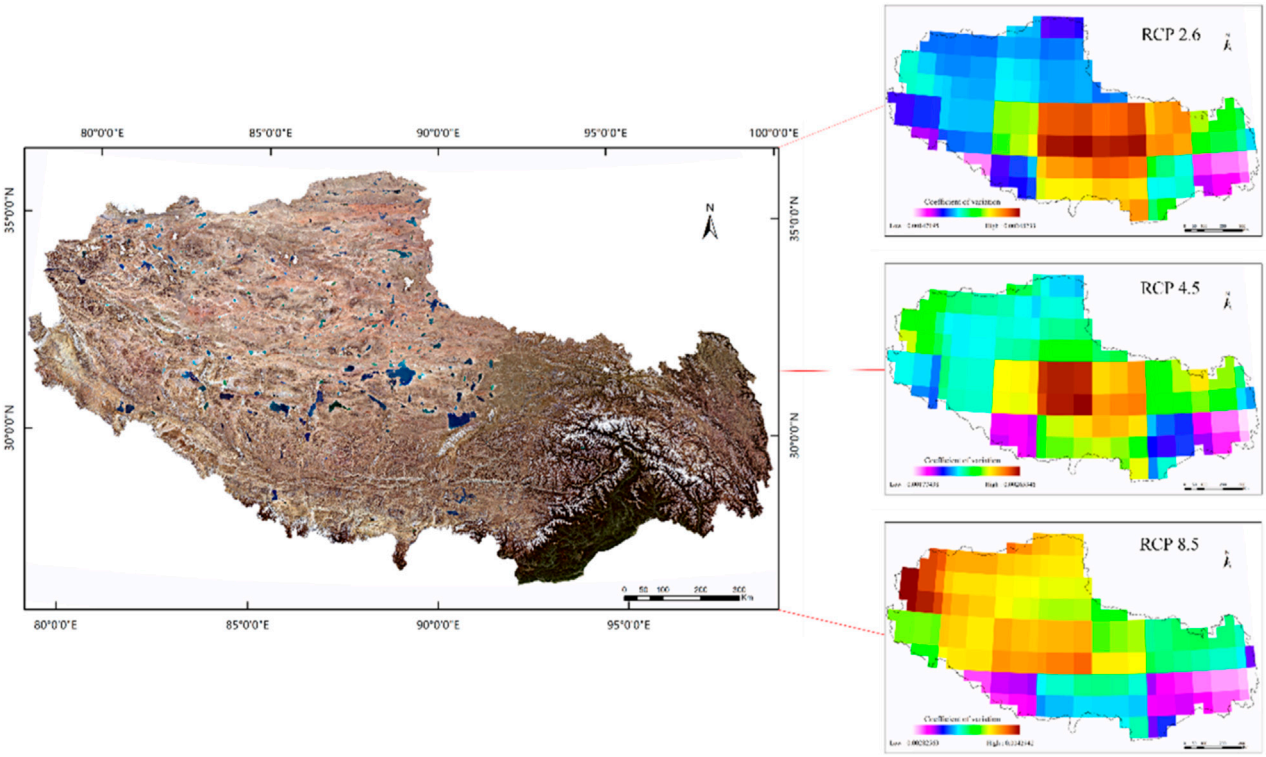

FIGURE 9
The distribution characteristics of CVs (RCP 2.6, RCP 4.5 and RCP 8.5 are displayed in the first, second and third rows on the right, respectively).

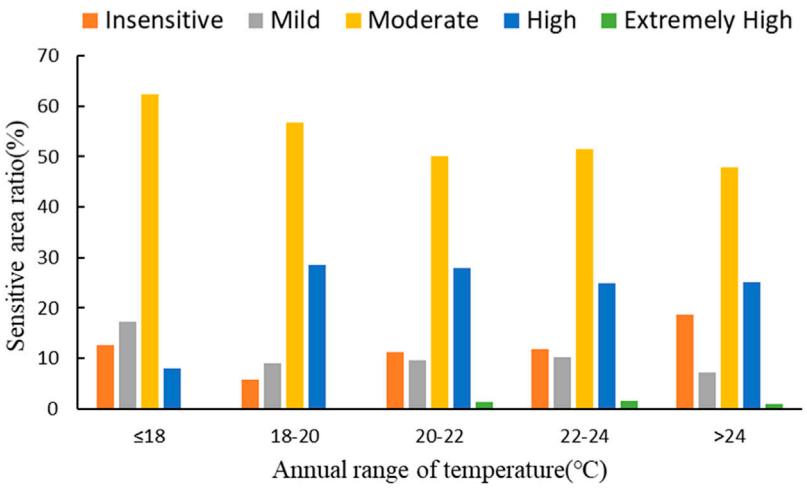

FIGURE 10
Ratios of different FT erosion sensitivities under various annual temperature ranges.

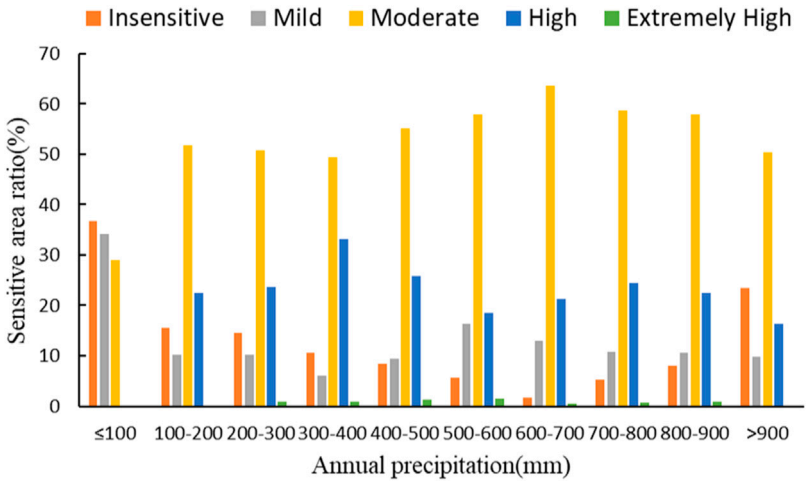

FIGURE 11
Ratios of different FT erosion sensitivities under various precipitation levels.

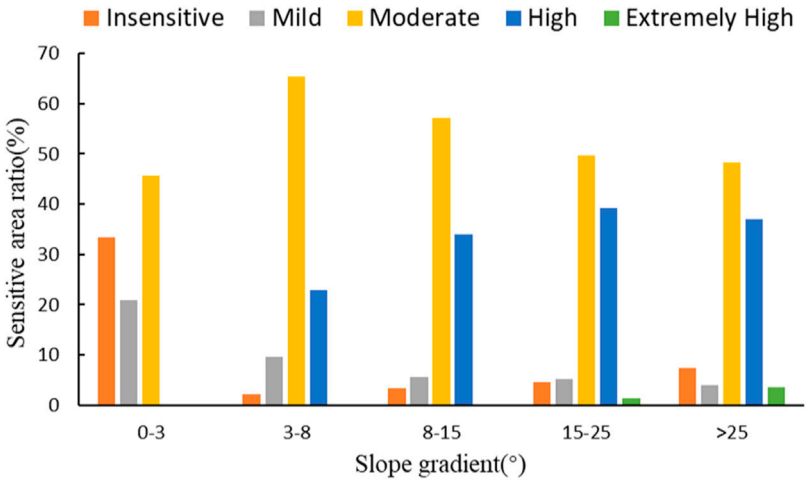

FIGURE 12
Ratios of different FT erosion sensitivities under various slope ranges.

high. Furthermore, we introduced the coefficient of variation (CV) to represent the future FT erosion probability.

Study area and materials

Study area

Tibet is located in Southwest China, spans between 26°50′-36°53′E and 78°25′-99°06′N, covers an area of 1,228,400 km^2 and belongs to an alpine subcontinent climate. It accounts for more than half of the Tibetan Plateau, and areas over 4,000 m above sea level account for 85.1% of the total area (Figure 1). The annual average temperature in Tibet is 4.2°C, and the average annual precipitation, which is mainly concentrated in summer, is 593.7 mm. The diverse soil types and the alternating FT cycles create conditions for the development of FT erosion. Tibet and its high mountainous regions are the most concentrated and intense regions of FT erosion in China (Li et al., 2005).

Data collection

The elevation data were provided by the NASA Shuttle Radar Topography Mission (SRTM) at a resolution of

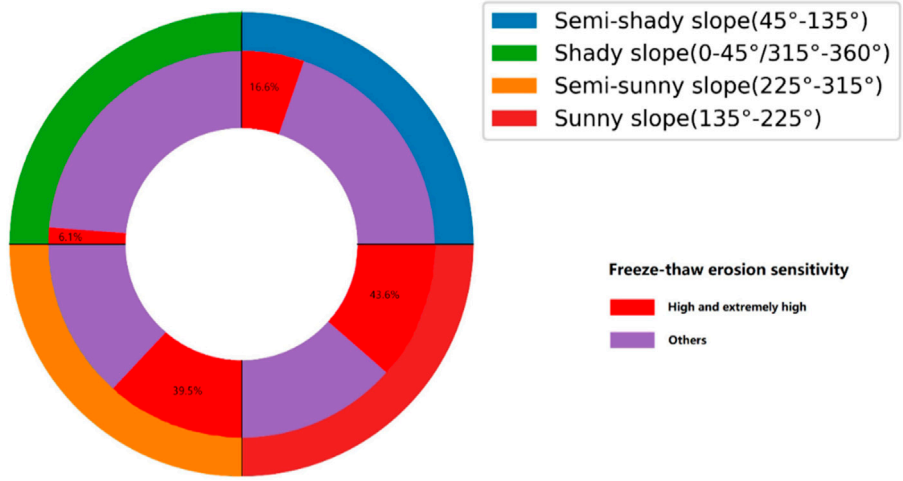

FIGURE 13
Ratios of different FT erosion sensitivities under various aspect ranges.

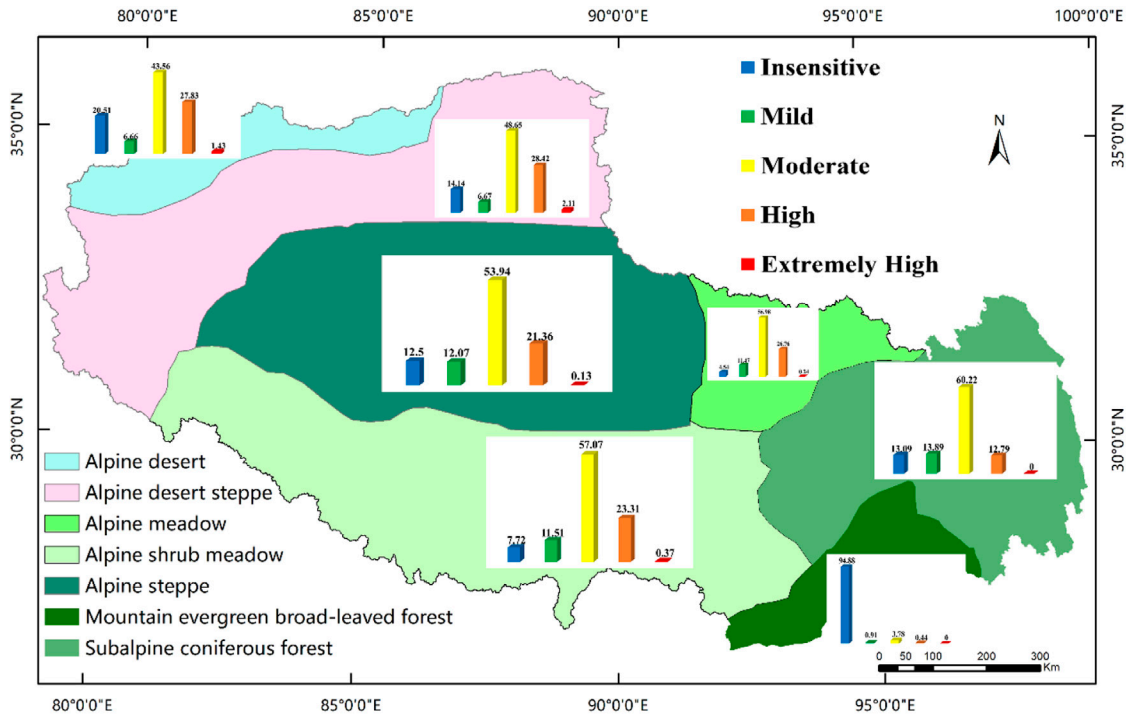

FIGURE 14
Vegetation distribution map and erosion ratios in Tibet.

approximately 30 m. The dataset has an absolute vertical accuracy of less than 16 m, and the relative vertical accuracy is less than 10 m (at the 90% confidence level) (Falorni et al., 2005). Slope and aspect were also derived based on the elevation, and the average pixel values were calculated to represent the surface morphology of the 90-m pixel.

TRMM precipitation data were provided by NASA (https://gpm.nasa.gov/data-access/downloads/trmm) (Huffman et al., 2010). The spatial resolution of the data was 0.25°, and the

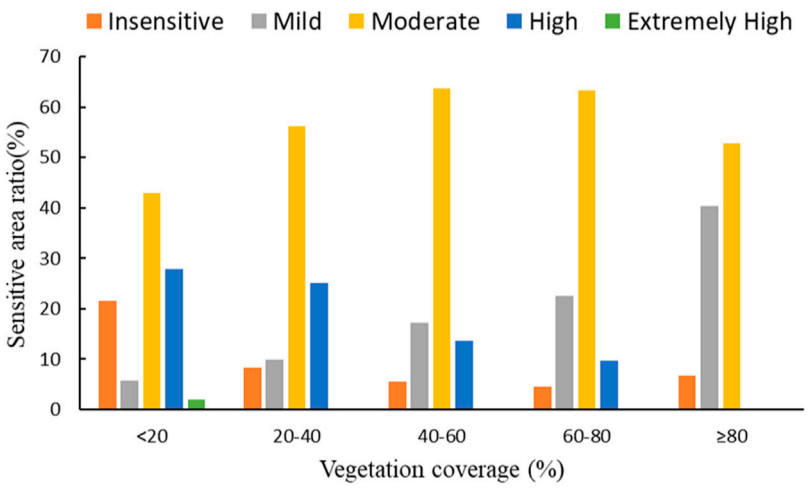

FIGURE 15
Ratios of different FT erosion sensitivities under various vegetation coverage ranges.

TABLE 3 Sensitivity grades of FT erosion.

	Sensitivity				
	Insensitive	**Mild**	**Moderate**	**High**	**Extremely high**
Evaluation of estimate (S)	<2	2–3.5	3.5–5.5	5.5–7.5	≥7.5

TABLE 4 Statistics on the sensitivity of FT erosion.

Sensitivity	**Area (10^4 km^2)**	**A (%)**	**B (%)**
Insensitive	9.56	12.05	7.95
Mild	8.19	10.32	6.81
Moderate	42.29	53.27	35.16
High	18.74	23.60	15.57
Extremely high	0.61	0.77	0.51
Total of FT zone	79.40	100.00	66.00
Non-FT zone	40.90	—	34.00
Total	120.30	—	100.00

Note: A is the percentage of FT, zone area; and B is the percentage of total area.

TABLE 5 Weighting of FT erosion indictors.

Factor	**Annual range of temperature**	**Annual precipitation**	**Slope**	**Aspect**	**Vegetation coverage**
Weight	0.38	0.23	0.14	0.06	0.19

temporal resolution was 3 h. All images were resampled to a 90-m spatial resolution using the nearest sampling method.

The Moderate Resolution Imaging Spectroradiometer (MODIS) normalized difference vegetation index (NDVI) products (MOD13Q1 and MYD13Q1) were downloaded from NASA Earthdata Search (https://search.earthdata.nasa.gov/). The data are generated every 16 days at a 250-m spatial resolution. In this paper, MODIS products from 2016 to 2018 were used, and the spatial resolution was resampled to 90 m using the nearest sampling method.

The Climatic Research Unit (CRU) time-series (TS) v. 4.05 dataset comprises month-by-month variations in climate over the period 1901–2020 (Morice et al., 2012; Harris et al., 2020); from this dataset, we selected daily mean temperature as the variable. In addition, we selected surface temperature from the CMIP5 model (Taylor et al., 2012; Knutti and Sedláček, 2013). The CMIP5 contains four experiments: a historical experiment (1901–2018) and 3 future emission scenarios for 2006–2,100. In detail, the 3 future scenarios are the representative concentration pathways (RCPs) developed for the IPCC Fifth Assessment Report (AR5). The RCPs—originally RCP2.6, RCP4.5, and RCP8.5—are labeled after a possible range of radiative forcing values in the year 2,100 (2.6, 4.5, and 8.5 W/m^2, respectively). The details of the datasets used in this study are shown in Table 1.

Methods

Extraction of the freezing and thawing region

Qiu et al. (2000) indicated that the lower boundary of permafrost in the Tibetan Plateau is equivalent to the −2°C −−3°C isotherm of the annual average temperature. Hence, the −2.5°C isotherm of the annual average temperature was selected as the lower bound of the permafrost. The lower bound of the FT erosion area in Tibet was 200 m lower than the −2.5°C isotherm of the annual average temperature (Zhou et al., 2000; Zhang and Liu, 2005). Therefore, we assumed that the altitude of the −2.5°C isotherm minus 200 m was the lower bound of the FT erosion zone in Tibet. The altitude of the FT erosion lower bound was acquired according to Eq. 1:

$$H = \frac{66.3032 - 0.9197X_1 - 0.1438X_2 + 2.5}{0.005596} - 200 \quad (1)$$

where H is the altitude of the FT erosion lower bound, X_1 is the latitude (°) and X_2 is the longitude (°).

The freezing and thawing regions were extracted *via* the following: 1) extracting the latitude (X_1) layer and longitude (X_2) layer using the DEM; 2) calculating the altitude (H) and obtaining the potential FT erosion zone based on DEM values; and 3) removing the glacier area, lake area, and desertification area from the potential FT erosion area using a land cover type map.

Selection of evaluation factors

FT erosion is closely related to climate, topography, hydrology and vegetation (Guo et al., 2015). Zhang et al. (2007) summarized the natural factors that contribute to FT erosion: 1) temperature, including mean annual soil temperature and annual soil temperature range in FT erosion zone. 2) landform, which has an influence on the type and degree of erosion. 3) precipitation, which has an influence on the type and degree of erosion. 4) vegetation, which can mitigate some of the effects. 5) soil, FT erosion is closely related to the soil physical property. In this study, the selection of indicators was considered on the basis of empirical evidence from previous research (Shi et al., 2012; Guo et al., 2015; Lu et al., 2021). In addition, soil physical properties are often influenced by temperature, precipitation, and vegetation. Therefore, this paper selected five factors as the influencing factors of FT erosion, including the annual temperature range, annual precipitation, slope, aspect and vegetation coverage.

Temperature is an important criterion used to judge the FT state, which mostly occurs when the soil temperature fluctuates at approximately 0°C (Wang et al., 2007). The soil temperature changes periodically in the FT erosion zone with periodic changes in air temperature. Thus, the air temperature can be used as a substitute factor for soil temperature (Zhang et al., 2007; Shi et al., 2012). The air annual temperature range was calculated *via* a regression Eq. 2 among latitude, longitude and altitude as follows:

$$A = 3.1052 + 1.2418X_1 - 0.2275X_2 - 0.0004133X_3 \quad (2)$$

Where A is the annual temperature range, X_1 is the latitude, X_2 is the longitude, and X_3 is the altitude.

Precipitation is a driving force for material movement of erosion, and it increases the possibility of FT erosion. We obtained daily precipitation data (years: 2016–2018) by summing the 3-hourly precipitation. Then, the average annual precipitation was calculated by Eq. 3:

$$Y = \sum_{i=1}^{n} Y_i \quad (3)$$

Where n is the length of the time series of one year.

In addition, the slope affects the amount of FT erosion and the magnitude of erosion displacement. Aspect can lead to different types of FT erosion. Slope and aspect were extracted by the DEM using the slope and aspect tools in ArcGIS.

Vegetation plays an important role in suppressing the FT erosion process. Based on the maximum value of the MODIS NDVI in summer over the past three years (2016–2018) and the vegetation type map, the vegetation coverages of different

vegetation types were obtained by using the pixel dichotomy model:

$$f_g = \frac{NDVI - NDVI_{soil}}{NDVI_{veg} - NDVI_{soil}} \quad (4)$$

where f_g is the vegetation coverage and $NDVI_{soil}$ and $NDVI_{veg}$ are the NDVI values of the full soil coverage pixels and full vegetation pixels, respectively.

Sensitivity of the evaluation factors

The comprehensive evaluation of FT erosion represents a synthesis of multiple factors affecting this complex process of FT erosion (Xie et al., 2017). The evaluation is worked out based to the distribution situation of various factors values in Tibetan freeze-thaw zone. According to the specific distribution of each factor value in the FT erosion area of Tibet and based on the results of previous studies, the sensitivity levels of various factors affecting FT erosion were determined (Table 2). Figure 2 shows the sensitivity of each factor.

Evaluation factors that affect FT erosion were integrated to obtain a comprehensive evaluation index for the sensitivity assessment of FT erosion (Wang et al., 2004). The comprehensive evaluation index can be calculated by using Eq. 5:

$$S = \sqrt[n]{\prod_{i=0}^{n} C_i} \quad (5)$$

where S is the comprehensive evaluation factor, C_i is the grading assignment of factor I, and n is the number of factors. The sensitivity of FT erosion in the study area was then divided into five grades (Table 3).

Importance calculation of evaluation factors

In the previous studies, Analytic Hierarchy Process (AHP) method is widely used in the evaluation of FT erosion. Zhang et al. (2007) chose six factors to build the model for relative classification of FT erosion using AHP method. Hu et al. (2021) selected seven evaluation factors to analyze the temporal and spatial characteristics of FT erosion based on the AHP method. AHP is a qualitative and quantitative, systematic and hierarchical analysis method (Hu et al., 2021). The factors are grouped at different levels according to the correlation and subordination, and finally a multi-level analysis structure model is formed. Further, the AHP semi-quantitatively assigns the weight of each factor according to the subjective judgment of experts and the importance of factors, making the weight allocation more reasonable. In this study, we utilized AHP to reflect the effects of each factor on FT erosion. In details, the importance of each factor was obtained by constructing a decision model of 5 factors affecting FT erosion. The AHP model can be generally carried out according to the following steps:

(1) Build a judgment matrix. Pairwise comparison of each factor is used to evaluate the grade according to its importance, and a judgment matrix is formed according to the result of the pairwise comparison. The formula is:

$$a_{ij} = \frac{1}{a_{ji}} \quad (6)$$

Where i and j represent the different factor.

(2) consistency test. According to the judgment matrix, the weight value of each factor is calculated. In order to test whether the weight value is scientific, the consistency test of the judgment matrix is also required:

$$\lambda_{max} = \sum_{i=1}^{n} \frac{[A\omega]_i}{n\omega_i} \quad (7)$$

$$CI = \frac{\lambda - n}{n - 1} \quad (8)$$

$$CR = \frac{CI}{RI} \quad (9)$$

where λ_{max} is the largest eigenvalue; A refers to judgment matrix; ω is feature vector; n is the order of matrix; CI is the indicator of consistency; CR is test coefficient; RI is the mean random consistency.

Temperature stability

The coefficient of variation (CV) was employed to estimate temperature stability. The CV can be calculated as follows (Wang et al., 2004):

$$CV = \sigma/\mu \quad (10)$$

$$\sigma = \sqrt{\frac{1}{n}\sum_{i=1}^{n}(x_i - \mu)^2} \quad (11)$$

$$\mu = \frac{1}{n}\sum_{i=1}^{n} x_i \quad (12)$$

where σ represents the standard deviation of the annual air temperature; μ represents the average air temperature during the study period; n represents the number of years; and x_i represents the air temperature in the i*th* year.

A flow chart of evaluating the FT erosion sensitivity is shown as Figure 3, specifically as follows: 1) Data processing. 2) Comprehensive evaluation of FT erosion. 3) Prediction of future FT erosion sensitivity.

Results

Freeze-thaw erosion sensitivity

The distribution of FT erosion regions was extensive in Tibet (Table 4), with an area of 79.4×10^4 km^2 accounting for 66.00% of the total area, which indicated that FT erosion may be one of the main types of soil erosion. The area sensitive to FT erosion is 69.83×10^4 km^2, among which the moderate and more sensitive area is 61.64×10^4 km^2, accounting for 77.63% of the total FT erosion area in Tibet.

Significant differences were observed in the spatial distribution of FT erosion sensitivity in Tibet. The sensitivity map (Figure 4) shows that the sensitivity of FT erosion in southern high-altitude areas is higher than that in northern high-latitude areas. High-sensitivity areas and extremely high-sensitivity areas were mainly distributed in the southwest region. Some areas in the southeast were insensitive-sensitivity and mild-sensitivity because they were situated in mountain canyons.

The contribution of each factor to the FT erosion susceptibility is different, it is necessary to weight each influencing factor. According to the AHP method, the weight of factors was calculated by building a judgment matrix, and consistency check of result was done (Table 5). The judgment matrix constructed in this paper is a 5th-order matrix, and the maximum eigenvalue λ_{max} = 5.252, CI = 0.063. Finally, the test coefficient CR = 0.056 is obtained, which is less than 0.1, indicating that the judgment matrix has passed the consistency test, so the obtained weight values of each ecological evaluation factor are available.

Validation of Freeze–thaw erosion sensitivity results

We compared our results with regional soil erosion intensity product overlapped with the study area in the bulletin of soil and water conservation issued by the ministry of water resources of the People's Republic of China in 2019. One of the main reasons for using this product as comparison was that the erosion intensity was the most authoritative results of the official release. It was also convenient to make such a comparison because the product provided high-spatial resolution result over Shenza County. A comparation between our FT erosion sensitivity results and soil erosion intensity product is shown in Figure 5. It is worth noting that our sensitivity grading is different from the erosion intensity grading. Only five ratings of our sensitivity correspond to the top five ratings of erosion intensity. In general, FT erosion show consistent distribution and similar level, they gradually weakened from northeast to southwest. Therefore, FT erosion sensitivity result in this study is reliable, and have a good accuracy.

Erosion sensitivity response to temperature change

Among the necessary climatic conditions for the occurrence of freeze-thaw erosion, temperature is the most important influencing factor, with a weight value of 0.38 (Table 5). Figure 6A shows the extent of variability in relation to the mean of the air temperature from 2016 to 2018. Our calculated CV indicated that air temperature stability is lower in western Tibet than in eastern Tibet, and the highest CV is located in northwestern Tibet, which means that the air temperature stability is lowest in the northwest. Figure 6B shows the mean CV in Tibet under different sensitivities, indicating that the CV has a high correlation with FT erosion sensitivity.

Prediction of future Freeze-thaw erosion sensitivity

In this study, we evaluated the agreement between CMIP5 air temperature anomalies and CRU observations. We took the average of the three CMIP5 scenarios as the air temperature. The correlation coefficient, RMSE and MAE were 0.70, 0.45°C, and 0.35°C, respectively. To further evaluate the agreement between the averaged CMIP5 air temperature and CRU observations in Tibet, we compared the time series and trends in annual temperatures (Figure 7). The time series of MAT (mean annual air temperature) showed increasing temperatures during 1901–2018 for the air temperatures from CMIP5 models and CRU observations. The MAT from CRU observations increased significantly at a rate of 0.079°C decade^{-1}, while the MAT trends from CMIP5 increased at a rate of 0.125°C decade^{-1}. The MAT time-series anomalies were very similar to those from CRU and CIMP5 for Tibet. This similarity indicated that CMIP5 scenarios correlate well with CRU and that the average MAT was increasingly warmer.

Figure 8 shows the trend of the overall annual average temperature in Tibet from 2019 to 2,100. The RCP2.6 scenario presented a decrease at a rate of 0.03°C decade^{-1} (p<0.05), the RCP4.5 scenario exhibited an increase at a rate of 0.202°C decade^{-1} (p<0.05), and the RCP8.5 scenario increased significantly at a rate of 0.488°C decade^{-1} (p<0.05). Both RCP 4.5 and RCP 8.5 between 2019 and 2,100 showed an obvious warming trend in temperature throughout this century, and only RCP 2.6 did not show a general increase with time. In addition, basing on the CVs of every three years, we analyzed the CV changes in Tibet over the next 30 years under different scenario models. As shown in Figure 8, the CV of RCP8.5 scenario has more significant volatility compared with

RCP2.6 and RCP4.5. It indicated that RCP8.5 scenario is more prone to FT erosion than RCP2.6 and RCP4.5, in the future.

To better understand the spatial and temporal variation characteristics of CV in Tibet, the air temperatures from CMIP5 under three scenarios were used to calculate the spatial distribution of CV from 2019 to 2,100. The mean CVs in RCP 2.6, 4.5 ,and 8.5 were 0.0020, 0.0023 and 0.0038 over Tibet, respectively. The distribution of CV varied greatly for different scenarios (Figure 9). The CVs of the three scenarios in central and western Tibet were higher than those in eastern Tibet, which means that midwestern Tibet is more prone to FT erosion.

Discussion

FT erosion is a soil erosion phenomenon in permafrost regions and represents the main type of soil erosion in alpine regions. FT erosion causes serious harm to farmlands, grasslands, roads and railways and is widespread in Tibet. Thus, evaluating the sensitivity of FT erosion is important. In this study, the sensitivity of FT erosion was obtained by comprehensively evaluating the temperature, precipitation, slope, aspect and vegetation coverage. To further explore the influence of each factor on FT erosion, the FT erosion under each factor condition was analyzed individually.

The influence of the annual temperature range on Freeze-thaw erosion

Figure 10 shows the sensitive area ratios (proportion of different degrees of FT erosion in the total FT area) of annual temperature in five ranges (≤18°C, 18–20°C, 20–22°C, 22–24°C ,and >24°C). High- and extremely high-sensitivity areas were mainly in the temperature range of >18°C, accounting for more than 25% of the FT erosion area. Extremely high-sensitivity areas occurred only in the temperature belt of >20°C, and the FT erosion area occupied by each temperature belt was less than 2%. With increases in the temperature difference, the FT process increases; additionally, with increases in the frozen layer and melted layer depths, the degree of FT erosion will become more severe.

The influence of annual precipitation on Freeze-thaw erosion

Precipitation, consisting of rainfall and snowfall, affects the intensity of FT erosion. Water content affects the stability of soil aggregates when soil is frozen (Lehrsch et al., 1991), and precipitation is an important source of soil water content that directly changes the soil content. Figure 11 shows the FT erosion area ratios under different precipitation levels of ≤100 mm, 100 mm–200 mm, 200 mm–300 mm, 300 mm–400 mm, and 400 mm–500 mm. Extremely high sensitivity occurred only in areas with precipitation greater than 100 mm. When the precipitation reached 600 mm, the proportions of high and extremely high sensitivities tended to be stable as precipitation increased because vegetation began to flourish, which effectively reduced the sensitivity of FT erosion.

The influence of slope and aspect on Freeze-thaw erosion

The sensitive area ratios for different slope ranges of 0–3, 3–8, 8–15, 15–25, and >25 are shown in Figure 12. With increasing slope, the FT erosion degree showed an increasing trend. Insensitive FT erosion was mainly concentrated in the 0–3 slope belt, which accounted for 34% of the FT area. High and extremely high values mainly occurred in areas with slopes greater than 3, which accounted for more than 20% of the FT area, and in areas with high and extremely high sensitivity at a slope >15. Intense and extremely high erosion dominated the areas where the slope was >25, compared with the other slope belts. To reduce the possibility of FT erosion, we must strengthen the restoration and improvement of sloping lands and cultivated land.

Figure 13 shows the FT erosion area ratios under the different aspect ranges of 0–45°/315°–360°, 45°–135°, 135°–225°, and 225°–315°. The outer ring represents four slope directions: sunny slope, semi-sunny slope, semi-shady slope, and shady slope. The inner ring indicates the sensitivity ratio of each slope direction. The ratio directly indicates the sensitivity of FT erosion to the four aspects. Among all aspects, sunny slopes had the largest ratio of high and extremely high sensitivities (with a ratio of 43.6%). In addition, the FT erosion on sunny slopes and semi-shady slopes was more serious than that on shady slopes and semi-shady slopes. The absorbed solar radiation difference between different slopes (sunny slope and shady slope) resulted in thermal differences (Chou et al., 2010; Pei et al., 2017), and the soil's temperature difference on sunny slopes was greater than that on shady slopes. The change in the temperature difference led to more serious erosion on the sunny slope than on the shady slope. In addition, the difference between the semi-sunny slope and sunny slope decreased gradually with increasing elevation; thus, erosion on the semi-sunny slope was more serious than that on shady and semi-shady slopes.

The influence of vegetation coverage on Freeze-thaw erosion

Vegetation not only improves the soil stability but also reduces the soil temperature range. Therefore, vegetation can effectively reduce the sensitivity of soil to FT erosion (Bargiel et al., 2013). Unique terrestrial ecosystems and atmospheric conditions have contributed to the development of diverse biomes and

characteristic altitudinal distribution patterns of vegetation in Tibet (Luo et al., 2002), which extend from subalpine coniferous forest to alpine desert (Figure 14). The influence of vegetation on FT erosion is obvious, as shown in Figure 15, as larger vegetation coverage corresponds to milder FT erosion action. In particular, when vegetation coverage was <20, high and extremely high sensitivities accounted for 27%. Different vegetation types play different roles in mitigating FT erosion. For instance, the ratios of extremely high probability in the alpine desert and alpine desert steppe were larger than others due to weaker mitigation (Figure 15). FT erosion was slight in mountain evergreen broad-leaved forest, where dense vegetation effectively protected the soil from erosion.

Conclusion

The main goal of this research was to assess FT erosion sensitivity and evaluate the distribution of FT erosion probability in Tibet. Five factors were selecteded, and we explored the influence of each factor individually on FT erosion. Specifically, the conclusions of this paper are as follows:

(1) The area sensitive to FT erosion covered 69.83 km^2×104 km^2, with the moderately and more sensitive areas covering 61.64 km^2×104 km^2 in Tibet.
(2) Moderate-sensitivity types were distributed in the alpine arid regions, and high and extremely high sensitivity were mainly distributed in alpine desert and alpine desert steppe areas.
(3) Annual temperature range, slope and aspect accelerate soil FT erosion. Vegetation coverage inhibit FT erosion. The proper increase of precipitation strengthened the role of vegetation. Under the comprehensive action of various factors, the melting of frozen layer in Tibet have accelerated the soil FT erosion.
(4) In the future, midwestern Tibet will be more prone to FT erosion than other areas.

Data availability statement

The original contributions presented in the study are included in the article/supplementary material, further inquiries can be directed to the corresponding author.

Author contributions

All authors listed have made a substantial, direct, and intellectual contribution to the work and approved it for publication.

Funding

This research was funded by the second Tibetan Plateau Scientific Expedition and Research Program (STEP), Grant No. 2019QZKK0603.

Conflict of interest

The authors declare that the research was conducted in the absence of any commercial or financial relationships that could be construed as a potential conflict of interest.

Publisher's note

All claims expressed in this article are solely those of the authors and do not necessarily represent those of their affiliated organizations, or those of the publisher, the editors and the reviewers. Any product that may be evaluated in this article, or claim that may be made by its manufacturer, is not guaranteed or endorsed by the publisher.

References

Bargiel, D., Herrmann, S., and Jadczyszyn, J. (2013). Using high-resolution radar images to determine vegetation cover for soil erosion assessments. *J. Environ. Manag.* 124, 82–90. doi:10.1016/j.jenvman.2013.03.049

Chou, Y., Sheng, Y., Li, Y., Wei, Z., Zhu, Y., and Li, J. (2010). Sunny–shady slope effect on the thermal and deformation stability of the highway embankment in warm permafrost regions. *Cold Regions Sci. Technol.* 63 (1), 78–86. doi:10.1016/j.coldregions.2010.05.001

Dong, R., Xu, Z., and Yang, Y. (2000). *Freeze-thaw erosion in qinghai-tibet plateau*. River: Yangtze, 39–41.

Eigenbrod, K. D. (1996). Effects of cyclic freezing and thawing on volume changes and permeabilities of soft fine-gained soils. *Can. Geotech. J.* 33 (4), 529–537. doi:10.1139/t96-079-301

Falorni, G., Teles, V., Vivoni, E. R., Bras, R. L., and Amaratunga, K. S. (2005). Analysis and characterization of the vertical accuracy of digital elevation models from the Shuttle Radar Topography Mission. *J. Geophys. Res.* 110 (2), F02005. doi:10.1029/2003jf000113

Ferrick, M. G., and Gatto, L. W. (2005). Quantifying the effect of a freeze–thaw cycle on soil erosion: Laboratory experiments. *Earth Surf. Process. Landf.* 30 (10), 1305–1326. doi:10.1002/esp.1209

Field, C. B., Barros, V. R., Mastrandrea, M. D., Mach, K. J., Abdrabo, M. K., Adger, N., et al. (2014). "Summary for policymakers," in *Climate change 2014: impacts, adaptation, and vulnerability. Part A: global and sectoral aspects. Contribution of Working Group II to the Fifth Assessment Report of the Intergovernmental Panel on Climate Change.* (Cambridge University Press), 1–32.

Gao, H., Zhang, W., and Chen, H. (2018). An improved algorithm for discriminating soil freezing and thawing using AMSR-E and AMSR2 soil moisture products. *Remote Sens.* 10 (11), 1697. doi:10.3390/rs10111697

Guo, B., and Jiang, L. (2017). Evaluation of freezing-thawing erosion intensity in qinghai-tibet plateau based on multi-source space-coupled data. *Bull. Soil Water Conserv.* 37, 12–19. doi:10.1080/19475705.2018.1564705

Guo, B., Zhang, F., Yang, G., and Jiang, L. (2017). Improved method of freeze–thaw erosion for the three-river source region in the qinghai–Tibetan plateau, China. *Geomatics, Nat. Hazards Risk* 8 (2), 1678–1694. doi:10.1080/19475705.2017.1370026

Guo, B., Zhou, Y., Zhu, J., Liu, W., Wang, F., Wang, L., et al. (2015). An estimation method of soil freeze-thaw erosion in the Qinghai–Tibet Plateau. *Nat. Hazards (Dordr).* 78 (3), 1843–1857. doi:10.1007/s11069-015-1808-5

Harris, I., Osborn, T. J., Jones, P., and Lister, D. (2020). Version 4 of the CRU TS monthly high-resolution gridded multivariate climate dataset. *Sci. Data* 7 (1), 109. doi:10.1038/s41597-020-0453-3

Hu, T., Fan, J., Yu, X., Zhou, Y., Zhang, P., and Han, L. (2019). Evaluation of freeze–thaw erosion in tibet based on cloud model. *Front. Earth Sci.* 15, 495. doi:10.20944/preprints201909.0201.v1

Huffman, G. J., Adler, R. F., Bolvin, D. T., and Nelkin, E. J. (2010). "The TRMM multi-satellite precipitation analysis (TMPA)," in *Satellite rainfall applications for surface hydrology* (Springer), 3–22.

Knutti, R., and Sedláček, J. (2013). Robustness and uncertainties in the new CMIP5 climate model projections. *Nat. Clim. Chang.* 3 (4), 369–373. doi:10.1038/nclimate1716

Kong, B., and Yu, H. (2013). Estimation model of soil freeze-thaw erosion in silingco watershed wetland of northern tibet. *Sci. World J.* 2013, e636521–7. doi:10.1155/2013/636521

Lehrsch, G. A., Sojka, R. E., Carter, D. L., and Jolley, P. M. (1991). Freezing effects on aggregate stability affected by texture, mineralogy, and organic matter. *Soil Sci. Soc. Am. J.* 55, 1401–1406. doi:10.2136/sssaj1991.03615995005500050033x

Li, D., Wei, X., Li, X., and Li, Y. (2015). Sensitivity evaluation of freeze-thaw erosion in Gansu province based one RS and GIS. *Res. Soil Water Conservation* 22, 1–6. doi:10.13869/j.cnki.rswc.2015.02.002

Li, H., Liu, S., Zhong, X., Zhang, J., and Wang, X. (2005). GIS-based sensitivity evaluation on freeze-thaw erosion in Tibet. *Soil Water Conservation China* 7, 44–46. doi:10.14123/j.cnki.swcc.2005.07.024

Li, S., Lai, Y., Pei, W., Zhang, S., and Zhong, H. (2014). Moisture–temperature changes and freeze–thaw hazards on a canal in seasonally frozen regions. *Nat. Hazards (Dordr).* 72 (2), 287–308. doi:10.1007/s11069-013-1021-3

Li, Z., Zhu, B., and Li, P. (2008). Advancement in study on soil erosion and soil and water conservation. *Actor Pedol. Sinaica* 45, 802–809. doi:10.3232/SJSS.2014.V4.N3.05

Liu, S., Liu, B., Tao, H., and Zhang, L. (2013). The current situation and countermeasures of freeze-thawing erosion in China. *Soil Water Conserv. China* 10, 41–44. doi:10.14123/j.cnki.swcc.2013.10.012

Liu, S., Zhang, J., and Gu, S. (2006). Study on the soil erosion types in Tibet. *J. Mt. Sci.* 24, 592–596. doi:10.3969/j.issn.1008-2786.2006.05.013

Lu, Y., Liu, C., Ge, Y., Hu, Y., Wen, Q., Fu, Z., et al. (2021). Spatiotemporal characteristics of freeze-thawing erosion in the source regions of the chin-sha, ya-lung and Lantsang rivers on the basis of GIS. *Remote Sens.* 13 (2), 309. doi:10.3390/rs13020309

Luo, T., Li, W., and Zhu, H. (2002). Estimated biomass and productivity of natural vegetation on the Tibetan plateau. *Ecol. Appl.* 12 (4), 980–997. doi:10.1890/1051-0761(2002)012[0980:EBAPON]2.0.CO;2

Morice, C. P., Kennedy, J. J., Rayner, N. A., and Jones, P. D. (2012). Quantifying uncertainties in global and regional temperature change using an ensemble of observational estimates: The HadCRUT4 data set. *J. Geophys. Res.* 117 (8). doi:10.1029/2011jd017187

Pei, W., Zhang, M., Li, S., Lai, Y., Jin, L., Zhai, W., et al. (2017). Geotemperature control performance of two-phase closed thermosyphons in the shady and sunny slopes of an embankment in a permafrost region. *Appl. Therm. Eng.* 112, 986–998. doi:10.1016/j.applthermaleng.2016.10.143

Qiu, G., Zhou, Y., and Cheng, G. (2000). *Geocryology in China*. Beijing: Science Press.

Reichstein, M., Bahn, M., Ciais, P., Frank, D., Mahecha, M. D., Seneviratne, S. I., et al. (2013). Climate extremes and the carbon cycle. *Nature* 500 (7462), 287–295. doi:10.1038/nature12350

Shi, Z., Tao, H., Liu, S., Liu, B., and Guo, B. (2012). Evaluation and analysis of freeze-thawing erosion in sanjiangyuan area based on GIS. *Trans. Chin. Soc. Agric. Eng.* 28, 214–221. doi:10.1007/s11707-021-0873-1

Taylor, K. E., Stouffer, R. J., and Meehl, G. A. (2012). An overview of CMIP5 and the experiment design. *Bull. Am. Meteorological Soc.* 93 (4), 485–498. doi:10.1175/bams-d-11-00094.1

Teng, H., Liang, Z., Chen, S., Liu, Y., Viscarra Rossel, R. A., Chappell, A., et al. (2018). Current and future assessments of soil erosion by water on the Tibetan Plateau based on RUSLE and CMIP5 climate models. *Sci. Total Environ.* 635, 673–686. doi:10.1016/j.scitotenv.2018.04.146

Wang, D., Ma, W., Niu, Y., Chang, X., and Wen, Z. (2007). Effects of cyclic freezing and thawing on mechanical properties of Qinghai–Tibet clay. *Cold Regions Sci. Technol.* 48 (1), 34–43. doi:10.1016/j.coldregions.2006.09.008

Wang, L. Y., Xiao, Y., Jiang, L., and Ouyang, Z. Y. (2017). Assessment and analysis of the freeze-thaw erosion sensitivity on the Tibetan Plateau. *J. Glaciol. Geocryol.* 39 (1), 61–69. doi:10.7522/j.issn.1000-0240.2017.0008

Wang, T., Yang, D., Yang, Y., Piao, S., Li, X., Cheng, G., et al. (2020). Permafrost thawing puts the frozen carbon at risk over the Tibetan Plateau. *Sci. Adv.* 6 (19), eaaz3513. eaaz3513. doi:10.1126/sciadv.aaz3513

Wang, X., Zhong, X., and Fan, J. (2004). Assessment and spatial distribution of sensitivity of soil erosion in Tibet. *J. Geogr. Sci.* 14 (1), 41–46. doi:10.1007/BF02873089

Wei, X., Ding, Y., and Li, X. (2012). Review and prospect of freeze-thawing-induced erosion research. *Res. Soil Water Conserv.* 19, 271–275.

Xie, S., Qu, J., Xu, X., and Pang, Y. (2017). Interactions between freeze–thaw actions, wind erosion desertification, and permafrost in the Qinghai–Tibet Plateau. *Nat. Hazards (Dordr).* 85 (2), 829–850. doi:10.1007/s11069-016-2606-4

Zhang, J., and Liu, S. (2005). A new method to define the distribution of freeze-thawing erosion areas in Tibet. *Geogr. Geo-Inf. Sci.* 21, 32–34.

Zhang, J., Liu, S., and Yang, S. (2007). The classification and assessment of freeze-thaw erosion in Tibet. *J. Geogr. Sci.* 17 (2), 165–174. doi:10.1007/s11442-007-0165-z

Zhang, K., and Liu, H. (2018). Research progress and prospect of freeze-thaw erosion in black soil areas in northeast China. *Sci. Soil Water Conserv.* 16, 17–24. doi:10.16843/j.sswc.2018.01.003

Zhang, R., Wang, X., Fan, H., Zhou, L., Wu, M., and Liu, Y. (2009). Study on the zonal erosion characteristics of freezing-thawing zone in China. *Sci. Soil Water Conserv.* 7, 24–28. doi:10.1051/e3sconf/202123701026

Zhou, Y., Guo, D., Qiu, G., Cheng, G., and Li, S. (2000). *Geocryology in China*. 1st ed. Beijing, China: Science Press, 15–115.

frontiers | Frontiers in Earth Science

TYPE Original Research
PUBLISHED 27 September 2022
DOI 10.3389/feart.2022.971655

OPEN ACCESS

EDITED BY
Jia-wen Zhou,
Sichuan University, China

REVIEWED BY
Min Xiong,
Tongji University, China
Elena Benedetta Masi,
University of Florence, Italy

*CORRESPONDENCE
Qigang Jiang,
jiangqigang@jlu.edu.cn

SPECIALTY SECTION
This article was submitted to Geohazards and Georisks, a section of the journal Frontiers in Earth Science

RECEIVED 17 June 2022
ACCEPTED 31 August 2022
PUBLISHED 27 September 2022

CITATION
Zhang S, Jiang Q, Xu X, Tao G, Zhang Z, Gao X and He C (2022), Influence of soil mechanical and hydraulic parameters on the definition of rainfall intensity and duration thresholds based on Transient rainfall infiltration and grid-based regional slope-stability model (TRIGRS). *Front. Earth Sci.* 10:971655. doi: 10.3389/feart.2022.971655

Influence of soil mechanical and hydraulic parameters on the definition of rainfall intensity and duration thresholds based on Transient rainfall infiltration and grid-based regional slope-stability model (TRIGRS)

Sen Zhang[1], Qigang Jiang[1]*, Xitong Xu[1], Guofang Tao[1], Zhenchao Zhang[1], Xin Gao[1] and Chunlong He[1]

[1]College of Geo-exploration Science and Technology, Jilin University, Changchun, China

As a supplement to empirical-statistical methods, physically based methods can be employed to define rainfall thresholds for triggering landslides in areas lacking records of landslides. The transient rainfall infiltration and grid-based regional slope-stability model (TRIGRS), as a physically based model, has been applied to define rainfall thresholds at the basin, slope unit, and grid cell scales. However, as far as we know to date, the influence of soil mechanical and hydraulic parameters on defining rainfall thresholds at various scales has not been comprehensively evaluated. In this study, TRIGRS was used to define rainfall intensity (I) and duration (D) thresholds at various scales for Buzhe village, Pu'an county, Guizhou province, China, under the conditions of different soil physical parameters. The results show that the number of rainfall thresholds decreased with cohesion (c) and internal friction angle (φ) and increased with soil unit weight (γ_s), excluding the basin scale. Threshold position varied positively with c and φ and negatively with γ_s. Soil mechanical parameters have a greater influence on the definition of rainfall thresholds based on TRIGRS than hydraulic parameters.

KEYWORDS

shallow landslides, rainfall thresholds, *I-D* thresholds, TRIGRS, physically based method, soil mechanical and hydraulic parameters

Introduction

Rainfall-induced shallow landslides mainly occur on slopes covered by a layer of colluvium or residual soil (Salciarini et al., 2006; Montrasio and Valentino, 2007; Montrasio and Valentino, 2008). Rainfall infiltration in slopes increases the pore-water pressure and decreases the shear strength, thereby triggering landslides (Lim

et al., 1996; Vanapalli et al., 1996). Thus, rainfall is recognized as the primary trigger of shallow landslides (Campbell, 1975; Keefer et al., 1987; Wilson, 2005), and rainfall thresholds are the most used tools to forecast landslides (Caine, 1980; Aleotti, 2004; Guzzetti et al., 2007; Guzzetti et al., 2008; Li et al., 2017; He et al., 2020). Guizhou province is located in the mountainous area of southwest China. As one of the landslide-prone provinces in China, shallow landslides frequently occur in Guizhou province (Yu et al., 2016; Zhang et al., 2017; Lin and Wang, 2018; Ma et al., 2020). However, only few defined rainfall thresholds or landslide early warning systems (LEWSs) exist in this area to address the risk of shallow landslides.

Empirical-statistical and physically based methods can be used to define rainfall thresholds (Aleotti, 2004; Guzzetti et al., 2007; Park et al., 2019). Empirical-statistical rainfall methods define rainfall thresholds through the statistical analysis of rainfall conditions that have triggered landslides (Brunetti et al., 2010; Peruccacci et al., 2012; Melillo et al., 2018). Currently, empirical-statistical rainfall thresholds have become the most common landslide model (i.e., the functional relationship between weather conditions and landslide events) in LEWSs (Calvello, 2017; Piciullo et al., 2018; Guzzetti et al., 2020). However, empirical-statistical methods mainly rely on the availability and quality of landslide records (Peres and Cancelliere, 2014). They are severely limited for the areas with incomplete or unavailable landslide records. In this case, physically based methods are the ideal alternative.

Physically based methods define rainfall thresholds by simulating the hydrological process of soil and slope stability during rainfall infiltration (Salciarini et al., 2008; Salciarini et al., 2012). TRIGRS is a physically based model for shallow landslide prediction (Baum et al., 2002; Baum et al., 2008; Baum et al., 2010; Alvioli and Baum, 2016). Thus, TRIGRS is widely used in modeling the timing and distribution of shallow landslides (Vieira et al., 2010; Lee et al., 2017; Tran et al., 2018; He et al., 2021; Ip et al., 2021) and landslide susceptibility mapping (Baum et al., 2005; Park et al., 2013; Marin and Mattos, 2020). In addition to these widespread applications, TRIGRS is applied in defining physically based rainfall thresholds given its ability to describe the scaling behavior of rainfall thresholds (Alvioli et al., 2014).

The Sendai Framework for Disaster Risk Reduction proposes the goal of substantially increasing the availability and access to multi-hazard early warning systems and disaster risk information and assessments to people by 2030 (UNISDR, 2015). Guzzetti et al. (2020) proposed that LEWSs can be deployed and operated worldwide, and suggested increasing the rate of LEWS deployment for landslide-prone areas. In some landslide-prone areas of China, the quality of records of landslides is poor. Although this situation has improved in recent years, the time span and quality of existing landslide records are insufficient

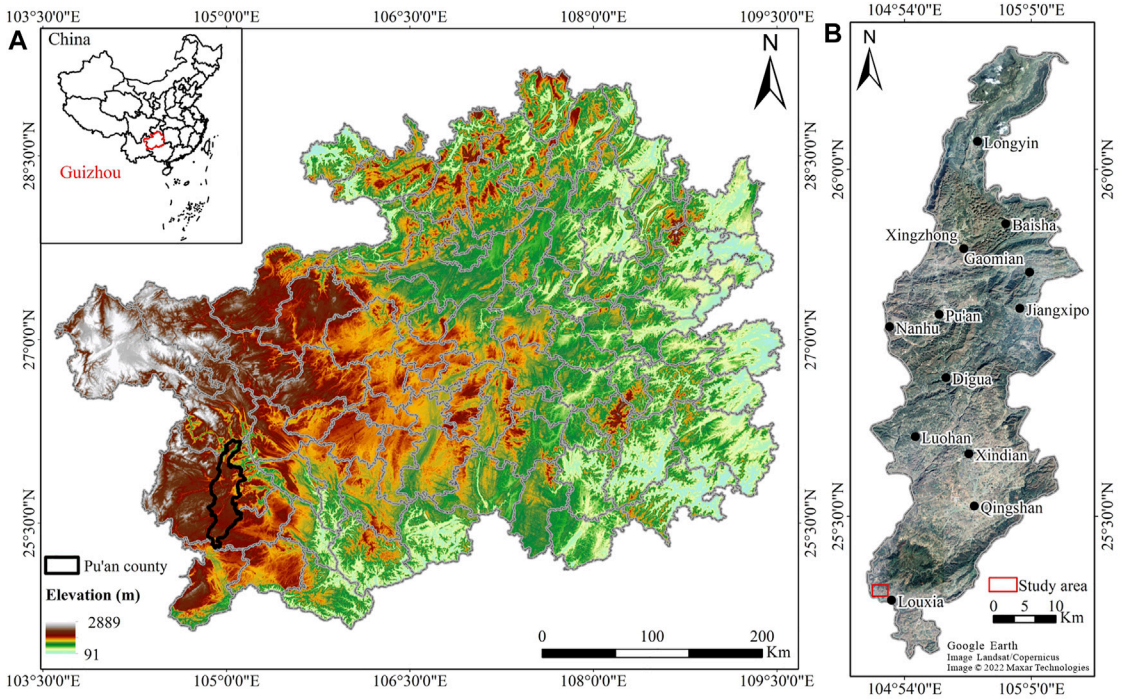

FIGURE 1
(A) Location of Pu'an county (image source: SRTM data) and **(B)** location of the study area.

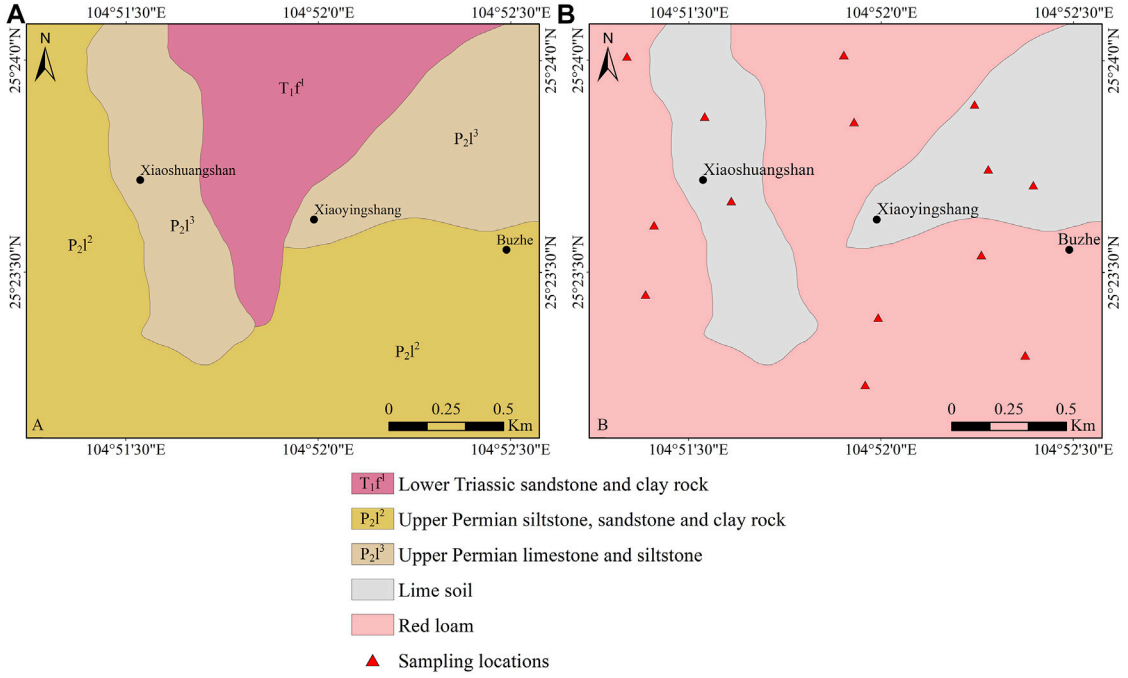

FIGURE 2
(A) Geology map of the study area and **(B)** spatial distribution of soil types.

TABLE 1 The range and average of soil samples measurements in the study area.

Parameters	Unit	Red loam (zone 1)		Lime soil (zone 2)	
		Range	Average	Range	Average
Cohesion (c)	Kpa	9.08–12.19	10.68	43.55–48.32	46.11
Internal friction angle (φ)	°	14.23–16.44	15.6	21.62–25.53	23.5
Unit weight of soil (γ_s)	KN/m	17.72–19.61	18.86	18.84–20.54	19.27
Saturated hydraulic conductivity (K_s)	m/s	4.36×10^{-6}–7.88×10^{-6}	6.12×10^{-6}	1.49×10^{-6}–3.17×10^{-6}	2.46×10^{-6}
Hydraulic diffusivity (D_0)	m/s	-	6.12×10^{-4}	-	2.46×10^{-4}
Saturated water content (θ_s)	-	-	0.54	-	0.63
Residual water content (θ_r)	-	-	0.03	-	0.01
Fitting parameter (α_G)	m^{-1}	-	0.5	-	1.3

to support the definition of empirical-statistical rainfall thresholds. For these areas, physically based methods can extend the application scenarios of LEWS based on rainfall thresholds, which is important for LEWS deployment.

TRIGRS can be employed to define rainfall thresholds at three scales, namely, basin, slope unit, and grid cell scales. At the basin scale, the rainfall threshold is defined for the whole area. Rainfall conditions exceeding the defined rainfall threshold can trigger several landslides in the entire area. Alvioli et al. (2018) used TRIGRS to define the rainfall event-duration (*E-D*) threshold for Upper Tiber River Basin in Italy. Bordoni et al. (2019) used TRIGRS to define the *E-D* threshold for an area of Oltrepò Pavese in Italy. Marin and Velásquez (2020) used TRIGRS to define the *I-D* thresholds for the Envigado Basin of Colombia under the conditions of different soil hydraulic properties. Marin et al. (2020) used TRIGRS to define the *I-D* thresholds for 93 small basins in Colombian Andes and analyzed the effect of basin morphometric parameters on defined *I-D*

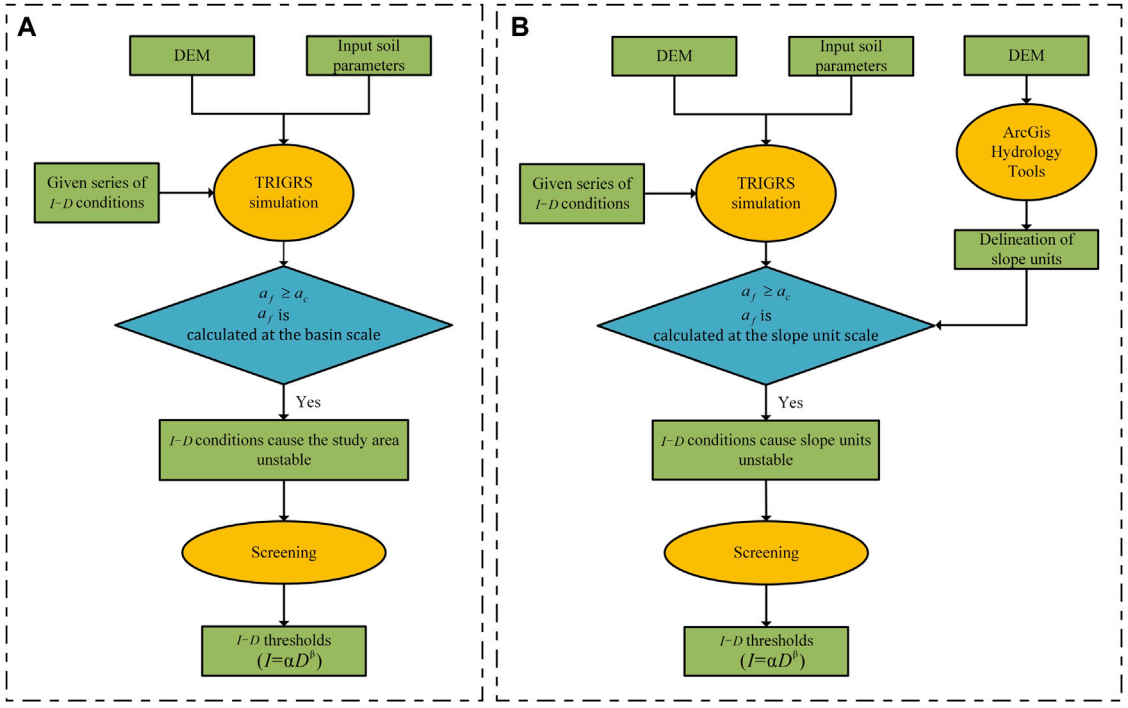

FIGURE 3
The flowchart of the definition of *I-D* thresholds based on TRIGRS **(A)** at the basin scale and **(B)** at the slope unit scale.

thresholds. Marin et al. (2021) used TRIGRS to define the *I-D* thresholds for La Arenosa and La Liboriana Basins in Colombian Andes. At the slope unit scale, rainfall thresholds are defined for slope units with critical rainfall. Rainfall conditions exceeding the defined rainfall thresholds can trigger landslides in the corresponding slope units. Alvioli et al. (2014) used TRIGRS to define the *I-D* thresholds for several sub-basins of the Upper Tiber River Basin. Zhang et al. (2022) divided Dabang village, Pu'an County, Guizhou Province, China, into several slope units and used TRIGRS to define the *I-D* thresholds for the slope units with critical rainfall. At the grid cell scale, rainfall thresholds are defined for grid cells with critical rainfall. Rainfall conditions exceeding the defined rainfall thresholds can trigger landslides in the area of the corresponding grid cells. Marin (2020) used TRIGRS to define the *I-D* thresholds for grid cells with critical rainfall in the Envigado Basin. Marin et al. (2021) used TRIGRS to define the *I-D* thresholds for grid cells with critical rainfall of La Arenosa and La Liboriana Basins.

Detailed and accurate soil parameters (e.g., soil depth, soil mechanical, and hydraulic parameters) are required to properly apply TRIGRS. However, obtaining substantial information on distributed soil properties at a large scale is a challenge, especially regarding soil physical properties (i.e., mechanical and hydraulic parameters) (Gariano and Guzzetti, 2016; Zhang et al., 2018). Uncertainties in soil parameters are caused by complex geological conditions, spatial variability, and laboratory measurement (Catani et al., 2010; Ho et al., 2012; Corominas et al., 2014; Bicocchi et al., 2015), which make it impossible to eliminate all uncertainties. In terms of using TRIGRS to predict the spatiotemporal information of shallow landslides and landslide susceptibility mapping, the influence of soil mechanical and hydraulic parameters on the prediction and mapping results has been extensively explored (Salciarini et al., 2006; Montrasio et al., 2011; Bordoni et al., 2015; Gioia et al., 2016; He et al., 2016; Ciurleo et al., 2017; de Lima Neves Seefelder et al., 2017; Weidner et al., 2018; Ciurleo et al., 2019). Some probabilistic approaches have been adopted with TRIGRS to quantitatively account for soil parameter uncertainties (Raia et al., 2014; Salciarini et al., 2017). In these probabilistic approaches, the input parameters are considered random variables, and the output is the probability of failure.

However, few studies have explored the influence of soil mechanical and hydraulic parameters on the definition of rainfall thresholds based on TRIGRS. Only Marin and Velásquez (2020) explored the effect of soil hydraulic parameters on the position of rainfall thresholds defined at the basin scale. The performance of the rainfall threshold requires evaluation before applying it in LEWSs (Piciullo et al., 2017; Segoni et al., 2018). Exploring the influence of soil physical parameters on the rainfall thresholds

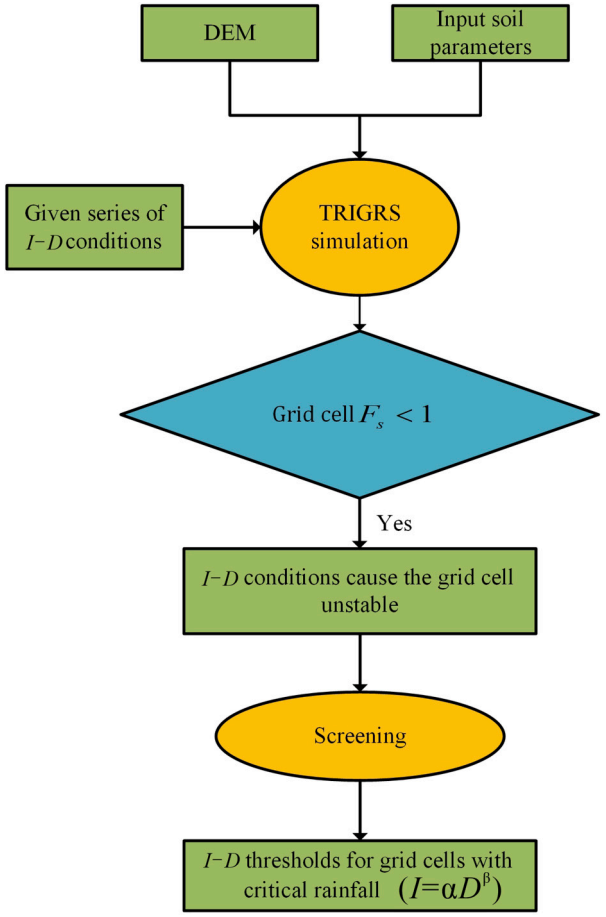

FIGURE 4
The flowchart of the definition of *I-D* thresholds based on TRIGRS at the grid cell scale.

defined by using TRIGRS can facilitate the evaluation of the physically based rainfall thresholds.

In this study, Buzhe village, Pu'an county, Guizhou province of China was taken as the study area. The soil mechanical and hydraulic parameters measured by field sampling were taken as standard values. In each TRIGRS simulation, a parameter was varied by the given proportion and the rest remained constant. Then, the *I-D* thresholds at various scales were defined under the conditions of given physical parameters. Finally, the influence of soil physical parameters on the number and position of rainfall thresholds was explored by comparing the simulated F_s maps and defined thresholds.

Study area

Pu'an county, which is located in southwest Guizhou province of China (Figure 1), has tremendous undulating terrains, and the dissolution and erosion of landforms are staggered. Moreover, soft rocks such as siltstone and sandstone are widespread. These soft rocks are easily weathered into the eluvium and slope wash. As for rainfall, the average annual precipitation of Pu'an county is 1,443 mm. Owing to the complex geological setting and rainy environment, Pu'an county is one of the landslide-prone counties in Guizhou province.

Lower Triassic sandstone and clay rock, Upper Permian siltstone, sandstone, and clay rock, and Upper Permian limestone and siltstone are distributed in the study area (Figure 2A). The soil types in the study area are red loam and lime soil (Figure 2B). The distribution of each soil type is consistent with the corresponding soil parent material. Red loam is distributed on sandstone, siltstone, and clay rock. Lime soil is distributed on limestone.

Data

Digital elevation model

The input data for TRIGRS are topographic factors, soil parameters, soil thickness, and initial conditions for surface flux and groundwater table. As for topographic factors, the 10-m resolution DEM was taken as input. Other required input slopes and flow direction maps were generated using ArcGIS software based on the DEM data.

Soil parameters

The input soil mechanical parameters include γ_s, φ, and c. The input hydraulic parameters include saturated hydraulic conductivity (K_s), hydraulic diffusivity (D_0), saturated water content (θ_s), residual water content (θ_r), and fitting parameter (α_G) of Gardner's model for the soil water characteristic curve (SWCC) (Gardner, 1958). A total of 18 samples of red loam and 10 samples of lime soil were collected at the 14 sampling locations (Figure 2B). The mechanical parameters were measured through laboratory static triaxial experiments. The hydraulic parameters were measured through laboratory variable tap penetration experiments. For each parameter, the average of the measurements was taken as the standard value (Table 1). Regarding θ_s, θ_r, and α_G, this study determined the parameters for the Gardner model (used in TRIGRS) based on the Van Genuchten model (Van Genuchten, 1980) for SWCC of typical soil types in Guizhou province (Zhao, 2021). The volumetric water contents were the same in the two models for each soil type, and α_G was fitted to be within the limits of the Van Genuchten curves, as suggested by Marin (2020).

c, φ, and γ_s were taken 0.8, 0.9, 1.1, and 1.2 times the standard values as input. K_s and D_0 were taken 0.7, 0.8, 1.2, and 1.3 times standard values as input. The input mechanical and hydraulic parameters were assigned to each grid cell according to the spatial

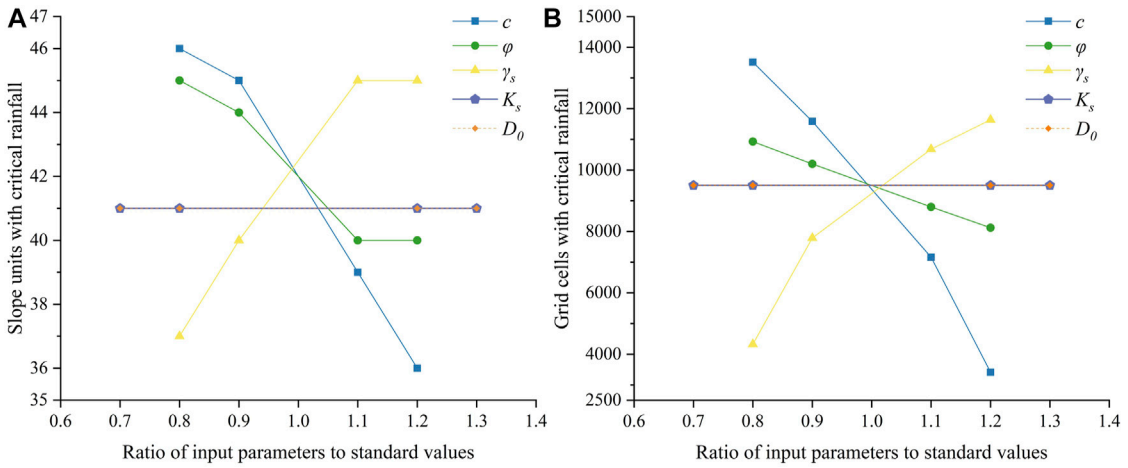

FIGURE 5
The number of objects with critical rainfall **(A)** slope units and **(B)** grid cells.

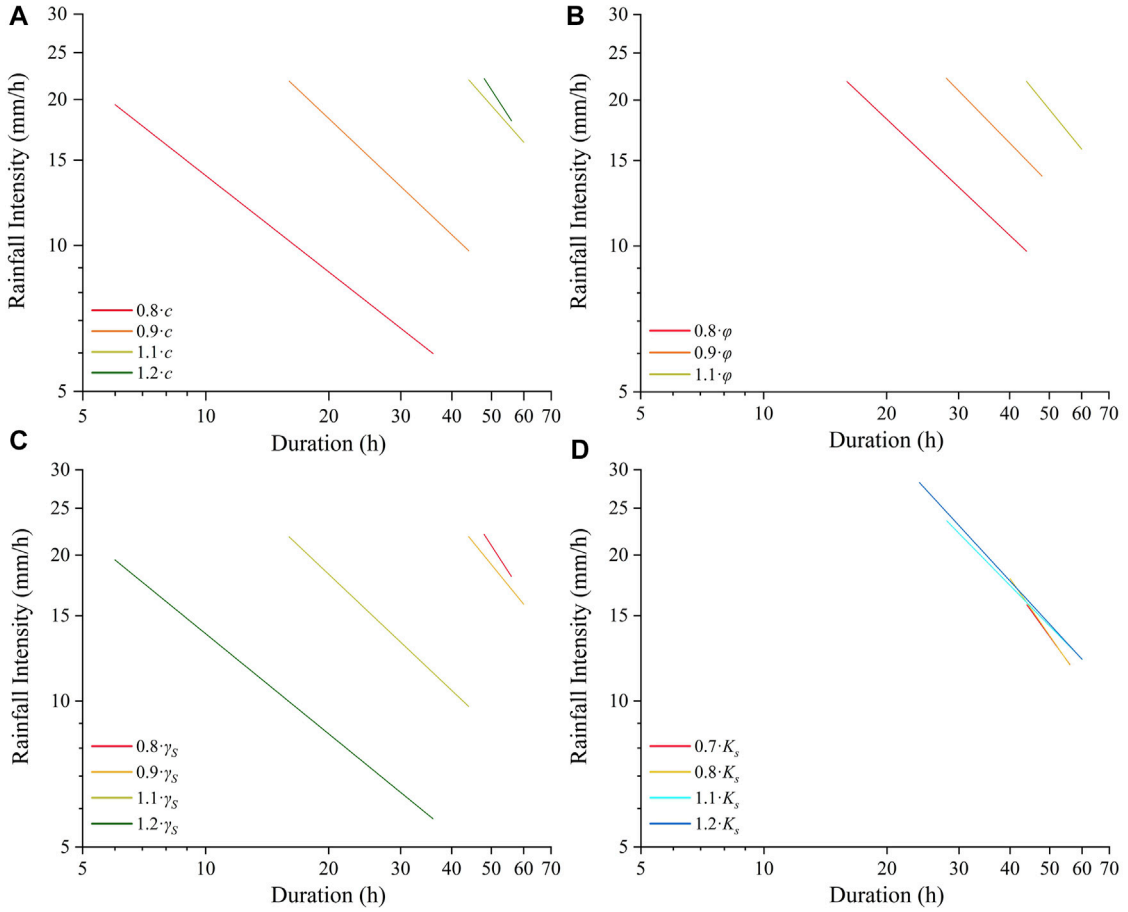

FIGURE 6
I-D thresholds defined at the basin scale under given soil mechanical and hydraulic parameters: **(A)** c, **(B)** φ (the thresholds were the same under the condition of 1.1·φ and 1.2·φ), **(C)** γ_s, and **(D)** K_s.

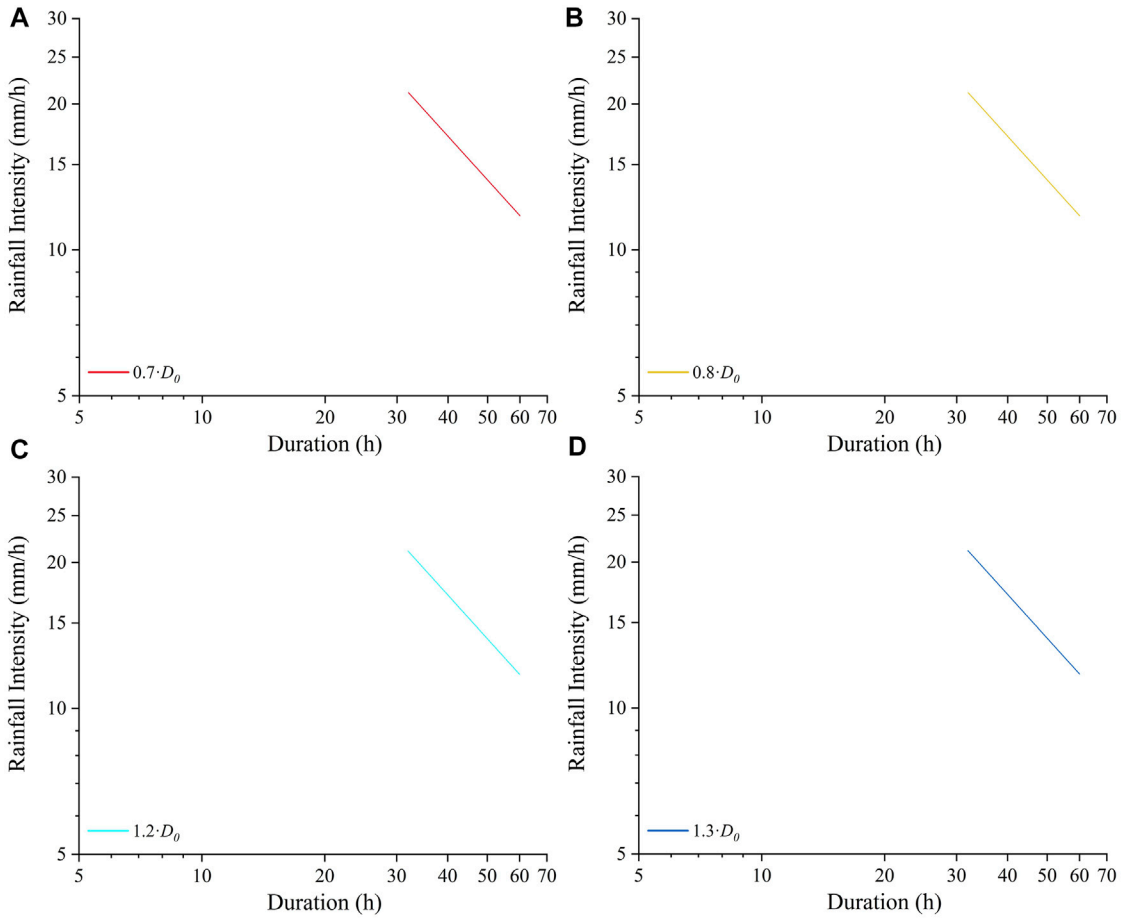

FIGURE 7
I-D thresholds defined at the basin scale under the conditions: **(A)** 0.8·D_0, **(B)** 0.9·D_0, **(C)** 1.1·D_0, and **(D)** 1.2·D_0.

distribution of soil types in the study area (Figure 2B). One parameter was changed, and the remaining parameters were kept constant for each simulation. A total of 20 simulations were performed.

Soil thickness significantly influences the simulation results of TRIGRS (Tran et al., 2018). Many studies have shown that the linear relation of slope angle and soil thickness to characterize the soil thickness map can obtain suitable simulation results of TRIGRS (Viet et al., 2017; Tran et al., 2018; He et al., 2021). The relationship assumes that soil thickness (y) is in inverse proportion to slope angle (x), that is, the minimum soil thickness (0.1 m) corresponds to the maximum slope (69.41°) and the maximum soil thickness (3.3 m) corresponds to the minimum slope (0.1°). From the relationship, the soil thickness map was generated by the linear equation (Eq. 1). The units of y and x are meter and degree, respectively.

$$y = -0.04617x + 3.3. \quad (1)$$

The input initial conditions include initial surface flux (I_z) and initial groundwater table. Given the complex properties of soil (e.g., void and uniformity), I_z is difficult to measure using laboratory tests. Thus, the empirical relationship between I_z and K_s was used to determine I_z. This study set I_z to be 0.01 of K_s and set the initial groundwater table to be the same as the soil thickness, as suggested by Kim et al. (2010), Park et al. (2013), Lee et al. (2017), and Viet et al. (2017).

Methods

TRIGRS model

The TRIGRS model is designed for simulating the timing and distribution of shallow landslides by computing the transient pore-pressure changes and attendant changes in the factor of safety of slope caused by rainfall infiltration (Baum et al., 2002; Baum et al., 2008; Baum et al., 2010; Alvioli and Baum, 2016).

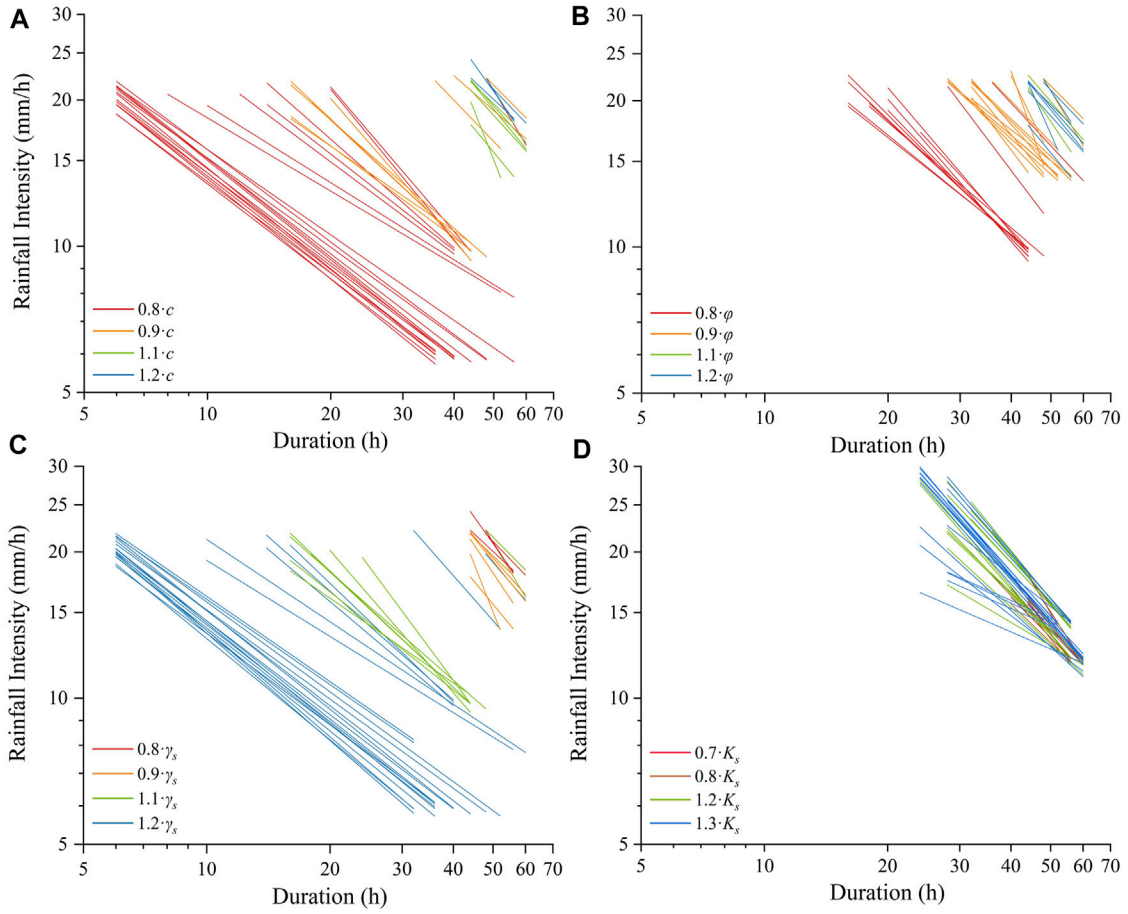

FIGURE 8
I-D thresholds defined at the slope unit scale under given soil mechanical and hydraulic parameters: **(A)** *c*, **(B)** φ, **(C)** γ_s, and **(D)** K_s.

Infiltration models include the models for saturated initial and unsaturated initial conditions. For saturated initial conditions, infiltration models in TRIGRS adopt Iverson's linearized solution (Iverson, 2000) of the Richards equation (Richards, 1931). For unsaturated initial conditions, infiltration models in TRIGRS adopt the analytical solution of the Richards equation for unsaturated soil proposed by Srivastava and Yeh (1991) to approximate the infiltration process and the Gardner model to describe SWCC (Gardner, 1958). TRIGRS simulates the slope stability based on the infinite-slope model (Taylor, 1948). The slope stability is represented by F_s, which is calculated as follows:

$$F_s(Z,t) = \frac{tan\phi'}{tan\delta} + \frac{c' - \psi(Z,t)\gamma_w tan\phi'}{\gamma_S Z sin\delta cos\delta}, \quad (2)$$

where γ_w and γ_S represent the unit weights of water and soil, respectively; c' is the effective soil cohesion; ϕ' is the effective soil internal friction angle; δ is the slope angle; and $\psi(Z,t)$ is the pressure head as a function of depth Z and time t. Failure is predicted when $F_s < 1$, and stability holds when $F_s \geq 1$. The simulation results of F_s are visualized on GIS software. The latest version (v2.1) of TRIGRS was used in this study (Alvioli and Baum, 2016).

Definition of *I-D* thresholds at the basin scale

In this study, the method proposed by Marin and Velásquez (2020), Marin et al. (2020), and Marin et al. (2021) was used to define the *I-D* thresholds at the basin scale. This method proposed two ratios, namely, the critical failure area ratio (a_c) and failing area ratio (a_f), where a_c is the ratio that excludes unconditionally unstable grid cells (i.e., $F_s < 1$ without rainfall). At the basin scale, a_f is calculated as the ratio of the area of grid cells with $F_s < 1$ to the area of study area.

Figure 3A shows the flowchart of the definition of *I-D* thresholds at the basin scale. TRIGRS was run with a set of *I-*

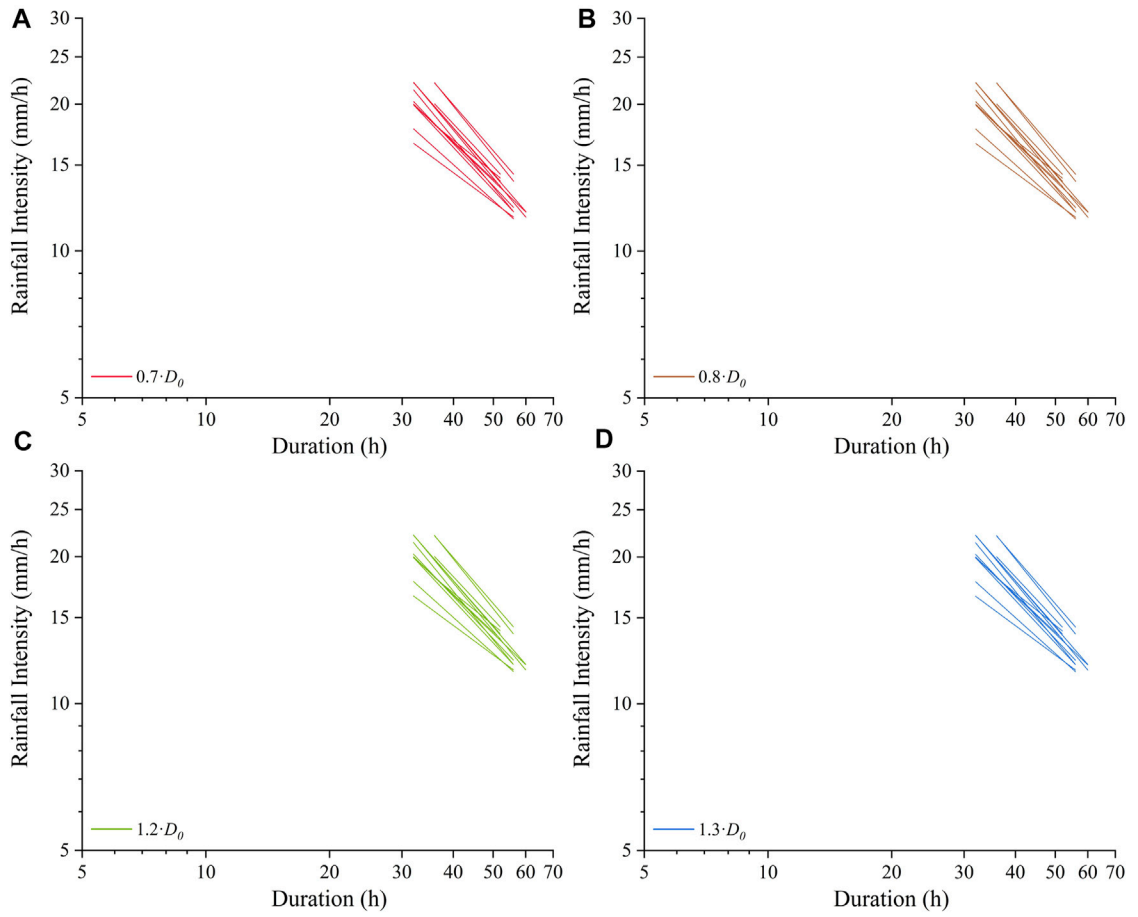

FIGURE 9
I-D thresholds defined at the slope unit scale under the conditions: **(A)** 0.8·D_0, **(B)** 0.9·D_0, **(C)** 1.1·D_0, and **(D)** 1.2·D_0.

D conditions to simulate. In the simulation, *I* was increased from 2 mm/h to 30 mm/h, with an increment step of 2 mm/h. *D* was increased from 2 to 60 h, ranging from 2 to 20 h with an increment step of 2 h and ranging from 20 to 60 h with an increment step of 4 h. For each *I-D* condition, a_f was calculated and compared with a_c. If $a_f \geq a_c$, the *I-D* condition was regarded to cause instability. This study defined rainfall thresholds using the a_c of 1%.

Before fitting, the *I-D* conditions that cause instability were screened to exclude the *I-D* conditions with the same *I* or *D* values (Zhang et al., 2022). Then, the screened *I-D* conditions were plotted in a log–log plot (log*I* vs log*D*). Also, the distribution of *I-D* conditions was fit to be the linear equation of Eq. 3.

$$\log I = \beta \log D + \log \alpha, \tag{3}$$

where *I* is the rainfall intensity (mm/h), *D* is the rainfall duration (h), β is the slope, and logα is the intercept. After getting the α and β, Eq. 3 was transferred into the power law equation (Eq. 4).

$$I = \alpha D^{\beta}, \tag{4}$$

Definition of *I-D* thresholds at the slope unit scale.

In this study, the method proposed by Zhang et al. (2022) was used to define *I-D* thresholds at the slope unit scale. The slope units were delineated based on ridge and valley lines obtained by using hydrology analysis tools in ArcGIS. (Xie et al., 2004; Wei et al., 2018).

The flowchart of the definition of *I-D* thresholds at the slope unit scale is shown in Figure 3B. The definition of rainfall thresholds at the slope unit scale involves defining rainfall

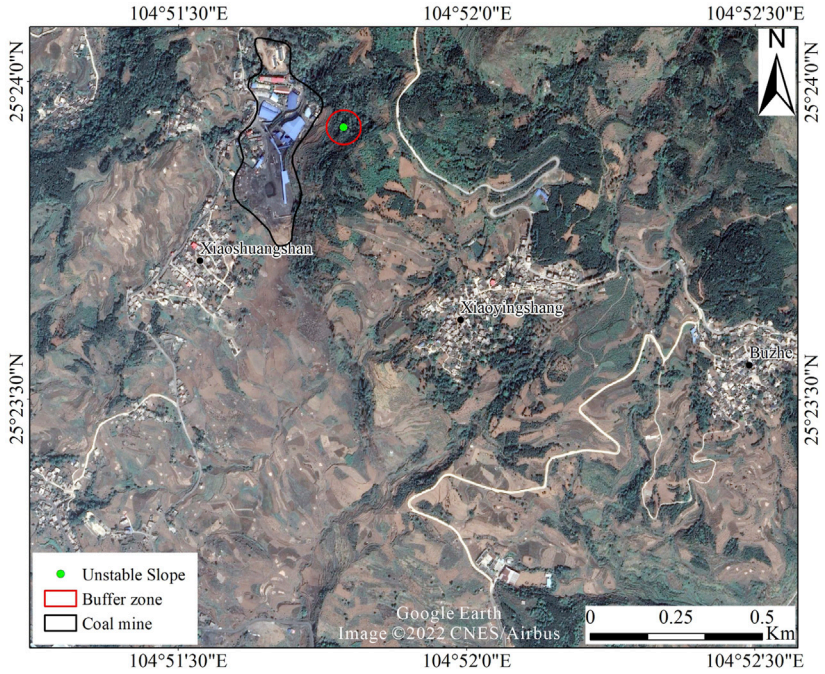

FIGURE 10
Location of the monitored unstable slope, coal mine, and built buffer zone.

thresholds for slope units with critical rainfall (i.e., under the given rainfall conditions, the slope units can reach instability). For each slope unit, a_f was calculated as the area of unstable grid cells within its range to the area of the slope unit. The remaining steps were the same as those for the basin scale.

Definition of *I-D* thresholds at the grid cell scale.

In this study, the method proposed by Marin (2020) was used to define *I-D* thresholds at the grid cell scale. Defining rainfall thresholds at the grid cell scale involves defining rainfall thresholds for grid cells with critical rainfall, that is, under the given rainfall conditions, the grid cells can reach instability. At the grid cell scale, the rule for determining *I-D* conditions causing instability was $Fs<1$. The remaining steps were the same as the abovementioned methods (Figure 4).

Rainfall thresholds defined at any scale are not applicable to rainfall events of any rainfall duration. The defined rainfall thresholds are valid for a range of duration with initial and final durations. The initial duration is the duration that causes the whole study area or each slope unit unstable for the first time. The final duration is the maximum duration at which the increase in duration no longer affects the stability for the given range of intensities.

Results

Factor of safety maps

When I and D are at the maximum, that is, $I = 30$ mm/h and $D = 60$ h, the F_s maps under different soil mechanical and hydraulic parameters conditions can reflect the number of slope units and grid cells with critical rainfall and whether the whole study area has critical rainfall.

Supplementary Video 1 (in the supplementary material) shows the distribution variation of grid cells with $F_s < 1$ under the maximum *I-D* condition when c, φ, and γ_s were 0.8, 0.9, 1.1, and 1.2 times the standard values. The whole study area had critical rainfall under given soil mechanical parameters. Figure 5 shows the number of slope units and grid cells with critical rainfall under given soil physical parameters. When c was 0.8, 0.9, 1.1, and 1.2 times the standard value, the number of slope units with critical rainfall was 46, 45, 39, and 36, respectively. The number of grid cells with critical rainfall was 13,518, 11,585, 7,613, and 3,414, respectively. The number of slope units and grid cells with critical rainfall decreased when c increased. When φ

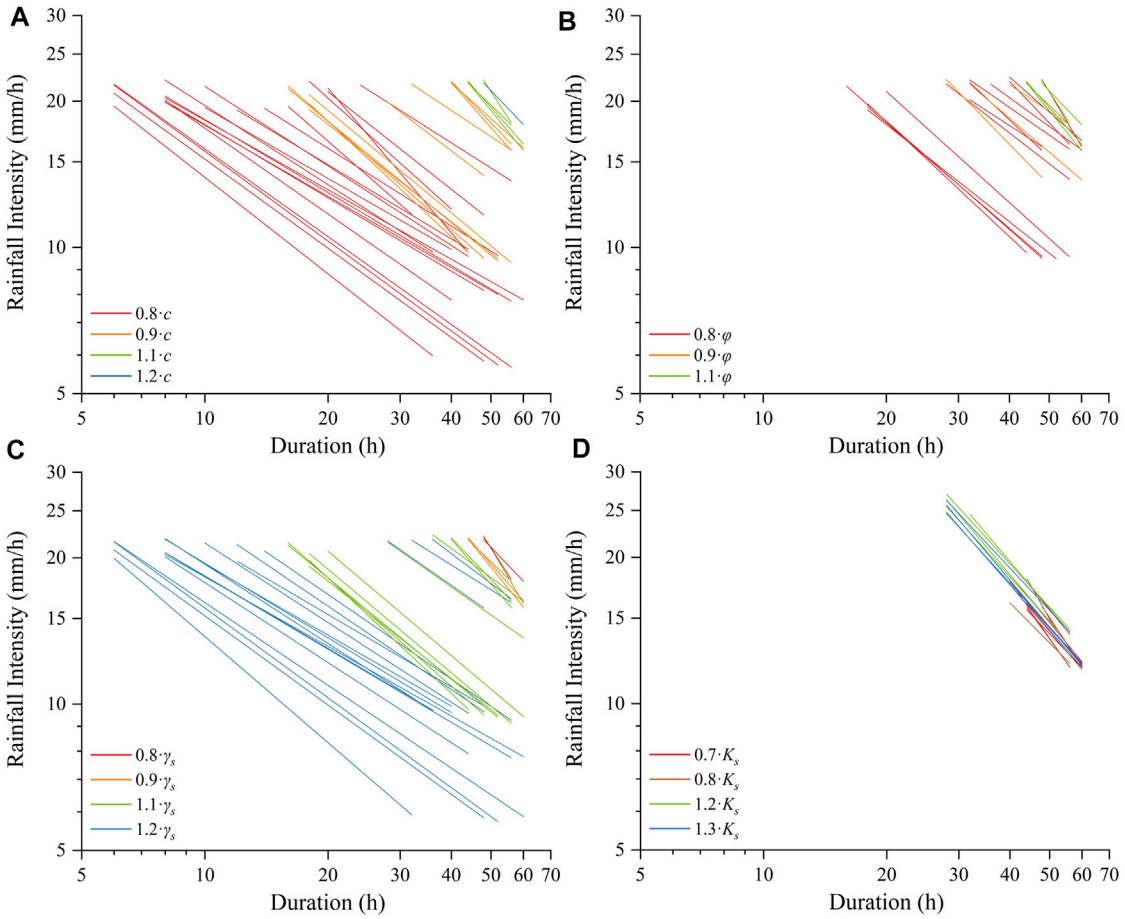

FIGURE 11
I-D thresholds defined at the grid cell scale under different soil mechanical and hydraulic parameters: **(A)** *c*, **(B)** φ (the thresholds were the same under the condition of 1.1·φ and 1.2·φ), **(C)** γ_s, and **(D)** K_s.

was 0.8, 0.9, 1.1, and 1.2 times the standard value, the number of slope units with critical rainfall was 45, 44, 40, and 40, respectively. The number of slope units with critical rainfall was 10,930, 10,201, 8,800, and 8,122, respectively. The number of slope units and grid cells with critical rainfall decreased when φ increased. When γ_s was 0.8, 0.9, 1.1, and 1.2 times the standard value, the number of slope units with critical rainfall was 37, 40, 45, and 45, respectively. The number of grid cells with critical rainfall was 4,324, 7,789, 10,680, and 11,639, respectively. The number of slope units and grid cells with critical rainfall increased when γ_s increased.

Supplementary Video 2 (in the supplementary material) shows the distribution variation of grid cells with $F_s < 1$ under the maximum *I-D* condition when K_s and D_0 were 0.7, 0.8, 1.2, and 1.3 times the standard values. In these cases, the whole study area had critical rainfall. The number of slope units and grid cells with critical rainfall was 41 and 9,502. The number of slope units and grid cells with critical rainfall did not vary with K_s or D_0.

I-D thresholds at the basin scale

Supplementary Video 3 (in the supplementary material) show the variation of *I-D* thresholds defined at the basin scale when *c*, φ, and γ_s were 0.8, 0.9, 1.1, and 1.2 times the standard values. Figures 6A–C show the comparison of thresholds defined at the basin scale under given *c*, φ, and γ_s values, respectively. The results showed that the threshold with higher *c* or φ was located on the higher part of the graph. The threshold with higher γ_s was located on the lower part of the graph.

Supplementary Video 4 (in the supplementary material) and Figure 7 show the variation of thresholds defined at the basin scale when K_s and D_0 were 0.7, 0.8, 1.2, and 1.3 times the standard values. Figure 6D shows the comparison of thresholds defined at the basin scale under given K_s values. The results showed that the variation in K_s did not significantly influence the position of thresholds defined at the basin scale. The threshold with higher K_s had a larger

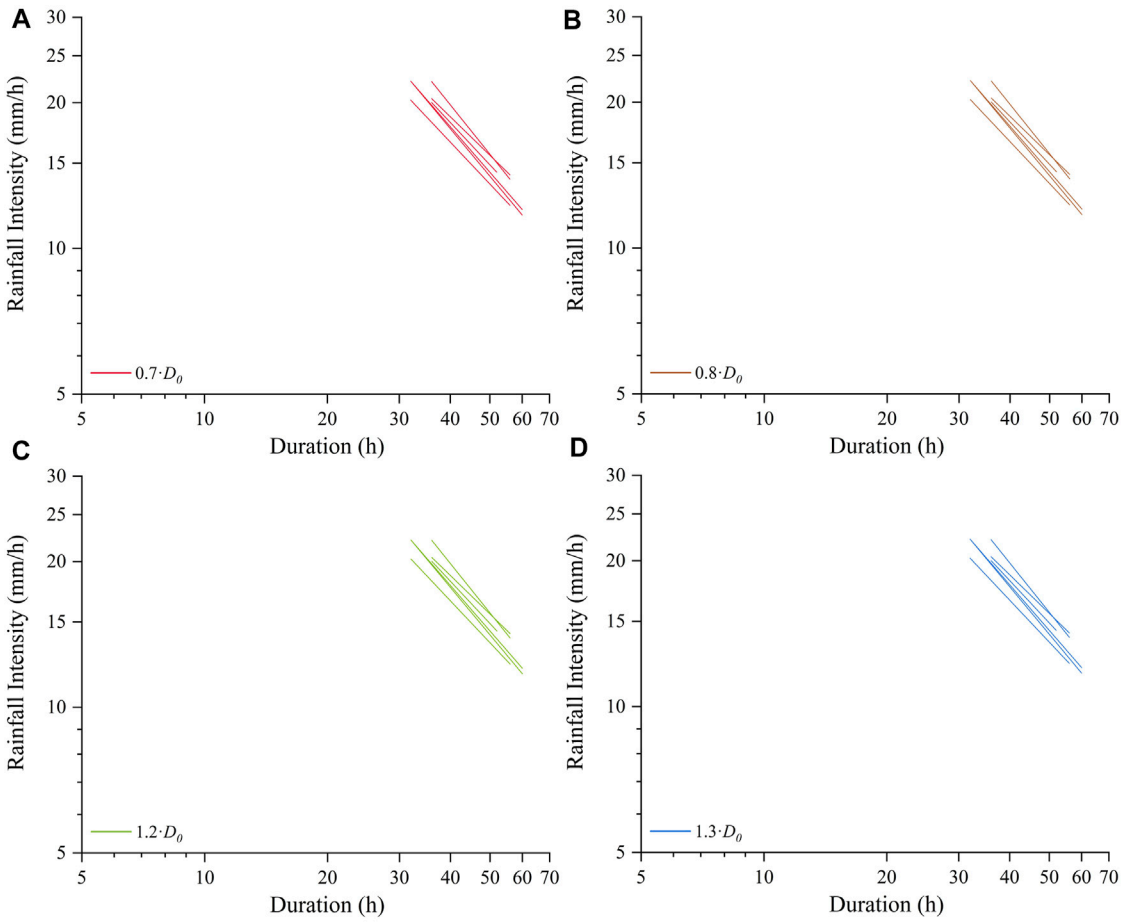

FIGURE 12
I-D thresholds defined at the grid cell scale under the conditions: **(A)** 0.8·D_0, **(B)** 0.9·D_0, **(C)** 1.1·D_0, and **(D)** 1.2·D_0.

applicable duration range. Meanwhile, under the condition evaluated, D_0 did not influence the position of thresholds defined at the basin scale.

I-D thresholds at the slope unit scale

Supplementary Video 5 (in the supplementary material) show the variation of *I-D* thresholds defined at the slope unit scale when$c$, φ, and γ_s were 0.8, 0.9, 1.1, and 1.2 times the standard values. Figures 8A–C show the comparison of thresholds defined at the slope unit scale under given c, φ, and γ_s values, respectively. The results showed that the thresholds with higher c or φ tended to be the higher part of the graph. The thresholds with higher γ_s tended to be the lower part of the graph.

Supplementary Video 6 (in the supplementary material) and Figure 9 show the variation of thresholds defined at the slope unit scale when K_s and D_0 were 0.7, 0.9, 1.1, and 1.2 times the standard values. Figure 8D shows the comparison of thresholds defined at the slope unit scale under given K_s values. The results showed that the variation in K_s did significantly influence the position of thresholds defined at the slope unit scale. The thresholds with higher K_s tended to be applicable to large duration ranges. D_0 did not influence the position of thresholds defined at the slope unit scale under the condition evaluated.

I-D thresholds at the grid cell scale

A monitored unstable slope is located near a coal mine in the study area. A buffer zone was built with a radius of 50 m around the unstable slope (Figure 10). *I-D* thresholds were defined for the grid cells with critical rainfall in the buffer zone.

Supplementary Video 7 (in the supplementary material) show the variation of *I-D* thresholds defined at the grid cell scale when c, φ, and γ_s were 0.8, 0.9, 1.1, and 1.2 times the

standard values. Figures 11A–C show the comparison of thresholds defined at the grid cell scale under given c, φ, and γ_s values, respectively. The results showed that the thresholds with higher c or φ tended to be the higher part of the graph. The thresholds with higher γ_s tended to be the lower part of the graph.

Supplementary Video 8 (in the supplementary material) and Figure 12 show the variation of *I-D* thresholds defined at the grid cell scale when K_s and D_0 were 0.7, 0.9, 1.1, and 1.2 times the standard values. Figure 11D shows the comparison of thresholds defined at the gird cell scale under given K_s values. The results showed that the variation in K_s did significantly influence the position of thresholds defined at the grid cell scale. The thresholds with higher K_s tended to be applicable to large duration ranges. D_0 did not influence the position of thresholds defined at the grid cell scale under the condition evaluated.

Discussion

The methods of defining rainfall thresholds at different scales have their own characteristics. At the basin scale, given that the threshold is defined for the entire area, the process is the simplest. However, the defined threshold can only judge the occurrence of landslides and cannot provide detailed spatial information for landslide prediction. At the slope unit scale, given that the thresholds are defined for slope units with critical rainfall, the process is relatively complicated. The defined thresholds can provide spatial information specific to the range of slope units for prediction. At the grid cell scale, given that the thresholds are defined for grid cells with critical rainfall, the process is the most complicated. The defined thresholds can provide the most spatial information (i.e., specific to the range of grid cells) for prediction. When defining rainfall thresholds at the basin and slope unit scales, an additional condition is used to determine whether *I-D* conditions cause instability ($a_f > a_c$). When defining rainfall thresholds at the grid cell scale, the rule for determining whether *I-D* conditions cause instability is simply $F_s < 1$ without additional conditions.

Soil physical parameters influence the number and position of rainfall thresholds defined at various scales. The number of rainfall thresholds is the number of objects warned by thresholds (i.e., the objects with critical rainfall). At the basin scale, the rainfall threshold was defined for the entire study area, and the entire study area had critical rainfall under the considered conditions in this study. At the slope unit and grid cell scales, the number of rainfall thresholds was positively correlated with γ_s and negatively correlated with c and φ. K_s and D_0 did not cause any variation (Figure 5).

For threshold position, the position of thresholds varied positively with c and φ and varied negatively with γ_s. Under the considered conditions, K_s did not significantly influence the threshold position. The thresholds with higher K_s were applicable to larger duration ranges. D_0 did not influence the threshold position. Marin and Velásquez (2020) discovered that K_s did not produce a noticeable variation on the position of the *I-D* threshold defined at the basin scale, and D_0 did not affect the position of threshold, which are in line with the results of this study. Wu et al. (2017) conducted a sensitivity analysis of soil physical parameters to evaluate the rainfall threshold determined by using TRIGRS. In the literature (Wu et al., 2017), rainfall threshold is defined as the critical rainfall condition causing the simulated F_s to be less than a specific critical value under a specific warning duration. Actually, this study conducted the sensitivity analysis of soil physical parameters to F_s. Wu et al. (2017) proposed that F_s varied positively with c and φ, negatively with γ_s. c, and φ, and γ_s affected F_s more significantly than K_s and D_0. Thus, the influence of soil physical parameters on the position of rainfall thresholds is the same as the influence on F_s.

TRIGRS does not have a function for defining rainfall thresholds. Rainfall thresholds are defined by analyzing the relationship between the output F_s grid and the input rainfall conditions of TRIGRS. The conditions for determining landslide occurrence differ in defining rainfall thresholds at various scales. The methods at the basin and slope unit scales take the condition that serval grid cells with $F_s < 1$ exist for given rainfall conditions to determine landslide occurrence, which is to analyze the overall behavior of unstable grid cells. The method at the grid cell scale analyzes the individual behavior of a single unstable grid cell by treating a single grid cell with $F_s < 1$ as a landslide. The variation of F_s of a random single grid cell directly influences the definition of rainfall thresholds at the grid cell scale. For example, under the conditions of c was 0.8 and 1.2 times the standard value, the variation in the number of grid cells with $F_s < 1$ is 10,104. The variation directly caused the variation of 10,104 for the number of rainfall thresholds defined at the grid cell scale. However, the variation only caused the variation of 10 for the number of rainfall thresholds defined at the slope unit scale. Thus, the method at the grid cell scale is easier affected by the uncertainty and spatial variability of soil physical parameters.

Conclusion

The influence of soil mechanical and hydraulic parameters on the definition of *I-D* thresholds based on TRIGRS can be divided into the influence on the number of rainfall thresholds and threshold position.

The number of rainfall thresholds defined at the slope unit and grid cell scale decreased with c and φ, increased with γ_s, and did not vary with K_s and D_0. Under the considered conditions, the number of thresholds defined at the basin scale was not affected by soil physical parameters.

The position of rainfall thresholds varied positively with c and φ and negatively with γ_s. K_s did not produce a noticeable variation in the threshold position. D_0 did not influence the threshold position. The thresholds with greater K_s were applicable to larger duration ranges.

Soil mechanical and hydraulic parameters have less effect on rainfall thresholds defined by analyzing the overall behavior of unstable grid cells (i.e., basin and slope unit scales) than the thresholds defined by analyzing the individual behavior of unstable grid cells (i.e., grid cell scale).

Data availability statement

The data analyzed in this study are subject to the following licenses/restrictions: The data presented in this research are available from the corresponding author by reasonable request. Requests to access these datasets should be directed to Qigang Jiang, jiangqigang@jlu.edu.cn.

Author contributions

SZ collected the soil samples, designed the analysis, performed the analysis, and wrote the original draft. XX developed a Python program for the definition of rainfall thresholds. The other authors helped to draft the manuscript.

Funding

This study was supported by The First Surveying and Mapping Institute of Guizhou Province under Grant number GZWH-2021-4536Y.

Acknowledgments

We thank The First Surveying and Mapping Institute of Guizhou Province for the assistance in the field sampling.

Conflict of interest

The authors declare that the research was conducted in the absence of any commercial or financial relationships that could be construed as a potential conflict of interest.

Publisher's note

Supplementary material

The Supplementary Material for this article can be found online at: https://www.frontiersin.org/articles/10.3389/feart.2022.971655/full#supplementary-material

References

Aleotti, P. (2004). A warning system for rainfall-induced shallow failures. *Eng. Geol.* 73, 247–265. doi:10.1016/j.enggeo.2004.01.007

Alvioli, M., and Baum, R. L. (2016). Parallelization of the TRIGRS model for rainfall-induced landslides using the message passing interface. *Environ. Model. Softw.* 81, 122–135. doi:10.1016/j.envsoft.2016.04.002

Alvioli, M., Guzzetti, F., and Rossi, M. (2014). Scaling properties of rainfall induced landslides predicted by a physically based model. *Geomorphology* 213, 38–47. doi:10.1016/j.geomorph.2013.12.039

Alvioli, M., Melillo, M., Guzzetti, F., Rossi, M., Palazzi, E., von Hardenberg, J., et al. (2018). Implications of climate change on landslide hazard in Central Italy. *Sci. Total Environ.* 630, 1528–1543. doi:10.1016/j.scitotenv.2018.02.315

Baum, R. L., Coe, J. A., Godt, J. W., Harp, E. L., Reid, M. E., Savage, W. Z., et al. (2005)., Regional landslide-hazard assessment for Seattle, Washington, USA. *Landslides* 2, 266–279. doi:10.1007/s10346-005-0023-y

Baum, R. L., Godt, J. W., and Savage, W. Z. (2010). Estimating the timing and location of shallow rainfall-induced landslides using a model for transient, unsaturated infiltration. *J. Geophys. Res.* 115, F03013. doi:10.1029/2009JF001321

Baum, R. L., Savage, W. Z., and Godt, J. W. (2002). TRIGRS—a fortran program for transient rainfall infiltration and grid-based regional slope-stability analysis. Golden, Colorado: *U. S. Geol. Surv. Open-File Rep.* 424, 38.

Baum, R. L., Savage, W. Z., and Godt, J. W. (2008). *Trigrs — a fortran program for transient rainfall infiltration and grid-based regional slope-stability analysis, version 2.0.* Denver, Colorado, USA: US Geological Survey Open-File. Report 2008-1159.

Bicocchi, G., D'Ambrosio, M., Vannocci, P., Nocentini, M., Tacconi-Stefanelli, C., Masi, E., et al. (2015). "Preliminary assessment of the factors controlling the geotechnical and hydrological properties in the hillslope deposits of eastern Tuscany (Central Italy)," in *IAMG 2015 proceedings*, 867–874.

Bordoni, M., Corradini, B., Lucchelli, L., Valentino, R., Bittelli, M., Vivaldi, V., et al. (2019). Empirical and physically based thresholds for the occurrence of shallow landslides in a prone area of Northern Italian Apennines. *WaterSwitzerl.* 11, 2653. doi:10.3390/W11122653

Bordoni, M., Meisina, C., Valentino, R., Bittelli, M., and Chersich, S. (2015). Site-specific to local-scale shallow landslides triggering zones assessment using TRIGRS. *Nat. Hazards Earth Syst. Sci.* 15, 1025–1050. doi:10.5194/nhess-15-1025-2015

Brunetti, M. T., Peruccacci, S., Rossi, M., Luciani, S., Valigi, D., and Guzzetti, F. (2010). Rainfall thresholds for the possible occurrence of landslides in Italy. *Nat. Hazards Earth Syst. Sci.* 10, 447–458. doi:10.5194/nhess-10-447-2010

Caine, N. (1980). The rainfall intensity-duration control of shallow landslides and debris flows. *Geogr. Ann. Ser. A Phys. Geogr.* 62, 23–27. doi:10.1080/04353676.1980.11879996

Calvello, M. (2017). Early warning strategies to cope with landslide risk. *Riv. Ital. Geotec.* 2017, 63–91. doi:10.19199/2017.2.0557-1405.063

Campbell, R. H. (1975). *Soil slips, debris flows, and rainstorms in the Santa Monica Mountains and vicinity, southern California*. Washington, DC, USA: US Geological Survey Professional Paper, 851.

Catani, F., Segoni, S., and Falorni, G. (2010). An empirical geomorphology-based approach to the spatial prediction of soil thickness at catchment scale. *Water Resour. Res.* 46, W05508. doi:10.1029/2008WR007450

Ciurleo, M., Cascini, L., and Calvello, M. (2017). A comparison of statistical and deterministic methods for shallow landslide susceptibility zoning in clayey soils. *Eng. Geol.* 223, 71–81. doi:10.1016/j.enggeo.2017.04.023

Ciurleo, M., Mandaglio, M. C., and Moraci, N. (2019). Landslide susceptibility assessment by TRIGRS in a frequently affected shallow instability area. *Landslides* 16, 175–188. doi:10.1007/s10346-018-1072-3

Corominas, J., van Westen, C., Frattini, P., Cascini, L., Malet, J. P., Fotopoulou, S., et al. (2014). Recommendations for the quantitative analysis of landslide risk. *Bull. Eng. Geol. Environ.* 73, 209–263. doi:10.1007/s10064-013-0538-8

de Lima Neves Seefelder, C., Koide, S., and Mergili, M. (2017). Does parameterization influence the performance of slope stability model results? A case study in rio de Janeiro, Brazil. *Landslides* 14, 1389–1401. doi:10.1007/s10346-016-0783-6

Gardner, W. R. (1958). Some steady-state solutions of the unsaturated moisture flow equation with application to evaporation from a water table. *Soil Sci.* 85, 228–232. doi:10.1097/00010694-195804000-00006

Gariano, S. L., and Guzzetti, F. (2016). Landslides in a changing climate. *Earth. Sci. Rev.* 162, 227–252. doi:10.1016/j.earscirev.2016.08.011

Gioia, E., Speranza, G., Ferretti, M., Godt, J. W., Baum, R. L., and Marincioni, F. (2016). Application of a process-based shallow landslide hazard model over a broad area in Central Italy. *Landslides* 13, 1197–1214. doi:10.1007/s10346-015-0670-6

Guzzetti, F., Gariano, S. L., Peruccacci, S., Brunetti, M. T., Marchesini, I., Rossi, M., et al. (2020). Geographical landslide early warning systems. *Earth. Sci. Rev.* 200, 102973. doi:10.1016/j.earscirev.2019.102973

Guzzetti, F., Peruccacci, S., Rossi, M., and Stark, C. P. (2007). Rainfall thresholds for the initiation of landslides in central and southern Europe. *Meteorol. Atmos. Phys.* 98, 239–267. doi:10.1007/s00703-007-0262-7

Guzzetti, F., Peruccacci, S., Rossi, M., and Stark, C. P. (2008). The rainfall intensity–duration control of shallow landslides and debris flows: An update. *Landslides* 5, 3–17. doi:10.1007/s10346-007-0112-1

He, J., Qiu, H., Qu, F., Hu, S., Yang, D., Shen, Y., et al. (2021). Prediction of spatiotemporal stability and rainfall threshold of shallow landslides using the TRIGRS and Scoops3D models. *Catena* 197, 104999. doi:10.1016/j.catena.2020.104999

He, S., Wang, J., and Liu, S. (2020). Rainfall event-duration thresholds for landslide occurrences in China. *Water* 12, 494. doi:10.3390/w12020494

He, X., Hong, Y., Vergara, H., Zhang, K., Kirstetter, P. E., Gourley, J. J., et al. (2016). Development of a coupled hydrological-geotechnical framework for rainfall-induced landslides prediction. *J. Hydrol. X.* 543, 395–405. doi:10.1016/j.jhydrol.2016.10.016

Ho, J.-Y., Lee, K. T., Chang, T.-C., Wang, Z.-Y., and Liao, Y.-H. (2012). Influences of spatial distribution of soil thickness on shallow landslide prediction. *Eng. Geol.* 124, 38–46. doi:10.1016/j.enggeo.2011.09.013

Ip, S. C. Y., Rahardjo, H., and Satyanaga, A. (2021). Three-dimensional slope stability analysis incorporating unsaturated soil properties in Singapore. *Georisk Assess. Manag. Risk Eng. Syst. Geohazards* 15, 98–112. doi:10.1080/17499518.2020.1737880

Iverson, R. M. (2000). Landslide triggering by rain infiltration. *Water Resour. Res.* 36, 1897–1910. doi:10.1029/2000WR900090

Keefer, D. K., Wilson, R. C., Mark, R. K., Brabb, E. E., Brown, W. M., Ellen, S. D., et al. (1987). Real-time landslide warning during heavy rainfall. *Science* 238, 921–925. doi:10.1126/science.238.4829.921

Kim, D., Im, S., Lee, S. H., Hong, Y., and Cha, K.-S. (2010). Predicting the rainfall-triggered landslides in a forested mountain region using TRIGRS model. *J. Mt. Sci.* 7, 83–91. doi:10.1007/s11629-010-1072-9

Lee, G., An, H., and Kim, M. (2017). Comparing the performance of TRIGRS and TiVaSS in spatial and temporal prediction of rainfall-induced shallow landslides. *Environ. Earth Sci.* 76, 315. doi:10.1007/s12665-017-6635-4

Li, W. Y., Liu, C., Scaioni, M., Sun, W. W., Chen, Y., Yao, D. J., et al. (2017). Spatio-temporal analysis and simulation on shallow rainfall-induced landslides in China using landslide susceptibility dynamics and rainfall *I-D* thresholds. *Sci. China Earth Sci.* 60, 720–732. doi:10.1007/s11430-016-9008-4

Lim, T. T., Rahardjo, H., Chang, M. F., and Fredlund, D. G. (1996). Effect of rainfall on matric suctions in a residual soil slope. *Can. Geotech. J.* 33, 618–628. doi:10.1139/t96-087

Lin, Q., and Wang, Y. (2018). Spatial and temporal analysis of a fatal landslide inventory in China from 1950 to 2016. *Landslides* 15, 2357–2372. doi:10.1007/s10346-018-1037-6

Ma, S., Xu, C., Xu, X., He, X., Qian, H., Jiao, Q., et al. (2020). Characteristics and causes of the landslide on july 23, 2019 in shuicheng, Guizhou province, China. *Landslides* 17, 1441–1452. doi:10.1007/s10346-020-01374-x

Marin, R. J., García, E. F., and Aristizábal, E. (2020). Effect of basin morphometric parameters on physically-based rainfall thresholds for shallow landslides. *Eng. Geol.* 278, 105855. doi:10.1016/j.enggeo.2020.105855

Marin, R. J., and Mattos, Á. J. (2020). Physically-based landslide susceptibility analysis using Monte Carlo simulation in a tropical mountain basin. *Georisk Assess. Manag. Risk Eng. Syst. Geohazards* 14, 192–205. doi:10.1080/17499518.2019.1633582

Marin, R. J. (2020). Physically based and distributed rainfall intensity and duration thresholds for shallow landslides. *Landslides* 17, 2907–2917. doi:10.1007/s10346-020-01481-9

Marin, R. J., Velásquez, M. F., García, E. F., Alvioli, M., and Aristizábal, E. (2021). Assessing two methods of defining rainfall intensity and duration thresholds for shallow landslides in data-scarce catchments of the Colombian Andean Mountains. *Catena* 206, 105563. doi:10.1016/j.catena.2021.105563

Marin, R. J., and Velásquez, M. F. (2020). Influence of hydraulic properties on physically modelling slope stability and the definition of rainfall thresholds for shallow landslides. *Geomorphology* 351, 106976. doi:10.1016/j.geomorph.2019.106976

Melillo, M., Brunetti, M. T., Peruccacci, S., Gariano, S. L., Roccati, A., and Guzzetti, F. (2018). A tool for the automatic calculation of rainfall thresholds for landslide occurrence. *Environ. Model. Softw.* 105, 230–243. doi:10.1016/j.envsoft.2018.03.024

Montrasio, L., and Valentino, R. (2008). A model for triggering mechanisms of shallow landslides. *Nat. Hazards Earth Syst. Sci.* 8, 1149–1159. doi:10.5194/nhess-8-1149-2008

Montrasio, L., and Valentino, R. (2007). Experimental analysis and modelling of shallow landslides. *Landslides* 4, 291–296. doi:10.1007/s10346-007-0082-3

Montrasio, L., Valentino, R., and Losi, G. L. (2011). Towards a real-time susceptibility assessment of rainfall-induced shallow landslides on a regional scale. *Nat. Hazards Earth Syst. Sci.* 11, 1927. doi:10.5194/nhess-11-1927-2011

Park, D. W., Nikhil, N. V., and Lee, S. R. (2013). Landslide and debris flow susceptibility zonation using TRIGRS for the 2011 Seoul landslide event. *Nat. Hazards Earth Syst. Sci.* 13, 2833–2849. doi:10.5194/nhess-13-2833-2013

Park, J. Y., Lee, S. R., Lee, D. H., Kim, Y. T., and Lee, J. S. (2019). A regional-scale landslide early warning methodology applying statistical and physically based approaches in sequence. *Eng. Geol.* 260, 105193. doi:10.1016/j.enggeo.2019.105193

Peres, D. J., and Cancelliere, A. (2014). Derivation and evaluation of landslide-triggering thresholds by a Monte Carlo approach. *Hydrol. Earth Syst. Sci.* 18, 4913–4931. doi:10.5194/hess-18-4913-2014

Peruccacci, S., Brunetti, M. T., Luciani, S., Vennari, C., and Guzzetti, F. (2012). Lithological and seasonal control on rainfall thresholds for the possible initiation of landslides in central Italy. *Geomorphology* 139–140, 79–90. doi:10.1016/j.geomorph.2011.10.005

Piciullo, L., Calvello, M., and Cepeda, J. M. (2018). Territorial early warning systems for rainfall-induced landslides. *Earth. Sci. Rev.* 179, 228–247. doi:10.1016/j.earscirev.2018.02.013

Piciullo, L., Gariano, S. L., Melillo, M., Brunetti, M. T., Peruccacci, S., Guzzetti, F., et al. (2017). Definition and performance of a threshold-based regional early warning model for rainfall-induced landslides. *Landslides* 14, 995–1008. doi:10.1007/s10346-016-0750-2

Raia, S., Alvioli, M., Rossi, M., Baum, R. L., Godt, J. W., and Guzzetti, F. (2014). Improving predictive power of physically based rainfall-induced shallow landslide models: A probabilistic approach. *Geosci. Model Dev.* 7, 495–514. doi:10.5194/gmd-7-495-2014

Richards, L. A. (1931). Capillary conduction of liquids through porous mediums. *Physics* 1, 318–333. doi:10.1063/1.1745010

Salciarini, D., Fanelli, G., and Tamagnini, C. (2017). A probabilistic model for rainfall—Induced shallow landslide prediction at the regional scale. *Landslides* 14, 1731–1746. doi:10.1007/s10346-017-0812-0

Salciarini, D., Godt, J. W., Savage, W. Z., Baum, R. L., and Conversini, P. (2008). Modeling landslide recurrence in Seattle, Washington, USA. *Eng. Geol.* 102, 227–237. doi:10.1016/j.enggeo.2008.03.013

Salciarini, D., Godt, J. W., Savage, W. Z., Conversini, P., Baum, R. L., and Michael, J. A. (2006). Modeling regional initiation of rainfall-induced shallow landslides in the eastern Umbria Region of central Italy. *Landslides* 3, 181–194. doi:10.1007/s10346-006-0037-0

Salciarini, D., Tamagnini, C., Conversini, P., and Rapinesi, S. (2012). Spatially distributed rainfall thresholds for the initiation of shallow landslides. *Nat. Hazards* 61, 229–245. doi:10.1007/s11069-011-9739-2

Segoni, S., Piciullo, L., and Gariano, S. L. (2018). A review of the recent literature on rainfall thresholds for landslide occurrence. *Landslides* 15, 1483–1501. doi:10.1007/s10346-018-0966-4

Srivastava, R., and Yeh, T. J. (1991). Analytical solutions for one-dimensional, transient infiltration toward the water table in homogeneous and layered soils. *Water Resour. Res.* 27, 753–762. doi:10.1029/90WR02772

Taylor, D. W. (1948). *Fundamentals of soil mechanics*. New York: Wiley.

Tran, T. V., Alvioli, M., Lee, G., and An, H. U. (2018). Three-dimensional, time-dependent modeling of rainfall-induced landslides over a digital landscape: A case study. *Landslides* 15, 1071–1084. doi:10.1007/s10346-017-0931-7

United Nations International Strategy for Disaster Reduction (UNISDR) (2015). Sendai framework for disaster risk reduction 2015–2030. Available at: http://www.wcdrr.org/uploads/Sendai_Framework_for_Disaster_Risk_Reduction_2015-2030.pdf (Access June 6, 2015).

Van Genuchten, M. T. (1980). A closed-form equation for predicting the hydraulic conductivity of unsaturated soils. *Soil Sci. Soc. Am. J.* 44, 892–898. doi:10.2136/sssaj1980.03615995004400050002x

Vanapalli, S. K., Fredlund, D. G., Pufahl, D. E., and Clifton, A. W. (1996). Model for the prediction of shear strength with respect to soil suction. *Can. Geotech. J.* 33, 379–392. doi:10.1139/t96-060

Vieira, B. C., Fernandes, N. F., and Filho, O. A. (2010). Shallow landslide prediction in the serra do mar, são paulo, Brazil. *Nat. Hazards Earth Syst. Sci.* 10, 1829–1837. doi:10.5194/nhess-10-1829-2010

Viet, T. T., Lee, G., Thu, T. M., and An, H. U. (2017). Effect of digital elevation model resolution on shallow landslide modeling using TRIGRS. *Nat. Hazards Rev.* 18, 04016011. doi:10.1061/(asce)nh.1527-6996.0000233

Wei, L. W., Huang, C. M., Chen, H., Lee, C. T., Chi, C. C., and Chiu, C. L. (2018). Adopting the <i>I</i>₃–<i>R</i>₂₄ rainfall index and landslide susceptibility for the establishment of an early warning model for rainfall-induced shallow landslides. *Nat. Hazards Earth Syst. Sci.* 18, 1717–1733. doi:10.5194/nhess-18-1717-2018

Weidner, L., Oommen, T., Escobar-Wolf, R., Sajinkumar, K. S., and Samuel, R. A. (2018). Regional-scale back-analysis using TRIGRS: An approach to advance landslide hazard modeling and prediction in sparse data regions. *Landslides* 15, 2343–2356. doi:10.1007/s10346-018-1044-7

Wilson, R. C. (2005). *The rise and fall of a debris-flow warning system for the San Francisco Bay region, California*. Chichester, England: Landslide hazard risk, 493–516. doi:10.1002/9780470012659.ch17

Wu, S. J., Hsiao, Y. H., Yeh, K. C., and Yang, S. H. (2017). A probabilistic model for evaluating the reliability of rainfall thresholds for shallow landslides based on uncertainties in rainfall characteristics and soil properties. *Nat. Hazards* 87, 469–513. doi:10.1007/s11069-017-2773-y

Xie, M., Esaki, T., and Zhou, G. (2004). GIS-based probabilistic mapping of landslide hazard using a three-dimensional deterministic model. *Nat. Hazards (Dordr).* 33, 265–282. doi:10.1023/B:NHAZ.0000037036.01850.0d

Yu, B., Wang, T., Zhu, Y., and Zhu, Y. (2016). Topographical and rainfall factors determining the formation of gully-type debris flows caused by shallow landslides in the Dayi area, Guizhou Province, China. *Environ. Earth Sci.* 75, 551–618. doi:10.1007/s12665-016-5243-z

Zhang, N., et al. (2017). A study of the instability mechanism and investigation methods of shallow bedrock landslides in karst mountain areas: Taking the jinxing landslide in dafang county as an example. *Hydrogeol. Eng. Geol.* 44, 142–146. (In Chinese).

Zhang, S., Jiang, Q., Wu, D., Xu, X., Tan, Y., and Shi, P. (2022). Improved method of defining rainfall intensity and duration thresholds for shallow landslides based on TRIGRS. *Water* 14, 524. doi:10.3390/w14040524

Zhang, S., Zhao, L., Delgado-Tellez, R., and Bao, H. (2018). A physics-based probabilistic forecasting model for rainfall-induced shallow landslides at regional scale. *Nat. Hazards Earth Syst. Sci.* 18, 969–982. doi:10.5194/nhess-18-969-2018

Zhao, G. (2021). *Soil physical characteristics of calcareous soil and yellow soil in a small catchment of typical karst area and their water regulation techniques*. Guiyang, Guizhou Province, China: Guizhou Minzu University (Guiyang). [master's thesis]. (In Chinese).

frontiers | Frontiers in Earth Science

TYPE Original Research
PUBLISHED 29 September 2022
DOI 10.3389/feart.2022.1021106

OPEN ACCESS

EDITED BY
Xiekang Wang,
Sichuan University, China

REVIEWED BY
Li Wu,
Anhui Normal University, China
Xiaozhong Huang,
Lanzhou University, China

*CORRESPONDENCE
Yuzhu Zhang,
xbdzyz05@nwu.edu.cn

SPECIALTY SECTION
This article was submitted to Quaternary Science, Geomorphology and Paleoenvironment, a section of the journal Frontiers in Earth Science

RECEIVED 17 August 2022
ACCEPTED 30 August 2022
PUBLISHED 29 September 2022

CITATION
Zhu Y, Wang H, Zhang Y, Huang CC, Zha X, Qiu H, Jia Y-n, Xiao Q, Chen D, Lin X and Liu T (2022), Sedimentary records and chronology of the late Pleistocene overbank flooding in the Yellow River source area, NE Tibetan Plateau.
Front. Earth Sci. 10:1021106.
doi: 10.3389/feart.2022.1021106

Sedimentary records and chronology of the late Pleistocene overbank flooding in the Yellow River source area, NE Tibetan Plateau

Yan Zhu[1], Haoyu Wang[2], Yuzhu Zhang[1]*, Chun Chang Huang[3], Xiaochun Zha[2], Haijun Qiu[1], Ya-na Jia[1], Qili Xiao[1], Dou Chen[1], Xu Lin[1] and Tao Liu[4]

[1]Shaanxi Key Laboratory of Earth Surface System and Environmental Carrying Capacity, College of Urban and Environmental Sciences, Northwest University, Xi'an, China, [2]Key Laboratory of Western China's Environmental Systems (Ministry of Education), College of Earth and Environmental Sciences, Lanzhou University, Lanzhou, China, [3]School of Geography and Tourism, Shaanxi Normal University, Xi'an, China, [4]Department of Hydrology and Atmospheric Sciences, University of Arizona, Tucson, AZ, United States

Paleohydrological investigations were carried out in the Yellow River source area on the northeast (NE) Tibetan Plateau. During our fieldwork investigations, two units of overbank flood deposits (OFD) were found in the Maqu-Kesheng reach. These OFD units were studied using a multi-index approach, including magnetic susceptibility, hygroscopic water, grain size distribution and micro-morphological features. It can be inferred that they have recorded two episodes of overbank flooding of the Yellow River. Using the optically stimulated luminescence (OSL) and AMS ^{14}C dating techniques, the first episode was dated to 34,680 ± 1880-29000 ± 1790 a and correlated with the late Marine Isotope Stage 3a (MIS 3a) with a warm and wet climate. The second episode occurred at 16,500 ± 1,250-14000 ± 1,280 a, which is coincided with the Bølling-Allerød warm stage during the last deglaciation, a period of coexisting global warming and rapidly shrinking ice sheets. At these two periods, the water was mainly derived from the accelerated melting of mountain glaciers surrounding the basin and/or the large-scale precipitation, which led to the overbank flooding events. At the same time, the related overbank flood deposits were interbedded within glacial outwash/flashflood deposits in the valley bottom of the Yellow River, which intensified the valley aggradation. These results are of great significance in enriching the paleoflood records in the Yellow River source area, recognizing the effect of river system on the development of valley landform, as well as understanding the hydro-climatic response of the Tibetan Plateau to global climate warming occurring presently.

KEYWORDS

Tibetan Plateau, Yellow River source area, late Pleistocene, environmental evolution, overbank flooding

1 Introduction

Paleoflood hydrology sub-discipline of paleohydrology that involves expertise from geomorphology, sedimentology, hydrology, modeling, and statistics, and concerns the study of past or ancient flood events using physical or botanical information, irrespective of any direct human observation (Schulte et al., 2019; Baker et al., 2022). The primary goal of paleoflood hydrology is to extend flood records over periods of time ranging from decades to millennia. The result is of great significance in providing data on the magnitude and frequency of floods and can indicate a limit to flood magnitude over a specified time interval (England et al., 2010; Guo et al., 2017; Munoz et al., 2018; Liu et al., 2019; Greenbaum et al., 2020; Panda et al., 2020; Baker et al., 2022; Benito et al., 2022; Mao et al., 2022), and understanding environmental and disaster effects of the interaction of hydrological processes, climate change, geomorphic factors and human activity (Knox, 2000; Benito et al., 2008; Huang et al., 2011; Srivastava et al., 2017; Wu et al., 2017; Liu et al., 2019; Zhang et al., 2019; Chen et al., 2021; Sharma et al., 2022). Consequently, since Kochel and Baker (1982) introduced "Paleoflood hydrology" in the journal *Science*, paleoflood investigates have been carried out over much of the world.

The geographic location of the Yellow River source area, influenced by the interplay among the Asian summer monsoon (ASM), Plateau monsoon, and Westerlies, provides great potential for elucidating climatic or environmental changes from sedimentary archives (Li et al., 1995; Wang et al., 1995; Shen et al., 1996; Zhou et al., 2010; Zhao et al., 2011; Wang et al., 2017; Hu et al., 2018; Li et al., 2020; Jia et al., 2022). The sensitivity of the region is shown in the temporal and spatial variability of natural indicators, such as floods, desertification, droughts and biodiversity, which are closely related to the global change drivers, climate and human activity (Li et al., 2011; Peng et al., 2014; Meng et al., 2016; Guo et al., 2022). In particular, the extreme floods in the Yellow River source area, characterized by high peak discharge, large area of influence, and long duration, can result in great damage and the loss of life and property (Peng et al., 2014). At present, scholars mainly rely on the measured data (no more than 60 years) from hydrometeorological stations and very limited historical documents to reveal the occurrence regularity of floods (Wang et al., 2009; Wang et al., 2012). However, extreme floods are events with low probabilities (IPCC, 2007). Therefore, it is necessary to carry out paleoflood studies and extend flood records to reveal the temporal spatial variability of extreme floods and the evolution tendency of the catchment system in the Yellow River source area.

The connection of the Zoige Basin with the Yellow River and the start of the basin excavation occurred at approximately 35,000 a BP (Li et al., 1995; Wang et al., 1995). After the endorheic Zoige catchment was captured by the Yellow River from the downstream basin at a much lower elevation, a rapid valley aggradation phase occurred at ca. 35,000-14600 a BP in the Maqu-Kesheng reach in the Yellow River source area (Wang et al., 2021). Scholars have revealed that valley aggradation often requires high sediment production from the catchment (climatically or human induced) and overbank (moderate or extreme) flows (Starkel, 2003; Benito et al., 2008; Srivastava et al., 2008; Chaudhary et al., 2015; Chahal et al., 2019; Prizomwala et al., 2019). It's worth noting that our research team has indeed found two units of late Pleistocene overbank flood deposits 2-6 m in thickness in the sediment sequences at Chameiqu (CMQ) and Zuhaka (ZHK) sites in the reach. And thus, the objectives of this study are as follows: 1) to enrich identification characteristics of these two units of overbank flood deposits; 2) to establish the chronology of overbank flooding by using the AMS ^{14}C and OSL dating techniques; and 3) to explore the possible triggering factors and climate background of overbank flooding. These results are very useful for reasonable utilization of water resources and mitigation of flood disasters in the Yellow River source area, and they will enrich theoretical results of the interaction of hydrological processes, climate change and geomorphic factors.

2 Geographical setting

The Yellow River source area is generally defined as the upstream catchment above the Tangnaihai (TNH) hydrological station, situated between 95°50′45″ E-103°28′11″ E and 32°12′10″ N-35°48′7″ N on the NE Tibetan Plateau (Figure 1). It has a main flow length of 1,553 km, a drainage area of 121,972 km^2, and an average channel gradient of ca. 1.1‰ (Li et al., 2014). The river flows southeast from the bedrock gorges into the Zoige Basin, which is a late Cenozoic faulted basin formed by tectonic movement (Lehmkuhl and Spönemann, 1994; Xue et al., 1998). The Zoige Basin is a relative subsidence area surrounded by East Kunlun Fault, Bailongjiang Fault, Awangcang Fault and so on (Figure 1B and Figure 2A). Originally, this basin was a paleolake (Zoige paleolake) with lacustrine sediments >300 m thick in the center (Xue et al., 1998).

The Yellow River meets the Jiaqu, Baihe and Heihe Rivers within the basin, and flows northwest into the Maqu-Kesheng reach forming a huge U-shaped bend (Figure 2A). In the Maqu-Oula reach, the well-developed huge pluvial fans from the Xiqing Mountains forced the Yellow River to move southward to the foot of bedrock hills of the northern Anyemaqen Mountains (Figure 2B). However, in the Oula-Kesheng reach, the huge pluvial fans from the Anyemaqen Mountains forced the Yellow River to move northward to the foot of bedrock hills of the Xiqing Mountains.

The climate in the Yellow River source area is sub-humid and semi-arid area characterized by low temperatures, drastic seasonal

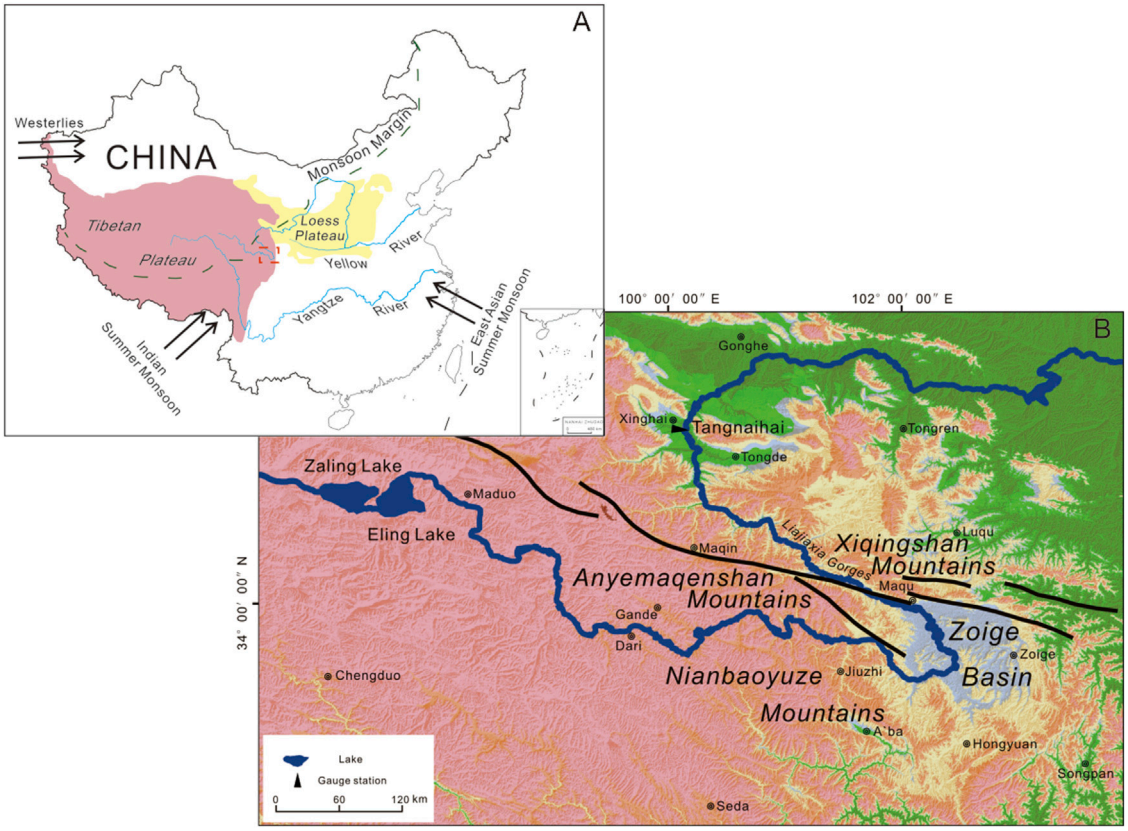

FIGURE 1
(A) Map showing the Maqu-Kesheng reach downstream of the Zoige Basin (red square) in the Yellow River source area on the NE Tibetan Plateau. **(B)** Map showing drainage basin, major fault zones (marked with "") (He et al., 2006) and topographical features of the Yellow River source area on the NE Tibetan Plateau.

variations in precipitation, frequent strong winds, high evaporation, and strong solar radiation. The mean annual temperature varies between -3.5°C and 2.4°C from southeast to northwest (1961-2014) (Shi et al., 2018). The mean annual precipitation ranges from 753.3 mm in the southeast to ca. 322.3 mm in the northwest (1961-2014) (Shi et al., 2018). Up to 75%-90% precipitation occurs between June and September because of the alpine hydro-climatic conditions with high seasonal variability. In addition, mean annual potential evaporation is 884.4 mm in the area (2000-2014) (Shi et al., 2018).

The Yellow River source area is often referred to as the water tower of the Yellow River as it contributes about 35% of the total annual runoff of the entire Yellow River (Hu et al., 2011). The area is covered with mountain glaciers, permafrost, snow, wetlands, lakes and grasslands, etc., forming a unique hydrological ecosystem. This causes extraordinary floods in the area with mixed recharge in the catchment derived from precipitation, snow melting and glacier ablation (LiG F et al., 2013). The hydrological data observed at the TNH gauge station show that the mean annual runoff volume is 1.78×10^{10} m^3, and the mean annual sediment concentration is 0.60 kg/m^3 (1991-2011) (Li et al., 2014). The gauged maximum flood discharge since 1955 is 5,450 m^3/s, which occurred in September 1981 (Peng et al., 2014).

3 Sampling sites and methods

3.1 Sampling sites

The Maqu-Kesheng reach in the Yellow River source area, is located in the downstream of the Zoige Basin and upstream of the Lajia Gorges (Figures 1, 2). The river valley is ca. 4-5 km in width developed along the East Kunlun Fault extending WNW-ESE between the Anyemaqen Mountains and the Xiqing Mountains (Zhou et al., 2021). Sediment sequences consist of aeolian loess-soil deposits, glacial outwash/flashflood deposits and periglacial slope deposits are widely distributed on the cliff river banks in the river reach. According to a variety of sedimentological criteria used in paleoflood hydrology (Benito et al., 2008; Huang et al.,

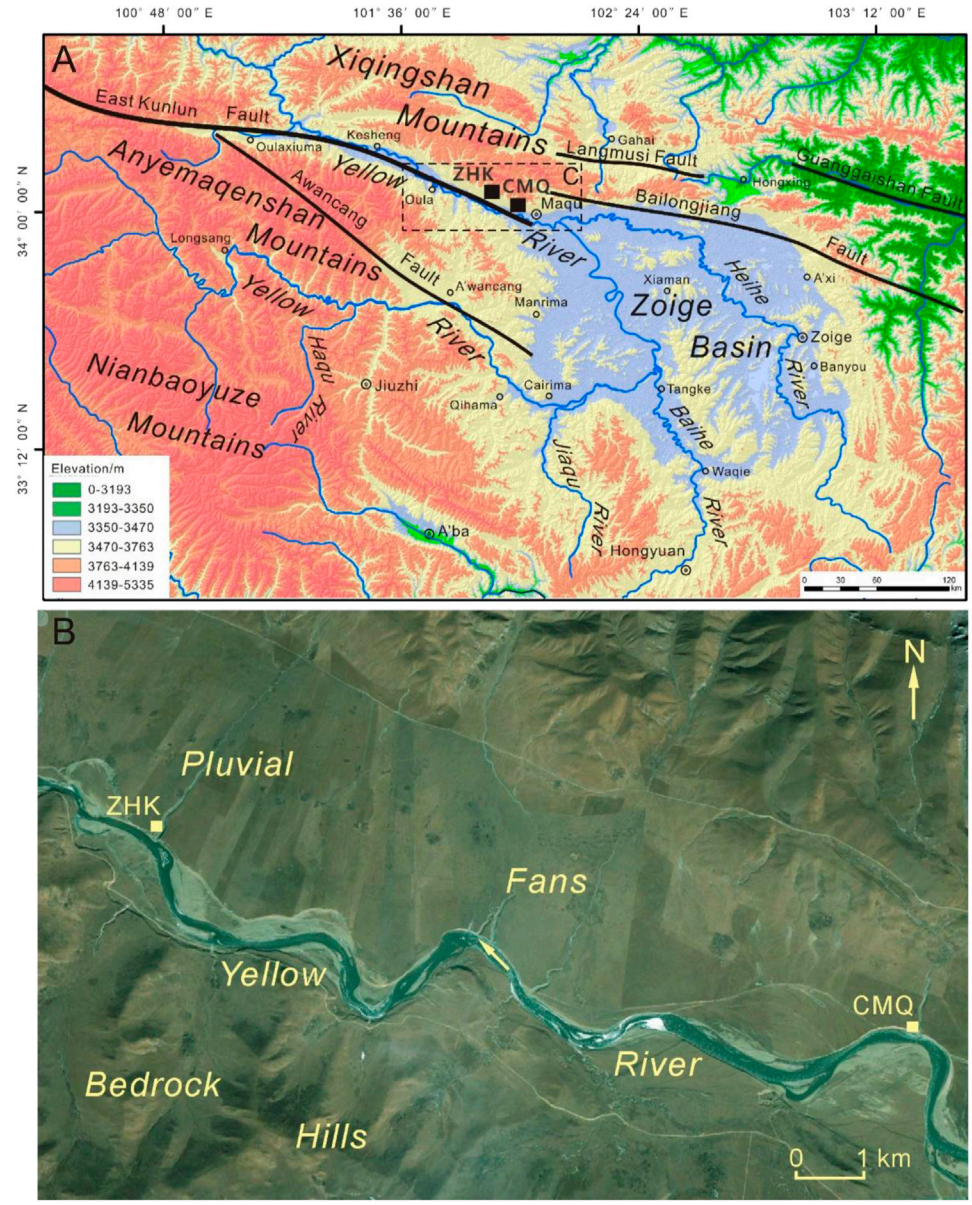

FIGURE 2
(A) Map showing the location of the CMQ and ZHK profiles (marked with "■") in the Maqu-Kesheng reach downstream of the Zoige Basin. **(B)** Google Earth image showing the location and the landscape at the CMQ and ZHK profiles (marked with "■").

2011), two units of overbank flood deposits (OFD) inserted into the large clastic sediments deposited from glacial outwash or flashflood have been identified on the right bank adjacent to Chameiqu (CMQ) and Zuhaka (ZHK) sites (Figure 3A,B). These sedimentological criteria include 1) sediment consisting of silt and medium sand with parallel beddings; 2) abrupt vertical change in color, grain size, texture and structure; 3) stratigraphic breaks between the beds; 4) a thin clay cap on top of a bed resulting from sorted deposition (Supplementary Figure S1); 5) presence of clastic sediments deposited from glacial outwash or flashflood between the units. The top of sediment profile at the CMQ site (102°0′30.5″ E, 33°59′36.8″ N; 3,341 m a.s.l.) is about 28 m above the normal water level of the Yellow River. The ZHK site is located ca. 13.5 km downstream from the CMQ site (Figure 2B). The front of the sediment profile at the ZHK site (101°53′9.9″ E, 34°1′13.6″ N; 3,437 m a.s.l.) is ca. 29 m above the normal water level of the Yellow River.

Pedo-stratigraphic subdivisions and sedimentological characteristics in the sediment sequences at the CMQ and

10.3389/feart.2022.1021106

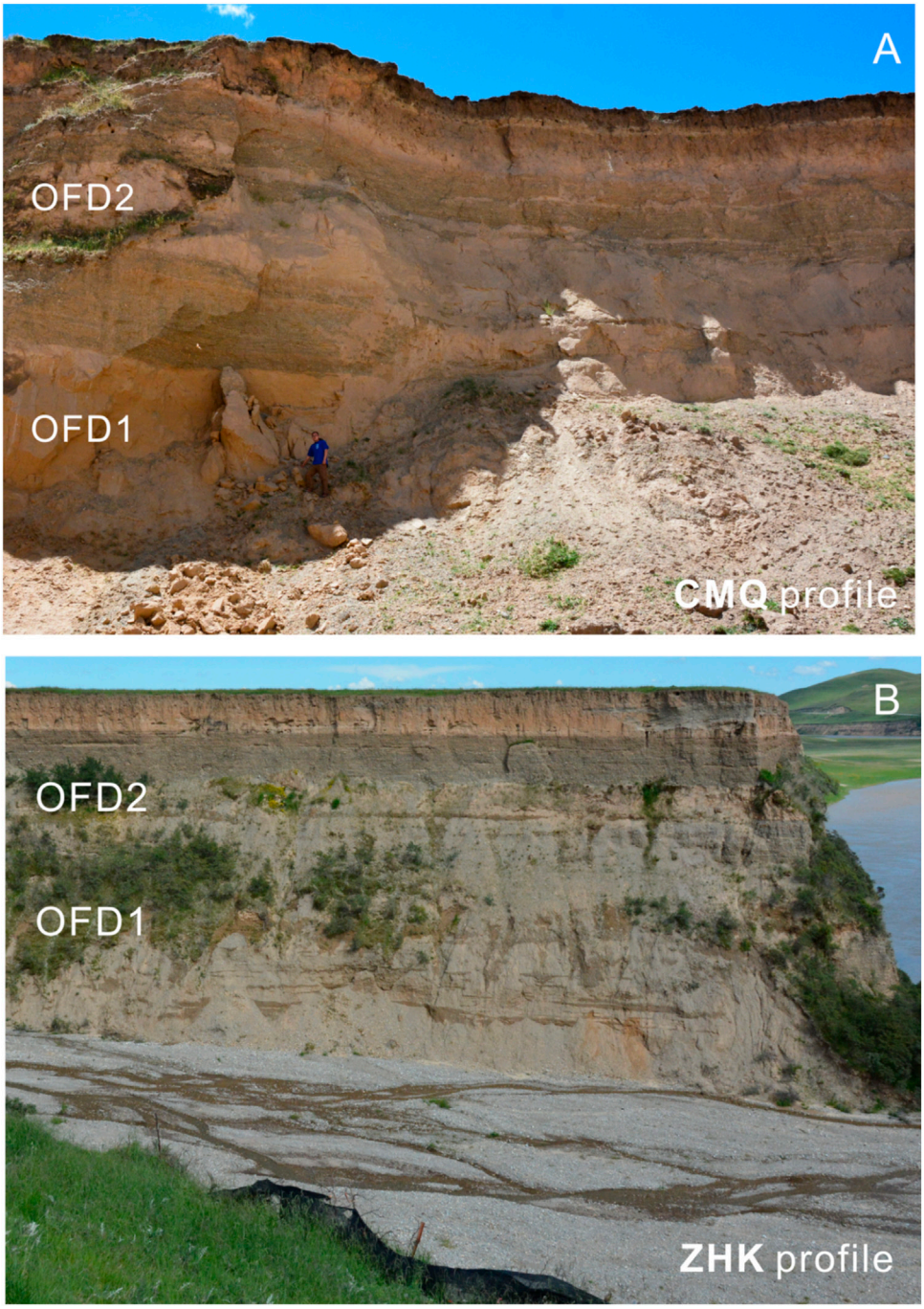

FIGURE 3
Photo showing the overbank flood deposits within the sediment profiles at the CMQ and ZHK sites in the Yellow River source area on the NE Tibetan Plateau.

ZHK sites were observed and described in detail during the fieldwork (Figure 3A,B; Tables 1, 2). After detailed observations and establishment of pedo-stratigraphical subdivisions, 228 bulk samples for sedimentary analysis were collected from modern soil, paleosol, loess, OFD units and paleochannel deposits in these two profiles. Four bulk samples for micro-morphological feature analysis were taken from paleosol, OFD1 unit in the CMQ profile and aeolian loess, OFD1 unit in the ZHK profile, respectively. Sixteen luminescence samples for OSL dating and nine organic sediment samples were collected from the ZHK and

TABLE 1 Pedo-stratigraphic subdivisions and descriptions of the CMQ profile in the Yellow River source area on the NE Tibetan Plateau.

Depth (m)	Pedo-stratigraphic subdivisions	Pedo-sedimentary descriptions
0.7–0	Modern soil	Grayish brown (7.5YR6/2), dark brown (7.5YR3/1) when wet, silt, crumb-clumpy structure, loose and porous, abundant plant roots
1.4–0.7	Paleosol	Brownish grey (7.5YR6/1), silt, crumb-clumpy structure, some pores with abundant calcareous pseudomycelium, vertical cracks, well-developed
2.1–1.4	Transitional loess	Dull yellowish orange (10YR7/4), fine sandy silt, uniform blocky structure, loose and many small pores with massive calcareous pseudomycelium, weak weathering and pedogenesis
2.6–2.1	Aeolian loess	Dull yellowish orange (10YR7/4), fine sandy silt, uniform blocky structure, loose and many small pores
7–2.6	Glacial outwash/flashflood deposits	Greyish variegated colour, variegated sand and gravel (1-10 cm), poorly rounded and poorly sorted, glacial outwash/flashflood deposits from the main peak of the Xiqing Mountains
9.7–7	Overbank flood deposits (OFD2)	Pale yellowish orange (10YR8/3), fine sandy silt/fine sand, well-sorted, with parallel beddings. The thickness of the OFD2 was about 2.7 m consisting of 9 individual overbank flood deposits beds which represented at least 9 palaeoflood events in the Yellow River source area
12–9.7	Glacial outwash/flashflood deposits	Greyish variegated colour, variegated sand and gravel (1-10 cm), poorly rounded and poorly sorted, glacial outwash/flashflood deposits from the main peak of the Xiqing Mountains
18–12	Overbank flood deposits (OFD1)	Pale yellowish orange (10YR8/3), fine sandy silt/fine sand, well-sorted, with parallel beddings. The thickness of the OFD1 was about 6 m consisting of 9 individual overbank flood deposits beds which represented at least 9 palaeoflood events in the Yellow River source area
>18	Glacial outwash/flashflood deposits	Greyish variegated colour, variegated sand and gravel (1-10 cm), poorly rounded and poorly sorted, glacial outwash/flashflood deposits from the main peak of the Xiqing Mountains

CMQ profiles according to the location of the lithostratigraphic boundaries (Table 3 and Table 4).

3.2 Methods

3.2.1 Paleo-environmental proxy analysis

Magnetic susceptibility can indicate the concentration of ferromagnetic minerals in the sediments and used for manifesting the changing intensity of weathering and pedogenic modification to accumulated dust in semi-humid and semi-arid regions (Liu, 1985; Kukla and An, 1989; Liu et al., 1993; Maher, 1998). Magnetic susceptibility was measured on a mass of 10 g of ground sediment with a Bartington MS-2B magnetic susceptibility meter (0.47/4.7 kHz) under the condition of no interference from magnetic objects.

Hygroscopic water concentration is closely related to the distribution of sediment grain size, which can indirectly reflect the intensity of soil weathering and pedogenisis as well as climate change (Huang, 2001; Zhao et al., 2012). The determination of hygroscopic water concentration is that 5 g of dried soil sample is put in an aluminum box and baked at 105°C for more than 24 h to constant weight, and then the percentage of hygroscopic water content is calculated.

Grain size distribution can be used to differentiate the paleoflood deposits from other kinds of sediments in the river valley (Zha et al., 2015; Mao et al., 2016; Zhang et al., 2019; Chen et al., 2021). Grain size distribution was analyzed using a LS13320 laser analyzer with $(NaPO_3)_6$ as a dispersing agent after pre-treatment with 30% H_2O_2 and 10% HCl to remove organic matter and carbonates, respectively.

Micro-morphological features can provide the key information that enables reconstruction of the pedo-sedimentary processes and associated paleoclimatic controls responsible for the formation of pedocomplexes (Kemp 1999; Przemyslaw, 2013; Zhang et al., 2018). The micro-morphological feature was observed under the Leica-DMRX polarizing microscope.

3.2.2 Optically stimulated luminescence and AMS ^{14}C dating

Sixteen OSL samples were prepared under subdued red light in the OSL laboratory in the Shaanxi Key Laboratory of Earth Surface System and Environmental Carrying Capacity, Xi'an. The outer 2-3 cm of deposits within the sample tubes were removed and reserved for measurement of U, Th, K and Rb concentrations. The remaining deposits within the tube were pretreated with 30% H_2O_2 (to remove organic materials), 10% HCl (to dissolve carbonates), and wet sieving to obtain the 90-125 μm grain fractions from the paleosol, transitional loess, aeolian loess, OFD and paleochannel deposits. And the 90-125 mm grain fractions were etched with 40% HF for 50 min (followed by an HCl rinse) to remove the outer (alpha-irradiated) layer of quartz grains and to eliminate feldspars.

Optically stimulated luminescence (OSL) dating was carried out on a Risø-TL/OSL-DA20 Dating System using the single-aliquot regenerative-dose (SAR) protocol (Murray and Wintle, 2000). The Risø-TL/OSL-DA20 Dating System was equipped with a new automated detection and stimulation head (DASH).

10.3389/feart.2022.1021106

TABLE 2 Pedo-stratigraphic subdivisions and descriptions of the ZHK profile in the Yellow River source area on the NE Tibetan Plateau.

Depth (m)	Pedo-stratigraphic subdivisions	Pedo-sedimentary descriptions
0.7–0	Modern soil	Grayish brown (7.5YR6/2), dark brown (7.5YR3/1) when wet, silt, crumb-clumpy structure, loose and porous, abundant plant roots
1.9–0.7	Paleosol	Brownish grey (7.5YR6/1), silt, crumb-clumpy structure, some pores with abundant calcareous pseudomycelium, vertical cracks, well-developed
2.4–1.9	Transitional loess	Dull yellowish orange (10YR7/4), fine sandy silt, uniform blocky structure, loose and many small pores with massive calcareous pseudomycelium, weak weathering and pedogenesis
2.95–2.4	Glacial outwash/flashflood deposits	2.85–2.4 m: greyish variegated colour, variegated sand and gravel (1-15 cm), poorly rounded and poorly sorted; 2.95–2.85 m: dull yellow orange (10YR7/4), sand, poorly sorted and relatively loose, glacial outwash/flashflood deposits from the main peak of the Xiqing Mountains
3.5–2.95	Aeolian loess	Dull yellowish orange (10YR7/4), fine sandy silt, uniform blocky structure, loose and many small pores
7.5–3.5	Glacial outwash/flashflood deposits	Greyish variegated colour, variegated sand and gravel (1-15 cm), poorly rounded and poorly sorted, glacial outwash/flashflood deposits from the main peak of the Xiqing Mountains
9.50–7.5	Overbank flood deposits (OFD2)	Pale yellowish orange (10YR8/3), fine sandy silt/fine sand, well-sorted, with parallel beddings. The thickness of the OFD2 was about 2 m consisting of 5 individual overbank flood deposits beds which represented at least 5 palaeoflood events
15–9.5	Glacial outwash/flashflood deposits	Greyish variegated colour, variegated sand and gravel (1–15 cm), poorly rounded and poorly sorted, glacial outwash/flashflood deposits from the main peak of the Xiqing Mountains
18–15	Overbank flood deposits (OFD1)	Pale yellowish orange (10YR8/3), fine sandy silt/fine sand, well-sorted, with parallel beddings. The thickness of the OFD1 was about 3 m consisting of 6 individual overbank flood deposits beds which represented at least 6 palaeoflood events
24–18	Glacial outwash/flashflood deposits	Greyish variegated colour, variegated sand and gravel (1-15 cm), poorly rounded and poorly sorted, glacial outwash/flashflood deposits from the main peak of the Xiqing Mountains
24.6–24	Paleochannel deposits	Consists of gravels and sands. Gravels are gray black, variegated sand and gravel (5-15 cm), moderately rounded and moderately sorted. The sands are dull yellowish orange (10YR7/4), coarse sand, loose, with lenticular beddings and rusty yellow spots (SupplementaryFigure S4A,B)
25.6–24.6	Glacial outwash/flashflood deposits	Greyish variegated colour, variegated sand and gravel (1-15 cm), poorly rounded and poorly sorted, glacial outwash/flashflood deposits from the main peak of the Xiqing Mountains
>25.6	Paleochannel deposits	Consists of gravels and sands. Gravels are gray black, variegated sand and gravel (5-15 cm), moderately rounded and moderately sorted. The sands are dull yellowish orange (10YR7/4), coarse sand, loose, with lenticular beddings and rusty yellow spots

TABLE 3 Calibrated radiocarbon dates of the CMQ and ZHK profile in the Yellow River source area on the northeast Tibetan Plateau.

Site	Sample ID	Sediment and stratigraphy	Dating material	Depth (m)	Radiocarbon date (a BP)	Calibrated age (cal a BP, 2σ)
CMQ	Beta-566789	Paleosol	Organic sediment	0.80–0.85	3,650 ± 30	3,953 ± 67
CMQ	Beta-561691	Paleosol	Organic sediment	1.30–1.35	5,810 ± 30	7,630 ± 47
CMQ	Beta-566792	OFD1	Organic sediment	17.80–17.90	26,460 ± 100	30,700 ± 312

The automated DASH includes blue LEDs (470 nm, ~80 mW/m^2), green LEDs (525 nm, ~40 mW/m^2) and infrared LEDs (850 nm, ~300 mW/m^2). Laboratory irradiation was carried out using ^{90}Sr/^{90}Y sources mounted on the reader. The OSL signal was detected using an ET PDM 9107Q-AP-TTL-03 photomultiplier tube in combination with a 7.5 mm thick Hoya U-340 glass filter and calculated by subtracting the average of the last 4 s (background signal) from the first 0.8 s of the signal decay curve (Figure 4). The OSL signals of the samples taken from the paleosol, transitional loess, aeolian loess, OFD and paleochannel deposits show rapid decay dominated by the fast component of the signal (Murray and Wintle, 2003). A preheat temperature of 220°C and a cut-heat of 180°C were selected for the regeneration and test doses, respectively, in routine equivalent dose (*De*) determination (Jia et al., 2022). All sensitivity-corrected dose response curves were fitted with saturating-exponential function to calculate *De* values using the software Analyst (Duller, 2015) (Figure 4).

In order to explain the distributions of *De* values and analyze the factors affecting the scatter in *De*, such as partial bleaching,

TABLE 4 Summary of the U, Th, K, Rb and dose rates for samples taken from overbank flood deposits (OFD), paleosol, aeolian loess, paleochannel deposits, glacial outwash/flashflood deposits in the CMQ and ZHK profiles in the Yellow River source area on the NE Tibetan Plateau.

Sample ID	Sediment and stratigraphy	Depth (m)	Grain size (μm)	Water content (%)	U (ppm)	Th (ppm)	Rb (ppm)	K (%)	Dose rate (Gy/ka)
CMQ-1	Paleosol	0.80–0.85	90–125	22 ± 3	1.99 ± 0.3	11.27 ± 0.7	103.86 ± 5	1.94 ± 0.04	2.98 ± 0.09
CMQ-2	Paleosol	1.30–1.35	90–125	22 ± 3	1.94 ± 0.3	11.22 ± 0.7	102.50 ± 5	1.94 ± 0.04	2.93 ± 0.09
CMQ-3	Aeolian loess	2.40–2.45	90–125	15 ± 3	2.12 ± 0.3	11.31 ± 0.7	95.46 ± 5	1.81 ± 0.04	2.96 ± 0.09
CMQ-4	Aeolian loess	2.50–2.55	90–125	15 ± 3	2.26 ± 0.3	9.73 ± 0.6	94.43 ± 5	1.87 ± 0.04	2.97 ± 0.09
CMQ-5	OFD2	7.10–7.15	90–125	20 ± 3	1.76 ± 0.3	10.37 ± 0.7	94.22 ± 5	1.92 ± 0.04	2.69 ± 0.08
CMQ-6	OFD2	9.60–9.65	90–125	20 ± 3	1.83 ± 0.3	9.85 ± 0.6	92.62 ± 5	1.82 ± 0.04	2.58 ± 0.08
CMQ-7	OFD1	15.10–15.15	90–125	20 ± 3	1.82 ± 0.3	10.94 ± 0.7	88.80 ± 4	1.75 ± 0.04	2.50 ± 0.08
CMQ-8	OFD1	17.80–17.90	90–125	20 ± 3	1.77 ± 0.3	10.30 ± 0.7	89.61 ± 4	1.73 ± 0.04	2.43 ± 0.08
ZHK-3	OFD2	8.50–8.60	90–125	20 ± 3	2.04 ± 0.3	11.63 ± 0.7	103.40 ± 5	1.98 ± 0.04	2.82 ± 0.08
ZHK-4	OFD1	15.10–15.20	90–125	20 ± 3	1.87 ± 0.3	11.24 ± 0.7	89.67 ± 4	1.96 ± 0.04	2.70 ± 0.08
ZHK-5	OFD1	16.50–16.60	90–125	20 ± 3	1.78 ± 0.3	9.74 ± 0.6	88.82 ± 4	1.72 ± 0.04	2.39 ± 0.08
ZHK-6	OFD1	17.80–17.90	90–125	20 ± 3	1.28 ± 0.3	7.44 ± 0.6	84.37 ± 4	1.67 ± 0.04	2.13 ± 0.07
ZHK-7	Paleochanneldeposits	25.90–26.00	90–125	20 ± 3	1.84 ± 0.3	12.52 ± 0.7	84.32 ± 4	1.67 ± 0.04	2.48 ± 0.08
ZHK-8	Paleochannel deposits	26.00–26.10	90–125	20 ± 3	1.72 ± 0.3	9.45 ± 0.6	76.07 ± 4	1.55 ± 0.04	2.18 ± 0.07

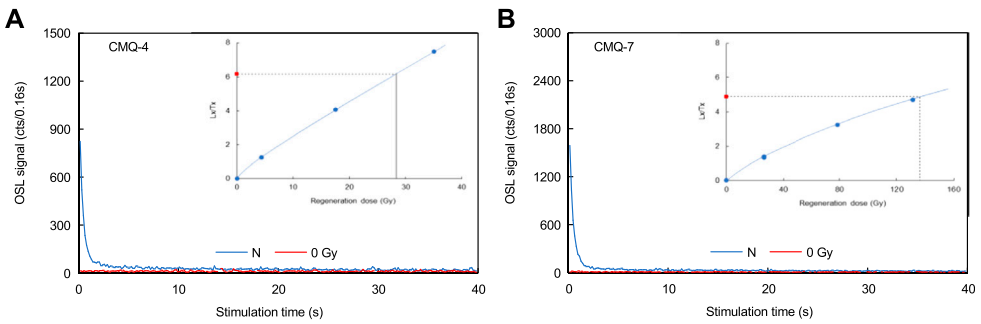

FIGURE 4
Growth and decay curves for the samples **(A)** CMQ-4 and **(B)** CMQ-7 from the CMQ and ZHK profiles in the Yellow River source area on the NE Tibetan Plateau.

post-depositional mixing or a combination of these, we used the R package 'Luminescence' (Kreutzer et al., 2012) that offers plot_KDE() (KDE: kernel density estimates) (Figure 5) and radial plots (Supplementary Figure S3) for dose distribution visualization to assess the luminescence samples. In addition, another approach is based on the assumption that partially bleached samples show not only a large scatter of *De* values but also a trend of rising paleodose with increasing OSL intensity. This can be identified by plotting the sensitivity corrected OSL signal against the corresponding *De* value (Li, 2001) (Supplementary Figure S4).

The central age model (CAM) and the minimum age model (MAM) were used to estimate the burial dose in this study (Galbraith et al., 1999). We used a formal decision process for selecting between these models, based on values of sample statistics such as overdispersion (*OD*), skewness (*sk*), kurtosis (*Kg*) and relative standard deviation (*RSD*) (Arnold et al., 2007). The CAM is used for estimating *De* values of well-bleached samples such as CMQ-1, CMQ-2, CMQ-3 and CMQ-4 with low *OD* values (<15%). In addition, the samples CMQ-7, CMQ-8 and ZHK-7 with high *OD* values (>15%) and a broad range of *De* values, but which display only slight asymmetry. The CAM is also appropriate for calculating *De* values for these samples (Arnold et al., 2007). However, other samples such as CMQ-5, CMQ-6, ZHK-3, ZHK-4, ZHK-5, ZHK-6 and ZHK-8 with high *OD* values (>15%) and asymmetric and/or positively skewed *De* values indicate incomplete zeroing and the MAM is more appropriate for calculating *De* values for these samples (Arnold et al., 2007) (Figure 5 and Table 5).

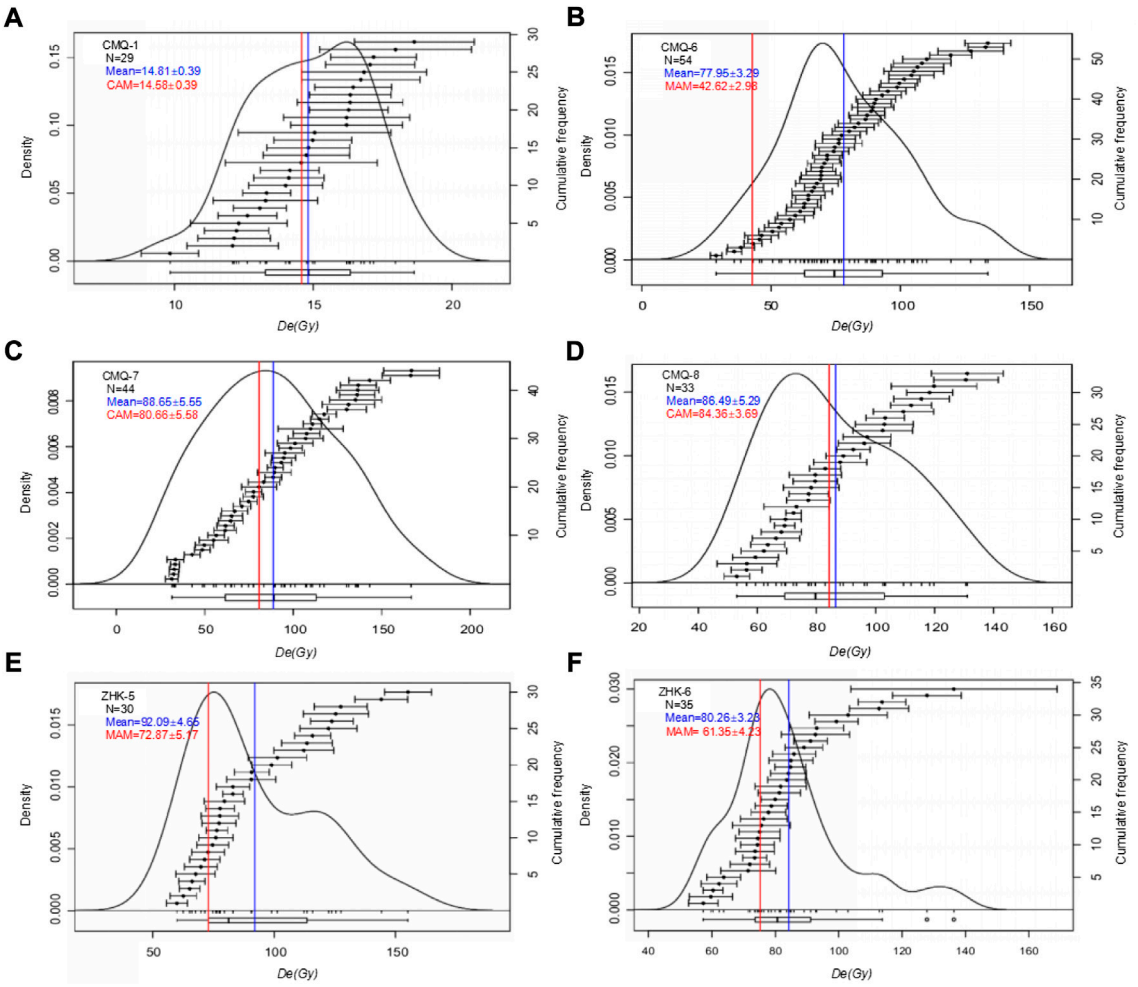

FIGURE 5
Plot_KDE() (KDE: kernel density estimates) for sample **(A)** CMQ-1, **(B)** CMQ-6, **(C)** CMQ-7, **(D)** CMQ-8 and **(E)** ZHK-5, **(F)** ZHK-6 from the CMQ and ZHK profiles in the Yellow River source area on the NE Tibetan Plateau.

The U, Th and Rb concentrations were measured by a Thermo Fisher iCAP 7,400 inductively coupled plasma-optical emission spectrometer (ICP-OES). And the K concentration was analyzed by a Thermo Fisher iCAP RQ inductively coupled plasma mass spectrometer (ICP-MS) (Table 4). The cosmic-ray dose rate was estimated for each sample as a function of depth, altitude and geomagnetic latitude (Prescott and Hutton, 1994). The total dose rates were calculated using the conversion factors of Guerin et al. (2011). The water content was estimated from field measurements of the water content when collected and the saturation water content.

AMS ^{14}C dating was measured in the Beta Analytic Radiocarbon Dating Laboratory in America, and the Calib 8.20 procedure and IntCal20 Northern Hemisphere radiocarbon age calibration curve were used for age correction (Stuiver and Reimer, 1993; Reimer et al., 2020).

4 Results and interpretations

4.1 Geophysical features

The variation curve of magnetic susceptibility is very similar to that of hygroscopic water in the CMQ profile in the Yellow River source area (Figure 6 and Table 6). The higher values of magnetic susceptibility (37.60×10^{-8}-78.20×10^{-8} m^3/kg, 85.80×10^{-8}-114.10×10^{-8} m^3/kg) and the hygroscopic water (1.13%-1.83%, 1.52%-2.04%) are shown in the paleosol and modern soil, suggesting the intensified pedogenic modification to the accumulated dust (Jia et al., 2022). The lower values of magnetic susceptibility (29.50×10^{-8}-34.60×10^{-8} m^3/kg, 29.70×10^{-8}-39.30×10^{-8} m^3/kg) and hygroscopic water (0.85–0.95%, 0.91–1.11%) in the loess levels (aeolian loess, transitional loess) indicating that they remained as

TABLE 5 The equivalent dose values and OSL ages for samples taken from overbank flood deposits (OFD), paleosol, aeolian loess, paleochannel deposits, and glacial outwash/flashflood deposits in the CMQ and ZHK profiles in the Yellow River source area on the NE Tibetan Plateau.

Sample ID	Sediment and stratigraphy	N	*OD* (%)	RSD (%)	*Sk*	σ_{sk}	*Kg*	σ_k	Mean De (Gy)	*De* (Gy)	OSL date (a)
CMQ–1	Paleosol	29	10	14	-0.29	0.45	-0.39	0.91	14.81 ± 0.39	14.58 ± 0.39CAM	4,890 ± 190
CMQ–2	Paleosol	21	5	12	0.16	0.53	-1.04	1.07	22.69 ± 0.60	22.32 ± 0.58CAM	7,630 ± 300
CMQ–3	Aeolian loess	16	1	12	0.27	0.61	0.19	1.22	39.11 ± 1.14	39.40 ± 1.09CAM	13,300 ± 550
CMQ–4	Aeolian loess	14	5	12	0.49	0.65	0.08	1.31	39.91 ± 1.23	39.74 ± 1.14CAM	13,400 ± 560
CMQ–5	OFD2	35	29	31	0.67	0.41	2.09	0.83	59.46 ± 3.10	37.66 ± 3.26 MAM	14,000 ± 1,280
CMQ–6	OFD2	54	31	31	0.34	0.33	-0.12	0.67	77.95 ± 3.29	42.62 ± 2.98MAM	16,500 ± 1,250
CMQ–7	OFD1	44	45	41	0.24	0.37	0.28	0.74	88.65 ± 5.55	80.66 ± 5.58CAM	32,260 ± 2,450
CMQ–8	OFD1	33	23	28	0.41	0.43	-0.84	0.85	86.49 ± 5.29	84.36 ± 3.69CAM	34,680 ± 1880
ZHK–3	OFD2	25	27	25	0.50	0.46	0.24	0.98	67.01 ± 3.58	43.60 ± 3.23MAM	15,460 ± 1,220
ZHK–4	OFD1	14	21	26	0.82	0.65	0.17	1.31	96.18 ± 6.69	79.40 ± 7.29MAM	29,450 ± 2,840
ZHK–5	OFD1	30	25	28	0.81	0.45	-0.27	0.89	92.09 ± 4.65	72.87 ± 5.17MAM	30,500 ± 2,370
ZHK–6	OFD1	35	21	21	0.43	0.41	0.74	0.83	80.26 ± 3.23	61.35 ± 4.23MAM	29,000 ± 1790
ZHK–7	Paleochannel deposits	22	23	27	1.28	0.52	2.38	1.04	102.81 ± 6.02	81.67 ± 7.18CAM	32,930 ± 2070
ZHK–8	Paleochannel deposits	27	20	22	-0.52	0.48	-0.14	0.94	88.22 ± 3.48	69.35 ± 5.67MAM	31,810 ± 2,780

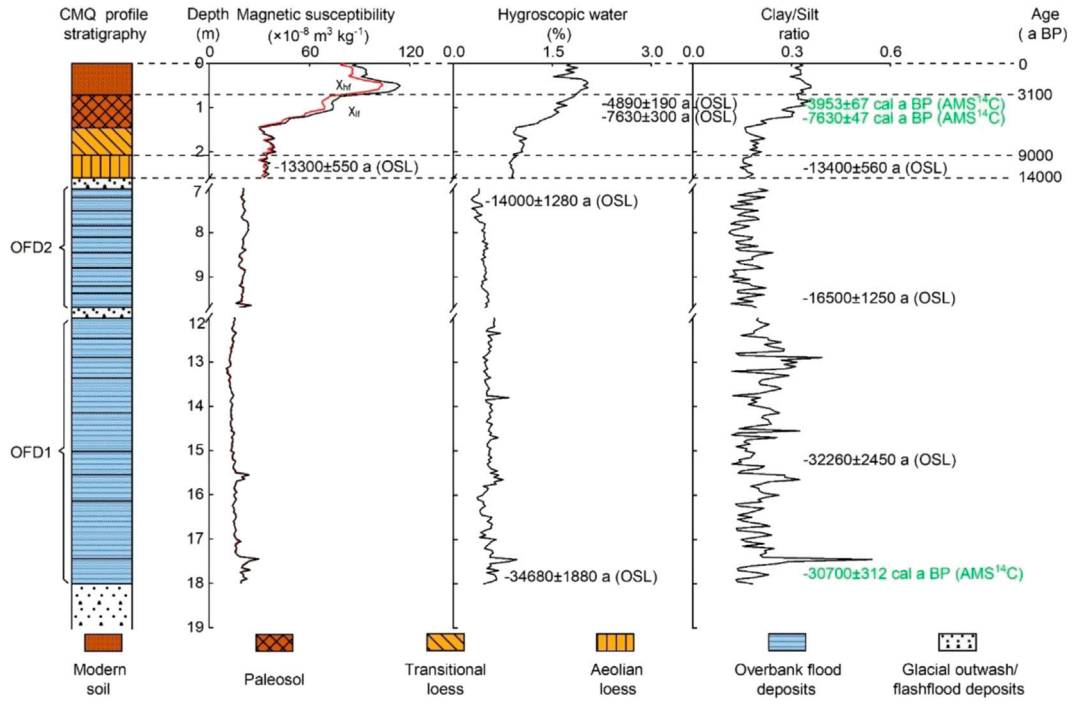

FIGURE 6
Pedo-stratigraphy, magnetic susceptibility, hygroscopic water concentration, clay/silt ratio in the CMQ profile in the Yellow River source area on the NE Tibetan Plateau.

accumulated dust and experienced very weak weathering and pedogenesis processes. The lowest values of magnetic susceptibility (10.10×10^{-8}–28.60×10^{-8} m^3/kg, 16.00×10^{-8}-25.00×10^{-8} m^3/kg) and hygroscopic water (0.37%-0.96%, 0.28%-0.54%) occur in the overbank flood deposits (OFD1, OFD2). This shows that these sediments were deposited in a

TABLE 6 Magnetic susceptibility, hygroscopic water concentration and grain size distribution in the Yellow River source area on the NE Tibetan Plateau.

Pedo-stratigraphic subdivisions	Magnetic susceptibility ($\times10^{-8}$ m^3/kg)	Hygroscopic water (%)	<2 μm (%)	2-16 μm (%)	16-63 μm (%)	>63 μm (%)	Md (μm)	Mz (μm)	Clay/Silt ratio
Modern soil	85.80–114.10	1.52–2.04	11.80–13.60	26.10–33.70	36.10–40.50	15.62–21.49	19.02–29.50	14.33–18.67	0.30–0.33
Paleosol	37.60–78.20	1.13–1.83	8.28–12.80	21.20–33.80	35.70–43.10	17.67–27.46	19.35–38.92	15.19–25.68	0.19–0.36
Transitional loess	29.70–39.30	0.91–1.11	6.89–9.39	18.80–23.00	42.20–45.30	23.16–30.90	34.24–42.66	35.24–43.66	0.16–0.22
Aeolian loess	29.50–34.60	0.85–0.95	6.55–8.16	17.00–21.20	41.40–45.70	25.91–34.60	37.77–46.81	38.77–47.81	0.14–0.18
OFD2	16.00–25.00	0.28–0.54	4.27–9.64	8.65–18.10	25.70–48.00	30.52–60.80	44.64–73.61	26.59–59.83	0.11–0.24
OFD1	10.10–28.60	0.37–0.96	2.28–15.20	3.81–41.20	12.70–60.90	12.50–78.00	11.76–96.61	11.61–94.15	0.12–0.54

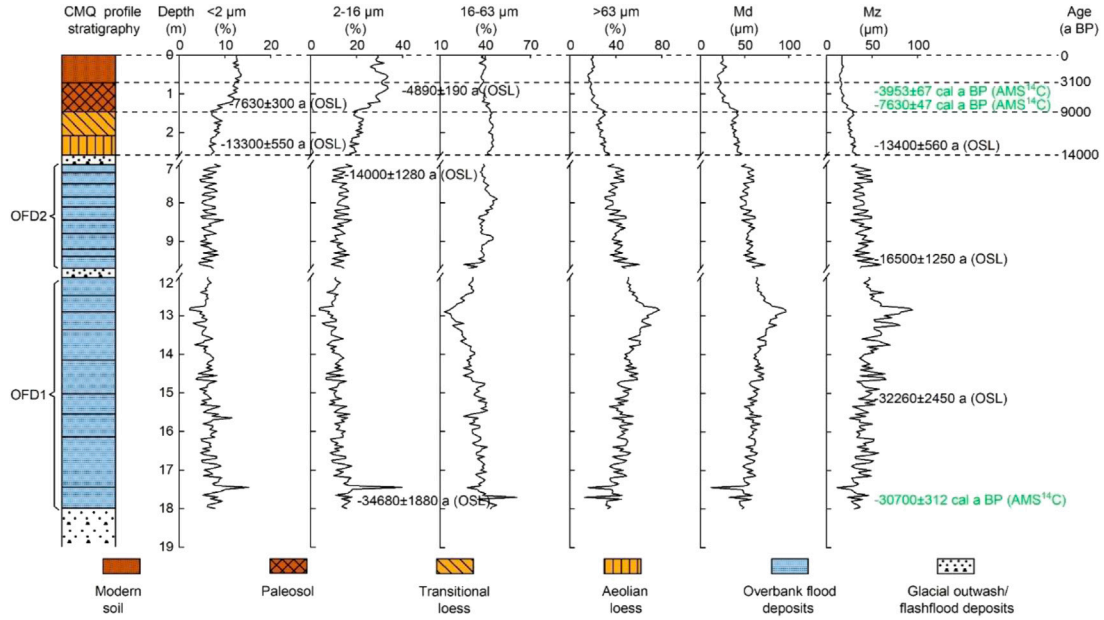

FIGURE 7
Pedo-stratigraphy and grain size distribution in the CMQ profile in the Yellow River source area on the NE Tibetan Plateau.

very short period of time and preserved immediately after the flood recession.

The grain size distribution and the statistical indices of these sediments in the CMQ profile are shown in Figure 7, Supplementary Figure S5 and Table 6. The variation curves of clay/silt ratio, clay (<2 μm) and fine silt (2-16 μm) concentrations are consistent with that of magnetic susceptibility and hygroscopic water. They are generally high in the paleosol/modern soil and low in the aeolian loess/transitional loess. That is, the paleosol and modern soil have a higher clay content because of pedogenic alteration of the accumulated aeolian dust. The sand (>63 μm) content is low in the paleosol/modern soil and high in the aeolian loess/transitional loess. It can be inferred that the loess levels with an increased sand content have recorded extremely intensified aeolian activity over the river valley, which resulted from the incursion of some fluvial deposits and slope clastics into the loess (Li et al., 2018). The sand (>63 μm) content of the OFD units is the highest in the profile, inferring that the overbank flooding with strong transporting energy that can carry coarse sediments.

Grain size distribution frequency curves of the CMQ profile are shown in Figure 8A and Figure 8B. Compared to the grain size distribution frequency curves of aeolian loess and transitional loess, the paleosol and modern soil in the CMQ profile present three peaks centered at: (i) 30-80 μm (peak 1); (ii) 2-10 μm (peak 2); and (iii) 200-300 μm (peak 3) (Figure 8A). It shows that the content of

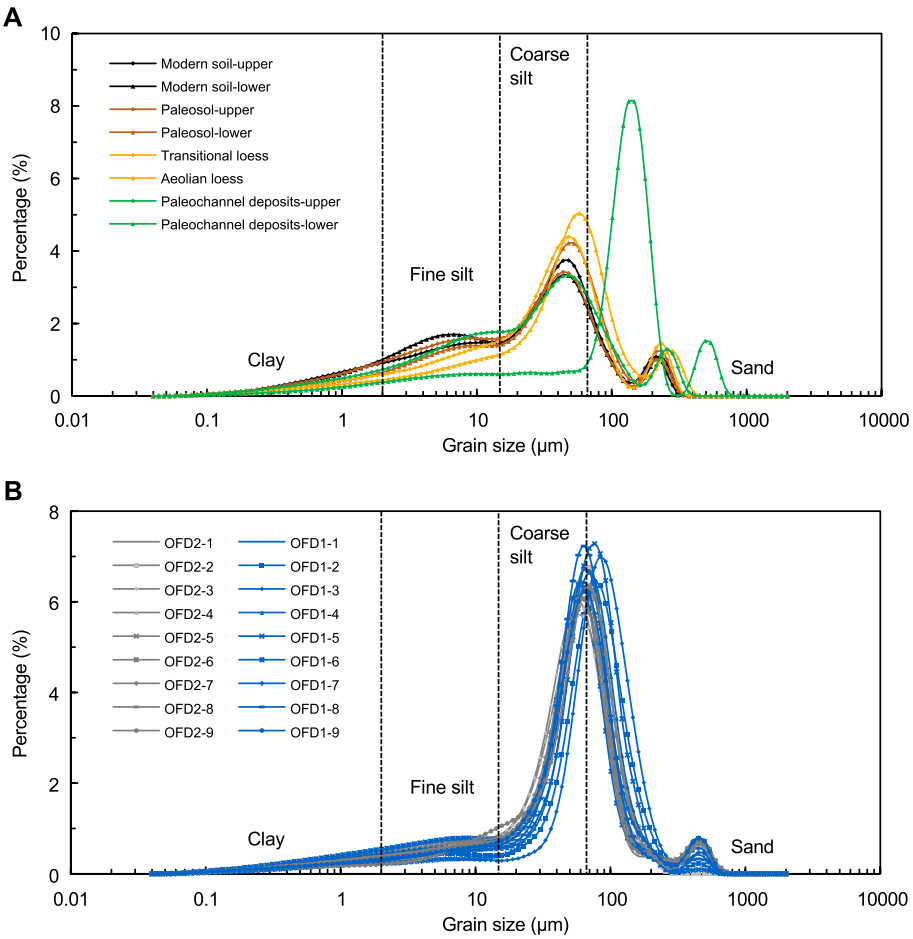

FIGURE 8
A comparison of grain size distribution frequency curves among **(A)** aeolian loess-paleosol deposits and Paleochannel deposits, **(B)** prehistoric overbank flooding deposits (OFD) in the CMQ profile in the Yellow River source area on the NE Tibetan Plateau.

secondary clay and fine silt are increasing under the influence of pedogenic alteration (Chen et al., 2021). Therefore, the paleosol and modern soil are defined as silt. It is also mixed with some fluvial deposits and slope clastics carried by valley wind from the nearby area (Li et al., 2018; Jia et al., 2022). The grain size distribution frequency curves of the upper and lower of the paleochannel deposits are significantly different, and their major peak centered at 25-75 μm and 90-200 μm, respectively. The shape of grain size distribution curves of the OFD units are very different from that of the aeolian loess/soil as well as paleochannel deposits, and are clearly shifted to the coarse side (Figure 8B). It shows a high-narrow major peak centered at 50-120 μm. The OFD1 and OFD2 units are classified as sandy silt or sand. The grain size indices, such as mode (*Md*), mean (*Mz*), skewness (*Sk*), and kurtosis (*Kg*), sorting (*S*) values also differentiate the OFD units, aeolian loess/soil and paleochannel deposits well in the profile (Supplementary Figure S5).

The micro-morphological features of the thin sections observed by the polarizing microscope can clearly differentiate the overbank flood deposits (OFD) from the aeolian loess/soil in the CMQ and ZHK profiles (Figure 9). The paleosol is characterized by round to sub-round coarse grains, high porosity and medium abundance of secondary calcite crystallite (pseudomycelia) in the pores (Figure 9A). The loess is characterized by angular to sub-angular coarse grains, simple packing bio-pores (Figure 9B). However, the OFD units consist of coarser well-rounding grains (Figure 9C and Figure 9D). Their distribution is very loose and the grain size is relatively uniformity, manifesting that they were mainly deposited from suspended sediment load in floodwaters.

4.2 OSL and AMS^{14}C ages

As shown in Figure 10, the pedo-stratigraphy in the CMQ profile is well synchronous with the ZHK profile in the Yellow River source area. Overall, the OSL and AMS^{14}C ages at the same

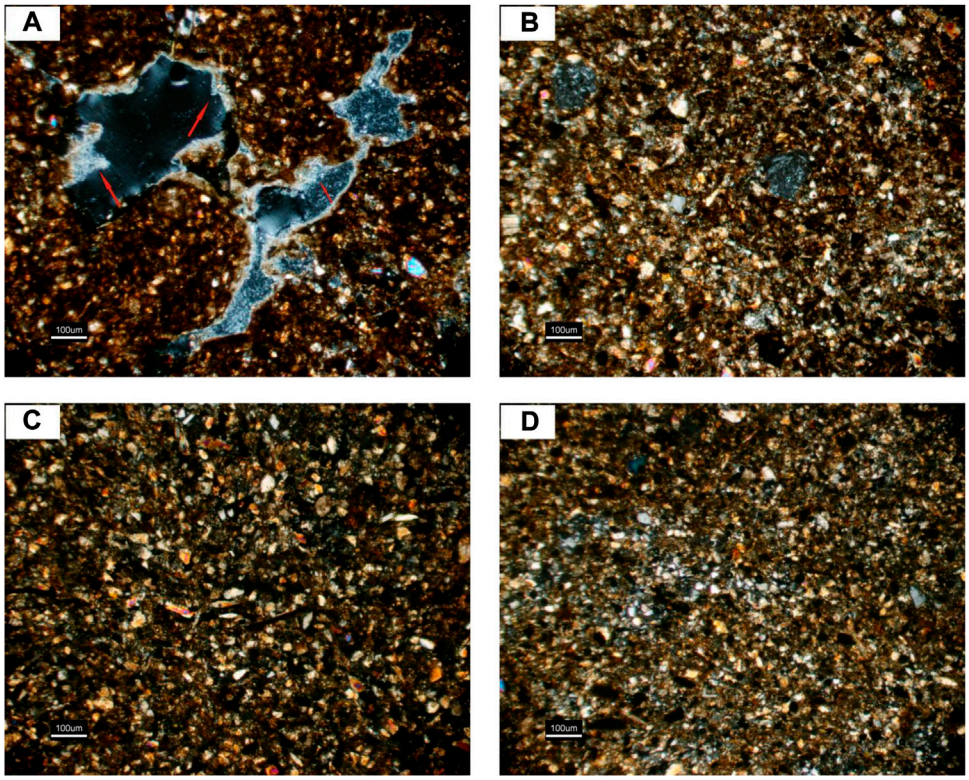

FIGURE 9
Micro-morphological features in the ZHK and CMQ profiles in the Yellow River source area on the NE Tibetan Plateau. **(A)** Micro-morphological features of the paleosol in the CMQ profile with needle-shaped secondary-calcite (10 × 5, crossed polarized light); **(B)** Micro-morphological features of the aeolian loess in the ZHK profile (10 × 5, crossed polarized light); **(C)** Micro-morphological features of the overbank flooding deposits (OFD1) in the CMQ profile (10 × 5, crossed polarized light); **(D)** Micro-morphological features of the overbank flooding deposits (OFD1) in the ZHK profile (10 × 5, crossed polarized light).

level in the CMQ and ZHK profiles are consistent (Figure 10). The OFD1 unit was found at the depth range of 12.00–18.00 m in the CMQ profile and 15.00–18.00 m in the ZHK profile. OSL ages from the middle (15.10–15.15 m) and the bottom (17.80–17.90 m) of the OFD1 in the CMQ profile are 32,260 ± 2,450 a and 34,680 ± 1880 a, respectively. In addition, the similar AMS^{14}C age (30,700 ± 312 cal a BP) is also obtained from the bottom of the OFD1 in the CMQ profile. And the top, middle and bottom of OFD1 in the ZHK profile were OSL dated to 29,450 ± 2,840 a, 30,500 ± 2,370 a and 29,000 ± 1790 a, respectively. The first episode of overbank flooding was therefore within a bracket of 34,680 ± 1880-29000 ± 1790 a. The OFD2 unit was identified at the depth range of 7.00–9.70 m in the CMQ profile and 7.50–9.00 m in the ZHK profile. The top (7.10–7.15 m) and the lower (9.60–9.65 m) of the OFD2 unit in the CMQ profile were OSL dated to 14,000 ± 1,280 a and 16,500 ± 1,250 a, respectively. The middle (8.50–8.60 m) of the OFD2 unit in the ZHK profile yielded an OSL age of 15,460 ± 1,220 a. It can be concluded that the second episode of overbank flooding occurred at 16,500 ± 1,250-14000 ± 1,280 a.

5 Discussion

5.1 The first episode of overbank flooding

The first episode overbank flooding occurred at 34,680 ± 1880-29000 ± 1790 a that correlated with the late Marine Isotope Stage 3a (MIS 3a) (Imbrie et al., 1984; Shi and Yu, 2003; Pu et al., 2010; Chen et al., 2014). Previous studies have shown that Asian summer monsoon is highly sensitive to the insolation difference caused by the earth orbital change (Prell and Kutzbach, 1992). During the period of MIS 3a, the incident radiation in the region between 50°N and 30°S was 20 W/m^2 higher than that of modern and the increase in the incident radiation resulted in the rise of air temperature (Shi et al., 1999) (Supplementary Figure S6), which led continental ice sheets retreated significantly, mountain glaciers melted and sea levels rose (Wang and Yao, 2002). Especially in the Yellow River source area, rising temperatures will inevitably lead to the melting of surrounding mountain glaciers. In addition, due to increased heat input, the difference of thermal

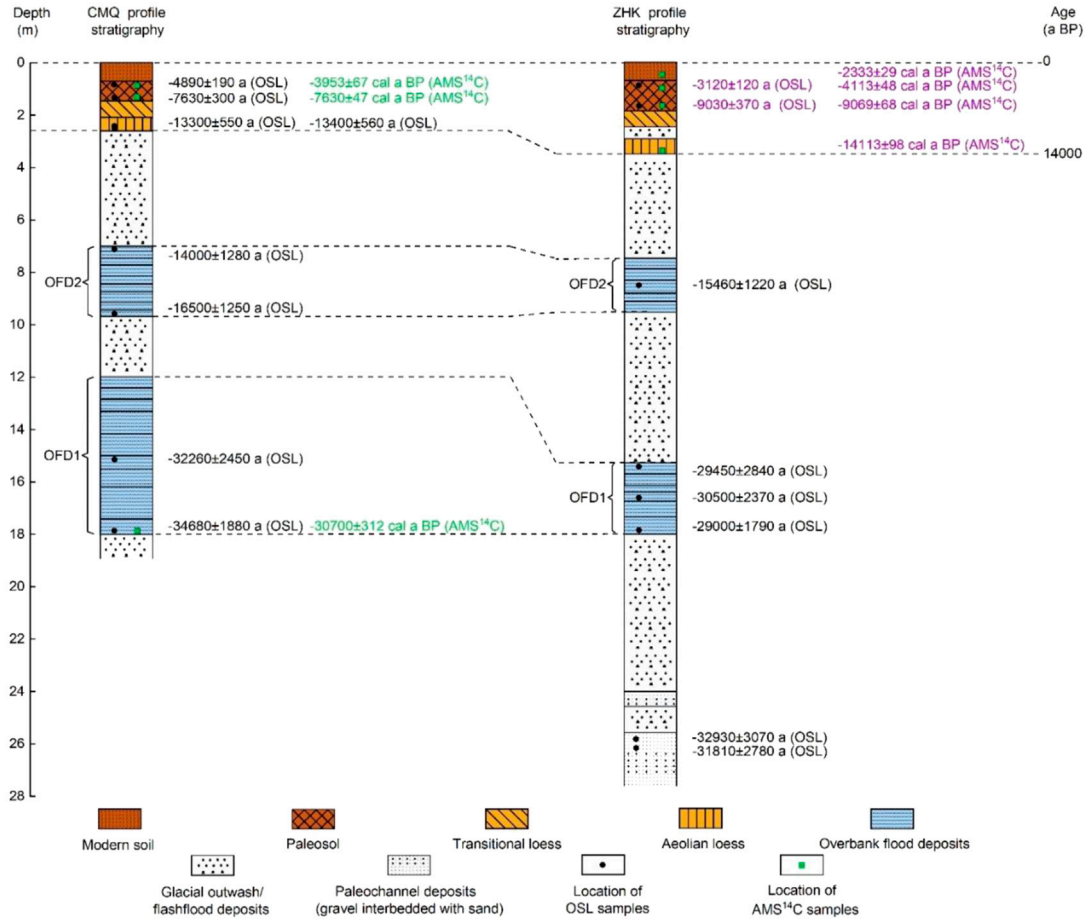

FIGURE 10
Pedo-stratigraphy and chronostratigraphic framework of the CMQ and ZHK profiles in the Yellow River source area on the NE Tibetan Plateau. [The dating data indicated in purple is taken from Jia et al. (2022)].

properties between land and sea increases, the East Asian summer monsoon (EASM) as well as the evaporation of the tropic and sub-tropic Indian Ocean surface was strengthened. At the same time, the cross-equatorial airflow moving towards the Northern Hemisphere may intensify the Indian summer monsoon (ISM). The ISM and EASM carried a large amount of moisture as moving over the ocean surface and formed the exceptionally strong summer monsoon on the Tibetan Plateau, which formed a large area of abundant precipitation (Shi et al., 1999).

Climate proxies in all over the world sensitively recorded the warm and wet climate characteristics during this period (Figure 11). Solar radiation in summer at 65°N (Berger and Loutre, 1991), <4 μm grain fractions of Shijiu Lake core (Wang, 2016), TOC content of cores LV53-23 in the Japan Sea (Zong, 2016), $\delta^{18}O$ concentration in Guliya ice core (Yao et al., 1997), $\delta^{18}O$ concentration in GRIP2 (Grootes et al., 1993; Stuiver and Grootes, 2000), CPI_h, ACL_h and pollen concentrations in Qarhan Salt Lake sediments (Pu et al., 2010) and simulated precipitation in Central Asia (Li X Z et al., 2013) were all higher during the MIS 3a. But the Mz of the Jingyuan loess profile (Wang, 2016), the Md of the South China Sea SO17940 core (Wang, 2016) and the $\delta^{18}O$ concentration of the Hulu Cave Stalagmite (Wang et al., 2001) are lower in this period, indicating that the global climate was mainly warm and wet during the MIS 3a.

In addition, high-resolution climatic proxies in the Tibetan Plateau and its surrounding areas record the warm and wet climatic characteristics in the MIS 3a. For example, the profiles containing trees and neutral herbaceous pollen in Qinghai Lake Basin, NE Tibetan Plateau, increased significantly at 39,000-26000 a, reflecting a relatively warm and humid environment (Shan et al., 1993). The profile in the eastern Bangong Co. paleolake on the western Tibetan Plateau was the most abundant in pollen and types at 36,000-28000 a, indicating that the climate was warmer and wetter than the present (Huang et al., 1989). The paleontological fossils of

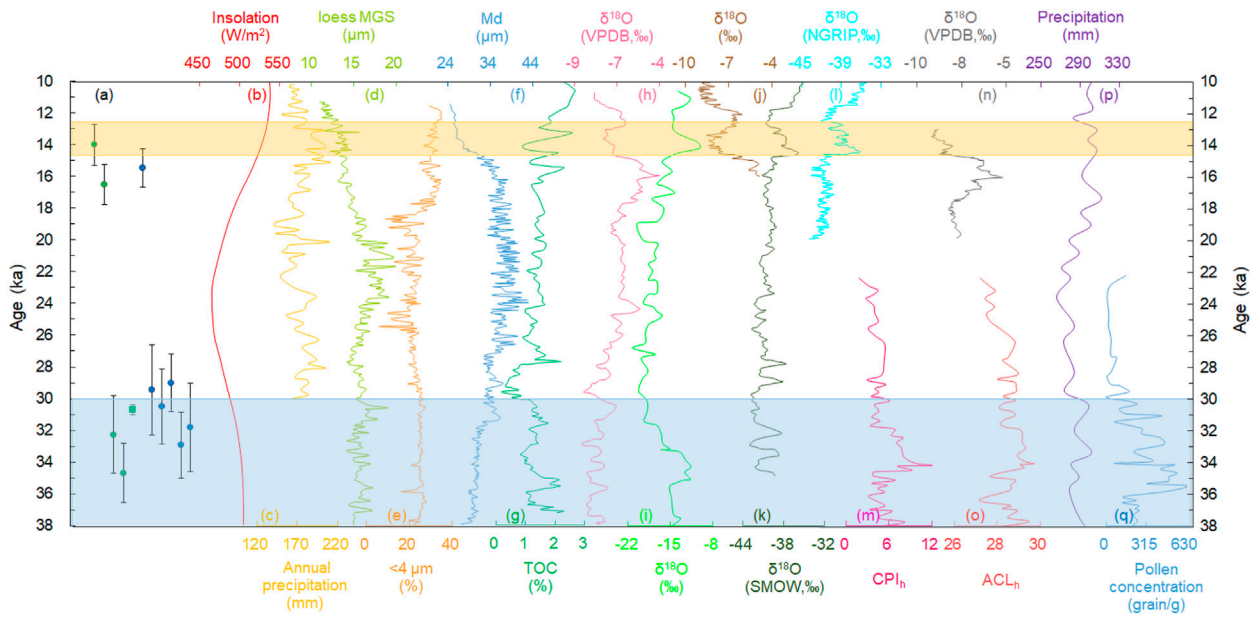

FIGURE 11
(A) The ages of OFD units in CMQ and ZHK profiles (Green and blue dots represent the OSL ages of CMQ and ZHK profile respectively; The green square represents AMS ^{14}C age of the CMQ profile), **(B)** Variation curve of solar radiation in summer at 65°N (Berger and Loutre, 1991), **(C)** precipitation reconstructed from rock core in Balikun Lake (Zhao, 2017), **(D)** The Mz of the Jingyuan loess profile (Wang, 2016), **(E)** <4 μm grain fractions of Shijiu Lake core (Wang, 2016), **(F)** The Md of the South China Sea SO17940 core (Wang, 2016), **(G)** TOC content of cores LV53-23 in the Japan Sea (Zong, 2016), **(H)** The $\delta^{18}O$ concentration of the stalagmite in Hulu Cave (Wang et al., 2001),**(I)** The $\delta^{18}O$ concentration in Guliya ice core (Yao et al., 1997), **(J)** The $\delta^{18}O$ concentration of the stalagmite in Dongge Cave (Dykoski et al., 2005), **(K)** The $\delta^{18}O$ concentration in GRIP2 (Grootes et al., 1993; Stuiver and Grootes, 2000), (L) The $\delta^{18}O$ concentrations in Greenland ice cores (Basak et al., 2018), (M) The CPI_h in Qarhan Salt Lake sediments (Pu et al., 2010), (N) The $\delta^{18}O$ concentration of the stalagmite in Haozhu Cave (Zhang et al., 2016), (O) The ACL_h in Qarhan Salt Lake sediments (Pu et al., 2010), (P) The simulated precipitation in Central Asia (Li X Z et al., 2013), (Q) The pollen concentrations in Qarhan Salt Lake sediments (Pu et al., 2010) (The blue and yellow rectangles represent MIS3a and Bøling-Allerød stages respectively).

pelobranchids, gastropods and ostracids in the shell deposits on the east of Qarhan Salt Lake indicate that the lake was fresh-brackish water at 38,000-28050 a BP, and the lake area was larger and the lake surface was higher during this period, which was about 2.56 times as large as the modern one (Chen and Bowler, 1985). The Baijian Lake in the tengger desert on the north of the Tibetan plateau appeared a high lake level 30 m higher than the modern lake level in 39,000–23000 a BP, suggesting that precipitation generally increased in the Tibetan Plateau during this period (Pachur et al., 1995; Li, 2000; Li et al., 2008). The $\delta^{18}O$ curve of Guliya ice-core in west Kunlun shows that the temperature is the highest in the MIS3a, the temperature and precipitation at this period are 2-4 °C and 40%-100% higher than those in modern, respectively (Shi et al., 2002, 1999). All these evidences indicated that the Tibetan Plateau had a warm and wet climate between 34,680 ± 1880 and 29,000 ± 1790 a.

Previous studies have shown that during the last glacial period, the ancient glaciers of the Anyemaqen Mountains may have reached the Yellow River, with an altitude of 2,650 m at the end and a snow line of 4,125 m (Kuhle et al., 1987). The total glacier area of Qiequ valley on the eastern slope and Zhihaidai valley on the western slope is 156.7 km^2 (Deng et al., 2004). In addition, geological and chronological evidence of glacial advance has been found at multiple sites on the Tibetan Plateau and surrounding mountains during the MIS 3b (Zhao et al., 2007; Wang, 2010). Significant glacial advance also took place in Anyemaqen and Nianbaoyuze Mountains during the MIS 3b (Owen et al., 2003, 2006). In both regions, glaciation was most extensive during the MIS3 (Anyemaqen and Jiukehe Glacial Stages) (Zheng et al., 1994; Lehmkuhl, 1998), which was represented by expanded ice caps and long valley glaciers that advanced ~15 km beyond the present glacier margins (Owen et al., 2003). However, mountain glaciers are very sensitive to temperature changes (Ali et al., 2015). With the advent of MIS 3a, the climate became warm-humid, and the mountain glaciers around the Yellow River Source area are bound to melt in large quantities. There are lateral moraines overtopped the surface of the lake on both sides of Ximen Co Lake on the NE Tibetan Plateau, and the moraines at both ends are obviously higher than the front of the lake. The age of aeolian loess on the moraine ridge is 32,000 ± 3,000 a, which indicates that the glacier had begun to

retreat before that period (Lehmkuhl, 1998). There are many moraine ridges in the 6-10 km north of the Ximen Co Lake, and the age of exposure moraine above them indicates that the glaciers retreat at 42,000-19000 a BP (Owen et al., 2003). Therefore, we have reason to believe that during the MIS 3a period with a very warm and humid climate, the water mainly derived from the accelerated melting of mountain glaciers from both sides and/or the large-scale precipitation flowed into the Yellow River source course, resulting in the overbank flooding. Moreover, the overbank flooding carried abundant sediment, which covered the glacial outwash/flashflood deposits, and intensified the channel accretion.

5.2 The second episode of overbank flooding

The second episode overbank flooding recorded by OFD2 unit in the CMQ and ZHK profiles was dated to 16,500 ± 1,250-14000 ± 1,280 a, which is coincided with the Bølling-Allerød warm and humid period (Dykoski et al., 2005; Basak et al., 2018) of the last deglaciation (19,000-11000 a BP) (Pedro et al., 2011; Clark et al., 2012). At that time, the incident radiation in the northern hemisphere in summer was 20 W/m^2 higher than that of present (Shi et al., 1999) (Supplementary Figure S6). Under this climate background, the increase of incident radiation would still result in the rise of air temperature in the Yellow River source area, which would lead to the massive melting of mountain glaciers. Beyond that, the increase of incident radiation would expand the difference of thermal properties between land and sea, which would contribute to intensifying the EASM and increasing precipitation on the Tibetan Plateau.

Various climate proxies around the world also have been recorded the climate characteristics of the period (Figure 11). Solar radiation in summer at 65°N (Berger and Loutre, 1991), precipitation reconstructed from rock core in Balikun Lake (Zhao, 2017), <4 μm grain fractions of Shijiu Lake core (Wang, 2016),TOC content of cores LV53-23 in the Japan Sea (Zong, 2016), δ^{18}O concentration in Guliya ice core (Yao et al., 1997), δ^{18}O concentration in GRIP2 (Grootes et al., 1993; Stuiver and Grootes, 2000), δ^{18}O concentrations in Greenland ice cores (Basak et al., 2018) and simulated precipitation in Central Asia (Li G F et al., 2013) were all higher in 14,700–12500 a BP. The *Mz* of the Jingyuan loess profile (Wang, 2016), the *Md* of the South China Sea SO17940 core (Wang, 2016) and the δ^{18}O concentration of the stalagmite in Hulu Cave (Wang et al., 2001), Dongge Cave (Dykoski et al., 2005) and Haozhu Cave (Zhang et al., 2016) are lower, indicating that the global climate was mainly warm and wet during this period.

The grain-size characteristics of Macheng profile on NE Jianghan Plain show that the temperature rose rapidly and the precipitation increased significantly at ca. 17,900-12050 a BP. And the climate is characterized by warm, wet and rainy as a whole (Zhang et al., 2020). High-resolution pollen records in the Dalianhai sediment cores on NE Tibetan Plateau show that tree pollen increased at 14,800–12900 cal a BP, indicating that forests developed in nearby mountains and the climate was warm and humid. In addition, the grassland coverage increases around Gonghe Basin (Cheng et al., 2010). In 14,100-12700 a BP, the Qinghai Lake vegetation changed from desert-steppe to forest-steppe, indicating a significant increase in temperature and humidity over the northeastern Tibetan Plateau during this period (Shen et al., 2005). Climate reconstruction of n-alkanes from Zabuye Lake cores in the Tibetan Plateau shows that woody plants are abundant and has a relatively warm climate in 15,600–12500 a BP (An et al., 2012; Jin, et al., 2015; Ling et al., 2017).

Previous studies have shown that during the Last Glacial Maximum (26,500-19000 a BP) (Clark et al., 2012), the global temperature was low, the glaciers were widely covered on the NE Tibetan Plateau, and the glacial advances of Anyemaqen and Nianbaoyuze mountains occurred during the Last Glacial Maximum. During this period, the glacial areas of Anyemaqen and Nianbaoyuze mountains were 8 and 206 times that of modern glaciers respectively. And their snow line height was 1,000 m lower than that of modern glaciers (Edward et al., 1991; Shi, 2022). However, since the last deglaciation, the global temperature has increased significantly. The mountain glaciers (or ice caps) on the NE Tibetan Plateau have inevitably melted in large quantities (Zhong et al., 2021). This large-scale meltwater event caused super floods in Europe, North and South America (Tomasson, 1996; Baker, 2013). The large-scale melting of the ice sheet also caused a large amount of meltwater to pour into the sea, which led the coastline retreated and the continental shelf was submerged. And the global average sea level rose substantially (Huang and Tian, 2008). Many lakes on the Tibetan Plateau such as Qinghai Lake, Selinco Lake and Longmuco Lake have rapidly increased due to the rapid increase of glacial melt water, and a large amount of ice water has been injected into the lakes, leading to the expansion of lakes and the rise of water level (Jia et al., 2001).

Therefore, we believe that second episode of overbank flooding recorded by OFD2 in the CMQ and ZHK profiles in the Yellow River Source area was due to the significant increase in temperature and the EASM significantly strengthened during the Bølling-Allerød period. In the meanwhile, the monsoon state is unstable, the mountain glaciers and ice caps melt rapidly in a large range, and the snowmelt water increases abnormally in the Yellow River source area. The water mainly derived from the accelerated melting of mountain glaciers surrounding the basin and/or the large-scale precipitation flowed into Yellow River, which led to the overbank flooding events (Qiu, 2008; Cuo et al., 2015; Chen et al., 2021).

6 Conclusion

During our paleohydrological investigations, two units of overbank flood deposits were found in the sediment sequences at Chameiqu (CMQ) and Zuhaka (ZHK) sites in the Maqu-Kesheng reach in the Yellow River source area. These paleoflood OFD units were studied using a multi-index approach, including magnetic susceptibility, hygroscopic water, grain size distribution and micro-morphological features. Based on field observations and laboratory analysis, it can be inferred that these paleoflood OFD units were deposited from the sediment load in Yellow River floodwaters. They have recorded two episodes of overbank flooding, which were dated to 34,680 ± 1880-29000 ± 1790 a and 16,500 ± 1,250-14000 ± 1,280 a respectively. The first episode was dated to 34,680 ± 1880-29000 ± 1790 a and correlated with the late Marine Isotope Stage 3a (MIS 3a) with a warm and wet climate. The second episode occurred at 16,500 ± 1,250-14000 ± 1,280 a, which is coincided with the Bølling-Allerød of the last deglaciation, a period of coexisting global warming and rapidly shrinking ice sheets. At these two periods, the water mainly derived from the accelerated melting of mountain glaciers surrounding the basin and/or the large-scale precipitation flowed into Yellow River, which led to the overbank flooding events. Obviously, the related overbank flood deposits were interbedded within glacial outwash/flashflood deposits in the valley bottom of the Yellow River, which intensified the valley aggradation.

Data availability statement

The original contributions presented in the study are included in the article/Supplementary Material, further inquiries can be directed to the corresponding author.

Author contributions

YaZ: Conceptualization, Methodology Software, Writing-Original Draft; HW: Data Curation, Writing-Original Draft; Investigation Formal Analysis YuZ: Conceptualization, Funding Acquisition, Writing-Review and Editing. CCH: Visualization, Investigation XZ: Resources, Supervision; HQ: Software Validation Y-nJ: Visualization, Writing-Review and Editing QX: Resources DC: Resources XL: Methodology Software TL: Supervision. All authors contributed to the article and approved the submitted version.

Funding

This work was supported by the grants from the Second Tibetan Plateau Scientific Expedition and Research Program (2019QZKK0903), the National Science Foundation of China (42277449, 41801060, 4197116), Strategic Priority Research Program of the Chinese Academy of Sciences (XDA20060201), and the Open Foundation of The State Key Laboratory of Loess and Quaternary Geology (SKLLQG2107).

Conflict of interest

The authors declare that the research was conducted in the absence of any commercial or financial relationships that could be construed as a potential conflict of interest.

Publisher's note

Supplementary material

The Supplementary Material for this article can be found online at: https://www.frontiersin.org/articles/10.3389/feart.2022.1021106/full#supplementary-material

SUPPLEMENTARY FIGURE S1
Close shot of the clay cap and silt at the top of OFD1-9 at CMQ profile in the Yellow River source area on the NE Tibetan Plateau.

SUPPLEMENTARY FIGURE S2
(A) Photo of deposits at the bottom of the ZHK profile and **(B)** riverbed gravels interbedded with sand in paleochannel deposits in the ZHK profile in the Yellow River source area on the NE Tibetan Plateau.

SUPPLEMENTARY FIGURE S3
Radial plots for sample **(A)** CMQ-1, **(B)** CMQ-6, **(C)** CMQ-7, **(D)** CMQ-8 and **(E)** ZHK-5, **(F)** ZHK-6 from the CMQ and ZHK profiles in the Yellow River source area on the NE Tibetan Plateau. These plots both present the D_e distributions and illustrate the spread in the data and how the modeled minimum or central age maps onto the distributions.

SUPPLEMENTARY FIGURE S4
Plots of single-aliquot D_e versus sensitivity corrected natural OSL signal for the sample **(A)** CMQ-1, **(B)** CMQ-6, **(C)** CMQ-7, **(D)** CMQ-8 and **(E)** ZHK-5, **(F)** ZHK-6 from the CMQ and ZHK profiles in the Yellow River source area on the NE Tibetan Plateau.

SUPPLEMENTARY FIGURE S5
Characteristic value diagram of grain size parameters showing the grain size distribution in the CMQ profile in the Yellow River source area on the NE Tibetan Plateau.**(A)** 3-D stereogram of skewness (*Sk*), standard deviation (δ) and kurtosis (*Kg*); **(B)** 3-D stereogram of mean (*Mz*), median (*Md*) and sorting coefficient (*S*).

SUPPLEMENTARY FIGURE S6
Insolation departures in July relative to the present values at various latitudes during the past 125 ka BP (W/m^2) (The blue rectangle and the yellow rectangle represent the Bølling-Allerød and MIS3a period) (Shi et al., 1999).

References

Ali, Z., Liu, W. L., Wang, X. D., Zainab, I., Zona, Z., Raza, S. T., et al. (2015). Glacier receding and ecological thresholds for Tibetan Plateau and associated cryosphere. *J. Animal Plant Sci.* 25 (3), 278–296.

An, Z. S., Colman, S. M., Zhou, W. J., Li, X. Q., Brown, E. T., Timothy Jull, A. J., et al. (2012). Interplay between the Westerlies and Asian Monsoon recorded in lake Qinghai sediments since 32 ka. *Sci. Rep.* 2, 619. doi:10.1038/srep00619

Arnold, L. J., Bailey, R. M., and Tuckerd, G. E. (2007). Statistical treatment of fluvial dose distributions from southern Colorado arroyo deposits. *Quat. Geochronol.* 2, 162–167. doi:10.1016/j.quageo.2006.05.003

Baker, V. R. (2013). 9.26 global late Quaternary fluvial paleohydrology: With special emphasis on paleofloods and megafloods. *Treatise Geomorphol.* 9, 511–527. doi:10.1016/b978-0-12-374739-6.00252-9

Baker, V. R., Benito, G., Brown, A. G., Carling, P. A., Enzel, Y., Greenbaum, N., et al. (2022). Fluvial palaeohydrology in the 21st century and beyond. *Earth Surf. Process. Landf.* 47, 58–81. doi:10.1002/esp.5275

Basak, C., Froellje, H., Lamy, F., Gersonde, R., Benz, V., Anderson, R., et al. (2018). Breakup of last glacial deep stratification in the South. Pacific. *Science* 359 (6378), 900–904. doi:10.1126/science.aao2473

Benito, G., Harden, T. M., and O'Connor, J. E. (2022). 6.35-Quantitative paleoflood hydrology. *Treatise Geomorphol.* 7, 743–764.

Benito, G., Thorndycraft, V. R., Rico, M., Sánchez-Moya, Y., and Sopeña, A. (2008). Palaeoflood and floodplain records from Spain: Evidence for long-term climate variability and environmental changes. *Geomorphology* 101, 68–77. doi:10.1016/j.geomorph.2008.05.020

Berger, A., and Loutre, M. F. (1991). Insolation values for the climate of the last 10 million years. *Quat. Sci. Rev.* 10, 297–317. doi:10.1016/0277-3791(91)90033-q

Chahal, P., Kumar, A., Sharma, C. P., Singhal, S., Sundriyal, Y. P., and Srivastava, P. (2019). Late Pleistocene history of aggradation and incision, provenance and channel connectivity of the Zanskar River, NW Himalaya. *Glob. Planet. Change* 178, 110–128. doi:10.1016/j.gloplacha.2019.04.015

Chaudhary, S., Shukla, U. K., Sundriyal, Y. P., Srivastava, P., and Jalal, P. (2015). Formation of paleovalleys in the Central Himalaya during valley aggradation. *Quat. Int.* 371, 254–267. doi:10.1016/j.quaint.2014.12.064

Chen, K. Z., and Bowler, J. M. (1985). Preliminary study on sedimentary characteristics and paleoclimate evolution of qarhan Salt Lake in Qaidam Basin. *Sci. Sin.* 5, 463–473.

Chen, M. Y., Xu, S. L., Wu, Z. H., Li, Y. H., Zhao, X. T., Zhang, K. Q., et al. (2014). The features and ages of lake beach rock around Sayram Lake in Western Tian Shan and its significance on lake level fluctuation during the last interglacial epoch MIS3. *J. Geomechanics* 20 (2), 174–184. (In Chinese with English abstract).

Chen, Y. L., Huang, C. C., Zhang, Y. Z., Zhou, Y. L., Zha, X. C., Wang, N. L., et al. (2021). Palaeoflood events during the last deglaciation in the Yellow River source area on the northeast Tibetan Plateau. *Geol. J.* 56, 4293–4309. doi:10.1002/gj.4164

Cheng, B., Chen, F. H., and Zhang, J. W. (2010). Palaeovegetational and palaeoenvironmental changes in GongheBasin since last deglaciation. *Acta Geogr. Sin.* 65 (11), 1336–1344. (In Chinese with English abstract).

Clark, P. U., Shakun, J. D., Baker, P. A., Bartlein, P. J., Brewer, S., Brook, E., et al. (2012). Global climate evolution during the last deglaciation. *Proc. Natl. Acad. Sci. U. S. A.* 109 (19), 1134–1142. doi:10.1073/pnas.1116619109

Cuo, L., Zhang, Y. X., Bohn, T. J., Zhao, L., Li, J. L., Liu, Q. M., et al. (2015). Frozen soil degradation and its effects on surface hydrology in the northern Tibetan Plateau. *J. Geophys. Res. Atmos.* 120 (6), 8276–8298. doi:10.1002/2015jd023193

Deng, X. F., Liu, S. Y., Ding, Y. J., Shen, Y. P., Zhao, L., and Xie, C. W. (2004). Quaternary glaciations and environment change in the Anyemaqen Mountains. *J. Glaciol. Geocryol.* 26 (3), 305–311. (In Chinese with English abstract).

Duller, G. (2015). The Analyst software package for luminescence data: Overview and recent improvements. *Anc. TL* 3, 35–42.

Dykoski, C. A., Edwards, R. L., Cheng, H., Yuan, D. X., Cai, Y. J., Zhang, M. L., et al. (2005). A high-resolution, absolute-dated Holocene and deglacial Asian Monsoon record from Dongge Cave, China. *Earth Planet. Sci. Lett.* 233 (1-2), 71–86. doi:10.1016/j.epsl.2005.01.036

Edward, D., Shi, Y. F., Li, J. J., Zheng, B. X., Li, S. J., and Wang, J. T. (1991). Quaternary glaciation of Tibet: The geological evidence. *Quat. Sci. Rev.* 10 (6), 485–510. doi:10.1016/0277-3791(91)90042-s

England, J. F., Jr., Godaire, J. E., Klinger, R. E., Bauer, T. R., and Julien, P. Y. (2010). Paleohydrologic bounds and extreme flood frequency of the Upper Arkansas River, Colorado, USA. *Geomorphology* 124 (1-2), 1–16. doi:10.1016/j.geomorph.2010.07.021

Galbraith, R. F., Roberts, R. G., Laslett, G. M., Yoshida, H., and Olley, J. M. (1999). Optical dating of single and multiple grains of quartz from Jinmium rock shelter, northern Australia. Part I. *Archaeometry* 41, 339–364. doi:10.1111/j.1475-4754.1999.tb00987.x

Greenbaum, N., Schwartz, U., Carling, P., Bergman, N., Mushkin, A., Zituni, R., et al. (2020). Frequency of boulders transport during large floods in hyperarid areas using paleoflood analysis-An example from the Negev Desert, Israel. *Earth-Science Rev.* 202, 103086. doi:10.1016/j.earscirev.2020.103086

Grootes, P. M., Stuiver, M., White, J. W. C., Johnsen, S., and Jouzel, J. (1993). Comparison of oxygen isotope records from the GISP2 and GRIP Greenland ice cores. *Nature* 366 (6455), 552–554. doi:10.1038/366552a0

Guerin, G., Mercier, N., and Adamiec, G. (2011). Dose-rate conversion factors: Update. *Anc. TL* 29, 5–8.

Guo, B., Wei, C. X., Yu, Y., Liu, Y. F., Li, J. l., Meng, C., et al. (2022). The dominant influencing factors of desertification changes in the source region of Yellow River: Climate change or human activity? *Sci. Total Environ.* 813, 152512. doi:10.1016/j.scitotenv.2021.152512

Guo, Y. Q., Huang, C. C., Pang, J. L., Zhou, Y. L., Zha, X. C., and Mao, P. N. (2017). Reconstruction palaeoflood hydrology using slackwater flow depth method in the Yanhe River valley, middle Yellow River basin, China. *J. Hydrology* 544, 156–171. doi:10.1016/j.jhydrol.2016.11.017

He, W. G., Xiong, Z., Yuan, D. Y., Ge, W. P., and Liu, X. W. (2006). Paleo-earthquake study on the Maqu fault of East Kunlun active fault. *Earthq. Res. China* 2, 126–134. [in Chinese with English abstract]

Hu, G. Y., Yu, L. P., Dong, Z. B., Lu, J. F., Li, J. Y., Wang, Y. X., et al. (2018). Holocene aeolian activity in the Zoige Basin, northeastern Tibetan Plateau, China. *Catena* 160, 321–328. doi:10.1016/j.catena.2017.10.005

Hu, Y. R., Maskey, S., Uhlenbrook, S., and Zhao, H. L. (2011). Stream flow trends and climate linkages in the source region of the Yellow River, China. *Hydrol. Process.* 25 (22), 3399–3411. doi:10.1002/hyp.8069

Huang, C. C., Pang, J. L., Zha, X. C., and Zhou, Y. L. (2011). Prehistorical floods in the Guanzhong Basin in the Yellow River drainage area: A case study along the Qishuihe River valley over the Zhouyuan loess tableland. *Sci. China Earth Sci.* 41 (11), 1658–1669. (In Chinese).

Huang, C. X., Zhang, Q. S., and Liu, F. T. (1989). A Preliminary study of paleovegetation and paleoclimate in the later period of late Pleistocene in the Bangong Co Lake region of Xizang. *J. Nat. Resour.* 3, 247–253. (In Chinese with English abstract).

Huang, C. Y. (2001). *Soil science*. Beijing: China Agriculture Press. (In Chinese).

Huang, E. Q., and Tian, J. (2008). Glacial meltwater events and abrupt climate change during the last deglaciation. *Chin. Sci. Bull.* 53 (12), 1437–1447. (In Chinese).

Imbrie, J., Hays, J. D., Martinson, D. G., McIntyre, A., and Shackleton, N. J. (1984). "The orbital theory of Pleistocene climate: Support from a revised chronology of the marine $\delta^{18}O$ record," in *Milankovitch and climate*. Editors A. Berger, J. Imbrie, J. Hays, G. Kukla, and B. Saltzman (Dordrecht: D. Reidel Publishing Company), 269–305.

IPCC (2007). *The fourth assessment report of the intergovernmental panel on climate change*. Cambridge: Cambridge University Press.

Jia, Y. L., Shi, Y. F., Wang, S. M., Jiang, X. Z., Li, S. J., Wang, A. J., et al. (2001). Preliminary study on four periods of lake flooding and their formation mechanism in the Tibetan Plateau since 40 ka. *Sci. Sin.* S1, 241–251 [(in Chinese with English abstract].

Jia, Y. N., Zhang, Y. Z., Huang, C. C., Wang, N. L., Qiu, H. J., Wang, H. Y., et al. (2022). Late pleistocene-holocene aeolian loess-paleosol sections in the Yellow River source area on the northeast Tibetan plateau: Chronostratigraphy, sediment provenance, and implications for paleoclimate reconstruction. *Catena* 28, 105777. doi:10.1016/j.catena.2021.105777

Jin, Z. D., An, Z. S., Yu, J. M., Li, F. C., and Zhang, F. (2015). Lake Qinghai sediment geochemistry linked to hydroclimate variability since the last glacial. *Quat. Sci. Rev.* 122, 63–73. doi:10.1016/j.quascirev.2015.05.015

Kemp, R. A. (1999). Micromorphology of loess–paleosol sequences: A record of paleoenvironmental change. *Catena* 35 (2-4), 179–196. doi:10.1016/s0341-8162(98)00099-x

Knox, J. C. (2000). Sensitivity of modern and Holocene floods to climate change. *Quat. Sci. Rev.* 19, 439–457. doi:10.1016/s0277-3791(99)00074-8

Kochel, R. C., and Baker, V. R. (1982). Paleoflood hydrology. *Science* 215, 353–361. doi:10.1126/science.215.4531.353

Kreutzer, S., Schmidt, C., Fuchs, M. C., Dietze, M., Fischer, M., and Fuchs, M. (2012). Introducing an R package for luminescence dating analysis. *Anc. TL* 30 (1), 1–8.

Kuhle, M., Hovemann, J., and Wang, W. J. (1987). *Reports on the northeastern part of the Qinghai-Xizang (Tibet) Plateau*. Beijing: Science Press. (In Chinese).The problem of a Pleisocene in land glaciation of the northeastern Qinghai-Xizang Plateau

Kukla, G., and An, Z. S. (1989). Loess stratigraphy in central China. *Palaeogeogr. Palaeoclimatol. Palaeoecol.* 72 (89), 203–225. doi:10.1016/0031-0182(89)90143-0

Lehmkuhl, F. (1998). Extent and spatial distribution of Pleistocene glaciations in eastern Tibet. *Quat. Int.* 45/46, 123–134. doi:10.1016/s1040-6182(97)00010-4

Lehmkuhl, F., and Spönemann, J. (1994). Morphogenetic problems of the upper Huang He drainage Basin. *GeoJournal* 34 (1), 31–40. doi:10.1007/bf00813967

Li, B. Y. (2000). The last greatest lakes on the Xizang (Tibetan) Plateau. *Acta Geogr. Sin.* 2, 174–182. (In Chinese with English abstract).

Li, G. F., Wang, C., Wang, Z. F., Hua, J. P., Ge, C. X., and Deng, J. H. (2013). Study on probable maximum flood in source region of Yellow River. *J. Hohai Univ. Nat. Sci.* 41 (2), 102–107. (In Chinese with English abstract).

Li, G. Q., Zhang, H. X., Liu, X. J., Yang, H., Zhang, X. J., Jonell, T. N., et al. (2020). Paleoclimatic changes and modulation of East Asian summer monsoon by high-latitude forcing over the last 130, 000 years as revealed by independently dated loess-paleosol sequences on the NE Tibetan Plateau. *Quat. Sci. Rev.* 237, 106283. doi:10.1016/j.quascirev.2020.106283

Li, J. C., Yang, Y. G., and Zhang, C. X. (2011). Quantitative study on influencing factors of desertification in headwater area of Yellow River. *J. Arid Land Resour. Environ.* 25 (2), 88–92 [in Chinese with English abstract].

Li, S. H. (2001). Identification of well-bleached grains in the optical dating of quartz. *Quat. Sci. Rev.* 20 (12), 1365–1370. doi:10.1016/s0277-3791(00)00156-6

Li, S. J., Shi, Y. F., and Wang, S. M. (1995). *The evolution, environment change and ecosystem study of Qinghai-Xizang Plateau*. Beijing: Science Press. (In Chinese).Geological record of climatic and environmental changes in Zoige Basin during the last 30000 years//The steering commission of the qinghai-xizang Program

Li, S. J., Zhang, H. L., Shi, Y. F., and Zhu, Z. Y. (2008). A high-resolution MIS 3 environmental change record derived from lacustrine deposit of Tianshuihai Lake, Qinghai-Tibet Plateau. *Quat. Sci.* 1, 122–131. (In Chinese with English abstract).

Li, S., Yang, S. L., Liang, M. H., Cheng, T., Chen, H., and Liu, N. N. (2018). The end member model analysis on grain size of loess in the eastern Tibetan plateau. *Earth Environ.* 46 (4), 331–338. (In Chinese with English abstract).

Li, X. Z., Liu, X. D., Qiu, L. J., An, Z. S., and Yin, Z. Y. (2013). Transient simulation of orbital-scale precipitation variation in monsoonal East Asia and arid central Asia during the last 150 ka. *J. Geophys. Res. Atmos.* 118, 7481–7488. doi:10.1002/jgrd.50611

Li, Z. W., Wang, Z. Y., Tian, S. M., and Zhang, C. D. (2014). Variation of stream-flow and sediment discharge rate and relationship with temperature change in Yellow River source area. *J. Sediment Res.* 3, 28–35. (In Chinese with Chinese abstract).

Ling, Y., Zheng, M. P., Sun, Q., and Dai, X. Q. (2017). Last deglacial climatic variability in Tibetan Plateau as inferred from n-alkanes in a sediment core from Lake Zabuye. *Quat. Int.* 454, 15–24. doi:10.1016/j.quaint.2017.08.030

Liu, T. S. (1985). *Loess and the environment*. Beijing: Science Press. (In Chinese).

Liu, W. M., Carling, P. A., Hu, K. H., Wang, H., Zhou, Z., Zhou, L. Q., et al. (2019). Outburst floods in China: A review. *Earth-Science Rev.* 197, 102895. doi:10.1016/j.earscirev.2019.102895

Liu, X. M., Liu, D. S., and John, S. (1993). Characteristics of magnetic minerals in Chinese loess and their paleoclimatic significance. *Quat. Sci.* 3, 281–287. (In Chinese with English abstract).

Maher, B. A. (1998). Magnetic properties of modern soils and Quaternary loessic paleosols: Paleoclimatic implications. *Palaeogeogr. Palaeoclimatol. Palaeoecol.* 137 (1-2), 25–54. doi:10.1016/s0031-0182(97)00103-x

Mao, P. N., Pang, J. L., Huang, C. C., Zha, X. C., Zhou, Y. L., Guo, Y. Q., et al. (2022). Paleoflood evidence for an upper limit of the maximum flood magnitudes along the Gold Gorge, the upper Hanjiang River, China. *Catena* 212, 106111. doi:10.1016/j.catena.2022.106111

Mao, P. N., Pang, J. L., Huang, C. C., Zha, X. C., Zhou, Y. L., Guo, Y. Q., et al. (2016). A multi-index analysis of the extraordinary paleoflood events recorded by slackwater deposits in the Yunxi Reach of the upper Hanjiang River, China. *Catena* 145, 1–14. doi:10.1016/j.catena.2016.05.016

Meng, F. C., Su, F. G., Yang, D. Q., Tong, K., and Hao, Z. C. (2016). Impacts of recent climate change on the hydrology in the source region of the Yellow River basin. *J. Hydrology Regional Stud.* 6, 66–81. doi:10.1016/j.ejrh.2016.03.003

Munoz, S. E., Giosan, L., Therrell, M. D., Remo, J. W. F., Shen, Z. X., Sullivan, R. M., et al. (2018). Climatic control of Mississippi River flood hazard amplified by river engineering. *Nature* 556, 95–98. doi:10.1038/nature26145

Murray, A. S., and Wintle, A. G. (2000). Luminescence dating of quartz using an improved single aliquot regenerative-dose protocol. *Radiat. Meas.* 32 (1), 57–73. doi:10.1016/s1350-4487(99)00253-x

Murray, A. S., and Wintle, A. G. (2003). The single aliquot regenerative dose protocol: Potential for improvements in reliability. *Radiat. Meas.* 37 (4-5), 377–381. doi:10.1016/s1350-4487(03)00053-2

Owen, L. A., Finkel, R. C., Haizhou, M., Spencer, J. Q., Derbyshire, E., Barnard, P. L., et al. (2003). Timing and style of late quaternary glaciation in northeastern Tibet. *Geol. Soc. Am. Bull.* 115 (11), 1356–1364. doi:10.1130/b25314.1

Owen, L. A., Finkel, R. C., Ma, H. Z., and Barnard, P. L. (2006). Late quaternary landscape evolution in the Kunlun Mountains and qaidam basin, northern Tibet: A framework for examining the links between glaciation, lake level changes and alluvial fan formation. *Quat. Int.* 154/155, 73–86. doi:10.1016/j.quaint.2006.02.008

Pachur, H. J., Wunneman, B., and Zhang, H. C. (1995). Lake evolution in the Tengger Desert, northwestern China, during the last 40, 000 years. *Quat. Res.* 44, 171–180. doi:10.1006/qres.1995.1061

Panda, S., Kumar, A., Das, S., Devrani, R., Rai, S., Prakash, K., et al. (2020). Chronology and sediment provenance of extreme floods of Siang River (Tsangpo-Brahmaputra River valley), northeast Himalaya. *Earth Surf. Process. Landf.* 45 (11), 2495–2511. doi:10.1002/esp.4893

Peng, H., Zheng, Y. S., and Shang, H. X. (2014). Analysis on flood variation characteristics in tangnaihe River and its upstream of the Yellow River. *J. North China Univ. Water Resour. Electr. Power (Natural Sci. Ed.* 35 (6), 18–20. (In Chinese with English abstract).

Prell, W. L., and Kutzbach, J. E. (1992). Sensitivity of the Indian monsoon to forcing parameters and implications for its evolution. *Nature* 360, 647–652. doi:10.1038/360647a0

Prescott, J. R., and Hutton, J. T. (1994). Cosmic ray contributions to dose rates for luminescence and ESR dating: Large depths and long-term time variations. *Radiat. Meas.* 23 (2-3), 497–500. doi:10.1016/1350-4487(94)90086-8

Prizomwala, P., Yadava, G. J., Solanki, T., Das, A., Chauhan, G., and Makwana, N. (2019). Style and stages of valley fill aggradation-incision cycles in the Northern Hill Range, Kachchh, Western India. *Quat. Int.* 510, 18–27. doi:10.1016/j.quaint.2018.11.020

Przemyslaw, M. (2013). Recycled loesses-a micromorphological approach to the determination of local source areas of Weichselian loess. *Quat. Int.* 296 (16), 241–250. doi:10.1016/j.quaint.2013.02.040

Pu, Y., Zhang, H. C., Lei, G. L., Chang, F. Q., Yang, M. S., Zhang, W. X., et al. (2010). Climate variability recorded by n-alkanes of paleolake sediment in Qaidam Basin on the northeast Tibetan Plateau in late MIS3. *Sci. China Earth Sci.* 40 (5), 624–631. (In Chinese).

Qiu, J. (2008). China: The third pole. *Nature* 454 (7203), 393–396. doi:10.1038/454393a

Reimer, P. J., Austin, W. E. N., Bard, E., Bayliss, A., Blackwell, P. G., Bronk, R. C., et al. (2020). The IntCal20 Northern Hemisphere radiocarbon age calibration curve (0-55 cal k BP). *Radiocarbon* 62, 725–757. doi:10.1017/rdc.2020.41

Schulte, L., Schillereff, D., and Santisteban, J. I. (2019). Pluridisciplinary analysis and multi-archive reconstruction of paleofloods: Societal demand, challenges and progress. *Glob. Planet. Change* 177, 225–238. doi:10.1016/j.gloplacha.2019.03.019

Shan, F. S., Du, N. Q., and Kong, Z. C. (1993). Vegetational and environmental changes in the last 350 ka in Erlangjian, Qinghai Lake. *J. Lake Sci.* 5 (1), 9–17. (In Chinese with English abstract). doi:10.18307/1993.0102

Sharma, C. P., Chahal, P., Kumar, A., Singhal, S., Sundriyal, Y. P., Ziegler, A. D., et al. (2022). Late Pleistocene–Holocene flood history, flood-sediment provenance and human imprints from the upper Indus River catchment, Ladakh Himalaya. *GSA Bull.* 134 (1-2), 275–292. doi:10.1130/b35976.1

Shen, C. M., Tang, L. Y., and Wang, S. M. (1996). Vegetation and climate during the last 22000 years in Zoige region. *Acta Micropaleontol. Sin.* 13 (4), 401–406. (In Chinese with English abstract).

Shen, J., Liu, X. Q., Wang, S. M., and Matsumoto, R. (2005). Palaeoclimatic changes in the Qinghai Lake area during the last 18, 000 years. *Quat. Int.* 136 (1), 131–140. doi:10.1016/j.quaint.2004.11.014

Shi, M. X., Lan, Y. C., Shen, Y. P., Tian, H., Wang, X., La, C. F., et al. (2018). Analyses of multiple time scale variation characteristics of pan evaporation and mutation in the source regions of the Yellow River from 1961 to 2014. *J. Glaciol. Geocryol.* 40 (4), 666–675. (In Chinese with English abstract).

Shi, Y. F. (2022). Discussion on temperature lowering values and equilibrium line altitude in the Qinghai-Xizang Plateau during the last Glacial Maximum and their simulated results. *Quat. Sci.* 22 (4), 312–322. (In Chinese with English abstract).

Shi, Y. F., Jia, Y. L., Yu, G., Yang, D. Y., Fan, Y. Q., Li, S. J., et al. (2002). Features, impacts and causes of the high temperature and large precipitation event in the Tibetan Plateau and its adjacent area during 40-30 ka BP. *J. Lake Sci.* 14 (1), 1–11. (In Chinese with English abstract).

Shi, Y. F., Liu, X. D., Li, B. Y., and Yao, T. D. (1999). A very strong summer monsoon event during 30-40 ka BP in the Qinghai-Xizang (Tibet) Plateau and its relation to precessional cycle. *Chin. Sci. Bull.* 44 (20), 1851–1858. doi:10.1007/bf02886339

Shi, Y. F., and Yu, G. (2003). Warm-humid climate and transgressions during 40-30 ka BP and their potential mechanisms. *Quat. Sci.* 23 (1), 1–11. (In Chinese with English abstract).

Srivastava, P., Kumar, A., Chaudhary, S., Meena, N., Sundriyal, Y. P., Rawat, S., et al. (2017). Paleofloods records in Himalaya. *Geomorphology* 284, 17–30. doi:10.1016/j.geomorph.2016.12.011

Srivastava, P., Tripathi, J. K., Islam, R., and Jaiswal, M. K. (2008). Fashion and phases of late Pleistocene aggradation and incision in the Alaknanda River valley, Western Himalaya, India. *Quat. Res.* 70, 68–80. doi:10.1016/j.yqres.2008.03.009

Starkel, L. (2003). Climatically controlled terraces in uplifting mountain areas. *Quat. Sci. Rev.* 22, 2189–2198. doi:10.1016/s0277-3791(03)00148-3

Stuiver, M., and Grootes, P. M. (2000). GISP2 oxygen isotope ratios. *Quat. Res.* 53 (5), 277–284. doi:10.1006/qres.2000.2127

Stuiver, M., and Reimer, P. J. (1993). Extended ^{14}C data base and revised Calib 3.0 ^{14}C age calibration Program. *Radiocarbon* 35 (1), 215–230. doi:10.1017/s0033822200013904

Tomasson, H. (1996). The jokulhlaup from Katla in 1918. *Ann. Glaciol.* 22, 249–254. doi:10.1017/s0260305500015494

Wang, G. X., Li, N., and Hu, H. C. (2009). Hydrologic effect of ecosystem responses to climatic change in the source regions of Yangtze River and Yellow River. *Clim. Change Res.* 5 (4), 202–208. (In Chinese with English abstract).

Wang, J. (2010). Glacial advance in the Qinghai-Xizang Plateau and peripheral mountains during the mid-MIS3. *Quat. Sci.* 30 (5), 1055–1065. (In Chinese with English abstract).

Wang, Q. F., Jin, H. J., Wu, Q. B., Zhang, T. J., and Huang, Y. D. (2017). Climatic evolution since 6 cal. ka B.P. recorded by frozen peat deposits in the source area of the Yellow River northeastern Qinghai-Tibet Plateau. *Quat. Sci.* 37 (2), 402–415. (in Chinese with English abstract).

Wang, X. Y., Liu, Y., Su, Q., Lu, H. Y., Miao, X., Li, Y., et al. (2021). Late Quaternary terrace formation from knickpoint propagation in the headwaters of the Yellow River, NE Tibetan Plateau. *Earth Surf. Process. Landf.* 46, 2788–2806. doi:10.1002/esp.5208

Wang, X. Y., Yang, T., Wang, B., Li, H. H., and Hao, X. B. (2012). Scenarios forecasting of runoff extreme value in source region of Yellow River based on multiple hydrological models. *Water Resour. Power* 30 (3), 27–30. (In Chinese with English abstract).

Wang, Y. (2016). *Climatic and environmental changes recorded in the sediments of Shijiu Lake during 38-11 ka BP*. Nanjing: Nanjing Normal University. (In Chinese with English abstract).

Wang, Y. F., Wang, S. M., Xue, B., Ji, L., Wu, J. L., Xia, W. L., et al. (1995). Sedimentological evidence of the piracy of fossil Zoige Lake by the Yellow River. *Chin. Sci. Bull.* 40 (8), 723–725. (In Chinese).

Wang, Y. J., Cheng, H. Y., Edwards, R. L., An, Z. S., Wu, J. Y., Shen, C. C., et al. (2001). A high-resolution absolute-dated late Pleistocene monsoon record from Hulu Cave, China. *Science* 294 (5550), 2345–2348. doi:10.1126/science.1064618

Wang, Y. Q., and Yao, T. D. (2002). Progresses in the studies of abrupt climatic change events recorded in Ice Cores during the Last Glacial-Interglacial Cycle. *J. Glaciol. Geocryol.* 5, 550–558. (In Chinese with English abstract).

Wu, L., Zhu, C., Ma, C. M., Li, F., Meng, H. P., Liu, H., et al. (2017). Mid-holocene palaeoflood events recorded at the Zhongqiao Neolithic cultural site in the Jianghan Plain, middle Yangtze River valley, China. *Quat. Sci. Rev.* 173, 145–160. doi:10.1016/j.quascirev.2017.08.018

Xue, B., Wang, S. M., Xia, W. L., Wu, J. L., Wang, Y. F., Qian, J. L., et al. (1998). The uplift and environmental change of the Qinghai Tibet Plateau since 900 ka BP revealed by the RM core within the Zoige Basin. *Sci. Sin. (Terrae)* 27 (6), 543–547. (In Chinese).

Yao, T. D., Thompson, L. G., Shi, Y. F., Qin, D. H., Jiao, K. Q., Yang, Z. H., et al. (1997). Records of climate change since the last interglacial period in the Guliya ice core. *Sci. Sin. (Terrae)* 5, 447–452. (In Chinese with English abstract).

Zha, X. C., Huang, C. C., Pang, J. L., Liu, J. F., and Xue, X. Y. (2015). Reconstructing the palaeoflood events from slackwater deposits in the upper reaches of Hanjiang River, China. *Quat. Int.* 380-381 (4), 358–367. doi:10.1016/j.quaint.2014.06.029

Zhang, H. B., Griffiths, M. L., Huang, J. H., Cai, Y. J., Wang, C. F., Zhang, F., et al. (2016). Antarctic link with East Asian summer monsoon variability during the Heinrich Stadial-Bølling interstadial transition. *Earth Planet. Sci. Lett.* 435, 243–251. doi:10.1016/j.epsl.2016.08.008

Zhang, Y. F., Li, C. A., Zhao, J. X., Mao, X., Xu, Y. S., Wei, C. Y., et al. (2020). Grain size characteristics and climatic environmental significance of sediments in the northeastern margin of the Jianghan Plain during the last deglaciation period. *Acta Sedimentol. Sin.* 39 (4), 1–14. (In Chinese with English abstract).

Zhang, Y. Z., Huang, C. C., Pang, J. L., Guo, Y. Q., and Zhou, Q. (2018). Identification of the prehistoric catastrophes at the Lajia Ruins using micromorphological analysis within the Guanting Basin, Minhe County, Qinghai Province. *Archaeol. Anthropol. Sci.* 3, 711–723. doi:10.1007/s12520-017-0509-2

Zhang, Y. Z., Huang, C. C., Tan, Z. H., Chen, Y. L., Qiu, H. J., Huang, C., et al. (2019). Prehistoric and historic overbank floods in the Luoyang Basin along the Luohe River, middle Yellow River basin, China. *Quat. Int.* 521, 118–128. doi:10.1016/j.quaint.2019.06.023

Zhao, J. D., Zhou, S. Z., Liu, S. Y., He, Y. Q., Liu, X. B., and Wang, J. (2007). A preliminary study of the glacier advance in MIS3b in the Western regions of China. *J. Glaciol. Geocryol.* 29 (2), 233–241. (In Chinese with English abstract).

Zhao, M., Zha, X. C., Huang, C. C., and Pang, J. L. (2012). Geochemical characteristics of the Holocene palaeoflood slackwater deposits in Weihe River basin. *J. Soil Water Conservation* 26 (1), 106–111. (In Chinese with English abstract).

Zhao, Y. T. (2017). *Vegetation and climate history around Balikun region from MIS3 to early Holocene (~60-9 ka BP) documented by multi-proxy data of Balikun Lake*. Lanzhou: Lanzhou University. (In Chinese with English abstract).

Zhao, Y., Yu, Z. C., and Zhao, W. W. (2011). Holocene vegetation and climate histories in the eastern Tibetan plateau: Controls by insolation-driven temperature or monsoon derived precipitation changes? *Quat. Sci. Rev.* 30 (9-10), 1173–1184. doi:10.1016/j.quascirev.2011.02.006

Zheng, B. X., Li, S. J., and Wang, S. M. (1994). "The Quaternary glacial evolution of the mountains surrounding Zoige Basin," in *The expert committee on the qingzang Program ed. Study on the formation and evolution of the qinghai-xizang plateau, environmental change and ecological annual academic* (Beijing: Science Press). (In Chinese).

Zhong, N., Jiang, H. C., Li, H. B., Xu, H. Y., and Liang, L. J. (2021). The Impact of climate transition on seismic activities on the eastern margin of the Tibetan Plateau during the last deglaciation. *Acta Geosci. Sin.* 42 (1), 21–31. (In Chinese with English abstract).

Zhou, L., Li, J., Zhang, P., and Jin, Y. (2021). Study on fault structure and stress field characteristics of Maqin-Maqu section of East Kunlun Fault. *J. Geodesy Geodyn.* 41 (1), 62–66. (In Chinese with English abstract).

Zhou, W. J., Yu, S. Y., Burr, G. S., Kukla, G. J., Jull, A. J. T., Xian, F., et al. (2010). Postglacial changes in the asian summer monsoon system: A pollen record from the eastern margin of the Tibetan Plateau. *Boreas* 39, 528–539. doi:10.1111/j.1502-3885.2010.00150.x

Zong, X. (2016). *Paleoenvironmental changes in the Japan Sea during the last hundred years and the last glacial respectively*. Nanjing: Nanjing University.

frontiers | Frontiers in Earth Science

TYPE Original Research
PUBLISHED 04 January 2023
DOI 10.3389/feart.2022.1049740

OPEN ACCESS

EDITED BY
Jie Dou,
China University of Geosciences
Wuhan, China

REVIEWED BY
Jianqi Zhuang,
Chang'an University, China
Zhilu Chang,
Nanchang University, China

*CORRESPONDENCE
Ning Shi,
564770359@qq.com
Liang-liang Li,
yantu05204108@163.com

SPECIALTY SECTION
This article was submitted to Geohazards and Georisks, a section of the journal Frontiers in Earth Science

RECEIVED 21 September 2022
ACCEPTED 02 December 2022
PUBLISHED 04 January 2023

CITATION
Shi N, Li L-l, Ma Y-b, Li Q-j and Bai L-y (2023), Study of deformation characteristics and a strain calculation model for pipelines impacted by landslides.
Front. Earth Sci. 10:1049740.
doi: 10.3389/feart.2022.1049740

Study of deformation characteristics and a strain calculation model for pipelines impacted by landslides

Ning Shi[1,2]*, Liang-liang Li[2]*, Yun-bin Ma[2,3], Qiu-juan Li[2] and Lu-yao Bai[2]

[1]College of Safety and Ocean Engineering, China University of Petroleum, Beijing, China, [2]General Institute of Science and Technology Company of PipeChina, LangFang, China, [3]School of Mechanical Engineering, Xian Jiaotong University, Xian, China

It is not uncommon to see pipelines damaged by landslides. If the maximum strain that landslides exert on pipelines can be calculated from available survey data, then pipeline damage can be more accurately predicted and the safety of the pipeline can be improved. Furthermore, this information can assist targeted prevention and control measures, which should greatly reduce the risk that landslides pose to pipelines. However, although researchers have conducted considerable research on landslide-induced pipeline deformation, there is no model that can calculate the change in pipeline strain under the displacement of landslide material. Based on geological data collected from a buried crude oil pipeline damaged by a landslide near a city in southeast China, this work uses numerical simulations to obtain the deformation parameters of pipelines affected by landslides at different orientations and for different landslide and pipeline parameters. This work also summarizes the deformation characteristics of pipelines affected by landslides under these different variables. A model is then constructed and verified that simulates the change in pipeline strain with soil displacement while considering the characteristics of the landslide mass and the pipeline itself. The results show that the model can sufficiently reflect the influence of various factors that act on pipeline deformation and can accurately calculate the maximum strain that landslides exert on pipelines.

KEYWORDS

deformation characteristics, strain calculation, pipeline, landslide, numerical simulation

1 Introduction

In recent years, oil and gas pipeline leaks caused by landslides have been frequent. These events are influenced by geological activity, extreme weather, and human engineering activities, and the resulting pipeline damage has led to environmental pollution, many casualties, and economic loss. For example, in July 2013, nearly 1 ton of crude oil leaked from a pipeline ruptured by landslides in Xi'an, Shaanxi, China, which polluted local waters (Wang et al., 2015). In

December 2015, the branch line of the West-East gas transmission project was damaged by a landslide that caused 94 casualties and direct economic losses of 881 million yuan in Shenzhen, China (Sun and Song, 2018). In July 2016, a landslide caused 250,000 L of crude oil to spill into the North Saskatchewan River in Canada, also leading to water pollution (Holliday et al., et al.). In July 2016, a landslide led to the fracture of a Sichuan gas pipeline, causing an explosion that killed two people and injured three in Cuijiaba, Enshi, China (Li, 2016). In December 2020, an oil pipeline broke and caught fire due to landslides in Salhoun, Iran. In-depth research on the deformation characteristics of pipelines subjected to landslides and improved models of how pipelines are deformed by landslides can inform predictions of pipeline safety during landslide events and aid in the development of landslide prevention and control measures.

The academic community has made some progress in the study of pipeline deformation characteristics under the action of landslides. For example, Feng et al. (2015) found that stress on pipelines is significantly concentrated in the middle and boundaries of a landslide. Niu et al. (2015) found that the location of maximum stress on a pipeline is related to the landslide stage and the burial condition of the pipeline. In recent years, numerical simulation techniques have been widely used in the study of landslide-induced pipeline deformation. For example, Xu et al. (2022) established a coupled model to examine how pipelines are deformed by landslides by combining smooth particle fluid dynamics with finite elements. The simulation found that the oil content of pipelines has a large effect on their displacement and deformation. Han and Fu (2020) used numerical simulations to analyze the relationship between pipeline deformation and landslides by changing the area of the landslide and the diameter of the pipeline. Zhang et al. (2018) developed a new finite element model with equal boundary springs and a new stiffness calculation method to effectively simulate the pipe-soil interaction in slope bodies. Scholars have also tried to construct computational models to more accurately simulate the deformation and damage characteristics of pipelines impacted by landslides,. For example, Zahid et al. (2020) proposed a mathematical model for calculating the ultimate axial strain of landslides on longitudinal gas pipelines by considering the effects of pipe-soil interaction, pipe pressure, weight, and temperature. Vasseghi et al. (2021) used the Winkler elastic foundation beam model to analyze the deformation and damage of natural gas pipelines impacted by landslides. Ma et al. (2022) established a physical model that couples oil pressure in the pipeline and soil to study the influence of oil pressure on pipeline deformation characteristics during landslide events. Wang et al. (2021) established a simplified mechanical model of the force deformation of buried pipelines under the action of lateral landslides based on the Winkler elastic foundation beam model and the lateral distribution model of landslide thrust. Zhang et al. (2022) analyzed the mechanical response of gas transmission pipelines to landslide thrusts by combining the Green-Ampt model and the Pasternak dual-reference model; they verified the accuracy of the analytical scheme. Han et al. (2022) established a static pipeline model based on consideration of the geotechnical properties at both ends of a pipeline.

These proposed models make it possible to predict the deformation characteristics of pipelines under landslide action; however, the following deficiencies remain:

1) Existing pipeline/landslide models can only determine the unidirectional deformation of buried pipelines. Additionally, most of these models focus on transversely buried pipelines.
2) Pipeline/landslide models do not consider the dynamic displacement process of the pipeline within the landslide soil and thus cannot determine the strain value of a pipeline during the landslide process.

Therefore, based on field-based analysis and numerical simulation, this study will investigate the effects of different slope shapes, buried pipeline directions, and pipeline properties on the deformation and damage characteristics of pipelines under landslide actions. Furthermore, it will construct a buried pipeline strain calculation model that considers landslide displacements and pipeline properties. The model considers pipelines that cross landslides laterally and longitudinally and which can provide the dynamic relationship between the maximum strain of the pipeline and landslide displacement, thereby laying the foundation for future predictions of pipeline safety during landslide events.

2 Field investigation of the threat landslides pose to pipelines

A site survey was carried out to obtain detailed information on and about the impact of landslide disasters on pipelines. The site investigated in this study is a buried crude oil pipeline located outside a city in southeast China, with six landslide disaster points: Cases 1 to 6 (see Table 1 for landslide parameters and Table 2 for pipeline information). The section of pipeline in Case 4 is located in the middle of the landslide, the section in Case 6 is located at the leading edge of the landslide, and the other four sections are located at the landslide's trailing edge. The pipeline was exposed but not significantly deformed after the landslide in Cases 1 and 3. In Cases 2, 5, and 6, the pipeline was deformed (e.g., bent and stretched) but did not break. In Case 4, the broken pipeline led to the leakage of crude oil and land pollution

TABLE 1 Statistics of landslide parameters in typical pipeline landslide cases.

No.	Width (m)	Length (m)	Thickness (m)	Slope gradient (°)
Case 1	15	10	0.7–2.2	15–30
Case 2	80	40	1.0–3.0	15–28
Case 3	30	20	2.0–3.5	15–28
Case 4	390	150	6.0–8.0	8.0–25
Case 5	100	85	6.0–8.0	30–40
Case 6	144	38	1.5–2.0	25–30

TABLE 2 Statistics of pipeline parameters in typical pipeline landslide cases.

No.	Relative location between pipeline and landslide	Depth (m)	Texture of pipeline	External diameter (mm)	Thickness of the pipeline (mm)	Fuel transfer pressure (MPa)
Case 1	Pipeline crosses the trailing edge of the landslide	0.89–2.29	L360 steel pipeline	648	7.9	2.3
Case 2	Pipeline crosses the trailing edge of the landslide	0.90–1.50	L360 steel pipeline	648	7.9	2.3
Case 3	Pipeline is 2–5 m away from the trailing edge of the landslide	0.72–1.20	L360 steel pipeline	610	7.9	2.3
Case 4	Pipeline runs across the middle of the landslide	1.20–1.50	L360 steel pipeline	559	11.9	4.8–6.4
Case 5	Pipeline is 7 m from the landslide trailing edge	0.50–1.60	L360 steel pipeline	864	14.3	8.85
Case 6	Pipeline crosses the landslide front	1.50–2.00	L360 steel pipeline	762	8.7	5–8.5

FIGURE 1
Oil pipeline ruptured by a landslide.

(Figure 1). The survey results show that small scale landslides are unlikely to cause a threat to the pipeline, and that the width of a landslide surface that can lead to pipeline deformation must exceed 30 m.

3 Numerical simulation of how landslides threaten pipelines

3.1 Simulation conditions and parameters

According to the investigation's results, the width, length, thickness, and gradient of a landslide are the main factors affecting pipeline deformation. To clarify the specific effects of these factors, this work calculates the impacts of landslides with different widths, lengths, thicknesses, and gradients on a pipeline. There are in fact three ways for a pipeline to cross a landslide. A pipeline can intersect with a landslide horizontally (i.e., longitudinally), vertically (i.e., latitudinally), or obliquely. The condition of pipelines that obliquely cross landslides can be revealed by analyzing those that intersect landslides vertically and horizontally. Therefore, these latter two orientations are considered in this study (Figure 2). Landslide mass is divided into three areas: the soil mass at the edge of a landslide consists of gravely soil, at its bottom is silty clay, and at the surface of a landslide is plain fill. The pipe is a hollow round pipe with an outer diameter of 600 mm and a wall thickness of 8 mm; it is made of L360 steel. A uniform pressure of 2.3 MPa was applied to the inner wall of the pipe. The friction coefficient between the

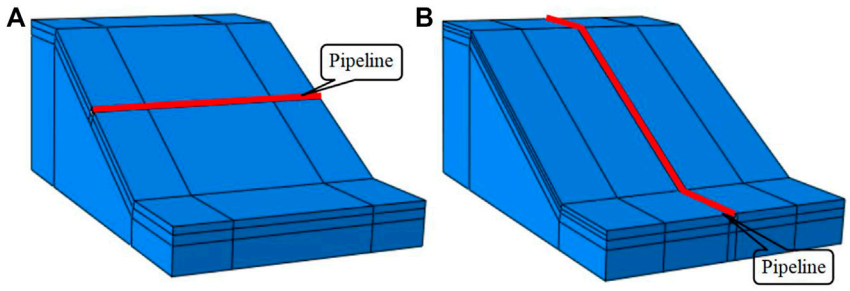

FIGURE 2
Schematic diagram of different conditions of pipelines crossing landslides.

TABLE 3 Values of landslide soil and pipeline parameters.

Material	Density (kg/m^3)	Elasticity modulus (MPa)	Poisson ratio	Internal friction angle (°)	Cohesion (kPa)
Plain fill	2360	20	0.35	15.0	13.0
Silty clay	1980	20	0.30	18.0	25.0
Gravelly soil	2600	55.6	0.23	35.0	26.0
L360 steel	7800	2.01×10^5	0.30	—	—

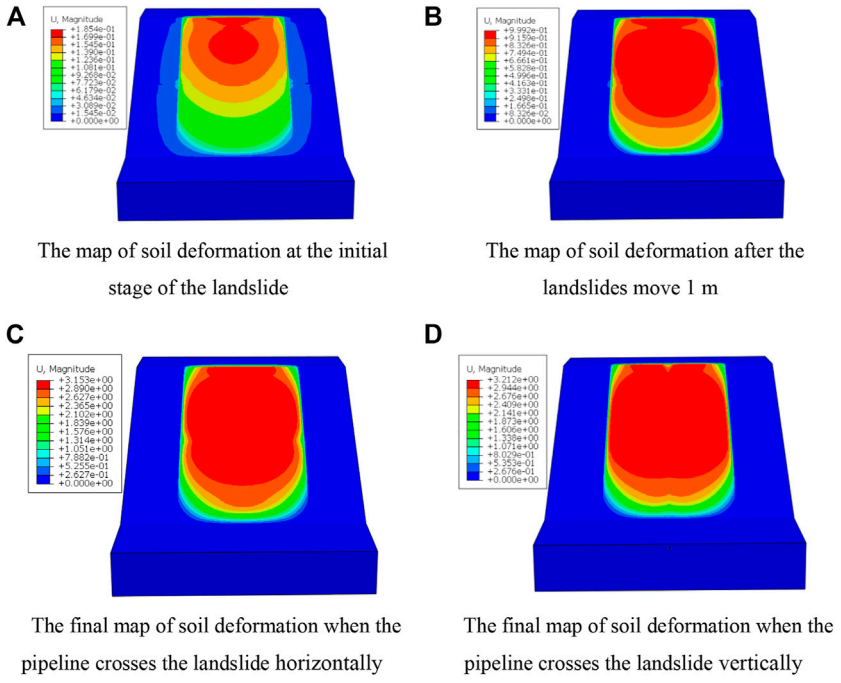

FIGURE 3
Landslide soil displacement and deformation map. **(A)** Map of soil deformation at the initial stage of the landslide. **(B)** Map of soil deformation after the landslides move 1 m. **(C)** Final map of soil deformation when the pipeline crosses the landslide horizontally. **(D)** Final map of soil deformation when the pipeline crosses the landslide vertically.

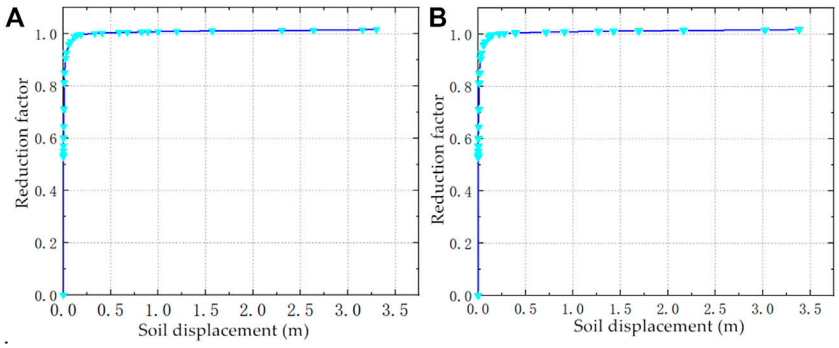

FIGURE 4
Variation diagram of the landslide reduction coefficient for pipelines passing through the landslide at different orientations: **(A)** horizontal, **(B)** vertical.

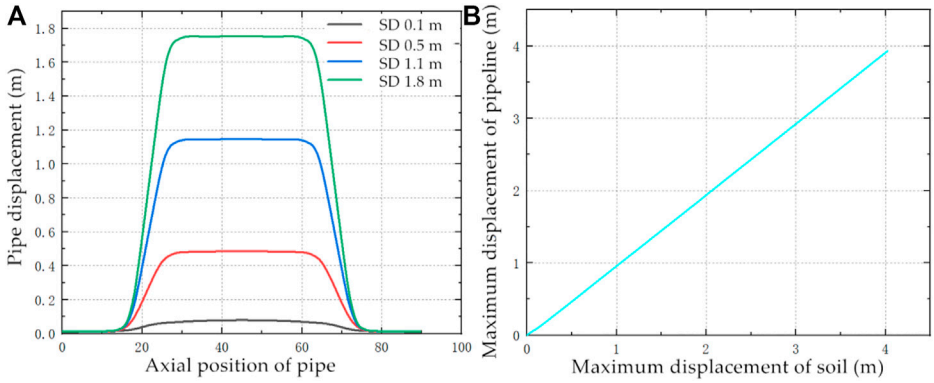

FIGURE 5
Relationship between pipeline displacement and landslide soil displacement (SD): **(A)** displacement at different positions along the pipeline, **(B)** maximum displacement of the pipeline.

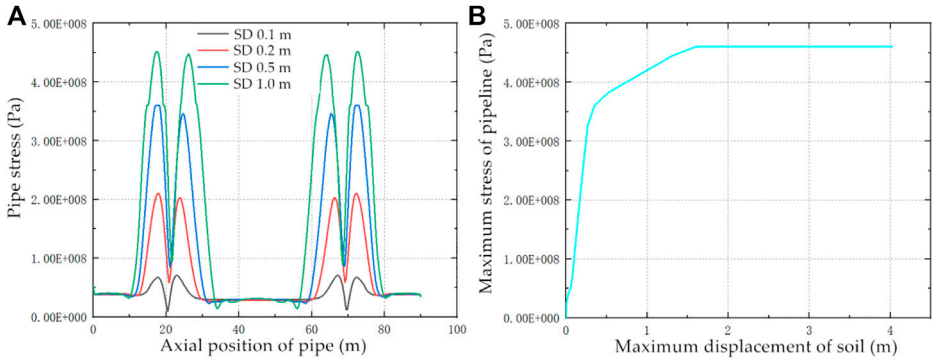

FIGURE 6
Relationship between pipeline stress and landslide soil displacement (SD): **(A)** stress at different positions of the pipeline, **(B)** maximum stress of the pipeline.

pipeline and the soil was 0.7, and the buried depth of the pipeline was 1.5 m. The length of the landslide was set at 60 m, its thickness at 6.0 m, its slope was 30°, and its width was 30 m.

According to the survey results, there are three different rock and soil materials in the landslide body. The parameters of the rock and soil mass obtained by the experimental results are shown in Table 3. The parameters of the L360 steel pipeline used in the exploration area are in accordance with the technical requirements for oil transportation steel pipelines and the standard "Steel Pipelines for Oil and Gas Industry Pipeline Conveying System" (GB/T9711-2011). For further detail, see Table 3.

3.2 Soil displacement and pipeline deformation characteristics

3.2.1 Pipeline influence on soil displacement

On the whole, due to the large scale of landslides, pipelines have little impact on the volume and location of soil displaced. Furthermore, a pipeline has little impact on the initial location of the landslide, the soil displacement during the landslide, and the area of soil deformation; it does, however, have a certain impact on the landslide's final accumulated form (Figure 3).

The stability of a soil mass is itself an important indicator of a slope's stability. The reduction coefficients for pipelines oriented horizontally and vertically to the landslide are extracted, as shown in Figures 4, 5. The changing values of the reduction coefficient are 1.0154 and 1.0153 for the horizontally and vertically oriented pipelines, respectively, which are similar. It can be seen that the way in which the pipeline crosses the landslide has not affected the soil's stability. It can be further inferred that, for large landslides, the presence of a pipeline has little impact on the slope itself.

3.2.2 Deformation characteristics of pipelines impacted by landslides

3.2.2.1 Pipeline crossing the landslide in a lateral orientation

3.2.2.1.1 Displacement of the pipeline. When a pipeline crosses a landslide with a lateral orientation, the displacement of the pipeline changes with the displacement of the landslide mass. In the initial stage of a landslide, the displacement of a pipeline is small, and the overall deformation is arc shaped. As the displacement of the soil increases, the pipeline's displacement increases significantly. The geometry of the displacement gradually changes from an arc shape to a "symmetric three-segment" pattern with a stepped distribution (Figure 5A). The pipeline located in the middle section of the landslide has the largest displacement and exhibits a linear distribution. The maximum displacement of the pipeline and the landslide body during the entire landslide deformation process was extracted for analysis. As shown in Figure 5B, it was found that the maximum displacement of the pipeline was linearly correlated with the maximum displacement of the soil body.

3.2.2.1.2 Stress of the pipeline. The stress acting on the pipeline is symmetrical to the axis of the landslide. With the increase in the displacement of the landslide, the stress on the pipeline increases gradually. The stress of the pipeline section near the edges of both sides of the landslide is the largest and shows a "hump" shape. The peak point of stress along the pipeline is located at the junction of the landslide mass and the stable soil mass. The pipeline stress in the middle section of the landslide body is small and relatively fixed; it does not increase with increasing landslide soil displacement (Figure 6A). The maximum stress of the pipeline is extracted, and the maximum displacement of the landslide soil is analyzed. In the initial stage of the landslide, the maximum stress on the pipeline changes rapidly with the displacement of the landslide soil, which shows a sharp linear change. However, when the soil displacement reaches approximately 0.3 m, the stress of the pipeline increases slowly, and the pipeline enters the yield stage. When the soil displacement reaches 1.6 m, the stress of the pipeline does not change much and only gradually reaches the maximum stress on the pipeline. At this point, the pipeline can be considered damaged (Figure 6B).

3.2.2.1.3 Strain of the pipeline. The strain on the pipeline is also distributed symmetrically on both sides of the landslide's central axis. The strain on the pipeline increases with the increase in the soil displacement of the landslide. The maximum strain point on the pipeline is located at the edge of the landslide body. The pipeline strain in the middle section of the landslide body is small and does not change with increasing landslide body displacement (Figure 7A). The maximum strain on the pipeline and the maximum displacement of the landslide soil are extracted, as shown in Figure 7B. The maximum strain on the pipeline increases with the displacement of the landslide soil. In the initial stage, the pipeline strain increases slowly with the displacement of the landslide soil and then increases rapidly. When the landslide soil displacement reaches 1.3 m, the pipeline strain further increases with the change rate of the landslide soil.

3.2.2.2 Pipeline crossing the landslide in a longitudinal orientation

3.2.2.2.1 Displacement of the pipeline. Figure 8A shows the displacement data for the pipeline at different positions under different landslide soil displacement distances. When the pipeline crosses the landslide longitudinally, the displacement of the pipeline increases with increasing landslide displacement. In the initial stage of the landslide, the displacement of the pipeline can be roughly considered as occurring in three stages. The pipeline outside the landslide has almost no displacement. The displacement of the pipeline inside the landslide increases gradually from the bottom to the top of the slope. There are

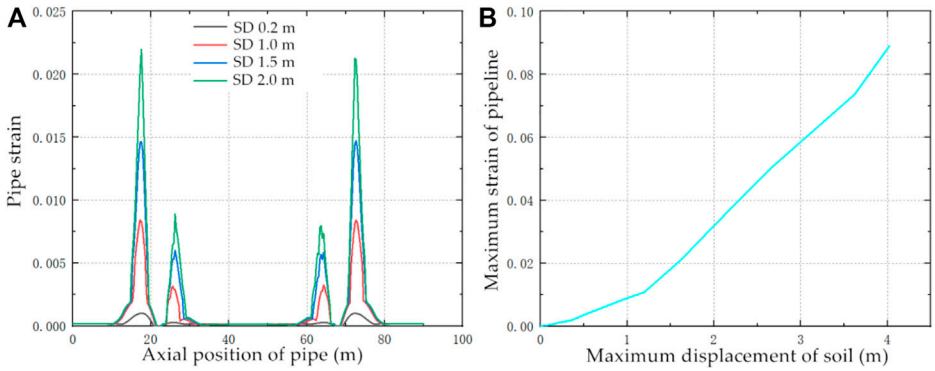

FIGURE 7
Relationship between pipeline strain and landslide soil displacement (SD): **(A)** strain at different positions along the pipeline, **(B)** maximum strain on the pipeline.

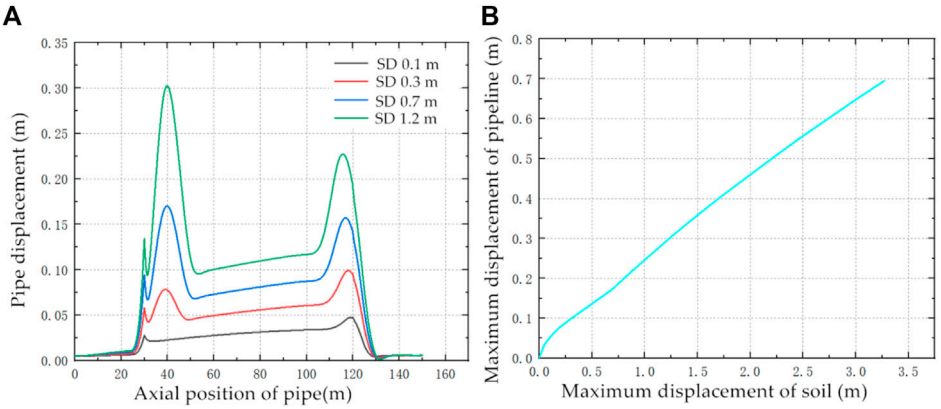

FIGURE 8
Relationship between pipeline displacement and landslide soil displacement (SD): **(A)** displacement at different positions of the pipeline, **(B)** maximum displacement of the pipeline.

obvious displacement points at the bottom and top of the slope. With the increase in the displacement of the landslide, the accumulation of soil at the bottom of the slope leads to a rapid increase in the displacement of the pipeline approximately 10 m from the foot of the slope and gradually becomes the maximum point of the pipeline displacement. The maximum soil displacement of the landslide body and the maximum displacement of the entire pipeline are extracted (Figure 8B). Initially, the maximum displacement of the pipeline increases significantly with the maximum displacement of the landslide. Then, the displacement of the pipeline slows down. Finally, the maximum displacement of the pipeline and the maximum displacement of the landslide body have an approximately linear increase. The displacement of the entire pipeline does not change strongly with the displacement of the landslide, and the linear relationship between the maximum displacement of the pipeline and the maximum displacement of the landslide is less than 0.2 from the overall analysis.

3.2.2.2.2 Stress of the pipeline. Stress data along different positions of the pipeline under different landslide soil displacement distances are shown in Figure 9A. The stress on the pipeline increases with increasing landslide displacement. In the initial stage of the landslide, the pipeline stress at the top of the slope is significantly greater than that at the bottom of the slope. As the displacement of the landslide increases, the stress of the pipeline at the bottom of the slope increases rapidly and then exceeds the stress of the pipeline at the top of the slope. The section of pipeline approximately 10 m from the bottom of the slope also increases sharply with the increase in the displacement of the landslide, eventually exceeding the stress on the pipeline section at the top of the slope.

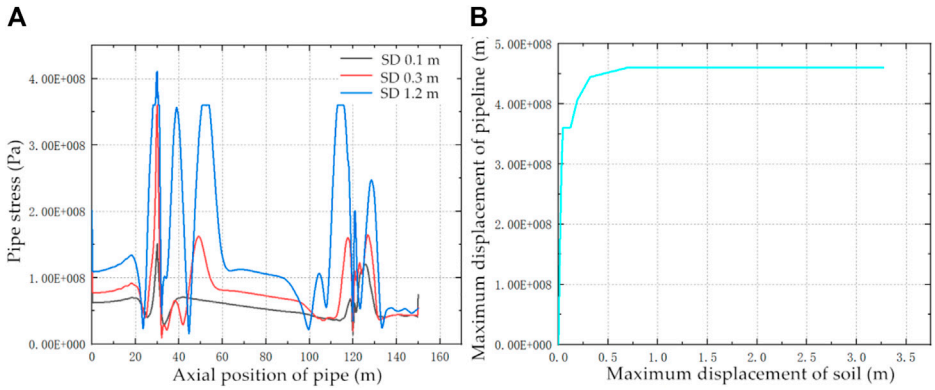

FIGURE 9
Relationship between pipeline stress and landslide soil displacement (SD): **(A)** stress at different positions of the pipeline, **(B)** maximum stress of the pipeline.

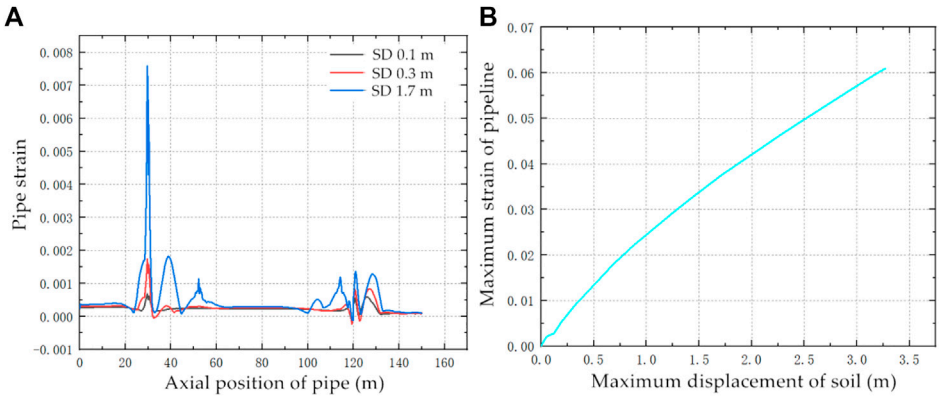

FIGURE 10
Relationship between pipeline strain and landslide soil displacement (SD): **(A)** strain at different positions of the pipeline, **(B)** maximum strain of the pipeline.

The maximum stress of the pipeline and the maximum displacement of the soil are shown in Figure 9B. When the pipeline crosses the landslide longitudinally, the maximum stress on the pipeline and the maximum displacement of the landslide have a three-stage relationship. In the initial stage of the landslide, the stress of the pipeline increases rapidly with the increase in the displacement of the landslide. With a further increase in the landslide displacement, the stress on the pipeline gradually increases until it reaches the strength limit of the pipeline.

3.2.2.2.3 Strain of the pipeline. Figure 10A shows the axial strain data at different positions of the pipeline under different landslide soil displacement distances. It is evident that the variable pattern of the strain along the whole pipeline is similar to the stress pattern of the pipeline observed for the longitudinal orientation. In the early stage of the landslide, the pipelines at the top and bottom of the landslide have the largest strain. Moreover, the strain of the pipeline at the top of the landslide, which is the maximum strain area of the entire pipeline, is greater than that at the bottom of the landslide. As the displacement of the landslide increases, the strain on the pipeline at the foot of the landslide exceeds the strain on the pipeline at the top of the landslide, thus becoming the largest strain area along the entire pipeline. Moreover, the strain on the pipeline at approximately 10 m from the bottom of the slope increases rapidly, which exceeds the strain on the pipeline at the top of the slope, becoming the second largest strain area of the pipeline. The pipeline at the top of the landslide is the third largest strain area of the pipeline. The strain on the other sections

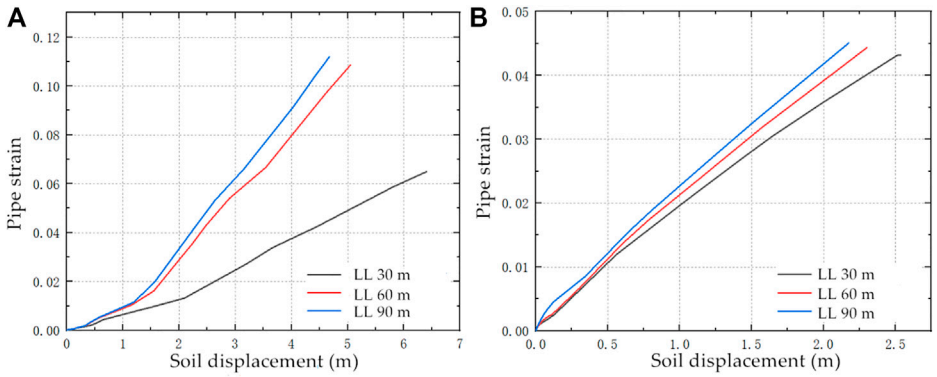

FIGURE 11
Influence of landslide length (LL) on the relationship between pipeline strain and landslide soil displacement: **(A)** pipeline crosses the landslide horizontally, **(B)** pipeline crosses the landslide vertically.

of the pipeline is small. In other pipeline sections, the strain changes are not large, despite increasing landslide displacement. The relationship of the maximum strain on the pipeline and the maximum displacement of the landslide soil are shown in Figure 10B. The pipeline strain increases with increasing landslide soil displacement. There is a linear relationship between pipeline strain and landslide soil displacement, with a correlation coefficient of 0.25.

3.2.2.3 Mechanism of pipeline deformation

Where the pipeline crosses the landslide body laterally, it can be concluded from the stress, strain, and displacement data for the pipeline that the pipeline receives the largest force at the junction of the landslide body and the stable soil body, and it is most prone to damage. The mechanism driving pipeline damage when crossing the landslide laterally is mainly the combination of unstable and stable soil which acts on the pipeline. Consequently, the pipeline is subjected to excessive shear stress at the junction of the stable and unstable soil, causing pipeline damage.

When pipelines are oriented longitudinally to landslides, the effect of the landslide material on the pipeline is different at different locations along the pipeline. The pipeline section located at the top of the slope at the landslide trailing edge was mainly affected by the shear and tensile action of the soil, the pipeline at the foot of the landslide was mainly affected by the pressure of the soil, and the rest of the pipeline was affected by the friction and push of the soil. According to the data, with the development of landslide damage due to the accumulation of the landslide's mass, the stress near the slope toe of the landslide increases rapidly, making that section of pipeline most likely to incur damage. Therefore, when the pipeline traverses the landslide vertically, the damage of the pipeline comes from the compression forces from the landslide body acting on the pipeline.

3.3 Influence of landslide geometry on pipeline deformation

3.3.1 Length of landslide

To conduct detailed analysis of the influence of landslide length on pipeline deformation and damage, landslide lengths of 30, 60, and 90 m were selected. Then, the maximum displacement of the landslide mass and maximum strain on the pipeline in the horizontal and vertical pipeline-crossing-landslide modes were extracted and analyzed (Figure 11) by numerically simulating the interaction between the pipeline and landslide.

When the pipeline crossed the landslide horizontally, the maximum strain on the pipeline generally increased with the maximum displacement of the landslide soil mass. Two inflection points in this relationship were affected by the characteristics of the pipeline material. The first was in the initial stage of the landslide. At first, the landslide caused the pipeline to deform only slightly. However, the change rate of the maximum strain on the pipeline increased with the increase in the maximum displacement of the landslide. The second inflection point was observed after the landslide had travelled a certain distance, when the maximum strain on the pipeline increased with the maximum displacement of the landslide soil. The variation in landslide length did not change the mechanical modes acting on the pipeline or the relationship between the maximum strain on the pipeline and the maximum displacement of the landslide soil mass; however, the increase in landslide length did increase the maximum strain on the pipeline when subjected to the same landslide soil mass displacement. When the landslide length was 30 m, the soil displacement at the second point was 2.1 m; when the landslide length was 60 m, the soil displacement at the second point was 1.5 m; and when the landslide length was 90 m, the soil displacement at the second point was 1.2 m. It is evident that the lengthening of the landslide will cause the second inflection point

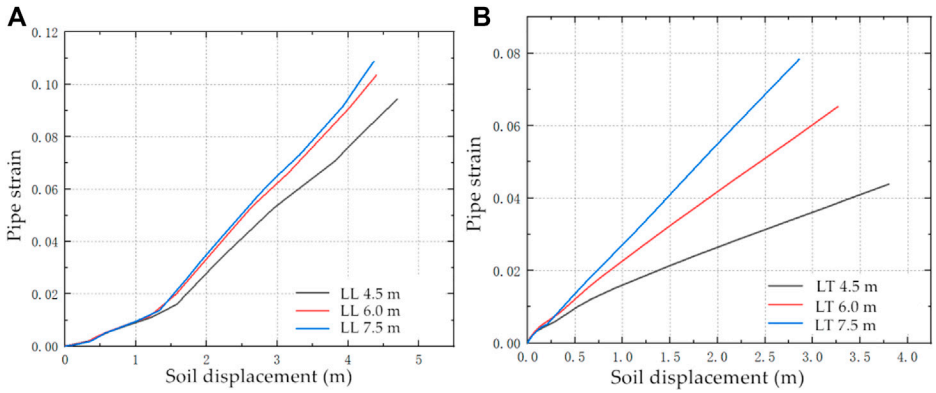

FIGURE 12
Influence of landslide thickness (LT) on the relationship between pipeline strain and landslide soil displacement: **(A)** pipeline crosses the landslide horizontally, **(B)** pipeline crosses the landslide vertically.

between the maximum strain on the pipeline and the maximum displacement of the landslide soil mass to decrease. Comparing the correlation curves between the maximum pipeline strain and the maximum landslide soil displacement of different landslide lengths, we found that the larger the landslide length is, the less influence it has on the relationship between soil displacement and maximum pipeline strain.

When the pipeline crossed the landslide vertically, the overall pipeline strain had an approximately linear relationship with the maximum displacement of the landslide soil mass. Under the same soil displacement, the length of the landslide increased, and the strain of the pipeline increased; however, larger landslide lengths did not have smaller influences on the relationship between the displacement of the landslide soil and the maximum strain of the pipeline.

3.3.2 Landslide thickness

In order to conduct detailed analysis of the influence of landslide thickness on pipeline deformation and damage, the landslide thickness was set at 30, 60, and 90 m. The maximum displacement of the landslide mass and maximum strain on the pipeline in the horizontal and vertical modes were extracted and analyzed (Figure 12) by numerically simulating the interaction between the pipeline and landslide.

When the pipeline crosses the landslide horizontally, the landslide thickness does not change the rule that the maximum strain on the pipeline changes with the maximum displacement of the landslide soil. Under the same soil displacement conditions, the greater the landslide thickness is, the greater the maximum strain on the pipeline, and the lower the impact of that strain has on the pipeline. The greater the landslide thickness is, the greater the force acting on the pipeline will be, which will lead to a greater strain on the pipeline. As the depth of the pipeline is fixed, while increasing the thickness of the landslide will lead to an increase in the overall force of the soil, the deeper the thickness of the landslide is, the farther away the soil from the pipeline will be and the smaller the effect it has on the pipeline. Therefore, the deeper the landslide thickness is, the less influence it will have on the pipeline strain growth rate.

When the pipeline crossed the landslide vertically, the maximum strain of the pipeline was linearly related to the maximum displacement of the landslide soil. Under the same landslide displacement conditions, the greater the landslide thickness, the greater the pipeline strain. In addition, compared with the horizontal orientation, the strain on the pipeline was more significantly affected by the thickness of the landslide when the pipeline crossed the landslide vertically. Based on the above, it can be concluded that the maximum strain on the pipeline is located at the foot of the slope, which is compressed by the accumulation of mass. The increase in landslide thickness can directly increase the landslide mass, thus increasing the strain on the pipeline.

3.3.3 Slope of landslide

Generally, the larger the slope of the landslide, the more likely the landslide will occur and the faster its rate of deformation. Additionally, different slopes will affect the degree of deformation and damage of pipelines impacted by landslides. According to the survey data, the slopes of six typical pipeline landslides were between 15° and 40°, most being approximately 30°. Therefore, landslide slopes of 20°, 30°, and 40° were set to analyze the influence of the landslide slope on the law of deformation and damage of the pipeline (Figure 13).

When the pipeline crosses the landslide horizontally, the overall trend of the relationship between the maximum strain of the pipeline and the maximum displacement of the landslide soil mass under different landslide slopes was consistent with the above two conditions. At the initial stage of the landslide, the

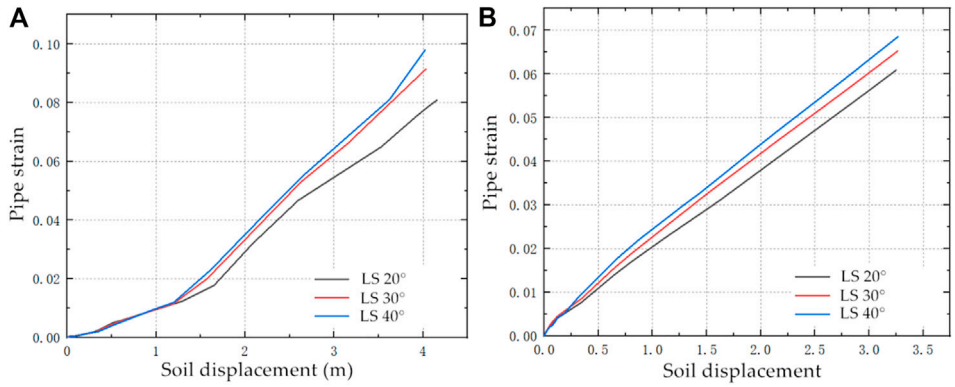

FIGURE 13
Influence of landslide slope on the relationship between pipeline displacement strain and landslide soil (LS): **(A)** pipeline crosses the landslide horizontally, **(B)** pipeline crosses the landslide vertically.

relationship between the maximum strain on the pipeline with different slopes and the maximum displacement of the soil mass was the same. With the increase in soil displacement, the maximum strain on the pipeline increased with the increase in landslide slope under the same conditions, but the impact of the landslide slope on the pipeline decreased.

When the pipeline crossed the landslide vertically, the landslide slope did not affect the relationship between the maximum strain on the pipeline and the maximum displacement of the soil. When the displacement of the soil was the same, the maximum strain on the pipeline increased with an increasing slope. Therefore, when the slope was larger, the displacement of the pipeline was smaller.

3.3.4 Width of landslides

The increase in the width of the landslide will lead to a larger area of deformation and failure length for pipelines that cross landslides horizontally. Furthermore, the deformation and failure degree of the pipeline will be different with the different landslide widths. The pipeline was placed in the middle of the landslide, and the change in the landslide width did not influence the consistency of the relationship between the maximum strain of the pipeline and the maximum displacement of the soil. Therefore, this study only analyzed the influence of landslide width on the deformation and failure law of pipelines that cross landslides horizontally.

The maximum strain on the pipeline and the maximum displacement of the landslide soil mass were extracted and analyzed (Figure 14) from the horizontal pipeline model. The change in landslide width did not change the relationship between the maximum strain on the pipeline and the maximum displacement of the landslide soil, but when the distance of the soil displacement was the same, the maximum strain on the pipeline decreased with increasing landslide width.

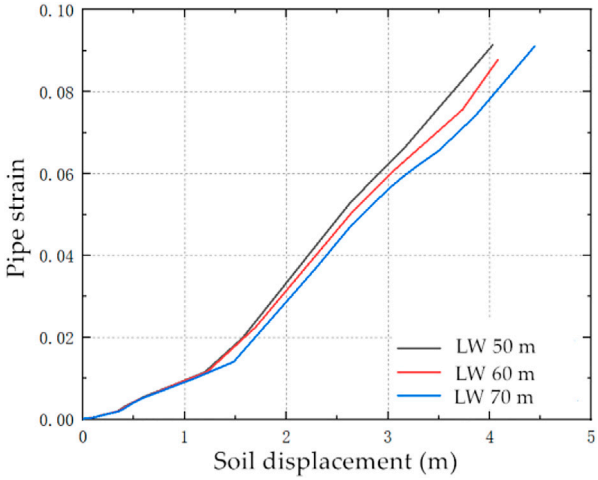

FIGURE 14
Influence of landslide width (LW) on the relationship between pipeline strain and landslide soil displacement.

As the maximum strain of the pipeline was caused by the pipeline bending at the landslide boundary, when the landslide displacement was kept constant, smaller landslide widths induced larger bends in the pipeline at the landslide boundary; thus, the maximum strain of the pipeline was larger. In contrast, when the width of the landslide increased, the bending of the pipeline at the landslide boundary decreased, and the maximum strain on the pipeline decreased.

3.3.5 The degree of influence

Different values of landslide geometric parameters (landslide length, thickness, slope, and width) will affect the deformation and failure law of pipelines within the landslide mass, but the

TABLE 4 Comparison of orthogonal tests of pipelines crossing landslides transversely.

Number	Length (m)	Width (m)	Slope (°)	Thickness (m)	Strain
1	30	50	20	4.5	0.0117
2	30	60	30	6.0	0.0088
3	30	70	40	7.5	0.0078
4	60	50	30·	7.5	0.0194
5	60	60	40	4.5	0.0132
6	60	70	20	6.0	0.0125
7	90	50	40	6.0	0.0206
8	90	60	20	7.5	0.0177
9	90	70	30	4.5	0.0134
R_j	0.0078	0.0060	0.0001	0.0021	

influence of different parameters of landslide geometry on the deformation and failure law of pipelines is not clear. Understanding the strength of their influence can provide a reference and basis for disaster prevention and mitigation in terms of pipeline engineering. Therefore, it is necessary to carry out sensitivity analysis on the influence of these geometric parameters on the deformation and failure law of pipelines.

There are many methods for analyzing the sensitivity of multiple factors to a certain index, among which orthogonal experiments is a common and effective method.

When the pipeline crosses the landslide horizontally, the geometric parameters of the landslide that affect the deformation and failure of the pipeline in the landslide mass include the length, width, thickness, and slope. To compare the influence of the four factors on the deformation and failure of the pipeline, orthogonal experiments were used to set three levels for the four factors; nine groups of simulation tests were conducted for the analysis. The strain index was extracted for the pipeline when the displacement of the landslide soil mass was 1.6 m for each working condition in the simulation results (Table 4), where R_j was the comparative value of the influence degree of each factor calculated by the intuitive analysis method. The length of the landslide has the greatest impact on the deformation and failure of the pipeline, followed by the width, thickness, and slope.

When the pipeline crosses the landslide vertically, because the pipeline was laid on the central axis of the sliding direction of the landslide mass, the width of the landslide did not affect the deformation or damage law of the pipeline; therefore, only three geometric landslide characteristics—length, slope, and thickness—needed to be analyzed. The orthogonal experiment was used to set up three levels for the three factors, and a total of nine groups of experiments were used to compare the influence of the three factors on the deformation and damage law of the pipeline subjected to landslides. Similarly, the strain on the pipeline was extracted when the displacement of the landslide soil mass under each working condition was 1.6 m, and the comparative value R_j of the influence degree of each factor was calculated (Table 5). We found that the thickness of the landslide had the greatest impact on the deformation and damage law of the pipeline, followed by the length of the landslide and, finally, the slope of the landslide.

TABLE 5 Orthogonal test comparison of pipelines crossing landslides longitudinally.

	Length (m)	Slope (°)	Depth (m)	Pipeline strain
1	30	20	4.5	0.0120
2	30	30	6.0	0.0257
3	30	40	7.5	0.0343
4	60	20	7.5	0.0384
5	60	30	6.0	0.0323
6	60	40	4.5	0.0202
7	90	20	6.0	0.0306
8	90	30	4.5	0.0224
9	90	40	7.5	0.0401
R_j	0.0070	0.0047	0.0194	

4 Model and evaluation of pipeline strain

The geometric landslide characteristics (length, width, thickness, and slope) and displacement are important parameters to assess the degree of pipeline deformation. Analyzing the relationship between the geometric

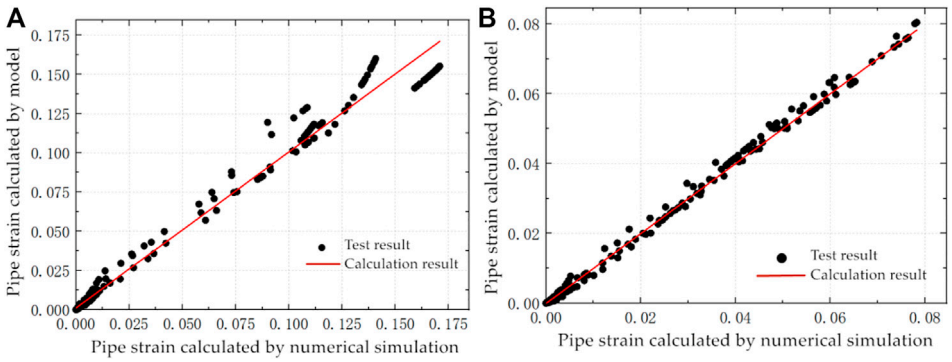

FIGURE 15
Comparison of strain model calculation results and numerical simulation results: **(A)** pipeline transversely crosses the landslide, **(B)** pipeline longitudinally crosses landslide.

characteristics and displacement of the landslide and the pipeline strain is key to establishing the pipeline strain calculation model.

The dimensional analysis method was used to analyze the relationship between the landslide and pipeline strain and to establish a calculation model. The length, thickness, slope, width, and displacement of the landslide are represented by L, D, A, W, and U, respectively. According to the dimensional analysis equation, the dimensions on the left and right sides are equal. Pipeline strain (ε) and landslide slope (A) are non-dimensional values. The dimensions of landslide length (L), thickness (D), width (W), and displacement (U) are, therefore, the dimensional values. However, these can be represented as the non-dimensional parameters L/d, D/d, W/d, and U/d, where d is the diameter of the pipeline.

When the pipeline is perpendicular to the direction of the landslide, the length, thickness, slope, width, and displacement of the landslide are the main factors affecting the deformation of the pipeline. The calculation model of the relationship between the pipeline strain and the geometric characteristics and displacement of the landslide is as follows:

$$\varepsilon = \mathrm{a1} \times \left(\frac{U}{d}\right)^{\mathrm{a2}} \times \left(\frac{L}{d}\right)^{\mathrm{a3}} \times \left(\frac{A}{180} \times \pi\right)^{\mathrm{a4}} \times \left(\frac{D}{d}\right)^{\mathrm{a5}} \times \left(\frac{W}{d}\right)^{\mathrm{a6}} \quad (1)$$

where ε_v is the strain on the pipeline when the pipeline is horizontal to the sliding direction of the landslide. a1, a2, a3, a4, a5, and a6 are fitting coefficients. From the numerical simulation results, MATLAB is used to fit the model parameters, and the results are as follows:

$$\varepsilon = 0.0001 \times \left(\frac{U}{d}\right)^{1.3952} \times \left(\frac{L}{d}\right)^{0.7970} \times \left(\frac{A}{180} \times \pi\right)^{0.5769} \times \left(\frac{D}{d}\right)^{1.1654} \times \left(\frac{W}{d}\right)^{-0.3413} \quad (2)$$

This model was used to calculate the maximum strain value of the pipeline under various working conditions. The results of the model and the numerical simulation are compared, as shown in Figure 15A. The results show that the model results and the numerical simulation results are linearly correlated, and the linear slope is 0.975. Therefore, the calculation results of the model are reasonable.

When the pipeline is parallel to the sliding direction of the landslide, the soil mass of the landslide is evenly distributed on both sides of the pipeline, and the width of the landslide has no effect on the deformation of the pipeline. Therefore, the calculation model of the relationship between the pipeline strain and the geometric characteristics and displacement of the landslide is as follows:

$$\varepsilon = \mathrm{a1} \times \left(\frac{U}{d}\right)^{\mathrm{a2}} \times \left(\frac{L}{d}\right)^{\mathrm{a3}} \times \left(\frac{A}{180} \times \pi\right)^{\mathrm{a4}} \times \left(\frac{D}{d}\right)^{\mathrm{a5}} \quad (3)$$

where ε_p is the pipeline strain when the pipeline and the sliding direction of the landslide are parallel. a1, a2, a3, a4, and a5 are fitting coefficients. From the numerical simulation results, MATLAB is used to fit the model parameters, and the results are as follows:

$$\varepsilon = 0.0002 \times \left(\frac{U}{d}\right)^{0.910} \times \left(\frac{L}{d}\right)^{0.1319} \times \left(\frac{A}{180} \times \pi\right)^{0.0578} \times \left(\frac{D}{d}\right)^{1.5911} \quad (4)$$

This model was used to calculate the maximum strain on the pipeline under various working conditions. The results of the model and the numerical simulation are compared, as shown in Figure 15B. The results show that the model results and the numerical simulation results are linearly correlated, and the linear slope is 1.007. Therefore, the calculation results of the model are reasonable.

5 Conclusion

In this study, the strain on a pipeline oriented horizontally and vertically to a landslide is analyzed. Based on the research results, a calculation model of pipeline strain is established, and the conclusions are as follows:

(1) The deformation and damage mechanisms are different for pipelines with different orientations to landslides. When the pipeline crosses the landslide laterally, it is affected by the combined action of stable and unstable soil. The pipeline is subjected to considerable shear stress at the interface between these soils, which results in pipeline damage. When the pipeline crosses the landslide longitudinally, the pipeline is compressed by the landslide at the bottom of the slope, which results in pipeline damage.
(2) When the pipeline crosses the landslide laterally, the influence of landslide parameters on the pipeline from greatest to least are length, width, thickness, and slope of the landslide. When the pipeline crosses the landslide longitudinally, the influence of landslide parameters on the pipeline from greatest to least are thickness, length, and slope of the landslide.
(3) The pipeline strain calculation model constructed from the dimensionless analysis method can well reflect the influence of the various factors that influence pipeline strain and can accurately calculate the maximum strain on the pipeline.

Data availability statement

The datasets presented in this study can be found in online repositories. The names of the repository/repositories and accession number(s) can be found in the article/supplementary material.

Author contributions

NS: conceptualization, methodology, software, validation, formal analysis, investigation, and resources. L-lL: validation, formal analysis, investigation, and resources. Y-bM: software, validation, and formal analysis. Q-jL: investigation. L-yB: resources.

Conflict of interest

NS, L-lL, Y-bM, Q-jL, and L-yB were employed by General Institute of Science and Technology Company of Pipeline China.

Publisher's note

References

Feng, W. K., Huang, R. A., Liu, J. A., Xu, X., and Luo, M. (2015). Large-scale field trial to explore landslide and pipeline interaction. *Soils Found.* 55 (6), 1466–1473. doi:10.1016/j.sandf.2015.10.011

Han, B., and Fu, Q. (2020). Study on the pipeline fragility appraisal indicators affected by landslide based on numerical simulation. *J. Phys. Conf. Ser.* 1549 (4), 042123–123. doi:10.1088/1742-6596/1549/4/042123

Han, J. J., Huang, D. W., and Wang, H. C., (2022). Research on failure mechanism of a fuel gas pipeline transversely crossing landslide. *Yangtze river* 53 (1), 209–215.

Holliday, C., Young, A., and Funk, T., The north Sasktchewan river valley landslide- slope and pipeline condition monitoring. *ASME13th Int. Pipeline Conf. (IPC).* 19, 12, 10.1115/IPC2020-9532,

Li, Y. (2016). Gas supply resumed on July 30 after the Sinopec Sichuan-East gas pipeline explosion and combustion accident in Enshi, which took 10d. *Gas Heat* 36 (09), 22.

Ma, H. Q., He, B. X., and Cai, W. H., (2022). Prediction model of deformation distribution of buried natural gas pipeline under longitudinal action of landslide debris flow. *J. Harbin Inst. Technol.* 12, 1–9.

Niu, W. Q., Zheng, J., and Wu, H. G., (2015). Experimental study on effect of orthogonal landslide on pipeline by model simulation. *Railw. Eng.* 12 (06), 117–120.

Sun, Y. J., and Song, E. (2018). Dynamic simulation of "12·20" Shenzhen landslide. *Chin. J. Geotechnical Eng.* 40 (03), 441–448.

Vasseghi, A., Haghshenas, E., Soroushian, A., and Rakhshandeh, M. (2021). Failure analysis of a natural gas pipeline subjected to landslide. *Eng. Fail. Anal.* 119, 105009. doi:10.1016/j.engfailanal.2020.105009

Wang, G. L., Li, T. L., Xing, X. L., and Zou, Y. (2015). Research on loess flow-slides induced by rainfall in July 2013 in Yan'an, NW China. *Environ. Earth Sci.* 73 (12), 7933–7944. doi:10.1007/s12665-014-3951-9

Wang, R. Y., Zhang, J. M., and Wang, Cong (2021). Comparative analysis of statics and numerical simulation of buried pipeline under the action of lateral landslide. *Sci. Technol. Eng.* 21 (1), 326–333.

Xu, T. L., Ma, X. L., Lan, X. B., Jiang, H., and Wang, J. (2022). Research on treatment scheme of soil landslide in aviation oil pipeline based on oil-pipeline-soil multi-physical field coupling and anti-sliding simulation. *Int. J. Press. Vessels Pip.* 200, 104780–104814. doi:10.1016/j.ijpvp.2022.104780

Zahid, U., Godio, A., and Mauro, S. (2020). An analytical procedure for modelling pipeline-landslide interaction in gas pipelines. *J. Nat. Gas Sci. Eng.* 81, 103474. doi:10.1016/j.jngse.2020.103474

Zhang, L. S., Fang, M. L., Pang, X., Yan, X., and Cao, Y. (2018). Mechanical behavior of pipelines subjecting to horizontal landslides using a new finite element model with equivalent boundary springs. *Thin-Walled Struct.* 124 (5), 501–513. doi:10.1016/j.tws.2017.12.019

Zhang, Z. G., Lv, X. L., Mao, M. D., Pan, Y., Fang, L., and Wu, Z. (2022). Mechanical response for rainfall-induced landslides on jointed gas pipelines. *Comput. Geotechnics* 146, 104708. doi:10.1016/j.compgeo.2022.104708

frontiers | Frontiers in Earth Science

TYPE Original Research
PUBLISHED 05 January 2023
DOI 10.3389/feart.2022.1023652

OPEN ACCESS

EDITED BY
Jia-wen Zhou,
Sichuan University, China

REVIEWED BY
Hongchao Zheng,
Tongji University, China
Vincenzo D'Agostino,
University of Padua, Italy

*CORRESPONDENCE
Xiaojun Wang,
wxjxxp@163.com

SPECIALTY SECTION
This article was submitted to Geohazards and Georisks, a section of the journal Frontiers in Earth Science

RECEIVED 20 August 2022
ACCEPTED 03 October 2022
PUBLISHED 05 January 2023

CITATION
Xie X, Wang X, Liu Z, Liu Z and Zhao S (2023), Regulation effect of slit-check dam against woody debris flow: Laboratory test.
Front. Earth Sci. 10:1023652.
doi: 10.3389/feart.2022.1023652

Regulation effect of slit-check dam against woody debris flow: Laboratory test

Xiangping Xie, Xiaojun Wang*, Zhenzhen Liu, Zhixuan Liu and Shenzhou Zhao

Anyang Institute of Technology, Anyang, China

Woody debris flows (i.e., debris flows carrying wood) are common in mountainous and forested areas. They can cause more severe hazards due to the effects of LW (woody debris larger than 1 m in length and 10 cm in width) compared to debris flows without LW. Mitigation structures for debris flows have considered little of the regulating effect on LW and the influence of LW on the regulation effect of sediment. Thus, model tests were conducted to discuss the regulation effects of slit-check dams on woody debris flow. Research results demonstrated that slit-check dams can effectively regulate woody debris flows without overflows. Once overflow occurs, sediment trapping efficiency and the wood retention rate dramatically decrease. The sediment trapping efficiency of slit-check dams on debris flows without LW shared a linear relationship with the relative opening width, the height-to-width ratio of the opening, and the opening density. However, this was also influenced by the wood retention rate for woody debris flow. A logarithmic relationship between the sediment trapping rate and wood retention rate was obtained. The wood retention rate is mainly determined by the ratio of the LW length to the opening width, the ratio of the LW length to the channel width and the opening density of the slit-check dam. Three draining patterns of woody debris flows at the slit-check dam and three clogging types of LW at the openings of the slit-check dam were observed. Some design criteria for the structure parameters of the slit-check dam were proposed. These research results promote a better understanding of the regulation effect of slit-check dams on woody debris flows and provide a basis for the optimal design of slit-check dams.

KEYWORDS

woody debris flow, large wood, slit-check dam, regulation effect, regression analysis

Introduction

With the recent increase of global warming and extreme weather, mountain disasters are occurring more frequently and with a high magnitude. With the phenomenon of mountain torrents and debris flows transporting woody debris, woody debris flows have been reported worldwide and the hazardous effects of LW (large wood more than 1 m in length and 10 cm in diameter) have been highlighted in many studies (Gao et al., 2005; Comiti et al., 2008; Ana et al., 2015; Henshaw et al., 2015; Steeb et al., 2016; Xie et al.,

2020a). An extreme flood that occurred in August 2005 in Switzerland was considered the costliest natural disaster in the history of Switzerland (Steeb et al., 2016), and one important factor responsible for the damage was LW. More than 69000 m^3 of LW were transported throughout the affected area (Steeb et al., 2016). LW accumulated at key cross sections, such as bridge piers and culverts, producing increased upstream water levels, large horizontal structural loadings, and flow field modifications that considerably exacerbated scour (Laursen 1956; Melville and Dongol, 1992; Pagliara and Carnacina, 2010; Schmocker et al., 2011; Schmocker and Hager, 2013; Jochner et al., 2015; Comiti et al., 2016; Hartlieb 2017; Panici and Almeida, 2018; Schalko et al., 2018; Schalko et al., 2019; Peng et al., 2021). LW can also block spillways of check dams, which causes sediment trapping upstream by subsequent debris flows and decreases their discharge ability and storage capacity (Doi et al., 2000; SEDALP WP6 Report 2014; Piton and Recking, 2016; Rossi and Armanini, 2019; Wang et al., 2017). LW transported by debris flow or flood waters can strike residential or other structures and exert a certain impact force that can be large enough to cause substantial damage to structures (Fu et al., 2001; Haehnel and Daly, 2002; Robert and Steven, 2004). Therefore, it is of great importance to study mitigation measures for LW and check the applicability of traditional mitigation measures based on traditional debris flows for woody debris flows.

Both engineering and non-engineering measures have been proposed to reduce the risk of flash floods and debris flows with LW. Several studies have conducted risk assessments that considered influencing factors such as LW amount and transport route. With the development of geographic information technology and advanced theories, the estimation and distribution model of LW quantity based on GIS and fuzzy decision theory has gradually developed (Rickenmann, 1999; Petraschek and Kienholz, 2003; Mazzorana et al., 2009; Mazzorana et al., 2012; Ruiz-Villanueva et al., 2014). Administrative measures include strategic and organizational procedures, such as emergency action plans, evacuation scenarios, or regional planning, that do not influence the river itself have also been developed in many countries (Lange and Bezzola, 2006; Schmocker et al., 2011). These measures lead to sustainable systems but are difficult to implement in many scenarios because the land use in densely populated regions is difficult to modify and change.

Structural engineering measures are often considered the most effective ways for debris flow mitigation (Comiti et al., 2016). Currently, woody debris mitigation structural measures can be divided into two main categories: 1) measures to guide woody debris safely downstream to protect certain objectives, such as debris deflectors and sweepers that are installed on protected objects (Bradley et al., 2004), and 2) measures to intercept woody debris at a certain location. Debris rakes and flexible barriers have been adopted to retain woody debris (Rimböck, 2004; Song et al., 2019; Wang et al., 2022; Xie et al.,2017). Slit-check dams, which are a traditional open-type check dam, have been most widely used for debris flow mitigation. Many researches have examined the sediment regulation effect of slit-check dams against debris flows through field investigations, model tests, and numerical simulations (Ishikawa and Mizuyama,1988; Han and Ou, 2006; Hassan-Esfahani and Banihabib, 2016; Chen and Tfwala, 2018; Zhao et al., 2019; Okamoto et al., 2019), while only a few researches have focused on the regulation effect of woody debris flows. D'Agostino et al. (2000) conducted investigations on open check dams for LW control. Shrestha et al. (2012) investigated the deposition process of debris flows with woody debris and woody debris jamming on slit-check dams. Kato et al. (2015) studied the characteristics of woody debris and sediment transportation around slit-check dams. Rossi and Armanini (2019) addressed the influence of intense sediment transport on the efficiency of structures aimed at the interception of wood logs. Xie et al. (2020b) conducted preliminary research on the regulation effect of slit-check dams on woody debris flows.

Although fundamental knowledge about slit-check dams and woody debris flows have been obtained from the previously mentioned studies, design criterion are still not explicit for slit-check dams regulating woody debris flows. Therefore, this study investigates the regulation effect of slit-check dams on woody debris flows through model tests. The whole process of woody debris flows including the initiation, transportation, and deposition is discussed. The regulating effect of slit-check dams on both sediment and woody components is analyzed. Certain criteria of the main parameters were obtained for the design of slit-check dams.

Methods and materials

Woody debris flow case

Many debris flows occurred in the Wenchuan earthquake area after it happened in 2008. Many of these debris flow events showed dam-breaking characteristics because of landslide dams and woody debris jams. A large number of woody debris and boulders were observed along gullies and clogged building structures, formed jams at narrow cross sections, and blocked open-type check dams (Figure 1).

Take the large-scale debris flow in Qipangou, Wenchuan County on 11 July 2013 as an example, this debris flow event lasted for approximately one and a half hours and the solid material flushed out was up to 78.2×10^4 m^3 and caused huge casualties and economic losses (Qin et al., 2016). The main valley of Qipangou is approximately 15.1 km long, 1300–4200 m a.s.l., and 20–120 m wide with an average longitudinal slope of 19.2%; the tributary channel is approximately 5–20 m in width with an

FIGURE 1
Woody debris in the debris flow events in the Wenchuan earthquake area.

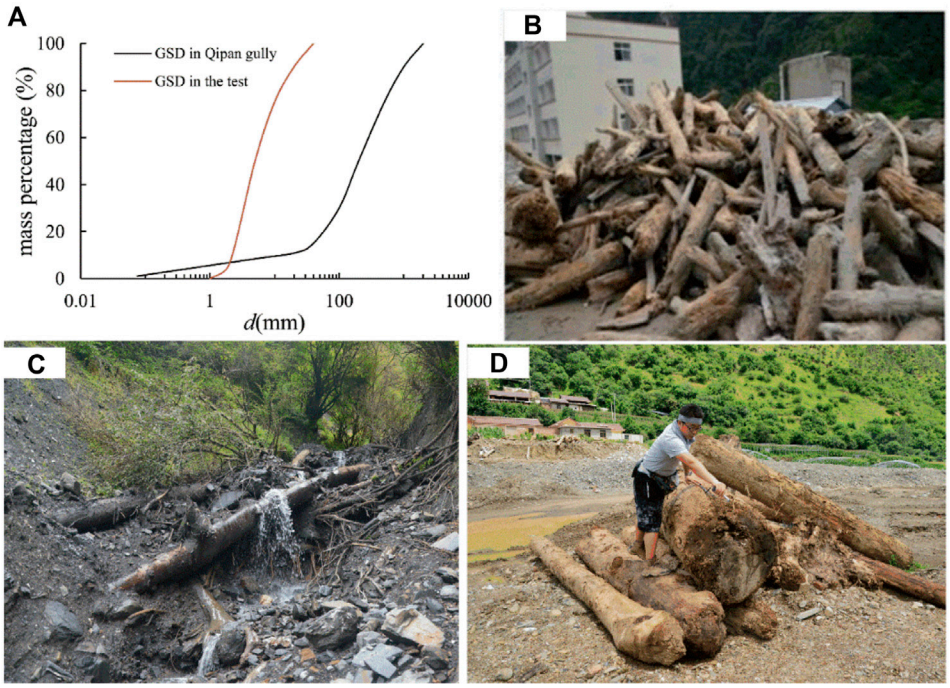

FIGURE 2
LW transported by the debris flow occurred on 11 July 2013 in Qipan Gully, **(A)** GSD of the sediment in the deposits, **(B)** LW artificially collected at the mouth of the main valley, **(C)** LW in the tributary channel, and **(D)** the measurement of LW.

average slope of 23.0%. The largest boulders we observed in the field at approximately 2.0 m. The grain size distribution (GSD) of the sediment obtained from the deposition is shown in Figure 2A. A large number of LWs were distributed both in the main valley and the tributary channel. Some of the LWs were artificially arranged and piled together near the residential area (Figure 2B). LW in the tributary maintained a more natural status (Figure 2C). We conducted detailed measurements of LW in two sections (Figure 2D), that is, the section A (within 1 km of depositing area in the main channel) and section B (1 km upstream from the mouth of the tributary valley). The statistics obtained are listed in Table 1.

Scaling

Small-scale flume tests have been widely used to investigate the complex flow interactions between mass movement and structures. Scaling issues play a crucial role in designing experiments involving grain fluid mixtures to ensure that the

TABLE 1 Statistical data of LW parameters in Qipangou, Wenchuan County on 11 July 2013.

Item	Section A	Section B
Average channel width (m)	20	5
Average channel slope (%)	14.3	16.5
Length of LW (m)	1–8	1–10
Diameter of LW (m)	0.1–0.5	0.1–0.5
Estimated volume of LW (m^3)	850	306
Estimated number of LW	1000	400
Maximum ratio of LW length to channel width	0.1–0.4	0.2–2.0
Density of LW (kg/m^3)	650–900	

test outcome is similar to that of the prototype (Rickenmann, 1999; Iverson, 2015). However, to transfer the entire dynamic process from prototype to laboratory experiment is difficult because the scaling laws are more complicated for debris flow than water (Heller, 2011; Kaitna et al., 2011). As debris flow is a type of gravity-driven motion, Froude similarity is often adopted to design the model tests for debris flow (Rickenmann, 1999; Iverson, 2015). According to the data of Qipangou debris flow, the length scale was set to be $\lambda_L=L_p/L_m=50$, where L_p and L_m are the length of the prototype and the model. The volume scale (λ_V) and velocity scale can be calculated as $\lambda_V=\lambda_L^3=125000$ and $\lambda v=\lambda_L^{0.5}=4.47$ based on Froude similarity.

Experimental device setup

The experimental device consisted of a hoper, a channel, a tailing pool and a water tank. The channel cross-section was rectangular with three dimensions of 6.0 m×0.43 m×0.5 m (length×width×depth) and a slope of 15.8% (9.0°) (Figure 3A). The right-side wall of the channel was made of transparent glass to permit easy observation. The wood sediment debris source was accumulated in the section of 0–1.5 m upstream, the slit dam was made of steel and installed in the channel 0.5 m from the downstream of the channel end, and the distance between the wood sediment source and the slit-check dam was equal to 3.5 m (Figure 3B). The wood sediment debris source was formed by the layered accumulation of sediment and wood as shown in Figure 3C. Figure 3D illustrates the slit-check dam model in which b represents the width of the openings, h is the height of the openings, and n is the number of openings. A water pump installed in the water tank was used to provide a constant water discharge of Q_w= 390 cm^3/s. Three high-definition cameras were installed on the top of the source area, the transportation section and on the top of the slit dam. Another camera was installed on the side of the transportation section.

Wood and sediment materials

The GSD used in the experiment was obtained from the field by removing fine particles smaller than 2 mm and coarse particles larger than 2 m, as shown in Figure 2A. There were two reasons to remove fine particles smaller than 2 mm: 1) d=2 mm was considered the lower acceptable limit particle size of the solid-liquid phase according to previous research on the two-phase flow theory regarding debris flow (Fei et al., 1991; Shu et al., 2008; Le et al., 2018) and 2) miniaturized debris flows exhibited disproportionately large effects of viscous shear resistance and cohesion exerted by the liquid phase (Iverson, 2015). The reason for removing coarse particles was related to the maximum particle size of the sediment (d_{max}), which should be less than 1/5 of the channel width to reduce the size effect in laboratory tests. Hence, the maximum diameter of the sediment d_{max} in this study was selected as equal to 40 mm with d_{30}=3.6 mm, d_{50}=5 mm, and d_{95}=30 mm. The sediment samples are shown in Figure 4A. The total mass of the sediment was 80 kg for each experiment with a bulk volume of 0.052 m^3.

The parameters of LW were designed based on the data in Table 1. The length of the LW model was 5 cm, 10 cm, 15 cm, 20 cm, and 25 cm with a diameter of 5–10 mm. The corresponding prototype was 2.5–12.5 m in length and 25–50 cm in diameter, which are mostly within the range of the prototype in Qipan gully. All LW models were made of natural branches in a cylindrical shape with an average density of 810 kg/m^3 as shown in Figure 4B. The volume and quantity of different LW are listed in Table 1. The ratio of LW volume to sediment volume (V/V_s) was set to be 0.038 and was within the range of 0.001–0.1 according to ESCD (2007). Different lengths of LW required different quantities (N) to satisfy the same V/Vs, which is also shown in Table 2.

Test conditions and measurements

Considering the different parameters of the slit-check dam and LW, two series of tests were set up. Test series A examined the regulation effect of a slit-check dam on debris flow without LW and had a total of 15 groups. Test series B was related to the regulation effect of the slit dam on woody debris flow and had a total of 45 groups. Each group of tests was coded with letters representing the different parameters of the slit-check dam and LW and the corresponding values, such as $n2b5h8L5N250$, which indicates quantities of the slit dam openings n = 2, the opening width b = 5 cm, the opening height h = 8 cm, the length of the LW L = 5 cm, and the quantity of LW N = 250.

A stony debris flow was formed from water eroding the accumulation of wood sediment debris. The duration of water discharge was 90 s. High-definition cameras were used to record the whole test progress. The debris flow density was measured using a cup and calculated *via* $\gamma_c=m_cg/V_c$, where m_c

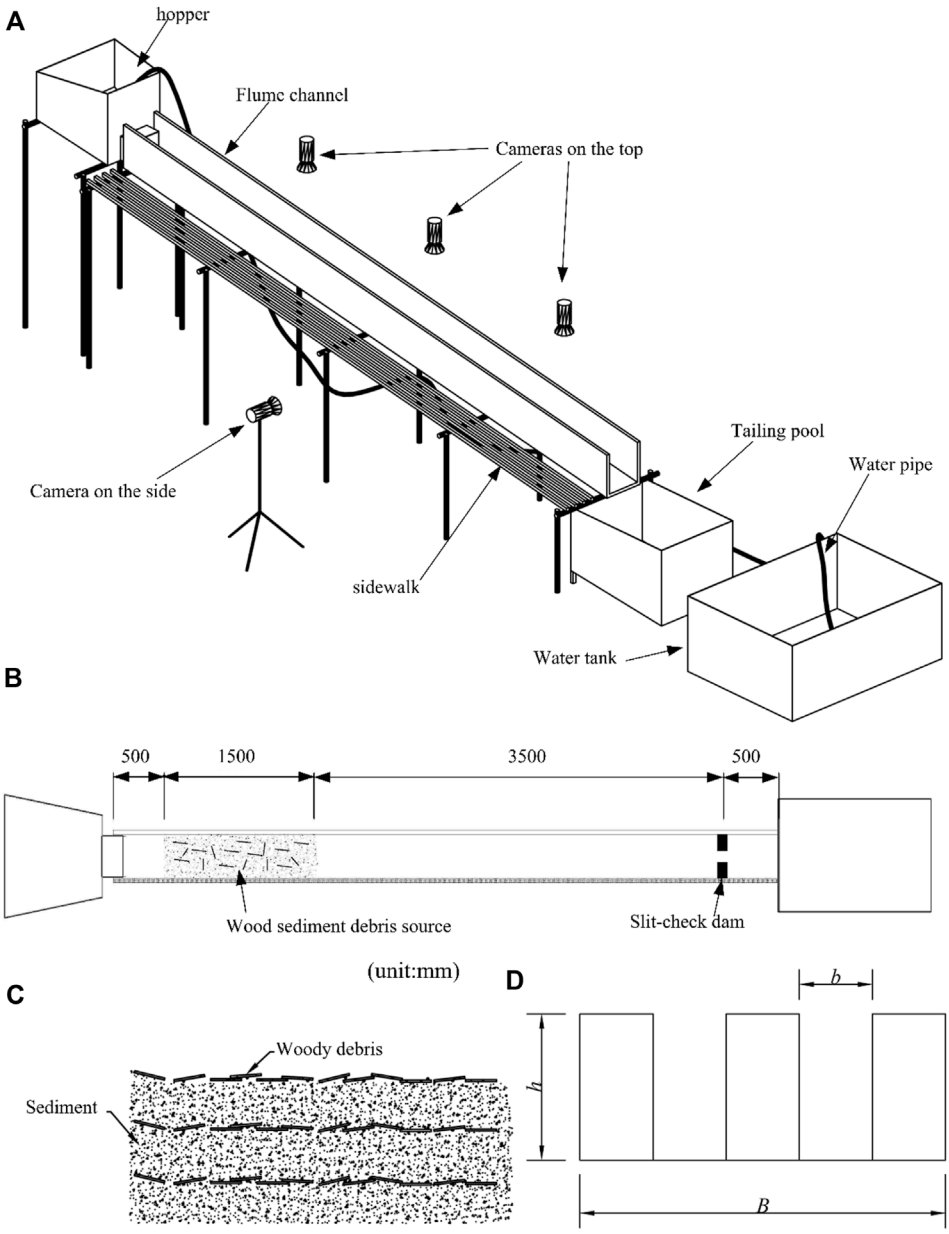

FIGURE 3
Schematic diagram of **(A)** a 3D view of the experimental device, **(B)** plain view of the experimental device, **(C)** accumulation of the wood sediment debris source, and **(D)** slit-check dam model.

is the mass of debris flow collected by the cup and V_c is the volume of the cup. The debris flow velocity was measured using the buoy method and calculated *via* $v=\triangle s/\triangle t$, where $\triangle s$ is the length of the measured section and $\triangle t$ is the duration of the buoy passing the measured section. Sediment and LW in the depositing area and that remaining in the source area was collected, dried, weighed, and sieved.

Results and analysis

Five parameters were first defined to depict the characteristic of the woody debris flow dynamics and the regulating effect of slit-check dam on sediment and woody debris, which are the sediment activation rate (P_{sa}), sediment trapping rate (P_{st}), wood retention rate (P_{wr}), wood clogging rate (P_{wc}), and opening blockage rate (P_{ob}) as expressed by Eqs. 1–(5).

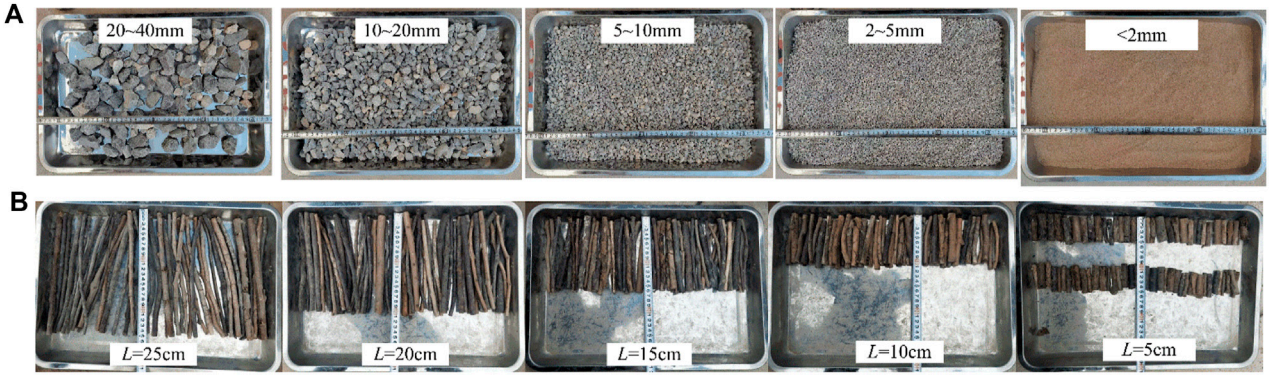

FIGURE 4
Sediment and LW model samples as **(A)** sediment samples and **(B)** LW model samples.

TABLE 2 Test parameters

	Variable	Specific value	Constants
Slit-check dam	Opening width (b) (cm)	5, 10, 15	Original sediment mass (M) (kg): 80 kg
	Opening height (h) (cm)	4, 8, 12	Original sediment bulk volume ($Vs.$) (m^3): 0.52
	Opening quantity (n)	1,2, 3, 4, 5	LW density: 810 kg/m^3
LW	Length (L) (cm)	5, 10,15, 20, 25	Clean water discharge (cm^3/s): 390
	Quantity (N)	50, 63, 83, 125, 250	Relative LW volume (V/Vs.): 0.038

$$P_{sa} = \frac{M - m_r}{M} \times 100\%, \quad (1)$$

$$P_{st} = \frac{m_t}{M - m_r} \times 100\%, \quad (2)$$

$$P_{wr} = \frac{N_t}{N - N_r} \times 100\%, \quad (3)$$

$$P_{wc} = \frac{N_c}{N_t} \times 100\%, \quad (4)$$

$$P_{ob} = \frac{A_b}{A} \times 100\%, \quad (5)$$

where M is the mass of the original source material (kg), which is 80 kg; m_r is the mass of sediment remaining in the source area (kg); m_t is the mass of sediment trapped by the slit-check dam (kg); N is the total amount of LW that is inputed; N_t is the total quantity of LW that stayed behind the slit-check dam; N_r is the quantity of LW that remained in the source area; N_c is the total amount of LW that blocked the slit-check dam openings. A_b and A are the blocked area and the total area of the slit-check dam openings, respectively.

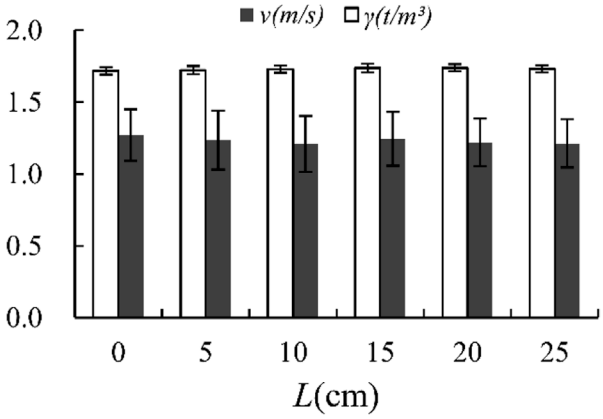

FIGURE 5
Density and velocity of debris flows under different conditions.

Woody debris flow properties

According to the test results, the density of the debris flow γ_c ranged from 1.65–1.76 t/m^3 with an average of 1.73 t/m^3. The sediment volume concentration C_v was calculated via $C_V = \frac{\gamma_c - \gamma_w}{\gamma_s - \gamma_w}$, where γ_w and γ_s are the density of water and sediment, respectively. The C_v ranged from 0.40 to 0.46 with a mean of 0.44. The average velocity of the debris flow under different

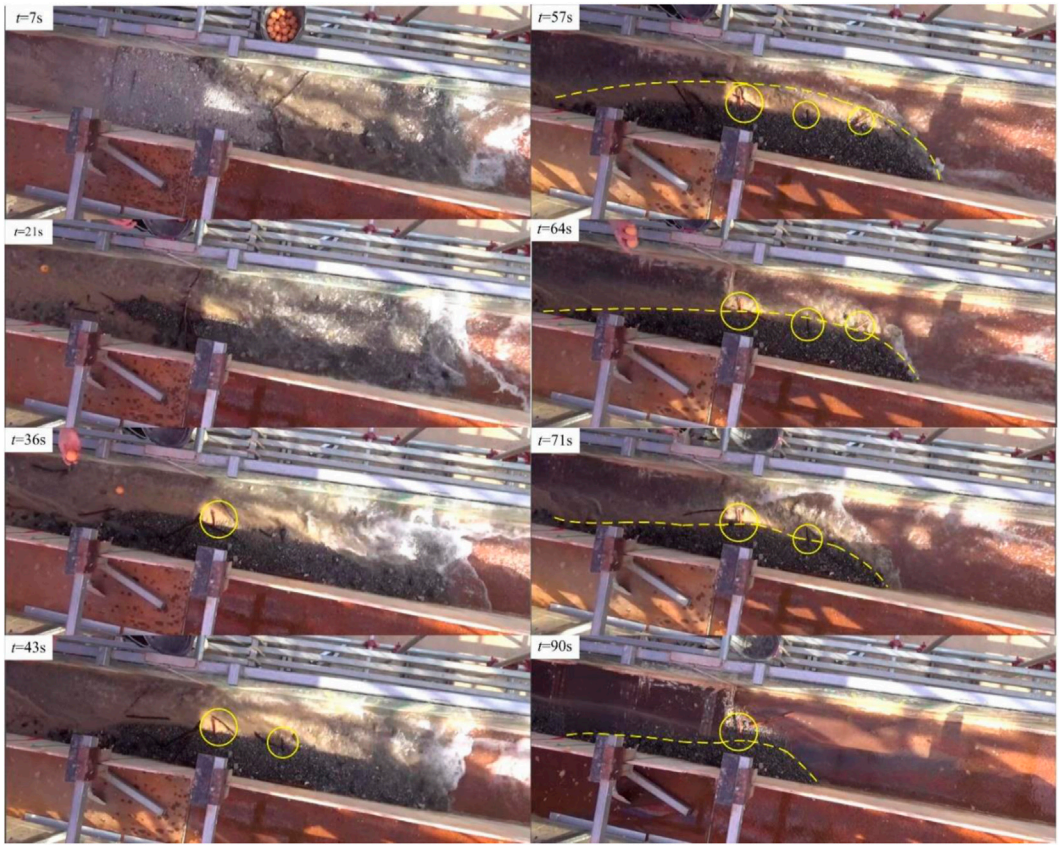

FIGURE 6
Initiation process of a woody debris flow.

conditions was approximately 1.2 m/s. Figure 5 shows that there was little difference in the density and velocity under debris flow conditions with or without LW, which indicates that LW exerted little influence on the properties of debris flow. The debris flow discharge Q_c was calculated according to Eq. 6 with an average of 700 cm^3/s.

$$Q_c = \frac{Q_w}{1 - C_v} \tag{6}$$

Characteristics of the woody debris flow dynamic process

The initiation of the woody debris flow

The formation of woody debris flows by hydraulic scour is a gradual process of erosion that starts with surface erosion and slowly forms erosion chutes until mass erosion collapses (Zheng et al., 2021) (Figure 6). The amount of the activated wood sediment source was variable under different conditions. A certain amount of wood and sediment remained in the source section under most test conditions. When LW was oblique or perpendicular to the direction of the flow in the wood sediment debris mixture, the key log was formed as illustrated by a circle in Figure 6. The sediment around the key log was much more stable and difficult to erode, which resulted in a convex shape around the key log in the wood sediment debris residual, as shown by dashed lines in Figure 6. We defined this effect as an anchoring effect of LW on the surrounding sediment. This phenomenon was also observed in the fields (Figure 7). These key logs can even form step-pool systems that play an important role in the topographic evolution of the channel (Brenda and Davies 2002; Curran and Wohl, 2003; Faustini and Jones, 2003).

Figure 8 illustrates that the sediment activation rate (P_{si}) decreased with an increase of the relative length of LW (L/b). This is because the longer the LW, the greater the probability of forming key logs and the more obvious the anchoring effect. However, due to the random distribution of the LW in each layer in this study, the changing trend of the sediment activation rate was not obvious.

FIGURE 7
LW store and anchor sediment around in the nature field.

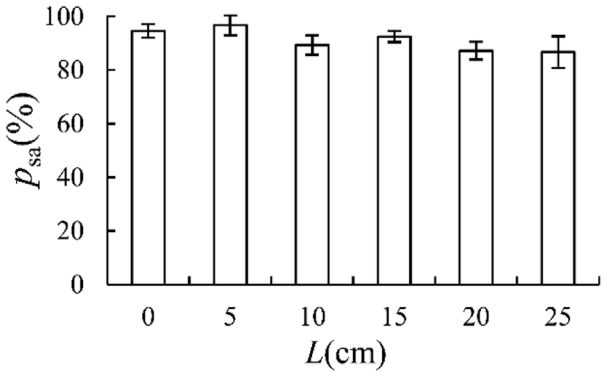

FIGURE 8
Sediment activation rate under different conditions of woody debris.

Transportation of woody debris flow

LW slides on the surface of the fluid with its long axis prone and parallel to the direction of the fluid. The closer the LW was to the wall of the flume, the more pronounced this phenomenon. Due to the large depth of the backwater behind the slit-check dam, LW that arrived before the sediment deposition occurrence floated and rotated in the backwater area and finally drained downstream. Sediment deposition occurred behind the slit-check dam as soon as large boulders reached the dam. Subsequent sediments accumulated and extended upstream, forming deposits within 2 m behind the slit-check dam. Many of the subsequent LW rotated along the long axis perpendicular to the direction of flow when moved to the sediment deposition section and rolled forward and then deposited on the surface of the sediment deposits due to decreased flow depth. As for those LWs that reached the slit-check dam, different draining processes at the slit dam could be observed under different conditions. We further discuss the overflow conditions and draining characteristics of LW at the slit-check dam in the following.

Overflow conditions

According to Lin et al. (2015), the designed maximum discharge of a slit-check dam with rectangular openings can be calculated by Eq. 7:

$$Q_m = n5Ch^{\frac{3}{2}}b, \tag{7}$$

$$C = -0.85\gamma_c + 0.02\theta + 0.24\frac{b}{B} + 1.79, \tag{8}$$

where n is the quantity of the openings; C is the flow discharge coefficient, which can be calculated by Eq. 8; b is the opening width; h is the opening height; γ_c is the flow discharge, t/m^3; θ is the slope of the channel, °; and B is the width of the channel.

Table 3 lists the maximum discharge of the slit-check dam under different conditions and the ratio of the maximum discharge to the measured discharge (Q_m/Q_c).

Table 3 shows that under the single-opening slit-check dam condition, full-section overflow (FO) occurred when Q_m/Q_c<0.6, that is, h=4 cm and b=5 cm, 10 cm, and 15 cm. Local overflow (LO) occurred when Q/Q_c =0.82 ($n1b5h12$) and no overflow phenomenon (NO) occurred when Q_m/Q_c >0.94. Under conditions of a multiple-opening slit-check dam, FO occurred when Q_m/Q_c =0.89 and LO happened even when Q_m/Q_c=1.34 ($n3b5h8$) and 1.78 ($n4b5h8$). As Q_m/Q_c increased, the overflow degree weakened but the characteristics of the opening and the total area influenced the discharge ability. When the opening height of the slit-check dam is too small, the overflow phenomenon may still occur by increasing the opening width. Similarly, when the opening width is too small, increasing the height and quantity of openings cannot prevent the overflow phenomenon. We conclude that the reasonable values of the width and height of a single opening are a prerequisite for a better discharge capacity of the slit-check dam.

Table 3 also shows that under the same opening area conditions, the larger the opening height-to-width ratio, the larger the Q_m/Q_c and the weaker the overflows, which infers that the discharge capacity of a narrow and deep opening is greater than that of a wide and shallow type.

TABLE 3 Overflow conditions

Test condition	Q_m (cm^3/s)	Q_m/Q_c	A (cm^2)	Overflow type[a]
*n*1*b*5*h*4	105.5	0.15	20	FO
*n*1*b*10*h*4	232.3	0.33	40	FO
*n*1*b*15*h*4	365.2	0.52	60	FO
*n*1*b*5*h*8	312.8	0.45	40	FO
*n*1*b*10*h*8	657.1	0.94	80	LO
*n*1*b*15*h*8	1033.0	1.48	120	NO
*n*1*b*5*h*12	574.6	0.82	60	LO
*n*1*b*10*h*12	1207.2	1.72	120	NO
*n*1*b*15*h*12	1897.8	2.71	180	NO
*n*2*b*5*h*8	625.5	0.89	80	FO
*n*3*b*5*h*8	938.3	1.34	120	FO
*n*4*b*5*h*8	1251.1	1.78	160	FO
*n*5*b*5*h*8	1563.9	2.22	200	NO

[a]FO, full-section overflow; LO, local overflow; NO, no overflow

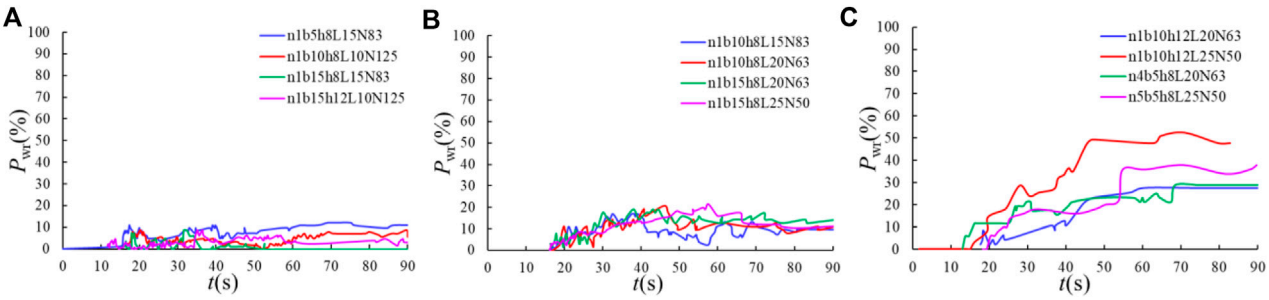

FIGURE 9
Different drainage patterns of LW at the slit-check dam. **(A)** Smoothly draining, **(B)** Intermittently blocking-breaking, and **(C)** Continuously clogging

LW draining characteristics at the slit-check dam

Three patterns of LW draining at the slit-check dam were concluded based on the relationship of wood retention rates (P_{wr}) with time, as shown in Figures 9A–C.

1) Smoothly draining downstream. This pattern indicates that all LWs reaching the slit-check dam could pass through and never block the openings. No clogging occurred at the openings and two specific cases can be subdivided further. One is draining from the top of the dam. For these conditions where overflow occurred, most of the LW reaching the slit-check dam was draining from the top of the dam no matter how long the LW was. The other is passing through the openings of the slit-check dam. This type mainly happened under the $L/b \leq 1.0$ condition. The wood retention rate was always lower than 10% during the whole process as shown in Figure 9A.
2) Intermittently blocking-breaking at the slit-check dam. This pattern mainly occurred under conditions of $1.0<L/b \leq 2.0$, where LW clogged the opening of the slit-check dam first and then partially or totally flowed away by the subsequent fluid. The wood retention rate dramatically fluctuated, as Figure 9B illustrates, and ranged from 10% to 20%.
3) Continuously clogging at the slit-check dam. This mode mostly occurred when $L/b>2.0$ and the logjam formed by LW was stable and hard to break once it was formed. The wood retention rate continued to increase with time and finally reached more than 30% in most cases. A slight fluctuation could also be observed from the P_{wt}-t curve in Figure 9C, which was caused by the phenomenon that a few members of LW were carried away by the subsequent flow without breaking the whole logjam.

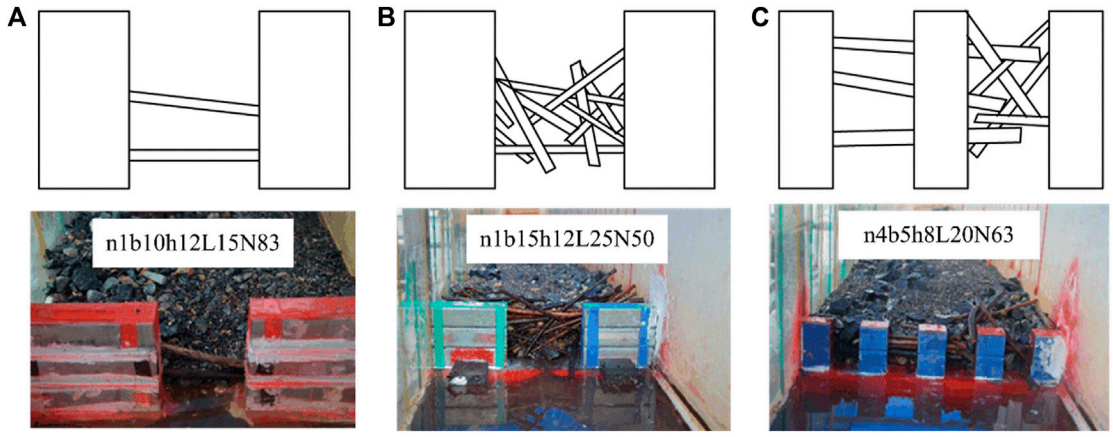

FIGURE 10
Three typical patterns of LW jams at slit-check dams. **(A)** bridging clogging, **(B)** intersecting clogging, and **(C)** hybrid clogging

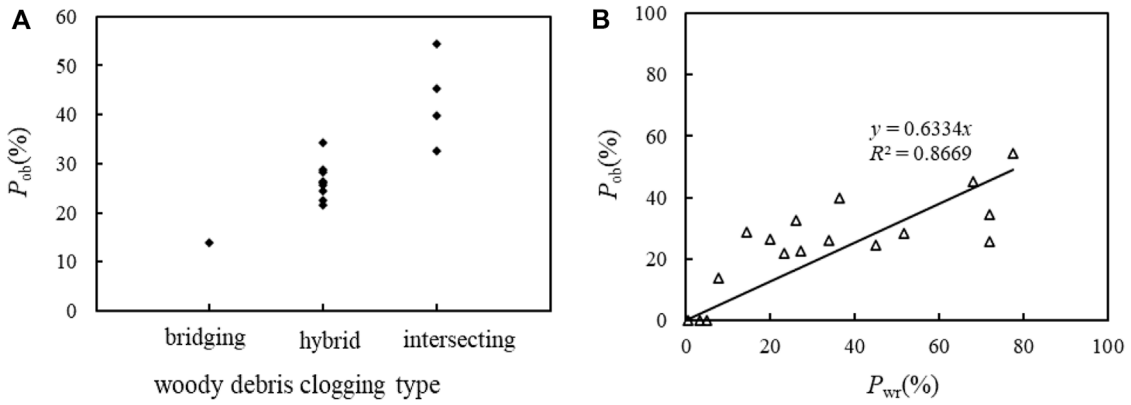

FIGURE 11
Characteristic of LW clogging at the slit-check dam. **(A)** Relationship of LW clogging types with the opening area blocking rate and **(B)** relationship between the wood retention rate and opening area blocking rate.

The characteristics of LW accumulation at the slit-check dam

The LW directly intercepted by the slit-check dam presented three typical forms of accumulation: 1) several LW members bridge across the openings (bridging clogging for short) (Figure 10A); 2) multiple LW members intersect with each other clogging the openings (intersecting clogging for short) (Figure 10B); and 3) both bridging members and intersecting members occurred in the accumulation (hybrid clogging for short) (Figure 10C). Usually, bridging clogging and intersecting clogging were easily formed in single-opening slit-check dams and hybrid clogging was observed in multi-openings of the slit-check dam. According to statistical analysis, the opening blockage rate (P_{oc}) caused by bridging clogging and intersecting clogging was generally less than 20% and more than 30%, respectively, and that caused by the hybrid clogging was between 20% and 30% (Figure 11A). The opening blocking area rate shared a linear relationship with the wood retention rate (Figure 11B).

Regulating effect of the slit-check dam

Regulation effect of the slit-check dam on debris flow without LW

Figure 12A demonstrates that the sediment trapping rate linearly decreased with an increase of the relative opening width, especially when h=4 cm, the sediment trapping rate decreased

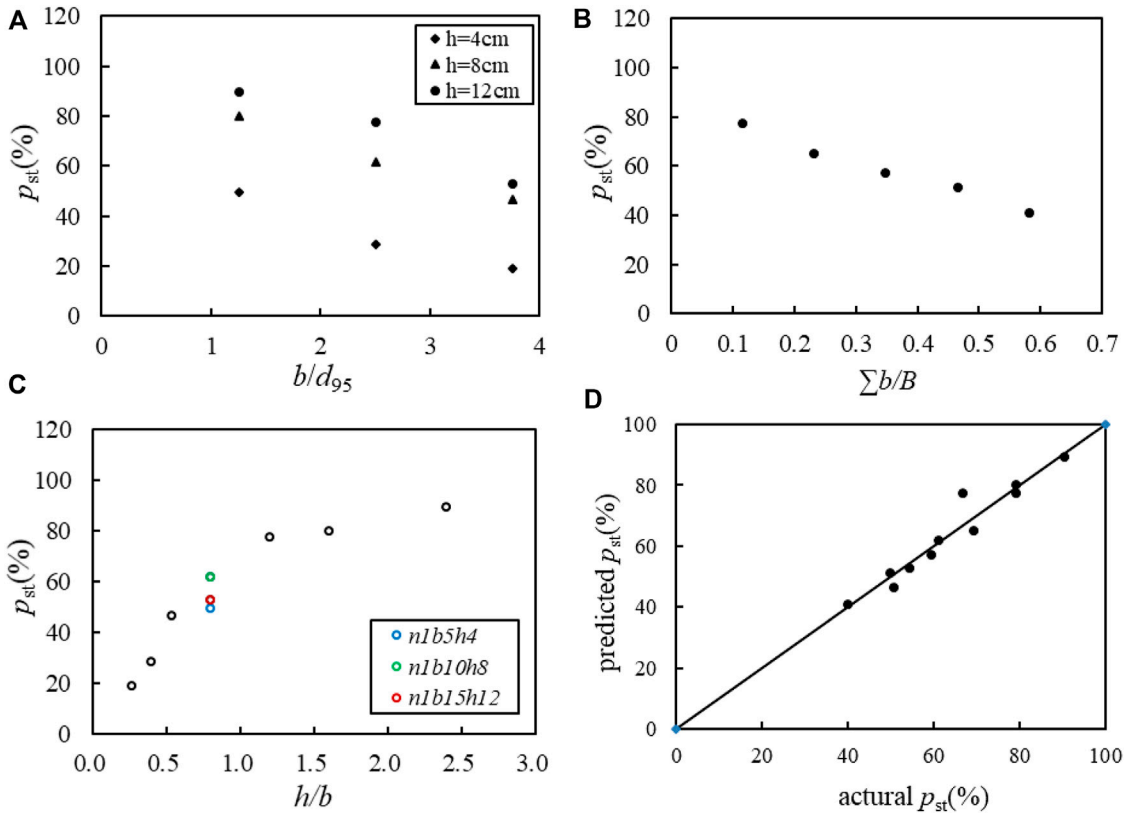

FIGURE 12
Sediment trapping rate under different conditions. **(A)** Different relative opening width, **(B)** different opening density, **(C)** different opening height-to-width ratio, and **(D)** verification of the regression result.

compared to that of h=8 cm and 12 cm. The main reason was that serious overflow occurred according to Table 3, which caused a large amount of sediment discharge from the top of the dam and resulted in a lower sediment trapping rate. Mizuyama and Mizuno (1997) reported that the open check dam could capture debris flows if the relative width of an opening b/d_{95} <2. To ensure more accurate capturing, opening of the check dams was proposed to satisfy the condition of $1.0 \leq b/d_{95} \leq 1.5$ by the Technical Standards on Debris Flow Control and Woody Debris Control in Japan (Osanai et al., 2010). Based on this study, when the opening width b=5 cm (b/d_{95}=1.67), the openings were severely blocked by large boulders and severe overflows occurred. Additionally, the slit-check dam would lose its function of trapping sediment and decreasing the discharge if all openings were blocked. Thus, a preliminary condition of $b/d_{95}>1.67$ is suggested from the perspective of preventing serious blocking of the openings.

Figure 12B shows that sediment trapping efficiency also decreased with an increase of the opening density. With low opening density, a high sediment trapping rate would accelerate sediment accumulation behind the dam and cause the storage capacity to be quickly consumed. Thus, the opening density suggested by Li. (1997) in the range of 0.3–0.6 is reasonable.

Figure 12C indicates that the sediment trapping rate increased with an increase in the height-to-width ratio. The sediment trapping rate increased dramatically when $h/b<1.2$ and then the increasing rate decreased when $h/b>1.2$. Figure 12C also demonstrates that the sediment trapping efficiency was different under the same height-to-width ratio conditions. For example, when b_1=5 cm, h_1=4 cm, b_2=10 cm, h_2=8 cm, and b_3=15 cm, h_3=12 cm all satisfied the condition of h/b=0.8, then the sediment trapping rate appeared the largest when b=10 cm, h=8 cm. The main reason was that under the condition of $n1b5$ $h4$, a serious overflow phenomenon occurred, which caused a large amount of sediment to be discharged from the top of the dam and resulted in a lower sediment trapping rate. While b=10 cm and 15 cm, the slit-check dam was not clogged by boulders so that the sediment trapping effect decreased with an increase of the opening width.

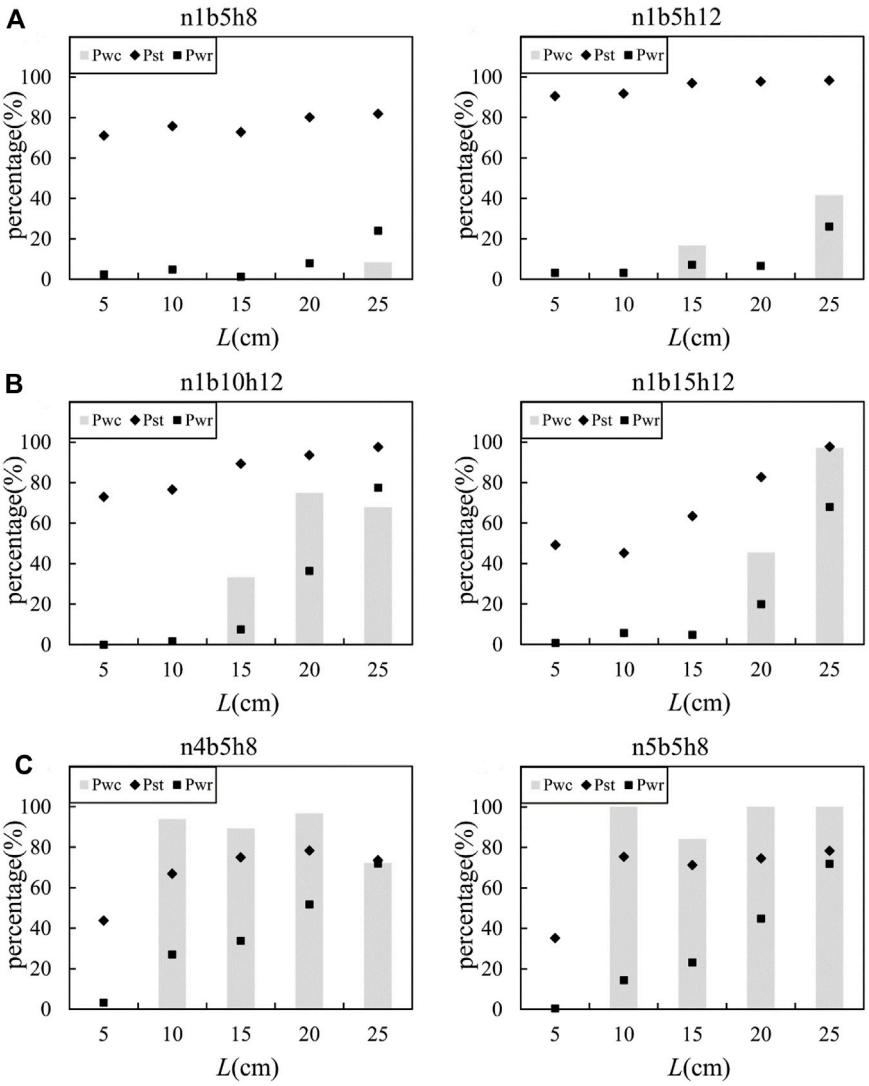

FIGURE 13
Sediment trapping rate (P_{st}), wood retention rate (P_{wr}), and wood clogging rate (P_{wc}) under different conditions. **(A)** Single-opening slit-check dams with overflows, **(B)** single-opening slit-check dams without overflow, and **(C)** multi-opening slit-check dams without overflow.

Considering the results of previous research and this study, the opening width and height of the slit-check dam are suggested to satisfy the conditions of $1.67 \leq b/d_{95} \leq 2.0$ and $h/b \geq 1.2$ to obtain a high sediment trapping efficiency without seriously clogging the openings. The opening density of the slit-check dam is suggested at a range of 0.3–0.6.

According to multiple linear regression analyses using data without overflow conditions, the sediment trapping rate had a relationship with the relative opening width (b/d_{95}), the height-to-width ratio (h/b), and the opening density of the slit-check dam ($\sum b/B$) as follows:

$$P_{st} = 63.3 + 1.86\left(\frac{b}{d_{95}}\right) + 14.1\left(\frac{h}{b}\right) - 84.6\left(\frac{\sum b}{B}\right) \quad R^2 = 0.902. \tag{9}$$

Figure 12D illustrates that the predicted values of the sediment trapping rate by Eq. 9 were well matched with the measured ones.

Regulation effect of the slit-check dam on woody debris flow

Figure 13A shows that the wood retention rates were mostly less than 10% under the conditions of L=5 cm, 10 cm, 15 cm, and

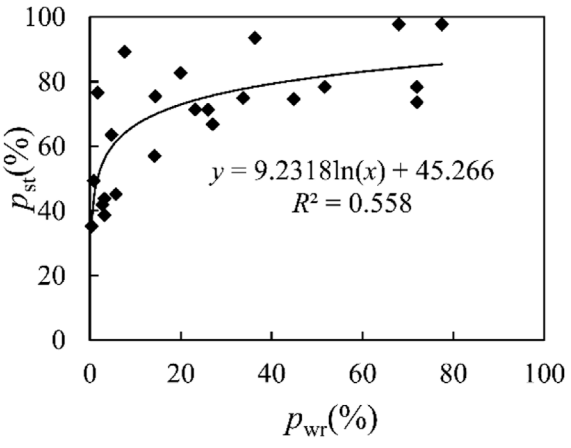

FIGURE 14
Relationship between the wood retention rate and the sediment trapping rate.

20 cm. For the LW with L=25 cm, the wood retention rate increased to 20%, which was mainly a contribution from the LW accumulated on the sediment deposits in the channel because of the low wood clogging rate. This is because LW is easy to deposit in the channel when the length of LW relative to the channel width L/B>0.5 (Lienkeaemper and Swanson, 1987; Abbe and Montgomery, 2003). Sediment trapping rates were relatively high and changed little under different LW conditions. We conclude that the regulation effect of a slit-check dam on LW was very poor, and the influence of LW on the sediment trapping efficiency could be neglected when overflow occurred. Thus, the follow-up analysis only focuses on cases without overflows. Figures 13B,C demonstrate that the wood retention rate linearly increased with the relative length of LW when L/b>1.0 and decreased with the increase of opening density. LW accumulation at the slit-check dam contributed to more than 60% of the wood retention rate. The intercepted LW accumulated at the opening of the slit-check dam and in turn promoted the interception of sediment.

We conclude from the above analysis that the length of LW relative to the width of the channel (L/B) affects its retention during the transportation process, while the length of LW relative to the opening width of the slit-check dam (L/b) and the opening density of the slit-check dam ($\sum b/B$) determined the interception of LW by the slit-check dam. The two aspects affected the wood retention rate together, which in turn affected the sediment trapping efficiency. Based on the regression analysis using data of all conditions without overflows, the relationship between the wood retention rate (P_{wr}) and L/B, L/b and $\sum b/B$ is shown in Eq. 10 and a logarithmic relationship was satisfied between the wood retention rate (P_{wr}) and the sediment trapping rate (P_{st}) as shown in Eq. 11 and Figure 14.

$$P_{wr} = -6.74 + 14.1\left(\frac{L}{b}\right) + 24.0\left(\frac{L}{B}\right) - 34.5\frac{\sum b}{B} \quad R^2 = 0.930 \tag{10}$$

$$P_{st} = 9.232\ln(P_{wr}) + 45.266 \quad R^2 = 0.558 \tag{11}$$

Discussion

Shrestha et al. (2012) proposed five mechanisms for LW jamming at the single-opening slit-check dam according to the geometric relationship and occurrence probability as shown in Figure 15. For this, the occurrence of (a), (b), and (c) needs to meet the basic condition of L/b>1.0. The pattern of (d) mainly occurs when the amount of LW is large, and the probability is related to the quantity and relative length of LW. The larger the amount and L/b, the greater the probability of jamming.

The basic types of LW clogging at the single-opening slit-check dam proposed in our study are bridging clogging and intersecting clogging, which can be explained by the above mechanism. The bridging type can be formed by the mentioned mechanism of (a) and (b), while the intersecting type can be formed by (c) and (d). All jamming observed in this study occurred under the condition of L/b>1.0, while Chen et al. (2020) produced intersecting jamming under the condition of 0.75<L/b<1.

Our study also proposed three draining patterns of LW at the slit-check dam according to the wood retention rate, which is smoothly draining mode, intermittently blocking-breaking mode and continuously clogging mode. The main factor determining the different patterns was L/b. These basic conclusions are consistent with Chen et al. (2020), but the specific conditions for each pattern were different. In this study, the smoothly draining mode mainly occurred under the condition of L/b<1.0, the intermittently blocking-breaking mode at 1.0<L/b<2.0, and the continuous clogging at L/b≥2.0. According to Chen et al. (2020), blocking-breaking phenomenon could be observed when L/b>0.5, and an amplification effect could be observed on debris flow discharge when blocking-breaking occurred. The amplification factor could be as high as 1.6 when L/b=0.85 and V/V_{max}=0.75. However, no obvious amplification effect was observed in either this study or in Shrestha et al. (2012).

The reasons for these differences in the model tests may be as follows: 1) the properties of debris flows are different. Debris flows in Chen et al. (2020) were prepared from real debris flow sediment samples from Jiangjia Valley, and this slurry contained a large number of fine particles; densities of 1.5 t/m^3, 1.7 t/m^3, and 1.9 t/m^3 were used. In this study, a stony debris flow with a density of 1.7 t/m^3 was formed by water eroding coarse-grained sediment accumulation. The existence of fine particles increased the stickiness of the debris flow and also filled the pores of the logjam, which caused a large increase in the upstream sediment storage capacity, and once the logjam broke up, an amplification of peak discharge occurred. 2) The dynamic parameters of debris flow

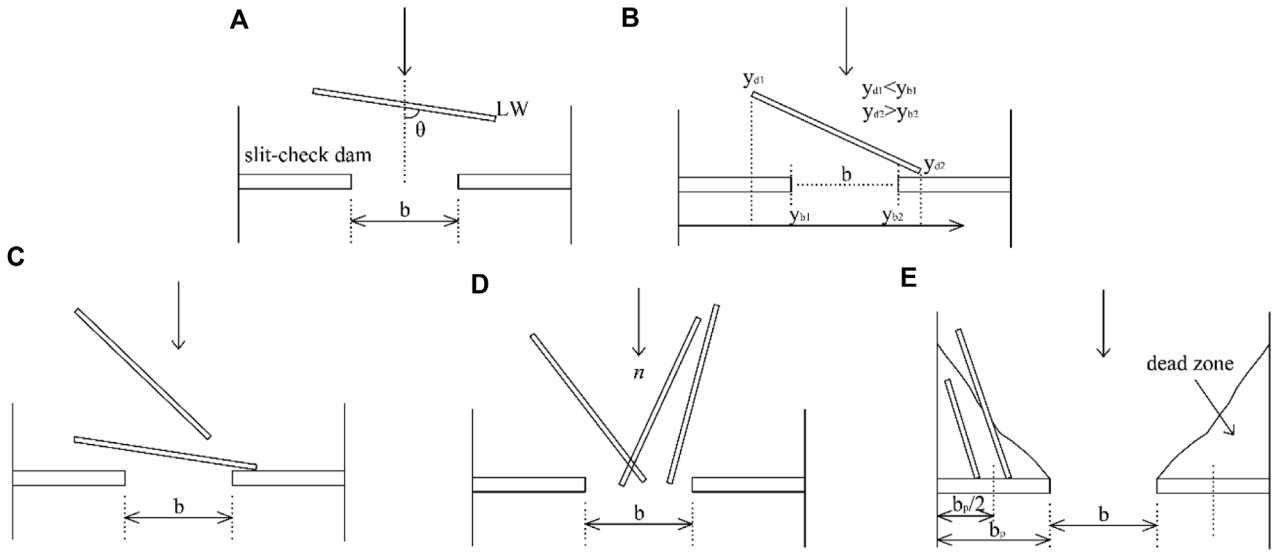

FIGURE 15
LW jamming at the slit-check dam. **(A)** A piece of driftwood was jammed with a large orientation ranging from 80° to 90°. **(B)** A piece of driftwood was jammed in a slit-check dam due to geometric conditions as yd1<yb1 and yd2<yb2. **(C)** A piece of driftwood coming from the rear was also jammed by the pieces of driftwood already jammed in a slit-check dam. **(D)** The pieces of driftwood were jammed when the number of pieces of driftwood arrived at the slit opening at the same time. **(E)** A piece of driftwood was jammed in an impermeable width of the slit-check dam when the centroid of the driftwood was located only inside the dead zone of flow (redrawn from Shrestha et al. (2012)).

are different. Chen et al. (2020) activated the debris flow of 0.75 m^3 by opening the gauge gate for a certain duration (10 s). The maximum discharge of the debris flow was approximately 3200–3600 cm^3/s. However, a constant discharge of 700 cm^3/s was produced by water scouring the sediment deposit in this study over a relatively long duration (90 s). Therefore, the instantaneous transport ability of debris flow to LW is different. Specifically, the larger the flow discharge, the more LWs can be transported at one time. 3) The input method of LW is different. LW was supplied in four groups upstream of the model dam with a frequency of 15 logs/s in Chen et al. (2020), which ensured the input LW to immediately participate in the movement. In this experiment, LWs were mixed with sediment in a layered occurrence as shown in Figure 3C and spread in the source area section. The quantity of LW that can participate in the movement was random in each test and the activation of LW requires more energy.

Based on the aforementioned analysis, the difference in fluid properties, dynamic parameters and input of LW all have an influence on the characteristics of LW transportation and deposition. Thus, future research should carry on stimulations based on real scenarios to make the research results more practical.

Conclusions

Through model tests, we analyzed the regulation effect of slit-check dams with different structural parameters on woody debris flows and discussed the influence of LW on the regulation effect of the slit-check dams. The main conclusions are as follows:

1) LW presented three draining modes at the slit-check dam: smoothly draining mode, intermittently blocking-breaking mode, and continuously clogging mode. Three types of logjams were observed by the intercepted LW at the slit-check dam, which are the bridging logjam, the intersecting logjam, and the hybrid logjam.
2) The opening width is a prerequisite for designing a slit-check dam concerning its regulation effects. This suggested the need to satisfy the conditions of $1.67<b/d_{95}<2.0$ and $1.0<L/b<2.0$ to obtain high sediment and woody trapping efficiency without serious clogging. A narrow and deep opening shape is preferred compared to a wide and shallow type. The height-to-width ratio is suggested to satisfy the condition of $h/b\geq1.2$. Multiple opening slit-check dams present a better regulation effect than single- opening slit-check dams when the opening area is the same. The opening density $\sum b/B$ is recommended and ranges from 0.3 to 0.6.
3) Overflow conditions should be taken into consideration when discussing the regulation effect of slit-check dams on woody debris flows. The ratio of the maximum discharge of the slit-check dam to the discharge of debris flow Q_m/Q_c is suggested to evaluate whether overflow would occur. Overflow will happen for a single-opening slit-check dam when Q_m/Q_c <1 and the value is even higher for multi-opening slit-check dams. Slit-check

dams have a weak regulation effect on LW when overflow occurs, but exert strong effects on LW without overflows. The sediment trapping rate could be predicted according to Eq. 9 for the debris flow without LW. The wood retention rate and sediment trapping rate could be predicted by Eqs. 10, 11, respectively, for woody debris flow.

Data availability statement

The original contributions presented in the study are included in the article/Supplementary Material, and further inquiries can be directed to the corresponding author.

Author contributions

XX and XW contributed to the conception and design of the study. XX, XW, Zhe L, Zhi L, SZ carried out all experiments and XW, Zhe L, and Zhi L organized the database. XW performed the statistical analysis and wrote the first draft of the manuscript. XX was responsible for the improvement of the manuscript. All authors contributed to manuscript revision and read and approved the submitted version.

Funding

This work is supported by the National Natural Science Foundation of China (Grant No 41907258) and Doctoral Research Start-up Fund of Anyang Institute of Technology (BSJ2019011).

Conflict of interest

The authors declare that this research was conducted in the absence of any commercial or financial relationships that could be construed as a potential conflict of interest.

Publisher's note

All claims expressed in this article are solely those of the authors and do not necessarily represent those of their affiliated organizations, or those of the publisher, editors, and reviewers. Any product that may be evaluated in this article, or claim that may be made by its manufacturer, is not guaranteed or endorsed by the publisher.

References

Abbe, T. B., and Montgomery, D. R. (2003). Patterns and processes of wood debris accumulation in the Queets River basin, Washington. *Geomorphology* 51 (1-3), 81–107. doi:10.1016/S0169-555X(02)00326-4

Ana, L., Comiti, F., Borga, M., Cavalli, M., and Marchi, L. (2015). Dynamics of large wood during a flash flood in two mountain catchments. *Nat. Hazards Earth Syst. Sci.* 12 (8), 1741–1755. doi:10.5194/nhess-15-1741-2015

Bocchiola, D., Rulli, M. C., and Rosso, R. (2006). Transport of large woody debris in the presence of obstacles. *Geomorphology* 76 (1–2), 166–178. doi:10.1016/j.geomorph.2005.08.016

Bradley, J. B., Richards, D. L., and Bahner, C. D. (2005). *Debris control structures–Evaluation and countermeasures[R], Hydraulic Engineering Circular 9*, 179.

Braudrick, C. A., and Grant, G. E. (2001). Transport and deposition of large woody debris in streams: A flume experiment. *Geomorphology* 41 (4), 263–283. doi:10.1016/S0169-555X(01)00058-7

Braudrick, C., Grant, G., and Ishikawa, Y. (1997). Dynamics of wood transport in streams: A flume experiment. *Earth Surf. Process. Landforms* 22 (7), 669–683. doi:10.1002/(SICI)1096-9837(199707)22:7<669::AID-ESP740>3.0.CO;2-L

Brenda, R. B., and Davies, R. T. (2002). Influence of large woody debris on channel morphology in native forest and pine plantation streams in the Nelson region, New Zealand. *N. Z. J. Mar. Freshw. Res.* 36 (4), 763–774. doi:10.1080/00288330.2002.9517129

Chen, J., Wang, D., Zhao, W., Chen, H., Wang, T., Nepal, N., et al. (2020). Laboratory study on the characteristics of large wood and debris flow processes at slit-check dams. *Landslides* 17 (2), 1703–1711. doi:10.1007/s10346-020-01409-3

Chen, S. C., and Tfwala, S. (2018). Evaluating an optimum slit check dam design by using a 2D unsteady numerical model. *E3S Web Conf.* 40, 03027. doi:10.1051/e3sconf/20184003027

Collins, B. D., Montgomery, D. R., Fetherston, K. L., and Abbe, T. B. (2012). The floodplain large-wood cycle hypothesis: A mechanism for the physical and biotic structuring of temperate forested alluvial valleys in the north pacific coastal ecoregion. *Geomorphology* 139-140, 460–470. doi:10.1016/j.geomorph.2011.11.011

Comiti, F., Lucía, A., and Rickenmann, D. (2016). Large wood recruitment and transport during large floods: A review. *Geomorphology* 269, 23–39. doi:10.1016/j.geomorph.2016.06.016

Comiti, F., Mao, L., Perciso, E., Picco, L., Marchi, L., and Borga, M. (2008). Large wood and flash floods: Evidence from the 2007 event in the davča basin (Slovenia). *WIT Trans. Eng. Sci.* 60. doi:10.2495/DEB080181

Curran, J. H., and Wohl, E. E. (2003). Large woody debris and flow resistance in step-pool channels, Cascade Range, Washington. *Geomorphology* 51, 141–157. doi:10.1016/S0169-555X(02)00333-1

D'Agostino, V., Degetto, M., and Righetti, M. (2000). "Experimental investigation on open check dam for coarse woody debris control," in *Dynamics of water and sediments in mountain basins Quaderni diIdronomia Montana* (Cosenza: Editoriale Bios), 201–212.

Davidson, S. L., and Eaton, B. C. (2013). Modeling channel morphodynamic response to variations in large wood: Implications for stream rehabilitation in degraded watersheds. *Geomorphology* 202, 59–73. doi:10.1016/j.geomorph.2012.10.005

Doi, Y., Minami, N., and Yamada, T. (2000). Experimental analysis of woody debris trapping by impermeable type Sabo dam, filled with sediment woody debris carried by debris flow. *J. Jpn. Soc. Eros. Control Eng.* 52 (6), 49–55. doi:10.11475/sabo1973.52.6_49

Erosion and Sediment Control Division (2007). *Manual of Technical Standard for establishing Sabo plan for debris flow and driftwood*. Technical Note of National Institute for Land and Infrastructure Management. AvaliableAt: http://www.sabo-int.org/guideline/index.html.

Faustini, J. M., and Jones, J. A. (2003). Influence of large woody debris on channel morphology and dynamics in steep, boulder-rich mountain streams, Western Cascades, Oregon. *Geomorphology* 51 (1), 187–205. doi:10.1016/S0169-555X(02)00336-7

Fei, X. J., Kang, Z. C., and Wang, Y. Y. (1991). Effect of fine grain and debris flow slurry bodies on debris flow motion. Mountain Research. *Mountain Research*(3), 143–152.

Fu, Z. P., Liu, M. M., and Liu, J. C. (2001). Study on measurement and characteristics of percussive force of float timber. *Adv. Sci. Technol. Water Resour.* 3, 33–34+6370.

Gao, K. C., Meng, C. G., and Wei, F. Q. (2005). Analysis and countermeasure for the large-scale landslide debris flow hazard in DeShong, Yunnan, China. *J. Disaster Prev. Mitig. Eng.* 25 (3), 251–257. doi:10.1360/gs050303

Gurnell, A. M., Bertoldi, W., and Corenblit, D. (2012). Changing river channels: The roles of hydrological processes, plants and pioneer fluvial landforms in humid temperate, mixed load, gravel bed rivers. *Earth-Science Rev.* 111, 129–141. doi:10.1016/j.earscirev.2011.11.005

Haehnel, R. B., and Daly, S. F. (2002). Maximum impact force of woody debris on floodplain structures. *J. Hydraul. Eng.* 130 (2), 112–120. doi:10.1061/(asce)0733-9429(2004)130:2(112)(2004)130:2(112)

Han, W. B., and Ou, G. Q. (2006). Efficiency of slit dam prevention against non-viscous debris flow. *Wuhan. Univ. J. Nat. Sci.* 11 (4), 865–869. doi:10.1007/bf02830178

Hartlieb, A. (2017). Decisive parameters for backwater effects caused by floating debris jams. *Open J. Fluid Dyn.* 07 (7), 475–484. doi:10.4236/ojfd.2017.74032

Hassan-Esfahani, L., and Banihabib, M. E. (2016). The impact of slit and detention dams on debris flow control using GSTARS 3.0. *Environ. Earth Sci.* 75, 328. doi:10.1007/s12665-015-5183-z

Heller, V. (2011). Scale effects in physical hydraulic engineering models. *J. Hydraulic Res.* 49 (3), 293–306. doi:10.1080/00221686.2011.578914

Henshaw, A. J., Bertoldi, W., and Harvey, G. L. (2015). *Large wood dynamics along the taliento river, Italy: Insights from field and remote sensing investigations*. Springer International Publishing. doi:10.1007/978-3-319-09054-2_30

Ishikawa, Y., and Mizuyama, T. (1988). "An experimental study of per-meable sediment control dams as a countermeasure against floating logs," in *6th congress asian and pacific regional division int. Association for hydraulic research kyoto* (Kyoto, Japan: Dept. of Civil Engineering, Kyoto Univ.).

Iverson, R. M. (2015). Scaling and design of landslide and debris-flow experiments. *Geomorphology* 2 (44), 9–20. doi:10.1016/j.geomorph.2015.02.033

Jochner, M., Turowski, J. M., Badoux, A., Stoffel, M., and Rickli, C. (2015). The role of log jams and exceptional flood events in mobilizing coarse particulate organic matter in a steep headwater stream. *Earth Surf. Dynam.* 3, 311–320. doi:10.5194/esurf-3-311-2015

Kaitna, R., Chiari, M., Kerschbaumer, M., Kapeller, H., Zlatic-Jugovic, J., Hengl, M., et al. (2011). Physical and numerical modelling of a bedload deposition area for an Alpine torrent. *Nat. Hazards Earth Syst. Sci.* 11, 1589–1597. doi:10.5194/nhess-11-1589-2011

Kato, Y., Hinokidani, O., Kajikawa, Y., and Nagatani, N. (2015). Characteristics of driftwoods and sediment transportation around a slit sabo dam. *Hydroengineering* 71 (4), 985–990. doi:10.2208/jscejhe.71.i_985

Lancaster, S. T., Hayes, S. K., and Grant, G. E. (2001). Effects of wood on debris flow run-out in small mountain watersheds. *Water Resour. Res.* 39 (6), 1168. doi:10.1029/2001WR001227

Lange, D., and Bezzola, G. R. (2006). in *Driftwood: Problems and solutions. Rep. VAW-mitteilung 188*. Editor H.-E. Minor (Zurich, Switzerland: Swiss Federal Institute of Technology).

Laursen, E. M. (1956). Scour around bridge piers and abutments. *Bulletin* 4 (60), 28–31.

Le, M. H., Han, Q. W., and Fang, C. M. (2018). The critical grain size of debris flow. *J. Sediment Res.* 43 (03), 1–6. doi:10.16239/j.cnki.0468-155x.2018.03.001

Li, D. J. (1997). *Debris flow mitigation theory and practices*. Beijing: Science Press.

Lienkaemper, G. W., and Swanson, F. J. (1987). Dynamics of large woody debris in streams in old-growth Douglas-fir forests. *Can. J. For. Res.* 17, 150–156. doi:10.1139/x87-027

Lin, X. P., You, Y., and Liu, J. F. (2015). Experimental study on discharge capacity of spillway of check dam for debris flow. *J. Nat. Disasters* 24 (1), 9–14.

Massong, T. M., and Montgomery, D. R. (2000). Influence of sediment supply, lithology, and wood debris on the distribution of bedrock and alluvial channels. *Geol. Soc. Am. Bull.* 112, 591–599. doi:10.1130/0016-7606(2000)112<591:iossla>2.0.co;2

Mazzorana, B., Comiti, F., Scherer, C., and Fuchs, S. (2012). Developing consistent scenarios to assess flood hazards in mountain streams. *J. Environ. Manag.* 94 (1), 112–124. doi:10.1016/j.jenvman.2011.06.030

Mazzorana, B., Zischg, A., Largiader, A., and Hubl, J. (2009). Hazard index maps for woody material recruitment and transport in alpine catchments. *Nat. Hazards Earth Syst. Sci.* 9 (1), 197–209. doi:10.5194/nhess-9-197-2009

Melville, B. W., and Dongol, D. M. (1992). Bridge pier scour with debris accumulation. *J. Hydraul. Eng.* 118118 (9), 1306–1310. doi:10.1061/(asce)0733-9429(1992)118:9(1306)

Mizuyama, T., and Mizuno, H. (1997). "Prediction of debris flow hydrograph passing through grid type control structure," in *Proceedings of first international conference on debris-flow hazard mitigation* (ASCE), 74–82.

Okamoto, T., Takebayashi, H., Sanjou, M., Suzuki, R., and Toda, K. (2019). Log jam formation at bridges and the effect on floodplain flow: A flume experiment. *J. Flood Risk Manag.* 13 (S1), 12562. doi:10.1111/jfr3.12562

Osanai, N., Mizuno, H., and Mizuyama, T. (2010). Design standard of control structures against debris flow in Japan. *J. Disaster Res.* 5, 307–314. doi:10.20965/jdr.2010.p0307

Pagliara, S., and Carnacina, I. (2010). Temporal scour evolution at bridge piers: Effect of wood debris roughness and porosity. *J. Hydraulic Res.* 48 (1), 3–13. doi:10.1080/00221680903568592

Panici, D., and de Almeida, G. A. M. (2018). Formation, growth, and failure of debris jams at bridge piers. *Water Resour. Res.* 54 (9), 6226–6241. doi:10.1029/2017WR022177

Peng, M., Guan, S., and Feng, S. (2021). Deposition characteristics of debris flows in a lateral flume considering upstream entrainment. *Geomorphology* 394, 1–16. doi:10.1016/j.geomorph.2021.107960

Petraschek, A., and Kienholz, H. (2003). Hazard assessment and mapping of mountain risks in Switzerland. *Bull. Eng. Geol. Environ.* 61 (3), 263–268. doi:10.1007/s10064-002-0163-4

Piton, G., and Recking, A. (2016) Design of sediment traps with open check dams II: Woody debris. *J. Hydraul. Eng.* 142, 04015046. doi:10.1061/(asce)hy.1943-7900.0001049

Qin, H. K., Zhang, H. Q., and Zhang, B. (2016). Formation conditions of the Qipangou multi stage dam-breaking debris flows in Wenchuan area after the earthquake. *J. Eng. Geol.* suppl, 100–107. doi:10.13544/j.cnki.jeg.2016.s015

Rickenmann, D. (1999). Empirical relationships for debris flows. *Nat. Hazards (Dordr).* 19 (1), 47–77. doi:10.1023/A:1008064220727

Rimböck, A. (2004). *Design of rope net barriers for woody debris entrapment: Introduction of a design concept*. Klagenfurt, Austria: International Research Society INTERPRAEVENT, 265–276.

Robert, B., and Steven, F. D. (2004). Maximum impact force of woody debris on floodplain structures. *J. Hydraul. Eng.* 130 (2), 112–120. doi:10.1061/(asce)0733-9429(2004)130:2(112)

Rossi, G., and Armanini, A. (2019). Experimental analysis of open check dams and protection bars against debris flows and driftwood. *Environ. Fluid Mech. (Dordr).* 1, 559–578. doi:10.1007/s10652-019-09714-9

Ruiz-Villanueva, V., Bodoque, J. M., Díez-Herrero, A., and Blade, E. (2014). Large wood transport as significant influence on flood risk in a mountain village. *Nat. Hazards (Dordr).* 74, 967–987. doi:10.1007/s11069-014-1222-4

Schalko, I., Lageder, C., Schmocker, L., Weitbrecht, V., and Boes, R. (2019). Laboratory flume experiments on the formation of spanwise large wood accumulations: I. Effect on backwater rise. *Water Resour. Res.* 55, 4854–4870. doi:10.1029/2018WR024649

Schalko, I., Schmocker, L., Weitbrecht, V., and Boes, R. M. (2018). Backwater rise due to large wood accumulations. *J. Hydraul. Eng.* 144 (9), 04018056. doi:10.1061/(ASCE)HY.1943-7900.0001501

Schmocker, L., Hager, W. H., and Asce, F. (2011). Probability of drift blockage at bridge decks. *J. Hydraul. Eng.* 137 (4), 470–479. doi:10.1061/(ASCE)HY.1943-7900.0000319

Schmocker, L., and Hager, W. H. (2013). Scale modeling of wooden debris accumulation at a debris rack. *J. Hydraul. Eng.* 139 (8), 827–836. doi:10.1061/(asce)hy.1943-7900.0000714

SEDALP WP6 Report (2014). Interactions with structures. Available at: http://www.sedalp.eu/download/dwd/reports/WP6_Report.pdf.191

Sediment Control (Sabo) Division (2000). *Driftwood countermeasure guideline (proposal)*. Japan: Sediment Control (Sabo) Department.

Shrestha, B. B., Nakagawa, H., Kawaike, K., Baba, Y., and Zhang, H. (2012). Driftwood deposition from debris flows at slit-check dams and fans. *Nat. Hazards (Dordr).* 61 (2), 577–602. doi:10.1007/s11069-011-9939-9

Shu, A. P., Zhang, Z. D., and Wang, L. (2008). Method for determining the critical grain size of viscous debris flow based on energy dissipation principle. *J. Hydraulic Eng.* 38 (3), 257–263. doi:10.3321/j.issn:0559-9350.2008.03.001

Song, D., Zhou, G. G., Xu, M., Choi, C., Li, S., and Zheng, Y. (2019). Quantitative analysis of debris-flow flexible barrier capacity from momentum and energy perspectives. *Eng. Geol.* 251, 81–92. doi:10.1016/j.enggeo.2019.02.010

Steeb, N., Rickenmann, D., Badoux, A., Rickli, C., and Waldner, P. (2016). Large wood recruitment processes and transported volumes in Swiss mountain streams

during the extreme flood of August 2005. *Geomorphology* 279, 112–127. doi:10.1016/j.geomorph.2016.10.011

Uchiogi, T., Shima, J., and Tajima, H. (1996). Design methods for wood-debris entrapment. *Interpraevent Int. Symp. Klagenf. Austria* 5 (1), 279–288.

Wang, D. Z., Chen, X. Q., Zhao, W. Y., Xu, M., and Choi, C. E. (2017). Movement and intercept characteristics of driftwood in debris flow. *Sci. Soil Water Conservation* 15 (06), 9–18. doi:10.16843/j.sswc.2017.06.002

Wang, L., Song, D., and Zhou, G. (2022). Debris flow overflowing flexible barrier: Physical process and drag load characteristics. *Landslides* 19, 1881–1896. doi:10.1007/s10346-022-01880-0

Wohl, E. (2011). Threshold-induced complex behavior of wood in mountain streams. *Geology* 39, 587–590. doi:10.1130/G32105.1

Xie, X. P. (2017). *The control effect of multi-herringbone water-separation system to debris flow and its design method based on experimental research*. Beijing: Chinese Academy of Sciences University.

Xie, X. P., Wang, X. J., and Qu, X. (2020b). Experimental study on mitigation effect of slit dam to debris flow with driftwood. *J. Eng. Geol.* 28 (6), 1300–1310. doi:10.13544/j.cnki.jeg.2020-130

Xie, X. P., Wang, X. J., and Yan, C. L. (2020a). A review of the research on woody debris related disaster and its prospect. *Mt. Res.* 38 (04), 552–560. doi:10.16089/j.cnki.1008-2786.000533

Xie, X. P., Wei, F. Q., Yang, H. J., and Xie, T. (2017). Experimental study on large wood filtration performance by herringbone water-sediment separation structure. *J. Mt. Sci.* 14 (2), 269–281. doi:10.1007/s11629-016-3922-6

Zhao, G. D., Hu, H., Song, D., Zhao, T., and Chen, X. Q. (2019). Experimental study on the regulation function of slit dam against debris flows. *Landslides* 16 (1), 75–90. doi:10.1007/s10346-018-1065-2

Zheng, H., Shi, Z., Yu, S., Zhao, T., and Chen, X. Q. (2021) Erosion mechanisms of debris flow on the sediment bed', Water Resources Research. *Water Resour. Res.* 57 (12), e2021WR030707. doi:10.1029/2021WR030707

Nomenclature

L the length of LW

N the quantity of LW

B the width of the channel, which equals the total width of the slit-check dam

b the width of a single opening of the slit-check dam

h the height of the opening of the slit-check dam

n the quantity of the openings of the slit-check dam

A the area of the openings of the slit-check dam

P_{sa} sediment activation rate

P_{st} sediment trapping rate

P_{wr} wood retention rate

P_{wc} wood clogging rate

P_{ob} opening blockage rate

γ_c debris flow density

C_v sediment volume concentration

Q_c debris flow discharge

v_c debris flow velocity Q_m: maximum discharge of the slit-check dam

V the volume of LW

V_s the volume of sediment

frontiers | Frontiers in Earth Science

TYPE Review
PUBLISHED 06 January 2023
DOI 10.3389/feart.2022.981068

OPEN ACCESS

EDITED BY
Xiekang Wang,
Sichuan University, China

REVIEWED BY
Chong Xu,
Ministry of Emergency Management, China
Tao Liu,
University of Arizona, United States

*CORRESPONDENCE
Qiming Zhong,
qmzhong@nhri.cn
Lin Wang,
linwang@xaut.edu.cn

SPECIALTY SECTION
This article was submitted to Geohazards and Georisks, a section of the journal Frontiers in Earth Science

RECEIVED 29 June 2022
ACCEPTED 22 December 2022
PUBLISHED 06 January 2023

CITATION
Zhong Q, Wang L, Shan Y, Mei S, Zhang Q, Yang M, Zhang L and Du Z (2023), Review on risk assessments of dammed lakes. *Front. Earth Sci.* 10:981068. doi: 10.3389/feart.2022.981068

Review on risk assessments of dammed lakes

Qiming Zhong[1]*, Lin Wang[2]*, Yibo Shan[1], Shengyao Mei[1], Qiang Zhang[2], Meng Yang[1], Lucheng Zhang[1] and Zhenhan Du[3]

[1]Key Laboratory of Reservoir and Dam Safety of the Ministry of Water Resources, Nanjing Hydraulic Research Institute, Nanjing, China, [2]State Key Laboratory of Eco-hydraulics in Northwest Arid Region, Xi'an University of Technology, Xi'an, China, [3]College of Civil and Transportation Engineering, Hohai University, Nanjing, China

As one type of natural disaster, dammed lakes pose a serious threat to the safety of lives and properties downstream. Scientific risk assessments of dammed lakes are key for pre-disaster prevention and post-disaster rescue. However, due to the lack of basic information and uncertainty surrounding materials and loads, risk assessments of dammed lakes are more complex than those of artificial reservoir dams, and comprehensive assessment methods are lacking. Based on the evolution of dammed lake hazard chains, starting with the concept of a dammed lake risk assessment, this paper focused on six aspects: worldwide dammed lake databases, hazard assessments for landslide dams, breach mechanisms and breach processes, flood routing after landslide dam breaching, loss assessments, and risk mitigation measures. A comprehensive review was conducted on the qualitative and quantitative risk assessment methods around the world, as well as future outlooks.

KEYWORDS

dammed lake, dam stability, breach process, flood routing, loss of life, risk mitigation

Highlights

- The hazard chain evolution process of dammed lake was focused.
- A worldwide database was compiled to provide basic information on dammed lakes.
- Hazard assessment methods of landslide dams were reviewed.
- The simulation methods of breach processes and flood routing were reviewed.
- Loss assessment methods and risk mitigation measures were reviewed.

1 Introduction

Triggered by earthquakes or rainfall, dammed lakes are a type of geological hazard in mountainous areas, and are caused by landslides that block rivers (Costa and Schuster, 1988; Korup, 2002; Ermini and Casagli, 2003; Fan et al., 2020). The accumulations blocking the rivers are called landslide dams. A global diagram of the distribution of 350 dammed lakes using topographic data from US Geological Survey from Ermini and Casagli (2003) showed that dammed lakes are widely spread around the world. Shen et al. (2020a) studied 1,393 documented dammed lakes and reported that 50.5% were earthquake-induced and 39.3% were rainfall-induced, which together made up nearly 90% of the total cases. The other causes were snowmelt, human-causes, and volcanic eruptions.

As the water retaining structures of dammed lakes, landslide dams are composed of Earth and stone materials, but there are significant differences between natural dams and artificial embankment dams. The main differences lie in (Zhong et al. 2021): 1) Dam geometry. Landslide dams are generally longer in the longitudinal direction and the crests are uneven. 2) Structure and materials. Most landslide dams have complex structures, strong heterogeneity and wide

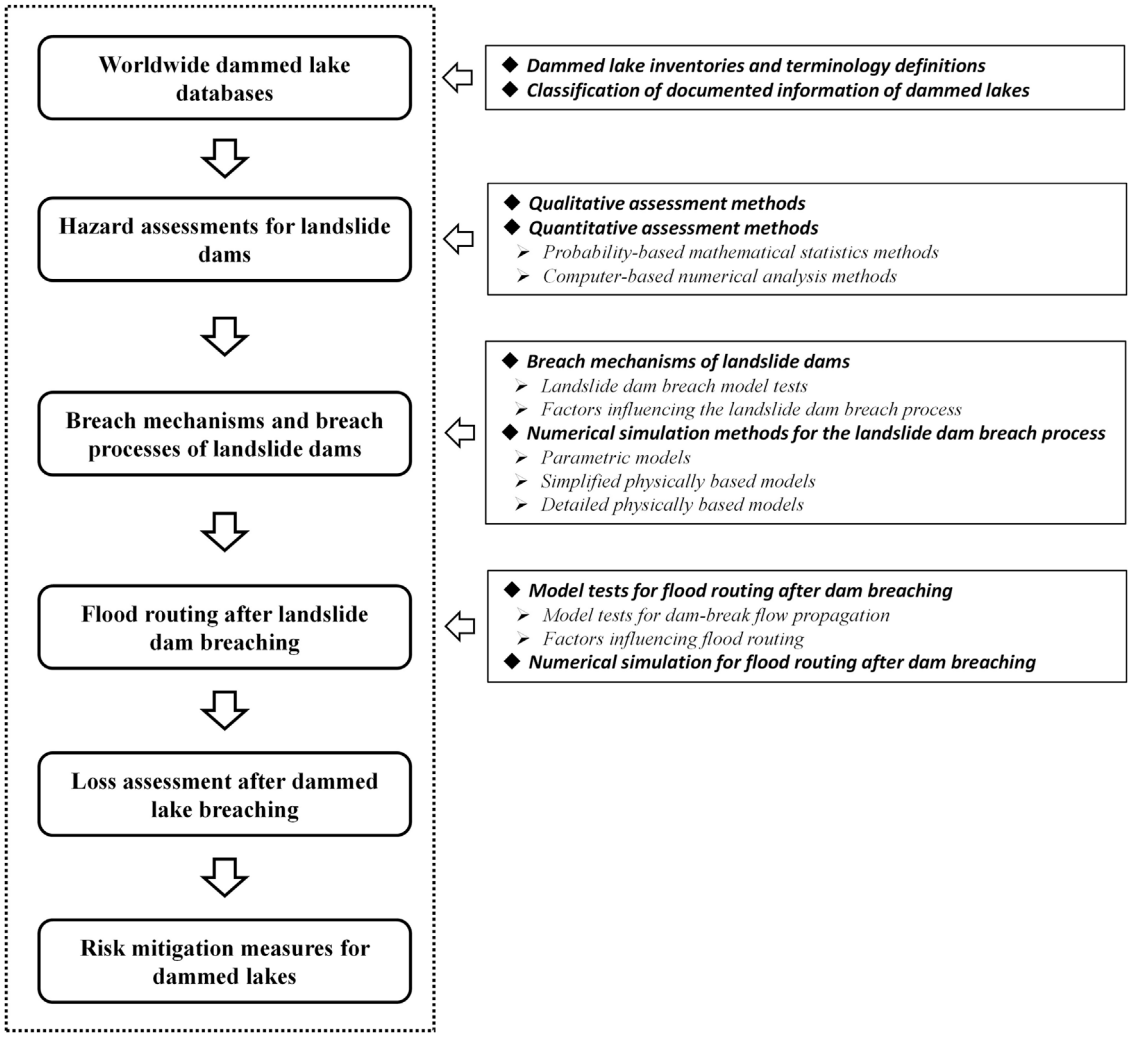

FIGURE 1
Overall architecture of the review.

grain-size distributions. 3) Hydrodynamic conditions. Because there are no flood discharge facilities on landslide dams, overtopping failures are prone to occur when water levels rise in dammed lakes; furthermore, due to the long length in the longitudinal direction, the maximum hydraulic gradient of a landslide dam is generally lower than that of an embankment dam. Hence, overtopping failures are the main failure type and more 90% of documented historical failures have been overtopping-induced (Costa and Schuster, 1988; Zhang et al., 2016).

Out of 73 dammed lakes around the world studied by Costa and Schuster (1988), 85% of the cases lasted less than 1 year, and 27% less than 1 day. Later, Peng and Zhang (2012a) and Shen et al. (2020a) also found similar statistical results based on 204 and 352 cases, respectively. In general, the failure probabilities of dammed lakes are much higher than those of artificial reservoirs. Once a dammed lake breaches, it may cause a serious flood disaster, so a reasonable assessment of the risk of the dammed lake can prepare emergency response, reduce the loss of property and environmental damage, as well as protect people's lives.

Risk is defined as the probability of injury or loss, which is a measurement of the likelihood and severity of negative effects on life, property, safety, health, or the environment. Although there are different understandings of risk, they are usually described from two perspectives: the first is possibility, as in the probability of occurrence; the second is consequence, as in the loss caused. According to the definition, risk can be quantified by the expected value of the consequences, which can be depicted by the product of the frequency of disasters and the losses. For a dammed lake, risk can be expressed as the product of failure probability and loss in Eq. 1.

$$R = P \times C \tag{1}$$

where R is the dammed lake risk; P is the failure probability; C is the loss after a dammed lake breach.

Since the 1980s, much research has focused on risk assessments of dammed lakes. After decades of development, great progress has been achieved in theoretical and practical aspects. A number of reviews covered the related topics (i.e., Costa and Schuster, 1988; Korup, 2002; Liu et al., 2019; Fan et al., 2019a; Fan et al., 2020; Fan et al., 2021;

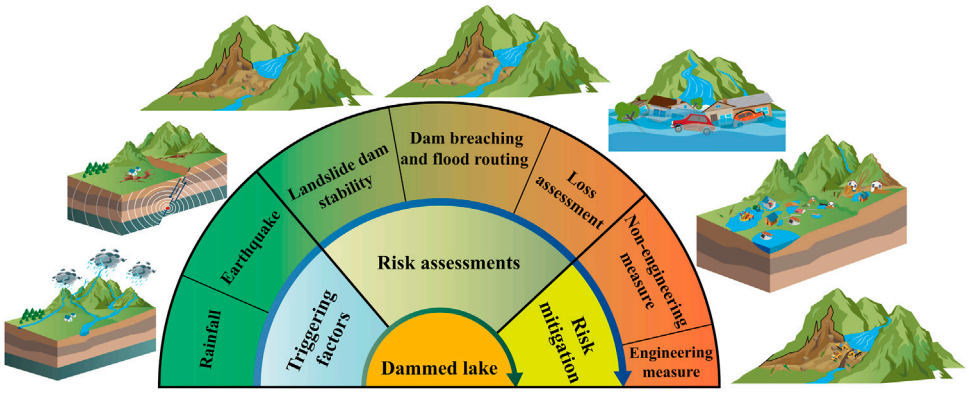

FIGURE 2
Geologic hazard chain triggered by dammed lake breaching and risk mitigation.

Zhong et al., 2021). Based on the information of 225 landslide dams, the publication of a benchmark review by Costa and Schuster (1988) first provided a comprehensive overview on the causes, classification, and grain size distribution of landslide dams, as well as their longevity and failure modes. Fourteen years later, with special attention to New Zealand, Korup (2002) emphasized the importance of high-quality essential data, and reviewed the state of knowledge at that time and elucidated several directions of future research potential on the formation and failure of landslide dams. Later, Liu et al. (2019) reviewed the outburst floods of landslide dams in China in terms of their characteristics, distribution, causes, as well as case studies and future research directions. Fan et al. (2019a), Fan et al. (2020), and Fan et al. (2021) presented a series of overviews on the patterns, mechanisms, and impacts geologic hazard chains, especially technological and methodological advances on landslide dam formation, stability, and impacts. Zhong et al. (2021) focused on the breach mechanisms and numerical modeling of embankment and landslide dam breaches, and illustrated model uncertainties, limitations, and further directions.

Despite these efforts, most of the reviews focused on landslide dam formation, stability, and breach processes; according to the definition of risk, a thorough review of dammed lake risk assessments has not been conducted, particularly with respect to advances in hazard chain evolution due to the damming of rivers by landslides.

This review focuses on hazard chain evolution of dammed lake formation and provides an overview of hazard assessments of landslide dams, breach processes, breach-induced flood routing, loss assessments, and risk mitigation measures.

Section 2 reports on data from landslide dam cases around the world. The cases in these databases are compiled to provide fundamental information on dammed lakes (Section 2.1). Furthermore, in order to unify the understanding, the terminology (Section 2.1) used for characterizing the stability of landslide dams, damming modes, and data classification (Section 2.2) based on the study purpose is also discussed in this section. Landslide dam stability is the prerequisite and foundation for a risk assessment, and Section 3 attempts to summarize hazard assessment methods for landslide dam stability, which includes qualitative (Section 3.1) and quantitative (Section 3.2) assessment methods. Section 4 is devoted to breach mechanisms and numerical simulation methods of landslide dam breach processes. A synopsis of the model tests for landslide dam breach processes and influencing factors is provided and illustrated (Section 4.1). Numeric simulation methods, including parametric, simplified physical, and detailed physical modeling are introduced and compared (Section 4.2). Then, model tests (Section 5.1) and numerical modeling (Section 5.2) to describe breach-induced flood routing are analyzed and summarized in Section 5, in which inundation is a key component of risk assessment. Section 6 reviews loss assessment methods after landslide dam breaching, while associated progresses in loss of life are introduced. Section 7 presents risk mitigation measures for dammed lakes, focusing on engineering measures. Section 8 discusses the uncertainties and limitations in the current study, and suggests several scientific issues for further study in the field of dammed lake risk assessments. Section 9 summarizes the research results based on the review work. The overall architecture of this review is shown in Figure 1. This review is a continuation of a study on breaches of embankment and landslide dams (Zhong et al., 2021). Herein, the advances of risk assessments methodologies for dammed lake geologic hazard chains are presented (Figure 2).

2 Worldwide dammed lake databases

2.1 Dammed lake inventories and terminology definitions

In recent decades, a high degree of study of dammed lakes has produced a multitude of documented cases. In this review, in order to comprehensively understand the fundamental information on dammed lakes, such as global distribution, geological and hydrological conditions, dam geomorphology, dam material composition, failure modes, and breach characteristics, an extensive collection of dammed lake cases was conducted. The published inventories that were closely related to the review and compiled in our database, are summarized in Table 1.

In Table 1, according to the stability classification, dammed lakes were classified into formed-stable, formed-unstable, and unknown in terms of landslide dam status. Herein, formed-stable refers to a landslide dam in which the blocked a river/valley still exists or has

TABLE 1 Summary of published dammed lakes inventories.

No.	Investigators	Country/ Region	No. of cases	Information
1	Costa and Schuster (1991)	World	463	Location, damming date, dammed river or lake, landslide type, trigger mechanism, landslide volume, dam type, dam height, dam length, dam width, lake length, lake volume, failure time, failure mechanism, breach dimensions, subsequent controls, and dam materials
2	Chai et al. (1995)	China	147	Damming date, dam volume, dammed river or lake, failure time, trigger mechanism, and subsequent hazards
3	Ermini and Casagli (2003)	World	350	Country, river or landslide name, damming year, catchment area, dam volume, dam height, and stability status
4	Casagli et al. (2003)	Italy	42	Grain size distribution of dam
5	Korup (2004)	New Zealand	232	Dam height, dam length, dam width, dam volume, dam type, trigger mechanism, age, current status, lake length, lake width, lake area, lake volume, catchment area, and upstream channel gradient
6	Tong (2008)	Japan and others	79 + 84	Japan (79 cases): Damming year, name, trigger mechanism, catchment area, mean/peak inflow rate, upstream/downstream channel gradient, lithology, horizontal travel distance, landslide volume, dam height, dam length, dam width, height of water level, lake area, dam volume, lake volume, and longevity
				Others (84 cases): River or landslide name, damming year, catchment area, dam volume, dam height, and stability classification
7	Cui et al. (2009)	China	257	Location (county/city), drainage basin, dam height, water storage capacity, width to height ratio, and composition of dam
8	Xu et al. (2009)	China	32	Name, County, dammed river, dam height, dam volume, lake volume, landslide type, dam materials, and failure mode
9	Chen et al. (2011)	Taiwan, China	17	Name, back water length, dam length, lake basin type, catchment area, and dam failure mechanism
10	Dong et al. (2011)	Japan	43	Catchment area, mean/peak flow, upstream/downstream channel gradient, landslide volume, landslide area, horizontal travel distance, slope height, dam height, dam width, dam length, lake depth, lake area, and dam volume
11	Hermanns et al. (2011b)	Argentina	61	Lake/river or site name, catchment area, dam volume, dam height, current status, and dam type
12	Peng and Zhang (2012a)	World	52	Name, location, damming date, dam height, dam width, dam volume, lake volume, dam erodibility, breach geometry (breach depth, top/bottom width), peak breach flow discharge, and breach time
13	Stefanelli et al. (2015)	Italy	300	Location, consequences, dam material, lithology, trigger mechanism, damming date, failure date, dam type, dam length, dam width, dam height, dam volume, dam condition, failure mechanism, name of dammed river, valley width, steepness of river bed, lake name, lake length, lake width, lake depth, lake surface area, lake volume, lake altitude, and longevity
14	Zhang et al. (2016)	World	1,044	Country, name, landslide type, trigger mechanism, dam type, dam volume, dam height, dam length, dam width, lake length, lake volume, failure time, failure mechanism, breach geometry (breach depth, top/bottom width), breach time, peak breach flow discharge, and loss of life
15	Stefanelli et al. (2018)	Peru	51	Location, lake volume, dam type, dam volume, dam condition, valley width, catchment area, steepness of river bed, and lake condition
16	Shen et al. (2020a)	World	70	Location, dammed river, damming date, dam materials, trigger mechanism, dam volume, dam height, dam width, dam length, lake volume, inflow rate, and longevity
17	Shan et al. (2020)	World	158	Country/region, name, damming date, dam height, dam length, dam width, dam volume, lake volume, catchment area, steepness of river bed, stability status, and dam materials

disappeared due to sediment infilling. Over its lifetime, inflow water may overtopped the dam crest, but neither total failure nor destructive flood occurred (Stefanelli et al., 2015; Stefanelli et al., 2016; Shan et al., 2020). Formed-unstable refers to a landslide dam that had disappeared when statistical work was conducted, and the longevity may have been minutes to centuries after its formation. A landslide dam can be classified as formed-unstable if human intervention has strongly influenced the dam morphology and hydrological conditions to prevent potential disasters (Stefanelli et al., 2015; Stefanelli et al., 2016; Shan et al., 2020). Unknown means the current status of a landslide dam could not be verified during the investigation. The unknown dams are not of concern in this review.

Based on the relationship with the stream/valley floor, landslide dams can be classified into six categories (Costa and Schuster, 1988; Hermanns et al., 2011a; Fan et al., 2020): 1) Partial blocking. A landslide did not reach the opposite bank of the stream/valley. 2) Complete blocking. A landslide reached the opposite bank of the stream/valley. 3) Longitudinal blocking. A landslide extended a long distance in the streamwise direction of the stream/valley. 4) Two sides blocking. Simultaneous movement of two landslides detached from opposite sides of the same stream/valley. 5) Multiple blocking. A single landslide sent multiple tongues of debris into a stream/valley and formed two or more landslide dams in the same section of the river. 6) Down-traverse blocking. A landslide involved one or more failure

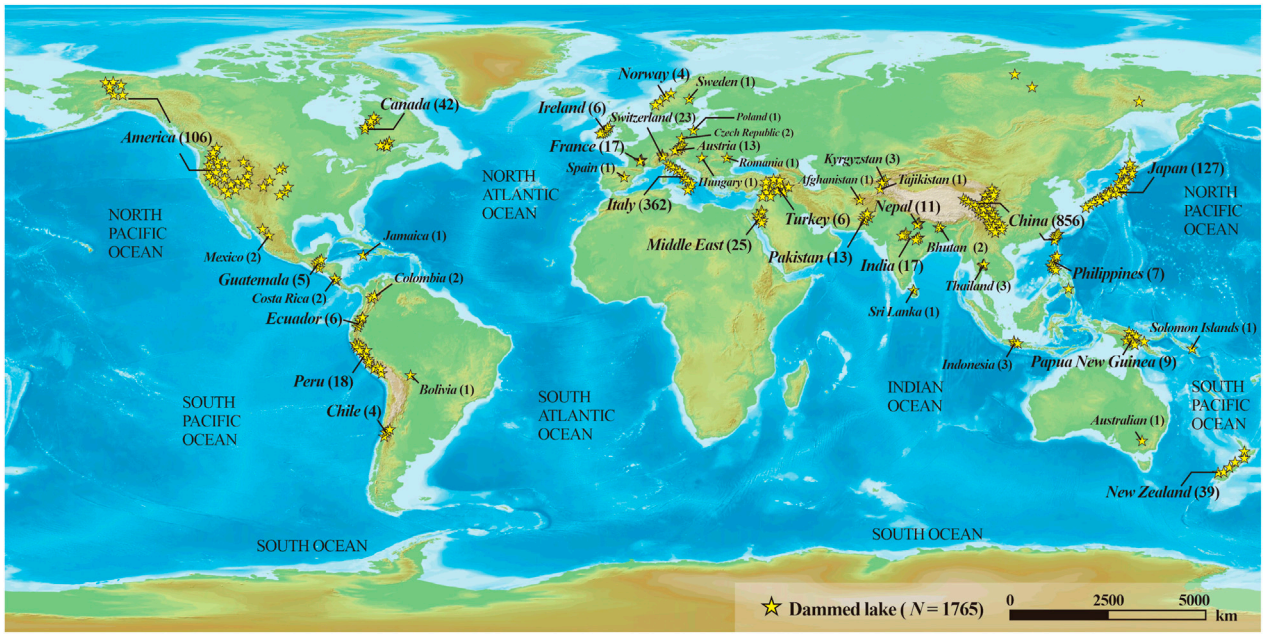

FIGURE 3
Worldwide distribution of 1,765 dammed lakes.

surfaces that extended under the stream/valley and emerged on the opposite side.

Based on the collection methods, theses inventories can be categorized as historical or event-based. The cases in the inventories of Cui et al. (2009), Xu et al. (2009), and Chen et al. (2011) are event-based. Of these, the first two referred to cases that were triggered by the 2008 Wenchuan earthquake in China, and the cases in the third inventory were triggered by the Morakot typhoon in 2009 in Taiwan, China. The other inventories are all historical cases.

In terms of the study purposes, the recorded information within these inventories have been used for geological surveys (i.e., Costa and Schuster, 1991; Chai et al., 1995; Cui et al., 2009; Xu et al., 2009; Chen et al., 2011; Hermanns et al., 2011b; Stefanelli et al., 2015; Stefanelli et al., 2018), landslide dam stability analysis (i.e., Ermini and Casagli, 2003; Casagli et al. 2003; Korup, 2004; Tong, 2008; Dong et al., 2009; Shen et al., 2020a; Shan et al., 2020) or dammed lake breach process simulations (Peng and Zhang, 2012a; Zhang et al., 2016).

In this review, based on the previous inventories and information collection, a database of 1,765 recorded dammed lakes was collected and sorted by the authors. The distribution of the 1,765 dammed lakes around the world is shown in Figure 3. Where cases were repeated across inventories, scientific inspection work was conducted to select the most accurate and complete information. Figure 4 chronologically presents the number of documented dammed lake cases in China. The landslide dam cases prior to the 1860s are listed together according to age, and other cases were organized every two decades until 2020. Because of the vast territory and special geographical conditions of China, the Tibetan Plateau and southwestern China located in a strong seismic activity zone have become high incidence areas of dammed lakes. It is worth mentioning that, the number of documented dammed lakes have increased in China in past decades.

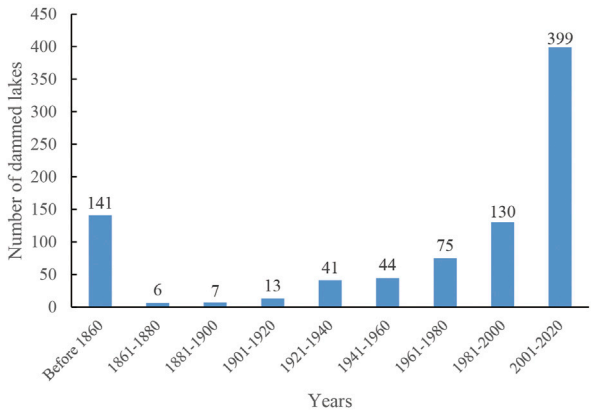

FIGURE 4
Number of documented dammed lake cases in China.

2.2 Classification of documented information of dammed lakes

As historical recorded dammed lakes have increased, global databases have shown an increasing trend. Depending on the purpose of a study, the documented information for dammed lakes varied from one to another. The information for dammed lakes can be categorized into three types: morphological indexes of landslide dams (i.e., dam height/width/length/volume), hydrodynamic conditions of dammed lakes (i.e., lake surface area/length/volume, catchment area, inflow discharge, dammed river steepness), and material composition of landslide deposits (i.e., lithology, material composition, grain-size distribution). Furthermore, for the formed-unstable dammed lakes, breaching information, such as breach flow discharge, breach size, and

TABLE 2 A brief overview of qualitative hazard assessment methods for landslide dams.

No.	Investigators	Survey methodology	Evaluation indexes	Assessment method
1	Weidinger (2006)	Remote sensing	Dam morphology, debris volume, material composition, climatic conditions, movement type of landslide, secondary compaction, catchment area, and sedimentation rate	Historical analysis method
2	Cui et al. (2009), Xu et al. (2009), Fan et al. (2019b)	Remote sensing	Dam height, material composition, and storage capacity	Engineering analogy method
3	Brideau et al. (2019)	Remote sensing	Dam morphology, material composition, temperature, rainfall, lake surface area, and flow channel dimension	Historical analysis method
4	Niazi et al. (2010)	Geoelectric survey (ERT)	Spatial variations in the resistivity, and seepage field	Historical analysis method
5	Bianchi-Fasani et al. (2011)	Geoelectric survey (ERT, VES), seismic survey (SRT, MASW)	Dam morphology, characteristics of debris, and flownet within the deposit	Historical analysis method
6	Ischuk (2011)	Seismic survey (VSP), geoelectric survey (ERT)	Dam morphology, permeability, debris compaction, and hydraulic gradient	Historical analysis method
7	Wang et al. (2013); Wang et al. (2014); Wang G. H. et al. (2016)	Seismic survey (MASW)	Internal structure of landslide deposit, and geotechnical properties of debris	Engineering analogy method
8	Wang et al. (2018)	Geoelectric survey (SP), seismic survey (MTM)	Seepage field	Historical analysis method

Note: ERT, electrical resistivity tomography; MASW, multichannel analysis of surface waves; MTM, micro-tremor; SP, self-potential; SRT, seismic refraction tomography; VES, vertical electrical sounding; VSP, vertical seismic profiling.

failure time, was the main concern. However, due to the scarcity of historical data, there was not complete information for most of the recorded cases. Of the available information, most had morphology indexes and some of the hydrodynamic conditions, such as lake surface area/length/volume or catchment area. In addition, dammed river steepness, lithology, material composition, and grain-size distribution of landslide deposits were available if the relevant field investigations were conducted, as well as the final breach size after dam breaching. In contrast, some information could not be found through retrospective analysis or field investigations, such as inflow discharge, breach flow discharge, and failure time, if the hydrological information was unavailable.

3 Hazard assessments for landslide dams

Dammed lakes are generally formed by the rapid accumulation of collapsible rock, debris, and Earth triggered by earthquake or rainfall. For a dammed lake, its hazard can be transformed into the stability of water-retaining structure, the landslide dam. Investigations have found that landslide dam stability is mainly related to the material composition, structural characteristics, hydrodynamic conditions of dammed lake, as well as local precipitation conditions and secondary disasters. Considering these influencing factors, a series of studies have assessed landslide dam stability, which can be divided into qualitative and quantitative assessment methods.

3.1 Qualitative assessment methods

The qualitative assessment methods for landslide dam stability are mainly based on formation mechanisms, geometry, material composition, catchment area, and inflow rate, to evaluate global stability. These methods do not use mathematical calculations, and the evaluation indexes can be obtained by means of remote sensing (Ermini et al., 2006; Scaioni et al., 2014; Fan et al., 2021) and geophysical methods (McCann and Forster, 1990; Jongmans and Garambois, 2007; Whiteley et al., 2019; Fan et al., 2021).

In recent decades, remote sensing technology has made significant advances in resolution, accuracy, acquisition time, and logistics, making it a powerful tool in landslide dam identification and investigation. It can be used for geometry mapping of landslide dams and dammed lakes, as well as the deformation monitoring of landslide dams. In addition, in regions without data, an alternative method of optical photogrammetry using unmanned aerial vehicles can be employed. Three types of geophysical methods are utilized to investigate landslide dams (Fan et al., 2021): electromagnetic surveys (i.e., active electromagnetics, ground penetrating radar, and magnetotellurics), geoelectric surveys (i.e., electrical resistivity tomography and self-potential), and seismic surveys (i.e., compressional P-waves and transverse S-waves).

Qualitative assessment methods can be divided into engineering analogy methods and historical analysis methods. The engineering analogy methods compare select landslide dams with similar ones in terms of the formation mechanisms and geological conditions, to assess the landslide dam stability. The historical analysis methods assess stability according to the landslide dam formation history and evolution process. Table 2 shows a brief overview of the qualitative hazard assessment methods for landslide dams. With the development of remote sensing and geophysical technologies, significant progress has been made in emergency response for dammed lake events. However, there are few studies that have focused only on qualitative assessments, most of which are used as the basic data support for quantitative assessments. Meanwhile, qualitative assessment is also the first step to judge the erosion resistance of the dam material. Accurate and rapid acquisition of topographic and hydrodynamic information, as well as geotechnical properties of landslide debris, is the basis for outburst flood analysis.

3.2 Quantitative assessment methods

The quantitative assessment methods for landslide dam stability can be classified into probability-based mathematical statistics methods and computer-based numerical analysis methods.

3.2.1 Probability-based mathematical statistics methods

Mathematical statistics is a branch of mathematics based on probability theory that studies the statistical regularity of a large number of random phenomena. In recent years, using measured data from formed-stable and formed-unstable landslide dams, a series of mathematical expressions and judgement criteria have been developed to rapidly evaluate landslide dam stability. With increased survey data for landslide dams around the world, the input parameters of the mathematical expressions of the assessment methods have gradually increased, and the influencing factors are more comprehensive. In this review, following the definition by Costa and Schuster (1991), landslide dam length is the crest length perpendicular to the valley axis, and landslide dam width is the base width parallel to the valley axis.

Starting from a database of 70 landslide dam cases collected in the northern Apennines, Casagli and Ermini (1999) defined the blockage index (*BI*) and proposed the first mathematical expression to evaluate landslide dam stability. In the expression, landslide dam volume and catchment area are the input parameters. The state of landslide dam stability can then be categorized into stable, unstable, and uncertain. Later on, based on 84 landslide dam cases, Ermini and Casagli (2003) introduced landslide dam height into the *BI* method and defined a new dimensionless blockage index (*DBI*). In 2004, based on 232 landslide dam cases in New Zealand, Korup (2004) proposed three dimensionless indexes, i.e., the backstow index (I_s), basin index (I_a), and relief index (I_r), to describe landslide dam stability. Landslide dam height and dammed lake volume are the input parameters for I_s, landslide dam height and catchment area are the input parameters for I_a, and landslide dam height and upstream relief are the input parameters for I_r. Subsequently, based on 300 cases, combining landslide dam volume, catchment area, and local longitudinal slope of the channel bed, Stefanelli et al. (2016) defined the hydromorphological dam stability index (*HDSI*) to discriminate between formed-stable and formed-unstable landslide dams.

In order to eliminate uncertainty in landslide dam stability assessments and establish judgement criteria, some mathematical statistics methods based on logistic regression algorithms have been proposed. The value 0 is set as the demarcation point, and a landslide dam is formed-stable if the calculated result is greater than 0. A dam is formed-unstable if the calculated result is less than 0. Based on 43 documented landslide dam cases in Japan, Dong et al. (2011) defined three indexes [i.e., $L_s(PHWL)$, $L_s(AHWL)$, and $L_s(AHV)$] to judge landslide dam stability. For $L_s(PHWL)$, parameters such as peak inflow rate, landslide dam height/width/length were selected; for $L_s(AHWL)$, catchment area, landslide dam height/width/length were selected; for $L_s(AHV)$, catchment area, landslide dam height and volume were selected as input parameters. Based on 79 landslide dam occurrences, Shi et al. (2020) proposed a three-parameter expression and two five-parameter expressions to evaluate landslide dam stability. Herein, landslide dam height and width, and dammed lake volume, were chosen for the three-parameter expression. In addition, for the five-parameter expressions, dimensional and dimensionless parameters were adopted, such as landslide dam height/width/length, dammed lake volume, and backwater length, as well as combinations of two for dimensionless input parameters.

It is well known that material composition has significant impacts landslide dam stability. Thus, according to the material composition of landslide dam debris, Shan et al. (2020) defined two indexes that can be classified as either detailed [$L_s(IVAS)$] or simplified [$L_s(IVAM)$] according to 27 and 150 cases, respectively. For $L_s(IVAS)$, the ratio of landslide dam height and width (to reflect the hydraulic gradient), landslide dam volume, catchment area, and particle composition index (to quantitative describe the grain size distribution) are the input parameters. Instead of a particle composition index, $L_s(IVAM)$ utilizes a particle characteristic parameter (to qualitative describe the material composition), and the other input parameters are the same as $L_s(IVAS)$. Table 3 presents an overview of the hazard assessment methods for landslide dams based on mathematical statistics.

As far as the current research status is concerned, regression analysis is the most used mathematical statistical method, but it depends on the reliability of samples and the rationality and representativeness of fitting factors. With the continuous accumulation of landslide dam data, the accuracy of landslide dam stability assessments using mathematical statistics methods have gradually improved.

3.2.2 Computer-based numerical analysis methods

Numerical analysis methods are usually used to analyze landslide dam stability according to dam configuration, internal structure, and geotechnical properties of landslide deposits, as well as the hydrodynamic conditions of the dammed lake. Because landslide dams are formed naturally, the upstream and downstream slope ratios (vertical/horizontal) are usually gentle, and numerical analysis is generally focused on landslide dam slope stability under different external loads, such as unsteady seepage flow (Shi et al., 2015a), aftershocks (Hu et al., 2011), and rainfall (Tsai et al., 2013). So far, the commonly used numerical analysis methods for landslide dam stability included the limit equilibrium method, finite element method, finite difference method, and discrete element method.

It is worth mentioning that, due to the longevity of most landslide dams, when the damming events occurred, the available time for hazard assessments was very short. In general, numerical analysis is relatively time-consuming; hence, this type of methods is relatively rare and most studies are retrospective analysis after landslide dam breach. Compared with landslide dam stability analysis, numerical analysis is applied more to evaluate mountain slope stability and simulate landslide damming processes.

4 Breach mechanisms and breach processes of landslide dams

The failure processes of landslide dams involve complex coupling effects of soil and water. Because landslide dams are usually located in mountain valleys with poor transportation, due to the rapid breach process and large peak breach flow, it is difficult to collect prototype data and documented failure processes of landslide dams are relatively scarce. Breach records from Tangjiashan (Liu et al., 2010) and Baige (Cai et al., 2020) in China are important reference values for this study. In order to better understand landslide breach mechanisms, numerous

TABLE 3 Hazard assessment methods of landslide dams based on mathematical statistics.

No.	Investigators	No. of cases	Expressions	Judgement criteria
1	Casagli and Ermini (1999)	70	$BI = \log(\frac{V_d}{A_b})$	$BI > 5$, Stability area
				$4 < BI < 5$, Uncertain area
				$3 < BI < 4$, Instability area
2	Ermini and Casagli (2003)	84	$DBI = \log(\frac{A_b \times H_d}{V_d'})$	$DBI < 2.75$, Stability area
				$2.75 < DBI < 3.08$, Uncertain area
				$DBI > 3.08$, Instability area
3	Korup (2004)	83	$I_s = \log(\frac{H_d'^3}{V_l'})$	$I_s > 0$, Stability area
				$-3 < I_s < 0$, Uncertain area
				$I_s < -3$, Instability area
		110	$I_a = \log(\frac{H_d^2}{A_b})$	$I_a > 3$, Stability area
				$I_a < 3$, Instability area
		108	$I_r = \log(\frac{H_d}{H_r})$	$I_r > -1$, Stability area
				$I_r < -1$, Instability area
4	Stefanelli et al. (2016)	300	$HDSI = \log(\frac{V_d}{A_b \times S_s})$	$HDSI > 7.44$, Stability area
				$5.74 < HDSI < 7.44$, Uncertain area
				$HDSI < 5.74$, Instability area
5	Dong et al. (2011)	43	$L_s(PHWL) = -2.55\log(P) - 3.64\log(H_d) + 2.99\log(W_d) + 2.73\log(L_d) - 3.87$	$L_s(PHWL) > 0$, Stability area
				$L_s(PHWL) < 0$, Instability area
		43	$L_s(AHWL) = -2.22\log(A_b') - 3.76\log(H_d) + 3.17\log(W_d) + 2.85\log(L_d) + 5.93$	$L_s(AHWL) > 0$, Stability area
				$L_s(AHWL) < 0$, Instability area
		84	$L_s(AHV) = -4.48\log(A_b') - 9.31\log(H_d) + 6.61\log(V_d') + 6.39$	$L_s(AHV) > 0$, Stability area
				$L_s(AHV) < 0$, Instability area
6	Shi et al. (2020)	79	$Z = 0.348\ln H_d + 0.254\ln W_d - 0.654\ln V_l' - 3.410$	$Z > 0$, Stability area
				$Z \leq 0$, Instability area
		79	$Z = 0.435\ln H_d + 0.076\ln L_d + 0.501\ln W_d + 1.352\ln L_l - 1.122\ln V_l' - 15.568$	$Z > 0$, Stability area
				$Z \leq 0$, Instability area
		79	$Z = -1.896\ln(\frac{H_d}{H_r}) + 1.126\ln(\frac{H_d}{W_d}) - 0.113\ln(\frac{L_l}{W_d}) - 1.101\ln(\frac{V_l'^{1/3}}{H_d}) - 0.387\ln(\frac{L_d}{W_d}) + 8.766$	$Z > 0$, Stability area
				$Z \leq 0$, Instability area
7	Shan et al. (2020)	27	$L_s(IVAS) = -0.264\log(I) + 1.166\log(V_d) - 1.551\log(A_b) - 0.168\log(S_d) - 4.847$	$L_s(IVAS) > 0$, Stability area
				$L_s(IVAS) < 0$, Instability area
		150	$L_s(IVAM) = -0.198\log(I) + 1.387\log(V_d) - 1.432\log(A_b) + 4.169M_i - 8.674$	$L_s(IVAM) > 0$, Stability area
				$L_s(IVAM) < 0$, Instability area

Note: BI, blockage index; DBI, dimensionless blockage index; I_s, backstow index; I_a, basin index; I_r, relief index; $L_s(PHWL)$, $L_s(AHWL)$, $L_s(AHV)$, $L_s(IVAS)$, $L_s(IVAM)$, Z, indexes of the logical regression; $HDSI$, hydromorphological dam stability index; A_b, catchment area with the unit of km^2; A_b', catchment area with the unit of m^2; V_d, landslide dam volume with the unit of m^3; V_d', landslide dam volume with the unit of 10^6 m^3; H_d, landslide dam height with the unit of m; H_d', landslide dam height with the unit of 10^2 m; V_l', dammed lake volume with the unit of 10^6 m^3; H_r, upstream relief with the unit of m; P, peak inflow rate with the unit of m^3/s; W_d, landslide dam width with the unit of m; L_d, landslide dam length with the unit of m; S_s, local longitudinal slope of the channel bed with the unit of °; L_l, backwater length with the unit of m; I, ratio of H_d and W_d; S_d, particle composition index; M_i, particle characteristic parameter.

physical model tests have been conducted to investigate failure processes and factors influencing breach morphology and hydrographs. Because most of the landslide dam failure model tests have focused on overtopping-induced dam breaching, this section only reviews the breach mechanisms and processes due to overtopping failure.

10.3389/feart.2022.981068

TABLE 4 Model tests of factors influencing landslide dam breach processes.

No.	Influencing factors	Investigators	No. of model tests	Conclusion
1	Downstream slope angle	Gregoretti et al. (2010)	168	Three types of failures were observed, which depended on the downstream slope angle of landslide dam. For the low values (≤7°), surface erosion was triggered by overtopping of the dam crest; for the intermediate values (7°–22°), backward erosion was the predominant type; for the high values (≥22°–25°), headcut erosion occurred after the sliding of downstream slope
		Jiang and Wei (2020)	5	With the increase of downstream slope angle, the breach flow discharge aggrandized, the failure time became shorter, the final sedimentation depth of the river channel bed decreased, the erosion rate increased in the early stage and changed little in the late stage, the peak sediment concentration first decreased and then increased, while the final morphology of the river channel bed was basically the same
		Zhu et al. (2021)	12	The downstream slope angle determined the breaching process and the stage of dam breach. If the value of downstream slope angle was small, resulting in the backward erosion; as the value gradually increased, causing retrogressive collapses; when the value was large enough, causing surface erosion
2	Dam height	Walder et al. (2015)	13	Peak breach flow increased almost linearly as a function of the dam height
		Zhu et al. (2021)	12	The dam height directly determined whether an accumulation body can be formed on the middle or lower parts of the downstream face
3	Grain size distribution	Cao et al. (2011a)	28	Cohesive clay may act to mitigate the seepage through the dam and modulate the dam breach process. Gravels in the dam may appreciably depress the rate of the erosion process and thus modify the flood
		Zhu et al. (2020)	11	The breach hydrographs were variable for different grain size distributions of the dam materials. The textural properties of loose materials determined the characteristics of failure modes and breach processes
4	Initial soil moisture	Chen S. C. et al. (2015)	64	Landslide dams with high soil initial moisture had low hydraulic conductivity, which increased the uplift speed of the impoundment, leading to overtopping failure and a shorter longevity
		Jiang and Wei (2019)	7	The peak breach flow increased with the increase in the initial soil moisture, while the failure time and residual dam height decreased. The backward erosion gradually weakened with the increase in the initial soil moisture. The breach deepened faster than it widened as the initial soil moisture increased, and the ratio of breach width to depth after dam breaching was greater than 1 at first and then less than 1
5	Soil hydraulic conductivity	Chen S. C. et al. (2015)	64	The soil hydraulic conductivity affected the dam longevity and its corresponding failure mode. Landslide dams in impermeable riverbeds tended to fail by overtopping, while the tests in permeable riverbeds had longer longevities
		Jiang et al. (2018)	159	For landslide dams with small soil hydraulic conductivities, stable seepage fields cannot be formed during the impoundment, so the overtopping failure mode played a leading role. For landslide dams with large soil hydraulic conductivities, the slope failure mode often occurred
6	Soil compactness	Chen S. C. et al. (2015)	64	The soil compactness affected the peak breach flow during dam breaching. Landslide dams of the looser material had larger peak discharges than the tests of the denser material
7	River channel bed gradient	Jiang and Wei (2019)	159	With an increase in river channel bed slope, the failure mode changed from the overtopping failure mode to the slope failure mode and back to the overtopping failure mode
		Zhu et al. (2021)	12	The river channel bed gradient determined the breach process and the stages of dam overtopping failure. With the increase of the river channel bed slope, the erosion process intensified, the time to peak breach flow occurred earlier
8	Inflow rate	Cao et al. (2011b)	28	The inflow rate dictated the landslide dam breach process and the flood. For a specific dammed lake size, the higher the inflow rate, the quicker the dam failed
		Chen S. C. et al. (2015)	64	Under low inflow rate conditions, dam material with high hydraulic conductivity can create an armoring layer without forming a sandbar downstream. Low hydraulic conductivity dams under high inflow rate conditions cause a braided river downstream after progressive erosion
		Jiang et al. (2018)	159	An increase in inflow rate can reduce the impoundment time, which is not conducive to the formation of a stable seepage field, so it is more difficult for the slope failure mode to occur
		Zhou et al. (2019)	4	The larger the inflow rate, the shorter the time it took to reach the inflection discharges, and the shorter the time to it took to reach the peak breach flow
9		Cao et al. (2011a)	28	

(Continued on following page)

TABLE 4 (*Continued*) Model tests of factors influencing landslide dam breach processes.

No.	Influencing factors	Investigators	No. of model tests	Conclusion
	With or without initial spillway			The dam without initial spillway reached a higher peak breach flow, and the time to peak flow was delayed compared with the tests with initial spillways. Due to the uneven morphology, lateral mass collapses were considerable where there was an initial breach in the landslide dam. Initial spillways were often excavated for alleviating the downstream flooding
10	Initial spillway shape	Zhao et al. (2018)	3	An initial spillway with a compound cross section has a higher initial discharge efficiency and lower peak breach flow, and the breach hydrograph corresponded to a "chunky-type." The draining from this type of an initial spillway could reduce the flood pressure and make the entire process smoother
11	Initial spillway location	Li D. Y. et al. (2021)	3	When the initial spillway was located close to the landslide dam abutment, the final breach width was smaller, and the volume of the residual dam was larger
12	Surge waves	Peng et al. (2019)	6	The landslide dam stability is determined by the difference between the effective water level (the sum of water level and wave height) and the dam height. The erosion in the breach initiation stage is much faster than that without surge wave, but the difference in the breach development stage is relatively small
		Peng et al. (2021)	9	The surge waves accelerate the breach process with more intense surface erosion and larger dynamic pore pressure. The total erosion volume and elapsed time decrease with the increase of mean grain size. With the increase of wave height, both the average erosion rate and peak discharge increase

4.1 Breach mechanisms of landslide dams

4.1.1 Landslide dam breach model tests

The common physical model tests of the landslide dam breach process can be mainly classified into small-scale flume model tests, large-scale field model tests, and centrifugal model tests. Landslide dam failure is a nonlinear erosion process of dam material during unsteady flow. Researchers have divided the failure process into different stages through different types of model tests. 1) Flume model tests. Based on seven flume model tests with landslide dam heights of 0.3 m, Yang et al. (2015) distinguished five stages of breaching: seepage erosion, formation of the initial breach, backward erosion, expansion and incision of the breach, and re-equilibration of the river channel through the breach. Using four flume model tests with dam heights of 0.7 m, Zhou et al. (2019) divided the whole hydrodynamic breaching process into three stages: headcut erosion process, accelerated erosional process, and attenuating erosional process. Based on 12 flume model tests with a maximum landslide dam height of 0.3 m, Zhu et al. (2021) divided the breaching process into four stages: initiation, head cutting, acceleration, and riverbed rebalancing. 2) Field model tests. Reports on large-scale model tests for landslide dam breaching have been relatively rare and are represented by three field model tests with dam heights of 2.5 m conducted by Li D. Y. et al. (2021). Li L. et al. (2021) divided the breach process into three stages: the initiation stage, the development stage, and the failure stage. Furthermore, in terms of the erosion characteristics during dam breaching, Zhang et al. (2021) found that the dominant erosion pattern is surface progressive erosion, and divided the breach process into three stages: headward erosion, rapid erosion, and attenuated erosion. Using two field model tests with dam heights of 1.0 m and different longitudinal dam shapes, Takayama et al. (2021) divided the overtopping-induced landslide dam breach process into two stages: progressive erosion and overtopping erosion. 3) Centrifugal model tests. Utilizing the "space-time amplification effect" of the centrifuge and a centrifugal model test system for dam breaching developed at the Nanjing Hydraulic Research Institute (NHRI), two centrifugal model tests with a dam height of 0.2 m and centrifugal acceleration of 30 g (the corresponding prototype dam height was 6 m) for breaching were conducted (Zhao et al., 2019). Zhao et al. (2019) divided the breach process into five stages: erosion on downstream slope, notch cutting, notch wall scouring, breach side slope collapse, and downstream slope coarsening.

In addition, based on the documentation of the "11·03" Baige landslide dam breach case, Zhong et al. (2020a) divided the breach process into four stages: uniform erosion, backward erosion, streamwise erosion, and breach rebalance.

Although there are different classification methods for the division of landslide dam breach processes, in terms of the sudden changes of breach hydrograph and morphology, the outburst process of landslide dams can be classified into the initial, accelerated, and stable stages. Further, backward erosion occurs in the initial stage, and the accelerated stage occurs after backward erosion enters an upstream dammed lake. The stable stage occurs when the inflow and outflow rates are balanced.

4.1.2 Factors influencing the landslide dam breach process

In order to further investigate breach mechanisms, a series of model tests have been conducted on landslide dam breach processes considering different influencing factors. There are five main categories of influencing factors: landslide dam morphology [i.e., downstream slope angle (Gregoretti et al., 2010; Jiang and Wei, 2020; Zhu et al., 2021), and dam height (Walder et al., 2015; Zhu et al., 2021)], physical and mechanical indexes of dam material [i.e., grain size distribution (Cao et al., 2011a; Zhu et al., 2020), initial soil moisture (Chen S. C. et al., 2015; Jiang and Wei, 2019), soil hydraulic conductivity (Chen S. C. et al., 2015; Jiang et al., 2018), and soil compactness (Chen S. C. et al., 2015)], hydrodynamic conditions of dammed lake [i.e., river channel bed gradient (Jiang and Wei, 2019;

Zhu et al., 2021), and inflow rate (Cao et al., 2011a; Chen S. C. et al., 2015; Jiang et al., 2018; Zhou et al., 2019)], initial spillway [i.e., with or without (Cao et al., 2011a), shape (Zhao et al., 2018), and location (Li D. Y. et al., 2021)], and surge waves [i.e., heights of surge waves above dam crest (Peng et al., 2019; Peng et al., 2021)]. By analyzing breach morphologies and hydrographs, useful information about breach mechanisms has been acquired. A brief introduction to model tests for influencing factors on landslide dam breach processes is shown in Table 4.

Based on the model tests in Table 4, a preliminary summary of the influencing factors on the breach process can be presented. The downstream slope angle of landslide dam does not have a simple increasing relationship with erosion rate and breach flow discharge, and there is a given threshold value. However, there is no clear understanding of the factors governing the threshold value. The higher the landslide dam height is, the higher the dammed lake volume would be, and hydrodynamic conditions would be enhanced, which results in an increase of peak breach flow. Whether the time to peak flow is advanced or not depends on the expansion rate of the breach morphology. When the landslide dam material is well graded, the dam is more stable. Peak breach flow is relatively low and the time to peak flow is delayed. The timing of the outburst process is relatively long and the breach hydrograph is relatively smooth. Peak breach flow usually increases as initial soil moisture increases, while the failure time and residual dam height decreases; however, the existing studies are not in agreement and lack model testing under high initial soil moisture conditions. Soil hydraulic conductivity plays an important role in the longevities and failure modes of landslide dams, and when the dam breach occurs, the effect of soil hydraulic conductivity on the outburst process is embodied by the initial soil moisture. As soil compactness increases the peak breach flow declines, and the time to peak flow would also lag behind. The river channel bed slope angle plus the downstream slope angle equals the breach flow gradient; hence, given the stability of the landslide dam slope, the sum of the two has an upper limit. In general, as the river channel bed gradient increases the erosion process intensifies and the time to peak breach flow occurs earlier. When the inflow rate increases, the outburst process is accelerated and the erosion rate increases. The excavation of the initial spillway is a problem to be considered when manual interference is involved. If the spillway is not excavated, the breach flow is significantly increased, aggravating the flood disaster downstream. Under the condition of the same excavation amount, the disposal of a compound spillway can effectively increase the discharge rate and make the breach hydrograph relatively gentle. When the initial spillway is located close to the bank, one-sided erosion occurs, the final breach width is smaller, and the volume of the residual dam is larger. In addition, when subjected to surge waves, landslide dam stability is determined by the difference between the effective water level and dam height, and dam material erosion rate is determined by the wave height and mean grain size.

In recent years, influencing factors, such as morphological indexes of landslide dam, physical and mechanical indexes of landslide deposits, hydrodynamic conditions of dammed lakes, manual intervention measures, and external loads, have been considered in the study of landslide dam breach mechanisms. However, due to the complexity in the grain-size distribution and internal structure, further validation is needed to determine whether the conclusions truly reflect the actual situation. There are two aspects that need more study: First, landslide deposits are generally composed of broadly graded soils and the upper limit of grain size in the scaled model tests is often less than 20 cm; thus, the similarity relation of erosion characteristics of landslide deposits needs further study. Second, triggered by different disaster factors, as well as the variations of slope materials and motion patterns, the internal structures of landslide dams are multifarious; however, the structural characteristics of landslide dam are not considered in traditional model tests.

4.2 Numerical simulation methods for the landslide dam breach process

Numerical simulation methods are widely used to analyze dam breach processes. Based on a report by the ASCE/EWRI (American Society of Civil Engineers/Environmental and Water Resources Institute) Task Committee on Dam/Levee Breaching (ASCE/EWRI Task Committee on Dam/Levee Breach, 2011), dam breach models can be classified as parametric, simplified physically based, or detailed physically based. Based on measured data from historical dam breach cases, regression analysis or machine learning are often utilized to develop empirical formulas to predict breaching parameters (i.e., peak breach flow, final breach size, and failure time) in the parametric models. Assumptions such as a regular shape (inverted triangle or rectangle or inverted trapezoidal) are adopted to confine the breach morphology, and various sediment transport equations and water flow formulas are respectively used to simulate the erosion process and breach flow discharge in simplified physically based models. In addition, some simplified physically based models consider the instability of breach side slopes during the failure processes. Unlike parametric models, the simplified physically based models can output breach flow discharge and breach size for each time step in the simulation period. Furthermore, some detailed physically based dam breach models have been developed to describe the morphology evolution process without the predefinition of breach shape, based on the shallow water hypothesis and sediment transport theory.

Recently, a numerical simulation method that coupled a discrete element method (DEM) and computational fluid dynamics (CFD) was used to simulate the breach process of landslide dams (Li L. et al., 2021). The advantage of the coupled DEM-CFD method is that it models landslide dam deposits through discontinuous particles, and reproduces the breach hydrograph with free water surface evolution, which is conducive to understanding the landslide dam breach mechanism of water and soil coupling. Although the DEM-CFD method can reflect the breach mechanisms more clearly, it distinctly restricted by spatial and temporal scales, and the grain size distribution of landslide dam materials and dam morphology indexes are set in a relatively narrow range. Due to the excessive computational costs, the applications of these models to real field scale cases still have a long way to go.

Nowadays, most of the dam breach models are reserved for embankment dams, while only a few numerical models are used to simulate landslide dam breaching; hence, the models for embankment dam breach are often used as substitutes. Because of obvious differences between the two types of dams, large errors may be produced due to the misapplication of the numerical models. In

TABLE 5 Existing parametric models for landslide dam breaching parameters.

No.	Investigators	No. of cases	Expressions
1	Costa (1985)	10	$Q_p = 6.3H_d^{1.59}$
			$Q_p = 672{V_l}'^{0.56}$
			$Q_p = 181\,(H_d{V_l}')^{0.43}$
2	Evans (1986)	29	$Q_p = 0.72V_l^{0.53}$
3	Costa and Schuster (1988)	12	$Q_p = 0.0158\,(PE)^{0.41}$
4	Walder and O'Connor (1997)	18	$Q_p = 1.6V_r^{0.46}$
			$Q_p = 6.7d_d^{1.73}$
			$Q_p = 0.99\,(d_d \cdot V_r)^{0.40}$
5	Peng and Zhang (2012a)	45	Full-variable equation: $\frac{Q_p}{g^{\frac{1}{2}}H_d^{\frac{5}{2}}} = (\frac{H_d}{H_0})^{-1.417}(\frac{H_d}{W_d})^{-0.265}(\frac{V_d^{\frac{1}{3}}}{H_d})^{-0.471}(\frac{V_l^{\frac{1}{3}}}{H_d})^{1.569}e^{a_1}$
			Simplified equation: $\frac{Q_p}{g^{\frac{1}{2}}H_d^{\frac{5}{2}}} = (\frac{H_d}{H_0})^{-1.371}(\frac{V_l^{\frac{1}{3}}}{H_d})^{1.536}e^{a_2}$
		13	Full-variable equation: $\frac{B_f}{H_0} = (\frac{H_d}{H_0})^{0.752}(\frac{H_d}{W_d})^{0.315}(\frac{V_d^{\frac{1}{3}}}{H_d})^{-0.243}(\frac{V_l^{\frac{1}{3}}}{H_d})^{0.682}e^{a_3}$
			Simplified equation: $\frac{B_f}{H_0} = (\frac{H_d}{H_0})^{0.911}(\frac{V_l^{\frac{1}{3}}}{H_d})^{0.271}e^{a_4}$
		10	Full-variable equation: $\frac{b_f}{H_0} = 0.004(\frac{H_d}{H_0}) + 0.050(\frac{H_d}{W_d}) - 0.044(\frac{V_d^{\frac{1}{3}}}{H_d}) + 0.088(\frac{V_l^{\frac{1}{3}}}{H_d}) + a_5$
			Simplified equation: $\frac{b_f}{H_0} = 0.003(\frac{H_d}{H_0}) + 0.070(\frac{V_l^{\frac{1}{3}}}{H_d}) + a_6$
		21	Full-variable equation: $\frac{D_f}{H_0} = (\frac{H_d}{H_0})^{0.882}(\frac{H_d}{W_d})^{-0.041}(\frac{V_d^{\frac{1}{3}}}{H_d})^{-0.099}(\frac{V_l^{\frac{1}{3}}}{H_d})^{0.139}e^{a_7}$
			Simplified equation: $\frac{D_f}{H_0} = (\frac{H_d}{H_0})^{0.923}(\frac{V_l^{\frac{1}{3}}}{H_d})^{0.118}e^{a_8}$
		14	Full-variable equation: $\frac{T_f}{T_0} = (\frac{H_d}{H_0})^{0.262}(\frac{H_d}{W_d})^{-0.024}(\frac{V_d^{\frac{1}{3}}}{H_d})^{-0.103}(\frac{V_l^{\frac{1}{3}}}{H_d})^{0.705}e^{a_9}$
			Simplified equation: $\frac{T_f}{T_0} = (\frac{H_d}{H_0})^{0.293}(\frac{V_l^{\frac{1}{3}}}{H_d})^{0.723}e^{a_{10}}$
6	Liu et al. (2013)	31	$B_{ave} = 0.367(\frac{V_l}{V_0})^{0.195}(\frac{L_d}{\tan\varphi})^{0.337}{H_d}^{0.5}$
			$H_{res} = 1.109(\frac{V_0}{V_l})^{0.065}{d_{90}}^{0.088}{H_d}^{0.912}$
7	Shi et al. (2014)	24	Full-variable equation: $Q_p = 3.130H_d^{0.120}W_d^{0.302}V_d^{-0.106}V_l^{0.453}e^{\alpha_1}$
		26	Simplified equation: $Q_p = 3.130H_d^{-0.046}V_l^{0.507}e^{\alpha_2}$
		23	Full-variable equation: $D_f = H_d^{0.840}W_d^{-0.169}V_d^{0.089}V_l^{0.040}e^{\alpha_3}$
		26	Simplified equation: $D_f = H_d^{0.875}V_l^{0.016}e^{\alpha_4}$
		11	Full-variable equation: $B_f = 1.593H_d + 85.249\frac{H_d}{W_d} - 3.438\frac{V_d^{\frac{1}{3}}}{H_d} + 15.963\frac{V_l^{\frac{1}{3}}}{H_d} + \alpha_5$
		11	Simplified equation: $B_f = H_d^{0.594}V_l^{0.182}e^{\alpha_6}$
		15	Full-variable equation: $b_f = -0.006H_d^2 - 0.047\frac{H_d^2}{W_d} + 0.017{V_d}^{\frac{1}{3}} + 0.047{V_l}^{\frac{1}{3}} + \alpha_7 H_d$

(Continued on following page)

10.3389/feart.2022.981068

TABLE 5 (*Continued*) Existing parametric models for landslide dam breaching parameters.

No.	Investigators	No. of cases	Expressions
		16	Simplified equation: $b_f = -0.007H_d^2 + 0.053V_l^{\frac{1}{3}} + \alpha_8 H_d$
		12	Full-variable equation: $T_f = H_d^{0.275}W_d^{-1.224}V_d^{0.439}V_l^{0.232}e^{\alpha_9}$
		12	Simplified equation: $T_f = H_d^{0.425}V_l^{0.236}e^{\alpha_{10}}$
8	Shan et al. (2022)	44	$Q_p = H_d^{0.229}W_d^{-0.04}V_l^{0.558}e^{C_m}$

Note: Q_p, peak breach flow with the unit of m^3/s; V_0, unit volume of landslide dam with the unit of m^3; V_l, dammed lake volume with the unit of m^3; H_0, unit height with the unit of m; T_0, unit time with the unit of h; g, gravitational acceleration with the unit of m/s^2; φ, internal friction angle with the unit of°; d_{90}, particle size for which 90% is finer by weight with the unit of m; PE, potential energy with the unit of joule; d_p, drop in dammed lake level with the unit of m; V_r, released water volume of dammed lake with the unit of m^3; B_f, final breach top with the unit of m; b_f, final breach bottom width with the unit of m; D_f, final breach depth with the unit of m; B_{ave}, final breach average width with the unit of m; H_{res}, residual landslide dam height after breaching with the unit of m; T_f, failure time with the unit of h; C_m, material composition-based coefficient.

$a_1 = 1.276$ for dam material with high erodibility, $a_1 = -0.336$ for dam material with medium erodibility, $a_1 = -1.532$ for dam material with low erodibility; $a_2 = 1.236$ for dam material with high erodibility, $a_2 = -0.380$ for dam material with medium erodibility, $a_2 = -1.615$ for dam material with low erodibility; $a_3 = 1.683$ for dam material with high erodibility, $a_3 = 1.201$ for dam material with medium erodibility, a_3 is unavailable for dam material with low erodibility; $a_4 = 0.588$ for dam material with high erodibility, $a_4 = 0.148$ for dam material with medium erodibility, a_4 is unavailable for dam material with low erodibility; $a_5 = 0.775$ for dam material with high erodibility, $a_5 = 0.532$ for dam material with medium erodibility, a_5 is unavailable for dam material with low erodibility; $a_6 = 0.624$ for dam material with high erodibility, $a_6 = 0.344$ for dam material with medium erodibility, a_6 is unavailable for dam material with low erodibility; $a_7 = -0.316$ for dam material with high erodibility, $a_7 = -0.520$ for dam material with medium erodibility, a_7 is unavailable for dam material with low erodibility; $a_8 = -0.673$ for dam material with high erodibility, $a_8 = -0.500$ for dam material with medium erodibility, a_8 is unavailable for dam material with low erodibility; $a_9 = -0.635$ for dam material with high erodibility, $a_9 = -0.518$ for dam material with medium erodibility, a_9 is unavailable for dam material with low erodibility; $a_{10} = -0.674$ for dam material with high erodibility, $a_{10} = -0.805$ for dam material with medium erodibility, a_{10} is unavailable for dam material with low erodibility.

$\alpha_1 = -0.489$ for dam material with high erodibility, $\alpha_1 = -1.918$ for dam material with low erodibility; $\alpha_2 = -0.565$ for dam material with high erodibility, $\alpha_2 = -1.836$ for dam material with low erodibility; $\alpha_3 = -0.977$ for dam material with high erodibility, $\alpha_3 = -1.218$ for dam material with low erodibility; $\alpha_4 = -0.322$ for dam material with high erodibility, $\alpha_4 = -0.709$ for dam material with low erodibility; $\alpha_5 = -66.094$ for dam material with high erodibility, $\alpha_5 = -86.005$ for dam material with low erodibility; $\alpha_6 = -0.498$ for dam material with high erodibility, $\alpha_6 = -1.178$ for dam material with low erodibility; $\alpha_7 = 1.304$ for dam material with high erodibility, $\alpha_7 = 0.639$ for dam material with low erodibility; $\alpha_8 = 1.360$ for dam material with high erodibility, $\alpha_8 = 0.710$ for dam material with low erodibility; $\alpha_9 = 2.346$ for dam material with high erodibility, $\alpha_9 = 2.104$ for dam material with low erodibility; $\alpha_{10} = -0.602$ for dam material with high erodibility, $\alpha_{10} = -0.662$ for dam material with low erodibility.

recent years, frequent events such as earthquakes and extreme rainstorms have directed attention to landslides that block rivers and research on numerical simulation technology for landslide dam breaching is gradually increasing. In this review, parametric, simplified and detailed physically based models are the main concerns.

4.2.1 Parametric models

Due to the simplicity and convenience of parametric models, they are often used in the rapid evaluation of disasters caused by landslide dam breaching. Compared to embankment dams, there are fewer parametric models available to predict the breaching parameters of landslide dams because of the complexity of structures and materials, as well as the uncertainty of parameters. Based on 10 landslide dam breach cases, Costa (1985) proposed three regression equations to predict the peak breach flow of landslide dams. Input parameters were landslide dam height or dammed lake volume, or the combination of both variables. Subsequently, another mathematical expression for the relationship between potential dammed lake energy and peak breach flow was established (Costa and Schuster, 1988). Based on 29 landslide dam breach cases, Evans (1986) developed an empirical relationship between peak breach flow and volume of water released during embankment dam failure that was thought to be applicable to landslide dam breaching. Later, based on 18 landslide dam breach occurrences, Walder and O'Connor (1997) provided the statistical relationships between peak breach flow and released water volume, or drop in dammed lake level, or the combination of both variables. The early parametric models only considered the morphological characteristics of landslide dams and dammed lake hydrodynamic conditions, and the mathematical expressions were single or double parametric. Further, the models only presented the expressions of peak breach flow.

Based on 45 documented landslide dam breach cases around the world, Peng and Zhang (2012a) developed a rapid prediction model of breaching parameters that considers the morphology of landslide dams, the hydrodynamic conditions of dammed lakes, and the erosion characteristics of dam materials (i.e., high, medium, and low erodibility coefficients). The model can be used to predict the peak breach flow during the outburst process, the final breach size (i.e., breach top width, bottom width, and depth), and the elapsed time of the landslide dam breach process. Later, a new regression model for estimating breaching parameters was established based on 41 cases with detailed information by Shi et al. (2014).

Landslide dams often retain a residual dam height after breaching. Based on 31 cases, Liu et al. (2013) proposed an empirical model to calculate the breaching parameters of landslide dams under natural conditions, including the final breach average width and residual dam height. The major factors included landslide dam morphology, hydrodynamic conditions of dammed lake, and physical and mechanical indexes of dam materials.

Table 5 describes the existing parametric models for landslide dam breaching parameters. With their small number of geomorphology parameters, some of which represent soil erosion features, parameter models can offer rapid access to the breaching parameters of landslide dams. However, the models cannot consider breach hydrographs and the evolution process of breach size, so they are generally used for rapid assessments of dam breaching disasters. For areas without hydrological data, parametric models are of great significance for emergency response.

TABLE 6 Typical simplified physically based models for the landslide dam breaching process.

No.	Investigators	Dam structure	Breach morphology		Breach flow discharge	Erosion characteristics	Mechanical mechanisms
			Cross section	Longitudinal section			
1	DABA [Chang and Zhang (2010), Peng et al. (2014), Shi et al. (2015a), Zhang et al. (2019), Chen C. et al. (2020)]	Multilayer	Breach side slope angle increased to a certain value, and then remain constant	Downstream slope angle increased to a certain value, and then remained constant	Broad-crested weir flow equation	Stress-based erosion rate equation considering variations in soil erodibility coefficient with depth	—
2	DB-IWHR [Chen Z. Y. et al. (2015), Wang L. et al. (2016), Chen et al. (2018), Chen Z. Y. et al. (2020)]	Monolayer	Breach side slope angle remain constant until instability occurred	Remain constant downstream slope angle	Broad-crested weir flow equation	Hyperbolic erosion rate equation	Instability of breach side slopes with circular or planar slip surface
3	DB-NHRI [Zhong et al. (2018), Zhong et al. (2020a), Zhong et al. (2020b), Shen et al. (2020b), Mei et al. (2021)]	Multilayer	Breach side slope angle remain constant until instability occurred	Continuous decrease of downstream slope angle	Broad-crested weir flow equation	Stress-based erosion rate equation considering variations in grain size distribution and soil erodibility coefficient with depth	Instability of breach side slopes with planar slip surface

4.2.2 Simplified physically based models

Simplified physically based models are the most popular models for dam breach modeling around the world, and are widely used for the numerical simulation of dams composed by soils and rocks (Zhong et al., 2016). In the early days, simplified physically based models describing embankment dam failures were often adopted to simulate landslide dam breach processes, such as the NWS (National Weather Services) BREACH model (Fread, 1988), which is one of the earliest and most used models. However, due to the large discrepancies between embankment and landslide dams, especially the characteristics of grain size distribution and dam structure, landslide dams do not always release all of the stored water. The application of models for embankment dams can introduce large errors by overestimating the breach flow discharge.

In the 21st Century, more attention has been paid to the numerical simulation of landslide dam breach process and simplified physically based models have been developed. For the landslide dam breaching process models, the cross section of the breach channel is often predefined to be an inverted trapezoid and outflow through the breach is simulated using the hydraulics of a broad-crested weir for most of the models. Hence, key points in the landslide dam breaching process modeling are how to reasonably reflect the structure features of landslide dams, the erosion rate of wide graded dam materials, and the evolution process of breach morphology in cross and longitudinal sections.

Field investigation have demonstrated stratification based on soil grain size distribution in the depth direction, and the grain size distribution in each layer varies for landslide dams with different accumulation forms (Fan et al., 2020). Using field test data or empirical formulas, some models can consider the landslide dam structure based on variations in soil erodibility (Chang and Zhang, 2010) or the grain size distribution of dam materials (Zhong et al., 2020b).

Stress-based erosion rate equations have been widely adopted to simulate breach bed erosion. The bed erosion rate can be expressed as the soil erodibility coefficient multiplied by the difference between the flow shear stress and the critical shear stress of the soil. For the flow shear stress, the Manning equation or shear stress equation for uniform flow is often adopted; for critical shear stress of soil and soil erodibility coefficient, empirical equations derived from erosion tests of wide graded dam materials have also been applied (Chang et al., 2011). Once the critical shear stress of soil is larger than the water shear stress, the bed erosion ceases. In addition, based on monitoring data from the Tangjiashan landslide dam breach process, Chen Z. Y. et al. (2015) proposed a hyperbolic model to describe the bed erosion rate. In this work, the maximum possible erosion rate was predefined according to regression on field measurements.

For breach development in the cross section, the lateral erosion rate is often assumed to be equal to the bed erosion rate or multiplied by a coefficient. The lateral enlargement due to the instability of breach side slopes is the main mechanism behind breach widening, and limited equilibrium methods with planar or circular slip surfaces are often utilized. For breach development in the longitudinal section, the main difference between the models is the assumption of downstream slope angle variability. Three assumption are often accepted, such as that the downstream slope angle remains constant, or decreases, or increases to a certain value and then remains constant.

In this section, three typical simplified physically based modes for landslide dam breaching, such as DABA (DAm Breach Analysis) (Chang and Zhang, 2010; Peng et al., 2014; Shi et al., 2015b; Zhang et al., 2019; Chen C. et al., 2020), DB-IWHR (Dam Breach—China Institute of Water Resources and Hydropower Research) (Chen Z. Y. et al., 2015; Wang G. H. et al., 2016; Chen et al., 2018; Chen Z. Y. et al., 2020), and DB-NHRI (Dam Breach—Nanjing Hydraulic Research Institute) (Zhong et al., 2018; Zhong et al., 2020a; Zhong et al., 2020b; Shen et al., 2020b; Mei et al., 2021), are introduced in Table 6. Although the simplified physically based landslide dam breach models have shortcomings, they are computationally efficient and have considered the necessary breach mechanisms.

Although the simplified physically based models can describe the breach process of landslide dams, they introduce many artificial assumptions in expressions of breach morphology, physical and mechanical properties of dam deposits, breach flow discharge, and breach side slope stability. In addition, because breach flow discharge

and breach size evolution are calculated separately, these types of models cannot consider the characteristics of high-velocity flow and broadly graded soils, or the coupling effect of soil and water in the dam breach process, so landslide dam breach mechanisms cannot be fully reflected.

4.2.3 Detailed physically based models

In recent years, with the development of computational fluid dynamics and sediment science, as well as hydrodynamics and sediment transport theory, a series of one-, two-, and three-dimensional numerical models for dam breach processes have been developed under the assumptions of shallow water and hydrostatic pressure distribution. These models are categorized as detailed physically based. They typically contain three modules, such as a hydrodynamic module (i.e., continuity and momentum conservation equations for clean or muddy water), a sediment transport module (i.e., equilibrium or nonequlibrium sediment transport equations), and a morphological evolution module (i.e., bed erosion equation, breach slope collapse equation). According to the types of sediment transport models selected in the dam breach models (Guan et al., 2015), the detailed physically based dam breach models can be divided into four categories: capacity models (i.e., Faeh, 2007; Swartenbroekx et al., 2010; Juez et al., 2014; Abderrezzak et al., 2016; Dazzi et al., 2019; Takayama et al., 2021), noncapacity models (i.e., Wu and Wang, 2007; Cao et al., 2011b; Wu et al., 2012; Guan et al., 2014; Marsooli and Wu, 2015), two-phase flow models (i.e., Rosatti and Begnudelli, 2013; Razavitoosi et al., 2014; Cristo et al., 2016), and two-layer transport models (i.e., Swartenbroekx et al., 2013; Li et al., 2013; Cantero-Chinchilla et al., 2016).

The capacity models are mainly composed of the shallow water equation and the Exner equation. The shallow water equation describes the flow movement of clear water and the Exner equation describes the breach morphology evolution process. In these models, the erosion process is dominated by bedload sediment transport where the velocity of dam material is less than that of the water flow. In addition, various empirical formulas for bedload erosion rate are often adopted.

In the noncapacity model, the flow is assumed to be muddy water and the shallow water equation containing the density of muddy water is used to describe the flow process. It is assumed that the erosion process consists of bedload transport and suspended load transport, and the interaction process between bedload and suspended load is determined by empirical formulas. The actual erosion rate is converted into the volume concentration of muddy water, and the erosion process is calculated by the volume concentration and the flow rate of muddy water.

Two-phase flow models assume that solid particles move in the liquid flow, the volume concentration of the solid particles is relatively low, and the solid particles move under the driving force of the liquid flow, but the interaction between the solid and liquid phases is weak. The solid and liquid phases are modeled based on the continuum hypothesis, and the continuity and momentum conservation equations describe the movement of the two phases, in which the solid phase has characteristics similar to particle flow.

In two-layer transport models, the water flow above the breach bottom bed is assumed to be made up of a upper clear water layer and the under bedload flow layer. Each layer has its own depth and concentration. There is clear water exchange between the clear water layer and the bedload flow layer, while there is soil exchange between the bedload flow layer and the breach bottom bed. The exchange capacity is often determined by empirical formulas. Continuity and momentum conservation equations are developed for the clear water and sand-water layers, respectively.

Mean grain size is commonly adopted to represent the dam material diameter in detailed physically based dam breach models. This is a suitable method for simulating the failure process of non-cohesive dams with relatively uniform particles. Some of the existing detailed physically based dam breach models in each of the four types are listed in Table 7.

The four types of detailed physically based models can simulate the breach hydrograph and rapid change in dam morphology during dam breaching under their own assumptions and theoretical frameworks. However, there are still some difficulties in their practical application. One of the key problems is how to select an appropriate erosion model. Most erosion formulas are obtained under the conditions of steady uniform flow, low sediment transport intensity, and slow riverbed deformation, while the theoretical results of breach slope instability are also obtained under many assumptions. These theoretical shortcomings greatly limit the simulation ability of detailed physically based models. Hence, there are few models that can reasonably reflect the erosion characteristics of broadly graded soils under high-velocity breach flow, which depends on the development of sediment theory.

In addition, although detailed physically based models can effectively improve accuracy in numerical simulation, they still have low computational efficiency when dealing with large-scale dam failure simulations. With the enhancement of computer processing capacity, GPU acceleration technology has been introduced into some models (Lacasta et al., 2014; Lacasta et al., 2015; Juez et al., 2016; Dazzi et al., 2019) to improve the calculation efficiency of dam breach flow. In general, future numerical simulation of landslide dam breach processes is moving in the direction of detailed physically based models.

5 Flood routing after landslide dam breaching

Once a landslide dam breaks, it forms a catastrophic outburst flood, then the dam-break flow spreads to the downstream area. Flooding can submerge riverine buildings and traffic facilities, causing direct harm to lives and properties. In addition, flood flow due to the failure of a landslide dam usually has fine to coarse sediment particles, and the characteristics of flood routing are different from those of clear water flow. Erosion or siltation on the riverbed results from the dam-break flood, altering the original river topography. In general, for dam-break flood routing, the inundated area, flow depth and velocity, riverbed elevation variability, and time to peak flood in a certain location are the main concerns.

5.1 Model tests for flood routing after dam breaching

5.1.1 Model tests for dam-break flow propagation

Flood routing after dam breaching is a strong and complex dynamic water-soil-riverbed coupled process with rapid changes in

10.3389/feart.2022.981068

TABLE 7 Existing typical detailed physically based dam breach models.

No.	Model type	Investigators	Breach morphology	Breach flow	Sediment transport	Geomechanics	Solution method
1	Capacity model	Faeh (2007)	2D Exner equation	2D shallow water equations	Equations for bed-load and suspended load	Vertical and lateral erosion, slope instability	Finite volume method (Roe and HLL Riemann solver)
		Swartenbroekx et al. (2010)	2D Exner equation	2D shallow water equations	Bed-load equation	Vertical and lateral erosion, slope instability	Finite volume method (HLLC Riemann solver)
		Juez et al. (2014)	2D Exner equation	2D shallow water equations	Different equations for bed-load	Vertical and lateral erosion	Finite volume method (Roe Riemann solver)
		Abderrezzak et al. (2016)	2D Exner equation	2D shallow water equations	Bed-load equation	Vertical and lateral erosion, slope instability	Finite element method (TELEMAC-2D)
		Dazzi et al. (2019)	2D Exner equation	2D shallow water equations	Stress-based erosion rate equation	Vertical and lateral erosion, slope instability	Finite volume method (HLLC Riemann solver)
		Takayama et al. (2021)	2D simplified Janbu's method	1D uniform flow equations	Equilibrium sediment transport equation	Vertical erosion and downstream slope instability	Finite difference method (explicit method)
2	Noncapacity model	Wu and Wang (2007)	1D nonequilibrium total-load transport equation	Generalized shallow water equations	Total-load capacity equation	Vertical erosion	Finite volume method (HLL Riemann solver)
		Cao et al. (2011b)	2D nonequilibrium total-load transport equation	Generalized shallow water equations	Bed-load equation	Vertical and lateral erosion, slope instability	Finite volume method (HLLC Riemann solver)
		Wu et al. (2012)	2D nonequilibrium total-load transport equation	Generalized shallow water equations	Total-load capacity equation	Vertical and lateral erosion, slope instability	Finite volume method (HLL Riemann solver)
		Guan et al. (2014)	2D nonequilibrium bed-load transport equation	2D shallow water equations	Bed-load equation	Vertical and lateral erosion, slope instability	Finite volume method (HLL Riemann solver)
		Marsooli and Wu (2015)	3D nonequilibrium total-load transport equation	Navier-Stokes (RANS) equations	Equations for bed-load and suspended load	Vertical and lateral erosion	Finite volume method (VOF method)
3	Two-phase flow model	Rosatti and Begnudelli (2013)	2D mass and momentum conservation equations (solid phase)	2D shallow water equations (water phase)	Equation of sand-water mixture flow concentration	Vertical and lateral erosion	Finite volume method (Generalized Roe Riemann solver)
		Razavitoosi et al. (2014)	2D N-S equations (solid phase, non-Newtonian fluid)	2D N-S equations (water phase, non-Newtonian fluid)	—	Vertical and lateral erosion	SPH method
		Cristo et al. (2016)	2D mass and momentum conservation equations (solid phase)	2D shallow water equations (water phase)	Equations for bed-load and suspended load	Vertical and lateral erosion, slope instability	Finite volume method (FIVFLOOD solver)
4	Two-layer transport model	Swartenbroekx et al. (2013)	2D mass and momentum conservation equations (bed-load)	2D shallow water equations	Erosion rate equation	Vertical and lateral erosion	Finite volume method (HLL Riemann solver)
		Li et al. (2013)	2D nonequilibrium suspended-load transport equation	2D shallow water equations	Erosion rate equation	Vertical and lateral erosion	Finite volume method (HLL and HLLC Riemann solver)
		Cantero-Chinchilla et al. (2016)	1D nonequilibrium total-load transport equation	1D Saint-Venant equations	Equations for bed-load and suspended load	Vertical erosion	Finite volume method (HLLC Riemann solver)

physical quantity; thus, the propagation process of a dam breach flood has its own special features.

Flume tests have been the principle physical model tests to study the characteristics of flood routing. In the model tests, a flood is often generated by the instantaneous dam breach or a prescribed flow curve, and the downstream river channel is generally set as fixed or movable bed. 1) Fixed bed model tests. In terms of the material composition of dam-break flow, fixed bed model tests can be classified as clean and muddy water flows. Regardless of whether the dam-break flow is clean or muddy water, the study main focuses on the propagation characteristics of dam-break waves in man-made river channels with different cross sections, such as a smooth rectangular and horizontal channel (Lauber and Hager, 1998), an initially dry channel with a 90° bend (Soares-Frazão and Zech, 2002), a frictional triangular channel (Wang et al., 2021), or a meandering channel (Itoh et al., 2018). Consequently, the mechanical properties of dam-break waves and water-soil mixture deposition are discussed. 2) Movable bed model tests. Dam-break flows in most of the movable bed model tests are clean water, so the study purpose is to describe the propagation characteristics of dam-break flows on the movable beds, as well as riverbed topography variations (i.e., Capart and Young, 1998; Spinewine and Zech, 2007; Goutiere et al., 2011; Carrivick et al., 2011; IAHR Working Group for Dam-break Flows over Mobile Beds, 2012; Qian et al., 2018). In general, compared with fixed bed model tests, dam-break flood waves on the movable bed propagate slower and attenuate faster.

The landslide dam breach process is not an instantaneous incident, but rather it is a nonlinear gradual process; in addition, natural river channel morphology is quite different from an experimental river channel. However, physical experimental studies of flood routing caused by the gradual collapse of a landslide dam in a natural river channel are still rare. Therefore, in the discussion on the influencing factors of flood routing in the next subsection, *in-situ* test results are the main basis for evaluation.

Dam-break flow propagation after landslide dam breaching is more complicated than that of clear water due to the high sediment content, which is almost sand-carrying flow or even debris flow. Experiments and *in-situ* tests have shown that the evolution of a sand-carrying flood caused by dam breaching in the lower reaches of a river involves erosion or deposition, as well as sediment sorting along the river channels.

5.1.2 Factors influencing flood routing

Flood routing after landslide dam breaching is mainly affected by flood rheology, breach flow hydrographs, dry and wet conditions downstream, river branches, river channel roughness, and downstream river topography (Liu et al., 2019). Because of the high sediment concentration in the flood water, the propagation of muddy water is more complicated than that of clear water. In addition, the dammed lake is generally formed in alpine valley areas with complex river terrain conditions; hence, flood routing in a mountainous area is obviously different from a plains area.

Because both sides of river banks are generally controlled by mountains, a dam-break flow propagates without planarization and water loss is relatively limited. Therefore, the flood discharge propagating along the downstream river channel decreases slowly, and its rate of decrease is significantly influenced by the breach hydrograph during the breach. In general, when peak breach flow is high and long in duration, the flood peak attenuates gradually downstream because the downstream river channel has been filled before the peak arrives (O'Connor and Beebee, 2009; Liu et al., 2019). Historical statistics have shown that the peak discharge of an outburst flood observed 60 km downstream of the Tangjiashan landslide dam in China showed no significant decline compared with the peak breach flow at the dam site (Liu et al., 2019). Similarly, at over 200 km and 100 km downstream of the Tanggudong and Dixi landslide dam sites, respectively, over 50% of the initial peak breach flow was maintained after long distance propagation (Chen et al., 1992; Wang et al., 2012).

In addition, after the landslide dam breaching, the outburst flood carries a large amount of sediment, which is deposited in the river channel and on both sides of the beach as flood velocity decreases during flood routing. Taking the 2018 failure event of the "11.03" Baige landslide dam on the Jinsha River, China as an example, on both sides of the river in the Shangri-La Development Zone, which is located about 600 km downstream of the dam site, the mud thickness on the beach was over 0.5 m after flood routing.

The huge amount of sediment carried in a dam-break flow that propagates downstream has serious impacts on downstream water environments in the river. Moderate amounts of sediment can increase nutrients in the water, while high sediment flows can be disastrous for most aquatic life. The formed-stable dammed lake may have positive effects on a mountain river ecosystem, but may be destroyed in 1 day in case the dammed lake fails.

5.2 Numerical simulation for flood routing after dam breaching

The model tests and *in-situ* tests demonstrated that dam-break flows contain shock and sparse waves, compared to conventional river floods. They also have the following characteristics (Aureli et al., 2000): 1) The peak breach flow of dam-break flood is relatively high; meanwhile, the water level is high, the water surface gradient is large, and the dam-break flow is often discontinuous during the propagation. 2) The topography of the area downstream of a landslide dam is commonly very irregular and it is easy to cause a flow regime transition. Supercritical, critical, and subcritical flows often occur simultaneously. Surge waves and hydraulic jumps often occur during dam-break flow propagation. 3) During flood routing, the dam-break flow often overflows the river channel and moves onto the dry bed, so there are complex dynamic boundary conditions.

The governing equations for dam-break flow routing simulation generally adopt Shallow Water Equations (for two-dimensional simulation) or Saint-Venant Equations (for one-dimensional simulation). The particularity of dam-break flow is mainly reflected in corresponding physical flow field discontinuities. Therefore, accurate simulation must capture this strong discontinuity or large gradient flow. There are two main approaches, such as the Shock Fitting Method and Shock Capture Method (Toro, 2000). With the rapid development of computer technology, the Shock Capture Method has been more widely used. However, the Shock Capture Method for non-conserved Shallow Water Equations may lead to calculation errors (Toro, 2000). Therefore, in order to correctly use the Shock Capture Method to solve the discontinuous problem, conservative variables, equation forms, and numerical solution methods should be used.

There are two main kinds of adaptive numerical solutions to capture discontinuities: 1) Discontinuities can be treated as special

cases with large gradients, which can be smoothed by artificially introducing a diffusion term with a viscosity effect when solving differential equations. This is called the artificial viscosity method. Or, when discretizing differential equations, a format with similar viscosity can be selected (i.e., Lax-Wendroff format, or Lax-Friedrichs format) (Anderson, 1995) to produce a smooth transition, called the format viscosity method. However, the first order precision scheme of this method will stretch the discontinuous transition zone too wide. 2) The Godunov Scheme (Godunov, 1959) was based on the idea of solving Riemann's approximate solution and is not only suitable for smooth classical solutions, but can also adapt to cases with large gradients or/and large deformation solutions, and can accurately and automatically capture the discontinuities. It has become one of the main methods for computing large gradient water surfaces.

As discussed above, dam-break flows have shock and sparse waves, which are usually expressed as the Saint-Venant or Shallow Water Equations, and the breach flow can be clear or muddy water. According to the discrete principle, numerical simulation methods can generally be classified as Method of Characteristics (MOC), the Finite Difference Method (FDM), the Finite Element Method (FEM), and the Finite Volume Method (FVM). The MOC, FDM, and FEM have achieved great success in many subcritical flow problems, but they are not completely suitable for solving the strong discontinuous flow of dam-break floods. The Finite Volume Method does not directly discretize the governing equations numerically, but starts from the integral form of conservative equations, forming the Riemann problem for discontinuous solutions on the boundary of a control body. For any region composed of one or more control bodies, even the whole computational region, physical conservation is strictly satisfied, there is no conservative error, and the discontinuity can be calculated correctly. After input/output flows and momentum fluxes are calculated along the normal direction of the computing element boundary, balance calculations of water volume and momentum are conducted for each element, and then the average water depth and velocity of each element at the end of the time step are obtained.

The Godunov scheme used in the Riemann solution is currently the main scheme for solving large gradient flows. The Roe scheme (Roe, 1981), Osher scheme (Osher and Solomon, 1982), HLL scheme (Harten et al., 1983), and HLLC scheme (Toro et al., 1994) are other widely used schemes. In addition, the high resolution methods of shock capture by the Finite Difference Method and others can be directly used in the Finite Volume Method. It is worth mentioning that there are some common software programs that can simulate dam-break flood propogation, such as FLDWAV (Fread and Lewis, 1988), DHI MIKE FLOOD (Danish Hydraulic Institute, 2021), HEC-RAS (US Army Corps of Engineers, 2021), and so on.

In recent years, numerous calculation methods have been developed to simulate flood routing after dam breaching, and the characteristics of downstream outburst flood (peak discharge, submergence area, average water depth, and average flow velocity) have been considered and discussed in-depth. However, more research is needed on the sensitivity of outburst floods to the dam breach process and the interaction mechanism involving sand-carrying flow and the downstream river channel.

Although many numerical models for flood routing can simulate sediment transport, the simulation of actual dam-break flow is mainly concerned with the propagation of flood flow, while the role of sediment carried by dam-break flow is ignored. The effects of rapidly releasing a huge amount of sediment on variable river topography and river ecology need to be further studied.

6 Loss assessments after dammed lake breaching

In order to effectively reduce life and property safety risks associated with dam-break floods, loss assessments are needed for the following purposes (Bowles et al., 2003): 1) To evaluate existing and residual risks against tolerable risk guidelines. 2) To evaluate the benefits associated with risk-reduction measures, such as more effective emergency plans and evacuation measures. 3) To estimate cost effectiveness and feasibility to aid in prioritizing and justifying expenditures on risk-reduction measures.

Therefore, a better understanding of flood-induced loss dynamics is of great importance for improving the scientific quality and availability of emergency response plans. Since the 1980s, scholars have studied loss assessments due to dam failures. In general, dam-break loss studies are still in the exploratory stage, and have mainly focused on the loss assessment of artificial dam reservoirs rather than dammed lakes. However, dam reservoirs and dammed lakes have common outburst flood propagation characteristics, so loss assessment methods for dam reservoirs can be used for reference in dammed lakes. According to the classification, loss assessments for dammed lake breaching can be classified as loss of life, loss of economy, and loss of ecology. However, compared to assessment methods for loss of life, there are fewer assessment methods for loss of economy and ecology. There are two main reasons for this (Ge et al., 2020): 1) The ability of potential inundation areas to endure losses of economy and ecology caused by dam failure changes over time due to constant economic and social development. 2) Economic and social development levels are distinct across different areas, resulting in significant differences in economic and ecology losses after a dam breach. It is difficult to establish a uniform assessment method for scientifically predicting these losses. Hence, in this review, the assessment methods for loss of life are the focus of attention.

Loss of life refers to the number of people potentially killed by flood disasters in the inundated area by a dam-break flood. It is coupled by qualitative and quantitative factors, and the disaster causing factor system is uncertain, which increases the difficulty of quantitative assessment. The state-of-the-art life loss assessment methods mostly use the main influencing factors as input parameters to develop models. The influencing factors can be classified into four categories, such as hazard factors, exposure factors, population-related factors, and rescue capability factors (Mahmoud et al., 2020), as shown in Figure 5.

A previous study divided the assessment methods for loss of life into three types: empirical models, physical models, and compromised models (Peng and Zhang, 2012b). These three categories are generally deterministic models quantified with a few independent parameters and may not sufficiently clarify the relationship between the input parameters and the calculated results. Therefore, a series of uncertainty models based on intelligent algorithms, fuzzy mathematics, and probability theory have been developed. The assessment methods for loss of life in this review are classified into four types, such as empirical, physical, compromised, and uncertainty models.

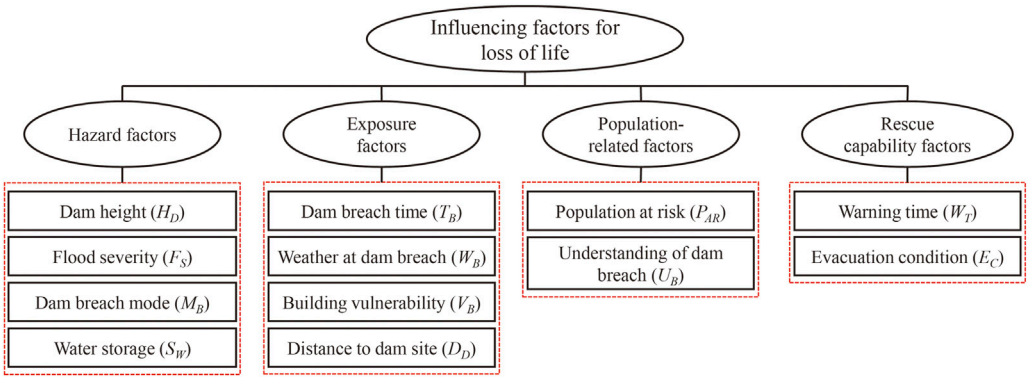

FIGURE 5
Factors influencing loss of life due to a dam breach [modified from Mahmoudet al. (2020)].

Empirical models describe the relationship between loss of life and influencing factors by integrating statistics of historical data and mathematical methods. Brown and Graham (1988) developed three empirical formulas to predict loss of life considering the population at risk and different available warning times based on statistics from historical dam failures of many countries around the world. Subsequently, more influencing factors have been considered to assess the loss of life (Table 8).

Physical models simulate human behavior in dam-break flood, and explore the stability of human beings in flood flow by taking individuals as the research object. Abt et al. (1989) first conducted a study to identify when an adult human could not stand or maneuver in a simulated flood flow. Then, a series of models were developed to measure human instability in flood flows with different combinations of water depth and flow velocity (Table 8).

Compromised models combine the characteristics of both empirical and physical models. A potential inundated area is often separated into several subareas based on physical concepts; simultaneously, flood-caused fatality mechanisms are considered. The relationship between loss of life and influencing factors in each subarea is calibrated with historical data or expert judgment in each subarea, then the assessment model for loss of life is developed (Table 8).

The above three types of models (empirical, physical, and compromised) can be generally defined as deterministic models, and loss of life can be quantified with a few independent input parameters. However, deterministic models may not sufficiently reveal the inter-relationships between the input parameters or include the uncertainties of these parameters, meanwhile, some important parameters cannot be quantified. Hence, uncertainty models came into existence. In these models, uncertainties in the predicted models are identified by performing uncertainty analyses regarding both the influence factors and their inter-relationships (Table 8).

Empirical models for loss of life are generally at a macroscale, developed and calibrated based on documented dam failure information and statistical data from disaster losses, which are easy to follow. However, due to the adoption of statistical approaches, this type of model cannot reflect the causes of flood-induced casualties the inter-relationships between the key influencing factors. In addition, empirical models are often established in terms of documented data from historical flood events, most of which are of low credibility or availability, resulting in relatively low accuracy in most of the applications.

Physical models for loss of life mainly focus on the instability of individual in the flood flow and most are complicated and cannot consider the subjective factors of individuals in danger. Hence, the theoretical analyses for every individual are very complicated and rarely applied in actual cases, while the correlation between human behavior in floods and loss of life needs further study and verification.

Compromised models for loss of life can describe the relationship between loss rate and dam-break flood characteristics by considering the causes of loss of life. This type of model combines the advantages of statistical approaches and theoretical analysis, which can quantitatively predict the loss of life under relevant risk criteria. However, the inter-relationships between the influence parameters are not included in these models.

Given the importance of subjective consciousness in empirical, physical, and compromise models, none of the deterministic models for loss of life can provide an accurate number of fatalities caused by a given dam breach case. Therefore, loss of life predicted by the deterministic models is subjective to uncertainty. Uncertainties in predicted loss of life due to dam-break floods can be identified by performing uncertainty analyses regarding the flood routing analysis results and loss of life estimations. Hence, uncertainty models are the future direction for loss of life assessments.

7 Risk mitigation measures for dammed lakes

Dammed lakes pose tremendous threats to people and properties in the inundation areas caused by landslide dam breaching floods. Due to the lack of flood discharge facilities, most landslide dams are breached naturally by overtopping flow a short time after the formation of dammed lakes. Therefore, quantitative risk assessment is urgently needed as the prerequisite and preliminary requirement to support the decision making in landslide-dam emergency response. Then, risk mitigation measures can be taken according to the dam failure risk assessment results. Risk mitigation measures for dammed lakes can be classified as non-engineering measures and engineering measures (Peng et al., 2014; Shi et al., 2016). Non-engineering

TABLE 8 Existing typical models for loss of life due to flood flow.

No.	Investigators	Model type	Expressions or influencing factors
1	Brown and Graham (1988)	Empirical	$LOL = \begin{cases} 0.5P_{AR} & W_T < 0.25\text{h} \\ P_{AR}^{0.56} & W_T < 1.5\text{h} \\ 0.0002P_{AR} & W_T > 1.5\text{h} \end{cases}$
2	Abt et al. (1989)	Physical	Human instability tests in flowing water (D, V, P_S)
3	Dekay and McClelland (1993)	Empirical	$LOL = \begin{cases} 0.075(P_{AR}^{0.560})e^{-0.759W_T} & \text{Low lethality area} \\ 0.075(P_{AR}^{0.560})e^{(-2.982W_T+3.790)} & \text{High lethality area} \end{cases}$
4	Graham (1999)	Empirical	Presented a framework for estimation of loss of life due to dam failures (P_{AR}, W_T, F_S, U_B)
5	Reiter (2001)	Physical	Human instability model tests in flowing water (D, V, P_S)
6	Lee (2003)	Uncertainty	Utilized the Monte Carlo simulation based on the Latin Hypercube Sampling technique (F_S, W_T, P_{AR}, N_s, E_M, T_M, F_M)
7	Lind et al. (2004)	Physical	Theoretical analysis based on hydrodynamic models (D, V, P_S)
8	Aboelata and Bowles (2005)	Compromised	Combined loss of life module with the probability distribution of fatality rates for each loss-of-shelter category/flood area (D, V, R, W_T, B_D)
9	Zhai et al. (2006)	Empirical	$P_{LOL} = \frac{LOL}{P_{AR}} = \frac{S(B_D)}{n \times B_D}$
10	Priest et al. (2007)	Compromised	Combined loss of life module with hazard and exposure thresholds and mitigating factors (D, V, R, W_T, B_D, P_S)
11	Jonkman (2007)	Compromised	Given the relationship between the intensity of physical effects and the mortality in the exposed population (D, V, R, W_T)
12	Jonkman and Penning-Rowsell (2008)	Physical	Human instability tests in flowing water (D, V, P_S)
13	Peng and Zhang (2012b)	Uncertainty	$P_{LOL} = \sum_{i=1}^{2}\sum_{j=1}^{2}\sum_{k=1}^{2} P(LOL = D_{IED}, E_{VA} = E_i, W_T = W_j, F_S = F_k)$
14	Brazdova and Riha (2014)	Empirical	$LOL = 0.075D_M^{0.384}(P_R + 2)^{-3.207}(W_A + 2)^{-1.017}$
15	Huang et al. (2017)	Empirical	Utilized two methods of multivariate nonlinear regression and leave-one-out cross-validation (F_S, E_C, P_{AR}, U_B, W_T, T_B, V_B, D_D, M_B, S_W, W_B)
16	Ge et al. (2019)	Compromised	Established an evaluation model for potential consequences of dam breach based on a catastrophe evaluation method (S_W, H_D, P_{AR}, U_B, W_T, V_B)
17	Mahmoud et al. (2020)	Empirical	Developed two empirical equations based on the multi-variable regression analysis for low flood severity, and medium and high flood severity (H_D, F_S, E_C, P_{AR}, U_B, W_T, T_B, V_B, D_D, M_B, S_W, W_B)
18	Ge et al. (2021)	Empirical	$LOL = PAR \times f_1(W_T, U_B) \times f_2(F_S, V_B)$

Note: LOL, loss of life; P_{AR}, population at risk; W_T, warning time; F_S, flood severity; U_B, understanding of dam breach; N_S, number of simulation; E_M, maximum flood elevation; T_M, time to maximum flood elevation; F_M, maximum flood flow; D, water depth; V, flow velocity; P_S, physical state of people; R, water rise rate; B_D, building damage; P_{LOL}, fatality probability; $S(B_D)$, function for the loss of life; n, number of residents per building; D_{IED}, number of died people; E_1, number of evacuated people; E_2, number of none-evacuated people; W_1, sufficient warning time; W_2, little warning time; F_1, high flood severity; F_2, low flow severity; D_M, material losses; P_R, general preparedness of society for flood management and control; W_A, factors influencing the warning of the population; E_C, evacuation condition; T_B, dam breach time; V_B, building vulnerability; D_D, distance to dam site; M_B, dam breach mode; S_W, water storage; W_B, weather at dam breach; H_D, dam height; $f_1(W_T,U_B)$, interval of the exposure rate of the population at risk influenced by the warning time and understanding of dam breach; $f_2(F_S,V_B)$, mortality interval of the exposed population influenced by the flood severity and building vulnerability.

measures mitigate risks by means of reducing the people and properties at risk through evacuation or reservoir regulation. In general, there are two kinds of implementation schemes: 1) Warning and evacuating people and movable assets at risk out of the potential inundated areas. 2) Emergency operation of upstream and downstream reservoirs on the river. This could mean reducing discharged water into an upstream reservoir, or emptying water stored in a downstream reservoir. Admittedly, non-engineering measures are low cost and high efficiency in rescuing people and movable assets at flood risk; however, measures of this category cannot reduce the loss of unmovable assets. Engineering measures mitigate risks by moving the people and properties at risk and limiting the dam failure probability, inundation area, flood severity, and vulnerability of population and assets at risk.

Sections 3–6 in this review are the basis for non-engineering measures, hence, engineering measures are the focus in this section.

After the formation of a landslide dam that threatens people and important infrastructure in the potential flooded area, immediate engineering measures must be taken if objective conditions are permitted. The purposes of this category are to prevent the water level in the dammed lake from reaching dangerous heights, or control the erosion rate if a landslide dam breach occurs (Peng et al., 2014). The most common engineering measures include: water level control by pumps or siphons, diversion tunnels through bedrock abutments, and drainage spillways through landslide dams.

For a dammed lake with small storage capacity and upstream inflow, pumps or siphons can be utilized to control the rising speed of water level in the dammed lake. For instance, on 5 June 2009, a landslide occurred in Wulong County, Chongqing City, China, and then blocked the river, resulted in a dammed lake. Pumps were installed to release the inflow water and keep the water level in the dammed lake below the dam crest (Figure 6).

FIGURE 6
Draining the Wulong dammed lake using pumps (Photo credit Xinhuanet.com).

FIGURE 7
Blasting a spillway for the Xiaogangjian dammed lake (Photo credit Xinhuanet.com).

Construction of diversion tunnels is a money- and time-consuming measure. This measure can be taken when the following requirements are met. 1) Geological conditions. The mountain slope upstream of the dam site should be made of bedrock for diversion tunnel construction. 2) Road and transport conditions. A temporary road to the dam site for transporting equipment and supplies is indispensable. For example, on 3 August 2014, the Mw 6.5 earthquake in Ludian County, Yunnan Province, China, resulted in the Hongshiyan landslide dam, which had a height of 83 m and a lake volume 260 million m^3, threatening more than 10,000 people (Shi et al., 2016). The landslide dam was located between an artificial dam and a hydropower plant; fortunately, there was an existing drainage tunnel that connected the dammed lake and the hydropower plant. Hence, the drainage tunnel was used as a natural diversion and played an important role in risk mitigation (Zhou et al., 2015; Shi et al., 2016).

Building a spillway across a dam is the most common measure for dammed lake risk mitigation. The function of a spillway is to control the breach process of landslide debris, preventing erosion from occurring too fast or slow. For a landslide dam with relatively small volume made of large blocks on the top, blasting can be used to break up the dam materials. The emergency disposal of the Xiaogangjian landslide dam, which was triggered by Wenchuan earthquake, 2008, China, is one example of this approach. The upper part of the Xiaogangjian landslide dam was composed of large blocks, while the lower part was composed of highly fragmented debris (Mei et al., 2021). Due to the traffic jams caused by earthquake, rescuers only accessed the dam site by rubber boats (Chen et al., 2018); thus, they considered various factors, and blasting a spillway was a preferable plan. After blasting, a spillway with 8 m depth and 30 m bottom width was constructed on the left bank of the dam (Figure 7). For landslide dams with large volume made of mixture of soil and stone, building a spillway with excavators is the most common measure. In terms of the workload and traffic conditions, as well as the rising speed of water level in the dammed lake, an emergency plan would be formulated. For example, in the risk mitigation of the Yigong dammed lake in China, a spillway with 30 m depth and 30 m bottom width was excavated before dam breaching (Figure 8), which significantly reduced the storage capacity in the dammed lake (Wang L. et al., 2016).

One must acknowledge the fact that because dammed lakes are generally trigged by earthquakes or rainfall, which are unforeseen emergencies that commonly result in inaccessible dam sites within the limited available time. Hence, although various measures for dammed lake risk mitigation can be adopted, non-engineering measures such as

FIGURE 8
Constructing a spillway for the Yigong dammed lake using excavators (Photo credit Xinhuanet.com).

warning and evacuating people in the potential inundated areas are more prevalent disposal countermeasure than engineering measures.

For the available engineering measures, building a spillway is an effective method for dammed lake risk mitigation. However, for the landslide dams with different material composition, how to design an optimal spillway to minimize dammed lake risks also requires further study. In addition, for a high-risk dammed lake, the combined utilization of engineering and non-engineering measures is usually more applicable in risk mitigation for a dammed lake breach disaster.

8 Discussion

Based on global databases, a comprehensive review on risk assessments of dammed lakes has been conducted considering the hazard chains that they trigger. Five topics have been discussed, such as hazard assessments for landslide dams, breach mechanisms and breach processes, flood routing after landslide dam breaching, loss assessments, and risk mitigation measures. In general, after systematic studies in recent decades, especially in the past 20 years, the basic framework for dammed lake risk assessments has been built, but there are still several scientific issues are encountered and worthy of further study:

1) Acquisition of basic information for dammed lakes. Due to the scarcity of historical documented data, modern technologies for field investigations should be adopted to obtain key information on dammed lakes for risk assessment, such as morphological indexes of landslide dams, hydrodynamic conditions of dammed lakes, and material composition of landslide deposits. Further, more attention is needed when a new dammed lake appears, such as *in-situ* measurements of breaches—especially breach hydrographs—which are key for validating risk assessment methods.
2) Uncertainty in hazard assessments of landslide dams. For dammed lakes, the occurrence of the breach disaster is a probability event. Therefore, it is necessary to utilize advanced technologies and methodologies to study landslide dams and delineate their internal structure, so that mechanical properties of the landslide deposits can be interpreted to assist assessment of the stability and erodibility of the materials. These measures help to overcome the uncertainty to a certain degree in the hazard assessment of landslide dams. Combining a large amount of basic information of dammed lakes, the near real probability of the landslide dam breach will be achieved through continuous algorithm improvement.
3) Accuracy of dammed lake outburst flood simulation. The simulation of landslide dam breaching involves complex coupling effects of water and soil. Because of the uncertainty of particle distribution in landslide deposits, accurate prediction of landslide dam breaching due to different triggering factors is key to flood routing and disaster consequences. Hence, it is necessary to reveal the damming mechanisms of landslides and obtain the material and structure of the landslide dams by making full use of remote sensing and geophysical prospecting methods. A dam-break flood has sand-carrying fluid, so to improve accuracy, the evolution of riverbed morphology under the action of erosion or deposition by a dam-break flood, as well as sediment sorting along the river channels, should be considered for flood routing simulation.
4) Quantitative methods for loss assessment of dammed lake breaching. Due to the lack of historical loss data, as well as the influence of sustained economic and social development, how to use limited historical data to quantitatively process input parameters in loss assessment models is a major problem that

needs to be solved. With the development of big data technology and the rise of multidisciplinary research, integrating survey data and deterministic/uncertainty methods under the proper algorithms may make up for the lack of historical data to a certain extent.

5) Quantitative risk assessments and risk mitigation for dammed lakes. The risk of a dammed lake is a dynamic process, but risk assessments are mostly conducted through static analysis, ignoring the uncertain evolution process of the hazard chain itself. A complete quantitative assessment system has not been established for the risk assessments of dammed lakes, and assessments of hazard chain evolution are independent of each other, while the quantitative degree is relatively low. Subsequent studies can consider the dynamic characteristics of human behavior and social organization evacuation, and combine satellite remote sensing and aerial photography techniques with unmanned aerial vehicles to dynamically assess the risk of dammed lakes. From the point of view of artificial intelligence, a reasonable overall risk assessment platform for dammed lakes should be explored through an intelligent network with forecasting and early warning. In addition, various uncertainties should be considered in engineering measures for risk mitigation, as well as the development of technologies to control the pace of landslide dam erosion progression.

9 Conclusion

The risk assessment of dammed lakes is a very complicated process that involves the geologic hazard chain triggered by dammed lake breaching and risk mitigation. Based on the overview of each aspect of dammed lake risk assessment, the following conclusion can be drawn:

Although a high degree of study of dammed lakes has produced a multitude of documented cases, the historical documented information is often insufficient in the risk assessment of dammed lakes. Great progresses on breach mechanisms and breach processes of landslide dams have been achieved by laboratory and field model tests, as well as by studying actual failure cases. However, the similarity relation of erosion characteristics of landslide deposits and the structural characteristics of landslide dam needs further study. A number of influencing factors (i.e., landslide dam morphology, physical and mechanical indexes of dam material, hydrodynamic conditions of dammed lake, downstream river topography, roughness of underlying surface, and so on) significantly affect the breach flow hydrographs and flood routing. Although a series of empirically and physically based models have been developed for dam-break flood and loss assessment, great uncertainties are still associated with predictions of the key parameters. Thus, it is very important to conduct mechanism investigations to improve the accuracy in the numerical modeling. In addition, for a high-risk dammed lake, the combined utilization of engineering (building a spillway) and non-engineering measures (evacuating people at risk) is usually an effective way in disaster mitigation.

Author contributions

QmZ: Conceptualization, methodology, writing-reviewing and editing. LW: Formal analysis, writing-reviewing and editing. YS: Conceptualization, methodology. SM: Conceptualization, methodology. QaZ: Formal analysis, Data curation. MY: Data curation, validation. LZ: Validation, investigation. ZD: Data curation.

Funding

This work was financially supported by the National Natural Science Foundation of China (Grant Nos U2040221, U22A20602, and 51909214), and the National Key Research and Development Program of China (Grant No. 2018YFC1508604).

Conflict of interest

The authors declare that the research was conducted in the absence of any commercial or financial relationships that could be construed as a potential conflict of interest.

Publisher's note

References

Abderrezzak, K.E.K., Moran, A.D., Tassia, P., Ata, R., and Hervouet, J.M. (2016). Modelling river bank erosion using a 2D depth-averaged numerical model of flow and non-cohesive, non-uniform sediment transport. *Advances in Water Resources* 93, 75–88.

Aboelata, M.A., and Bowles, D.S. (2005). *LIFESim: a model for estimating dam failure life loss*. Logan, USA: Report to Institute for Water Resources, US Army Corps of Engineers and Australian National Committee on Large Dams, Institute for Dam Safety Risk Management, Utah State University.

Abt, S.R., Wittler, R.J., Taylor, A., and Love, D.J. (1989). Human stability in a high flood hazard zone. *Water Resources Bulletin* 25 (4), 881–890. doi:10.1111/j.1752-1688.1989.tb05404.x

Anderson, J.D. (1995). *Computational fluid dynamics: The basics with applications*. New York, USA: McGraw-Hill, Inc.

ASCE/EWRI Task Committee on Dam/Levee Breach (2011). Earthen Embankment Breaching. *Journal of Hydraulic Engineering* 137 (12), 1549–1564. doi:10.1061/(asce)hy.1943-7900.0000498

Aureli, F., Mignosa, P., and Tomorotti, M. (2000). Numerical simulation and experimental verification of dam-break flows with shocks. *Journal of Hydraulic Research* 38 (3), 197–206. doi:10.1080/00221680009498337

Bianchi-Fasani, G., Esposito, C., Petitta, M., Scarascia-Mugnozza, G., Barbieri, M., Cardarelli, E., Cercato, M., and Di Filippo, G. (2011). *The importance of geological models in understanding and predicting the life span of rockslide dams: the case of Scanno Lake, Central Italy. Natural and Artificial Rockslide Dams*. Springer, 323–345.

Bowles, D.S., Anderson, L.R., Glover, T.F., and Chauhan, S.S. (2003). "Dam safety decision-making: Combining engineering assessments with risk information," in *Proceedings of the 2003 US Society on Dams Annual Lecture*. USA: Charleston.

Brazdova, M., and Riha, J. (2014). A simple model for the estimation of the number of fatalities due to floods in Central Europe. *Natural Hazards and Earth System Sciences* 14 (7), 1663–1676. doi:10.5194/nhess-14-1663-2014

Brideau, M.A., Shugar, D.H., Bevington, A.R., Willis, M.J., and Wong, C. (2019). Evolution of the 2014 Vulcan Creek landslide-dammed lake, Yukon, Canada, using

field and remote survey techniques. *Landslides* 19 (6), 1823–1840. doi:10.1007/s10346-019-01199-3

Brown, C.A., and Graham, W.J. (1988). Assessing the threat to life from dam failure. *Journal of the American Water Resources Association* 24 (6), 1303–1309. doi:10.1111/j.1752-1688.1988.tb03051.x

Cai, Y.J., Cheng, H.Y., Wu, S.F., Yang, Q.G., Wang, L., Luan, Y.S., and Chen, Z.Y. (2020). Breaches of the Baige barrier lake: Emergency response and dam breach flood. *Science China: Technological Sciences* 63 (7), 1164–1176. doi:10.1007/s11431-019-1475-y

Cantero-Chinchilla, F.N., Castro-Orgaz, O., Dey, S., and Ayuso-Muñoz, J.L. (2016). Nonhydrostatic dam break flows. II: One-dimensional depth-averaged modeling for movable bed flows. *Journal of Hydraulic Engineering* 142 (12), 04016069. doi:10.1061/(asce)hy.1943-7900.0001206

Cao, Z.X., Yue, Z.Y., and Gareth, P. (2011a). Landslide dam failure and flood hydraulics. Part I: experimental investigation. *Natural Hazards* 59 (2), 1003–1019. doi:10.1007/s11069-011-9814-8

Cao, Z.X., Yue, Z.Y., and Pender, G. (2011b). Landslide dam failure and flood hydraulics. Part II: coupled mathematical modelling. *Natural Hazards* 59 (2), 1021–1045. doi:10.1007/s11069-011-9815-7

Capart, H., and Young, D.L. (1998). Formation of a jump by the dam-break wave over a granular bed. *Journal of Fluid Mechanics* 372, 165–187. doi:10.1017/s0022112098002250

Carrivick, J.L., Jones, R., and Keevil, G. (2011). Experimental insights on geomorphological processes within dam break outburst floods. *Journal of Hydrology* 408, 153–163. doi:10.1016/j.jhydrol.2011.07.037

Casagli, N., Ermini, L., and Rosati, G. (2003). Determining grain size distribution of the material composing landslide dams in the Northern Apennines: Sampling and processing methods. *Engineering Geology* 69, 83–97. doi:10.1016/s0013-7952(02)00249-1

Casagli, N., and Ermini, L. (1999). Geomorphic analysis of landslide dams in the Northern Apennine. *Transactions of the Japanese Geomorphological Union* 20 (3), 219–249.

Chai, H.J., Liu, H.C., and Zhang, Z.Y. (1995). The catalog of Chinese landslide dam events. *Journal of Geological Hazards and Environment Preservation* 6 (4), 1–9. (in Chinese).

Chang, D.S., and Zhang, L.M. (2010). Simulation of the erosion process of landslide dams due to overtopping considering variations in soil erodibility along depth. *Natural Hazards and Earth System Sciences* 10 (4), 933–946. doi:10.5194/nhess-10-933-2010

Chang, D.S., Zhang, L.M., Xu, Y., and Huang, R.Q. (2011). Field testing of erodibility of two landslide dams triggered by the 12 May Wenchuan earthquake. *Landslides* 8 (3), 321–332. doi:10.1007/s10346-011-0256-x

Chen, C., Zhang, L.M., Xiao, T., and He, J. (2020). Barrier lake bursting and flood routing in the Yarlung Tsangpo Grand Canyon in October 2018. *Journal of Hydrology* 583, 124603. doi:10.1016/j.jhydrol.2020.124603

Chen, S.C., Hsu, C.L., Wu, T.Y., Chou, H.T., and Cui, P. (2011). "Landslide dams induced by typhoon Morakot and risk assessment," in 5th International Conference on Debris-Flow Hazards Mitigation: Mechanics (Padua, Italy: Prediction and Assessment), 653–660.

Chen, S.C., Lin, T.W., and Chen, C.Y. (2015). Modeling of natural dam failure modes and downstream riverbed morphological changes with different dam materials in a flume test. *Engineering Geology* 188, 148–158. doi:10.1016/j.enggeo.2015.01.016

Chen, S.J., Chen, Z.Y., Tao, R., Yu, S., Xu, W.J., Zhou, X.B., and Zhou, Z.D. (2018). Emergency response and back analysis of the failures of earthquake triggered cascade landslide dams on the Mianyuan River, China. *Natural Hazards Review* 19 (3), 05018005. doi:10.1061/(asce)nh.1527-6996.0000285

Chen, Y.J., Zhou, F., Feng, Y., and Xia, Y.C. (1992). Breach of a naturally embanked dam on Yalong River. *Can. J. Civ. Eng.* 19 (5), 811–818. (in Chinese). doi:10.1139/l92-092

Chen, Z.Y., Ma, L.Q., Yu, S., Chen, S.J., Zhou, X.B., Sun, P., and Li, X. (2015). Back analysis of the draining process of the Tangjiashan barrier lake. *Journal of Hydraulic Engineering* 141 (4), 05014011. doi:10.1061/(asce)hy.1943-7900.0000965

Chen, Z.Y., Zhang, Q., Chen, S.J., Wang, L., and Zhou, X.B. (2020). Evaluation of barrier lake breach floods - insights from recent case studies in China. *WIREs Water* 7 (2), e1408. doi:10.1002/wat2.1408

Costa, J.E., and Schuster, R.L. (1988). The formation and failure of natural dams. *Geological Society of America Bulletin* 100 (7), 1054–1068. doi:10.1130/0016-7606(1988)100<1054:tfafon>2.3.co;2

Costa, J.E., and Schuster, R.L. (1991). *Documented historical landslide dams from around the world*. Open-File Report 91-239. Washington D C, USA: U.S. Geological Survey.

Costa, J.E. (1985). *Floods from dam failures*. Open-File Report 85-560. Washington D C, USA: U.S. Geological Survey.

Cristo, C.D., Greco, M., Iervolino, M., Leopardi, A., and Vacca, A. (2016). Two-dimensional two-phase depth-integrated model for transients over mobile bed. *Journal of Hydraulic Engineering* 142 (2), 04015043. doi:10.1061/(asce)hy.1943-7900.0001024

Cui, P., Zhu, Y.Y., Han, Y.S., Chen, X.Q., and Zhuang, J.Q. (2009). The 12 May Wenchuan earthquake-induced landslide lakes: distribution and preliminary risk evaluation. *Landslides* 7 (6), 209–223. doi:10.1007/s10346-009-0160-9

Danish Hydraulic Institute (2021). *MIKE FLOOD: Modelling of urban flooding*. Copenhagen, Denmark: Danish Hydraulic Institute.

Dazzi, S., Vacondio, R., and Mignosa, P. (2019). Integration of a levee breach erosion model in a GPU-accelerated 2D shallow water equations code. *Water resources research* 55 (1), 682–702. doi:10.1029/2018wr023826

DeKay, M.L., and McClelland, G.H. (1993). Predicting Loss of Life in Cases of Dam Failure and Flash Flood. *Risk Analysis* 13 (2), 193–205. doi:10.1111/j.1539-6924.1993.tb01069.x

Dong, J.J., Tung, Y.H., Chen, C.C., Liao, J.J., and Pan, Y.W. (2009). Discriminant analysis of the geomorphic characteristics and stability of landslide dams. *Engineering Geology* 110, 162–171. doi:10.1016/j.geomorph.2009.04.004

Dong, J.J., Tung, Y.H., Chen, C.C., Liao, J.J., and Pan, Y.W. (2011). Logistic regression model for predicting the failure probability of a landslide dam. *Engineering Geology* 117, 52–61. doi:10.1016/j.enggeo.2010.10.004

Ermini, L., and Casagli, N. (2003). Prediction of the behaviour of landslide dams using a geomorphological dimensionless index. *Earth Surface Processes and Landforms* 28 (1), 31–47. doi:10.1002/esp.424

Ermini, L., Casagli, N., and Farina, P. (2006). Landslide dams: analysis of case histories and new perspectives from the application of remote sensing monitoring techniques to hazard and risk assessment. *Italian Journal of Engineering Geology and Environment Special Issue* 1, 45–52.

Evans, S.G. (1986). The maximum discharge of outburst floods caused by the breaching of man-made and natural dams. *Canadian Geotechnical Journal* 23 (3), 385–387. doi:10.1139/t86-053

Faeh, R. (2007). Numerical modeling of breach erosion of river embankments. *Journal of Hydraulic Engineering* 133 (9), 1000–1009. doi:10.1061/(asce)0733-9429(2007)133:9(1000)

Fan, X.M., Dufresne, A., Subramanian, S.S., Strom, A., Hermanns, R., Stefanelli, C.T., Hewitt, K., Yunus, A.P., Dunning, S., Capra, L., Geertsema, M., Miller, B., Casagli, N., Jansen, J.D., and Xu, Q. (2020). The formation and impact of landslide dams – State of the art. *Earth-Science Reviews* 203, 103116. doi:10.1016/j.earscirev.2020.103116

Fan, X.M., Scaringi, G., Korup, O., West, A.J., van Westen, C.J., Tanyas, H., Hovius, N., Hales, T.C., Jibson, R.W., Allstadt, K.E., Zhang, L.M., Evans, S.G., Xu, C., Li, G., Pei, X.J., Xu, Q., and Huang, R.Q. (2019a). Earthquake-induced chains of geologic hazards: Patterns, mechanisms, and impacts. *Reviews of Geophysics* 57, 421–503. doi:10.1029/2018rg000626

Fan, X.M., Dufresne, A., Whiteley, J., Yunus, A.P., Subramanian, S.S., Okeke, C.A.U., Pánek, T., Hermanns, R.L., Peng, M., Strom, A., Havenith, H.B., Dunning, S., Wang, G.H., and Stefanelli, C.T. (2021). Recent technological and methodological advances for the investigation of landslide dams. *Earth-Science Reviews* 218, 103646. doi:10.1016/j.earscirev.2021.103646

Fan, X.M., Xu, Q., Alonso-Rodriguez, A., Siva Subramanian, S., Li, W.L., Zheng, G., Dong, X.J., and Huang, R.Q. (2019b). Successive landsliding and damming of the Jinsha River in eastern Tibet, China: prime investigation, early warning, and emergency response. *Landslides* 16 (5), 1003–1020. doi:10.1007/s10346-019-01159-x

Fread, D.L. (1988). *National Oceanic and Atmospheric Administration*. USA: National Weather Service, Silver Spring.BREACH: An erosion model for earthen dam failures (Model description and user manual)

Fread, D.L., and Lewis, J.M. (1988). "FLDWAV: A generalized flood routing model," in Proceedings of National Conference on Hydraulic Engineering, Colorado Springs, USA.

Ge, W., Sun, H.Q., Zhang, H.X., Li, Z.K., Guo, X.Y., Wang, X.W., Qin, Y.P., Gao, W.X., and van Gelder, P. (2020). Economic risk criteria for dams considering the relative level of economy and industrial economic contribution. *Science of the Total Environment* 725, 138139. doi:10.1016/j.scitotenv.2020.138139

Ge, W., Jiao, Y.T., Sun, H.Q., Li, Z.K., Zhang, H.X., Zheng, Y., Guo, X.Y., Zhang, Z.S., and van Gelder, P. (2019). A method for fast evaluation of potential consequences of dam breach. *Water* 11 (11), 2224. doi:10.3390/w11112224

Ge, W., Wang, X.W., Li, Z.K., Zhang, H.X., Guo, X.Y., Wang, T., Gao, W.X., Lin, C.N., and van Gelder, P. (2021). Interval analysis of the loss of life caused by dam failure. *Journal of Water Resources Planning and Management* 147 (1), 04020098. doi:10.1061/(asce)wr.1943-5452.0001311

Godunov, S.K. (1959). Finite difference method for the computation of discontinuous solutions of the equations of fluid dynamics. *Sbornik Mathematics* 47, 271–306.

Goutiere, L., Soares-Frazão, S., and Zech, Y. (2011). Dam-break flow on mobile bed in abruptly widening channel: experimental data. *Journal of Hydraulic Research* 49 (3), 367–371. doi:10.1080/00221686.2010.548969

Graham, W.J. (1999). *A procedure for estimating loss of life caused by dam failure*. Denver, USA: U.S. Bureau of Reclamation. Dam Safety Office, Report No. DSO-99-06.

Gregoretti, C., Maltauro, A., and Lanzoni, S. (2010). Laboratory experiments on the failure of coarse homogeneous sediment natural dams on a sloping bed. *Journal of Hydraulic Engineering* 136 (11), 868–879. doi:10.1061/(asce)hy.1943-7900.0000259

Guan, M.F., Wright, N.G., and Sleigh, P.A. (2015). Multimode morphodynamic model for sediment-laden flows and geomorphic impacts. *Journal of Hydraulic Engineering* 141 (6), 04015006. doi:10.1061/(asce)hy.1943-7900.0000997

Guan, M.F., Wright, N.G., and Sleigh, P.A. (2014). 2D process-based morphodynamic model for flooding by noncohesive dyke breach. *Journal of Hydraulic Engineering* 140 (7), 04014022. doi:10.1061/(asce)hy.1943-7900.0000861

Harten, A., Lax, P.D., and van Leer, B. (1983). On upstream differencing and Godunov-Type schemes for hyperbolic conservation laws. *SIAM Review* 25 (1), 35–61. doi:10.1137/1025002

Hermanns, R.L., Hewitt, K., Strom, A., Evans, S.G., Dunning, S.A., and Scarascia-Mugnozza, G. (2011a). *The classification of rockslide dams. Natural and Artificial Rockslide Dams*. Springer, 581–593.

Hermanns, R.L., Folguera, A., Penna, I., Fauqué, L., and Niedermann, S. (2011b). Landslide dams in the central Andes of Argentina (northern Patagonia and the Argentine northwest). *Natural and Artificial Rockslide Dams*, 147–176. Springer.

Hu, X.W., Luo, G., Lv, X.P., Huang, R.Q., and Shi, Y.B. (2011). Analysis on dam-breaking mode of Tangjiashan barrier dam in Beichuan County. *Journal of Mountain Science* 8 (2), 354–362. doi:10.1007/s11629-011-2097-4

Huang, D.J., Yu, Z.B., Li, Y.P., Han, D.W., Zhao, L.L., and Chu, Q. (2017). Calculation method and application of loss of life caused by dam break in China. *Natural Hazards* 85 (1), 39–57. doi:10.1007/s11069-016-2557-9

IAHR Working Group for Dam-break Flows over Mobile BedsCanelas, R., Cao, Z., Cea, L., Chaudhry, H. M., Die Moran, A., et al. (2012). Dam-break flows over mobile beds: experiments and benchmark tests for numerical models. *Journal of Hydraulic Research* 50 (4), 364–375. doi:10.1080/00221686.2012.689682

Ischuk, A.R. (2011). *Usoi rockslide dam and lake Sarez, Pamir mountains, Tajikistan. Natural and Artificial Rockslide Dams*. Springer, 423–440.

Itoh, T., Ikeda, A., Nagayama, T., and Mizuyama, T. (2018). Hydraulic model tests for propagation of flow and sediment in floods due to breaking of a natural landslide dam during a mountainous torrent. *International Journal of Sediment Research* 33, 107–116. doi:10.1016/j.ijsrc.2017.10.001

Jiang, X.G., and Wei, Y.W. (2020). Erosion characteristics of outburst floods on channel beds under the conditions of different natural dam downstream slope angles. *Landslides* 17 (4), 1823–1834. doi:10.1007/s10346-020-01381-y

Jiang, X.G., and Wei, Y.W. (2019). Natural dam breaching due to overtopping: effects of initial soil moisture. *Bulletin of Engineering Geology and the Environment* 78, 4821–4831. doi:10.1007/s10064-018-01441-7

Jiang, X.G., Wei, Y.W., Wu, L., and Lei, Y. (2018). Experimental investigation of failure modes and breaching characteristics of natural dams. *Geomatics, Natural Hazards and Risk* 9 (1), 33–48. doi:10.1080/19475705.2017.1407367

Jongmans, D., and Garambois, S. (2007). Geophysical investigation of landslides: a review. *Bulletin de la Soci´et´e g´eologique de France* 178 (2), 101–112. doi:10.2113/gssgfbull.178.2.101

Jonkman, S.N. (2007). *Loss of life estimation in flood risk assessment: theory and applications*. Ph.D. Thesis. Delft, Netherlands: Delft University of Technology.

Jonkman, S.N., and Penning-Rowsell, E. (2008). Human instability in flood flows. *Journal of the American Water Resources Association* 44 (5), 1208–1218. doi:10.1111/j.1752-1688.2008.00217.x

Juez, C., Murillo, J., and García-Navarro, P. (2014). A 2D weakly-coupled and efficient numerical model for transient shallow flow and movable bed. *Advances in Water Resources* 71, 93–109. doi:10.1016/j.advwatres.2014.05.014

Juez, C., Lacasta, A., Murillo, J., and García-Navarro, P. (2016). An efficient GPU implementation for a faster simulation of unsteady bed-load transport. *Journal of Hydraulic Research* 55 (3), 275–288. doi:10.1080/00221686.2016.1143042

Korup, O. (2002). Recent research on landslide dams - a literature review with special attention to New Zealand. *Progress in Physical Geography* 26 (2), 206–235. doi:10.1191/0309133302pp333ra

Korup, O. (2004). Geomorphometric characteristics of New Zealand landslide dams. *Engineering Geology* 73, 13–35. doi:10.1016/j.enggeo.2003.11.003

Lacasta, A., Morales-Hernández, M., Murillo, J., and García-Navarro, P. (2014). An optimized GPU implementation of a 2D free surface simulation model on unstructured meshes. *Advances in Engineering Software* 78, 1–15. doi:10.1016/j.advengsoft.2014.08.007

Lacasta, A., Juez, C., Murillo, J., and García-Navarro, P. (2015). An efficient solution for hazardous geophysical flows simulation using GPUs. *Computers and Geosciences* 78, 63–72. doi:10.1016/j.cageo.2015.02.010

Lauber, G., and Hager, W.H. (1998). Experiments to dambreak wave: Horizontal channel. *Journal of Hydraulic Research* 36 (3), 291–307. doi:10.1080/00221689809498620

Lee, J.S. (2003). Uncertainties in the predicted number of life loss due to the dam breach floods. *KSCE Journal of Civil Engineering* 7 (1), 81–91. doi:10.1007/bf02841991

Li, L., Yang, X.G., Zhou, J.W., Zhang, J.Y., and Fan, G. (2021). Large-scale field test study on failure mechanism of non-cohesive landslide dam by overtopping. *Frontiers in Earth Science* 9, 660408. doi:10.3389/feart.2021.660408

Li, D.Y., Zheng, D.F., Wu, H., Shen, Y.Q., and Nian, T.K. (2021). Numerical simulation on the longitudinal breach process of landslide dams using an improved coupled DEM-CFD method. *Frontiers in Earth Science* 9, 673249. doi:10.3389/feart.2021.673249

Li, J., Cao, Z.X., Pender, G., and Liu, Q.Q. (2013). A double layer-averaged model for dam-break flows over mobile bed. *Journal of Hydraulic Research* 51 (5), 518–534. doi:10.1080/00221686.2013.812047

Lind, N, Hartford, D, and Assaf, H (2004). Hydrodynamic models of human instability in a flood. *Journal of the American Water Resources Association* 40 (1), 89–96. doi:10.1111/j.1752-1688.2004.tb01012.x

Liu, J.K., Cheng, Z.L., and Wu, J.S. (2013). An empirical model calculating the breach parameters of landslide and debris-flow dam. *Journal of Sichuan University (Engineering Science Edition)* 45 (S2), 84–89. (in Chinese).

Liu, N., Chen, Z.Y., Zhang, J.X., Lin, W., Chen, W.Y., and Xu, W.J. (2010). Draining the Tangjiashan barrier lake. *Journal of Hydraulic Engineering* 136 (11), 914–923. doi:10.1061/(asce)hy.1943-7900.0000241

Liu, W.M., Carling, P.A., Hu, K.H., Wang, H., Zhou, Z., Zhou, L.Q., Liu, D.Z., Lai, Z.P., and Zhang, X.B. (2019). Outburst floods in China: A review. *Earth-Science Review* 197, 102895. doi:10.1016/j.earscirev.2019.102895

Mahmoud, A.A., Wang, J.T., and Jin, F. (2020). An improved method for estimating life losses from dam failure in China. *Stochastic Environmental Research and Risk Assessment* 34, 1263–1279. doi:10.1007/s00477-020-01820-1

Marsooli, R., and Wu, W.M. (2015). Three-dimensional numerical modeling of dam-break flows with sediment transport over movable beds. *Journal of Hydraulic Engineering* 141 (1), 04014066. doi:10.1061/(asce)hy.1943-7900.0000947

McCann, D., and Forster, A. (1990). Reconnaissance geophysical methods in landslide investigations. *Engineering Geology* 29 (1), 59–78. doi:10.1016/0013-7952(90)90082-c

Mei, S.Y., Chen, S.S., Zhong, Q.M., and Shan, Y.B. (2021). Effects of Grain Size Distribution on Landslide Dam Breaching—Insights From Recent Cases in China. *Frontiers in Earth Science* 9, 658578. doi:10.3389/feart.2021.658578

Niazi, F.S., Habib Ur, R., and Akram, T. (2010). Application of electrical resistivity for subsurface characterization of Hattian Bala landslide dam, GeoFlorida 2010. *Adv. Analysis Model. Desig.*, 480–489.

O'Connor, J.E., and Beebee, R.A. (2009). *Floods from natural rock-material dams*. New York: Cambridge University Press.

Osher, S., and Solomon, F. (1982). Upwind difference schemes for hyperbolic systems of conservation laws. *Mathematics of Computation* 158, 339–374. doi:10.1090/s0025-5718-1982-0645656-0

Peng, M., and Zhang, L.M. (2012a). Breaching parameters of landslide dams. *Landslides* 9 (1), 13–31. doi:10.1007/s10346-011-0271-y

Peng, M., and Zhang, L.M. (2012b). Analysis of human risks due to dam-break floods – part 1: a new model based on Bayesian networks. *Natural Hazards* 64, 903–933. doi:10.1007/s11069-012-0275-5

Peng, M., Jiang, Q.L., Zhang, Q.Z., Hong, Y., Jiang, M.Z., Shi, Z.M., and Zhang, L.M. (2019). Stability analysis of landslide dams under surge action based on large-scale flume experiments. *Engineering Geology* 259, 105191. doi:10.1016/j.enggeo.2019.105191

Peng, M., Ma, C.Y., Chen, H.X., Zhang, P., Zhang, L.M., Jiang, M.Z., Zhang, Q.Z., and Shi, Z.M. (2021). Experimental study on breaching mechanisms of landslide dams composed of different materials under surge waves. *Engineering Geology* 291, 106242. doi:10.1016/j.enggeo.2021.106242

Peng, M., Zhang, L.M., Chang, D.S., and Shi, Z.M. (2014). Engineering risk mitigation measures for the landslide dams induced by the 2008 Wenchuan earthquake. *Engineering Geology* 180, 68–84. doi:10.1016/j.enggeo.2014.03.016

Priest, S., Wilson, T., Tapsell, S., Penning-Rowsell, E., Viavattene, C., and Fernandez-Bilbao, A. (2007). *Building a model to estimate Risk to Life for European flood events - final report*. Integrated flood risk analysis and management methodologies. Available at: http://www.floodsite.net/html/partner_area/search_results3b.asp?docID=265.

Qian, H.L, Cao, Z.X., Liu, H.H., and Pender, G. (2018). New experimental dataset for partial dam-break floods over mobile beds. *Journal of Hydraulic Research* 56 (1), 124–135. doi:10.1080/00221686.2017.1289264

Razavitoosi, S.L., Ayyoubzadeh, S.A., and Valizadeh, A. (2014). Two-phase SPH modelling of waves caused by dam break over a movable bed. *International Journal of Sediment Research* 29 (3), 344–356. doi:10.1016/s1001-6279(14)60049-4

Reiter, P. (2001). *Loss of life caused by dam failure: the RESCDAM LOL method and its application to Kyrkosjarvi dam in Seinajoki*. Helsinki: PR Water Consulting Ltd.

Roe, P.L. (1981). Approximate Riemann solvers, parameter vectors, and difference schemes. *Journal of Computational Physics* 43, 357–372. doi:10.1016/0021-9991(81)90128-5

Rosatti, G., and Begnudelli, L. (2013). Two-dimensional simulation of debris flows over mobile bed: Enhancing the TRENT2D model by using a well-balanced Generalized Roe-type solver. *Computers and Fluids* 71, 179–195. doi:10.1016/j.compfluid.2012.10.006

Scaioni, M., Longoni, L., Melillo, V., and Papini, M. (2014). Remote sensing for landslide investigations: an overview of recent achievements and perspectives. *Remote Sensing* 6 (10), 9600–9652. doi:10.3390/rs6109600

Shan, Y.B., Chen, S.S., and Zhong, Q.M. (2020). Rapid prediction of landslide dam stability using the logistic regression method. *Landslides* 17 (12), 2931–2956. doi:10.1007/s10346-020-01414-6

Shan, Y.B., Chen, S.S., Zhong, Q.M., Mei, S.Y., and Yang, M. (2022). Development of an empirical model for predicting peak breach flow of landslide dams considering material composition. *Landslides* 19 (6), 1491–1518. doi:10.1007/s10346-022-01863-1

Shen, D.Y., Shi, Z.M., Peng, M., Zhang, L.M., and Jiang, M.Z. (2020a). Longevity analysis of landslide dams. *Landslides* 17 (8), 1797–1821. doi:10.1007/s10346-020-01386-7

Shen, G.Z., Sheng, J.B., Xiang, Y., Zhong, Q.M., and Yang, D.W. (2020b). Numerical modeling of overtopping-induced breach of landslide dams. *Natural Hazards Review* 21 (2), 04020002. doi:10.1061/(asce)nh.1527-6996.0000362

Shi, Z.M., Cheng, S.Y., Zhang, Q.Z., and Xue, D.X. (2020). A fast model for landslide dams stability assessment: a case study of Xiaogangjian (Upper) landslide dam. *Journal of Water Resources and Architectural Engineering* 18 (2), 95–100+146. (in Chinese).

Shi, Z.M., Guan, S.G., Peng, M., and Xiong, X. (2015a). "Research on the influence of material permeability to landslide dam seepage stability," in 10th Asian Region Conference of IAEG, Kyoto, Japan, Sept. 26-27, 2015.

Shi, Z.M., Ma, X.L., Peng, M., and Zhang, L.M. (2014). Statistical analysis and efficient dam burst modelling of landslide dams based on a large-scale database. *Chinese Journal of Rock Mechanics and Engineering* 33 (9), 1780–1790. (in Chinese).

Shi, Z.M., Guan, S.G., Peng, M., Zhang, L.M., Zhu, Y., and Cai, Q.P. (2015b). Cascading breaching of the Tangjiashan landslide dam and two smaller downstream landslide dams. *Engineering Geology* 193, 445–458. doi:10.1016/j.enggeo.2015.05.021

Shi, Z.M., Xiong, X., Peng, M., Zhang, L.M., Xiong, Y.F., Chen, H.X., and Zhu, Y. (2016). Risk assessment and mitigation for the Hongshiyan landslide dam triggered by the 2014 Ludian earthquake in Yunnan, China. *Landslides* 14 (1), 269–285. doi:10.1007/s10346-016-0699-1

Soares-Frazão, S., and Zech, Y. (2002). Dam break in channels with 90° bend. *Journal of Hydraulic Engineering* 128 (11), 956–968. doi:10.1061/(asce)0733-9429(2002)128:11(956)

Spinewine, B., and Zech, Y. (2007). Small-scale laboratory dam-break waves on movable beds. *Journal of Hydraulic Research* 45 (S1), 73–86. doi:10.1080/00221686.2007.9521834

Stefanelli, C. T., Catani, F., and Casagli, N. (2015). Geomorphological investigations on landslide dams. *Geoenvironmental Disasters* 2 (2), 21. doi:10.1186/s40677-015-0030-9

Stefanelli, C.T., Segoni, S., Casagli, N., and Catani, F. (2016). Geomorphic indexing of landslide dams evolution. *Engineering Geology* 208, 1–10. doi:10.1016/j.enggeo.2016.04.024

Stefanelli, C.T., Vilímek, V., Emmer, A., and Catani, F. (2018). Morphological analysis and features of the landslide dams in the Cordillera Blanca, Peru. *Landslides* 15 (3), 507–521. doi:10.1007/s10346-017-0888-6

Swartenbroekx, C., Soares-Frazão, S., Staquet, R., and Zech, Y. (2010). Two-dimensional operator for bank failures induced by water-level rise in dam-break flows. *Journal of Hydraulic Research* 48 (3), 302–314. doi:10.1080/00221686.2010.481856

Swartenbroekx, C., Zech, Y., and Soares-Frazão, S. (2013). Two-dimensional two-layer shallow water model for dam break flows with significant bed load transport. *International Journal for Numerical Methods in Fluids* 73 (5), 477–508. doi:10.1002/fld.3809

Takayama, S., Miyata, S., Fujimoto, M., and Satofuka, Y. (2021). Numerical simulation method for predicting a flood hydrograph due to progressive failure of a landslide dam. *Landslides* 18, 3655–3670. doi:10.1007/s10346-021-01712-7

Tong, Y.X. (2008). *Master Thesis*. Taoyuan: National Central University. (in Chinese).Quantitative analysis for stability of landslide dams

Toro, E.F. (2000). *Shocking methods for free surface shallow flows*. New York, USA: Wiley.

Toro, E.F., Spruce, M., and Speares, W. (1994). Restoration of the contact surface in the HLL-Riemann solver. *Shock Waves* 4 (4), 25–34. doi:10.1007/bf01414629

Tsai, P.H., Feng, Z.Y., Yu, F.C., and Lin, J.H. (2013). "Stability analysis of landslide dam under rainfall," in IACGE 2013 - Challenges and Recent Advances in Geotechnical and Seismic Research and Practices, Chengdu, China, October 25-27, 2013.

US Army Corps of Engineers (2021). *HEC-RAS, River analysis system user's manual*. Davis, USA: Hydrologic Engineering Center, US Army Corps of Engineers.

Walder, J.S., Iverson, R.M., Godt, J.W., Logan, M., and Solovitz, S.A. (2015). Controls on the breach geometry and flood hydrograph during overtopping of noncohesive earthen dams. *Water Resources Research* 51 (8), 6701–6724. doi:10.1002/2014wr016620

Walder, J.S., and O'Connor, J.E. (1997). Methods for predicting peak discharge of floods caused by failure of natural and constructed earthen dams. *Water Resources Research* 33 (10), 2337–2348. doi:10.1029/97wr01616

Wang, B., Zhang, F.J., Liu, X., Guo, Y.K., Zhang, J.M., and Peng, Y. (2021). Approximate analytical solution and laboratory experiments for dam-break wave tip region in triangular channels. *Journal of Hydraulic Engineering* 147 (9), 06021015. doi:10.1061/(asce)hy.1943-7900.0001928

Wang, F.W., Okeke, A.C.U., Kogure, T., Sakai, T., and Hayashi, H. (2018). Assessing the internal structure of landslide dams subject to possible piping erosion by means of microtremor chain array and self-potential surveys. *Engineering Geology* 234, 11–26. doi:10.1016/j.enggeo.2017.12.023

Wang, G.H., Huang, R.Q., Kamai, T., and Zhang, F.Y. (2013). The internal structure of a rockslide dam induced by the 2008 Wenchuan (Mw7.9) earthquake, China. *Engineering Geology* 156, 28–36. doi:10.1016/j.enggeo.2013.01.004

Wang, G.H., Huang, R.Q., Lourenço, S.D., and Kamai, T. (2014). A large landslide triggered by the 2008 Wenchuan (M8.0) earthquake in Donghekou area: Phenomena and mechanisms. *Engineering Geology* 182, 148–157. doi:10.1016/j.enggeo.2014.07.013

Wang, G.H., Furuya, G., Zhang, F.Y., Doi, I., Watanabe, N., Wakai, A., and Marui, H. (2016). Layered internal structure and breaching risk assessment of the Higashi-Takezawa landslide dam in Niigata, Japan. *Geomorphology* 267, 48–58. doi:10.1016/j.geomorph.2016.05.021

Wang, K.W., Deng, C.J., and Zhang, F. (2012). Formation process of Tanggudong landslide and Yuri accumulation body in Yalong River valley in southwest. China. *J. Eng. Geol.* 20 (6), 955–970. (in Chinese).

Wang L., L., Chen, Z.Y., Wang, N.X., Sun, P., Yu, S., Li, S.Y., and Du, X.H. (2016). Modeling lateral enlargement in dam breaches using slope stability analysis based on circular slip mode. *Engineering Geology* 209, 70–81. doi:10.1016/j.enggeo.2016.04.027

Weidinger, J.T. (2006). Landslide dams in the high mountains of India, Nepal and China - Stability and life span of their dammed lakes. *Italian Journal of Engineering Geology and Environment Special Issue* 1, 67–80.

Whiteley, J., Chambers, J., Uhlemann, S., Wilkinson, P., and Kendall, J. (2019). Geophysical monitoring of moisture-induced landslides: a review. *Reviews of Geophysics* 57, 106–145. doi:10.1029/2018rg000603

Wu, W.M., and Wang, S.S.Y. (2007). One-dimensional modeling of dam-break flow over movable beds. *Journal of Hydraulic Engineering* 133 (1), 48–58. doi:10.1061/(asce)0733-9429(2007)133:1(48)

Wu, W.M., Marsooli, R., and He, Z.G. (2012). Depth-averaged two-dimensional model of unsteady flow and sediment transport due to noncohesive embankment break/breaching. *Journal of Hydraulic Engineering* 138 (6), 503–516. doi:10.1061/(asce)hy.1943-7900.0000546

Xu, Q., Fan, X.M., Huang, R.Q., and Westen, C.V. (2009). Landslide dams triggered by the Wenchuan earthquake, Sichuan Province, south west China. *Bulletin of Engineering Geology and the Environment* 68, 373–386. doi:10.1007/s10064-009-0214-1

Yang, Y., Cao, S.Y., Yang, K.J., and Li, W.P. (2015). Experimental study of breach process of landslide dams by overtopping and its initiation mechanisms. *Journal of Hydrodynamics* 27 (6), 872–883. doi:10.1016/s1001-6058(15)60550-9

Zhai, G.F., Fukuzono, T., and Ikeda, S. (2006). An empirical model of fatalities and injuries due to flood in Japan. *Journal of the American Water Resources Association* 42 (4), 863–875. doi:10.1111/j.1752-1688.2006.tb04500.x

Zhang, J.Y., Fan, G., Li, H.B., Zhou, J.W., and Yang, X.G. (2021). Large-scale field model tests of landslide dam breaching. *Engineering Geology* 293, 106322. doi:10.1016/j.enggeo.2021.106322

Zhang, L.M., Peng, M., Chang, D. S., and Xu, Y. (2016). *Dam failure mechanisms and risk assessment*. Singapore: John Wiley & Sons Singapore Pte. Ltd.

Zhang, L.M., Xiao, T., He, J., and Chen, C. (2019). Erosion-based analysis of breaching of Baige landslide dams on the Jinsha River, China, in 2018. *Landslides* 16 (10), 1965–1979. doi:10.1007/s10346-019-01247-y

Zhao, T.L., Chen, S.S., Fu, C.J., and Zhong, Q.M. (2019). Centrifugal model test on the failure mechanism of barrier dam overtopping. *KSCE Journal of Civil Engineering* 23 (4), 1548–1559. doi:10.1007/s12205-019-0375-9

Zhao, T.L., Chen, S.S., Fu, C.J., and Zhong, Q.M. (2018). Influence of diversion channel section type on landslide dam draining effect. *Environmental Earth Sciences* 77 (2), 54–62. doi:10.1007/s12665-017-7217-1

Zhong, Q.M., Wang, L., Chen, S.S., Chen, Z.Y., Shan, Y.B., Zhang, Q., Ren, Q., Mei, S.Y., Jiang, J.D., Hu, L., and Liu, J.X. (2021). Breaches of embankment and landslide dams – State of the art review. *Earth-Science Reviews* 216, 103597. doi:10.1016/j.earscirev.2021.103597

Zhong, Q.M., Chen, S.S., Wang, L., and Shan, Y.B. (2020a). Back analysis of breaching process of Baige landslide dam. *Landslides* 17 (7), 1681–1692. doi:10.1007/s10346-020-01398-3

Zhong, Q.M., Wu, W.M., Chen, S.S., and Wang, M. (2016). Comparison of simplified physically based dam breach models. *Natural Hazards* 84 (2), 1385–1418. doi:10.1007/s11069-016-2492-9

Zhong, Q.M., Chen, S.S., and Shan, Y.B. (2020b). Prediction of the overtopping-induced breach process of the landslide dam. *Engineering Geology* 274, 105709. doi:10.1016/j.enggeo.2020.105709

Zhong, Q.M., Chen, S.S., Mei, S.A., and Cao, W. (2018). Numerical simulation of landslide dam breaching due to overtopping. *Landslides* 15 (6), 1183–1192. doi:10.1007/s10346-017-0935-3

Zhou, G.G.D, Zhou, M.J., Shrestha, M.S., Song, D.R., Choi, C.E., Cui, K.F.E., Peng, M., Shi, Z.M., Zhu, X.H., and Chen, H.Y. (2019). Experimental investigation on the longitudinal evolution of landslide dam breaching and outburst floods. *Geomorphology* 334, 29–43. doi:10.1016/j.geomorph.2019.02.035

Zhou, X.B., Chen, Z.Y., Yu, S., Wang, L., Deng, G., Sha, P.J., and Li, S.Y. (2015). Risk analysis and emergency actions for Hongshiyan barrier lake. *Natural Hazards* 79 (3), 1933–1959. doi:10.1007/s11069-015-1940-2

Zhu, X.H., Liu, B.X., Peng, J.B., Zhang, Z.F., Zhuang, J.Q., Huang, W.L., Leng, Y.Q., and Duan, Z. (2021). Experimental study on the longitudinal evolution of the overtopping breaching of noncohesive landslide dams. *Engineering Geology* 288, 106137. doi:10.1016/j.enggeo.2021.106137

Zhu, X.H., Peng, J.B., Liu, B.X., Jiang, C., and Guo, J. (2020). Influence of textural properties on the failure mode and process of landslide dams. *Engineering Geology* 271, 105613. doi:10.1016/j.enggeo.2020.105613

frontiers | Frontiers in Earth Science

TYPE Original Research
PUBLISHED 11 January 2023
DOI 10.3389/feart.2022.1053634

OPEN ACCESS

EDITED BY
Tianshou Ma,
Southwest Petroleum University, China

REVIEWED BY
Ke Zhang,
Kunming University of Science and Technology, China
Shui-Hua Jiang,
Nanchang University, China

*CORRESPONDENCE
Yongdong Meng,
meng@ctgu.edu.cn

SPECIALTY SECTION
This article was submitted to Geohazards and Georisks, a section of the journal Frontiers in Earth Science

RECEIVED 26 September 2022
ACCEPTED 27 October 2022
PUBLISHED 11 January 2023

CITATION
Cai Z, Shou S, Zhou J, Tian B, Xiong B and Meng Y (2023), System reliability analysis of landslides involving sliding surfaces using intelligent multiple response surfaces.
Front. Earth Sci. 10:1053634.
doi: 10.3389/feart.2022.1053634

System reliability analysis of landslides involving sliding surfaces using intelligent multiple response surfaces

Zhenglong Cai[1,2], Silong Shou[2], Jiawen Zhou[3], Bin Tian[1], Bobo Xiong[2] and Yongdong Meng[1]*

[1]Hubei Key Laboratory of Disaster Prevention and Mitigation, China Three Gorges University, Yichang, China, [2]College of Hydraulic and Environmental Engineering, China Three Gorges University, Yichang, China, [3]State Key Laboratory of Hydraulics and Mountain River Engineering, Sichuan University, Chengdu, China

The shear strength reduction method provides an effective tool of numerical analysis for landslides reliability analysis. However, it ignores the failure probability of the secondary failure surfaces and requires huge computational cost. To avoid these common criticisms, an intelligent multiple response surfaces method for system reliability using multiple response-surface method (MRSM) and least-squares support vector machine (LSSVM) is presented to evaluate the stability of complex multistage historic landslides with multiple sliding surfaces. Deterministic analysis of each sliding surface is first performed using the finite element method of sliding surface stress analysis, which is applied to obtain the safety factors of different sliding surfaces from the stress fields generated by finite element simulations. The LSSVM model with excellent nonlinear fitting ability is then employed to construct the multiple response-surface method (MRSM) of the sliding surfaces and a genetic algorithm (GA) is adopted to optimize the LSSVM. This proposed methodology is finally applied to investigate the probability of system failure of the Zhenggang landslide in southwestern China. The results indicate that the proposed approach can reduce the computational cost of finite element analysis in direct Monte Carlo simulation (MCS) by proper training using a limited of samples, and the calculation accuracy meets the engineering requirements of complex multistage historic landslides.

KEYWORDS

landslide, system reliability, multiple response surfaces, least-squares support vector machine, finite element limit equilibrium method

1 Introduction

Evaluation of landslide stability is an important topic in geotechnical engineering and disaster prevention. However, large uncertainties of landslide stability are commonly associated with rock and soil properties and measurement errors (Su et al., 2011; Hong et al., 2016; Li et al., 2019). Reliability analysis is an effective approach to account for the

uncertainties associated with the underlying landslide stability parameters (Griffiths and Fenton 2004; Ji et al., 2012). For example, Wu et al. (2014) used Monte Carlo simulations (MCS) to study the random-fuzzy reliability of the Liangshuijing landslide, and Dadashzadeh et al. (2017) employed an integrated response surface method to investigate the reliability of rock slopes. However, a complex historic landslide may have experienced several sliding episodes and formed multiple sliding surfaces (i.e., potential failure modes). Considering the single most critical failure mode (i.e., the most critical surface) may not give a complete picture of the overall reliability of the landslide. System reliability, which considers all significant failure modes and their correlations, should therefore be employed to study landslide stability.

Due to the stochastic characteristic of probability analysis, it is necessary to implement a large number of deterministic analyses to obtain the safety factors of the landslide stability probabilistically. The deterministic analysis for landslide system reliability is almost based on rigid limit equilibrium methods in literatures (Liu and Cheng 2016; Wang et al., 2020). This is because the strength reduction method cannot simultaneously estimate the safety factors of landslide with multiple potential sliding surfaces, and it requires the long solution time in the iterative process of shear strength reduction, which has dramatically increase because of the large number of deterministic analyses. Finite element method of sliding surface stress analysis (Zou et al., 1995; Kim and Lee 1997), the hybrid of limit element method (LEM) and finite element method (FEM), can calculate directly the safety factor of multiple potential sliding surfaces based on stress field generated by a FEM simulation, and thus expands greatly the application of numerical simulation in landslide system reliability.

Currently, the system reliability methods for landslide mainly include Monte Carlo simulation (MCS) (Wang and Goh 2021; Pei et al., 2022), bounds method (Ditlevsen 1979; Low et al., 1997, 2011), *mvncdf* method (Liu and Low 2017) and multiple response-surface method (MRSM) (Li et al., 2015). The Monte Carlo simulation (MCS) is one of the most popular methods for analyzing the system reliability without closed-form solutions. However, the MCS requires extensive computational efforts due to a large number of sampling needed to ensure a sufficiently accurate estimation of the failure probability (Dong and Lu 2021). The bounds method and *mvncdf* method are based on the situation where an explicit mathematical function exists (Fu et al., 2019), but it is often difficult to obtain the explicit relationship function between the safety factor of landslide and the shear strength parameters. The MRSM is a metamodel-based method for replacing a complex model by approximating the actual limit state functions (Li et al., 2015). It can thus effectively alleviate the cost of functions evaluation in the response surfaces of all failure modes, and provides efficient strategies for system reliability analysis.

Generally, traditional MRSM employs multiple polynomial functions to model low-order problems, and corresponding computational efficiency of response surface models can satisfy the requirements of probabilistic numerical models. Low-order polynomial response surfaces, however, are difficult to approximate the actual response state function (RSF) with obvious nonlinear characteristics of landslide. Thus, several researchers proposed the intelligent algorithms to construct more accurate RSF in the literatures. For example, Li et al. (2013) employed a support vector machine (SVM) to approach the RSF of landslide stability because of its excellent fitting ability with a limited number of samples. Sung (2008) developed artificial neural network (ANN) as an approximate RSF to express the relationship function of landslide between the safety factor and the shear strength parameters. Tan et al. (2011) studied the similarities and differences between these RSFs using ANN and SVM. Applying the similar method, intelligent multiple response surfaces method can be used for probabilistic numerical modeling of landslide stability considering multiple sliding surfaces.

In this study, a system reliability method is proposed for probabilistic numerical study of landslide stability based on LSSVM and MRSM. The safety factors of multiple sliding surfaces, which form the basis of system reliability analysis, are obtained from results of finite element method of sliding surface stress analysis. The MRSM, which integrates LSSVM and genetic algorithm (GA) is then applied to generate the explicit relationship function between the safety factor and random variables of landslide. Next, the system failure probability of a landslide with multiple sliding surfaces can be obtained by the MCS approach. As a case study, the system failure probability method is finally applied to the Zhenggang landslide in southwestern China to illustrate the proposed approach.

2 Methodology

2.1 Finite element method of sliding surface stress analysis

The deterministic analysis of landslide is determined using finite element method of sliding surface stress analysis in this paper, which is a numerical technique based on the limit equilibrium method (LEM) and finite element method (FEM). The finite element method of sliding surface stress analysis can be applied to evaluate the safety factors of multiple potentially active sliding surfaces using a finite element simulation (Farias and Naylor 1998). The nodal stress components (σ_x, σ_y, τ_{xy}) on a sliding surface can be obtained from the FEM analysis. The two-dimensional curve of a sliding surface is discretized into several segments. The stresses of the two end-points of a segment are used to approximate the stress components in the segment by

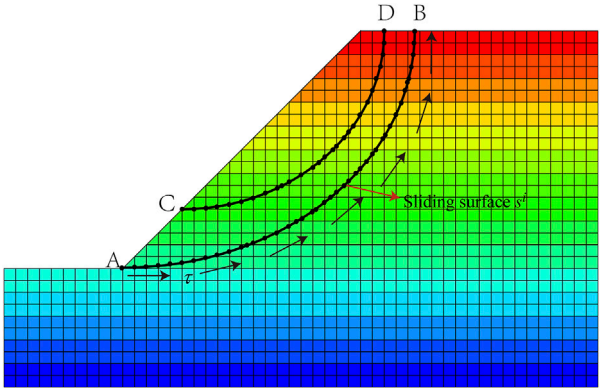

FIGURE 1
Schematic diagram for the *i*th sliding surface of a discrete slope.

interpolation. The normal stress σ_n and shear stress τ of each segment are expressed as (Yang et al., 2015):

$$\sigma_n = \frac{\left[\left(\sigma_x + \sigma_y\right) + \left(\sigma_y - \sigma_x\right)\cos 2\alpha\right]}{2} + \tau_{xy}\sin 2\alpha, \tag{1}$$

$$\tau = \frac{\left(\sigma_y - \sigma_x\right)\sin 2\alpha}{2} + \tau_{xy}\cos 2\alpha, \tag{2}$$

where α is the angle between the sliding surface and horizontal plane. For a discrete ith sliding surface s^i of landslide (Figure 1), the safety factor Fs_i can be defined as:

$$Fs_i = \frac{\sum_{j=1}^{n}\tau_{fj}s_j^i}{\sum_{j=1}^{n}\tau_j s_j^i} = \frac{\int \tau_f ds^i}{\int \tau ds^i}. \tag{3}$$

where s_j^i is the length of segment j in ith sliding surface s^i; n is the number of discrete segments, and τ_{fj} and τ_j are, respectively, the shear strength and shear stress on the plane of the jth segment of the sliding surface. According to the Mohr-Coulomb strength criterion, the safety factor Fs_i along sliding surface s^i can be expressed as:

$$Fs_i = \frac{\int \left(c + \sigma_n \tan\phi\right) ds^i}{\int \tau ds^i}, \tag{4}$$

where c and ϕ are respectively cohesion and friction angle.

2.2 Least-squares support vector machine

The LSSVM is introduced by Suykens (1999) as a modified form of the support vector machine (SVM), which can transform the quadratic optimization problem of the SVM into a linear system of equations based on linear least squares criteria. For a given data set $(\boldsymbol{x}_k, y_k)_{k=1}^m \in R^m \times R$ with input data $\boldsymbol{x}_k$ and output data y_k. The LSSVM regression model can be described as (Tan et al., 2016):

$$f(\boldsymbol{x}) = \sum_{k=1}^{m} a_k K(\boldsymbol{x}, \boldsymbol{x}_k) + b, \tag{5}$$

where $K(\boldsymbol{x}, \boldsymbol{x}_k)$ is a symmetric kernel function, and the Gaussian radial basic function (RBF) $K(\boldsymbol{x}, \boldsymbol{x}_k) = \exp\left(-(\boldsymbol{x} - \boldsymbol{x}_k)^2/(2\sigma^2)\right)$ is adopted as the kernel function in this paper. Where σ is the kernel parameter; m is the sample number; a_k is the Lagrange multiplier; b is a bias term; and a linear equation can be obtained (Cai et al., 2016):

$$\begin{bmatrix} 0 & 1_v^T \\ 1_v & \Omega + \frac{1}{\gamma}\mathrm{I} \end{bmatrix} \begin{bmatrix} b \\ \boldsymbol{a} \end{bmatrix} = \begin{bmatrix} 0 \\ \boldsymbol{y} \end{bmatrix}, \tag{6}$$

where γ is a e tolerance error; $\boldsymbol{y} = [y_1, y_2, \cdots, y_m]^T$; $1_v = [1, 1, \cdots, 1]^T$; $\boldsymbol{a} = [a_1, a_2, \cdots, a_m]^T$; Ω is a symmetric matrix, $\Omega = \phi(x)^T\phi(x_m) = K(x, x_m)$. The analytical of $\boldsymbol{a}$ and b can be obtained by:

$$\begin{bmatrix} b \\ \boldsymbol{a} \end{bmatrix} = \Phi^{-1} \begin{bmatrix} 0 \\ \boldsymbol{y} \end{bmatrix}, \tag{7}$$

Where

$$\Phi = \begin{bmatrix} 0 & 1_v^T \\ 1_v & \Omega + \frac{1}{\gamma}\mathrm{I} \end{bmatrix}. \tag{8}$$

Note that there are two user-determined parameters (kernel parameter σ and tolerance error γ) in the LSSVM model. Generally, the kernel parameter σ determines the local properties of RBF function, and the tolerance error γ balances the training error and model complexity (Roy et al., 2019). Therefore, the optimal selection of parameters is crucial to improve the accuracy of LSSVM model.

2.3 Parameters optimization of least-squares support vector machine using genetic algorithm

Genetic algorithm (GA) is a global searching method for handling optimization problems (Li et al., 2018). Actually, GA is an evolutionary algorithm inspired from the evolution theory of genetics and natural selection based on the implementation of natural genetic mechanisms such as selective reproduction, crossover and mutation. Compared with other optimization algorithms, GA requires fewer adjustment parameters to obtain the globally optimal solution and is easy to implement. Hence, GA is applied to seek the optimum parameters of LSSVM considering its excellent global search abilities in this paper. The GA optimization strategy starts by initializing a randomly generated population. Next, a population with new individuals

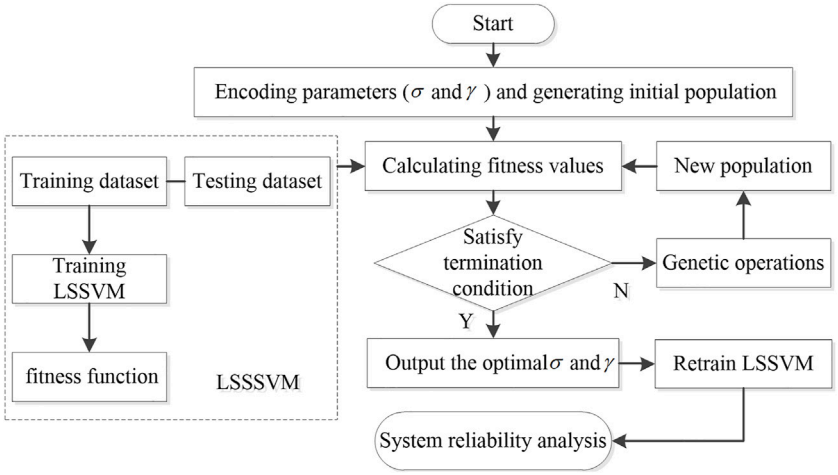

FIGURE 2
Calculation diagram of GA optimized LSSVM in system reliability analysis of landslide.

can be formed by genetic operations, and the process is repeated in computational iterations of the evolving population. Subsequently, each individual is evaluated by the statistical fitness function until the best individual (the optimal parameters) are attained. The calculating process of optimal LSSVM parameters using GA for system reliability analysis of landslide is described in Figure 2.

In this paper, the root mean square error (RMSE) is used as the fitness function to evaluate the fitting performance of LSSVM. It can be defined as:

$$RMSE = \sqrt{\frac{1}{m}\sum_{i=1}^{m}(y_i - \tilde{y}_i)^2}, \tag{9}$$

where m is the number of sample points, y_i and $\tilde{y}_i$ are the actual values and fitting values by the LSSVM model, respectively.

2.4 least-squares support vector machine-based multiple response-surface method for system reliability of landslide

For a complex multistage historic landslide with several failure modes, i.e., sliding surfaces, the limit state function for ith failure mode $g_i(\boldsymbol{X})$ can be written as:

$$g_i(\boldsymbol{X}) = Fs_i(\boldsymbol{X}) - 1. \tag{10}$$

Note that an explicit equation $Fs_i(\boldsymbol{x})$ for ith sliding surface of landslide is difficult to obtain by the FEM simulation. The GA-LSSVM model is adopted to construct the RSF $\tilde{g}_i(\boldsymbol{X})$ to approximate the implicit relationship function of landslide between the safety factor and the shear strength parameters. Applying the similar method, a multiple RSFs with all sliding surfaces can be established for the system reliability analysis. According to Eq. 5, the ith LSSVM-based RSF $\tilde{g}_i(\boldsymbol{X})$ can be expressed as:

$$\tilde{g}_i(\boldsymbol{X}) = \sum_{k=1}^{m} a_{i,k} K(\boldsymbol{X}, \boldsymbol{X}_k) + b_i. \tag{11}$$

After a LSSVM-based MRSM is constructed, a direct Monte-Carlo simulation (MCS) approach (Liu and Low 2017) can be applied to obtain the failure probability of ith sliding surface p_{f_i} and system failure probability p_f^{sys} as follows:

$$p_{fi} = \frac{1}{N_p}\sum_{k=1}^{N_p} I[\tilde{g}_i(\boldsymbol{X}) < 0], \tag{12}$$

$$p_f^{\text{sys}} = \frac{1}{N_p}\sum_{k=1}^{N_p} I\left[\min_{i=1,2,\cdots N_m} \tilde{g}_i(\boldsymbol{X}) < 0\right], \tag{13}$$

where N_p and N_m are the number of MCS simulations and sliding surfaces of landslide, respectively; $I(\cdot)$ is an indicator function.

Once the LSSVM-based MRSM is generated, the evaluation of the safety factors can be obtained directly by the evaluation of the algebraic expression without deterministic analysis of landslide stability. This means that the computational cost of the MCS is greatly reduced, especially for the deterministic analysis of finite element simulations. In addition, for deterministic multiple sliding surfaces of multistage landslides, the hybridization of the limit equilibrium method (LEM) and finite element method (FEM) only needs one finite element simulation to calculate the safety factors of all potentially

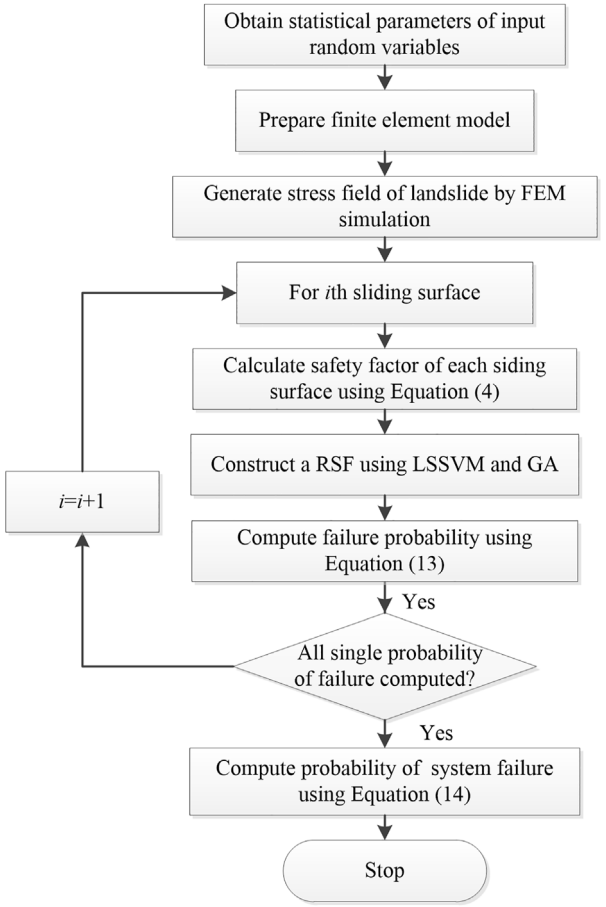

FIGURE 3
The flowchart of the system reliability analysis for landslide.

sliding surfaces from the stress fields generated, which will further reduce the computation of FEM. The flow chart of this proposed approach for system reliability of landslide can be shown in Figure 3.

3 Case study

3.1 Characterization and geology features of landslide

To illustrate the proposed methodology, the Zhenggang landslide, which is located on the right bank of the Gushui hydroelectric power station along the Lancang River near the village of Zhenggang in Yunnan Province, China, is considered. The landslide volume is approximately 47.5 million m^3 with an elevation of 2180–3220 m, and its external boundary is indicated by the yellow line in Figure 4A. The landslide, which has formed three dynamic sliding stages, lies mainly between the right No. 7 gully on the right bank and the Yagong gully. Because intensive erosion of the Zhenggang gully has generated the deepest terrain incision depth, the landslide can be divided into two geomorphological zones (I and II).

According to a geological reconnaissance survey, the Zhenggang landslide has undergone three episodes of large-scale sliding in the past and formed three potential sliding surfaces, as evidenced by its long-term deformation evolution and the destructive features in the surrounding environment (Wang et al., 2017). The largest bedrock landslide formed in the first stage and was caused by fracturing, i.e., shear failure of layered rock, which was subjected to large bending and/or toppling forces. A transfixion surface gradually formed with the continuous development of the shear plane and tensile cracking at the trailing edge, which led to rapid offsets along Lancang River and formation of the first stage of the landslide mass. The second- and third-stage landslides occurred inside the first stage of the landslide body. Their formation mechanisms are essentially the same: all slides deformed locally in the late reformation of the oldest landslide. Heavy rainfall, snowfall, groundwater flow, earthquakes, long-term erosion by melting glaciers, and weathering are factors that led to the two subsequent large-scale sliding events, forming the current second and third landslides. Figure 4B shows it can be clearly seen that the sliding zone of the Zhenggang landslide is between the landslide deposit and bedrock in the site.

Figure 5 shows that the landslide deposit formed three potential sliding surfaces. The same transfixion surface observed in all stages indicates high correlation between the three surfaces. The landslide deposit is mainly composed of diluvium (Q^{dl}), glacial and fluvial deposits (Q^{fgl}), and landslide deposits (Q^{del}). A typical profile of the Zhenggang landslide, as shown in Figure 5, is chosen for the case study.

3.2 Statistical parameters

The values of some material properties, such as unit weights γ, Young's modulus E, and Poisson's ratio μ, typically have a limited rate of change and have little influence on the reliability analysis (Tan et al., 2011). They can therefore be considered as deterministic variables in this case. Furthermore, the slide mass of the Zhenggang landslide is mainly in landslide deposit and sliding zone; as a result, it is acceptable to ignore the randomness of bedrock parameters. The randomness of shear strength parameters c and φ for deposit and sliding zone is considered in this paper.

To determine statistical characteristics of shear strength parameters of the Zhenggang landslide, a certain number of shear tests are conducted for 22 deposit samples and 3 samples of sliding zone. The laboratory tests result shows the cohesion c_d and friction angle φ_d of deposits can be modelled as

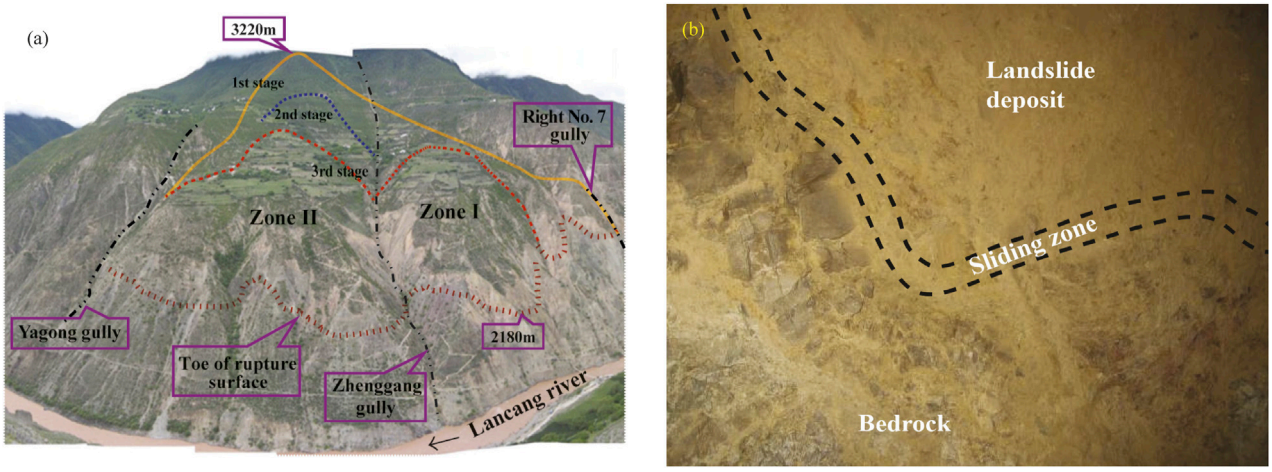

FIGURE 4
Aerial view and geomorphic features of the Zhenggang landslide (Xu 2010).p

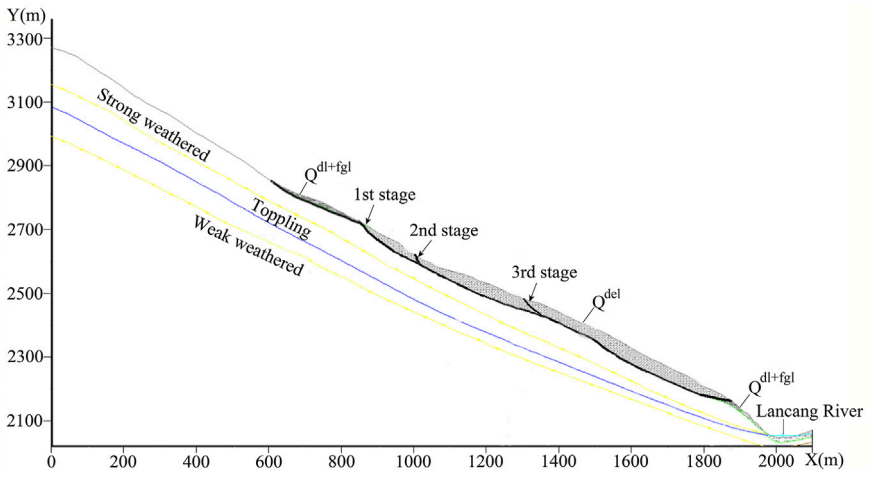

FIGURE 5
A typical profile of the Zhenggang landslide with three sliding surfaces.

normally distributed random variables (Xu 2010), and the corresponding histograms are shown in Figure 6. However, we could not make definite conclusions regarding the statistical distribution types of shear strength parameters for the sliding zone because of the small number of acquisition trials. Combined with the parameter inversion analysis and statistical results of similar engineering, the cohesion c_s and friction angle φ_s of sliding zone can be considered as standard normally distribution of random variables. Descriptive statistical parameters for the Zhenggang landslide are listed in Table 1.

4 Results

4.1 Validation of the finite element model

Deterministic methods, i.e., finite element model and simplified Bishop method, are employed to analyze the Zhenggang landslide stability using the mean parameter values listed in Table 1. The FEM analysis on Zhenggang landslide is built based on the lastic-plastic constitutive model and Mohr-Coulomb criterion. The vertical borders of the landslide model are horizontally constrained, and the bottom is completely fixed.

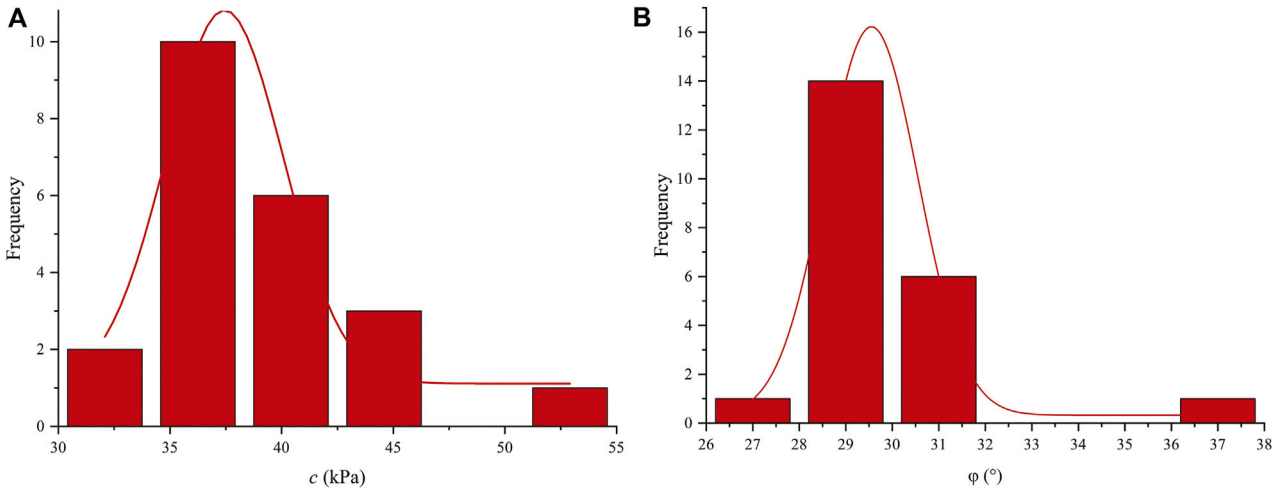

FIGURE 6
Histograms of material properties of landslide deposit **(A)** cohesion and **(B)** friction angle.

TABLE 1 Descriptive statistics parameters for the Zhenggang landslide.

	E (GPa)	γ (kN/m^3)	μ	c (kPa)		φ (°)	
				Mean	Standard deviation	Mean	Standard deviation
Deposit	0.10	21.50	0.32	37.44	2.63	29.55	1.01
Slip zone	0.05	20.50	0.35	20.55	2.37	27.0	1.80
Bedrock	5.0	24.00	0.30	250	—	40.00	—

The calculation results of the three sliding surfaces are respectively 1.119, 1.090 and 1.052, which is in good agreement with that (i.e., 1.140, 1.069 and 1.059) calculated from the simplified Bishop. This verifies the accuracy and feasibility of the sliding surface stress as the deterministic method of landslide numerical modeling. All safety factors are greater than 1.05, which demonstrates that the Zhenggang landslide remains in an essentially stable state. The third stage (i.e., front area) of the landslide has the lowest safety factor value, indicating that it is most likely to destabilize; the first failure is expected to occur in the front area of the landslide. When not supported by the third sliding body, the landslide gradually disintegrates and moves towards the Lancang River.

Moreover, for system reliability analysis of landslides involving deterministic multiple sliding surfaces, the sliding surface stress analysis has an incomparable advantage than shear strength reduction. The shear strain colour plot of Figure 7 indicates that finite element strength reduction technique can only obtain the most dangerous failure plane (Third-stage landslide) but cannot reflect the effects of the secondary failure surfaces on the system stability of landslide. In contrast, the sliding surface stress analysis can calculate the

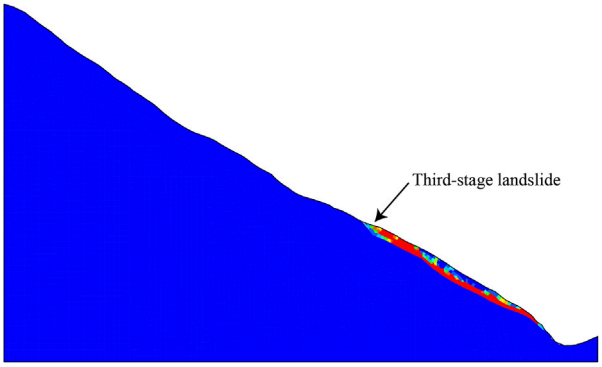

FIGURE 7
Landslide failure plane deduced from finite element simulation.

TABLE 2 Calculation results of intelligent multiple response surfaces for the Zhenggang landslide.

Stages of typical profile	Optimum parameters		Failure probability (%)
	σ	γ	
1st	2.99	543.50	2.15
2nd	3.23	548.12	5.65
3rd	5.12	513.51	16.95
System			16.95

safety factors of multiple potentially active sliding surfaces from the stress fields generated by a finite element simulation, which will effectively expand the application of FEM analysis in landslide system reliability analysis.

4.2 Validation of least-squares support vector machine-based multiple response-surface method

The key to system reliability analysis is to construct the MRSM of Fs for all sliding surfaces using the random variables of landslide. In this paper, a total of 400 samples with four random variables, i.e., c_d and φ_d of deposit, c_s and φ_s of sliding zone, are first randomly generated as training samples based on normal distribution characters of random variables. These training samples are generated using the Latin hypercube sampling method (Huang et al., 2020). The safety factors of the three sliding surfaces from the 400 training samples are subsequently used to determine the multiple response-surface functions. That means that perform 400 runs of FEM analyses to obtain the corresponding safety factors of the three sliding surfaces.

The LSSVM models for the three sliding surfaces are then used to construct the MRSM based on the 400 training samples, and GA is used to search for optimum parameters of LSSVM (σ and γ). During the build process, three different and independent suites of LSSVM models are trained simultaneously, each of which corresponds to a response surface of sliding surface. The population size of GA is set to 50 and the maximum generation number is set to 50, the crossover probability and mutation probability are set to 0.8 and 0.08 respectively. The results of optimum parameters σ and γ of multiple LSSVM models with the three sliding surfaces are presented in Table 2.

After the LSSVM-based MRSM is constructed, an additional dataset of 2000 samples are generated using the Latin hypercube sampling. The trained LSSVM models are then adopted to predict the safety factors of the three sliding surfaces associated with the 2000 random samples. A MCS method is applied to obtain the failure probability of ith sliding surface p_{f_i} and system failure probability p_f^{sys} from the 2000 LSSVM-predicted values of safety factors, and the results of calculation are presented in Table 2.

The failure probabilities of the three sliding surfaces are respectively 2.15%, 5.65%, 16.95%, which is consistent with the evaluation of landslide safety factor, that is, system failure of the Zhengang landslide is mainly contributed by the third sliding. Although the safety factors of the Zhenggang landslide with the three sliding surfaces are all greater than 1.05, the failure probability of the third stage landslide is as high as 16.95%. It is suggested that accurate evaluation of landslide stability based on deterministic analysis of the landslide alone is insufficient and system reliability analysis is essential to have a complete picture of the risk of land sliding. The system failure probability (16.95%) demonstrates that engineering measures be taken to reinforce the Zhenggang landslide because of low landslide stability.

For comparison, a direct finite element MCS with 2000 samples is used to estimate the system failure probability of the Zhenggang with the three sliding surfaces. This means that the FEM of the sliding surface stress analyses are conducted with 2000 simulations. The calculation result of the three sliding surfaces are respectively 2.20%, 5.60% and 16.70%, which is in good agreement with that (i.e., 2.15%, 5.65% and 16.95%) calculated from the LSSVM-based MRSM. The good agreement signifies the promising performance of LSSVM-based MRSM as metamodel of the FEM models.

4.2.1 Nonlinear characteristics of multiple response surfaces

To study the nonlinear characteristics of multiple response surfaces of the Zhenggang landslide, four different training sample sizes, 100, 200, 300 and 400, are used to construct the multiple response surfaces with the three sliding surfaces in this paper. Figures 8–11 show the safety factors of three sliding surfaces with different training sample sizes. Each subplot contains different number of scatter points that correspond to the training samples. Label of X-axis, Y-axis and Z-axis represents respectively the c_d and φ_d of deposit and c_s of sliding zone, and the size of scatters is φ_d of sliding zone. According to the calculation results of the FEM method, the safety factors are marked in different colors on the scatters, where

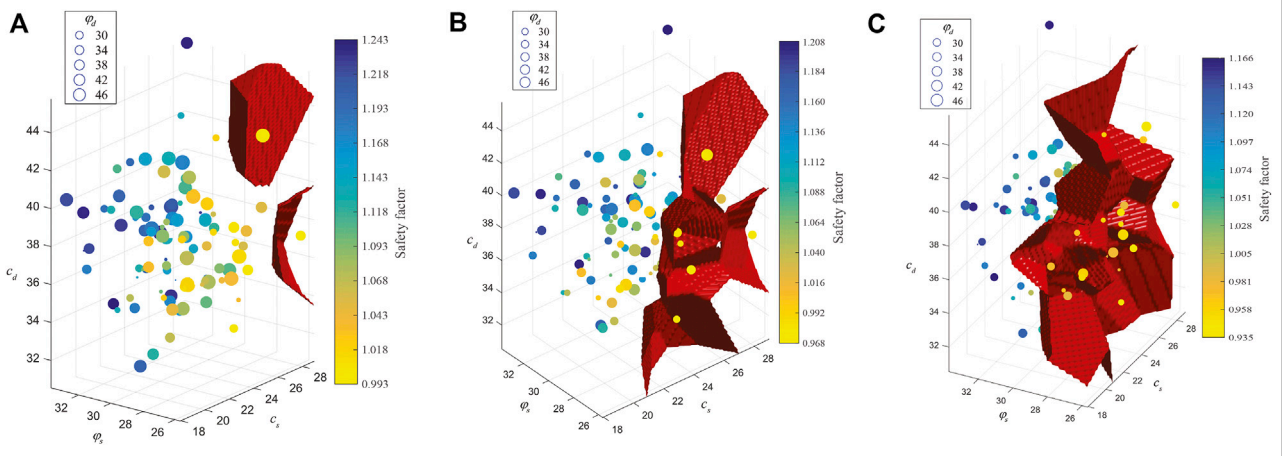

FIGURE 8
Safety factors of three sliding surfaces with 100 training samples. **(A)** 1st sliding surface **(B)** 2nd sliding surface **(C)** 3rd sliding surface.

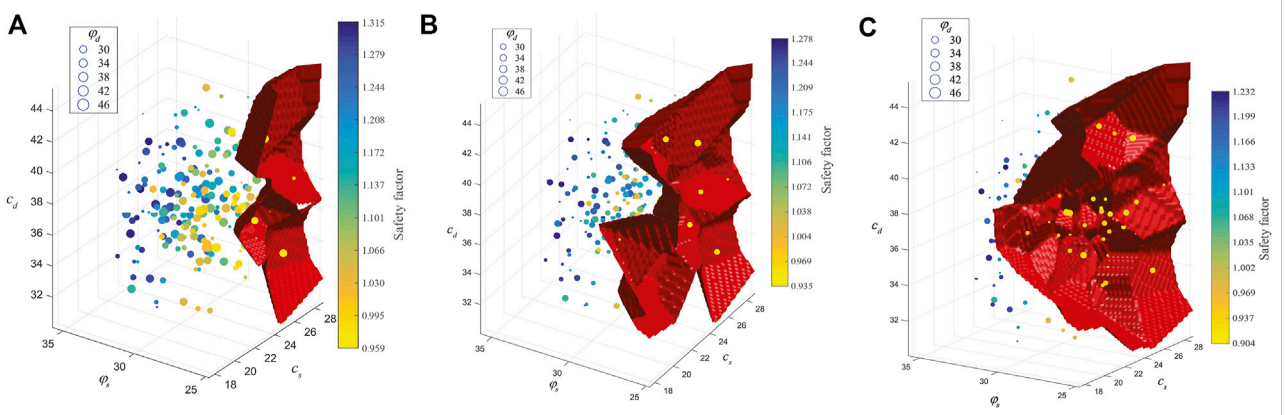

FIGURE 9
Safety factors of three sliding surfaces with 200 training samples. **(A)** 1st sliding surface **(B)** 2nd sliding surface **(C)** 3rd sliding surface.p

yellow and blue are safety factors less than 1 and greater than 1 respectively. As shown in Figures 8–11, failure points ($Fs < 1$) of each failure sliding surface increase obviously as the increase of training sample size. There are the most failure points and the largest failure zone in the third sliding surface, indicating that the third stage is most likely to destabilize, which is consistent with the evaluation of landslide safety factor. What's more, the shape of response surfaces (red surfaces) with safety factor of 1 is complex and changeable under the condition of multi-dimensional parameters. It is obvious that the traditional polynomial-based RSMs are difficult to fit the red response surfaces with highly nonlinear characteristics. Therefore, the LSSVM model with excellent nonlinear fitting ability is used to build the MRSM of Zhenggang landslide in this paper.

4.2.2 Performance of least-squares support vector machine-based multiple response-surface method

Figure 12 shows the predicted safety factors of LSSVM are compared with the FEM of the sliding surface stress analysis calculated values under the four different training samples (100, 200, 300 and 400). The 2000 safety factors results from the direct finite element MCS are taken as the "exact" solutions to examine the accuracy of the trained LSSVM with the four training sample sizes. The calculation results show the training sample size directly affects the prediction performance of the proposed method. As expected, more training samples means that the GA optimized LSSVM model can learn more nonlinear features to describe the mapping relationships between the safety factor and random variables, resulting in decrease RMSE values.

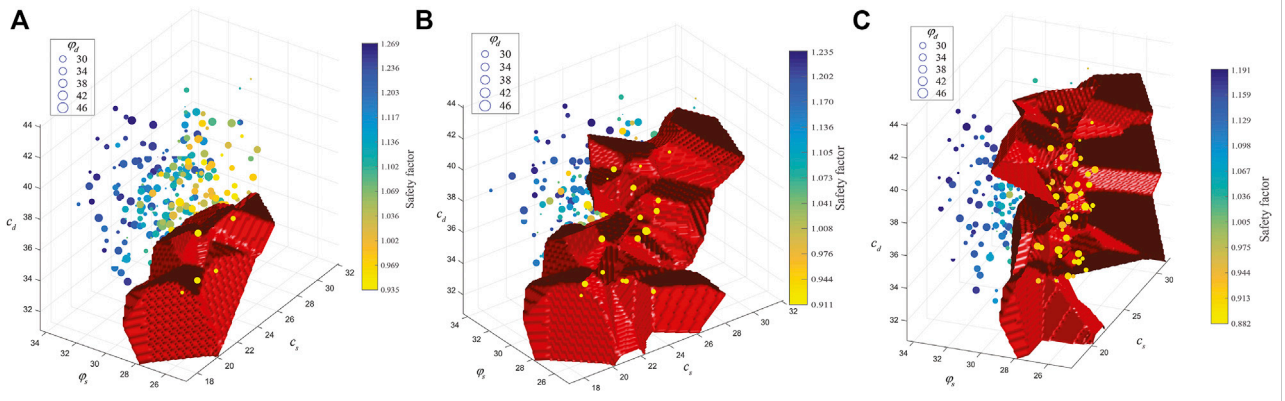

FIGURE 10
Safety factors of three sliding surfaces with 300 training samples. **(A)** 1st sliding surface **(B)** 2nd sliding surface **(C)** 3rd sliding surface.

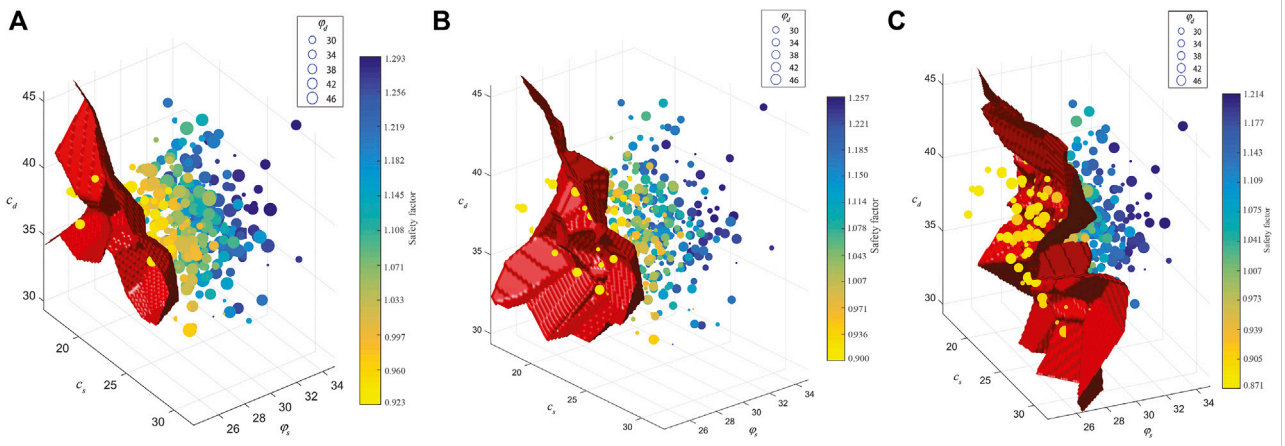

FIGURE 11
Safety factors of three sliding surfaces with 400 training samples. **(A)** 1st sliding surface **(B)** 2nd sliding surface **(C)** 3rd sliding surface.

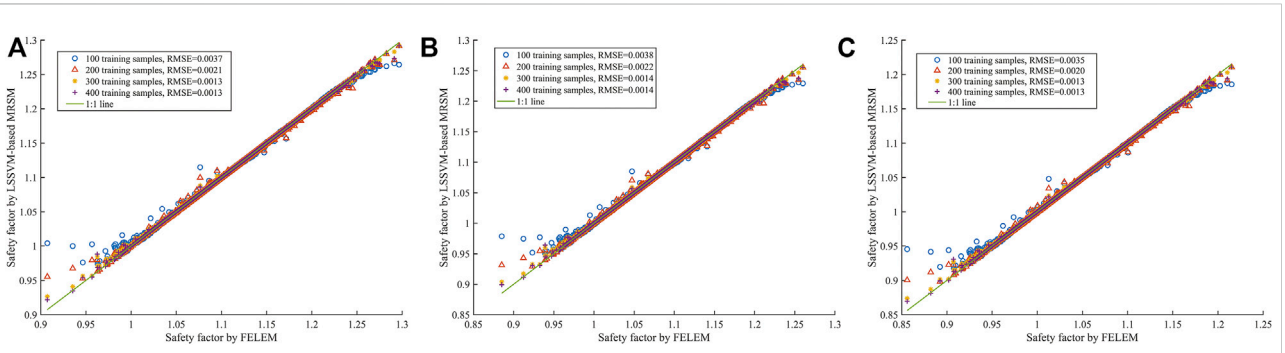

FIGURE 12
Comparison of safety factor predicted by LSSVM-based MRSM with the four training sample sizes. **(A)** 1st sliding surface **(B)** 2nd sliding surface **(C)** 3rd sliding surface.

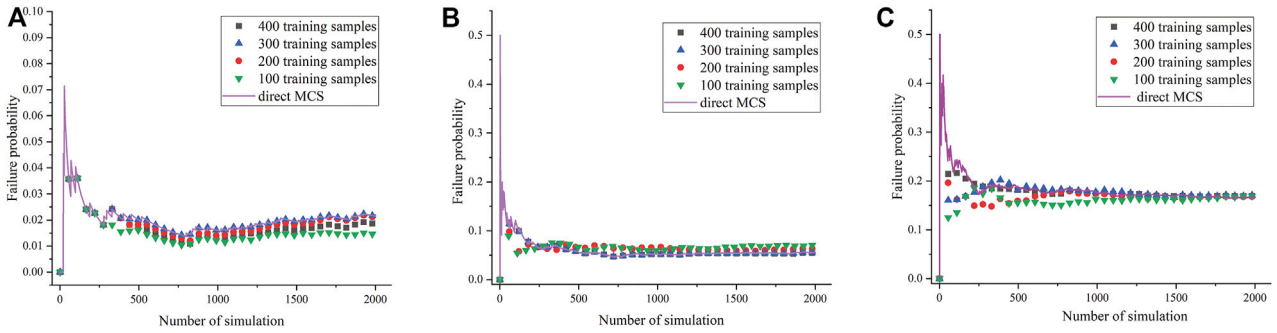

FIGURE 13
Comparison of failure probability for different number of simulation.p

Moreover, the RMSE values are all smaller than 0.04, which indicates the safety factors predicted by LSSVM agree reasonably well with the FEM calculated values in all three subplots. However, a bias in the trends is also easily observed when the safety factor is greater than 1.15 or less than 0.97. The convergence of the bias is generally attained within 300 training samples, which implies that 400 training samples performed for this study are sufficient.

Figure 13A–C show the failure probability of the three sliding surfaces with different number of simulations, for both the LSSVM-based MRSM and direct MCS results. As the number of simulations increases, failure probability gradually decreases and converges within 1500 MCS simulations, indicating that the 2000 simulations are suitable. Some discrepancies between the safety factors predicted by LSSVM and calculated by finite element are observed, and the discrepancies gradually reduce by using more training samples. The good agreement of the three sliding surfaces further demonstrates 400 training samples are the appropriate sample size, and the LSSVM model shows good prediction performance for the nonlinear response surface.

In summary, from the perspective of both accuracy and efficiency, it can be seen that the use of LSSVM-based MRSM provides a highly promising method for probabilistic numerical modeling of landslide stability considering multiple sliding surfaces.

5 Discussion

The promising performance of system reliability analysis heavily depends on the computational cost of deterministic landslide analysis and the number of samplings. Considering the deterministic analysis adopted by the proposed method, sliding surface stress analysis can effectively avoid the iterative calculation in the process of shear strength reduction. The computational cost associated with the construction of probabilistic numerical modeling can be quite high should the other shear strength reduction is applied.

Besides, the accuracy and time costs of system reliability increase linearly with the number of samplings, and more samples means more deterministic analyses are performed. Compared the directly MCS, the MRSM adopts metamodels with a small number of samples to replace the deterministic analysis procedure, which greatly improves the computational efficiency. However, the traditional MRSM method is limited to the design of sample number and ranges, and quadratic polynomial functions are difficult to approximate true RSFs nonlinearities for this case are presented in Figure 8–11.

The proposed intelligent multiple response surfaces method employs the robust generality of the LSSVM to approximate the values of implicit RSFs, which combines the advantages of the LSSVM and traditional MRSM approach. As shown in Figure 12, the proposed method is quite capable of representing the RSFs by using only 400 training samples that system reliability analysis can be implemented with acceptable accuracy. Therefore, it is applicable to a wide range of system reliability problems in engineering geology, including the complex system reliability analysis of multistage landslide involving sliding surfaces.

There are some shortcomings associated with the present study. The minimum failure probability of the three sliding surfaces is approximately 2% in this case, and the landslide reliability problem with low levels of failure probability has not yet been considered. It is well known that reliability calculation could be very time consuming especially when the failure probability is less than 10^{-4} (Jiang and Huang 2016). Additional studies of geotechnical problems involving the inherent spatial variability of soil properties will be implemented to further illustrate the promising performance of the proposed method in future work.

6 Conclusion

An intelligent multiple response surfaces method is proposed to study the probability of system failure of a landslide by using the MRSM combined with GA optimized LSSVM. The method is applied to investigate the system reliability of the Zhenggang landslide, in Yunnan Province, China, involving sliding surfaces. The following conclusions can be drawn:

1 The sliding surface stress analysis can calculate simultaneously the safety factors of multiple sliding surfaces for system reliability analysis, which is not possible using shear strength reduction method. This effectively expands the application of FEM analysis in system reliability analysis of landslides involving deterministic multiple sliding surfaces.
2 The GA optimized LSSVM can effectively improve the fitting accuracy of the multiple response-surface method with a limited number of samples, from which they obtain substantially obtain the ability to make high-quality FEM predictions.
3 By comparing the LSSVM-based MRSM against direct MCS method, the accuracy and validity of the proposed intelligent multiple response surfaces method are verified using the Zhenggang landslide case study involving sliding surfaces. Wong, 1985.

Data availability statement

The original contributions presented in the study are included in the article/supplementary material, further inquiries can be directed to the corresponding author.

Author contributions

ZC: Conceptualization, Methodology, Software, Investigation, Formal Analysis, Writing—Original Draft; SS: Data Curation, Writing—Original Draft; JZ: Writing—Review andamp; Editing; BT: Investigation, Software; BX: Resources, Supervision; YM: Conceptualization, Funding Acquisition, Resources, Supervision, Writing—Review and Editing.

Funding

The work presented in this paper is financially supported by the National Natural Science Foundation of China (U2240221 and 51939004).

Conflict of interest

The authors declare that the research was conducted in the absence of any commercial or financial relationships that could be construed as a potential conflict of interest.

Publisher's note

All claims expressed in this article are solely those of the authors and do not necessarily represent those of their affiliated organizations, or those of the publisher, the editors and the reviewers. Any product that may be evaluated in this article, or claim that may be made by its manufacturer, is not guaranteed or endorsed by the publisher.

References

Cai, Z. L., Xu, W. Y., Meng, Y. D., Shi, C., and Wang, R. (2016). Prediction of landslide displacement based on GA-LSSVM with multiple factors. *Bull. Eng. Geol. Environ.* 75 (2), 637–646. doi:10.1007/s10064-015-0804-z

Dadashzadeh, N., Duzgun, H. S. B., and Yesiloglu-Gultekin, N. (2017). Reliability-based Stability Analysis of rock slopes using numerical analysis and response surface method. *Rock Mech. Rock Eng.* 50 (8), 2119–2133. doi:10.1007/s00603-017-1206-2

Ditlevsen, O. (1979). Narrow reliability bounds for structural systems. *J. Struct. Mech.* 7 (4), 453–472. doi:10.1080/03601217908905329

Dong, B., and Lu, Z. Z. (2022). Efficient adaptive Kriging for system reliability analysis with multiple failure modes under random and interval hybrid uncertainty. *Chin. J. Aeronautics* 35, 333–346. doi:10.1016/j.cja.2021.08.017

Farias, M. M., and Naylor, D. J. (1998). Safety analysis using finite elements. *Comput. Geotechnics* 22 (2), 165–181. doi:10.1016/s0266-352x(98)00005-6

Fu, X. Q., Zhang, X. R., Qiao, Z., and Li, G. (2019). Estimating the failure probability in an integrated energy system considering correlations among failure patterns. *Energy* 178, 656–666. doi:10.1016/j.energy.2019.04.176

Griffiths, D. V., and Fenton, G. A. (2004). Probabilistic slope stability analysis by finite elements. *J. Geotech. Geoenviron. Eng.* 130 (5), 507–518. doi:10.1061/(asce)1090-0241(2004)130:5(507)

Hong, Y., Yu, G. M., and He, K. Q. (2016). Probabilistic landslide risk assessment of a historic and cultural site on the north slope of Lishan Mountain, Xian, China. *Environ. Earth Sci.* 75, 646. doi:10.1007/s12665-016-5434-7

Huang, Y., Chen, S., Chen, Z., Hu, W., and Huang, Q. (2020). Improved probabilistic load flow method based on D-vine copulas and Latin hypercube sampling in distribution network with multiple wind generators. *IET Gener. Transm. &amp. Distrib.* 14 (5), 893–899. doi:10.1049/iet-gtd.2019.1126

Ji, J., Liao, H. J., and Low, B. K. (2012). Modeling 2-D spatial variation in slope reliability analysis using interpolated autocorrelations. *Comput. Geotech.* 40, 135–146. doi:10.1016/j.compgeo.2011.11.002

Jiang, S. H., and Huang, J. S. (2016). Efficient slope reliability analysis at low-probability levels in spatially variable soils. *Comput. Geotechnics* 75, 18–27. doi:10.1016/j.compgeo.2016.01.016

Kim, J. Y., and Lee, S. R. (1997). An improved search strategy for the critical slip surface using finite element stress fields. *Comput. Geotechnics* 21 (4), 295–313. doi:10.1016/s0266-352x(97)00027-x

Li, D. Q., Jiang, S. H., Cao, Z. J., Zhou, W., Zhou, C. B., and Zhang, L. M. (2015). A multiple response-surface method for slope reliability analysis considering spatial variability of soil properties. *Eng. Geol.* 187, 60–72. doi:10.1016/j.enggeo.2014.12.003

Li, K., Wang, L. Y., Wu, J. J., Zhang, Q. J., Liao, G., and Su, L. (2018). Using GA-SVM for defect inspection of flip chips based on vibration signals. *Microelectron. Reliab.* 81, 159–166. doi:10.1016/j.microrel.2017.12.032

Li, S. J., Zhao, H. B., and Ru, Z. L. (2013). Slope reliability analysis by updated support vector machine and Monte Carlo simulation. *Nat. Hazards (Dordr).* 65 (1), 707–722. doi:10.1007/s11069-012-0396-x

Li, Z., Hu, Z., Zhang, X. Y., Du, S., Guo, Y., and Wang, J. (2019). Reliability analysis of a rock slope based on plastic limit analysis theory with multiple failure modes. *Comput. Geotechnics* 110, 132–147. doi:10.1016/j.compgeo.2019.02.021

Liu, H. X., and Low, B. K. (2017). System reliability analysis of tunnels reinforced by rockbolts. *Tunn. Undergr. Space Technol.* 65, 155–166. doi:10.1016/j.tust.2017.03.003

Liu, L. L., and Cheng, Y. M. (2016). Efficient system reliability analysis of soil slopes using multivariate adaptive regression splines-based Monte Carlo simulation. *Comput. Geotechnics* 79, 41–54. doi:10.1016/j.compgeo.2016.05.001

Low, B. K. (1997). Reliability analysis of rock wedges. *J. Geotech. Geoenviron. Eng.* 123 (6), 498–505. doi:10.1061/(asce)1090-0241(1997)123:6(498)

Low, B. K., Zhang, J., and Tang, W. H. (2011). Efficient system reliability analysis illustrated for a retaining wall and a soil slope. *Comput. Geotechnics* 38, 196–204. doi:10.1016/j.compgeo.2010.11.005

Pei, L., Chen, C., He, K., and Lu, X. (2022). System reliability of a gravity dam-foundation system using Bayesian networks. *Reliab. Eng. Syst. Saf.* 218, 108178. doi:10.1016/j.ress.2021.108178

Roy, A., Manna, R., and Chakraborty, S. (2019). Support vector regression based metamodeling for structural reliability analysis. *Probabilistic Eng. Mech.* 55, 78–89. doi:10.1016/j.probengmech.2018.11.001

Su, Y. H., Li, X., and Xie, Z. Y. (2011). Probabilistic evaluation for the implicit limit-state function of stability of a highway tunnel in China. *Tunn. Undergr. Space Technol.* 26, 422–434. doi:10.1016/j.tust.2010.11.009

Sung, E. C. (2009). Probabilistic stability analyses of slopes using the ANN-based response surface. *Comput. Geotechnics* 36 (5), 787–797. doi:10.1016/j.compgeo.2009.01.003

Suykens, J. A. K., and Vandewalle, J. (1999). Least squares support vector machines classifiers. *Neural Process Lett.* 9 (3), 293–300.

Tan, X. H., Bi, W. H., Hou, X. L., and Wang, W. (2011). Reliability analysis using radial basis function networks and support vector machines. *Comput. Geotechnics* 38, 178–186. doi:10.1016/j.compgeo.2010.11.002

Wang, B., Liu, L. L., Li, Y. H., and Jiang, Q. (2020). Reliability analysis of slopes considering spatial variability of soil properties based on efficiently identified representative slip surfaces. *J. Rock Mech. Geotechnical Eng.* 12 (3), 642–655. doi:10.1016/j.jrmge.2019.12.003

Wang, S. N., Xu, W. Y., Shi, C., and Chen, H. J. (2017). Run-out prediction and failure mechanism analysis of the Zhenggang deposit in southwestern China. *Landslides* 14 (2), 719–726. doi:10.1007/s10346-016-0770-y

Wang, Z. Z., and Goh, H. S. (2021). Novel approach to efficient slope reliability analysis in spatially variable soils. *Eng. Geol.* 281, 105989. doi:10.1016/j.enggeo.2020.105989

Wong, F. S. (1985). Slope reliability and response surface method. *J. Geotech. Engrg.* 111 (1), 32–53. doi:10.1061/(asce)0733-9410(1985)111:1(32)

Wu, Y. P., Cheng, C., He, G. F., and Qiuxia, Z. (2014). Landslide stability analysis based on random-fuzzy reliability: Taking liangshuijing landslide as a case. *Stoch. Environ. Res. Risk Assess.* 28 (7), 1723–1732. doi:10.1007/s00477-013-0831-x

Xu, W. Y. (2010). *Further research report on the Zhenggang landslide deposits of Gushui hydropower station project in Lancang river*. Nan Jing: Hohai University. (in Chinese).

Yang, Y. C., Xing, H. G., YangHuang, K. x., and Zhou, J. w. (2015). Two-dimensional stability analysis of a soil slope using the finite element method and the limit equilibrium principlenite element method and the limit equilibrium principle. *fiThe IES J. Part A Civ. Struct. Eng.* 8 (4), 251–264. doi:10.1080/19373260.2015.1072299(

Zou, J. Z., Willians, D. J., and Xiong, W. L. (1995). Search for critical slip surfaces based on finite element method. *Can. Geotech. J.* 32 (2), 233–246. doi:10.1139/t95-026

frontiers | Frontiers in Earth Science

TYPE Original Research
PUBLISHED 19 January 2023
DOI 10.3389/feart.2022.1062981

OPEN ACCESS

EDITED BY
Biswajeet Pradhan,
University of Technology Sydney, Australia

REVIEWED BY
Li Wang,
China Three Gorges University, China
Kun He,
Southwest Jiaotong University, China

*CORRESPONDENCE
Qiming Zhong,
qmzhong@nhri.cn

SPECIALTY SECTION
This article was submitted to Geohazards and Georisks, a section of the journal Frontiers in Earth Science

RECEIVED 06 October 2022
ACCEPTED 23 November 2022
PUBLISHED 19 January 2023

CITATION
Zhang L, Zhong Q, Yang M, Peng M, Liu J, Mei S, Yan Z and Shan Y (2023), Centrifugal model tests and numerical modeling on overtopping-induced breach processes of landslide dams. *Front. Earth Sci.* 10:1062981. doi: 10.3389/feart.2022.1062981

Centrifugal model tests and numerical modeling on overtopping-induced breach processes of landslide dams

Lucheng Zhang[1], Qiming Zhong[1,2]*, Meng Yang[1], Ming Peng[3], Jiaxin Liu[4], Shengyao Mei[1], Zhikun Yan[1] and Yibo Shan[1]

[1]Department of Geotechnical Engineering, Nanjing Hydraulic Research Institute, Nanjing, China, [2]Key Laboratory of Reservoir and Dam Safety of the Ministry of Water Resources, Nanjing, China, [3]Department of Geotechnical Engineering, Tongji University, Shanghai, China, [4]College of Civil and Transportation Engineering, Hohai University, Nanjing, China

This study used the 400 g-ton geotechnical centrifuge model test system at the Nanjing Hydraulic Research Institute (NHRI) to investigate the breach evolution characteristics and hydrograph process of overtopping-induced breaching of landslide dams. It was achieved by taking advantage of the "time-space amplification" effect created by high-speed rotation using a centrifuge overweight force field. The effects of dam height, slope ratio, and soil gradation on the overtopping failure process of landslide dams were investigated by centrifugal model tests for the first time. In addition, a detailed physically-based dam breach model was developed to simulate the overtopping failure of landslide dams. Results show that the breach process of a landslide dam can be divided into four stages based on the measured breach morphology evolution process and the abrupt variations of breach flow discharge: initial scour on the downstream slope, retrogressive erosion to the dammed lake, erosion along the breach channel, and breach stabilization. Moreover, the peak breach flow is most sensitive to the dam height, followed by the average particle size; the time to peak is mainly affected by the slope ratio, and the relative residual dam height is primarily susceptible to the average particle size. In practice, the calculated results are consistent with the measured results. This study provides a scientific reference for the cognition of the overtopping-induced breach mechanism of landslide dams.

KEYWORDS

landslide dam, overtopping, breach process, breach mechanism, centrifugal model test, numerical simulation

1 Introduction

Landslide dams are accumulations formed by blocking valleys or river channels as a result of landslides, debris flows, lava flows, and other mass-wasting events caused by earthquakes, rainfall, or volcanic eruptions under specific geological and geomorphological conditions (Costa and Schuster, 1988; Korup and Tweed, 2007;

Hermanns, 2013; Fan et al., 2019). As a result of natural processes, landslide dams exhibit wide gradations, irregular shapes, and complex structures (Zhong et al., 2021). Landslide dams are widespread throughout the world. Extreme weather and geological disasters have occurred frequently in recent years, leading to increased landslide dams (Mei et al., 2021; Zheng et al., 2021). Unlike artificial dams, landslide dams are formed by a mixture of unconsolidated soil and rock in a naturally unstable state (Zhong et al., 2018). They lack channelized spillways or other protected outlets (Zhong et al., 2021). Therefore, once the upstream flow continues, the failure risk of landslide dams is much higher than that of artificial dams. Shen et al. (2020a) performed statistical analysis on 352 landslide dams with longevity information and found that 29.8% of the cases lasted for less than 1 day, 68.2% lasted for less than 1 month, and 84.4% lasted for less than 1 year. Other researchers presented similar statistics (Costa and Schuster, 1988; Peng and Zhang, 2012).

Landslide dams generally have a wide area of rainwater collection and a large volume of water storage. Once the dam fails, the breached flood can bring severe life, economic, and ecological losses to the downstream inundated area, causing profound social impact. For instance, the burst of the Diexi landslide dam in China in 1933 washed away numerous villages and massive farmland, causing over 9,000 deaths (Liu et al., 2016). On 25 April 1974, a massive landslide occurred on the Mantaro River in Peru, creating a huge dammed lake that burst 2 months later, and destroying roads, farms, and bridges (Lee and Duncan, 1975). Overtopping and seepage are the most common failure modes for landslide dams (Zheng et al., 2021). Almost 94% of landslide dams failed due to overtopping and 5% due to piping (Zhong et al., 2021). Hence, it is vital to investigate the dam breach process and breach mechanism of overtopping-induced failure of landslide dams to conduct emergency treatments efficiently to minimize losses.

The overtopping breach of landslide dams is a highly complex process involving water-soil coupling and structural failures. The current research methods for the overtopping failure of landslide dams are mainly divided into physical model tests and mathematical models (Zheng et al., 2021; Zhong et al., 2021). The physical model test is a common and indispensable technique for studying dam failure mechanisms. Recently, a series of landslide dam failure model tests were developed based on the artificial dam erosion models. The principal research methodologies include *in situ* tests (i.e., Chang and Zhang, 2010; Chang et al., 2011; Zhou et al., 2022) and laboratory model tests (i.e., Davies et al., 2007; Niu et al., 2012; Yang et al., 2015; Zhou et al., 2019; Peng et al., 2021; Zhu et al., 2021). The flume test is currently the primary method for the laboratory model test. It's widely applied to study the breach morphology evolution and breach hydrograph during landslide dam overtopping failure, and the influence of various factors on the dam failure process. Due to the significant difference in stress levels between the model and the prototype, the test results often vary from reality, and the conclusions of different scholars regarding various influencing factors are also inconsistent. Although the results of the large-scale *in situ* tests are closer to the prototype dam, the test costs are high, the test period is long, and the risks are difficult to control.

In recent years, with the continuous advancement in the simulation theory of landslide dam failure and the rapid development of computer technology, more studies have been conducted on the mathematical models of overtopping-induced landslide dam breaching. Generally, these models can be classified as empirical models and physically based numerical models (Wahl, 1998; ASCE/EWRI Task Committee on Dam/Levee Breach, 2011; Zhong et al., 2016, 2021). Based on the statistical regression of the collected measured data of landslide dam breach cases, empirical models were developed to predict the breaching parameters, such as peak breach flow, final breach size, and failure time (Costa, 1985; Evans, 1986; Costa and Schuster, 1988; Walder and O'Connor, 1997; Peng and Zhang, 2012; Shan et al., 2022). The empirical models are easy to use, allowing for rapid prediction of the consequences due to landslide dam failure. In contrast, physically based numerical models have the advantage of reflecting the dam breach mechanisms and failure processes, and can provide the breach morphology evolution processes and the breach flow hydrographs (Zhong et al., 2018; Shen et al., 2020b; Mei et al., 2022). The physically based numerical models can be further divided into simplified and detailed physically based models. Simplified physically based numerical models consider the necessary physical processes and have high computational efficiency. In these models, the breach cross-section is often simplified as a trapezoid, and the overtopping flow through the breach is simulated using the broad-crested weir flow equation, and the erosion at the breach is determined using sediment transport models (Chang and Zhang, 2010; Chen et al., 2015; Zhong et al., 2018). Based on the Navier-Stokes equations and sediment transport models, detailed physically based numerical models can consider the complex flow characteristics and rapid breach topography evolution in the landslide dam breach process, thus effectively improving the accuracy of simulation results (Cao et al., 2011; Li et al., 2021).

In summary, the existing physical model tests and mathematical models for the overtopping-induced landslide dam breach process have apparent shortcomings. The stress levels of small-scale dam breach model tests differ significantly from those of the prototype, while the large-scale dam breach model tests are costly and time-consuming. An empirical model cannot consider the physical and mechanical properties of the wide-graded dam materials, and cannot provide the breach flow discharge process. In addition, the reliability of the empirical models depends on the accuracy of landslide dam information. The simplified physically based numerical models introduce significant simplifications and assumptions, so they

TABLE 1 The similarity criteria of common physical quantities in centrifugal model tests.

Physical quantities	Acceleration	Length	Area	Volume	Normal stress	Shearing stress	Strain	Permeability coefficient
Similarity ratio (model/prototype)	N	$1/N$	$1/N^2$	$1/N^3$	1	1	1	$1/N$

Physical quantities	Quality	Flow	Void ratio	Viscosity	Force	Moment	Density	Time
Similarity ratio (model/prototype)	$1/N^3$	$1/N^2$	1	1	$1/N^2$	$1/N^3$	1	$1/N$

cannot really consider the erosion characteristics of wide graded soil and the hydrodynamic conditions of high-velocity flow during landslide dam breaching. Furthermore, multidimensional, specifically 3D detailed physically based breach models, are still at the early stage of development.

Under the condition of high-speed rotation, the hypergravity field generated by a geotechnical centrifuge has the effect of "time-space amplification". It can generate prototype-level effective stress in a small-scale model. At the same time, similar conditions, such as geometry, dam materials, and hydrodynamic conditions, can be satisfied. Therefore, the centrifugal model test can be regarded as a practical method for investigating the failure of landslide dams. They can reproduce the overtopping failure process of a landslide dam in a short period at a low cost. This is important and valuable for correctly revealing the breach mechanism and breach process of a landslide dam composed of wide-graded dam materials.

This study investigates the failure of a landslide dam due to overtopping using centrifugal model tests. It reveals the breach mechanism, breach evolution characteristics, and hydrograph during the dam failure. The effects of dam height, slope ratio, and gradation of dam materials on the dam failure process are addressed by centrifugal model tests for the first time. In addition, a 3D detailed physically based numerical model of overtopping-induced failure of landslide dams is developed, which can consider the complex hydrodynamic characteristics of turbulent flow, and the bedload and suspended load transportation during the landslide dam breach process with actual topography. Finally, the calculated results are compared with the measured data of the centrifugal model tests to verify the rationality of the proposed mathematical model.

2 Centrifugal model test system for landslide dam breaching

To conduct landslide dam breach model tests in a geotechnical centrifuge, three fundamental technical problems must be solved: 1) establish a similarity criterion for the centrifugal model test of landslide dam breaching, 2) continuously provide stable water flow to the high-speed rotating centrifuge, and 3) accurately record and measure the breach flow discharge. A centrifugal model test system for landslide dam breaching was developed based on the 400 g-ton geotechnical centrifuge at the Nanjing Hydraulic Research Institute (NHRI). The following is a description of the similarity criteria and centrifugal model test system.

2.1 Similarity criterion

The breach of a landslide dam is a typical water-soil coupling process. When a centrifuge is used to explore the dam breach process, it is necessary to establish similar criteria for the dam materials and the dam breach flow. The following briefly introduces the similar criteria used in the model tests.

2.1.1 Stress similarity criterion

The force of gravity endured by the prototype is consistent with the centrifugal force physical effects experienced by the model in the centrifuge, where the materials properties of the soil are hardly changed. The centrifugal model test simulates gravity using centrifugal force so that the dead weight of the model in the centrifuge is raised to match that of the prototype, and the stress state of the model and prototype are identical.

In the centrifuge, the model's geometric size is reduced to $1/N$ of the prototype, and the model's stress force corresponds to the stress force of the prototype. The physical relationship is as follows:

$$\begin{cases} L_m = L_p/N \\ \sigma_m = \sigma_p \\ q_m = q_p \end{cases} \tag{1}$$

where subscript m represents model, p represents prototype, L = length, σ = stress, q = hydrostatic pressure, and N = model geometry scale.

In rock and soil mass, the force of gravity is the essential stress. For the gravity of the model to be equal to the prototype, when the model is identical to that of the prototype materials, the

TABLE 2 The main technical parameters of NHRI-400 g-ton geotechnical centrifuge.

Main technical parameters	Value
Capacity	400 g-ton
Effective radius	5 m
Maximum acceleration	200 g
Acceleration stability	±0.2%
Allowable space for hanging basket	1.32 m × 1.2 m × 1.14 m

1/N model must bear the centrifugal acceleration of Ng in the centrifuge:

$$g_m = Ng_p = Ng \tag{2}$$

where g_m is the centrifugal acceleration of the model, g_p is the prototype acceleration, and g is the acceleration of gravity.

2.1.2 Flow similarity criterion

The centrifugal model test of an overtopping dam breach involves the process of breach flow. The similarity criteria of flow velocity, flow rate, and time are derived from the Chezy formula and energy conservation law.

Using the Chezy formula and assuming that the flow at the breach of the dam is uniform and stable, the flow velocity v is:

$$v = C\sqrt{RJ} \tag{3}$$

$$R = A/\chi \tag{4}$$

where R = hydraulic radius, A = wetted cross-section area, χ = wetted perimeter, J = hydraulic gradient, and C is the Chezy coefficient.

In the centrifugal model test, the water body conforms to the geometric similarity criterion whether the water is static or flowing.

$$\begin{cases} R_m = R_p/N \\ J_m = J_p \end{cases} \tag{5}$$

Chezy coefficient can be expressed as:

$$C = \sqrt{8g/\lambda} \tag{6}$$

where λ is the resistance coefficient along the path, the resistance coefficient λ_m of the model is equal to that of the prototype, and the inertia acceleration g_m of the model flow is N times that of the prototype, so the Chezy coefficient C_m of the model flow is N times that of the prototype.

$$\begin{cases} g_m = Ng_p = Ng \\ \lambda_m = \lambda_p \\ C_m = C_p\sqrt{N} \end{cases} \tag{7}$$

Therefore, the flow velocity of the model is entirely equal to that of the prototype.

$$v_m = v_p \tag{8}$$

The cross-section in the model is $1/N^2$ times that of the prototype, and the breach flow Q_m of the model is:

$$Q_m = \frac{Q_p}{N^2} \tag{9}$$

Time can be extrapolated according to the velocity and length of the model flow:

$$t_m = \frac{L_m}{v_m} = \frac{L_p/N}{v_p} = \frac{t_p}{N} \tag{10}$$

Table 1 details the similarity criteria of common physical quantities in centrifugal model tests.

2.2 Centrifugal model test system

The centrifugal model test system mainly comprised a large geotechnical centrifuge, a special model box, a servo water valve flow control system, a data acquisition system, and image-recording devices.

2.2.1 Large geotechnical centrifuge

Figure 1A shows the large geotechnical centrifuge, while Table 2 lists the main technical parameters of the NHRI-400 g-ton geotechnical centrifuge.

2.2.2 Model box

2.2.2.1 Appearance and size

A special box (Figure 2A) was developed to investigate the process of the dam breach. The effective size of the model box was 1.2 m × 0.4 m × 0.8 m (length × width × height). In order to easily observe and record the process of a dam breach, one side of the box was made of highly transparent tempered glass. The other side of the box, the head cover, and the bottom of the model box were high-strength aluminum alloy plates with a thickness of 65 mm.

2.2.2.2 Rectangular sharp-crested weir

To investigate the breach process and mechanism of landslide dams, a rectangular sharp-crested weir (Figures 2B,C) was embodied in the downstream end of the model box to obtain an accurate breach flow discharge process. Two pore pressure sensors were installed inside the box's downstream end, as shown in Figure 2D. The sensor's output signal is a voltage signal, which can be converted to water depth.

The breach flow discharge can be calculated based on the water depth using the following formula.

$$Q = m_0 B_w \sqrt{2Ng}h\,(t)^{1.5} \tag{11}$$

where Q is the breach flow discharge, m_0 is the discharge coefficient which will be calibrated before the test, B_w is the

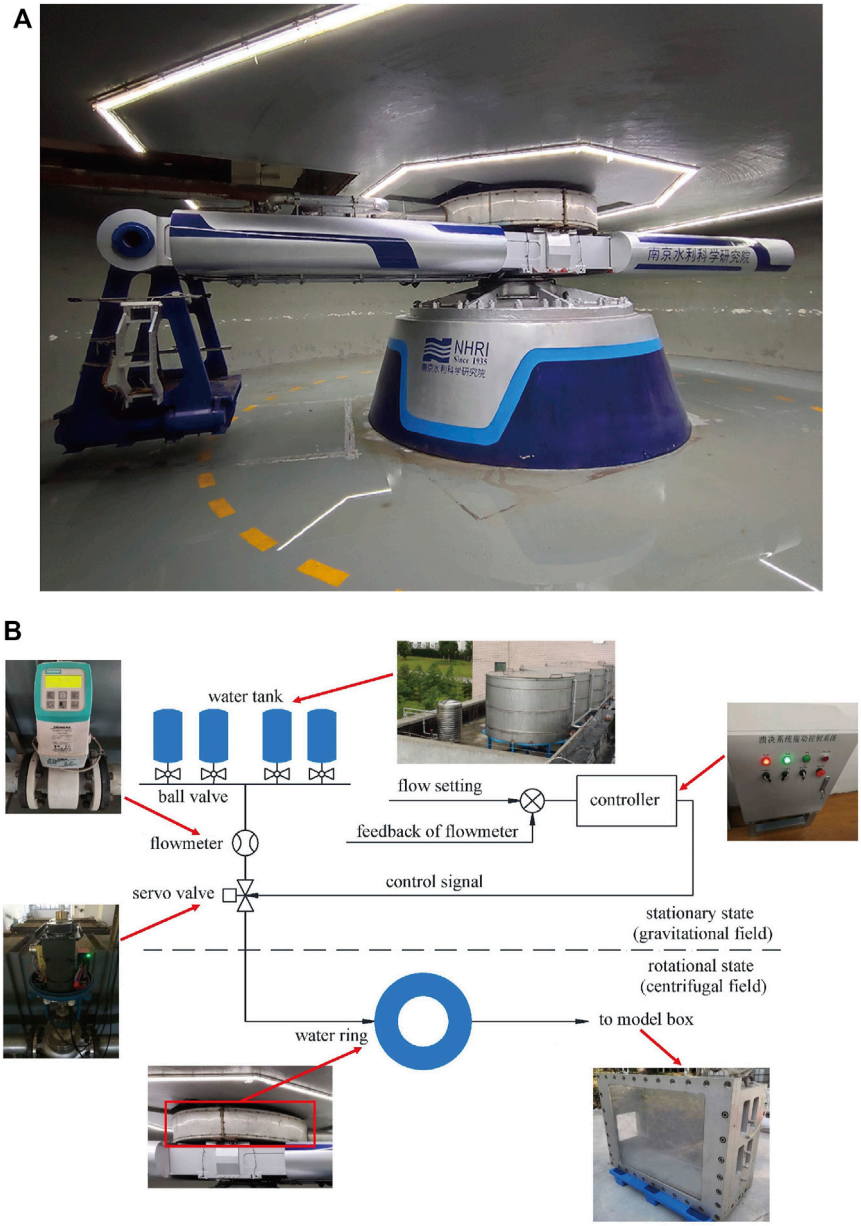

FIGURE 1
Centrifugal model test system. **(A)** NHRI-400 g ton large geotechnical centrifuge. **(B)** Schematic diagram of the servo water valve flow control system.

width of the rectangular sharp-crested weir, Ng is the centrifuge acceleration, h is the depth of water, and t is the time.

2.2.2.3 Water tank

A 200 mm × 400 mm × 500 mm water tank was constructed to store water upstream and stabilize the upstream flow. The front of the water tank was a perfect fit for the model box and was covered with a 3 mm diameter unidirectional pore.

2.2.3 Servo water valve flow control system

Figure 1B demonstrates the servo water valve flow control system. Four 2.5 m^3 water tanks were installed on top of the laboratory roof. The flowmeter monitored the water supply flow and generated a negative feedback signal, and then the controller drove the openness of the servo valve according to the PID (proportion integral differential) control algorithm based on the supply flow process set before the test. Water flowed through the

servo valve into the water ring. There was no hardware contact between the water supply pipe and the water ring, which avoided wear and leakage of the hydraulic rotary head. Water flowed into the model box through a rotary arm, was discharged to the laboratory floor through a rectangular sharp-crested weir, and then recycled by a water collector.

2.2.4 Data acquisition system and image-recording devices

The data acquisition system consisted of the data acquisition module on the rotary arm and the industrial computer on the ground. The data acquisition module can synchronously record signals from 90 measuring channels, including 70 channels of the strain signal and 20 channels of the voltage signal. The flow control system recorded the flow process. The pore pressure sensors installed within the water tank and at the rectangular mouth were connected to the data acquisition module. The image-recording devices were two cameras, one on the top of the model box (Figure 2E) and the other on the side of the centrifuge hanging basket (Figure 2F).

3 Test setup and procedure

In this study, the centrifugal model test system was utilized to conduct the overtopping failure test of landslide dams under different conditions. The centrifugal acceleration was set to 50 *g*. The breach morphology evolution process, the breach flow discharge process, and the influence of various factors on the overtopping failure process were investigated to reveal the breach mechanism of landslide dams in greater detail. Based on the size of the model box, the water supply condition of the servo water valve flow control system, and the dam materials selected for the test, the three influencing factors of dam height, slope ratio, and gradation of dam materials were chosen for the test design. The reason for the choice of three influencing factors is that the dam height is known to be the determinant of the dammed lake volume and potential energy of water, the slope ratio determines the breach morphology in cross and longitudinal sections, and the gradation of dam materials determines the soil erosion rate under particular flow shear stress. Therefore, this paper selected four conditions for the centrifugal model test.

Because the rectangular sharp-crested weir was 200 mm away from the bottom of the model box, clay was placed at the bottom, followed by a cushion plate to make downstream flood and eroded dam materials discharge smoothly. The top surface of the cushion plate was 100 mm away from the bottom of the model box.

3.1 Design of parameters

3.1.1 Dam height

After arranging the clay layer and cushion plate inside the model box, the effective height was 700 mm. To make full use of the model box space, considering the slope ratio and the outlet height of the water tank, this study specified dam heights of 250 and 350 mm, with the corresponding actual dam heights of 12.5 and 17.5 m under

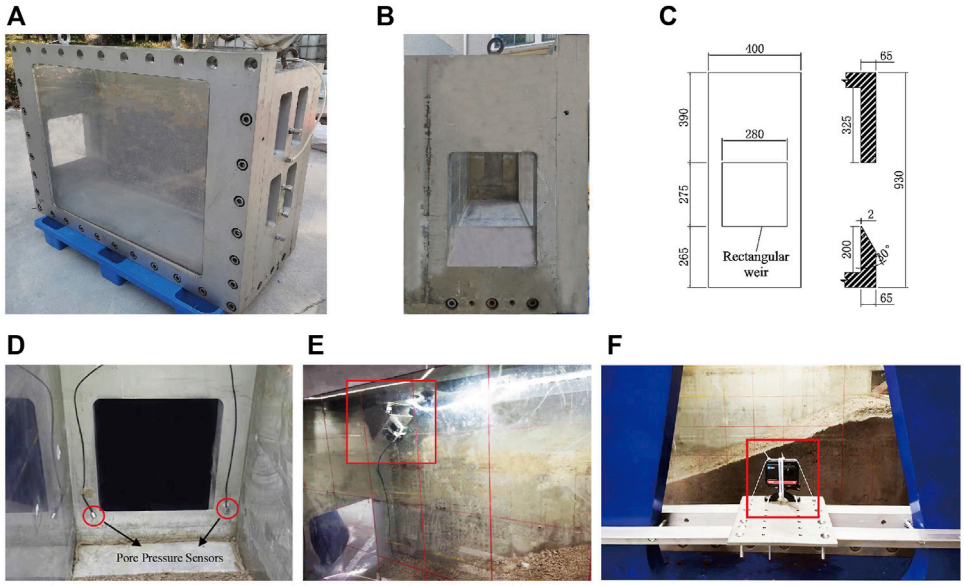

FIGURE 2
The special model box, layout of the pore pressure sensors and the image-recording devices. **(A)** Photograph of the model box **(B)** Photograph of the rectangular weir. **(C)** Schematic diagram of rectangular weir (unit: mm). **(D)** The pore pressure sensors. **(E)** Camera No. 1. **(F)** Camera No. 2.

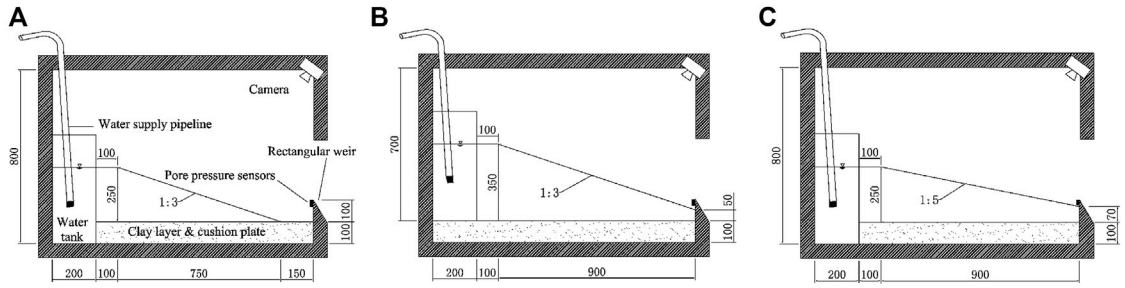

FIGURE 3
Schematic diagrams of each model (unit: mm). **(A)** Condition 1 and 4. **(B)** Condition 2. **(C)** Condition 3.

the gravity acceleration of 50 g. The cushions under different dam heights were adjusted to cause the water tank outlet to be slightly higher than the top of the dam, and the height difference between the outlet and the top remained constant. When the model dam height was 250 mm, the water tank was placed at the bottom of the model box (Condition 1, Figure 3A). When the model dam height was 350 mm, the water tank was on the cushion (Condition 2, Figure 3B).

3.1.2 Slope ratio

The slope ratio of the downstream dam has an important influence on the breach process of landslide dams. Usually, the dam slope of a natural landslide dam is gentle, with a slope ratio between 1:2 and 1:5.5. Considering the length of the water tank was 200 mm, the effective length of the model box was 1,000 mm, and to make full use of the space of the model box, two slope ratios of 1:3 (Condition 1, Figure 3A) and 1:5 (Condition 3, Figure 3C) were selected.

3.1.3 Gradation

Due to the wide gradation characteristics of the dam materials of landslide dams, the gradation curve obtained from five boreholes of the Tangjiashan landslide dam (Liu et al., 2010) was used in this study. The maximum particle size of the model gradation was controlled to 40 mm by the average gradation as the prototype gradation and scaled down utilizing the mixed method. The mean particle size (d_{50}) was used to characterize the different gradations. The mean particle size of Conditions 1 to 3 was controlled at 5 mm by a similar gradation method, and the particles larger than 40 mm were replaced with 40–5 mm. To investigate the effect of gradation on landslide dam failure, the d_{50} of Condition 4 was set to 1 mm, and Figure 4 depicts the gradation curves. The model size of Condition 4 was identical to that of Condition 1. Table 3 summarizes the parameter settings of the three influencing factors of the centrifugal model tests on the overtopping-induced breach processes of landslide dams.

Rockfill materials for dam construction were selected for the test. After drying and screening, the materials were divided into

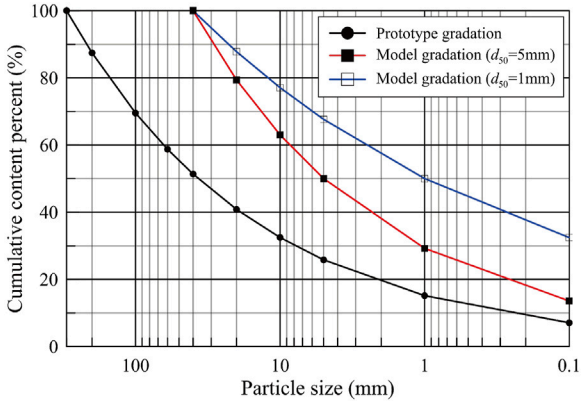

FIGURE 4
Gradation curves of prototype and model.

TABLE 3 Parameter settings of the three influencing factors for the four conditions.

Condition	Dam height (mm)	Slope ratio	d_{50} (mm)
1	250	1:3	5
2	350	1:3	5
3	250	1:5	5
4	250	1:3	1

five particle size groups, 40–20, 20–10, 10–5, 5–1, and <1 mm, respectively, as shown in Figures 5A–E. The specific gravity of soil is 2.75. For the four conditions, the porosity of the sample was set to 28%, and the moisture content was set to 5%. Based on the specific gravity of the soil and the sample porosity, the dry density of the model was determined to be 1.98 g/cm^3.

3.1.4 Initial breach location and size

The initial breach was opened on the tempered glass side of the model box to observe changes in the breach and erosion of the

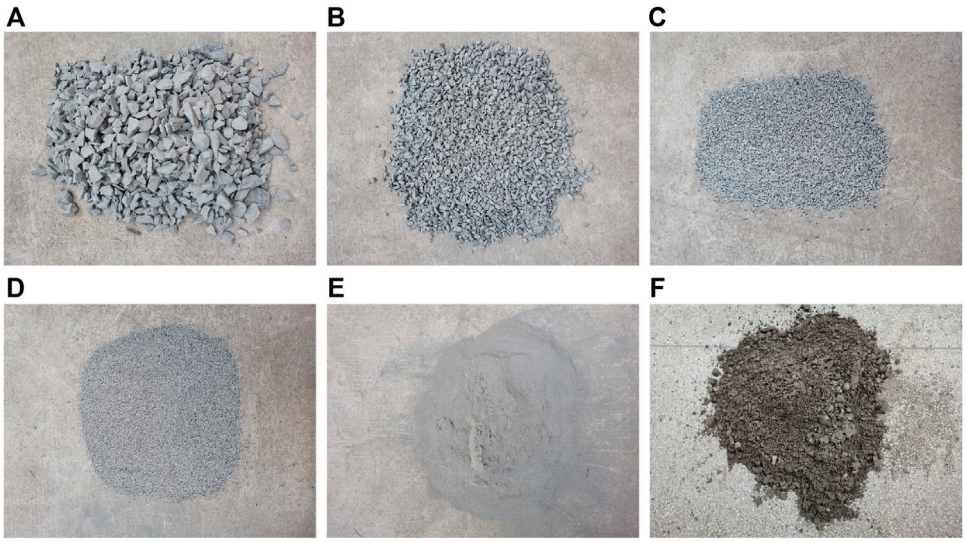

FIGURE 5
Particles in each particle size group and preparation of model dam materials. **(A)** 40–20 mm. **(B)** 20–10 mm. **(C)** 10–5 mm. **(D)** 5–1 mm. **(E)** <1 mm. **(F)** Dam materials after mixing evenly with water.

FIGURE 6
Excavation size of the initial breach and the model dam of Condition 1. **(A)** Schematic diagram of the initial breach (unit: mm). **(B)** Actual excavation of initial breach of Condition 1. **(C)** Photo of the side of the model dam of Condition 1.

downstream slope. The breach shape was trapezoidal, with a top width of 70 mm, a bottom width of 30 mm, and a height of 40 mm (Figure 6A).

3.2 Procedure of test

The test of each working condition was conducted according to the following steps.

Step 1: Model materials preparation. The total mass of soil particles was calculated using the model dimensions and dry density. Due to the loss during sample preparation, the soil materials were prepared at 1.2 times the mass. The mass of each particle size group was calculated based on the sample gradation. After weighing, water was added until a moisture content of 5% was reached. The dam materials were stirred evenly for later use, as shown in Figure 5F.

Step 2: Model dam construction. The clay layer and backing plate were prepared in the model box, and the model dam was filled based on its size and porosity. The initial breach was excavated on the side of the tempered glass. The model dam for Condition 1 is illustrated in Figures 6B,C.

Step 3: Centrifuge counterweight. The model box was weighed and placed into the hanging basket of the centrifuge. The iron sheet of corresponding mass was placed on the other rotary arm of the centrifuge according to the calculated counterweight.

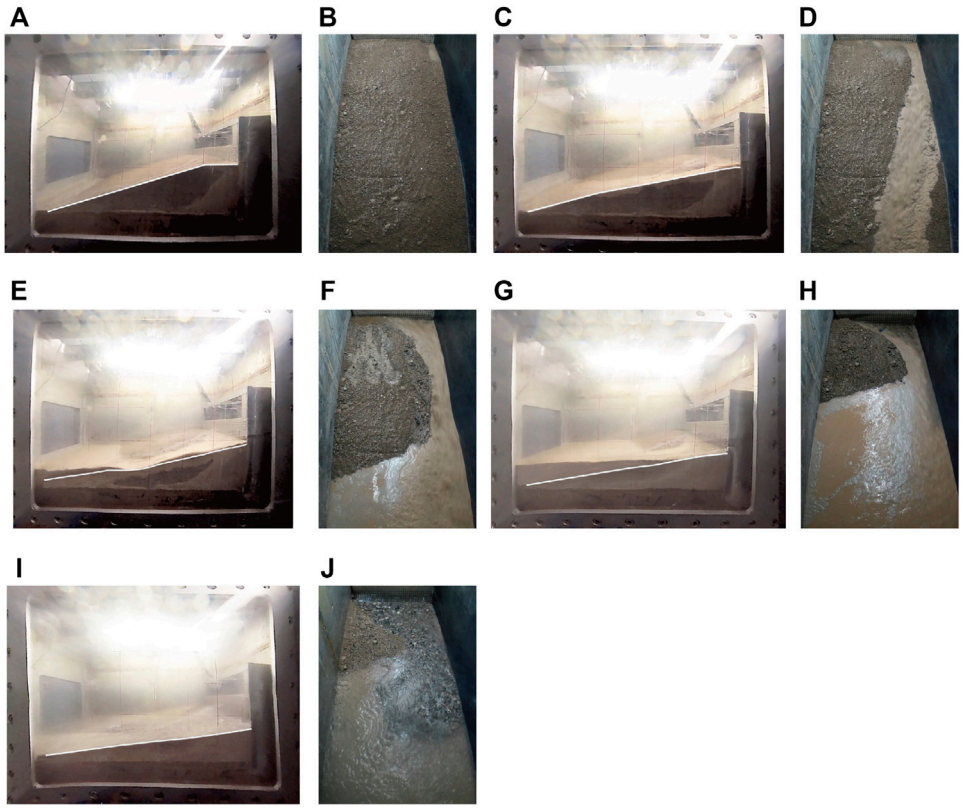

FIGURE 7
Typical dam images of breach process of Condition 4. **(A)** The initial moment of dam failure (Camera No. 1). **(B)** The initial moment of dam failure (Camera No. 2). **(C)** Stage 1 (Camera No. 1). **(D)** Stage 1 (Camera No. 2). **(E)** Stage 2 (Camera No. 1). **(F)** Stage 2 (Camera No. 2). **(G)** Stage 3 (Camera No. 1). **(H)** Stage 3 (Camera No. 2). **(I)** Stage 4 (Camera No. 1). **(J)** Stage 4 (Camera No. 2).

Step 4: Pore pressure sensors and camera installation. The pore pressure sensors were installed and fixed inside the water tank, at the rectangular mouth, and connected to the data acquisition system. Cameras were placed and fixed above the model box and on the side of the tempered glass, and then the centrifuge chamber door was closed.

Step 5: Dam breach test. The servo water valve flow control system and data acquisition system were activated, and the centrifuge was started after setting the parameters. The water supply process was established, and the automatic flow control system was turned on once the centrifuge reached the target acceleration.

Step 6: End of test. After the water supply process was over, the automatic flow control system and the centrifuge were deactivated, and the sensors data were saved. After the centrifuge came to a complete stop, the model dam was measured and recorded. The centrifuge chamber and model box were cleaned and prepared for the next test.

4 Analysis of the centrifugal model test results

The following test results were converted into the physical quantities of the prototype dam according to the similarity criterion in Section 2.1. The breach process and mechanism of overtopping-induced failure of landslide dams were analyzed utilizing Condition 4 as an example. The effects of dam height, slope ratio, and gradation on the dam failure process were compared separately based on the findings of four conditions.

4.1 Breach evolution characteristics

Figure 7 illustrates the typical dam images captured during the breach process as a result of a thorough analysis of the two-camera-recorded video of the dam breach process of Condition 4. The overtopping-induced failure of landslide dams can be divided into the following four stages.

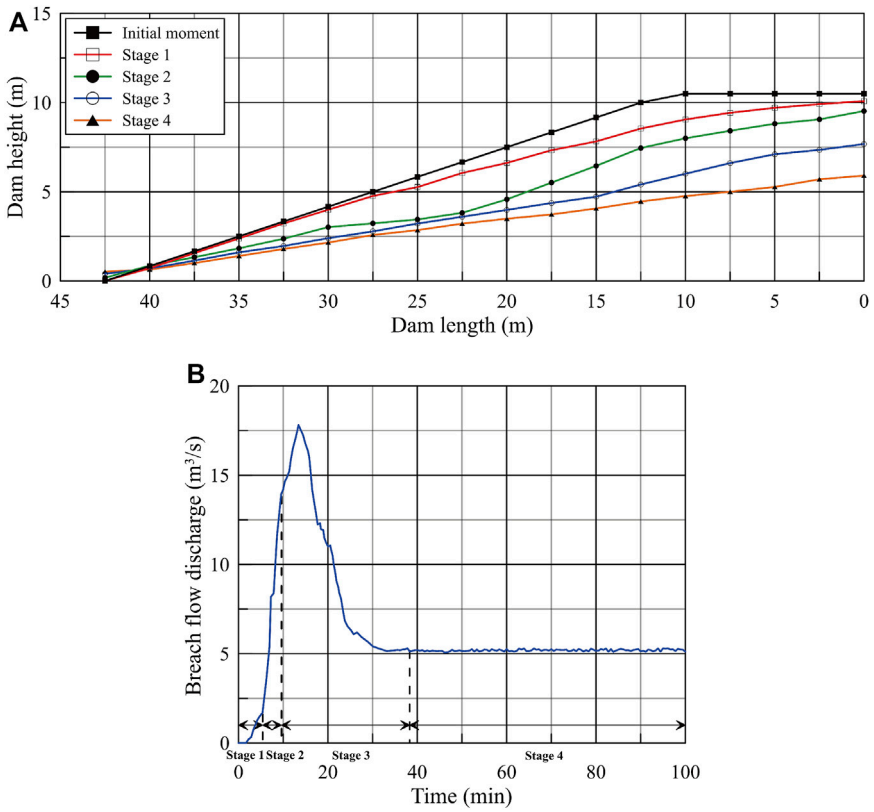

FIGURE 8
Breach morphology and breach hydrograph of Condition 4 (prototype dam). **(A)** Longitudinal section at the breach during dam breaching. **(B)**. Breach flow discharge process.

Stage 1: Initial scour on the downstream slope. In the initial stage of the dam breach, overtopping water overflowed from the initial breach and eroded the downstream slope. The fine particles on the dam surface were taken away by the water flow, forming a high-concentration sand-laden water flow. At this stage, surface erosion was dominant, and the breach gradually expanded.
Stage 2: Retrogressive erosion to the dammed lake. Compared to the breach, the flow velocity at the foot of the downstream slope was faster, and the erosion effect was more substantial, resulting in more extensive dam erosion and a gentler slope ratio. This process developed gradually upstream, which is known as retrogressive erosion. At this stage, the size of the breach grew rapidly with the speed of vertical cutting exceeding the rate of width expansion.
Stage 3: Erosion along the breach channel. After the end of the previous stage, the slope ratio of the downstream slope was significantly reduced. Due to insufficient hydrodynamic conditions, the breach cutting rate slowed down, and the longitudinal dimension of the breach gradually increased, accompanied by lateral broadening.
Stage 4: Breach stabilization. The upstream water level dropped, and the erosion ability of the water flow receded. For the landslide dam of wide gradation, the coarse particles remained on the downstream slope because the critical start-up condition was not reached, resulting in a coarsening of the slope. At this stage, the breach gradually stabilized and no longer developed.

Meanwhile, Figure 8A depicts the longitudinal section of the prototype dam at the breach for the various stages of the dam failure shown in Figure 7. With the development of the dam breach, the downstream slope became gentler.

4.2 Breach flow discharge process

Before the test, the discharge coefficient of the rectangular weir was measured to be 0.278. The breach flow discharge can be determined with Eq. 11, where $h(t)$ can be obtained from the pore pressure sensor readings.

Figure 8B depicts the breach flow discharge process of the prototype dam in Condition 4. When time equalled zero, the overtopping water flow overflowed from the breach. It is simple to determine that the breach flow discharge process indicates the following features. First, in the first few minutes of the dam

TABLE 4 Breach parameters of prototype dams for the four conditions.

Condition	Variable	Peak discharge (m^3/s)	Time to peak (min)	Relative residual dam height (%)
1	—	11.4	18.9	66.4
2	Dam height	18.6 (+62.6%)	16.1 (−14.8%)	55.4 (−16.5%)
3	Slope ratio	9.5 (−16.6%)	24.5 (+30.0%)	75.2 (+13.3%)
4	Gradation	17.8 (+56.0%)	13.4 (−29.0%)	47.2 (−28.9%)

failure, the flow discharge increased slowly, corresponding to Stage 1. Second, the flow discharge rose rapidly and reached 14.0 m^3/s at t = 9.6 min, corresponding to Stage 2. Subsequently, the increase in flow discharge rate slowed down slightly and reached the peak discharge of 17.8 m^3/s at t = 13.4 min and then rapidly decreased, corresponding to Stage 3. Finally, when t = 38.3 min, the flow gradually stabilized, and the breach flow was the inflow, corresponding to Stage 4.

4.3 Influence of different factors on breach process

In this paper, the dam height, slope ratio, and gradation were changed respectively to research the influence of these factors on the dam break process with Condition 1 as the control test. By sorting the test results, three dam breach parameters, peak discharge, time to peak, and relative residual dam height (defined as the ratio of residual dam height to initial dam height), were selected for comparison and analysis. The test results are summarized in Table 4, where the percentage in brackets represents the increment of dam breach parameters compared to Condition 1.

The influence of the three factors on the breach parameters is as follows. When the dam height increased or the average particle size of the dam materials decreased, the peak discharge grew significantly, the time to peak advanced, and the relative residual dam height decreased. The peak discharge decreased, the time to peak was observably delayed, and the relative residual dam height increased when the slope ratio became gentler. Further analysis found that the peak breach flow was most sensitive to the dam height, followed by the average particle size, the time to peak was most sensitive to the slope ratio, and the relative residual dam height was most susceptible to the average particle size.

These phenomena are because of various inner-physical mechanical mechanisms. By comparing Condition 1 and Condition 2, when the dam height of the landslide dam increases, the upstream water storage increases, so the peak discharge increases. The potential energy of the overtopping water flow increases, and the erosion effect on the downstream slope is stronger, accelerating the dam breach process and making the dam breach more sufficient. Therefore, the time to peak advances, and the relative residual dam height decreases. By comparing Condition 1 and Condition 3, when the downstream slope ratio of the landslide dam decreases, the dam body itself is more stable and not easily eroded. The process of releasing the potential energy of the overtopping water flow slows down, thus inhibiting the development of the dam breach and slowing down the dam breach process. Therefore, the peak discharge decreases, the time to peak delays, and the relative residual dam height increases. By comparing Condition 1 and Condition 4, under the same hydrodynamic conditions, when the mean particle size of the barrier dam decreases, that is, when the dam materials become finer, the number of particles satisfying the critical start-up condition increases. The dam body is easily eroded and the dam breach is more thorough. Therefore, the peak discharge increases, the time to peak advances, and the relative residual dam height decreases.

5 Numerical simulation test

To further study the breach process and mechanism, a detailed physically based numerical model was adopted to simulate the overtopping-induced failure of landslide dams.

5.1 Numerical simulation method and model

5.1.1 Governing equations

Based on the Cartesian coordinate system and assuming that water is an incompressible fluid, the continuity equation and momentum equations of the Reynolds-Averaged Navier-Stokes (RANS) equations are given by Eqs 12, 13, respectively (Kocaman et al., 2020).

$$V_F \frac{\partial \rho_w}{\partial t} + \frac{\partial}{\partial x_i}\left(\rho_w u_i A_i\right) = 0 \tag{12}$$

$$\frac{\partial u_i}{\partial t} + \frac{1}{V_F}\left(u_j A_j \frac{\partial u_i}{\partial x_j}\right) = -\frac{1}{\rho_w}\frac{\partial P}{\partial x_i} + g_i + f_i \tag{13}$$

where ρ_w is the water density, V_F is the fractional volume open to flow, t is time, x_i represents the coordinate along the three directions (subscript i traverses the three directions of x, y, and z, respectively, and so does j), u_i, A_i, g_i, and f_i represent the components of velocity,

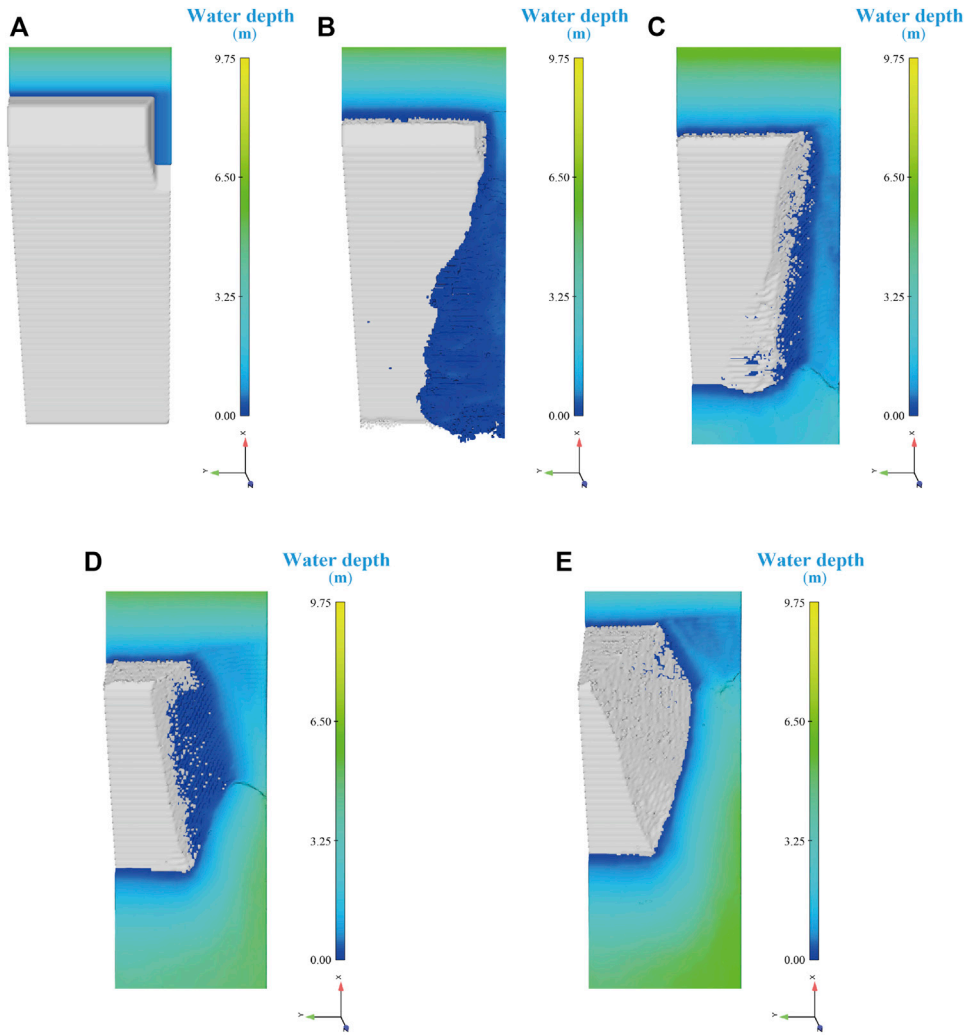

FIGURE 9
Typical top view of the dam body shape at each stage of the numerical model. **(A)** The initial moment of dam failure. **(B)** Stage 1. **(C)** Stage 2. **(D)** Stage 3. **(E)** Stage 4.

flow passing area, mass acceleration and viscous acceleration in subscript direction, respectively, and p is pressure.

During the breach process of a landslide dam, the sediment movement modes can be converted between bedload and suspended load (Mei et al., 2022).

5.1.2 Discretization of governing equations and initial and boundary conditions

To solve the above governing equations, it is necessary to discretize the grid calculation region, which is divided into multiple continuous subregions using grid nodes. In this study, the finite volume method (FVM) was applied for discretization, and a three-dimensional rectangular staggered grid was used to decompose the whole calculation domain.

The calculation object of the numerical simulation is the prototype dam of Condition 4. The whole computational domain is covered by a 0.2 m three-dimensional uniform rectangular grid.

The initial upstream water level was identical to the bottom elevation of the breach. The upstream boundary adopted a constant inflow condition, and the inflow was constant at 5.2 m^3/s. The boundary conditions were set based on the centrifugal model test.

5.2 Analysis of calculation results

5.2.1 Breach process

Figure 9 depicts the top views of the dam body shape at each stage. A comparison of the longitudinal section of the dam body at the breach in each stage of the two test methods is shown in

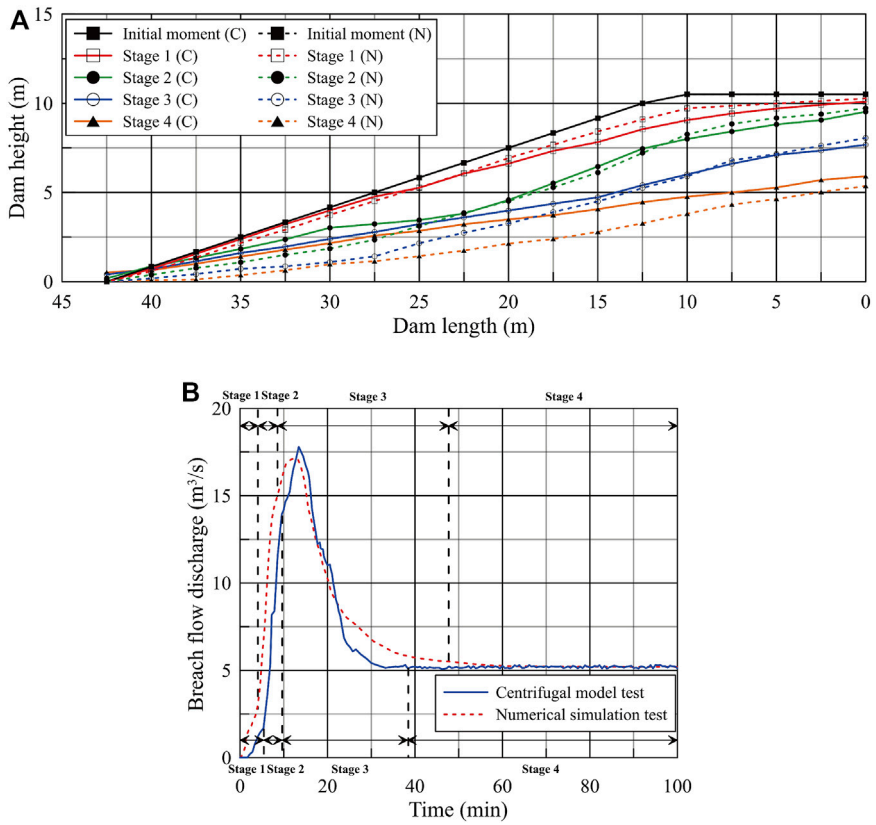

FIGURE 10
Breach morphology and breach hydrograph of Condition 4 (prototype dam). **(A)** Comparison of longitudinal section during dam breaching (prototype dam). **(B)** Comparison of breach flow discharge process of Condition 4 (prototype dam).

Figure 10A, where the C and N in brackets represent the centrifugal model test and numerical simulation test, respectively. Similar to the centrifugal model test, the dam breach process can also be divided into four stages.

During Stage 1, the water level was low, and the water flow was slow, resulting primarily in surface erosion of the downstream dam surface and the slow development of the breach. During Stage 2, the hydrodynamic conditions were enhanced as the water level continued to rise, and the breach undercut rapidly. During Stage 3, the speed of the lateral breach expansion increased compared to the undercut. During Stage 4, the breach gradually stopped developing. Dam failure was complete when the breach flow was approximately equal to the inflow. The evolution of breach morphology played an essential part in the overtopping breach process of landslide dams. In Stages 2 and 3, the downstream dam was heavily eroded.

Compared to the centrifugal model test (Figure 7), the breach process of the numerical simulation test was slightly different.

Stage 1: For the centrifugal model test, the breach had a preliminary development, and the downstream slope toe near the left bank was not eroded. For the numerical simulation test, the breach almost did not develop, and the water flow scoured the downstream slope along the left bank boundary.
Stage 2: For the centrifugal model test, the breach had obvious transverse broadening and longitudinal development, and the downstream slope toe was eroded entirely. For the numerical simulation test, the breach had a preliminary transverse widening, the longitudinal development was obvious, and the downstream slope toe was partially eroded.
Stage 3: For the centrifugal model test, the breach was further widened horizontally, and the downstream slope was obviously eroded. For the numerical simulation test, the breach rapidly widened horizontally and developed vertically, and the downstream slope toe was slowly eroded.
Stage 4: For the centrifugal model test, the breach was fully widened, and the dam shape reached a stable state. For the numerical simulation test, the breach was almost completely widened and no longer developed, and the dam shape reached a stable state.

In general, the difference between the two tests was because in the high-speed rotating centrifuge, the water flow had a

TABLE 5 Comparison of breach parameters (prototype dam).

Test method	Peak discharge (m^3/s)	Time to peak (min)
Centrifugal model test	17.8	13.4
Numerical simulation test	17.1 (−3.9%)	12.3 (−8.2%)

velocity component pointing to the right bank under the action of Coriolis force, which accelerated the transverse widening of the breach.

5.2.2 Breach hydrograph

Figure 10B compares the breach flow discharge process between the numerical simulation test and the centrifugal model test. The comparison shows that the calculated breach hydrograph was consistent with the measured hydrograph trend. For the numerical simulation of the dam breach process, predicting the peak breach flow and the time to peak was crucial. Table 5 indicates the results of these two breach parameters, with the percentage in brackets representing the relative error between the calculated and measured values. The calculated peak discharge was 17.1 m^3/s, 3.9% less than the measured value. The time to peak was 12.3 min, 8.2% earlier than the measured value. The relative errors of the two breach parameters were within ±10%, indicating that the numerical simulation test breach hydrograph matched the results of the centrifugal model.

Overall, the calculation results demonstrated that the numerical method adopted in this paper was feasible and able to simulate the overtopping failure process of landslide dams.

6 Conclusion

This study performed centrifugal model tests to study the mechanisms and processes of overtopping-induced failure of landslide dams to overcome the problems in existing physical model tests and mathematical models. It intuitively showed various stages during a landslide dam breach and revealed its breach mechanisms. Furthermore, this study investigated the effects of dam height, slope ratio, and gradation of dam materials on the dam failure process by centrifugal model tests for the first time. In addition, a 3D detailed physically based numerical model was adopted to simulate the overtopping breach of landslide dams. The results of the numerical simulation test and the centrifugal model test were compared and analyzed. The conclusions are as follows.

(1) Based on the abrupt change in erosional characteristics and the breach morphological evolutionary process in the centrifugal model tests of overtopping-induced failure of landslide dams, the breach process can be divided into four stages: 1) initial scour on the downstream slope, 2) retrogressive erosion to the dammed lake, 3) erosion along the breach channel, and 4) breach stabilization. Further, a detailed description of the development in each stage was elucidated. However, it is worth noting that, for the centrifugal model tests, the water flow deflected to the right bank under the action of Coriolis force, which accelerated the transverse widening of the breach.

(2) Dam height, slope ratio, and gradation of dam materials greatly influence the overtopping-induced breaching of landslide dams. The peak breach flow is mainly influenced by the dam height, followed by the average particle size. Furthermore, the time to peak is most sensitive to the slope ratio, and the relative residual dam height is mainly affected by the average particle size. The internal physical and mechanical mechanisms of the influence of various factors on the dam breach process were analyzed.

(3) A detailed 3D physically-based numerical model was developed to simulate the overtopping-induced breach process of the landslide dam based on the RANS equations, and bedload and suspended load transport formula. The comparison between the calculated and measured results showed that the proposed model is consistent with the experimental observation data, with relative errors within ±10% for the key breaching parameters. Overall, this model can be used to simulate the overtopping breach process of landslide dams.

Data availability statement

The raw data supporting the conclusion of this article will be made available by the authors, without undue reservation.

Author contributions

LZ: writing—original draft, and analysis. QZ: supervision, methodology, and funding acquisition. MY: writing—original draft. MP: methodology and funding acquisition. JL: data

processing. SM: calculation. ZY and YS: methodology and advise. All authors contributed to the article and approved the submitted version.

Funding

The authors greatly acknowledge the financial support from the National Natural Science Foundation of China (Grant Nos. U2040221 and U22A20602), the Open Fund of the Key Laboratory of Earth-rock Dam Failure Mechanism and Prevention and Control Technology of the Ministry of Water Resources (Grant No. YK321001), and the Fundamental Research Funds for Central Public Research Institutes (Grant No. Y320005).

Conflict of interest

The authors declare that the research was conducted in the absence of any commercial or financial relationships that could be construed as a potential conflict of interest.

Publisher's note

References

ASCE/EWRI Task Committee on Dam/Levee Breach (2011). Earthen embankment breaching. *J. Hydraul. Eng.* 137 (12), 1549–1564. doi:10.1061/(ASCE)HY.1943-7900.0000498

Cao, Z. X., Yue, Z. Y., and Pender, G. (2011). Landslide dam failure and flood hydraulics. Part II: Coupled mathematical modelling. *Nat. Hazards* 59 (2), 1021–1045. doi:10.1007/s11069-011-9815-7

Chang, D. S., and Zhang, L. M. (2010). Simulation of the erosion process of landslide dams due to overtopping considering variations in soil erodibility along depth. *Nat. Hazards Earth Syst. Sci.* 10 (4), 933–946. doi:10.5194/nhess-10-933-2010

Chang, D. S., Zhang, L. M., Xu, Y., and Huang, R. Q. (2011). Field testing of erodibility of two landslide dams triggered by the 12 May Wenchuan earthquake. *Landslides* 8 (3), 321–332. doi:10.1007/s10346-011-0256-x

Chen, Z. Y., Ma, L. Q., Yu, S., Chen, S. J., Zhou, X. B., Sun, P., et al. (2015). Back analysis of the draining process of the Tangjiashan barrier lake. *J. Hydraul. Eng.* 141 (4), 05014011. doi:10.1061/(ASCE)HY.1943-7900.0000965

Costa, J. E. (1985). *Floods from dam failures*. Washington D C, USA: U.S. Geological Survey. Open-File Report 85-560.

Costa, J. E., and Schuster, R. L. (1988). The formation and failure of natural dams. *Geol. Soc. Am. Bull.* 100 (7), 1054–1068. doi:10.1130/0016-7606(1988)100<1054:tfafon>2.3.co;2

Davies, T. R., Manville, V., Kunz, M., and Donadini, L. (2007). Modeling landslide dambreak flood magnitudes: Case study. *J. Hydraul. Eng.* 133 (7), 713–720. doi:10.1061/(asce)0733-9429(2007)133:7(713)

Evans, S. G. (1986). The maximum discharge of outburst floods caused by the breaching of man-made and natural dams. *Can. Geotech. J.* 23 (3), 385–387. doi:10.1139/t86-053

Fan, X. M., Scaringi, G., Korup, O., West, A. J., van Westen, C. J., Tanyas, H., et al. (2019). Earthquake-induced chains of geologic hazards: Patterns, mechanisms, and impacts. *Rev. Geophys.* 57 (2), 421–503. doi:10.1029/2018RG000626

Hermanns, R. L. (2013). *"Landslide dam" in encyclopedia of natural hazards*. Editor P. Bobrowsky (Berlin: Springer), 602–606.

Kocaman, S., Güzel, H., Evangelista, S., Ozmen-Cagatay, H., and Viccione, G. (2020). Experimental and numerical analysis of a dam-break flow through different contraction geometries of the channel. *Water* 12 (4), 1124. doi:10.3390/w12041124

Korup, O., and Tweed, F. (2007). Ice, moraine, and landslide dams in mountainous terrain. *Quat. Sci. Rev.* 26, 3406–3422. doi:10.1016/j.quascirev.2007.10.012

Lee, K. L., and Duncan, J. M. (1975). *Landslide of 25 April, 1974 on the Mantaro River, Peru*. Washington, DC: National Academy of Sciences, 72.

Li, J., Cao, Z. X., Cui, Y. F., Fan, X. M., Yang, W. J., Huang, W., et al. (2021). Hydro-sediment-morphodynamic processes of the baige landslide-induced barrier lake, Jinsha River, China. *J. Hydrology* 596, 126134. doi:10.1016/j.jhydrol.2021.126134

Liu, N., Chen, Z. Y., Zhang, J. X., Lin, W., Chen, W. Y., and Xu, W. J. (2010). Draining the Tangjiashan barrier lake. *J. Hydraul. Eng.* 136 (11), 914–923. doi:10.1061/(ASCE)HY.1943-7900.0000241

Liu, N., Yang, Q. G., and Chen, Z. Y. (2016). *Hazard mitigation for barrier lakes*. Wuhan, China: Changjiang Press. (in Chinese).

Mei, S. Y., Chen, S. S., Zhong, Q. M., and Shan, Y. B. (2022). Detailed numerical modeling for breach hydrograph and morphology evolution during landslide dam breaching. *Landslides* 19, 2925–2949. doi:10.1007/s10346-022-01952-1

Mei, S. Y., Chen, S. S., Zhong, Q. M., and Shan, Y. B. (2021). Effects of grain size distribution on landslide dam breaching-insights from recent cases in China. *Front. Earth Sci.* 9, 658578. doi:10.3389/feart.2021.658578

Niu, Z. P., Xu, W. L., Li, N. W., Xue, Y., and Chen, H. y. (2012). Experimental investigation of the failure of cascade landslide dams. *J. Hydrodyn.* 24 (3), 430–441. doi:10.1016/S1001-6058(11)60264-3

Peng, M., Ma, C. Y., Chen, H. X., Zhang, P., Zhang, L. M., Jiang, M. Z., et al. (2021). Experimental study on breaching mechanisms of landslide dams composed of different materials under surge waves. *Eng. Geol.* 291, 106242. doi:10.1016/j.enggeo.2021.106242

Peng, M., and Zhang, L. M. (2012). Breaching parameters of landslide dams. *Landslides* 9 (1), 13–31. doi:10.1007/s10346-011-0271-y

Shan, Y. B., Chen, S. S., Zhong, Q. M., Mei, S. Y., and Yang, M. (2022). Development of an empirical model for predicting peak breach flow of landslide dams considering material composition. *Landslides* 19 (6), 1491–1518. doi:10.1007/s10346-022-01863-1

Shen, D. Y., Shi, Z. M., Peng, M., Zhang, L. M., and Jiang, M. Z. (2020a). Longevity analysis of landslide dams. *Landslides* 17 (3), 1797–1821. doi:10.1007/s10346-020-01386-7

Shen, G. Z., Sheng, J. B., Xiang, Y., Zhong, Q. M., and Yang, D. W. (2020b). Numerical modeling of overtopping-induced breach of landslide dams. *Nat. Hazards Rev.* 21 (2), 04020002. doi:10.1061/(ASCE)NH.1527-6996.0000362

Wahl, T. L. (1998). *Prediction of embankment dam breach parameters: A literature review and needs assessment*. Denver, USA: U. S. Dept. of the Interior. Dam Safety Rep. No. DSO-98-004Bureau of Reclamation.

Walder, J. S., and O'Connor, J. E. (1997). Methods for predicting peak discharge of floods caused by failure of natural and constructed earthen dams. *Water Resour. Res.* 33 (10), 2337–2348. doi:10.1029/97WR01616

Yang, Y., Cao, S. Y., Yang, K. J., and Li, W. P. (2015). Experimental study of breach process of landslide dams by overtopping and its initiation mechanisms. *J. Hydrodyn.* 27 (6), 872–883. doi:10.1016/S1001-6058(15)60550-9

Zheng, H. C., Shi, Z. M., Shen, D. Y., Peng, M., Hanley, K. J., Ma, C. Y., et al. (2021). Recent advances in stability and failure mechanisms of landslide dams. *Front. Earth Sci.* 9, 659935. doi:10.3389/feart.2021.659935

Zhong, Q. M., Chen, S. S., Mei, S. A., and Cao, W. (2018). Numerical simulation of landslide dam breaching due to overtopping. *Landslides* 15 (6), 1183–1192. doi:10.1007/s10346-017-0935-3

Zhong, Q. M., Wang, L., Chen, S. S., Chen, Z. Y., Shan, Y. B., Zhang, Q., et al. (2021). Breaches of embankment and landslide dams-State of the art review. *Earth-Science Rev.* 216, 103597. doi:10.1016/j.earscirev.2021.103597

Zhong, Q. M., Wu, W. M., Chen, S. S., and Wang, M. (2016). Comparison of simplified physically based dam breach models. *Nat. Hazards* 84 (2), 1385–1418. doi:10.1007/s11069-016-2492-9

Zhou, G. G. D., Zhou, M., Shrestha, M. S., Song, D., Choi, C. E., Cui, K. F. E., et al. (2019). Experimental investigation on the longitudinal evolution of landslide dam breaching and outburst floods. *Geomorphology* 334, 29–43. doi:10.1016/j.geomorph.2019.02.035

Zhou, G. G., Li, S., Lu, X., and Tang, H. (2022). Large-scale landslide dam breach experiments: Overtopping and "overtopping and seepage" failures. *Eng. Geol.* 304, 106680. doi:10.1016/j.enggeo.2022.106680

Zhu, X. H., Liu, B. X., Peng, J. B., Zhang, Z. F., Zhuang, J. Q., Huang, W. L., et al. (2021). Experimental study on the longitudinal evolution of the overtopping breaching of noncohesive landslide dams. *Eng. Geol.* 288, 106137. doi:10.1016/j.enggeo.2021.106137

frontiers | Frontiers in Earth Science

TYPE Original Research
PUBLISHED 23 February 2023
DOI 10.3389/feart.2023.1144283

OPEN ACCESS

EDITED BY
Jia-Wen Zhou,
Sichuan University, China

REVIEWED BY
Huei-Fen Chen,
National Taiwan Ocean University, Taiwan
Shengli Yang,
Lanzhou University, China

*CORRESPONDENCE
Yuzhu Zhang,
xbdzyz05@nwu.edu.cn

SPECIALTY SECTION
This article was submitted to Quaternary Science, Geomorphology and Paleoenvironment, a section of the journal Frontiers in Earth Science

RECEIVED 14 January 2023
ACCEPTED 13 February 2023
PUBLISHED 23 February 2023

CITATION
Wang S, Wang N, Zhang Y, Huang C, Zhu Y, Xiao Q, Chen D, Wang H, Ming Y, Huang X and Wang S (2023), Geochemistry of a paleo-oxbow lake sediments and its implications for the late Holocene extreme overbank flooding history of the Yellow River within the Zoige Basin, NE Tibetan Plateau. *Front. Earth Sci.* 11:1144283. doi: 10.3389/feart.2023.1144283

Geochemistry of a paleo-oxbow lake sediments and its implications for the late Holocene extreme overbank flooding history of the Yellow River within the Zoige Basin, NE Tibetan Plateau

Shuo Wang[1], Ninglian Wang[1,2], Yuzhu Zhang[1,3]*, Chang Huang[1], Yan Zhu[1], Qili Xiao[1], Dou Chen[1], Haoyu Wang[1], Yisen Ming[1], Xiaoling Huang[1] and Sikai Wang[1]

[1]Shaanxi Key laboratory of Earth Surface System and Environmental Carrying Capacity, College of Urban and Environmental Science, Northwest University, Xi'an, China, [2]CAS Center for Excellence in Tibetan Plateau Earth Sciences, Beijing, China, [3]State Key Laboratory of Loess and Quaternary Geology, Institute of Earth Environment, Chinese Academy of Sciences, Xi'an, China

Paleo-oxbow lake sediments can provide archives to reconstruct paleo-channel evolution and flooding history of the river. Multi-proxy approaches including detailed sediment stratigraphy, sedimentology and geochemistry have been implemented in a high-resolution sedimentary section of paleo-oxbow lake of the Yellow River within the Zoige Basin on the NE Tibetan Plateau, to reconstruct regional environmental changes and extreme overbank flooding history. Our results suggest that not only traditional sedimentological proxies, but also chemical elements can be applied in defining sequences with different genetic types, especially the paleoflood deposits in the paleo-oxbow profile. Two units of late-Holocence extreme overbank flooding deposits (OFDs) are identified in terms of the significantly higher proportions of sand, high contents of SiO_2, Na_2O, Ba, low contents of Al_2O_3, Fe_2O_3, MgO, K_2O, Ti, Rb and high values of Zr/Fe, Zr/Rb ratios. These extraordinary flood events within the Zoige Basin were dated back to 2,960 ± 240–2,870 ± 270 a and 1840 ± 200–1700 ± 160 a, in response to the mid-Holocene climatic optimum to the late Holocene and the Dark Age Cold Period (DACP). And the strong rainfall caused by the abnormal atmospheric circulation during the period of climate transition and abrupt change may led to the frequent occurrence of extreme flood events in the source region of the Yellow River. These findings are important for understanding the response of regional fluvial system to high climatic instability and provide a new perspective for us to analyze the risk of flood disasters on the Tibetan Plateau under the background of climate change.

KEYWORDS

Yellow River, Tibetan Plateau (TP), oxbow lake, paleoflood, climatic variability

1 Introduction

It is generally accepted that lakes are highly sensitive to environmental change and its response to the major climate fluctuations is extremely complex (Woolway and Merchant, 2019; Zhang et al., 2020). Oxbow lakes, as a special type of abandoned channels formed by curve cut-off of meandering rivers in the alluvial plain, play an important role in describing relationships between environmental change and the fluvial dynamics of the systems (Pawłowski et al., 2015). Sediment delivery and deposition at low energy locations result in the accumulation of organic matter, silt, and clay, and these undisturbed sediment fines preserve the sedimentation and geochemical record in the oxbow lake watershed (Bábek et al., 2011; Petr et al., 2013). In recent years, the multi-proxy approaches including pollen analyses, radiocarbon dating, detailed sediment stratigraphy, micromorphology and geochemistry, have been implemented in high-resolution lacustrine deposits of oxbow lakes to reconstruct paleohydrological environment and track past climatic change (Xiao et al., 2022; Antczak-Orlewska et al., 2021; Galicki et al., 2018; Petr et al., 2013).

The element geochemistry has been used as an indicator of past climatic and environmental changes across a wide range of timescales (Wennrich et al., 2014; Arnaud et al., 2016; Francke et al., 2020). For example, Rb/Sr ratios have been widely applied to reflect chemical weathering intensity and climate change on geological timescales (Chen et al., 1999a; Fritz et al., 2018; Yang et al., 2020). The chemical index of alteration (CIA) were used as a paleoclimatic indicator to reconstruct weathering process and pedogenesis as well as the intensity of the East Asian summer monsoon and westerlies (Goldberg and Humayun, 2010; Jia et al., 2022). The elemental distribution (such as Al, Fe, K, Mg, Mn, Ca, and Na) of river and lake sediment have important tracing significance on studies about the regional features of the catchment, the transformation of soils, and the hydrogeological conditions (Brown, 2011; Vogel et al., 2015; Hasberg et al., 2019).

The northeastern (NE) Tibetan Plateau is affected by the Prevailing westerlies (PW), East Asian summer monsoon (EASM) and Indian summer monsoon (ISM), which is a sensitive area in response to global climate change (An et al., 2012; Chen et al., 2016; Li et al., 2019). Channel migration of the Yellow River and its tributaries have left countless meander scars, abandoned channels, and (paleo-) oxbow lakes across the Zoige Basin on the NE Tibetan Plateau, after the demise of the Zoige paleo-lake in the last stage of the late Pleistocene (Huang, 2021). These (paleo-) oxbow lakes experienced the transition from distant river sediment input to the nearby lake sediment, providing the valuable archives to document the entire basin's evolution during the late Pleistocene and Holocene. However, previous researches of the (paleo-) oxbow lakes within the basin were mainly on the channel stability and ecological effects rather than its indicative significance of paleo-environmental changes (Li and Gao, 2019; Zhou et al., 2019; Wang et al., 2020; Guo et al., 2021).

Oxbow lake deposits may also include a continuous record of flood events and are appropriate to reconstruct the flooding history of a river over time intervals of several millennia (Wolfe et al., 2006; Berner et al., 2012; Munoz et al., 2018; Fuller et al., 2019; Toonen et al., 2020). Under the influence of the river system, oxbow lake sedimentation is primarily dominated by local flooding, backwater flooding, overland river flow, and tributary runoff (Galicki et al., 2018). High energy discharge during floods can result in an increase in coarse-grained material and is accompanied with significant changes in chemical-mineralogical contents in oxbow lake sediments (Wolfe et al., 2006; Berner et al., 2012). Predicted climate warming is likely to change future flood magnitude and frequency as the hydrological cycle intensifies in the headwater region on the Tibetan Plateau (Lutz et al., 2016; Wang et al., 2016; Gu et al., 2018). Hence, there is a need to better understand relationships between climatic changes and extreme flood event variability and requires paleoflood reconstruction to improve our ability to assess the risk of low-frequency, high-magnitude flood events (Baker, 1987; Wilhelm et al., 2018). This paper presents our new paleoflood investigations in the source region of Yellow River. Based on field observations and sedimentological analysis, a representative paleo-oxbow lake fill at NYQ-B site (NYQ-B profile) within the Zoige Basin was studied. Using different geochemical characteristics in overbank flood deposits and paleo-oxbow lake deposits, combined with other lithological and sedimentological proxies, we reconstruct paleoflood activities of the Yellow River within the Zoige Basin, and demonstrate the fluvial and geomorphic response to climatic changes on the NE Tibetan Plateau during the late Holocene.

2 Geographical settings

The Zoige Basin is a Cenozoic fault depression (pull-apart basin) located on the NE Tibetan Plateau between latitudes 32°17′N and 32°7′N and longitudes 101°30′E and 103°22′E, covering an area of 19,400 km^2 (Figure 1; Wang and Xue, 1997). The majority of the area is 3,400–3,600 m a.s.l, surrounded by the Anyemaqen, Nianbaoyuze and Qionglai Mountains of elevations >4,000 m (Figure 1). These surrounding mountains are annually snow-covered and have paleo-glacier relics. The basin is affected by PW, EASM and ISM, which is a sensitive area in response to global climate change (An et al., 2012; Chen et al., 2016; Li and Gao, 2019). The annual average temperature ranges from 0.6°C to 1.2 °C (the minimum and maximum monthly temperature is −9.0°C in January and 11.5°C in July, respectively). The mean annual precipitation ranges from 600 to 700 mm and monthly precipitation is mainly concentrated between May and October, accounting for 90% of the annual total (610 mm) (Hu et al., 2018).

The Zoige Basin is characterized by wide river valleys and lakes are distributed among low hills. The main rivers within the Zoige Basin include the Yellow River and its tributaries such as the White River, the Black River, and the Jiaqu River. The Yellow River flows southeast into the basin about 110 km, turns northwest at the intersection with the White River and flows out after receiving the Black River, which forms a huge U-shaped bend known as the "First Bend of the Yellow River" (Figure 1). Along the way, variations of stream gradient and bed sand constituent make the river pattern of the Yellow River changes repeatedly, leaving more than 150 oxbow lakes within Zoige Basin (Li and Gao, 2019; Huang, 2021).

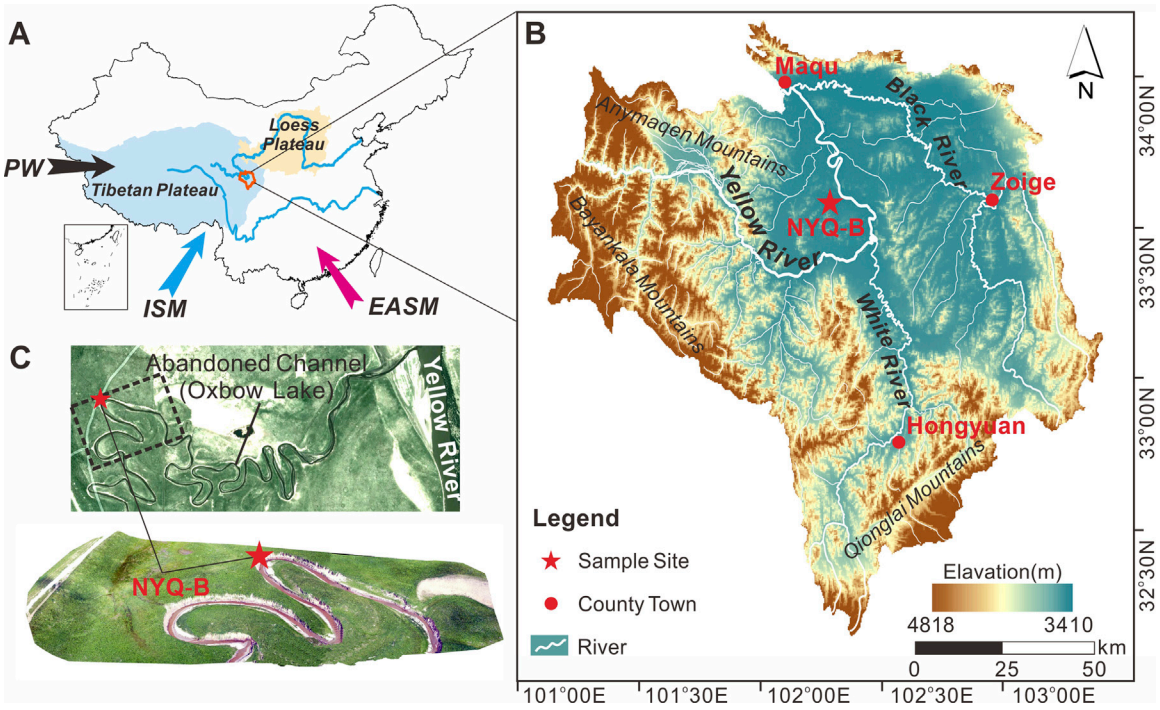

FIGURE 1
Overview of the study area. **(A)** Map shows the Zoige Basin (the outlined area) on the NE Tibetan Plateau; Abbreviation: PW, Prevailing Westerlies; ISM, Indian summer Monsoon; EASM, East Asian summer Monsoon. **(B)** Geomorphology of the Zoige Basin and the location of the paleo-oxbow lake fill at NYQ-B site in the Yellow River within the Zoige Basin. **(C)** The satellite image (Google Earth) and our UAV aerial image shows the location of the paleo-oxbow lake fill at NYQ-B site in the Yellow River within the Zoige Basin.

3 Materials and methods

3.1 Fieldwork

A detailed geological survey showed that a large number of paleo-oxbow lakes formed along the huge U-shaped bend of the Yellow River within the Zoige Basin on the NE Tibetan Plateau. The paleo-oxbow lake fill at the NYQ-B site (33°37′12″N, 102°18′44″E) in the Yellow River within the basin was studied (Figure 1C). The NYQ-B profile is situated in a Ω-shaped paleochannel at the back edge of the first river terrace (T_1) and 5 m above the present normal water level of the Yellow River. As the paleochannel is deeply cut by the Niangyiqu branch, the profile is freshly exposed and has clear stratigraphic boundaries (Figure 2). Detailed filed observation and stratigraphic description (color, structure and texture) were made in the field (Table 1).

3.2 Geochemical and sedimentological analysis

Chemical composition was determined in 69 samples taken every 5 cm, using a Bruker S2 RANGER Energy Dispersive X-Ray fluorescence spectrometer. 4 g of dried and homogenized sediments were put into the mold and smoothed, using boric acid base to edge. Then the sample was put into the press machine (30 t pressure) and pressed into circular sheets for measurements. Precision and accuracy of the chemical analysis for major (K, Ca, Na, Mg, Al, Fe, Si) and trace elements (Co, Zr, Rb, Sr, Ti, Zn, Cu, Pb, Ba, Cr, Mn, As, P, S) was checked by repeated measurements of the certified reference material including a Cu disk and a glass BAXS-S2 with the determination error <5%. For a typical analyses process and the precision of all elements refer to Shehata Ahmed Hussein (2016). Magnetic susceptibility was measured on a mass of 10 g of sediment with a Bartington MS-2B magnetic susceptibility meter (0.47/4.7 kHz). Grain-size distribution was measured by a Backman Coulter LS13320 laser analyzer with $(NaPO_3)_6$ as a dispersing agent after pre-treatment with 30% H_2O_2 (to remove organic matter) and 10% HCl (to remove carbonates), respectively.

3.3 Principal component analysis

The principal component analysis (PCA) is used to represent the elemental dataset with a few components instead of a large number of variables, group the elemental variables and detect main influential factors of element distribution (Ringnér, 2008). In this study, the function rda in the core package of vegan in R language was used to extract the feature quantity of the element concentration data to complete the principal component analysis (Borcard et al., 2018). The functions of summary and loadings ware used to query the information of each principal component and check the contribution of each variable to the principal component. The function biplot (using scaling 1 and scaling 2, respectively) was applied to plot the samples and project the elements over the principal component, visualizing

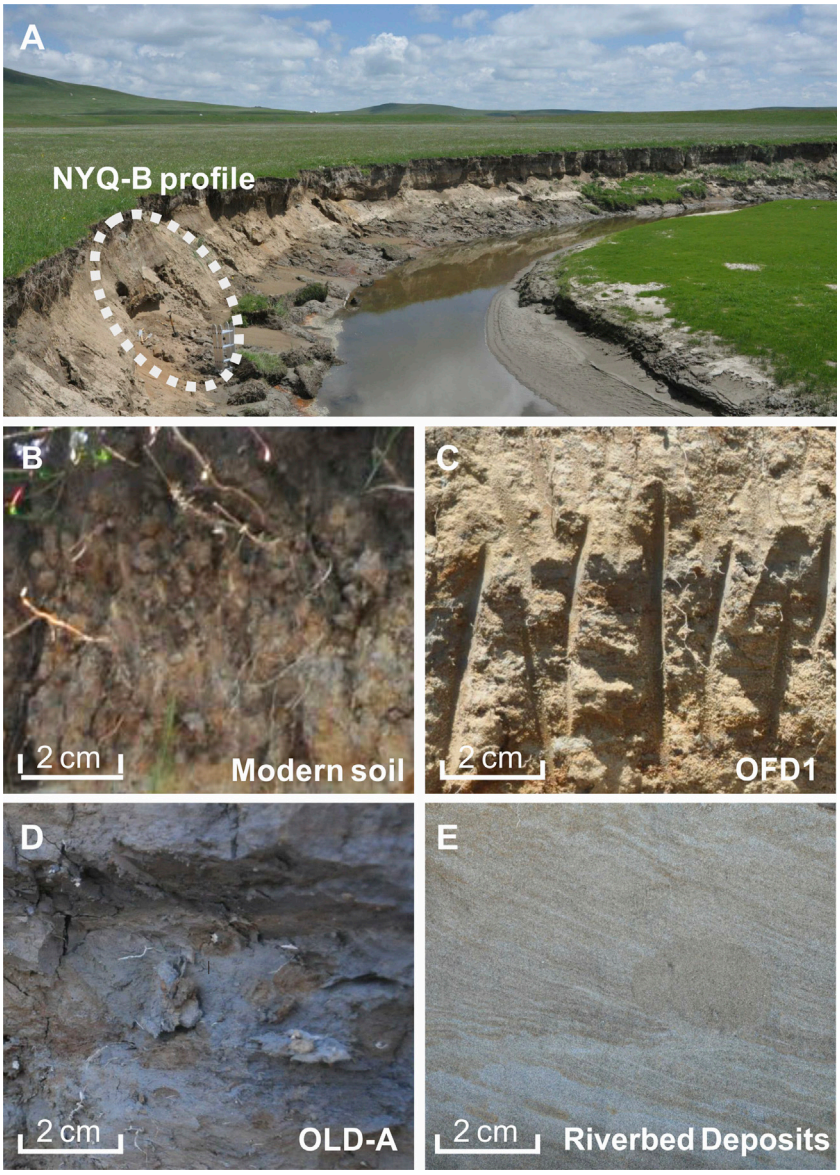

FIGURE 2
(A) Photo showing the paleo-oxbow lake fill at NYQ-B site within the Zoige Basin on the NE Tibetan Plateau. **(B–E)** Close-up shots showing difference between modern soil, overbank flooding deposits (OFD), paleo-oxbow lake deposits (OLD) and riverbed deposits (RD) at the NYQ-B site.

correlations between samples and determine whether samples can be grouped (Borcard et al., 2018). The arrow lengths of elements in distance biplot (scaling 1) showing their contribution to the principal components, and the correlation biplot (scaling 2) reveals distinct element clusters and the elements within the one cluster are highly correlated (Ter Braak, 1983; Legendre and Gallagher, 2001).

4 Results

4.1 Stratigraphy and chronology

In the NYQ-B profile within the Zoige Basin on the NE Tibetan Plateau, the sediment sequence was divided into six units according to the lithology and sedimentary structures from the base upwards (Figure 3). The unit of riverbed deposits consisting of fine sand and medium sand with parallel beddings were clearly visible at the bottom (340–215 cm). And two units of the paleo-oxbow lake deposits (OLD-A and OLD-B) were found in the depth range of 215–200 cm and 170–80 cm, which were composed of brown black clayey silt, with a hard texture and rich in organic matter. Two units of overbank flood deposits (OFD1, OFD2) with parallel and wavy beddings were also identified at 200–170 cm and 80–35 cm, respectively. The OFD2 unit was split into three sublayers, OFD2-1, OFD2-2 and OFD2-3, indicating that several episodes of overbank flooding occurred during the late Holocene (Huang et al., 2011a; 2011b; 2010; Xiao et al., 2022). The layer of typical subalpine meadow

TABLE 1 Pedosedimentary descriptions of the paleo-oxbow lake fill at NYQ-B site within the Zoige Basin on the NE Tibetan Plateau.

Depth (cm)	Pedostratigraphic subdivisions	Pedosedimentary descriptions
35–0	Modern soil (MS)	Gray, clayey silt, granular-block structure, loose and porous, some earthworm burrows and excrement, well-developed plant roots.
50–35	Overbank flood deposits (OFD2-3)	Yellowish orange, silty fine sand, some rust spots, very loose.
68–50	Overbank flood deposits (OFD2-2)	Grayish-white, silty fine sand, some rust spots, very loose.
80–68	Overbank flood deposits (OFD2-1)	Yellowish orange, silty fine sand, some rust spots, unconformable contact with the underlying oxbow lacustrine deposits.
80–170	Paleo-oxbow lake deposits (OLD-B)	Brown, interbedding of clayey silt and fine sandy silt, some rust spots, relatively firm.
200–170	Overbank flood deposits (OFD1)	Yellowish orange, medium sandy fine sand, some rust spots, very loose, some parallel or waving beddings.
215–200	Paleo-oxbow lake deposits (OLD-A)	Brown black, clayey silt, rich in organic matter, relatively firm.
340–215	Riverbed deposits (RD)	Dull yellowish orange, fine sandy medium sand, some rust spots, with inclined beddings.

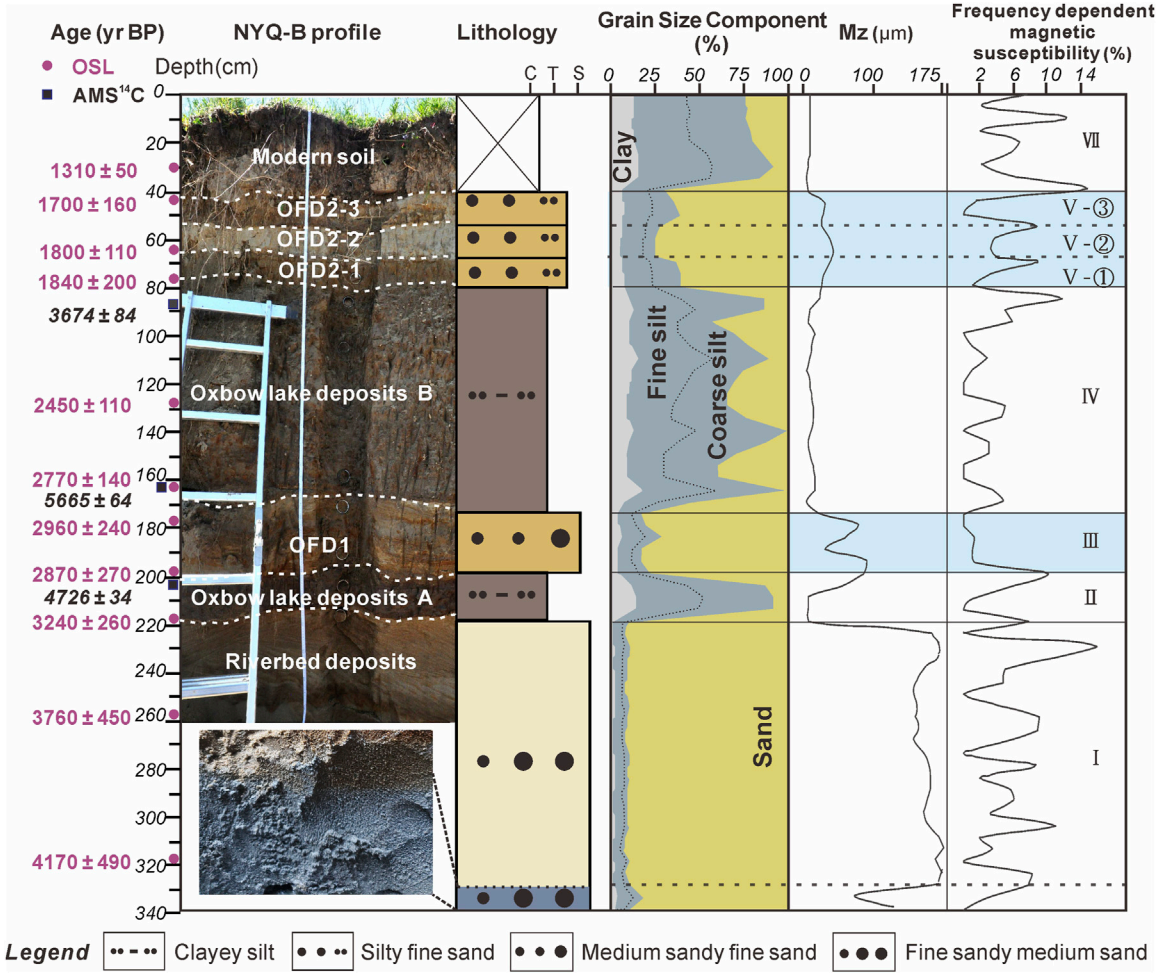

FIGURE 3
Sedimentary framework of the paleo-oxbow lake fill at NYQ-B site within the Zoige Basin on the NE Tibetan Plateau, including lithology, dating results, grain size parameters, magnetic susceptibility and frequency dependent magnetic susceptibility. The results of AMS ^{14}C and OSL dating in Figure 3 refer to Xiao et al., 2022.

soil were found at surface (35–0 cm), which comprised grey clayey silt with abundant earthworm burrows and plant roots. In particular, the chronology of the NYQ-B profile was dated by using the AMS ^{14}C and OSL dating techniques (Xiao et al., 2022) (Figure 3). However, the AMS ^{14}C ages are inverted and obviously older than OSL ages as a result of the re-working of old carbon during the paleo-oxbow lake depositional process (Zhou et al., 2016; Kołaczek et al., 2017). And then, these AMS ^{14}C ages were dropped. In summary, the dating results showed that two episode of extraordinary overbank flooding recorded by the OFDs occurred at 2,960 ± 240 to 2,870 ± 270 a and 1840 ± 200 to 1700 ± 160 a, respectively (Xiao et al., 2022).

4.2 Grain-size distribution and magnetic susceptibility

The grain-size distribution in the NYQ-B profile within the Zoige Basin is shown in Figure 3. The clay (<2 μm), fine silt (2–16 μm), coarse silt (16–63 μm), and sand (>63 μm) ratio vary considerably in the six units of the profile NYQ-B. The significant low values of the mean grain size show in the paleo-oxbow lake deposits (OLD-A and OLD-B), while high values in the overbank flood deposits (OFD1 and OFD2) and riverbed deposits.

Unit I (from the bottom to 215 cm) is composed of riverbed deposits, therefore, the sediment is the coarsest and dominated by sand (90.2%), with a little bit of silt (7.6%) and clay (2.2%). The sediment of Unit II (215–200 cm, OLD-A) is the finest and the sand component sharply reduces to 8.2%, while the silt component reaches its highest levels of the profile (76.8%) and clay content is 15.0% Unit III (200–170 cm, OFD1) is dominated by sand content again (79.2%), while silt content decreases to 16.0% and clay content falls further to 4.8% In Unit IV (170–80 cm, OLD-B), Mean silt content increases to 63.7% on average and sand reduces to 24.8% (Figure 3). It is noteworthy that sand content has been reduced to <1% at some depths. There is also substantial variation here in mean particle size, from 8.5 to 41.6 μm, with a mean value of 20.8 μm. Unit V (80–35 cm, OFD2) is divided into three sections, OFD2-1, OFD2-2 and OFD2-3 according to the mean particle size. Mean particle size of OFD2-2 (72.2 μm) is much coarser than the OFD2-1 and OFD2-3 (51.2 and 50.5 μm, respectively), and the sand content of OFD2-2 further increased to 74.3% than 60.4% and 65.0% in the OFD2-1 and OFD2-2. Unit VI (35–0 cm) is dominated by silt again (68.0%) with clay (13.8%) and sand (18.2%). Mean grain size also decrease to 9.9–18.3 μm.

In water-laid deposits, the frequency magnetic susceptibility reflects predominantly the supply of exogenic very fine-grained material, which means clay minerals deposited from suspension (Petr et al., 2013). Grain-size and Magnetic susceptibility data have been reported in previous papers (Xiao et al., 2022), but the frequency dependent magnetic susceptibility (χ_{fd}) is calculated in this study (Figure 3), to indicate the concentration of ferromagnetic minerals in the sediments and distinguish between the flooding units and the paleo-oxbow lake deposits combined with grain size distribution. The units with high frequency dependent susceptibility (χ_{fd}) have a finer average grain size. For example, the average χ_{fd} of surface layer (modern soil) is 6.61%, and the highest reach to 14.8%; the average χ_{fd} value of the OLD-A is 5.01% with the maximum value of 10.2% and the layer of the OLD-B has the maximum value of 11.7%. It means that magnetic minerals in sediments are composed of a relatively high proportion of super fine particles (superparamagnetic/single-domain threshold) which only contribute to the low-frequency susceptibility (Zhou et al., 1990; Liu et al., 2005). In contrast, the χ_{fd} of OFD1, OFD2 layers are lower than those of the pale-oxbow lake deposits, with the mean values of 0.70%, 3.82%; the highest value of OFD1, OFD2 layers are 1.3%, 8.9% and the lowest value is close to 0. And the χ_{fd} value of riverbed deposits fluctuates greatly and the average value is 5.11%. We infer that extreme hydrodynamic force during flood events brought more coarse terrigenous material into the paleo-oxbow lake fill at NYQ-B site, leading to a decrease in the contribution of superparamagnetic particles to magnetic susceptibility and a very low frequency magnetic susceptibility (Wu, 1993).

4.3 Element geochemistry

The variation of representative major element oxides and trace elements and their ratios can be roughly divided into 6 units from bottom to top (Figures 4, 5).

Unit I (340–215 cm, RD): The element content in this unit shows little fluctuation (Figures 4, 5). The average content of SiO_2 is the maximum of the whole section; while the mean values of Al_2O_3, Fe_2O_3, CaO, K_2O, MgO, Ti, P, S, Zr, Rb, Sr, Zn, Cu are the minimum of the whole section (Table 2; Figures 4, 5). The average contents of Ba, Cr are as the maximum values in all sedimentary units. The average Zr/Rb, Cu/Zn ratios are the minimum of the whole section and the average Zr/Fe ratio is as a comparatively small value (Table 2; Figure 5).

Unit II (215–200 cm, OLD-A): The element content in this unit appears change suddenly compared with those in Unit I. The average content of SiO_2 is a comparatively small value of the whole section (Table 2; Figure 4). The mean values of Al_2O_3, K_2O, MgO, Ti, Mn, Zr, Rb, Zn, Cu increase to the maximum of the whole section, the contents of Ba, Cr, Na_2O significantly decrease and CaO, Sr change little. The average Zr/Fe, Zr/Rb and Cu/Zn ratios are higher than those of the Unit I (Table 2; Figures 4, 5).

Unit III (200–170 cm, OFD1): The distribution of element content in this unit is obviously different from that in the previous unit. The SiO_2, Na_2O, Ba, Cr contents increase sharply to relatively large values in the whole section. The mean values of Al_2O_3, Fe_2O_3, K_2O, MgO, Ti, Mn, P, S, Zr, Zn, Cu and Rb drop significantly. The content of CaO increases and the content of Sr decreases slightly. The average Zr/Rb, Cu/Zn ratios decrease and the Zr/Fe ratio keeps as 0.007 (Table 2; Figures 4, 5).

Unit IV (170–80 cm, OLD-B): The element contents in this unit are similar to those in Unit II but fluctuate markedly (Figures 4, 5). The average content of SiO_2 drops dramatically to the minimum of the whole section and the Na_2O, Ba, Cr contents also decrease sharply. The mean values of Al_2O_3, Fe_2O_3, K_2O, MgO, Ti, Mn, P, S, Zr, Rb, Zn, Cu increase significantly. The average contents of CaO and Sr increase sharply to the highest value (Table 2; Figures 4, 5). The Zr/Fe ratio decreases to the minimum with the value of 0.005. The average Cu/Zn ratio increases to the maximum value of 0.36 in the whole section (Table 2; Figures 4, 5).

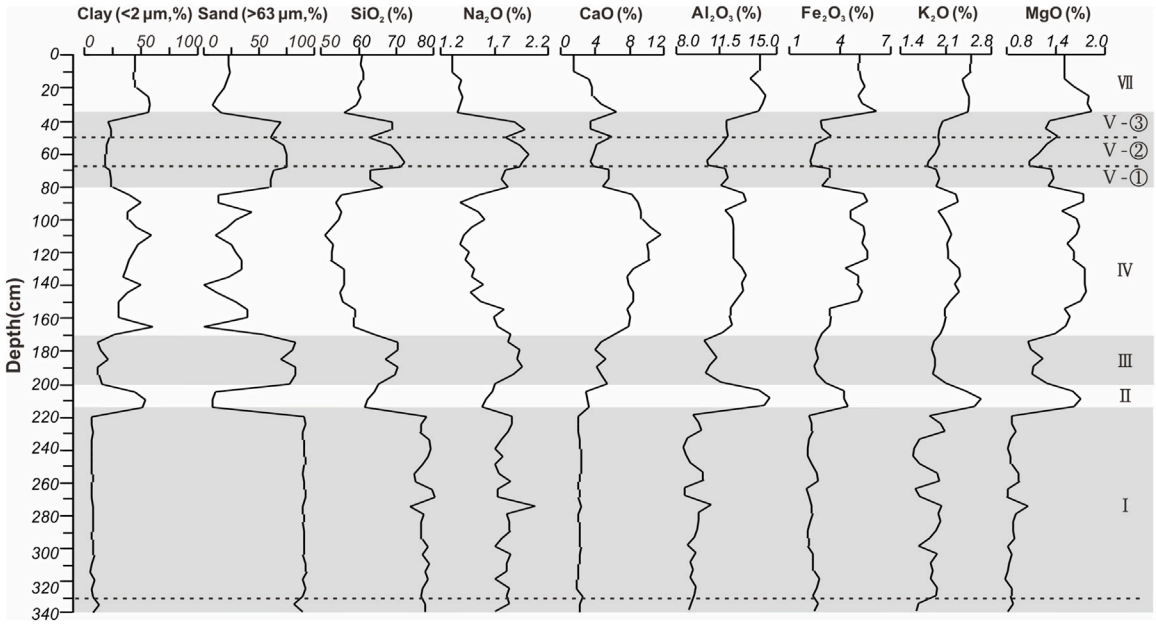

FIGURE 4
Grain size distribution and major element SiO_2, Na_2O, CaO, Al_2O_3, Fe_2O_3, K_2O, and MgO concentrations of the paleo-oxbow lake fill at NYQ-B site within the Zoige Basin on the NE Tibetan Plateau.

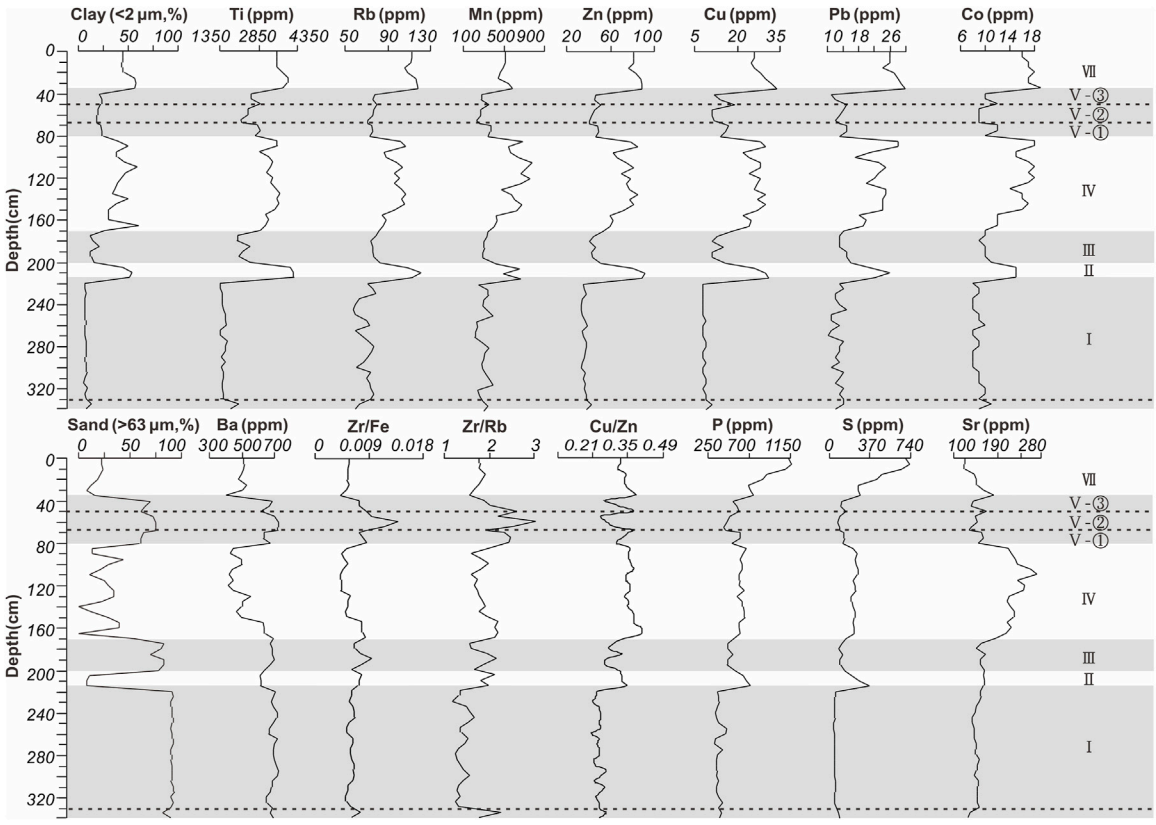

FIGURE 5
Grain size distribution and trace element Ti, Rb, Mn, Zn, Cu, Pb, Co, Ba, P, S, Sr concentrations and element ratios of Zr/Fe, Zr/Rb, and Cu/Zn of the paleo-oxbow lake fill at NYQ-B site within the Zoige Basin on the NE Tibetan Plateau.

TABLE 2 Average content of major elements oxides, trace elements and element ratios of the paleo-oxbow lake fill at NYQ-B site within the Zoige Basin on the NE Tibetan Plateau.

Elements	Modern soil	Riverbed deposits	Oxbow lacustrine deposits		Overbank flood deposits			
			OLD-A	OLD-B	OFD1	OFD2-1	OFD2-2	OFD2-3
SiO_2 (%)	59.93	77.50	62.84	55.61	69.01	64.24	70.78	66.84
Al_2O_3 (%)	13.77	9.27	14.14	12.15	10.49	11.41	10.58	11.54
Fe_2O_3 (%)	5.30	2.33	4.30	4.73	2.70	3.21	2.35	3.06
CaO (%)	3.22	2.08	3.03	8.81	4.63	5.27	3.73	4.19
K_2O (%)	2.45	1.85	2.53	2.17	1.95	1.98	1.90	2.02
Na_2O (%)	1.35	1.80	1.63	1.56	1.87	1.80	1.96	1.89
MgO (%)	1.63	0.84	1.64	1.63	1.14	1.33	1.14	1.33
Ti (ppm)	3698	1505	4151	3328	2222	2802	2297	2666
Ba (ppm)	491.63	691.24	613.00	507.67	674.67	647.00	718.75	659.33
Mn (ppm)	508.50	298.76	609.00	589.83	323.83	359.33	255.75	298.33
P (ppm)	905.38	364.96	670.00	610.61	486.00	569.33	453.25	556.67
S (ppm)	477.13	55.44	283.33	227.78	112.67	134.67	91.25	128.00
Cr (ppm)	115.63	146.04	93.33	89.89	119.50	94.33	121.50	103.33
Zr (ppm)	197.31	97.24	223.67	177.94	138.17	179.33	177.75	168.33
Rb (ppm)	112.94	69.00	114.33	96.50	77.50	74.67	73.75	78.00
Sr (ppm)	142.94	145.40	161.67	224.94	156.67	156.67	139.50	147.67
Zn (ppm)	83.50	36.20	87.00	71.94	44.33	47.67	41.75	47.33
Cu (ppm)	28.31	8.48	29.00	26.00	12.83	15.67	12.25	15.00
Pb (ppm)	27.00	12.68	23.00	22.22	14.17	14.33	13.00	12.67
As (ppm)	22.50	4.44	11.67	22.17	6.67	7.33	4.75	7.00
Co (ppm)	17.19	8.80	15.00	15.44	10.00	11.33	9.00	10.67
Zr/Fe	0.005	0.006	0.007	0.005	0.007	0.008	0.011	0.008
Zr/Rb	1.75	1.42	1.96	1.86	1.79	2.40	2.40	2.15
Cu/Zn	0.34	0.23	0.33	0.36	0.29	0.33	0.29	0.31

Unit V (80–35cm, OFD2): This unit can be divided into three sections according to the element content distribution (Figures 4, 5). As a whole, the SiO_2, Na_2O, Ba, Cr contents increase and the contents of Al_2O_3, Fe_2O_3, CaO, K_2O, MgO, Ti, Mn, P, S, Zr, Zn, Cu, Rb and Sr decrease significantly in this unit. Notable, the high content elements such as SiO_2, Na_2O, Ba, Cr are more abundant in OFD2-2 than OFD2-1 and OFD2-3 and the low-value elements in OFD2-2 are even scarcer (Table 2; Figures 4, 5). The average Zr/Fe, Zr/Rb ratios increase significantly and reach the maximum (0.011, 2.40) in OFD2-2. The average Cn/Zn ratio decrease and reach the minimum of the whole section in OFD2-2 with the values of 0.29 (Table 2; Figures 4, 5).

Unit VI (35–0 cm): The SiO_2, Ba, Cr contents drop sharply and the Al_2O_3, Fe_2O_3, K_2O, MgO, Ti, Mn, Zr, Rb, Zn, Cu contents in this unit appear high values again compared with those in Unit V (Figures 4, 5). The contents of Na_2O, CaO, Sr drop sharply to minimum in the surface layer while the contents of P, S increase dramatically to the maximum of the whole section. The Zr/Fe ratio decreases to the minimum and the average Cu/Zn ratio increases (Table 2; Figures 4, 5).

4.4 Results of principal component analysis

The element geochemistry is vertically consistent with stratigraphic change in the profile NYQ-B revealing distinct distribution patterns (Figures 4, 5). Principal component analysis (PCA) is used to extract the important information from a multivariate data table and to express this information as a set of few new variables called principal components (PC). The PCA of the element concentration data from the NYQ-B profile revealed that 84.06% of the sample variance is associated with the first two principal components (PC1 and PC2) and the first principal

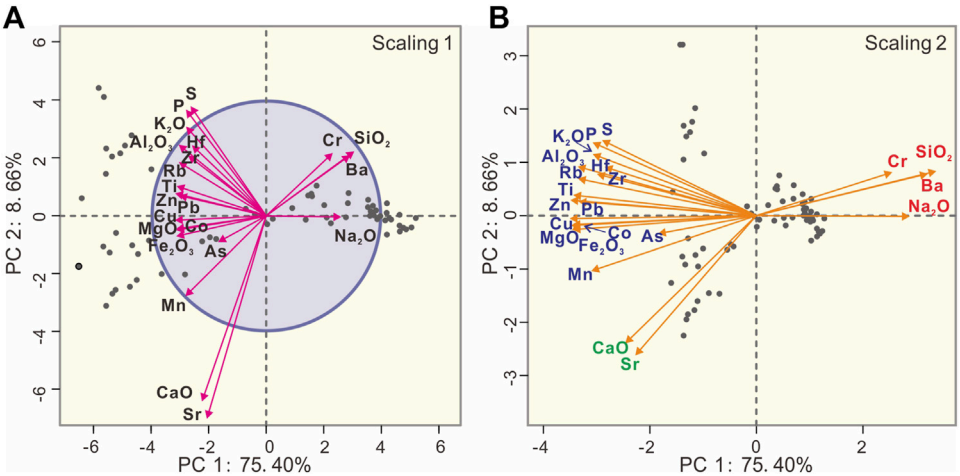

FIGURE 6
Principal component analysis of element concentration data of the paleo-oxbow lake fill at NYQ-B site within the Zoige Basin on the NE Tibetan Plateau. Elemental projections over the distance biplot using scaling 1 **(A)** and over the correlation biplot using scaling 2 **(B)** onto the first two principal components (PC1 and PC2).

component (PC1) account for 75.4% of the total variance (Figure 6). Therefore the PC 1 predominantly contribute toward the variability in the elemental dataset. The samples are plotted and elements are projected over the distance biplot (scaling 1) and the correlation biplot (scaling 2) (Figure 6). The correlation biplot reveals that elements distributed in sedimentary strata can be divided into three distinct element clusters (Figure 6B). A cluster comprising Ba, Cr, Na and SiO_2 is characterized by high positive scores of the PC1, slightly positive scores of the PC2 (Figure 6B), whose concentrations tend to increase in the most prominent sandy layers (Figures 4, 5). And another cluster with high negative PC1 scores, slightly positive or negative PC2 scores (Figure 6B), comprises Al_2O_3, Fe_2O_3, MgO, K_2O, Cu, Zn, Pb, Zr, Rb, Mn, P, S and other trace elements, showing decreasing concentrations in the sandy layers (Figures 4, 5). So we suggest that the PC 1 can be associated with the grain-size, which means the element distribution of the paleo-oxbow lake fill at NYQ-B site is controlled mainly by grain-size variation. A cluster comprising Sr, CaO is characterized by high negative PC1 scores and high negative PC2 scores (Figure 6B). In addition, the arrow lengths of the P, S, Sr and CaO in distance biplot are much longer than the radius of the circle of equilibrium contribution (Figure 6A), indicating that their contribution to the PC1 and PC2 are greater than the average contribution of other variables. PC2 (8.66% of sample variance) is presumably related to the effect of the element source. The highly negative scores of Sr and CaO are assumed to indicate source from authigenic carbonate (Chen et al., 1999b).

5 Discussion

5.1 Identification of oxbow lake evolution and extreme overbank flooding

Oxbow lakes form from the cut-off and sealing of previous meanders due to bank erosion and flooding within the Zoige Basin on the NE Tibetan Plateau (Li and Gao, 2019; Huang, 2021), and provide archives to reconstruct the paleo-channel evolution and the flooding history of the Yellow River during the Holocene. The elemental distribution in each sedimentary unit of the NYQ-B profile show obviously different characteristics (Figures 4, 5) and our PCA results prove that distribution pattern is controlled mainly by grain-size variation (Figure 6). Wolfe et al. (2006) report on a close correlation between flood events and high energy discharge marked by an increased influx of coarse grained detrital material into the river coupled with a relative decrease in the clay fraction. Significant correlations between turbidity and some trace elements were interpreted by Berner et al. (2012) due to the sorption of metals onto fine-grain size particles particles. So we suggest that chemical elements can be applied in defining the paleoflood deposits in the paleo-oxbow profile and have important tracing significance on studies about the regional channel evolution (Zhang et al., 2012). Meanwhile, the Zr/Rb and the Zr/Fe ratios provides a robust geochemical proxy for flood deposits across floodplain in this study (Fuller et al., 2018; Munoz et al., 2018). The element Zr is found principally in the resistant mineral zircon, tending to become concentrated in fine sand to coarse silt, while Rb and Fe is found in a range of minerals including clay minerals and concentrates in fine silt and clay, which means an increasing Zr/Rb and Zr/Fe ratio can be associated with an increase in grain size (Jones et al., 2012). Besides, the Cu/Zn ratio is used as a reference to judge the oxidation-reduction status of the sedimentary environment of the paleochannel (Fan et al., 2022). On the basis of the lithological, grain size, and compelling geochemical evidence presented, we propose that the development of the paleo-river channel NYQ-B including 6 phases: a fluvial environment, two oxbow lake environment and a steppe environment, interrupted by two episodes of overbank flooding.

Phase I: The dull yellowish orange medium sands can be identified at the bottom of the profile NYQ-B (Unit I-Riverbed deposits). The Unit I (215–340 cm) is dominated by coarse sand with some rust spots and inclined beddings (Figure 3) and characterized by the high contents of SiO_2 contained in sand-

sized quartz grains in local river systems (Figure 4), which can represent the riverbed deposits of the ancient Yellow River. It can be indicated that the ancient Yellow River flowed through the site before 3,240 ± 260 a (Xiao et al., 2022). This riverbed deposits of the ancient Yellow River below 330 cm is blue-gray and has a low value of Cu/Zn ratio, which indicates that it is a weakly reducing environment (Mei, 1988). It is speculated that the gleying process occurred because the lower part of the section was submerged by water for a long time due to the high groundwater level, which transformed the ferric iron into ferrous compound (Lu et al., 2012).

Phase II: The Unit II (215–200 cm, OLD-A) has a sharp contact with the Unit I and is composed of brown black clayey silt, with a hard texture and rich in organic matter. Such vertical changes in the sedimentary texture and structure indicate that the previous river channel was cut off and the abandoned river channel was filled up by suspended-load sediments on floodplains in an environment of slowly flowing to stagnant water (Toonen et al., 2012). It suggests that the fluvial sedimentary environment was replaced by the oxbow lake sedimentary environment. This is also proven by the results of the concentration of lithophilic elements (Al, Fe, K and Mg) and elements concentrate in fine silt and clay (Ti, Rb), which are highly correlated by according to our PCA results and indicate the abundant delivery of fine-grained detrital material into the paleo-oxbow lake (Sedláček et al., 2019; Antczak-Orlewska et al., 2021). We considered that the ancient Yellow River completed the nature cutoff (neck cutoff) at 3,240 ± 260 a, and this river channel was gradually abandoned and formed the paleo-oxbow lake (Xiao et al., 2022).

Phase III: The Unit III (200–170 cm, OFD1) has a sharp boundary with Unit II, which comprises yellowish orange sand with some rust spots and parallel or waving beddings. This stratigraphical structures is typical of overbank flood deposits. According to the grain size analysis, significantly higher proportions of sand occurred in Unit III. Sandy layers and low χ_{fd} values give evidence of the accumulation phase during flood events and represent typical overbank flood deposits (Figure 3). The high contents of SiO_2 reveals that the OFD1 unit is also dominated by the coarse sand-sized quartz grains (Galicki et al., 2018). It can be concluded that although the paleochannel (paleo-oxbow lake type) of the Yellow River has formed at 3,240 ± 260 a, extreme overbank flooding at 2,960 ± 0.24–2,870 ± 270 a accessed into the paleo-oxbow lake and resulted in high sedimentation rates (Wolfe et al., 2006; Xiao et al., 2022).

Phase IV: the grain size of the Unit IV (170–80 cm, OLD-B) became fine rapidly and the color changed from yellowish orange to brown, indicating the sedimentary environment is transformed to the oxbow lake environment again. Compared to the previous paleo-oxbow environment (Phase II), this layer is characterized by the obvious interbedding of the clay silt and fine sandy silt, a comparatively large fluctuation of element contents and the highly concentrated soluble elements (Ca, Sr). The high values of Sr and CaO in the lake sediments were caused by authigenic carbonate precipitation, suggesting a shrinking and progressively more saline lake as the climate gradually became drier (Chen et al., 2010). A generally drier climate and weaker vegetation coverage in the basin after 3000 BP was also indicated by the pollen record from the eastern margin of the Tibetan Plateau (Zhou et al., 2010). This implies that the intensity of the summer monsoon was weakening during this period (Wang et al., 2005; Hu et al., 2008).

Phase V: The Unit V (80–35 cm, OFD2) can be divided into three sublayers: the OFD2-1 and OFD2-3 comprises yellowish orange silty fine sand, while the OFD2-2 has a lighter color and a coarser grain size composed of grayish-white silty fine sand, and it could be resulted from three episodes of extreme overbank flooding with different magnitudes at 1840 ± 200–1700 ± 160 a. The OFD2 unit is also detected by the Zr/Fe, Zr/Rb ratios, which reach to the maximum value of the whole profile, due to the large amount of heavy mineral transported into the lake environment by high energy discharge during floods (Fuller et al., 2018; Munoz et al., 2018).

Phase VI: The Unit V merges gradually into Unit VI (35–0 cm, Modern soil) after 1,310 ± 50 a, a layer of typical subalpine meadow soil, which comprises grey clayey silt with abundant earthworm burrows and plant roots. The fine-grained sediment and the enrichment of Al, Fe, K, Mg, Ti, Rb indicate that pedogenesis processes occurred at the NYQ-B site (Jia et al., 2022). The high concentration of P and S in surface layer are presumed to indicate the influence of anthropogenic pollution (Akhtar et al., 2003).

5.2 The link between climate change and extreme overbank flooding

The general characteristics of climatic and environmental changes during Holocene can be reflected by the evolution phases of the paleo-oxbow lake fill at NYQ-B site within the Zoige Basin on the NE Tibetan Plateau. Especially, the climatic background and inducing factors of extreme overbank flooding recorded by flood units are inferred in this study. Previous studies have proposed that extraordinary floods often result from an abrupt change of climate and climatic deterioration (Guo et al., 2000; Huang et al., 2007). The OFDs in the NYQ-B profile are easily differentiated from oxbow lake deposits in terms of the significantly higher proportions of sand, enriched content of SiO_2 (even above 80%) and the increase in silicate-bound elements (Na, Ba and Cr). It is confirmed that two phases of extreme overbank flooding prevailed within the Zoige Basin between 2,960 ± 240–2,870 ± 270 a and 1840 ± 200–1700 ± 160 a, respectively. And we infer these high intensity of floods on the NE Tibetan Plateau result from increase in extreme rainstorms during the late Holocene climatic deterioration and are considered as a response of the regional fluvial system to high climatic variability and instability.

The first extreme flooding episode (2,960 ± 240–2,870 ± 270 a) recorded by OFD1 in the NYQ-B profile is coincide with the climatic deterioration during mid-Holocene climatic optimum to the late Holocene (Peng et al., 2005; Huang et al., 2009). Because the Megathermal fell into decline and global climate entered a drastic fluctuation period around 3,000 a BP, the climate became highly variable and instabilized in the transition from the dominance of the maritime monsoon to continental monsoon (Xiao et al., 2004; Wang et al., 2005; Hu et al., 2008). Studies on the relationships between modern floods and the monsoonal climate have indicated that extraordinary flood events often resulted from infrequent rainstorms in connection with unusual atmospheric circulation

patterns (Knox, 2000; Huang et al., 2007; Guo et al., 2016; Huang, 2021). Therefore, we infer that an abrupt climatic deterioration with extreme climate variability around 3,000 a BP at the end of the mid-Holocene Climate Optimum caused a series of disasters in different areas in China's monsoonal regions, including extraordinary floods due to increased precipitation in the source region of Yellow River (Kale et al., 2000; Grossman, 2001; Bohorquez et al., 2013; Lillios et al., 2016). Previous researches of the middle Yellow River also provide evidence that some extreme flooding events occurred at the Weihe River, Jinghe River and Beiluo River between 3,200 a BP to 2,800 a BP (Huang et al., 2012; Wan et al., 2015; Li et al., 2019). Historical documents show that the collapses of the Shang Dynasty (1,600–1046 BCE) were attributed to disastrous events including extreme floods, droughts, famines and desiccation of the Yellow River and its tributaries during this period (Huang et al., 2009).

Moreover, severe droughts resulting from shortage of rainfall and extraordinary floods resulting from rainstorms were two parts of the extreme climate variability during climatic events (Huang et al., 2007; Huang et al., 2010; Huang et al., 2013; Guo et al., 2015; Guo et al., 2016; Li et al., 2019; Li et al., 2021). Although great floods occurred as a result of extreme rainstorms in the Zoige Basin, deposits from Qinghai Lake and its surrounding aeolian deposits have documented decreasing temperature and increasing aridity after ca. 3,100 a BP (Shen et al., 2005; Li et al., 2017). Meanwhile, the colder and drier regime around 3,000 a BP is also identified in Nile Delta and severe centennial-scale droughts may have affected civilizations in northern Africa, southwestern Asia and mid-continental North America Middle (Bernhardt et al., 2012). It was suggested that the precipitation variability might be resulted from the complex feedback process between various high- and low-latitude competing driving forces, implying a large-scale climatic teleconnection across the Northern Hemisphere (Li et al., 2017).

The second episode of extreme flooding events recorded by OFD2 in the NYQ-B profile occurred at 1840 ± 200–1700 ± 160 a correlated with cooling and desiccation periods during the Dark Age Cold Period (DACP) (1800–1,100 a; Patterson et al., 2010). This flood episode on the NE Tibetan Plateau shows good agreement in terms of the low values of $\delta^{18}O$ from ice-cores of the GRIP which indicates that the climate cooled significantly during this period (Dansgaard et al., 1993). Some high resolution climatic proxies and precise dating from stalagmites provide information on weakening of monsoon activities at that time (Wang et al., 2005; Hu et al., 2008). The increased flood activities during the Dark Age Cold Period are also correspond to the reconstructed paleoflood events in the middle Yangtze River (Guo et al., 2016) and reported by other documentary and sedimentary archives from the Austrian Pre-Alps (Swierczynski et al., 2012) and the western Europe (Pears et al., 2020). This flood phase generally corresponds to the period of the Eastern Han Dynasty (CE 25–220) in Chinese history and the floods, droughts, large-scale famine and frequent change of dynasties are recorded in ancient Chinese documents (Zheng et al., 1999).

Overall, two episodes of increased flood activities on the NE Tibetan Plateau occurred at global deterioration periods with highly climate instability. Great floods occurred as a result of extreme rainstorms caused by special atmospheric circulation patterns that determine the location of storm tracks and air mass boundaries, resulting in excessive runoff and flooding (Knox, 2000). In particular, glacier advanced and the glacial meltwater supply decreased on the NE Tibetan Plateau due to the colder and drier climate from 3,100 to 2,600 a and 1800–1,300 a (Lehmkuhl, 1997; Mischke and Zhang, 2010), which means the contribution of ice and snow melting to the two episodes of overbank flooding may be relatively weak. However, when climate departed from its normal condition during late Holocene, the weak summer monsoon and strong Western Pacific Subtropical High (WPSH) occur in the Yellow River catchment, and the warm-humid air masses brought by EASM and ISM meets the northern cold airflow brought by northwestern continental monsoon (Ma and Xu, 1982). Therefore, we consider that large-magnitude floods on the NE Tibetan Plateau is caused by long-duration rainstorms due to the quasistationary front hovers above the upper Yellow River catchment (Guo et al., 2016). Similar historical and modern flooding events within the Zoige Basin due to the extreme precipitation have been reported by previous studies (Wang, 2012). Therefore, we believe that the strong rainfall caused by abnormal atmospheric circulation during the period of climate transition/abrupt change may be the main triggering factor of these two episodes of extreme overbank flooding (Xiao et al., 2022).

6 Conclusion

The sedimentary section of the paleo-oxbow lake fill at NYQ-B site was discovered after the observation of aerial photographs and maps within the Zoige Basin on the NE Tibetan Plateau. The multi-proxy approach especially geochemical proxy to the interpretation of the NYQ-B paleo-oxbow sedimentary infill enables us to reconstruct the evolution of river channel, local sedimentation processes and extreme flooding history linked to global climate changes. The following conclusions are drawn:

1. The sediment of the paleo-oxbow lake fill at NYQ-B site contained the paleoenvironmental record during middle to late Holocene. The paleo-oxbow lake fill was occupied by the ancient Yellow River during 4,170 ± 490–3,240 ± 260 a. After the neck cutoff of the Yellow River and abandonment of the channel, the shallow oxbow lake appeared at 3,240 ± 260 a, interrupted by two episodes of extraordinary overbank flooding, changed to a steppe environment at 1,310 ± 50 a and continue to the present day.
2. Geochemical characteristics can be used as the robust proxy to identify the flood deposits accurately in the Holocene stratum of the fluvial plain on the NE Tibetan Plateau. The elemental distribution in each sedimentary unit of the profile NYQ-B show obviously different characteristics with a certain relationship with grain-size variation. Layers of overbank flood deposits are characterized by the high contents of SiO_2, Na_2O, Ba, low contents of Al_2O_3, Fe_2O_3, MgO, K_2O, Ti, Rb and high values of Zr/Fe, Zr/Rb ratios.
3. Two episodes of extraordinary overbank flooding in the upper Yellow River occurred during 2,960 ± 240–2,870 ± 270 a and 1840 ± 200–1700 ± 160 a, which are in good agreement with the transition periods from the mid-Holocene climatic optimum to the late Holocene and the Dark Age Cold

Period (DACP). Abnormal atmospheric circulation and strong rainfall during the period of climate transition and abrupt change triggered extreme flooding on the NE Tibetan Plateau, which is helpful in understanding the regional response of hydroclimatic system to climatic variations in source region of the largest rivers of Asia.

Data availability statement

The original contributions presented in the study are included in the article/Supplementary Material, further inquiries can be directed to the corresponding author.

Author contributions

ShW: analyzing and synthesizing study data, writing the initial draft; NW: Management and coordination responsibility for the research activity planning and execution; YuZ: Formulation of overarching research goals and design of methodology; CH: Data collection and software programming; YaZ: Conducting the investigation process; QX: Performing the OSL dating experiments; DC: Performing the geochemical experiments; HW: Performing the experiments of Magnetic susceptibility; YM and XH: Performing the experiments of Grain-size distribution; SiW: Reviewing and editing the manuscript.

Funding

This work was supported by the grants from the National Science Foundation of China (42277449, 4197116), the Chinese Postdoctoral Science Foundation (2022M722570), the Second Tibetan Plateau Scientific Expedition and Research Program (2019QZKK0903), Strategic Priority Research Program of the Chinese Academy of Sciences (XDA20060201), and the Open Foundation of The State Key Laboratory of Loess and Quaternary Geology (SKLLQG2107).

Conflict of interest

The authors declare that the research was conducted in the absence of any commercial or financial relationships that could be construed as a potential conflict of interest.

Publisher's note

All claims expressed in this article are solely those of the authors and do not necessarily represent those of their affiliated organizations, or those of the publisher, the editors and the reviewers. Any product that may be evaluated in this article, or claim that may be made by its manufacturer, is not guaranteed or endorsed by the publisher.

References

Akhtar, M., Richards, B., Medrano, P., deGroot, M., and Steenhuis, T. (2003). Dissolved phosphorus from undisturbed soil cores. *Soil Sci. Soc. Am. J.* 67, 458–470. doi:10.2136/sssaj2003.0458

An, Z., Colman, S., Zhou, W., Li, X., Brown, E., Jull, A., et al. (2012). Interplay between the westerlies and asian monsoon recorded in lake Qinghai sediments since 32 ka. *Sci. Rep.* 2, 619. doi:10.1038/srep00619

Antczak-Orlewska, O., Okupny, D., Pawłowski, D., Kotrys, B., Krąpiec, M., Luoto, T. P., et al. (2021). The environmental history of the oxbow in the Luciąża River valley – study on the specific microclimate during Allerød and Younger Dryas in central Poland. *Quat. Int.* 644-645, 178–195. doi:10.1016/j.quaint.2021.08.011

Arnaud, F., Poulenard, J., Giguet-Covex, C., Wilhelm, B., Révillon, S., Jenny, J.-P., et al. (2016). Erosion under climate and human pressures: An alpine lake sediment perspective. *Quat. Sci. Rev.* 152, 1–18. doi:10.1016/j.quascirev.2016.09.018

Bábek, O., Faměra, M., Hilscherová, K., Kalvoda, J., Dobrovolný, P., Sedláček, J., et al. (2011). Geochemical traces of flood layers in the fluvial sedimentary archive; implications for contamination history analyses. *Catena* 87, 281–290. doi:10.1016/j.catena.2011.06.014

Baker, V. (1987). Paleoflood hydrology and extraordinary flood events. *J. Hydrology* 96, 79–99. doi:10.1016/0022-1694(87)90145-4

Berner, Z., Bleeck-Schmidt, S., Stüben, D., Neumann, T., Fuchs, M., and Lehmann, M. (2012). Floodplain deposits: A geochemical archive of flood history – a case study on the river rhine, Germany. *Appl. Geochem.* 27, 543–561. doi:10.1016/j.apgeochem.2011.12.007

Bernhardt, C., Horton, B., and Stanley, J. (2012). Nile Delta vegetation response to Holocene climate variability. *Geology* 40, 615–618. doi:10.1130/g33012.1

Bohorquez, P., García-García, F., Pérez-Valera, F., and Martínez-Sánchez, C. (2013). Unsteady two-dimensional paleohydraulic reconstruction of extreme floods over the last 4000 yr in Segura River, southeast Spain. *J. hydrology* 477, 229–239. doi:10.1016/j.jhydrol.2012.11.031

Borcard, D., Gillet, F., and Legendre, P. (2018). "Unconstrained ordination," in *Numerical ecology with R* (Springer), 151–201.

Brown, E. (2011). Lake Malawi's response to "megadrought" terminations: Sedimentary records of flooding, weathering and erosion. *Palaeogeogr. Palaeoclimatol. Palaeoecol.* 303, 120–125. doi:10.1016/j.palaeo.2010.01.038

Chen, F., Bloemendal, J., Zhang, P., and Liu, G. (1999b). An 800 ky proxy record of climate from lake sediments of the Zoige Basin, eastern Tibetan Plateau. *Palaeogeogr. Palaeoclimatol. Palaeoecol.* 151, 307–320. doi:10.1016/s0031-0182(99)00032-2

Chen, J., An, Z., and Head, J. (1999a). Variation of Rb/Sr ratios in the loess-paleosol sequences of central China during the last 130,000 Years and their implications for monsoon paleoclimatology. *Quat. Res.* 51, 215–219. doi:10.1006/qres.1999.2038

Chen, H., Song, S., Lee, T., Löwemark, L., Chi, Z., Wang, Y., et al. (2010). A multiproxy lake record from Inner Mongolia displays a late Holocene teleconnection between Central Asian and North Atlantic climates. *Quat. Int.* 227, 170–182. doi:10.1016/j.quaint.2010.03.005

Chen, F., Wu, D., Chen, J., Zhou, A., Yu, J., Shen, J., et al. (2016). Holocene moisture and East Asian summer monsoon evolution in the northeastern Tibetan plateau recorded by lake Qinghai and its environs: A review of conflicting proxies. *Quat. Sci. Rev.* 154, 111–129. doi:10.1016/j.quascirev.2016.10.021

Dansgaard, W., Johnsen, S., Clausen, H., Dahl-Jensen, D., Gundestrup, N., Hammer, C., et al. (1993). Evidence for general instability of past climate from a 250-kyr ice-core record. *nature* 364, 218–220. doi:10.1038/364218a0

Fan, Q., Xia, G., Li, G., and Yi, H. (2022). Analytical methods and research progress of redox conditions in the paleo-ocean. *Acta Sedimentol. Sin.* 40, 1151–1171. (In Chinese with English abstract). doi:10.14027/j.issn.1000-0550.2021.023

Francke, A., Holtvoeth, J., Codilean, A., Lacey, J., Bayon, G., and Dosseto, A. (2020). Geochemical methods to infer landscape response to quaternary climate change and land use in depositional archives: A review. *Earth-Science Rev.* 207, 103218. doi:10.1016/j.earscirev.2020.103218

Fritz, M., Unkel, I., Lenz, J., Gajewski, K., Frenzel, P., Paquette, N., et al. (2018). Regional environmental change versus local signal preservation in Holocene thermokarst lake sediments: A case study from herschel island, yukon (Canada). *J. Paleolimnol.* 60, 77–96. doi:10.1007/s10933-018-0025-0

Fuller, I., Macklin, M., Toonen, W. H., and Holt, K. (2018). Storm-generated Holocene and historical floods in the manawatu river, New Zealand. *Geomorphology* 310, 102–124. doi:10.1016/j.geomorph.2018.03.010

Fuller, I., Macklin, M., Toonen, W., Turner, J., and Norton, K. (2019). A 2000 year record of palaeofloods in a volcanically-reset catchment: Whanganui River, New Zealand. *Glob. Planet. Change* 181, 102981. doi:10.1016/j.gloplacha.2019.102981

Galicki, S., Bujenovic, M., Woehnker, T., Galtney, J., and Galicki, T. (2018). Mid-late Holocene anthropogenic and natural variations in geochemistry and sedimentation in the yazoo basin: Clark lake, sharkey county, Mississippi. *Phys. Geogr.* 40, 209–226. doi:10.1080/02723646.2018.1516395

Goldberg, K., and Humayun, M. (2010). The applicability of the chemical index of alteration as a paleoclimatic indicator: An example from the permian of the paraná basin, Brazil. *Braz. Palaeogeogr. Palaeoclimatol. Palaeoecol.* 293, 175–183. doi:10.1016/j.palaeo.2010.05.015

Grossman, M. (2001). Large floods and climatic change during the Holocene on the Ara river, central Japan. *Geomorphology* 39, 21–37. doi:10.1016/s0169-555x(01)00049-6

Gu, H., Yu, Z., Yang, C., and Ju, Q. (2018). Projected changes in hydrological extremes in the Yangtze River basin with an ensemble of regional climate simulations. *Water* 10, 1279. doi:10.3390/w10091279

Guo, Z., Petit-Maire, N., and Kröpelin, S. (2000). Holocene non-orbital climatic events in present-day arid areas of northern Africa and China. *Glob. Planet. Change* 26, 97–103. doi:10.1016/s0921-8181(00)00037-0

Guo, Y., Huang, C., Pang, J., Zha, X., Zhou, Y., Wang, L., et al. (2015). Investigating extreme flood response to Holocene palaeoclimate in the Chinese monsoonal zone: A palaeoflood case study from the hanjiang river. *Geomorphology* 238, 187–197. doi:10.1016/j.geomorph.2015.03.014

Guo, Y., Huang, C., Zhou, Y., Pang, J., Zha, X., Zhou, L., et al. (2016). Extraordinary flood events and the response to monsoonal climatic change during the last 3000 years along the middle Yangtze River valley, China. *Palaeogeogr. Palaeoclimatol. Palaeoecol.* 462, 70–84. doi:10.1016/j.palaeo.2016.09.005

Guo, X., Gao, P., and Li, Z. (2021). Morphological characteristics and changes of two meandering rivers in the Qinghai-Tibet Plateau, China. *Geomorphology* 379, 107626. doi:10.1016/j.geomorph.2021.107626

Hasberg, A., Bijaksana, S., Held, P., Just, J., Melles, M., Morlock, M., et al. (2019). Modern sedimentation processes in Lake Towuti, Indonesia, revealed by the composition of surface sediments. *Sedimentology* 66, 675–698. doi:10.1111/sed.12503

Hu, C., Henderson, G., Huang, J., Xie, S., Sun, Y., and Johnson, K. (2008). Quantification of Holocene Asian monsoon rainfall from spatially separated cave records. *Earth Planet. Sci. Lett.* 266, 221–232. doi:10.1016/j.epsl.2007.10.015

Hu, G., Yu, L., Dong, Z., Lu, J., Li, J., Wang, Y., et al. (2018). Holocene aeolian activity in the Zoige Basin, northeastern Tibetan plateau, China. *Catena* 160, 321–328. doi:10.1016/j.catena.2017.10.005

Huang, C. (2021). Palaeoflood deposits in the Zoige Basin and the enlightening on the formation of the Yellow River drainage system on the Tibetan plateau. *Acta Geogr. Sin.* 76, 612–625. (In Chinese with English abstract). doi:10.11821/dlxb202103009

Huang, C., Pang, J., Zha, X., Su, H., Jia, Y., and Zhu, Y. (2007). Impact of monsoonal climatic change on Holocene overbank flooding along Sushui River, middle reach of the Yellow River, China. *Quat. Sci. Rev.* 26, 2247–2264. doi:10.1016/j.quascirev.2007.06.006

Huang, C., Pang, J., Su, H., Li, S., and Ge, B. (2009). Holocene environmental change inferred from the loess–palaeosol sequences adjacent to the floodplain of the Yellow River, China. *Quat. Sci. Rev.* 28, 2633–2646. doi:10.1016/j.quascirev.2009.05.024

Huang, C., Pang, J., Zha, X., Zhou, Y., Su, H., and Li, Y. (2010). Extraordinary floods of 4100– 4000 a BP recorded at the late neolithic ruins in the Jinghe River gorges, middle reach of the Yellow River, China. *Palaeogeogr. Palaeoclimatol. Palaeoecol.* 289, 1–9. doi:10.1016/j.palaeo.2010.02.003

Huang, C., Pang, J., Zha, X., Su, H., and Jia, Y. (2011a). Extraordinary floods related to the climatic event at 4200 a BP on the Qishuihe River, middle reaches of the Yellow River, China. *Quat. Sci. Rev.* 30, 460–468. doi:10.1016/j.quascirev.2010.12.007

Huang, C., Pang, J., Zha, X., Zhou, Y., Su, H., Wan, H., et al. (2011b). Sedimentary records of extraordinary floods at the ending of the mid-Holocene climatic optimum along the Upper Weihe River, China. *Holocene* 22, 675–686. doi:10.1177/0959683611409781

Huang, C., Pang, J., Zha, X., Zhou, Y., Su, H., Zhang, Y., et al. (2012). Holocene palaeoflood events recorded by slackwater deposits along the lower Jinghe River valley, middle Yellow River basin, China. *J. Quat. Sci.* 27, 485–493. doi:10.1002/jqs.2536

Huang, C., Pang, J., Zha, X., Zhou, Y., Yin, S., Su, H., et al. (2013). Extraordinary hydro-climatic events during the period AD 200– 300 recorded by slackwater deposits in the upper Hanjiang River valley, China. *Palaeogeogr. Palaeoclimatol. Palaeoecol.* 374, 274–283. doi:10.1016/j.palaeo.2013.02.001

Jia, Y., Zhang, Y., Huang, C., Wang, N., Qiu, H., Wang, H., et al. (2022). Weathering and pedogenesis of the late Pleistocene and Holocene aeolian loess-paleosol sections in the Yellow River source area, NE Tibetan Plateau. *Palaeogeogr. Palaeoclimatol. Palaeoecol.* 208, 111065. doi:10.1016/j.palaeo.2022.111065

Jones, A., Macklin, M., and Brewer, P. (2012). A geochemical record of flooding on the upper River Severn, UK, during the last 3750years. *Geomorphology* 179, 89–105. doi:10.1016/j.geomorph.2012.08.003

Kale, V., Singhvi, A., Mishra, P., and Banerjee, D. (2000). Sedimentary records and luminescence chronology of late Holocene palaeofloods in the luni river, thar desert, northwest India. *Catena* 40, 337–358. doi:10.1016/s0341-8162(00)00091-6

Knox, J. (2000). Sensitivity of modern and Holocene floods to climate change. *Quat. Sci. Rev.* 19, 439–457. doi:10.1016/s0277-3791(99)00074-8

Kołaczek, P., Gałka, M., Apolinarska, K., Gębica, P., Superson, S., Michno, A., et al. (2017). Lost in dating – problems with the absolute chronologies and sedimentation rates of Late Glacial and Early Holocene oxbow lake deposits in Central Europe. *Quat. Geochronol.* 41, 187–201. doi:10.1016/j.quageo.2017.05.002

Legendre, P., and Gallagher, E. (2001). Ecologically meaningful transformations for ordination of species data. *Oecologia* 129, 271–280. doi:10.1007/s004420100716

Lehmkuhl, F. (1997). Late Pleistocene, late-glacial and Holocene glacier advances on the Tibetan plateau. *Quat. Int.* 38, 77–83. doi:10.1016/s1040-6182(96)00025-0

Li, J., Dodson, J., Yan, H., Cheng, B., Zhang, X., Xu, Q., et al. (2017). Quantitative precipitation estimates for the northeastern Qinghai-Tibetan Plateau over the last 18,000 years. *J. Geophys. Res. Atmos.* 122, 5132–5143. doi:10.1002/2016jd026333

Li, Y., Huang, C., Ngo, H., Pang, J., Zha, X., Liu, T., et al. (2019). *In situ* reconstruction of long-term extreme flooding magnitudes and frequencies based on geological archives. *Sci. total Environ.* 670, 8–17. doi:10.1016/j.scitotenv.2019.03.066

Li, Y., Huang, C., Ngo, H., Yin, S., Dong, Z., Zhang, Y., et al. (2021). Analysis of event stratigraphy and hydrological reconstruction of low-frequency flooding: A case study on the fenhe river, China. *J. Hydrology* 603, 127083. doi:10.1016/j.jhydrol.2021.127083

Li, Z., and Gao, P. (2019). Channel adjustment after artificial neck cutoffs in a meandering river of the Zoige basin within the Qinghai-Tibet Plateau, China. *Catena* 172, 255–265. doi:10.1016/j.catena.2018.08.042

Lillios, K., Blanco-González, A., Drake, B., and López-Sáez, J. (2016). Mid-late Holocene climate, demography, and cultural dynamics in iberia: A multi-proxy approach. *Quat. Sci. Rev.* 135, 138–153. doi:10.1016/j.quascirev.2016.01.011

Liu, Q., Torrent, J., Maher, B., Yu, Y., Deng, C., Zhu, R., et al. (2005). Quantifying grain size distribution of pedogenic magnetic particles in Chinese loess and its significance for pedogenesis. *J. Geophys. Res. Solid Earth* 110, B11102. doi:10.1029/2005jb003726

Lu, S., Zhu, L., and Yu, J. (2012). Mineral magnetic properties of Chinese paddy soils and its pedogenic implications. *Catena* 93, 9–17. doi:10.1016/j.catena.2012.01.002

Lutz, A., Immerzeel, W., Kraaijenbrink, P., Shrestha, A., and Bierkens, M. (2016). Climate change impacts on the upper indus hydrology: Sources, shifts and extremes. *PLoS One* 11, e0165630. doi:10.1371/journal.pone.0165630

Ma, J., and Xu, G. (1982). Extreme flood of the upper Yellow River in the fall of 1981. *Meteorol. Mon.* 8, 7–9. (In Chinese). doi:10.7519/j.issn.1000-0526.1982.04.002

Mei, S. (1988). Application of rock chemistry in the study of presinian sedimentary environment and the source of uranium mineralization in Hunan province. *Hunan Geol.* 7, 25–49. (In Chinese with English abstract).

Mischke, S., and Zhang, C. (2010). Holocene cold events on the Tibetan Plateau. *Glob. Planet. Change* 72, 155–163. doi:10.1016/j.gloplacha.2010.02.001

Munoz, S., Giosan, L., Therrell, M., Remo, J., Shen, Z., Sullivan, R., et al. (2018). Climatic control of Mississippi River flood hazard amplified by river engineering. *Nature* 556, 95–98. doi:10.1038/nature26145

Patterson, W., Dietrich, K., Holmden, C., and Andrews, J. (2010). Two millennia of North Atlantic seasonality and implications for Norse colonies. *Proc. Natl. Acad. Sci.* 107, 5306–5310. doi:10.1073/pnas.0902522107

Pawłowski, D., Kowalewski, G., Milecka, K., Płóciennik, M., Woszczyk, M., Zieliński, T., et al. (2015). A reconstruction of the palaeohydrological conditions of a flood-plain: A multi-proxy study from the grabia river valley mire, central Poland. *Boreas* 44, 543–562. doi:10.1111/bor.12115

Pears, B., Brown, A., Toms, P., Wood, J., Sanderson, D., and Jones, R. (2020). A sub-centennial-scale optically stimulated luminescence chronostratigraphy and late Holocene flood history from a temperate river confluence. *Geology* 48, 819–825. doi:10.1130/g47079.1

Peng, Y., Xiao, J., Nakamura, T., Liu, B., and Inouchi, Y. (2005). Holocene East Asian monsoonal precipitation pattern revealed by grain-size distribution of core sediments of Daihai Lake in Inner Mongolia of north-central China. *Earth Planet. Sci. Lett.* 233, 467–479. doi:10.1016/j.epsl.2005.02.022

Petr, L., Sádlo, J., Žáčková, P., Lisá, L., Novák, J., Rohovec, J., et al. (2013). Late-glacial and Holocene environmental history of an oxbow wetland in the polabí lowland (river elbe, Czech republic); a context-dependent interpretation of a multi-proxy analysis. *Folia Geobot.* 49, 137–162. doi:10.1007/s12224-013-9171-3

Ringnér, M. (2008). What is principal component analysis? *Nat. Biotechnol.* 26, 303–304. doi:10.1038/nbt0308-303

Sedláček, J., Kapustová, V., Šimíček, D., Bábek, O., and Sekanina, M. (2019). Initial stages and evolution of recently abandoned meanders revealed by multi-proxy methods in the Odra River (Czech Republic). *Geomorphology* 333, 16–29. doi:10.1016/j.geomorph.2019.02.027

Shehata Ahmed Hussein, A. (2016). *The role of mineral composition, rock permeability, and connate-water composition on the performance of low-salinity waterflooding in sandstone reservoirs*. Doctoral dissertation. College Station, TX: Department of Petroleum Engineering, Texas A&M University, 29–32.

Shen, J., Liu, X., Wang, S., and Matsumoto, R. (2005). Palaeoclimatic changes in the Qinghai Lake area during the last 18,000 years. *Quat. Int.* 136, 131–140. doi:10.1016/j.quaint.2004.11.014

Swierczynski, T., Brauer, A., Lauterbach, S., Martín-Puertas, C., Dulski, P., von Grafenstein, U., et al. (2012). A 1600 yr seasonally resolved record of decadal-scale flood variability from the Austrian Pre-Alps. *Geology* 40, 1047–1050. doi:10.1130/g33493.1

Ter Braak, C. (1983). Principal components biplots and alpha and beta diversity. *Ecology* 64, 454–462. doi:10.2307/1939964

Toonen, W., Kleinhans, M., and Cohen, K. (2012). Sedimentary architecture of abandoned channel fills. *Earth Surf. Process. Landforms* 37, 459–472. doi:10.1002/esp.3189

Toonen, W., Munoz, S., Cohen, K., and Macklin, M. (2020). "High-resolution sedimentary paleoflood records in alluvial river environments: A review of recent methodological advances and application to flood hazard assessment," in *Palaeohydrology* (Springer), 213–228.

Vogel, H., Russell, J., Cahyarini, S., Bijaksana, S., Wattrus, N., Rethemeyer, J., et al. (2015). Depositional modes and lake-level variability at Lake Towuti, Indonesia, during the past ~29 kyr BP. *J. Paleolimnol.* 54, 359–377. doi:10.1007/s10933-015-9857-z

Wan, H., Huang, C., and Pang, J. (2015). Major elements in the Holocene loess-paleosol sequence in the upper reaches of the Weihe River valley, China. *J. Arid Land* 8, 197–206. doi:10.1007/s40333-015-0020-5

Wang, Y., Cheng, H., Edwards, R., He, Y., Kong, X., An, Z., et al. (2005). The Holocene asian monsoon: Links to solar changes and north atlantic climate. *Science* 308, 854–857. doi:10.1126/science.1106296

Wang, J., Liang, Z., Wang, D., Liu, T., and Yang, J. (2016). Impact of climate change on hydrologic extremes in the upper basin of the Yellow River basin of China. *Adv. Meteorology* 2016, 1–13. doi:10.1155/2016/1404290

Wang, D., Li, Z., Li, Z., Pan, B., Tian, S., and Nie, X. (2020). Environmental gradient relative to oxbow lake-meandering river connectivity in Zoige Basin of the Tibetan Plateau. *Ecol. Eng.* 156, 105983. doi:10.1016/j.ecoleng.2020.105983

Wang, S., and Xue, B. (1997). Environmental evolution of zoigê basin since 900 ka B.P. And comparison study with loess plateau. *Sci. China Ser. D-Earth Sci.* 26, 329–336. (in Chinese). doi:10.1007/bf02877543

Wang, Z. (2012). Estimation of PMF for large-sized hydropower stations at the upper reach of longyangxia hydropower station on the Yellow River. *Northwest Hydropower* 130, 1–6. (In Chinese with English abstract). doi:10.3969/j.issn.1006-2610.2012.01.001

Wennrich, V., Minyuk, P., Borkhodoev, V., Francke, A., Ritter, B., Nowaczyk, N., et al. (2014). Pliocene to Pleistocene climate and environmental history of Lake El'gygytgyn, Far East Russian Arctic, based on high-resolution inorganic geochemistry data. *Clim. Past* 10, 1381–1399. doi:10.5194/cp-10-1381-2014

Wilhelm, B., Ballesteros Cánovas, J., Macdonald, N., Toonen, W., Baker, V., Barriendos, M., et al. (2018). Interpreting historical, botanical, and geological evidence to aid preparations for future floods. *Wiley Interdiscip. Rev. Water* 6, e1318. doi:10.1002/wat2.1318

Wolfe, B., Hall, R., Last, W., Edwards, T., English, M., Karst-Riddoch, T., et al. (2006). Reconstruction of multi-century flood histories from oxbow lake sediments, Peace-Athabasca Delta, Canada. *Hydrol. Process.* 20, 4131–4153. doi:10.1002/hyp.6423

Woolway, R., and Merchant, C. (2019). Worldwide alteration of lake mixing regimes in response to climate change. *Nat. Geosci.* 12, 271–276. doi:10.1038/s41561-019-0322-x

Wu, R. (1993). Magnetic susceptibility (χ) and frequency dependent susceptibility (χ_{fd}) of lake sediments and their paleoclimatic implication. *J. Lake Sci.* 5, 128–135. (In Chinese with English abstract). doi:10.18307/1993.0204

Xiao, J., Xu, Q., Nakamura, T., Yang, X., Liang, W., and Inouchi, Y. (2004). Holocene vegetation variation in the daihai lake region of north-central China: A direct indication of the asian monsoon climatic history. *Quat. Sci. Rev.* 23, 1669–1679. doi:10.1016/j.quascirev.2004.01.005

Xiao, Q., Zhang, Y., Wang, N., Huang, C., Qiu, H., Zhu, Y., et al. (2022). Paleochannel of the Yellow River within the Zoige Basin and its environmental significance on the NE Tibetan plateau. *Sci. Total Environ.* 853, 158242. doi:10.1016/j.scitotenv.2022.158242

Yang, H., Zhao, Y., Cui, Q., Ren, W., and Li, Q. (2020). Paleoclimatic indication of X-ray fluorescence core-scanned Rb/Sr ratios: A case study in the Zoige Basin in the eastern Tibetan plateau. *Sci. China Earth Sci.* 64, 80–95. doi:10.1007/s11430-020-9667-7

Zhang, Y., Huang, C., Pang, J., Zha, X., Zhou, Y., Zhou, Z., et al. (2012). Geochemical characteristics of the Holocene flooding slackwater deposits in the lower reaches of the Jinghe river. *Acta Sedimentol. Sin.* 30, 900–908. (In Chinese with English abstract). doi:10.14027/j.cnki.cjxb.2012.05.020

Zhang, G., Yao, T., Xie, H., Yang, K., Zhu, L., Shum, C. K., et al. (2020). Response of Tibetan Plateau lakes to climate change: Trends, patterns, and mechanisms. *Earth-Science Rev.* 208, 103269. doi:10.1016/j.earscirev.2020.103269

Zheng, J., Ge, Q., and Zhang, P. (1999). Abrupt climatic change: Evidence and implication. *Adv. Earth Sci.* 14, 76–81. (In Chinese with English abstract). doi:10.3321/j.issn:1001-8166.1999.02.013

Zhou, L., Oldfield, F., Wintle, A., Robinson, S., and Wang, J. (1990). Partly pedogenic origin of magnetic variations in Chinese loess. *Nature* 346, 737–739. doi:10.1038/346737a0

Zhou, W., Yu, S., Burr, G., Kukla, G., Jull, A., Xian, F., et al. (2010). Postglacial changes in the asian summer monsoon system: A pollen record from the eastern margin of the Tibetan plateau. *Boreas* 39, 528–539. doi:10.1111/j.1502-3885.2010.00150.x

Zhou, W., Liu, T., Wang, H., An, Z., Cheng, P., Zhu, Y., et al. (2016). Geological record of meltwater events at Qinghai Lake, China from the past 40 ka. *Quat. Sci. Rev.* 149, 279–287. doi:10.1016/j.quascirev.2016.08.005

Zhou, X., Xu, M., Wang, Z., Yu, B., and Shao, X. (2019). Responses of macroinvertebrate assemblages to environmental variations in the river-oxbow lake system of the Zoige wetland (Bai River, Qinghai-Tibet Plateau). *Sci. Total Environ.* 659, 150–160. doi:10.1016/j.scitotenv.2018.12.310

frontiers | Frontiers in Earth Science

TYPE Original Research
PUBLISHED 13 March 2023
DOI 10.3389/feart.2023.1106920

OPEN ACCESS

EDITED BY
Biswajeet Pradhan,
University of Technology Sydney, Australia

REVIEWED BY
Jianqi Zhuang,
Chang'an University, China
Hongchao Zheng,
Tongji University, China
Kun He,
Southwest Jiaotong University, China

*CORRESPONDENCE
Shengtao Zhou,
stzhou@cug.edu.cn

SPECIALTY SECTION
This article was submitted to Geohazards and Georisks, a section of the journal Frontiers in Earth Science

RECEIVED 24 November 2022
ACCEPTED 27 February 2023
PUBLISHED 13 March 2023

CITATION
Dai Z, Zhou S, Yin Y, Fu X, Zhang Y, Guo J, Du Z, Tao Y and Wu X (2023), Experimental study on the mechanical properties and failure modes of BFRP bar anchor systems under static tension loading.
Front. Earth Sci. 11:1106920.
doi: 10.3389/feart.2023.1106920

Experimental study on the mechanical properties and failure modes of BFRP bar anchor systems under static tension loading

Zhenwei Dai[1], Shengtao Zhou[2,3]*, Yueping Yin[4], Xiaolin Fu[1], Yanjun Zhang[1], Jinjun Guo[5], Zhigang Du[5], Yawen Tao[6] and Xiaolei Wu[7]

[1]Wuhan Center, China Geological Survey (Central South China Innovation Center for Geosciences), Wuhan, China, [2]Faculty of Engineering, China University of Geosciences, Wuhan, China, [3]Oulu Mining School, University of Oulu, Oulu, Finland, [4]China Institute of Geo-environment Monitoring, Beijing, China, [5]School of Civil Engineering, Luoyang Institute of Science and Technology, Luoyang, China, [6]College of Civil Engineering and Architecture, Henan University of Technology, Zhengzhou, China, [7]School of Civil Engineering, Henan Polytechnic University, Jiaozuo, China

Basalt fiber-reinforced polymer bars are lightweight composite materials with high strength, low density, and excellent corrosion resistance. The anchor system made from basalt fiber-reinforced polymer bars is worthy of being developed and expected to be used in rock anchoring projects. In this work, four different basalt fiber-reinforced polymer anchor systems were designed, the influences of different design parameters on the ultimate bearing capacity of the anchor system were investigated through tension tests, and the failure modes of different anchor systems were elucidated. The test results indicated that failure modes, such as the transverse fracture of these bars and debonding of the bonding medium, were widely present in the wedge-modified anchor system and the steel-pipe-protected anchor system. These two anchor systems performed poorly with the wedge anchorage, whereas the basalt fiber-reinforced polymer bars protected by seamless steel pipes burst under the tension imposed by a universal testing machine. The threaded steel-pipe-bonded anchor system and the steel strand–basalt fiber-reinforced polymer bar composite anchor system had maximum anchorage efficiency coefficients of 97.7% and 98.5%, respectively. The bars in the corresponding test groups all exhibited burst failure, indicating that these two anchoring structures achieved effective anchorage of the basalt fiber-reinforced polymer bars.

KEYWORDS

basalt fiber-reinforced polymer bar, rock anchoring, anchor system, ultimate bearing capacity, failure mode

Abbreviations: BFRP, Basalt fiber-reinforced polymer; CRD, Cleaned of rust in the coupler and dried; CG, Cut grooves; CRO, Cleaned of rust and oil; PS, Paste quartz sand on the steel strand; SBCAS, Steel strand–BFRP bar composite anchor system; SBAS, Steel sleeve-protected BFRP anchor system; SS, Sprayed fine steel shot; TSAS, Threaded steel-pipe-bonded anchor system; UBC, Ultimate bearing capacity; UCS, Uniaxial compressive strength; WMAS: Wedge-modified anchor system.

1 Introduction

Prestressed anchor cables have been widely applied as an effective rock mass reinforcement method in slopes (Koca et al., 2011; Yang et al., 2015; Xu et al., 2018), tunnels (Gao et al., 2016; Sun et al., 2019), mine roadways (Cao et al., 2020; Shan et al., 2022), dams (Brown, 2015), geological disasters (Zheng H. et al., 2021; Xia et al., 2022; Yin et al., 2022), and other projects (Tistel et al., 2017; Zheng K. et al., 2021). Prestressed anchor cables are usually made of steel strands or high-strength steel wires. Steel is prone to stress corrosion in humid environments and brackish groundwater (Zhu et al., 2022), leading to a loss in the prestress of the anchor cable (Wang et al., 2019; Ma et al., 2021). After a substantial loss of prestressing, the stability of the rock mass is affected, easily causing a series of geological disasters, such as landslides or the collapse of underground cavities (Yi et al., 2014; Wang et al., 2018; Guo et al., 2020; Li et al., 2020; Zhu et al., 2020). In rock engineering, prestressed anchor cables are always buried deep in rock masses. Their corrosion conditions are detected using non-destructive techniques (Furse et al., 2009; Xu and Li, 2011; Ivanović and Neilson, 2013; Shi et al., 2018), significantly increasing the anchor cable operation and maintenance costs. The durability of prestressed anchor cables has recently become a topic of major interest in the rock anchoring field. Many studies have attempted to protect steel anchor cables by coating the cable with resin or zinc (Zhang, 2015; Meikle et al., 2017). However, these protective treatment methods can only prolong the service life of the anchor cables and cannot fundamentally resolve the problem of corrosion.

Basalt fiber-reinforced polymer (BFRP) bars are an advanced high-strength material. Their tensile strength is approximately 3–4 times higher than that of ordinary rebar, and their density is approximately 1/3–1/4 of that of prestressed steel bars. They can not only resist static loads, but also resist dynamic loads including fluctuating pressure (Zheng et al., 2022), explosion (Feng et al., 2017), and blast vibration (Zhou et al., 2023). Moreover, since they are resistant to acid and alkali corrosion (Inman et al., 2017; Xu et al., 2019; Li et al., 2021; Mohamed et al., 2021), BFRP bars could provide a reliable way to solve the corrosion of steel prestressed anchor cables. Therefore, they are expected to be widely applied in the rock anchoring field. In recent years, BFRP bars have mainly been applied in structural engineering. The use of BFRP bars can improve the stiffness and crack resistance of concrete sections, the structures durability of concrete (Wu and Yamamoto, 2013), and the yielding and ultimate load of the structure (Wang et al., 2015). Moreover, it is indicated from the blast experiments that the engineering structures reinforced with BFRP bars have a higher loading-bearing capacity (Lan et al., 2022; Zhao et al., 2022). BFRP bars are mostly used to make bolts in the field of geotechnical engineering. Although the bonding performance between the BFRP bolt and the grouting body is slightly worse than that of the steel bolt, the ultimate bearing capacity (UBC) of the BFRP bolt and the steel bolt is close. When applying it in the loess slope, the failure mode of the BFRP bolt anchor system is controlled by the relative interface strength of the bolt anchor system (Feng et al., 2019a; Feng et al., 2019b). It is indicated from the field support tests that BFRP bolts can be effectively applied to soil slope support (Zhao et al., 2016; Gao et al., 2017).

Since BFRP was developed after aramid fiber-reinforced polymer, carbon fiber-reinforced polymer, and glass fiber-reinforced polymer, the anchorage used for BFRP bars is still in its infancy. Aramid fiber-reinforced polymer has poor creep resistance and is prone to large deformation under long-term load. When glass fiber-reinforced polymer is bonded with alkaline concrete, a slow chemical reaction will occur, so it is not particularly suitable for bonding with concrete directly. Carbon fiber-reinforced polymer is expensive and has a poor ability to coordinate deformation with concrete. But BFRP bars perform well in these aspects, so it is valuable to develop the BFRP anchor system. When using the industrial wedges applicable to steel strand anchor cables and GFRP anchor cables to tension BFRP bars, the anchoring efficiency of BFRP bars is between 59% and 79% (Motwani et al., 2020), so these existing wedges cannot be used directly. A variable-stiffness composite wedge suitable for BFRP bars was designed to improve the anchoring efficiency by Wang et al. (2020) and Shi et al. (2022). This wedge is wound with organic materials of different stiffnesses from the loading end to the free end. When using this wedge to hold the BFRP bar, the anchoring efficiency could reach as high as 91%, so this wedge can effectively avoid the notch effect and increase the UBC of the BFRP anchor system.

Although the use of the variable-stiffness composite wedge in applications has been shown to be feasible, this special wedge still cannot be widely applied due to its complex processing requirements. To produce a BFRP anchor system with a good anchoring effect and low processing difficulty, in this study, we designed four different BFRP anchor systems, investigated the impact of different design parameters on their UBCs, and elucidated the failure modes of the different anchor systems.

2 Load transfer material of the BFRP anchor systems

Anchoring structures for FRP bar anchor systems can be either mechanical or bonded. In mechanical anchoring structures, the stiffness of the wedge affects the stress of its tip. When the wedge stiffness is very high, a notch effect will appear at the tip, and the FRP bar will fail through transverse fracture, preventing its UBC from being reached. In bonded anchoring structures, the bonding strength of each interface in the anchoring cable structure is affected by the bonding material strength. When the bonding material strength is low, the bonding interface fails first without destroying the FRP bars. Regardless of whether a mechanical or bonded anchoring structure is used, it is critical to select an appropriate wedge material and bonding material for load transfer. In the manufacturing of these anchoring structures, different types of epoxy resins to prepare eight kinds of load transfer materials were used, i.e., Type A-G resins. Their mixing ratio designs are shown in Table 1.

To evaluate the strength and hardening characteristics of the load transfer materials, a large number of resin samples were prepared with curing times of 7, 14, and 28 days according to the mixing ratios of the eight materials mentioned above. The preparation process involved six steps: dosing materials, blending, pouring, curing, demolding, and polishing and cutting. The samples

TABLE 1 Mixing ratio design of load transfer materials.

Name	Composition of material	Mixing ratio
Type A	128 epoxy resin, curing agent, accelerator	100:75:3.5
Type B	128 epoxy resin, curing agent, accelerator, 9-mm-long basalt fiber	100:75:3.5:15
Type C	Bisphenol A epoxy resin, curing agent	100:10
Type D	Bisphenol A epoxy resin, curing agent	100:50
Type E	XT-modified epoxy resin, polyamide resin, acetone, curing agent	100:50:10:100
Type F	XT general purpose epoxy, polyamide resin, acetone, hardener, quartz sand, steel fiber	100:50:10:100:150:35
Type G	XT-A deep penetrating epoxy, polyamide resin, acetone, curing agent, quartz sand, steel fiber	100:50:10:100:150:35
Type H	XT-modified epoxy resin, polyamide resin, acetone, hardener, quartz sand, steel fiber	100:50:10:100:150:35

(Note: 128 epoxy resin was manufactured by Shanxi Guangling Epoxy Paint Co., Ltd., bisphenol A epoxy resin was manufactured by Nanjing Mankate Company, and the epoxy resin materials in Types E-H were manufactured by Guangzhou Huaguan Engineering Co., Ltd.).

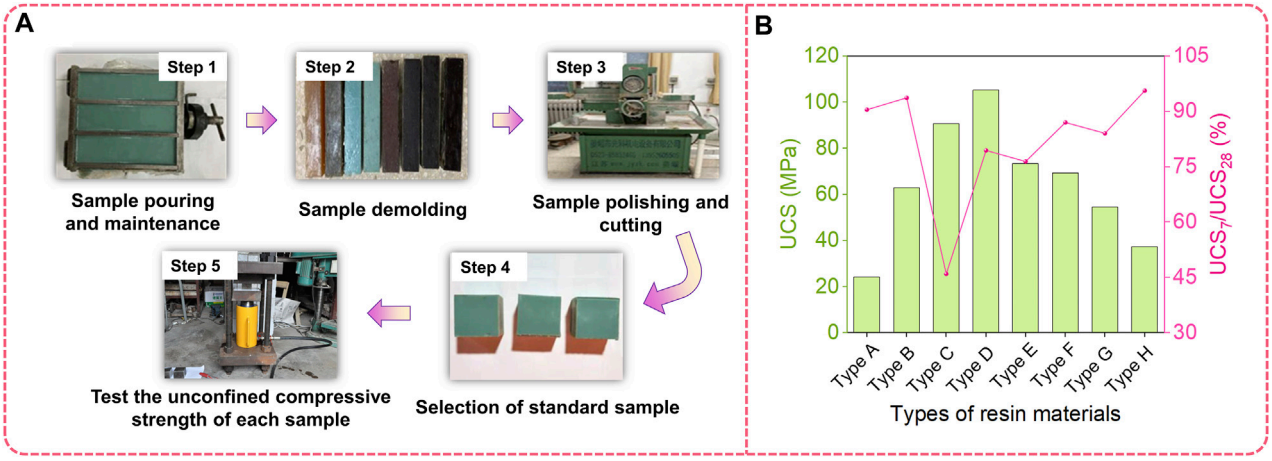

FIGURE 1
UCS test preparation steps and test results of different loading transfer materials: **(A)** UCS test preparation steps, **(B)** UCS test results of eight loading transfer materials.

were demolded 48 h after pouring and then maintained at a temperature of 18°C ± 2°C and humidity of 50%. Upon completion, the YBZ2×2(1.5)-50(63) oil pump with the YDC-650 center hole jack was used for a UCS test. The key process for the preparation of load transfer materials and the mechanical test is shown in Figure 1A. Each group contained three epoxy resin material samples to eliminate the errors resulting from sample discreteness. Furthermore, the ratio of the UCS of the material at 7 days to that at 28 days were selected to evaluate the early strength. The test results are shown in Figure 1B.

As shown in Figure 1B, Type D resin has the highest UCS, and after 7 days of curing, the strength of Type H resin can reach more than 95% of the final UCS. According to the early strength ratio of the eight resins, Type B, D, and F resins have high UCS and a high hardening efficiency. Hence, these three resins could be considered to have good performance.

3 Design and test process of BFRP anchor systems

Mechanical anchorage is one of the most widely used methods among rock mass reinforcement methods. The wedge is generally made of high-stiffness steel in the traditional mechanical anchor system. However, steel wedges cannot be directly applied as anchors to FRP bars due to the notch effect. Thus, it is important to either modify the steel wedge or design a new anchor system. In this case, reducing the wedge stiffness, protecting the BFRP bars, or using a bonded anchor system may be effective methods. In this study, four anchor systems and tested their ultimate bearing capacity were developed. These four anchor systems are the wedge-modified anchor system, the steel sleeve-protected BFRP anchor system, the threaded steel-pipe-bonded anchor system, and the steel strand–BFRP bar composite anchor system.

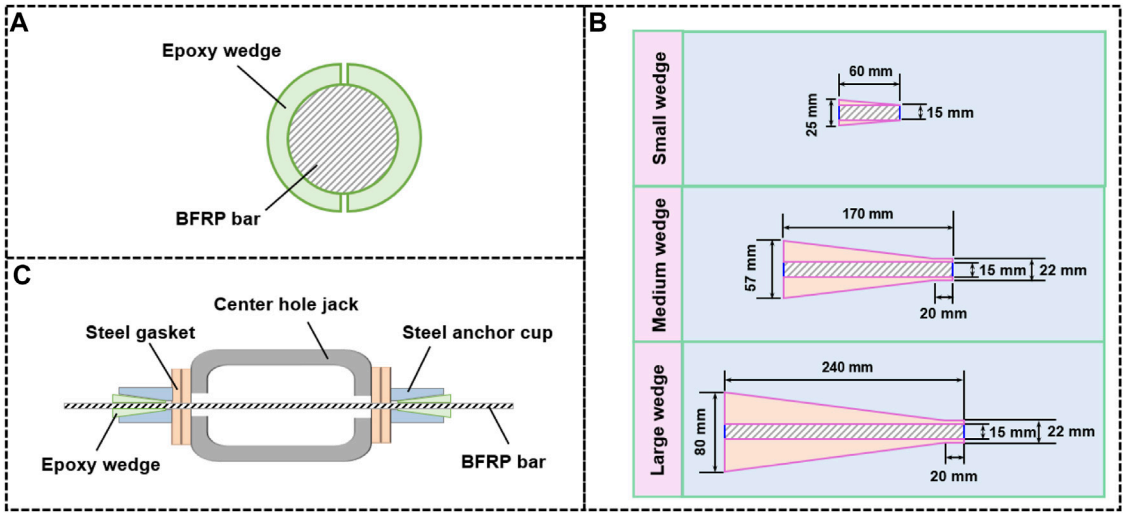

FIGURE 2
Structure of key components in the TSAS and the corresponding tension device: **(A)** Wedge holding methods in WMAS, **(B)** Epoxy wedges with different sizes, **(C)** Tension device of the TSAS.

TABLE 2 Tensioning test design of the WMAS under static load.

No.	Wedge material	Type of BFRP bar	Wedge size
W1	Type F	Smooth	Small
			Medium
			Large
W2	Type B	Smooth	Medium
W3	Type F	Sand bonded	Small
			Medium
			Large
W4	Type B	Sand bonded	Medium
			Large

3.1 Wedge-modified anchor system

When modifying the wedge, we directly use an epoxy resin wedge to hold the BFRP bar, as shown in Figure 2A. In this design, the epoxy resin wedge reduces the stiffness of the wedge tip.

The wedge size usually has a strong impact on the wedge holding force. In this test, three types of epoxy wedges were made with different sizes, namely, large, medium, and small wedges, as shown in Figure 2B. The inner wall of these wedges has internal threads with a tooth height of 2–2.5 mm. Type B and F resins were chosen to make these epoxy wedges because they harden rapidly and have high strength. Under these conditions, wedge fabrication was more rapid, and the wedge could withstand high stress.

In this test, the diameter of the BFRP bar was 12.6 mm, and the corresponding strength and elastic modulus were 1,170 MPa and 45 GPa, respectively. Depending on whether sand was bonded to the surface, BFRP bars were divided into sand-bonded BFRP bars and smooth BFRP bars. Five groups of tensioning tests were carried out by YDC-650 center hole jack and YBZ2×2(1.5)-50(63) oil pump, as shown in Table 2. Resin wedges were used in Groups J1-J4, and a 40Cr steel wedge with a coating group was used in Group J5. When tensioning the BFRP bar, the load was applied at a constant rate of 100 MPa/min based on the Chinese Standard JGJ 85–2010. When the load reached 20% and 40% of the nominal UBC of the BFRP bar, the load was maintained for 10 min. After the load reached 50% of the nominal UBC, the load was maintained for 20 min. Then, the loading was continually applied until the WMAS failed. The corresponding tensioning test device is shown in Figure 2C.

3.2 Steel sleeve-protected BFRP anchor system

In addition to WMAS, we also fabricated the SBAS wedge anchor system. With a steel sleeve bonded to the outside of the BFRP bar and clamped by the wedge, in this structure the steel sleeve rather than the BFRP bar bears the radial pressure at the wedge tip. Bivalve, trivalve, and seamless steel sleeves with a length of 300 mm were used in this test. The bivalve and trivalve steel sleeves were processed by cutting equally along the axes of the seamless steel sleeves with a laser. To bond the steel sleeve to the BFRP bar as a single unit, Type D resin with the highest strength was chosen as a bonding medium. The BFRP bars used in this test are the same as for WMAS, and the wedge is made of 40Cr Steel, with a length of 48.8 mm and an inclination of 6°. When the BFRP bars were tensioned, three pieces of wedges held the steel sleeves. To increase the roughness of the inner face of the steel sleeve, a part of the inner wall of the steel sleeve was sandblasted. The cross-sectional view of these three bonded

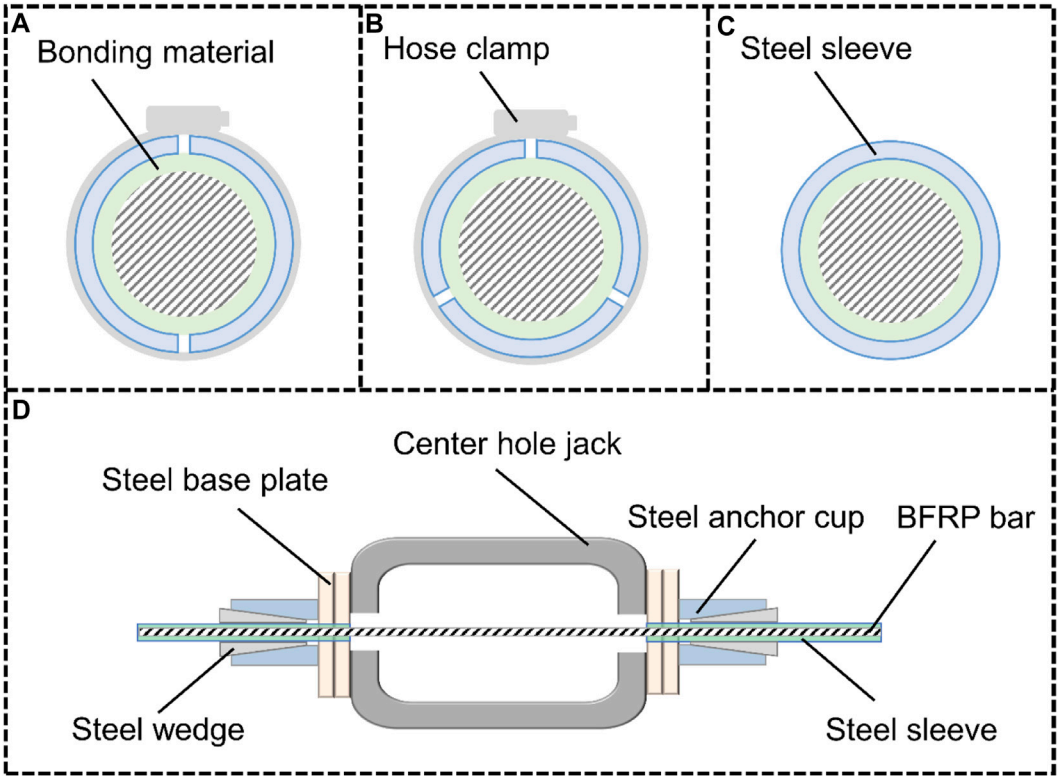

FIGURE 3
Cross-sectional view of bonded structures and the tension device of the SBAS: **(A)** Bivalve steel sleeve, **(B)** Trivalve steel sleeve, **(C)** seamless steel sleeve, **(D)** Tension device of the SBAS.

TABLE 3 Tensioning test parameters of the SBAS.

No.	Number of valves	Material	Steel sleeve processing method	Inner diameter/mm	Outer diameter/mm
S1	2	Q235 steel	Sandblasting	14	16
S2	2	45# steel	Sandblasting	15	17
S3	2	45# steel	Polishing	15	17
S4	3	45# steel	Polishing	15	17
S5	3	45# steel	Sandblasting	15	17
S6	-	45# steel	Polishing	14	17
S7	-	45# steel	Polishing	15	17

structures is shown in Figures 3A–C. Note that the hose clamp was only used in the bonding process and should be removed prior to tensioning.

The bivalve and trivalve SBAS were tensioned with the center hole jack and the 40Cr Steel wedges, as shown in Figure 3D. The loading method and device were the same as in the WMAS. The seamless SBAS was tensioned by a universal testing machine at a loading speed of 100 MPa/min. Seven sets of static load tests were carried out, and more details about the test parameters are shown in Table 3.

3.3 Threaded steel-pipe-bonded anchor system

Although the mechanical anchor system is widely used, the bonded anchor system is also a reliable option. By bonding BFRP bars and the threaded steel pipe, a new TSAS was also developed, as shown in Figure 4A. The anchor cable was composed of two threaded steel pipes, one BFRP bar, and the bonding medium. Both ends of the BFRP bar were centered in and bonded to the threaded steel pipes. Threads were present on both the inner and outer walls of the steel

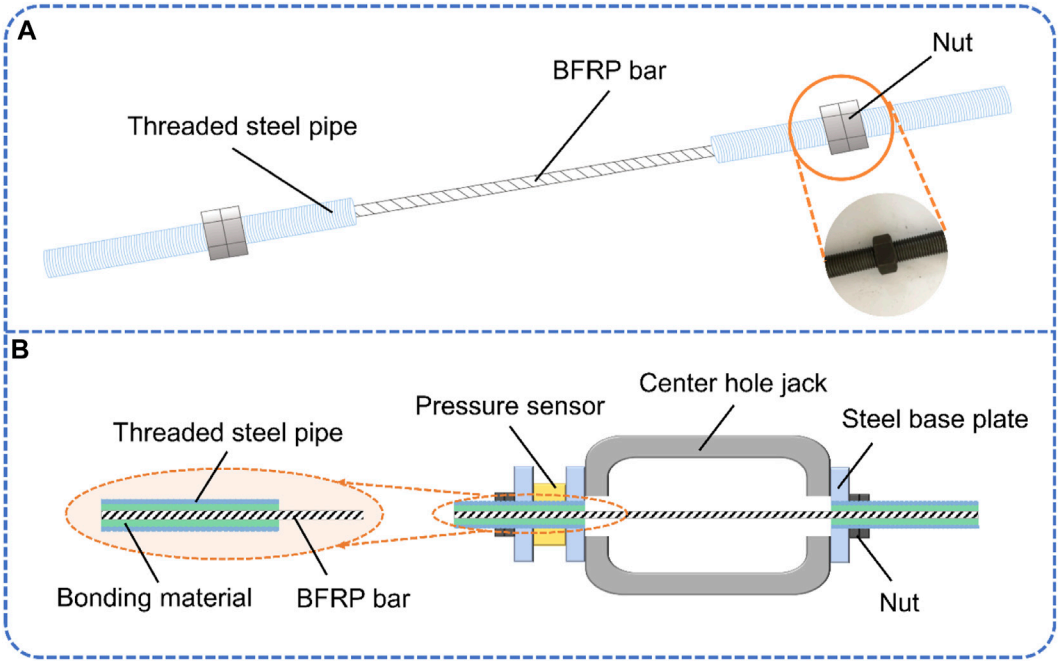

FIGURE 4
Structure of the TSAS and the corresponding tension device: **(A)** Structure of the TSAS, **(B)** Tension device of the TSAS.

TABLE 4 Tensioning test parameters for the TSAS.

No.	Material of steel pipe	Bonding material	Threaded steel pipe parameter (mm)	Inner diameter of threaded steel pipe (mm)	Number of BFRP bars
T1	45# steel	Type A resin	M30*300	15	1
T2	45# steel	Type B resin	M30*300	15	1
T3	45# steel	Type C resin	M30*300	15	1
T4	45# steel	Type D resin	M30*300	15	1
T5	45# steel	Type G resin	M22*300	15	1
T6	45# steel	Type D resin	M22*300	15	1
T7	45# steel	Type D resin	M30*300	18	1
T8	40Cr steel	Type D resin	M42*400	32	3

pipe. Two mutually contacting nuts were installed on the outer wall of every steel pipe, and the steel base plate was set inside the two groups of nuts. When the TSAS was tensioned, the center hole jack directly applied the load to the steel base plate, transferring the load to the threaded steel pipe through the nuts to tension the BFRP bar.

The bonding medium is important for preventing premature failure of the interfaces of the TSAS. To ensure sufficient strength of the bond interface, Type D resin was also chosen in this test. Some comparative tests were carried out with Types A, B, and C resins. A sand-bonded BFRP bar with a nominal UBC of 145.9 kN was used. For the threaded steel pipe, the outer threads were used to install the necessary nuts, the inner thread was used to increase the contact area between the inner wall and the bonding medium, and the pitch of these two types of threads was 1 mm. During the tensioning tests, the center hole jack and oil pump same as WMAS and SBAS tests were used (Figure 4B), with a single-stage load of 26.3 kN maintained for 10 min. The load on the TSAS was monitored by the center-hole pressure sensor. For the TSAS, eight groups of tests were carried out, and the details of these tests are shown in Table 4.

3.4 Steel strand–BFRP bar composite anchor system

Inspired by the structures of the above-mentioned wedge anchor system and bonded anchor system, a steel strand–BFRP bar

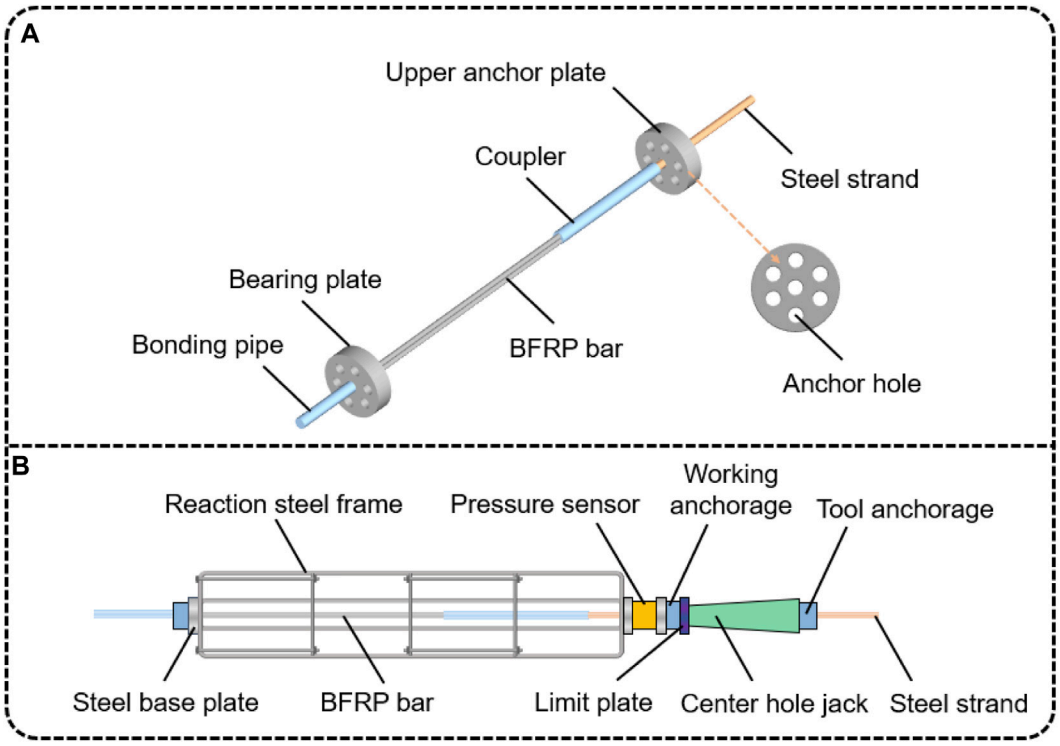

FIGURE 5
Structure of the SBCAS and the corresponding tension device: **(A)** Structure of the SBCAS, **(B)** Tension device of the SBCAS.

composite pressure-type anchor system that combines the advantages of these two typical anchor systems was further developed, as shown in Figure 5A. Three BFRP bars with equal length are bound together as the primary stress component in the SBCAS. One end of the three BFRP bars is bonded to the single-stranded steel strands in the coupler after centering, and the other ends are bonded to the tail bonding pipes. A single steel strand and bonded BFRP bars take half of the length of the coupler. The free end of the steel strand passes through the upper anchor plate, where there are steel wedges for clamping the steel strand. The tail bonding pipe is inserted into the bearing plate. When applying the prestress, the wedge first holds the steel strand, and then the prestress is transferred to the BFRP bar through the coupler.

A 220-cm-long BFRP bar with 20–40 mesh quartz sand on the surface, manufactured by Shanxi ECIC Basalt Development Co., Ltd. was used in this test. This BFRP bar had a tensile strength of 891 MPa. The steel strand had dimensions of 1×7–21.6 mm, and its tensile strength was 1893.7 MPa. Type D resin was poured into the coupler to bond the BFRP bar and the steel strand. With an outer diameter of 38 mm and an inner diameter of 32 mm, the coupler was made of 40Cr steel and has a total length of 80 cm. The tail bonding pipe with a length of 40 cm was also made of 40Cr steel, and a 32 × 1 mm threaded tooth was present on the inner wall.

Prior to the UBC test, a tension test system was assembled, as shown in Figure 5B. The center hole jack applied tension to the steel strand by horizontally pushing the working anchorage. The tail bonding pipe was confined in the bearing plate, the other side of which was provided with a steel base plate in direct contact with the steel reaction frame. This arrangement can convert the tensile force on the BFRP bar into pressure on the reaction frame. The reaction frame was fixed on the ground to provide support for applying prestress to the anchor system. A pressure sensor for the evaluation of the tensile load of the jack was set on the tension side of the anchor system. Two steel base plates were provided on both sides of the pressure sensor. A working anchorage in which a steel wedge was installed to clamp the steel strand was set outside the external steel base plate of the pressure sensor. A limit plate, a center hole jack, and a tool anchorage were arranged in sequence outside the working anchorage.

Some processing parameters of the anchor system (i.e., coupler injection method, steel strand treatment method, and the internal thread pitch of the coupler) were selected as variables in order to evaluate their effects on the UBCs. The three injection methods are as follows:

(1) Water drainage method: fill the water first in the coupler and then pour the Type D resin into the coupler through a catheter to replace the water to ensure that no air bubbles occur.
(2) Direct injection method: Slowly pour the bonding material into the coupler.
(3) Extended injection method: A 10-cm-long PVC pipe was added to the steel strand outlet of the coupler, and the PVC pipe was filled with the bonding material to extend the bonding length of the steel strand.

TABLE 5 UBC test parameters for the SBCAS.

Test group	Number of tested samples	Inner thread pitch	Injection method	Bonding method
C1	6	1 mm	Water drainage	CRO
C2	7	1 mm	Direct injection	CRO
C3	3	1 mm	Direct injection	CRO, CG
C4	3	1 mm	Direct injection	CRO, SS
C5	4	1 mm	Direct injection	CRO, CG, CRD
C6	2	1 mm	Direct injection	CRO, PS, CRD
C7	3	1 mm	Extended injection	CRO, CG, CRD
C8	2	1.5 mm	Extended injection	CRO, CG, CRD

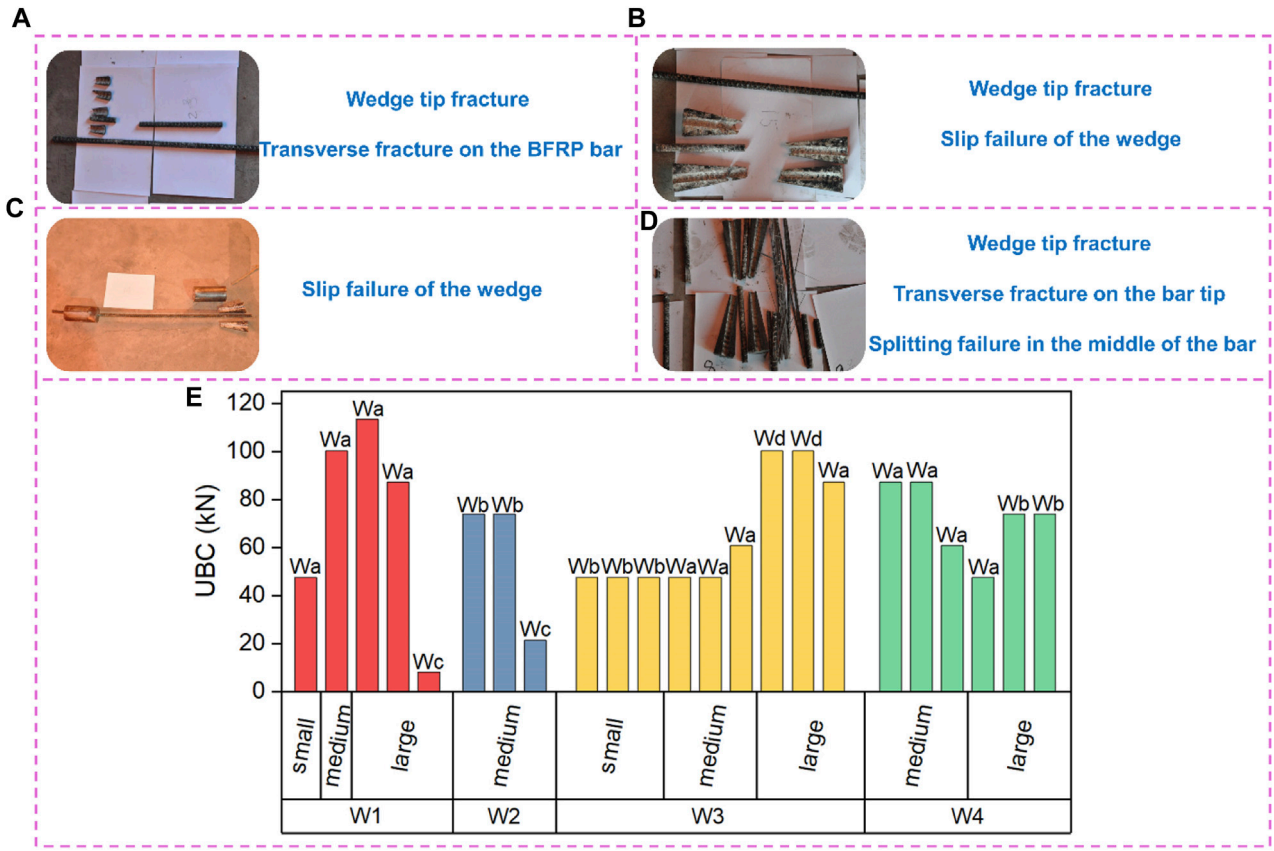

FIGURE 6
Failure modes and UBC test results of the WMASs: **(A)** Failure mode Wa, **(B)** Failure mode Wb, **(C)** Failure mode Wc, **(D)** Failure mode Wd, **(E)** UBC test results of WMASs.

Since the steel strand surface is smooth and often has oil stains and rust, the bonding interface strength between the bonding material and the steel strand is low, and the rust and oil on the bonding section of all steel strands were removed. Furthermore, surface treatment of the steel strand was carried out with three other methods in this test, namely, paste quartz sand onto the steel strand surface, spray of fine steel shot onto the steel strand surface, and 1-mm-deep grooves cut on the steel strand surface at a 3-mm spacing. When carrying out the tests, a YCQ45Q-200 center-hole jack was used. The oil pressure loading gradient of the jack was 2 MPa, and the load was applied at 100 MPa/min until the anchor system failed. More UBC test parameters are listed in Table 5.

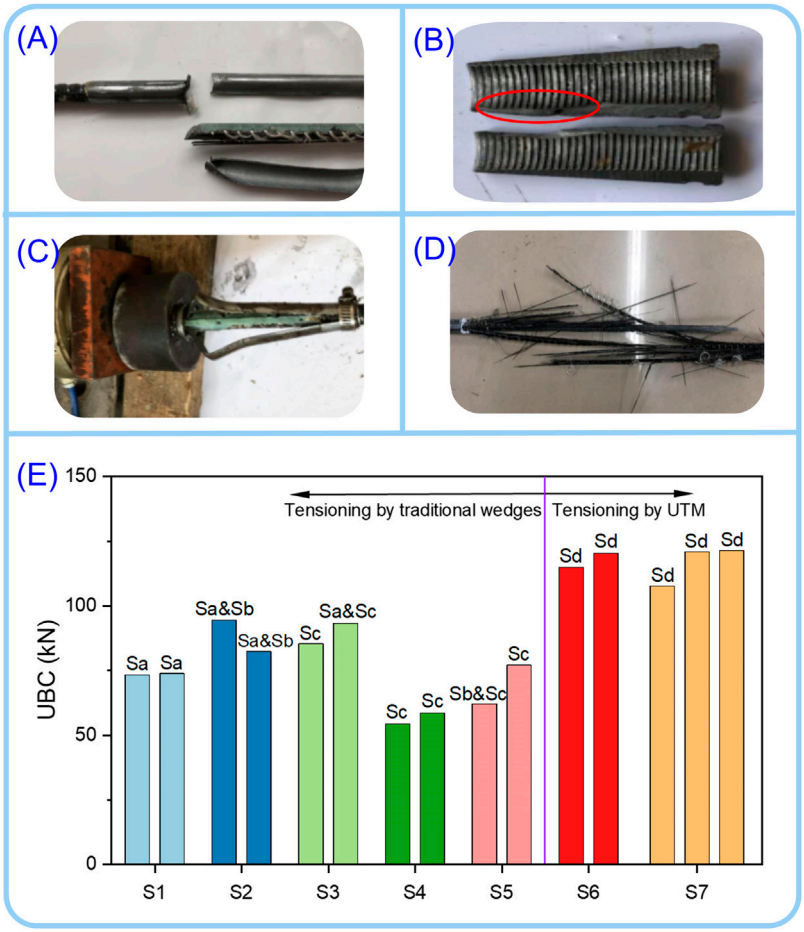

FIGURE 7
Failure modes and UBC test results of the SBAS: **(A)** Transverse fracture of the BFRP bar (Sa), **(B)** local fracture of the wedge (Sb), **(C)** deformation and debonding of the steel sleeve (Sc), **(D)** BFRP bar bursting (Sd), **(E)** UBC test results of the SBAS.

4 Test results

4.1 Tensioning test results of WMAS

When the BFRP bar suffers a tension failure, it will burst instantly. However, the BFRP bars did not burst in any of the WMAS tensioning experiments. Four typical failure modes occurred in these tests, as shown in Figures 6A–D. In the first failure mode, a transverse fracture of the BFRP bar occurred, and the wedge tip failed at the same time. In this case, the transverse strength of the anchor cable is still too low to undergo concentrated stress. Within the second failure mode, the wedge was first damaged and slipped from the anchorage. Only slip failure occurred in another failure mode. The lack of friction between the wedge and the BFRP bar led to wedge slipping. In the two tests where large wedges were used (Group W3), the two WMASs had breakage and transverse fracture on the wedge tip, and local splitting failure occurred on the BFRP bar. All tensioning results are shown in Figure 6E, where the four failure modes are marked as Wa–Wd.

Figure 6E indicates that the UBC of the anchor system increased with the increase in the wedge size in W3. When tensioning, a small wedge had slip failure. For medium and large wedges, the BFRP bars showed transverse breakages, and a lower UBC was obtained during slip failure. Note that except for the sample using the large wedge in group W4, the UBC during slip failure in each test group was lower. In groups W1–W4, the wedge material and type of BFRP bar had little impact on the UBC.

During the above tests, because no total bursting failure occurred with the BFRP bars, these WMASs designed in this study are unreliable. The efficiency coefficient of WMAS was less than 0.9; according to Chinese Standard GB/T 14370-2015, this anchor system can also be regarded as ineffective.

4.2 Tensioning test results of SBAS

When tensioning the SBAS with steel wedges, four failure phenomena were observed alone or in combination, as shown in Figures 7A–D. For the two samples in group S1, the steel sleeve containing the BFRP bar exhibited transverse fracture (Figure 7A). Different from group S1, in group S2, the BFRP bars failed along the cross-section, and the wedges popped out

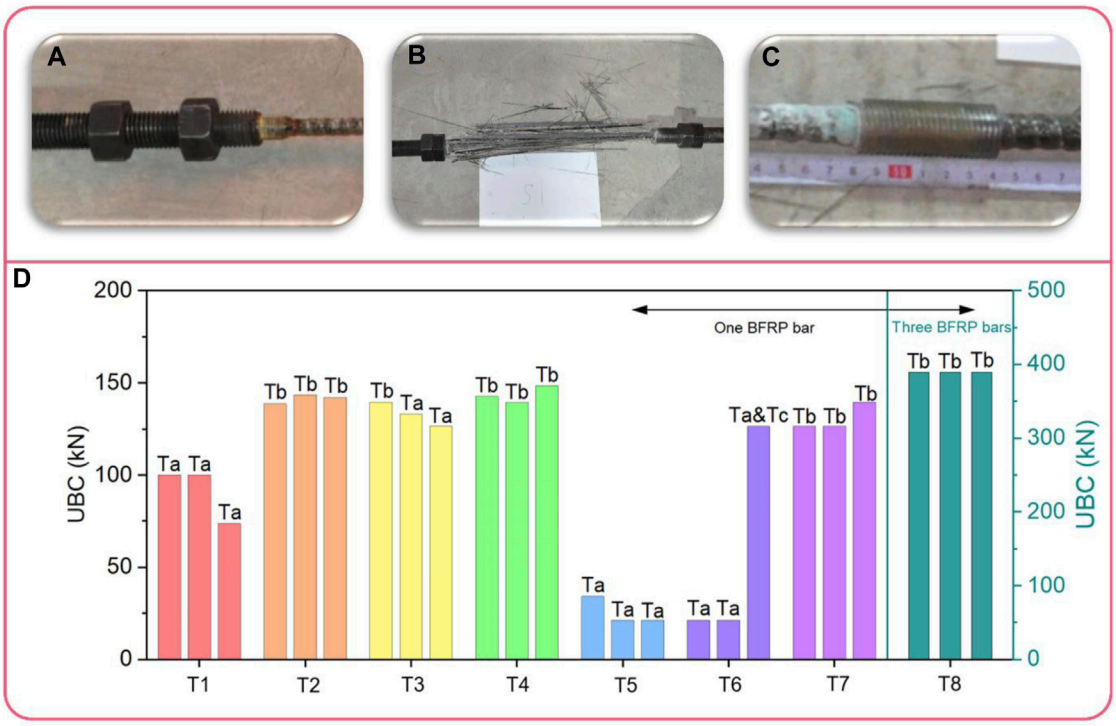

FIGURE 8
Failure modes and UBC test results of the TSAS: **(A)** Slip failure of the interface (Ta), **(B)** BFRP bar bursting (Tb), **(C)** Fracture of the threaded steel pipe (Tc), **(D)** UBC test results of the TSAS.

from the anchorage with a local fracture (Figure 7B). Another type of failure, the steel sleeve deformed and debonded, was observed with all samples in test groups S3–S5 (Figure 7C). Therefore, a steel wedge cannot be used to tension the BFRP bar when an external steel sleeve protects the BFRP bar. When applying the load by the universal testing machine, all samples in the two groups failed with the bursting of BFRP bars (Figure 7D). In this case, the tensile stress in the BFRP bar was greater than the tensile strength, indicating that the ideal failure mode of the BFRP bar occurred. As long as the steel sleeve was not subjected to an excessive holding force, even if the inner wall of the steel sleeve was only polished, the bonding interface between all components did not fail prior to the bursting of the BFRP bar. The UBCs and failure modes of all samples are shown in Figure 7E, and Sa–Sd represents the four failure phenomena in Figures 7A–D.

Burst failure did not occur in the BFRP bars of groups S1–S5. The BFRP bars in groups S1 and S2 failed with transverse fracture, but the UBC of Group S2 was higher because the strength of #45 steel was higher than that of the Q235 steel. The transverse strength of these two types of steel sleeves is not sufficiently high to overcome the notch effect. The anchor systems in groups S4 and S5 had similar failure modes, but the average UBC in group S5 was greater than that in group S4, demonstrating that sandblasting treatment improved the strength of the interface between the steel sleeve and the bonding medium. The trivalve SBASs had a lower UBC than those using bivalve steel sleeves because a greater number of slits in the steel sleeve resulted in lower strength and made it more difficult to resist the external load. After the steel sleeve deformed, it was prone to separating from the bonding medium, causing failure of the anchor system. When the wedge anchorage was not employed, all samples in groups S6–7 failed by bursting, demonstrating that the strength of the interface between the bonding medium and polished steel sleeve was sufficient to maintain the interface completely prior to the bursting of the BFRP bar. In this case, the inner wall of the steel sleeve does not need sandblasting treatment.

4.3 Tensioning test results of TSAS

When loading the TSAS, three different failure modes occurred in the test results, as shown in Figures 8A–D. When the interface strength of the threaded steel pipe and bonding medium is low, slip failure will occur at the bond interface (Figure 8A). The bursting of the BFRP bar also occurred, indicating that the tensile stress in the bar reached the tensile strength, as shown in Figure 8B. The third failure mode was the failure of the threaded steel pipe, which appeared in one sample of group T6, as shown in Figure 8C. The UBCs and the corresponding failure modes are shown in Figure 8D, where the failure modes in Figures 8A–C were marked as Ta–Tc.

Four types of bonding materials were used in T1–T4, and the corresponding slip–load curves for the anchor systems were monitored. All failures of the anchor system in test group

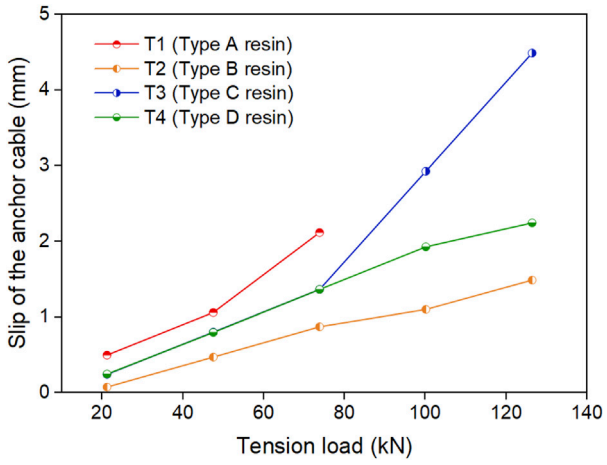

FIGURE 9
Slip–load curves of TSAS with different resins.

T1 were caused by the failure of the interface between the inner wall of the threaded steel pipe and the bonding material. In both groups T2 and T4, all BFRP bars underwent burst failures. This result indicated that the strength of the bonding between Types B and D materials and the threaded steel pipe was sufficient to lead to tension failure of the BFRP bar. For group T3, the interfaces between the bonding material and the threaded steel pipe of the two bonded anchor cables were damaged, and the BFRP bar from one anchor cable underwent burst failure. This result may be associated with the curing process of Type C resin. Since the Type C resin contains a small amount of curing agent, when tensioned, the epoxy resin in some samples may not be completely cured, resulting in low interface strength.

The monitored slip–load curves are given in Figure 9. When using the Type A and C resins as bonding media, the slip–load curves show obvious plastic stages, which is not conducive to the application of prestress. The slip amounts of Type B and D resins both increase linearly with increasing tensile load, demonstrating that they were always in the elastic stage under tensioning. The anchor cable using Type D resin slipped more under the same load. When anchoring the rock mass toward slope treatment or another rock engineering, the reinforced rock mass may deform strongly. Therefore, the anchor cable used in this condition should exhibit larger deformation in the elastic stage to ensure the coordination of deformation between the anchor cable and the rock mass. Although the BFRP bars failed by bursting in group T2, the Type D resin is considered better.

The inner interface of the threaded steel pipe in group T5 detached, and two BFRP bars in group T6 showed interface failure. This result occurred because when the tension load increased, the friction and chemical bonding force on the interface between the bonding material and the steel pipe decreased with the deformation until the interface failed. During this process, the BFRP bar was not damaged. Combined with the tension test results of group T4, it is found that if the steel pipe has a low thickness, the bonding medium easily slips from the steel pipe with the BFRP bar wrapped. In the third sample of group T6, the threaded steel pipe failed with 1 mm threads with a length of 8 cm provided at both ends of this pipe. Upon completion of steel pipe bonding, the bonding media at both ends were slightly thicker than those in the middle. The teeth between the threads and the bonding media are not easily continuously cut off, improving the bonding strength of the interface. Nevertheless, the third sample in group T6 finally failed due to the fracture of the steel pipe. Therefore, when BFRP bars were bonded with threaded steel pipes, pipes with thicker walls should be selected.

In addition to groups T2 and T4, the bursting of the BFRP bar also occurred in groups T7 and T8. With the same bonding material, the average UBC of group T7 was slightly lower than that of group T4, indicating that an increase in the inner diameter of the steel pipe may adversely influence the UBC. The average UBC of groups T4 and T7 was 142.415 kN, with an anchorage efficiency coefficient of 97.7%. All BFRP bars in group T8 also underwent burst failures. The average UBC of a single BFRP bar was only 129.86 kN because the “buckets effect” arises when multiple BFRP bars were subjected to loads simultaneously. In this case, if one of the BFRP bars broke first, the tension load on the other two BFRP bars would instantaneously exceed the tensile strength. As a result, the three BFRP bars in a single threaded steel pipe broke off together. In this case, the UBC of the anchor system depends on the BFRP bar that failed first.

4.4 Tensioning test results of SBCAS

After tensioning tests, four failure modes were observed with the failure of SBCAS. These four failure modes were slipping out of the steel strand (Figure 10A), slip failure of the steel strand (Figure 10B), BFRP bar bursting (Figure 10C) and fracture of the coupler (Figure 10D). They can be simply called Sa–Sd. The average UBC and the corresponding failure mode are shown in Figure 10E.

The samples of groups C1–C4 and C6 had the same failure mode, but their average UBCs differed. Although the strength of the interface between the resin and the steel strand in these five groups is too low and could not ensure the bursting of the BFRP bar, the results indicate that the processing method of SBCAS is important for the interface strength. The UBC of SBCAS using water drainage is lower than that using the direct injection method because in the water drainage method, the water attached to the steel strand surface may weaken the adhesive force. Even if the use of the water drainage method can avoid the creation of air bubbles during the bonding process, the bond strength of the soaked steel strand to the epoxy resin was also reduced. Therefore, the drainage method is not recommended. The CG, SS, PS, and CRD treatments all helped increase the UBC to varying degrees. For the treatment methods of steel strands, the best bonding method is CG, followed by SS, while PS is the worst.

All BFRP bars in test group C7 burst, other parts of the anchoring structure were undamaged, and the anchorage efficiency coefficient was 98.5%, indicating that the extended injection method was better than the direct injection method. In one sample of group C8, the tail bonding pipe was first crushed, and the BFRP bar burst; in another test, the coupler fractured, and then the BFRP bar burst. When using the coupler with an internal thread

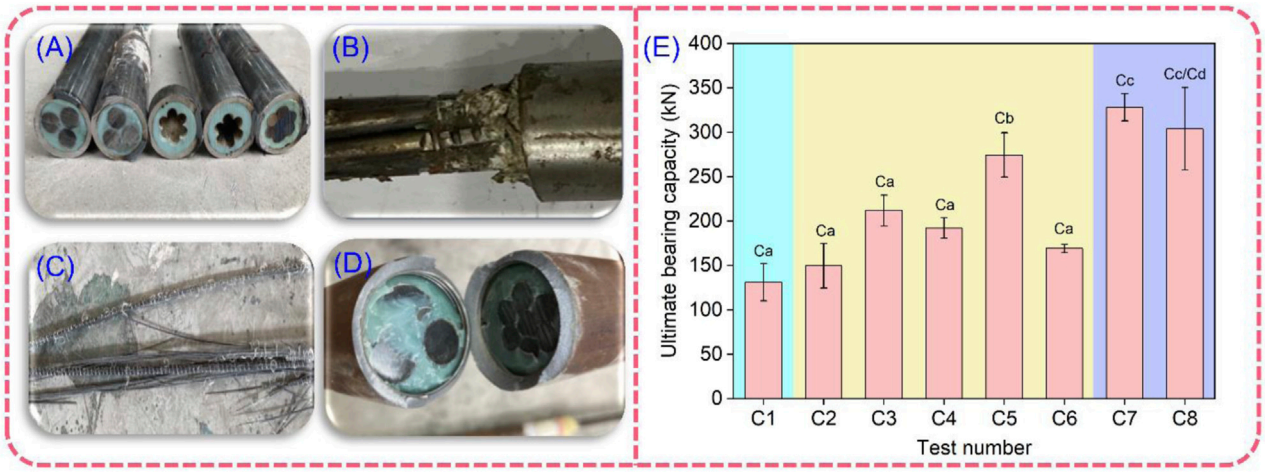

FIGURE 10
Failure modes of the SBCASs and UBC of SBCAS with different manufacturing parameters: **(A)** Slipping out of the steel strand (Ca), **(B)** Slip failure of the steel strand (Cb), **(C)** BFRP bar bursting (Cc), **(D)** Fracture of the coupler (Cd), **(E)** UBC test results of SBCASs.

of 1.5 mm, the UBC of the anchor system was lower than that using the coupler with an internal thread of 1 mm.

5 Discussion

To develop an effective BFRP bar anchor system for rock mass reinforcement, four BFRP bar anchor systems were designed. It is indicated from laboratory tensioning tests that, two anchor systems (TSAS and SBCAS) were identified as feasible, and other anchor systems (WMAS and SBAS) were demonstrated to be unusable. The test results demonstrate that both TSAS and SBCAS can achieve a good anchor effect. Moreover, the processing method and structure of these two anchor systems are also very simple. It should be noted that they also have some shortcomings. For TSAS, the tension load needs to be applied through the nut. The nut has a certain thickness. When multiple BFRP anchor cables were expected to use in one borehole, the thickness of the nut may limit the number of BFRP bars. For the SBCAS, the processing of the anchor system is time-consuming due to the pre-treatment of the steel strands and couplers. In the future, better designs may alleviate these problems.

Due to funding limitations, only a number of tests with limited parameters were carried out in this study. The failure modes and mechanical properties of anchor systems depend strongly on the material used, particularly on the types of steel pipes and resin materials. In the future, more types of load transfer materials and steel pipes should be used to develop more anchor systems, and more precise tests should be carried out, which will not only help us further develop an improved anchor system but also help to understand the coupling effect of different components on the UBC. For the WMAS, when the wedge strength is too high, a transverse fracture of the BFRP bar will occur. By contrast, if the wedge strength is too low, the wedge will fracture during tensioning. Currently, it is difficult to find a suitable material for making wedges directly. However, in future work, a flexible coating inside the steel wedge can be set to overcome the notch effect. For the SBAS, when tensioning with wedge anchors, the relative strength of the steel sleeve and the wedge is critical. The size of the wedge must be considered further. The effectiveness of the remaining two anchor systems has been demonstrated. Several possible directions can be pursued for the further optimization of these anchor systems. In this study, their failure mode and mechanical properties were investigated, but the production costs of anchor systems were still not taken into account. In fact, a superior anchor system requires not only good anchoring properties and a simple production process but also low production costs. Future work should focus on reducing production costs and simplifying the production process while ensuring the performance of these anchor systems.

6 Conclusion

(1) The failure modes of wedge-modified anchor systems include transverse fracture of the basalt fiber-reinforced polymer bar and wedge slip failure. The corresponding efficiency coefficient is less than 90%. The modified resin wedges in this study were not applicable to basalt fiber-reinforced polymer bars.

(2) When a wedge anchorage is used to load a steel sleeve-protected BFRP anchor system, the failure modes of bivalve and trivalve steel sleeve-protected BFRP anchor systems include transverse fracture of the basalt fiber-reinforced polymer bar, deformation and debonding of the sleeve, and breakage and pop-up of the wedge. However, when tensioning the anchor system by the universal testing machine, bursting of the basalt fiber-reinforced polymer bar occurred in the anchor system with a basalt fiber-reinforced polymer bar bonded in a seamless steel sleeve.

(3) When one basalt fiber-reinforced polymer bar was bonded in a #45 steel pipe, the maximum anchorage efficiency coefficient of the threaded steel-pipe-bonded anchor system reached 97.7%. When three basalt fiber-reinforced polymer bars were bonded in

a 40Cr steel pipe, even if the basalt fiber-reinforced polymer bar in this threaded steel-pipe-bonded anchor system still burst, the average ultimate bearing capacity of each basalt fiber-reinforced polymer bar decreased due to the bucket effect. The threaded steel-pipe-bonded anchor system is a reliable anchor system.

(4) For the steel strand–basalt fiber-reinforced polymer bar composite anchor system, the internal thread pitch of the couple should be 1 mm rather than 1.5 mm. The composite anchor system subject to steel strand grooving, coupler rust removal and drying, and extended injection has the highest ultimate bearing capacity, with an anchorage efficiency coefficient of 98.5%. It is regarded as an effective basalt fiber-reinforced polymer anchor system.

Data availability statement

The original contributions presented in the study are included in the article/Supplementary material, further inquiries can be directed to the corresponding author.

Author contributions

ZD: Conceptualization, Funding acquisition, Writing. SZ: Supervision, Writing-Review and Editing. YY: Methodology, Supervision. XF: Formal analysis, Visualization. YZ: Investigation, Writing—Review and Editing. JG: Data Curation, Resources. ZD: Data Curation, Validation. YT: Investigation, Data Curation. XW: Investigation.

Funding

This work was supported by a follow-up of the Geological Disaster Prevention and Control Project in the Three Gorges area (Grant No. 000121 2019C C60 001 and Grant No. 000121 2021C C60 001), the Natural Science Foundation of Hubei Province (Grant No. 2020CFB352), Qianlong Plan Top Talent Project of Wuhan Center of China Geological Survey (Grant No. QL2022-06), the Fundamental Research Funds for National University, China University of Geosciences (Wuhan) (Grant No. CUGDCJJ202217), and the Key Consulting Project of Chinese Academy of Engineering (Grant No. 2021-XZ-1). The second author thanks the China Scholarship Council for the financial support of his studying in Finland (Grant No. 202106410041).

Conflict of interest

The authors declare that the research was conducted in the absence of any commercial or financial relationships that could be construed as a potential conflict of interest.

Publisher's note

References

Brown, E. T. (2015). Rock engineering design of post-tensioned anchors for dams–a review. *J. Rock Mech. Geotech.* 7, 1–13. doi:10.1016/j.jrmge.2014.08.001

Cao, J., Zhang, N., Wang, S., Qian, D., and Xie, Z. (2020). Physical model test study on support of super pre-stressed anchor in the mining engineering. *Eng. Fail Anal.* 118, 104833. doi:10.1016/j.engfailanal.2020.104833

Feng, J., Wang, Y., Wu, H., Lai, B., and Xie, X. (2019a). Field pullout tests of basalt fiber-reinforced polymer ground anchor. *Rock Soil Mech.* 40, 2563–2573. doi:10.16285/j.rsm.2018.0552

Feng, J., Wang, Y., Zhang, Y., Huang, L., He, C., and Wu, H. (2019b). Experimental comparison of anchorage performance between basalt fiber and steel bars. *Rock Soil Mech.* 40, 4185–4193. doi:10.16285/j.rsm.2018.1640

Feng, J., Zhou, Y., Wang, P., Wang, B., Zhou, J., Chen, H., et al. (2017). Experimental research on blast-resistance of one-way concrete slabs reinforced by BFRP bars under close-in explosion. *Eng. Struct.* 150, 550–561. doi:10.1016/j.engstruct.2017.07.074

Furse, C., Smith, P., and Diamond, M. (2009). Feasibility of reflectometry for nondestructive evaluation of prestressed concrete anchors. *IEEE Sens. J.* 9, 1322–1329. doi:10.1109/jsen.2009.2019309

Gao, S., Chen, J., Zuo, C., Wang, W., and Sun, Y. (2016). Structure optimization for the support system in soft rock tunnel based on numerical analysis and field monitoring. *Geotech. Geol. Eng.* 34, 1089–1099. doi:10.1007/s10706-016-0029-3

Gao, X., Xie, Q., Zhao, W., and Hu, Y. (2017). Experimental study on determining design parameters of non-prestressed BFRP anchor for supporting soil slope. *J. Highw. Transp. Res. Dev.* 34, 20–28+36. doi:10.3969/j.issn.1002-0268.2017.07.004

Guo, J., Zhang, P., Zhang, Q., Huang, B., and Qin, Z. (2020). Study on landslide hazard identification Technology based on multispectral remote sensing images in Wu gorge. *Geol. Mineral Resour. South China* 36 (2), 38–45. doi:10.3969/j.issn.1007-3701.2020.01.005

Inman, M., Thorhallsson, E. R., and Azrague, K. (2017). A mechanical and environmental assessment and comparison of basalt fibre reinforced polymer (BFRP) rebar and steel rebar in concrete beams. *Energy Procedia* 111, 31–40. doi:10.1016/j.egypro.2017.03.005

Ivanović, A., and Neilson, R. D. (2013). Non-destructive testing of rock bolts for estimating total bolt length. *Int. J. Rock Mech. Min.* 64, 36–43. doi:10.1016/j.ijrmms.2013.08.017

Koca, M. Y., Kincal, C., Arslan, A. T., and Yilmaz, H. R. (2011). Anchor application in karatepe andesite rock slope, izmir—Türkiye. *Izmir—Türkiye. Int. J. Rock Mech. Min.* 48, 245–258. doi:10.1016/j.ijrmms.2010.11.006

Lan, Y., Zhang, R., Jin, L., and Du, X. (2022). Impact performance of BFRP and steel-reinforced concrete beams with different span-to-depth ratios: Numerical and analytical studies. *Sci. China Technol. Sci.* 66, 301–319. doi:10.1007/s11431-022-2206-2

Li, C., Zhang, R., Zhu, J., Liu, Z., Lu, B., Wang, B., et al. (2020). Model test of the stability degradation of a prestressed anchored rock slope system in a corrosive environment. *J. Mt. Sci-Engl* 17, 2548–2561. doi:10.1007/s11629-019-5835-7

Li, S., Guo, S., Yao, Y., Jin, Z., Shi, C., and Zhu, D. (2021). The effects of aging in seawater and SWSSC and strain rate on the tensile performance of GFRP/BFRP composites: A critical review. *Constr. Build. Mater* 282, 122534. doi:10.1016/j.conbuildmat.2021.122534

Ma, F., Zeng, Q., Lu, X., Wu, T., Lu, X., Zhang, T., et al. (2021). Electrochemical study of stainless steel anchor bolt corrosion initiation in corrosive underground water. *Processes* 9, 1553. doi:10.3390/pr9091553

Meikle, T., Tadolini, S. C., Sainsbury, B. A., and Bolton, J. (2017). Laboratory and field testing of bolting systems subjected to highly corrosive environments. *Int. J. Min. Sci. Tech.* 27, 101–106. doi:10.1016/j.ijmst.2016.11.017

Mohamed, O. A., Al Hawat, W., and Keshawarz, M. (2021). Durability and mechanical properties of concrete reinforced with basalt fiber-reinforced polymer (BFRP) bars: Towards sustainable infrastructure. *Polymers* 13, 1402. doi:10.3390/polym13091402

Motwani, P., Perogamvros, N., Taylor, S., and Laskar, A. (2020). Performance of industrial wedge-anchors for pre-stressing BFRP bars: Experimental and numerical studies. *Compos. Struct.* 251, 112592. doi:10.1016/j.compstruct.2020.112592

Shan, R., Huang, P., Yuan, H., Meng, C., and Zhang, S. (2022). Research on the full-section anchor cable and C-shaped tube support system of mining roadway in

island coal faces. *J. Asian Archit. Build.* 21, 298–310. doi:10.1080/13467581.2020.1869556

Shi, J., Wang, X., Zhang, L., Wu, Z., and Zhu, Z. (2022). Composite-wedge anchorage for fiber-reinforced polymer tendons. *J. Compos Constr.* 26, 04022005. doi:10.1061/(asce)cc.1943-5614.0001194

Shi, Z. M., Liu, L., Peng, M., Liu, C. C., Tao, F. J., and Liu, C. S. (2018). Non-destructive testing of full-length bonded rock bolts based on HHT signal analysis. *J. Appl. Geophys.* 151, 47–65. doi:10.1016/j.jappgeo.2018.02.001

Sun, X., Zhang, B., Gan, L., Tao, Z., and Zhao, C. (2019). Application of constant resistance and large deformation anchor cable in soft rock highway tunnel. *Adv. Civ. Eng.* 2019, 1–19. doi:10.1155/2019/4347302

Tistel, J., Grimstad, G., and Eiksund, G. (2017). Testing and modeling of cyclically loaded rock anchors. *J. Rock Mech. Geotech.* 9 (6), 1010–1030. doi:10.1016/j.jrmge.2017.07.005

Wang, J., Huang, B., Zhao, Y., Zhang, Z., and Hu, M. (2018). Study on deformation and failure mechanism of huangnanbeixi dangerous rock in three Gorges reservoir area. *Geol. Mineral Resour. South China* 34 (4), 339–346. doi:10.3969/j.issn.1007-3701.2018.04.009

Wang, X., Shi, J., Wu, G., Yang, L., and Wu, Z. (2015). Effectiveness of basalt FRP tendons for strengthening of RC beams through the external prestressing technique. *Eng. Struct.* 101, 34–44. doi:10.1016/j.engstruct.2015.06.052

Wang, X., Zhou, J., Ding, L., Song, J., and Wu, Z. (2020). Static behavior of circumferential stress-releasing anchor for large-capacity FRP cable. *J. Bridge Eng.* 25, 04019127. doi:10.1061/(asce)be.1943-5592.0001504

Wang, Y., Sun, X., and Ren, A. (2019). Investigations of rock anchor corrosion and its influence factors by exhumations in four typical field sites. *Eng. Fail Anal.* 101, 357–382. doi:10.1016/j.engfailanal.2019.03.022

Wu, Z., and Yamamoto, M. (2013). "Study on the basic performance of FRP-concrete Structures using basalt fibre reinforced polymer rods," in The 68th Annual Meeting of the Japan Society of Civil Engineers JSCE. (in Japanese).

Xia, D., Tang, H., Sun, S., Tang, C., and Zhang, B. (2022). Landslide susceptibility mapping based on the germinal center optimization algorithm and support vector classification. *Remote Sens.* 14 (11), 2707. doi:10.3390/rs14112707

Xu, H., and Li, Q. (2011). Factors affecting the dynamic response of pre-stressed anchors after transient excitation. *Min. Sci. Technol. (China)* 21, 395–399. doi:10.1016/j.mstc.2011.05.018

Xu, M., Tang, Y., Liu, X., Yang, H., and Luo, B. (2018). A shaking table model test on a rock slope anchored with adaptive anchor cables. *Int. J. Rock Mech. Min.* 112, 201–208. doi:10.1016/j.ijrmms.2018.10.021

Xu, X., Rawat, P., Shi, Y., and Zhu, D. (2019). Tensile mechanical properties of basalt fiber reinforced polymer tendons at low to intermediate strain rates. *Compos Part B-Eng* 177, 107442. doi:10.1016/j.compositesb.2019.107442

Yang, G., Zhong, Z., Zhang, Y., and Fu, X. (2015). Optimal design of anchor cables for slope reinforcement based on stress and displacement fields. *J. Rock Mech. Geotech.* 7, 411–420. doi:10.1016/j.jrmge.2015.04.004

Yi, H., Liu, W., Zhang, X., Yang, H., Yu, H., and Li, L. (2014). Study on deformation mechanism of high stress and broken roadway and its controlling measures. *Appl. Mech. Mater* 501, 1798–1803. doi:10.4028/www.scientific.net/amm.501-504.1798

Yin, Z., Zhao, B., and Ye, R. (2022). Identification of potential landslides in the head area of the Three Gorges Reservoir based on time series InSAR. *South China Geol.* 38, 273–280. doi:10.3969/j.issn.2097-0013.2022.02.008

Zhang, H. (2015). *Preparation and properties of electroless plating coating on anchor rod in support engineering*. Taiyuan, China: Taiyuan University of Technology.

Zhao, C., Tang, Z., Wang, P., Feng, J., Zhou, J., Kong, X., et al. (2022). Blast responses of shallow-buried prefabricated modular concrete tunnels reinforced by BFRP-steel bars. *Undergr. Space* 7, 184–198. doi:10.1016/j.undsp.2021.07.004

Zhao, W., Wang, H., Chen, Y., and Hu, Y. (2016). Laboratory and field tests use of BFRP anchor bolt in supporting soil slope. *J. Eng. Geol.* 24, 1008–1015. doi:10.13544/j.cnki.jeg.2016.05.032

Zheng, H., Shi, Z., Haas, D. T., Shen, D., Hanley, K. J., and Li, B. (2022). Characteristics of the impact pressure of debris flows. *J. Geophys Res-Earth* 127, e2021JF006488. doi:10.1029/2021jf006488

Zheng, H., Shi, Z., Yu, S., Fan, X., Hanley, K. J., and Feng, S. (2021). Erosion mechanisms of debris flow on the sediment bed. *Water Resour. Res.* 57, e2021WR030707. doi:10.1029/2021wr030707

Zheng, K., Shi, C., Lin, Y., Lei, M., and Liu, J. (2021). Transfer station cracks induced by cutting anchor cables and crack stabilization: A case study. *Eng. Fail Anal.* 126, 105460. doi:10.1016/j.engfailanal.2021.105460

Zhou, S., Yao, Y., Luo, X., Jiang, N., and Niu, S. (2023). Dynamic response evaluation for single-hole bench carbon dioxide blasting based on the novel SSA–VMD–PCC method. *Int. J. Geomech.* 23, 04022248. doi:10.1061/(asce)gm.1943-5622.0002589

Zhu, B., Song, Y., Wang, H., and Li, Y. (2020). Coupling effect of creep deformation and prestress loss of anchored jointed rock. *Adv. Civ. Eng.* 2020, 1–10. doi:10.1155/2020/8850975

Zhu, H., Xiang, Q., Luo, B., Du, Y., and Li, M. (2022). Evaluation of failure risk for prestressed anchor cables based on the AHP-ideal point method: An engineering application. *Eng. Fail Anal.* 138, 106293. doi:10.1016/j.engfailanal.2022.106293

frontiers | Frontiers in Earth Science

TYPE Original Research
PUBLISHED 20 March 2023
DOI 10.3389/feart.2023.1121690

OPEN ACCESS

EDITED BY
Biswajeet Pradhan,
University of Technology Sydney,
Australia

REVIEWED BY
Muhammet Gul,
Istanbul University, Türkiye
Kun He,
Southwest Jiaotong University, China
Sarita Gajbhiye Meshram,
WRAM Research Lab Pvt. Ltd., India

*CORRESPONDENCE
Hui-ge Xing,
hgxing@scu.edu.cn

SPECIALTY SECTION
This article was submitted
to Geohazards and Georisks,
a section of the journal
Frontiers in Earth Science

RECEIVED 12 December 2022
ACCEPTED 02 March 2023
PUBLISHED 20 March 2023

CITATION
Yu M, Hu S-y, Cai J-m, Guo P-n, Li H-b and Xing H-g (2023), A comprehensive evaluation method for the site selection of new healthcare facilities in geological hazard-prone areas.
Front. Earth Sci. 11:1121690.
doi: 10.3389/feart.2023.1121690

A comprehensive evaluation method for the site selection of new healthcare facilities in geological hazard-prone areas

Miao Yu[1], Shi-yu Hu[2], Jian-min Cai[1], Peng-ning Guo[1], Hai-bo Li[3] and Hui-ge Xing[1]*

[1]College of Architecture and Environment, Sichuan University, Chengdu, China, [2]Institute for Disaster Management and Reconstruction (IDMR), Sichuan University, Chengdu, China, [3]State Key Laboratory of Hydraulics and Mountain River Engineering, Sichuan University, Chengdu, China

Healthcare facilities in geological hazard-prone areas not only are responsible for local basic medical services but also are the main provider of hazard emergency rescue work. The selection of their sites is further complicated by the need to consider both the equalization of regional medical services and resource allocation and the impact of geological hazards on site safety. Shimian County in Sichuan Province, a geological disaster-prone area, was chosen as the study area. First, suitability analysis of the construction land was used to determine the site alternatives for new healthcare facilities, and an evaluation index system of construction land suitability consisting of geological hazard susceptibility, slope and aspect was established. Then, the suitability was evaluated by the Ordered Weighted Averaging (OWA) operator, and the Analytic Hierarchy Process (AHP) and the quantitative method of Regular Increasing Monotone (RIM) were used to calculate the criterion weights and order weights in the Ordered Weighted Averaging operator respectively. The suitability results were classified into five levels: high, moderate, average, barely suitable, and unsuitable. Twelve site alternatives were identified in the highly and moderately suitable areas. Finally, a comprehensive evaluation index system consisting of indices such as construction land suitability and medical service accessibility was established, the PROMETHEE II method was conducted to comprehensively evaluate the site alternatives, and ranked results for the 12 site alternatives were obtained. These ranked results were analyzed by subindexes and Graphical Analysis for Interactive Aid (GAIA) to obtain a score for each alternative index and its similarity to the alternative, which could significantly help decision-making. This study achieves reasonable and scientific site selection for healthcare facilities in geological hazard-prone areas, and the results can provide references for relevant decision-makers.

KEYWORDS

geological hazard, healthcare facility, site selection, GIS, PROMETHEE II

1 Introduction

Healthcare facilities are closely related to social development and health (Bahadori et al., 2017). With the rapid development of urbanization and the improvement of residents' living standards, the demand for medical services is increasing. China has a large number of mountainous areas where geological hazard activities are frequent (Lin, Chen, Qi, & Hou, 2021). Geological hazards seriously threaten the life and property safety of residents and affect socioeconomic development (Ma & Mei, 2021). Healthcare facilities in geological hazard-prone areas are not only responsible for providing basic medical services (Tripathi, Agrawal, & Gupta, 2021), but also a key part of the post-hazard emergency rescue management. Nevertheless, China suffers from an imbalance between the supply and demand of medical resources, especially in mountainous regions, where the population distribution and economic development are heterogeneous. Scientific and reasonable site selection of healthcare facilities is essential to meet residents' medical needs, improve the efficiency of the regional medical system, and enhance hazard prevention and mitigation (Dell'Ovo et al., 2017; Sara & Abbas, 2014). The geological hazard factors should be considered in the site selection study of healthcare facilities (Gul & Guneri, 2021). Therefore, this paper examined the scientific and rational site selection of new healthcare facilities in geological hazard-prone areas to improve the safety of healthcare facility sites and make the spatial layout more reasonable.

The site selection of new healthcare facilities requires consideration of criteria such as geological hazard susceptibility, construction land suitability, accessibility, and medical equalization, which is a multidimensional and complex multicriteria decision-making (MCDM) problem in nature (Eldemir & Onden, 2016; Senvar, Otay, & Bolturk, 2016; Wang, Shi, & Gan, 2018). MCDM is a method for solving decision-making and planning problems involving multiple criteria by evaluating alternatives based on a set of decision criteria (Tyagi & Singh, 2019). The MCDM method is used to select healthcare facility sites in many studies, and the criteria and methods used in some of these studies are shown in Supplementary Table S9. Scholars generally consider the criteria for healthcare facility site selection in terms of accessibility, competition, cost, demand, and environment, with the accessibility criterion being used by all scholars, indicating that the proximity of healthcare facilities to the transportation road network is one of the criteria that must be considered. Meanwhile, GIS is widely used in the site selection of healthcare facilities (Tripathi et al., 2021) because it can create a problem-solving environment for spatially referenced data. The integration of MCDM methods and GIS enables the manipulation and presentation of spatial data, providing effective ranking of alternatives based on multiple criteria (Sara & Abbas, 2014), as well as reducing errors and increasing the efficiency of the decision-making process (Eghtesadifard, Afkhami, & Bazyar, 2020). Some researchers have identified areas suitable for the site selection of healthcare facilities in the study areas based on GIS (Ajaj et al., 2019; Dell'Ovo, Capolongo, & Oppio, 2018; Dulin et al., 2010; Halder, Bandyopadhyay, & Banik, 2020), but did not prioritize suitable locations for site selection, leading to decision-makers' own judgment for selection. Zolfani, Yazdani, Torkayesh, and Derakhti (2020), Adali and Tus (2021), and Yilmaz and Atan (2021) used the MCDM method to identify the ranking of the advantages and disadvantages of healthcare facility site alternatives based on the corresponding criteria but lacked a basis for selection when determining the site alternatives. Based on the above analysis, this paper will combine GIS and MCDM methods to study the site selection of new healthcare facilities in geological hazard-prone areas, identify site alternatives in the study area and comprehensively evaluate and rank them to help decision-makers make appropriate choices.

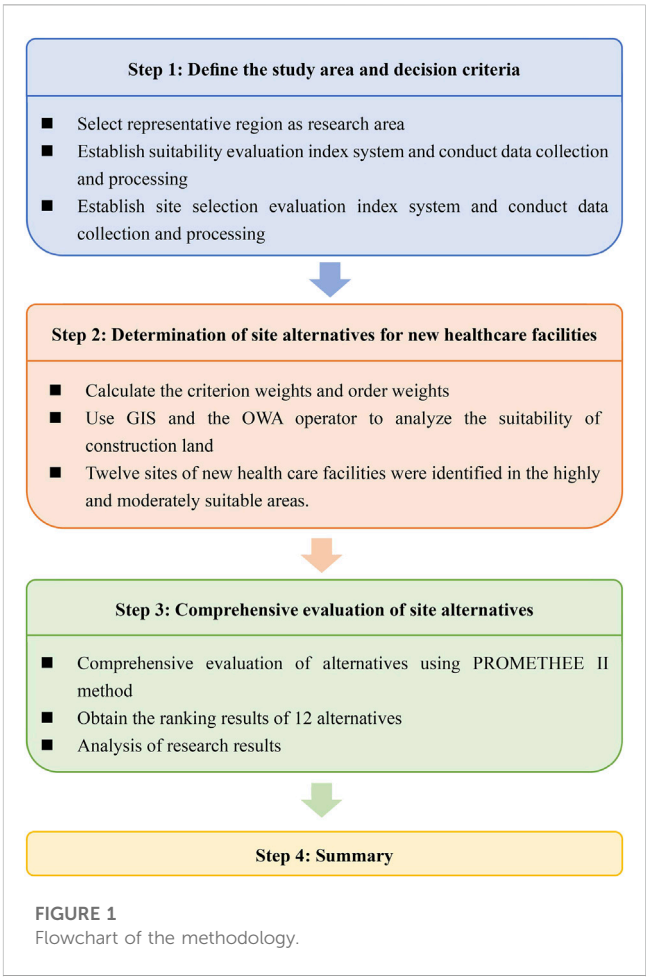

FIGURE 1
Flowchart of the methodology.

Judging from the research content of this paper, the types of evaluation indices required in this paper are extensive and the data are diverse. Therefore, the MCDM method was chosen in the study, which required less data processing and could reflect various index information. Of course, the MCDM method must be applicable to siting selection research. Based on relevant researches (Chai, Liu, & Ngai, 2013; Wu et al., 2020b; Guo, Gao, Men, Fan, & Liu, 2021), the advantages and disadvantages of common MCDM methods are summarized as Supplementary Table S10. Preference Ranking Organization Methods for Enrichment Evaluations (PROMETHEE) is a ranking method among multicriteria decision-making methods that can rank and select a limited set of alternatives among conflicting criteria (Behzadian, Kazemzadeh, Albadvi, & Aghdasi, 2010). As shown in Supplementary Table S10, it has the advantages of no need to process raw data, little missing information, and the ability to reflect various characteristics of indicator attributes, which meets the research requirements of this paper and can better solve the ranking problem of site alternatives. Sennaroglu and Celebi (2018), Wu, Zhang, Wu, Zhang, and Liu (2019), Wu et al., 2020a, and Guo et al. (2021) all applied the PROMETHEE method to facility site studies and

successfully ranked and selected the site alternatives, reducing the difficulty for decision-makers to identify the best alternative. To sum up, the PROMETHEE method is selected for comprehensive evaluation of site selection alternatives. The PROMETHEE method has many derivative versions, among which the PROMETHEE II method can obtain a complete ranking of the alternatives instead of a partial ranking by improving the PROMETHEE I method.

In summary, this paper proposes a comprehensive evaluation method for the site selection of new healthcare facilities based on GIS and PROMETHEE II methods in geological hazard-prone areas. The flowchart of the methodology in this paper is shown in Figure 1. The study area is Shimian County, Ya'an City, Sichuan Province, which is prone to geological hazards. The suitability map for construction and site alternatives for new healthcare facilities are determined based on GIS and OWA methods in the study area. The PROMETHEE II method is used to comprehensively evaluate the alternatives and obtain the ranking results of the alternatives. The method proposed in this paper can take full advantage of the combination of GIS and PROMETHEE II, which can ensure the safety and suitability of the site and consider the comprehensive and developmental aspects of new healthcare facilities. Thus, the purpose of reasonable and scientific site selection for new healthcare facilities in geological hazard-prone areas can be achieved.

The rest of the paper is organized as follows: Section 2 briefly introduces the research methodology, Section 3 details the process of determining the study area and the evaluation index system, Section 4 details the results of the site alternative identification and comprehensive evaluation of new healthcare facilities, Section 5 discusses the study results and concludes the paper, and Section 6 proposes future research directions.

2 Methods

2.1 Ordered Weighted Averaging operator

In methods of combining GIS with multicriteria decision-making, the linear weighted combination approach can result in some criteria compensating for other criteria that have obvious constraints (Bagheri, Sulaiman, & Vaghefi, 2013; Kapoor & Bansal, 2021; Aghmashhadi, Azizi, Zahedi, Hoseinkhani, & Cirella, 2022) since the selection of evaluation indices is usually interrelated. Thus, it may make the obtained results not as restrictive as intended by the evaluator (Liu Y. et al., 2014). The ordered weighted averageing (OWA) operator involves two types of weights: criterion weights and order weights (Yager, 1988). First, the weighting method is used to calculate the weight of the criterion, and the criterion is ranked according to the weight. Then, different order weights are assigned to the criterion according to the order. The OWA operator can reduce the influence of extreme values on the results and increase the influence of central values and the importance of the weighted measure values (in relation to other values) while maintaining independence from the original information source (Csiszar, 2021). Moreover, the OWA operator can simulate scenarios that indicate the suitability of construction land under different decision-making preferences by setting the decision preference coefficient α. The OWA operator has been widely used in land suitability studies (Liu R. et al., 2014; Kumar & Kumar, 2014; Billaud, Soubeyrand, Luque, & Lenormand, 2020; Cosimo, Martins, & Gleriani, 2021; Luan, Liu, & Peng, 2021; Yang, Tang, & Li, 2021). Thus, this paper uses the OWA operator to analyze construction land suitability and determine the suitable sites of new healthcare facilities in the study areas. The calculation process is as follows:

$$OWA_i = \sum_{j=1}^{n} \left(\frac{u_j v_j}{\sum_{j=1}^{n} u_j v_j} \right) Z_{ij} \tag{1}$$

In the formula, OWA_i is the suitability analysis result of the ith pixel; j is the rank; n is the number of evaluation indices; Z_{ij} is the attribute value corresponding to the jth index of the ith pixel; u_j is the criterion weight; and v_j is the order weight.

The Analytic Hierarchy Process (AHP) is used to calculate the criterion weights of the evaluation indices, the quantitative method of Regular Increasing Monotone (RIM) is used to determine the order weights (Yager, 1996), and v_j is calculated as follows:

$$v_j = Q_{RIM}\left(\frac{j}{n}\right) - Q_{RIM}\left(\frac{j-1}{n}\right) \tag{2}$$

$$Q_{RIM}(r) = r^{\alpha} \tag{3}$$

where r is the independent variable and α is the decision-makers' preference coefficient. When α=1, the order weights are equal, and the calculation turns into a linear weighted combination of criterion weights; when $0<\alpha<1$, the greater the criterion weights of the indices are, the greater their order weights. At this time, the evaluation results can visually show the most important attributes of the index system. When $\alpha>1$, the order weights of indices with larger criterion weights are smaller, and the less important indices at the back receive more attention. The study area is prone to geological hazards; therefore, the impact of geological hazards is the most important factor and must be considered. Finally, we take α=0.5.

2.2 PROMETHEE II

The PROMETHEE II method compares each attribute of the alternatives in pairs to obtain the ranking of the alternatives according to certain criteria (recognized criterion). The specific computational process is as follows:

1) Construction of decision matrix

Suppose a multicriteria decision problem with m alternatives $A=\{a_1,a_2, \ldots a_m\}$, each corresponding to n evaluation indices, the set of evaluation indices $C=\{c_1,c_2, \ldots c_n\}$, and the weight vector $w=(w_1, w_2, \ldots, w_n)$ corresponding to the evaluation indices and satisfying $w_j \in [0,1]$ and $\sum w_j = 1$, (j = 1,2, … n).

2) Construction of preference functions

$$P_j(a_p, a_q) = F_j\left[d_j(a_p, a_q)\right] \tag{4}$$

$$d_j(a_p, a_q) = f_j(a_p) - f_j(a_q) \tag{5}$$

where $P_j(a_p,a_q)$ $(0 \le P_j(a_p,a_q) \le 1)$ is a preference function that is used to describe the priority of alternative a_p relative to a_q for indicator c_n; $f_j(a_p)$ is the value of evaluation index c_j for alternative a_p, and $f_j(a_q)$ is the same.

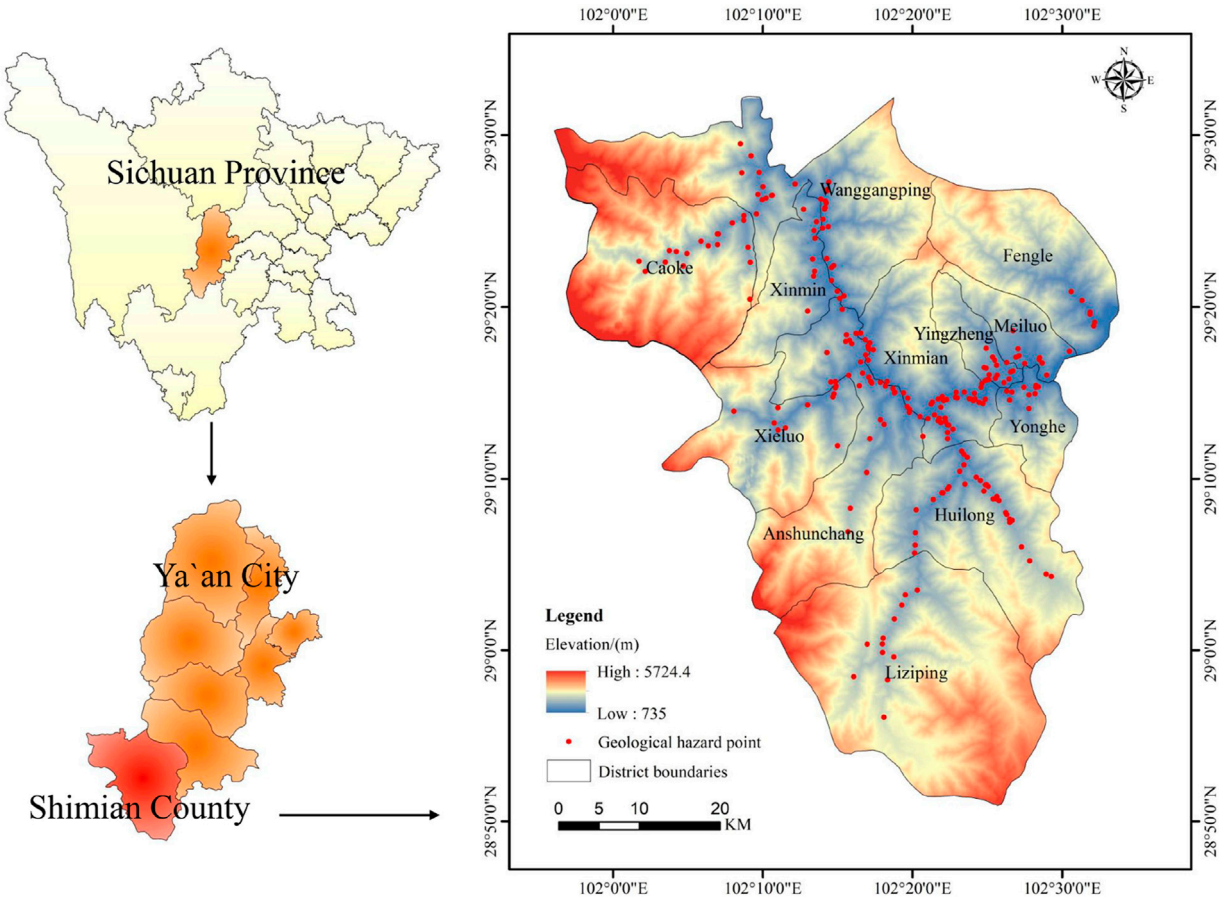

FIGURE 2
Study area overview.

3) Calculation of the overall preference indices G (ap,aq) and G (aq,ap)

$$G(a_p, a_q) = \sum_{j=1}^{n} w_j P_j(a_p, a_q) \tag{6}$$

$$G(a_q, a_p) = \sum_{j=1}^{n} w_j P_j(a_q, a_p) \tag{7}$$

where $G(a_p,a_q)$ indicates that alternative a_p is superior to alternative a_q and $G(a_p,a_q)$ indicates that alternative a_q is superior to alternative a_p.

4) Calculation of the positive flow φ+(ap) and negative flow φ-(ap) of alternative a_p

$$\varphi^{+}(a_p) = \frac{1}{m-1} \sum_{x \in A} G(a_p, x) \tag{8}$$

$$\varphi^{-}(a_p) = \frac{1}{m-1} \sum_{x \in A} G(x, a_p) \tag{9}$$

5) Calculation of net flow φ(ap)

$$\varphi(a_p) = \varphi^{+}(a_p) - \varphi^{-}(a_p) \tag{10}$$

The net flow reflects the priority of alternative a_p. The alternative is ranked according to the net flow of each alternative, and the higher the net flow value, the higher the priority of the alternative and the ranking.

3 Determination of study area and decision criteria

3.1 Study area

Rational planning of the site layout of new healthcare facilities in the county is a strategic need for national development. Geological hazards are frequent in Shimian County, Ya'an City, Sichuan Province. According to data from the Geospatial Data Cloud platform, there were 442 geological hazard sites in Shimian County from 1949 to 2018, accounting for 24.26% of the total geological hazard sites in Sichuan Province. Shimian County is one of the most prominent hazard prevention and mitigation areas in Sichuan Province. Therefore, the selection of Shimian County as the study area has practical significance and representativeness.

Shimian County is located in the eastern part of the Hengduan Mountains on the Qinghai-Tibet Plateau in the middle reaches of

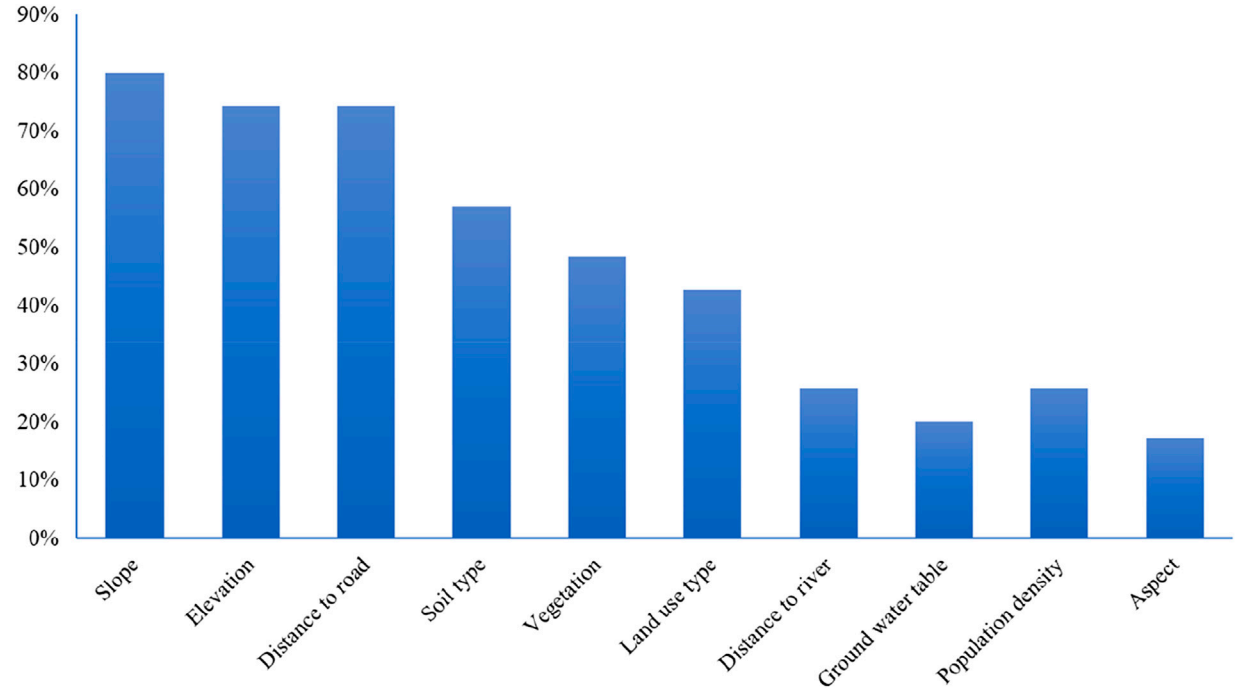

FIGURE 3
Frequency diagram of initial evaluation indices for construction land suitability.

the Dadu River. The geographical coordinates are 101°55′-102°34′E and 28°51′-29°32′N (Figure 2). The maximum horizontal distance from east to the west in Shimian County is 60 km, and the maximum vertical distance from north to south is 76.5 km. It is a typical mountainous county with an elevation of more than 1,000 m accounting for approximately 90% of the total area, while the river valley and flat areas only account for 2%.

3.2 Establishment of the evaluation index system

3.2.1 Establishment of the suitability evaluation index system

Based on the principles of scientificity, comprehensiveness, accessibility and comparability, literature analysis are used to identify and filter indices for construction land suitability analysis, and the final evaluation index system is established by making corrections in the context of the study area. According to Kapoora and Bansalb's study, we compile a total of 35 papers on the topics of "Spatial suitability", "Land use suitability", "Urban land suitability" and "Construction land suitability", which involve a total of 29 evaluation indices (Kapoor & Bansal, 2021). After eliminating the irrelevant indices, the frequency statistics of the indices were conducted, and the indices that appear≥6 times are selected as the initial evaluation indices. The frequency diagram of the initial evaluation indices is shown in Figure 3.

The initial filtering process could potentially result in two situations. One is that the indices with strong relevance to construction land suitability in geological hazard-prone areas are not selected due to insufficient frequency, and the other is that the evaluation indices do not conform to the selection principles of this study. To ensure that the indices could accurately evaluate construction land suitability in geological hazard-prone areas, the indices in Figure 3 are adjusted as follows: 1) The geological hazard-prone index is added to ensure the safety of the site selection. 2) The distance to fault is added because Shimian County is located at the compound intersection of three fault zones, namely, Xianshui River, Anning River and Longmen Mountain, and thus the strata in the territory are fragmented and earthquake prone, so the buildings should not be built close to the fault. 3) The vegetation is excluded because it has been considered in the geological hazard susceptibility index and thus is not repeatedly selected here. 4) The groundwater table data do not conform to the principle of availability, hence, the evaluation index is excluded. 5) The precision and comparability of the soil type in the study area is not high, and the land use type can replace the soil type to a certain extent; thus, the soil type is also excluded.

Based on the above analysis, nine indices of geological hazard susceptibility, slope, aspect, elevation, distance to fault, distance to river, population density, distance to road and land use type are determined as the suitability evaluation index system for construction land. These indices are classified from four aspects: geological hazards, topography, geohydrology and socioeconomics. Based on previous studies (Kapoor & Bansal, 2021; Luan et al., 2021; Yang et al., 2021) and the situation of Shimian County, the grading standard of the suitability evaluation index is determined. The results are shown in Table 1. Grades 1–5 correspond to unsuitable, barely suitable, generally suitable, moderately suitable and highly suitable, i.e., the suitability gradually increases with

TABLE 1 Suitability evaluation index system and grading criteria.

Category	Evaluation	Suitability grading				
	Indices	1	2	3	4	5
Geological hazard	Geological hazard susceptibility	I	II	III	IV	V
Topography	Aspect	North	Northeast, Northwest	East, West	Southeast, Southwest	South, Flatland
	Slope (degrees)	≥25	10–25	5–10	2–5	<2
	Elevation m)	≥3000	2000–3000	1500–2000	1000–1500	<1000
Geohydrology	Distance to fault m)	<200	200–500	—	—	—
	Distance to river m)	<50	50–100	100–300	300–500	≥500
Socioeconomic	Population density (per sq. km)	4.51–35.32	35.32–59.17	59.17–98.92	98.92–164.50	164.50–258.91
	Land use type	Permanent Snow and Ice, Water Bodies	Forest, Wetland	Cultivated Land, Shrubland	Grassland	Artificial Surfaces
	Distance to road m)	≥1000	750–1000	500–750	250–500	<250

TABLE 2 Evaluation index data sources and preprocessing.

Evaluation indices	Data source	Data preprocessing
Elevation	Geospatial Data Cloud	DEM data (30 m resolution)
Slope	(http://www.gscloud.cn/)	Extracted from DEM data using slope analysis function in ArcGIS.
Aspect		The slope direction analysis function is used in ArcGIS to extract from the DEM data
Land use type	National Catalog Service For Geographic Information (http://www.webmap.cn/)	Land use type raster data (30 m resolution)
Distance to river		The river system data is processed using the multiring buffer function of ArcGIS and converted to raster data
Distance to road		The road network data is processed using the multiring buffer function of ArcGIS and converted to raster data
Distance to fault	Geocloud (http://geocloud.cgs.gov.cn/)	The fault data is processed using the Multiple Ring Buffer tool of ArcGIS and converted to raster data
Population density	Seventh National Census Data	After calculating the population density of each township, the population density map is obtained by interpolation using the inverse distance weighting method

increasing grade. The Jenks natural breaks classification method is a data clustering method that determines how values are optimally arranged in different classes by reducing within-class variance and maximizing between-class variance. Therefore, this paper used the Jenks natural breaks classification method to classify the population density index.

The geological hazard susceptibility is obtained by calculating and correcting 11 evaluation indices of elevation, aspect, distance to fault, lithology, river system density, NDVI, road network density, population density, slope, mean annual precipitation, and land use type using the information value-logistic regression coupled model (Yu, Xing, & Hu, 2021). The data sources and processing of the remaining indices are shown in Table 2.

The Multiple Ring Buffer and Reclassifies Tool of ArcGIS are used for grading processing, and the evaluation indices are all raster data with a size of 30 m*30 m; a detailed map of the evaluation index grading is shown in Figure 4.

3.2.2 Establishment of the site selection evaluation index system

1) Selection of site selection evaluation indices

The frequency of evaluation indices is counted in the literature of Supplementary Appendix SA. The indices that appear ≥4 times are selected as the preliminary evaluation indices, whose frequency diagram is shown in Figure 5.

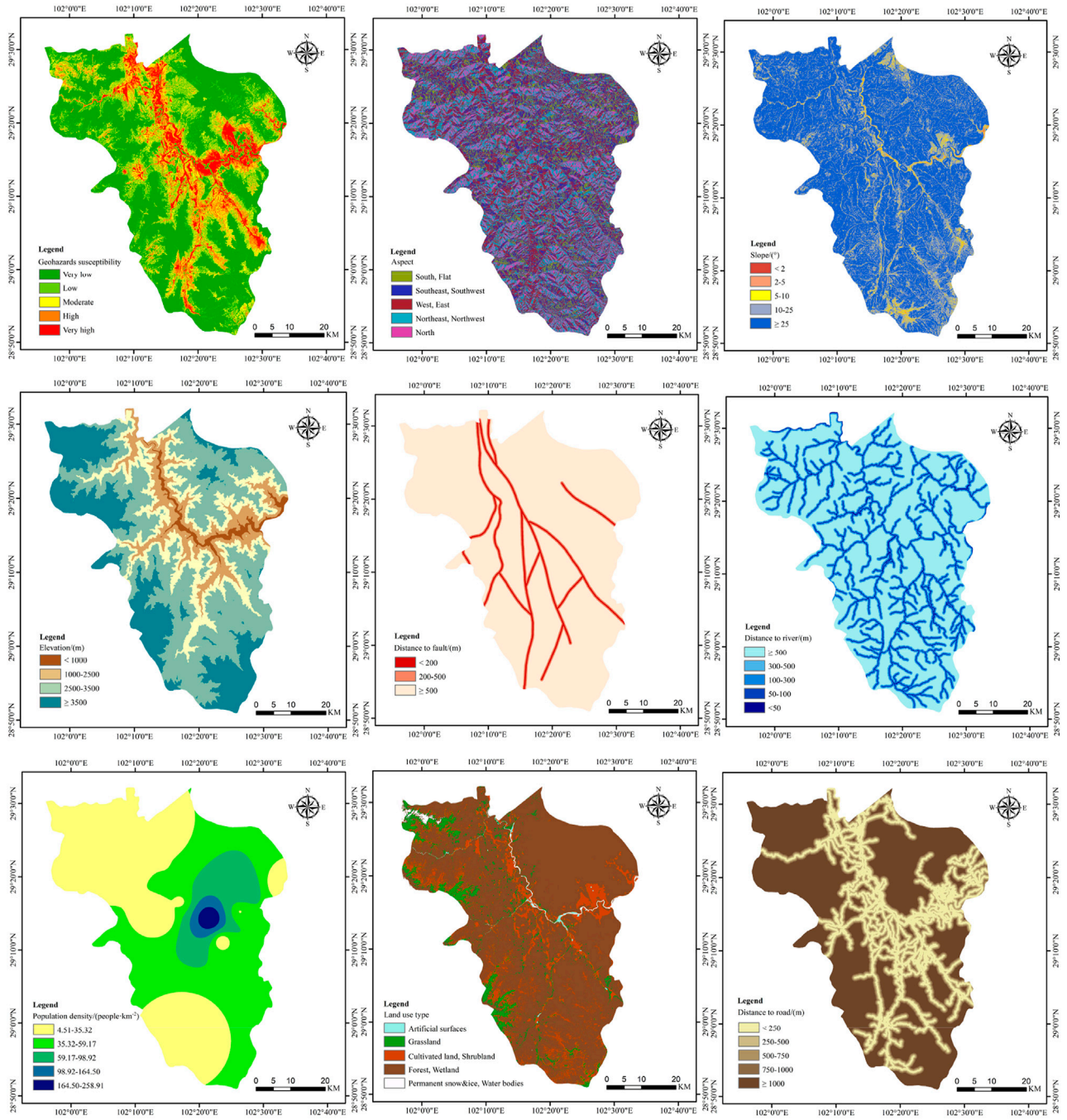

FIGURE 4
Detailed diagram of suitability evaluation index classification.

The indices are adjusted in Figure 5 *via* the following: 1) indices for construction land suitability are increased and the alternative with the highest suitability level is selected as often as possible; 2) the evaluation index of medical service equalization is increased. Improving the level of equalization of basic public services is a clear requirement in China's 14th Five-Year Plan period. 3) The distance to roads and population density have been considered in construction land suitability, so they are excluded. 4) The data for land cost, land expansion and green area do not conform to the principle of accessibility, so they are excluded. 5) The study area has better air quality, and the air pollution data do not meet the principle of comparability, so the air pollution data are excluded. 6) The demand for healthcare facilities are characterized by medical service accessibility. If the new healthcare facility in a certain place has the largest sum of medical service accessibility at the demand points of the residents in the study area, then the demand for healthcare facilities in that place is the largest. 7) The total distance to healthcare facilities is used to characterize the distance to

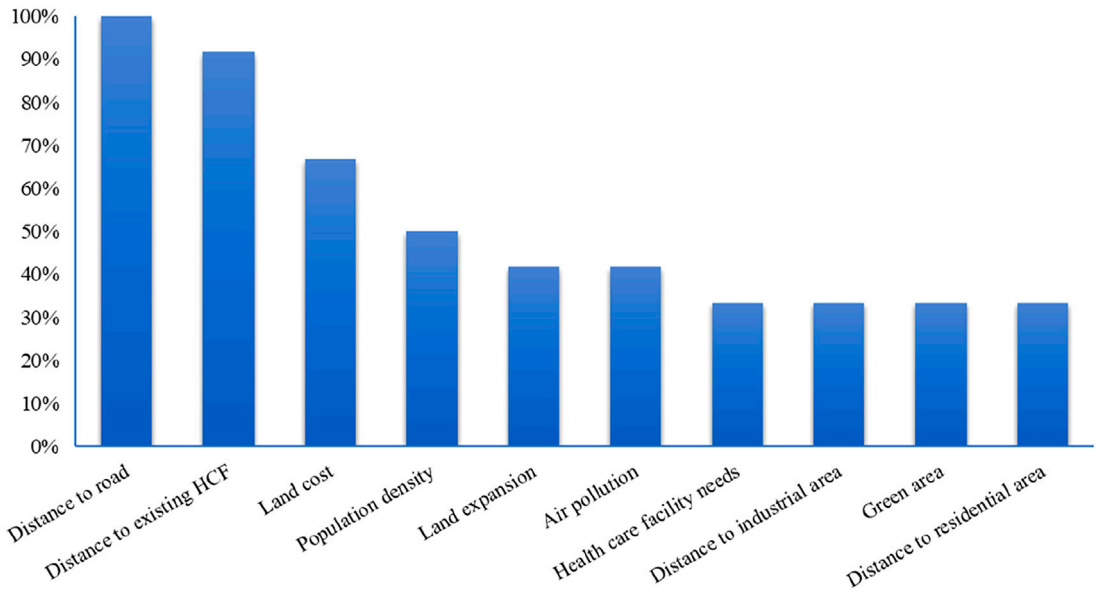

FIGURE 5
Frequency diagram of the preliminary evaluation indices.

TABLE 3 New healthcare facility site selection evaluation index system.

Category	Evaluation indices
Quantitative indices	Distance to existing HCF D1
	Accessibility to medical service D2
	Medical service equalization D3
	Total distance to HCF D4
Qualitative indices	Construction land suitability D5
	Distance to industrial area D6

residential points. Based on the above analysis, the site selection evaluation index system of the new healthcare facility is determined as shown in Table 3, which contains two categories of quantitative and qualitative evaluation indices.

2) Data sources
   1) Resident demand point data. Most of the population demand data take streets, communities and other residential surfaces as a whole and extract the geometric center as the resident demand point. However, this practice will cause certain errors in the calculation results of travel impedance for mountainous cities with uneven population distribution. In this paper, the median center of natural villages in each township and street is calculated, and the median center of natural villages is used as the resident demand point, as shown in Figure 6A.
   2) Healthcare facility data. The healthcare facilities in Shimian County include 4 hospitals, 15 rural township health centers, 1 community health service center, 1 disease control and prevention center, and 1 maternal and child healthcare hospital. The data are obtained from Gao De Map POI interest points, as shown in Figure 6B. Since the internal data of some healthcare facilities are not available, the following healthcare facilities refer to hospitals.
   3) Traffic road network data. Based on the Open Streets Map, the carriageway is drawn with reference to the road data in the National Catalog Service for Geographic Information and Google Earth. After topologically processing the road network data, the travel impedance between resident demand points and healthcare facilities is calculated. According to the road types in Shimian County, *Technical code for urban road engineering GB51286-2018* and *Regulation on the Implementation of the Road Traffic Safety Law of the People's Republic of China*, the vehicle travel speed is assigned to the traffic road network, where the vehicle travel speeds of Class I, Class II, Class III and Class IV are set to 60 km/h, 45 km/h, 40 km/h and 30 km/h, respectively, as shown in Figure 6C.
3) Data calculation
   1) Distance to existing HCF (D1). To make the distribution of healthcare resources more balanced, the distance between the new healthcare facilities and the existing healthcare facilities should be as far as possible. Therefore, the following equation is used to calculate the distance between the two kinds of healthcare facilities:

$$D_k = AVERAGE \sum d_{jk} \tag{11}$$

where D_k is the average distance from the new healthcare facility k to the existing healthcare facility j and d_{jk} is the distance from the new healthcare facility k to the existing healthcare facility j. The network analysis function of ArcGIS is used to calculate d_{jk}.

   2) Accessibility to medical service (D2). Accessibility refers to the sum of the accessibility to medical services at resident demand points in the study area, including the sum of the original

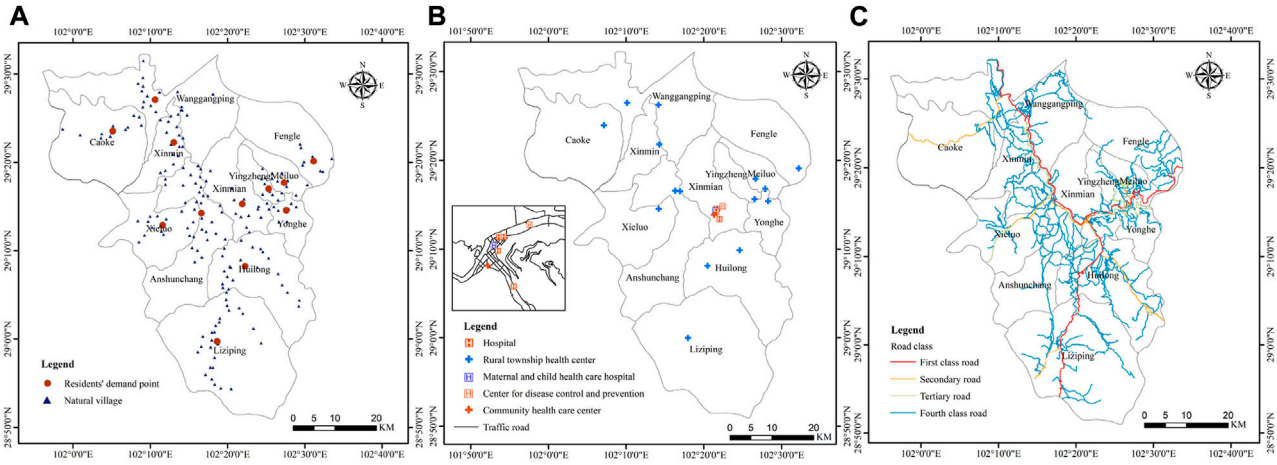

FIGURE 6
(A) resident demand point distribution map; **(B)** healthcare facilities distribution map; **(C)** traffic road network distribution map.

accessibility to medical services at resident demand points and the increased accessibility after the addition of healthcare facilities. The greater the accessibility to medical services in the study area is, the better. The specific equation is as follows:

$$A_k^* = \sum_{i=1}^{m} OA_i + \sum_{i=1}^{m} A_{ik} \tag{12}$$

where A_k* is the medical service accessibility at resident demand points in the study area after the addition of healthcare facility k, OA_i is the original medical service accessibility at resident demand point i, *and* A_{ik} is the medical service accessibility increased by resident demand point i after the addition of healthcare facility k. An improved potential model is used to calculate the accessibility to medical service (Joseph & Bantock, 1982).

3) Medical service equalization (D3). The fairness of accessibility to medical services is used to measure medical service equalization in the study area, which is represented by the deviation degree (variance) of accessibility (Zhang, Cao, Liu, & Huang, 2016). The smaller the variance of accessibility is, the better. The specific equation is as follows:

$$E_k = Var\{A_i\} \tag{13}$$

$$A_i = pop_i * \left[\frac{(OA_i + A_{ik})}{A_k^*} \right], \; i = 1, 2, \ldots\ldots n \tag{14}$$

where E_k is the medical service equalization in the study area after the addition of healthcare facility k, Var(A_i) is the variance of the sequence A_i of the accessibility at resident demand point i, and pop_i is the population at resident demand point i.

4) Total distance to HCF (D4). Total distance to HCFs is calculated by the sum of the weighted distance between resident demand points and their nearest healthcare facilities (existing and new). The smaller the total distance to HCFs is, the more suitable the site. The weight of demand points is the population of the site, and the specific equation is as follows:

$$TD_k = \sum_i^m pop_i * Min\left(d_{ij`}\right) \tag{15}$$

where TD_k is the total distance to the HCF at resident demand points after the addition of new healthcare facility k, $Min(d_{ij`})$ is the shortest distance from resident demand point $i$ to healthcare facility $j$`, and j` includes existing and new healthcare facilities. The calculation process of $d_{ij`}$ is the same as Eq. 11.

5) Construction land suitability (D5). The evaluation results of construction land suitability are used to measure the suitability of alternative sites for new healthcare facilities. The multivalue extraction to points function of ArcGIS is utilized to extract the suitability rating to the alternative, which is considered the evaluation value of this index.
6) Distance to industrial area (D6). There are two industrial parks in Shimian County, the Sichuan Shimian Industrial Park and the Xiaoshui Industrial Complex. To avoid possible damage to healthcare facilities caused by unexpected environmental events under special circumstances in industrial parks, healthcare facilities should be as far away from industrial parks as possible. The distance to the industrial area is classified with reference to "Basic requirements of safety technology for enterprise handing hazardous chemicals business GB18265-2019" (Table 4).

4 Results

4.1 Determination of site alternatives for new healthcare facilities

4.1.1 Suitability results

The Analytic Hierarchy Process (AHP) is used to calculate the criterion weights of the evaluation indices. The evaluation indices are ranked according to the values of criterion weights from large to small, and then the order weights of the evaluation indices are

TABLE 4 Distance classification to industrial area.

Evaluation indices	Classification				
	1	2	3	4	5
Distance to industrial area (m)	<1000	1000–3000	3000–5000	5000–10000	≥10,000

TABLE 5 Weights of suitability evaluation indices.

Category	Evaluation index	Criterion weight	Order weight
Geological hazard	Geological hazard susceptibility	0.381	0.333
Topography	Aspect	0.029	0.065
	Slope	0.075	0.089
	Elevation	0.066	0.071
Geohydrology	Distance to fault	0.228	0.138
	Distance to river	0.114	0.106
Socioeconomic	Population density	0.026	0.061
	Land use type	0.067	0.079
	Distance to road	0.015	0.057

calculated according to Eqs 2, 3. The results of the criterion and order weights are shown in Table 5.

According to the criterion and order weights of evaluation indices, the suitability of construction land in geological hazard-prone areas is evaluated in ArcGIS using the raster calculator combined with suitability grading values and Eq. 1. The results of the suitability analysis range from 1.01 to 4.90. Then, the results are classified as highly suitable, moderately suitable, generally suitable, barely suitable, and unsuitable by using the natural breakpoint method (Figure 7).

4.1.2 Determination of the site alternatives for new healthcare facilities

According to the suitability analysis results and the resident point data of Shimian County, the highly suitable and moderately suitable sites are selected as the site alternatives for new healthcare facilities in the residential surface layer coverage area of each township and street in Shimian County (Figure 8).

4.2 Comprehensive evaluation of site alternatives based on PROMETHEE II

Based on the characteristics of 6 common preference functions in PROMETHEE II, the linear preference is the best choice for quantitative criteria when needing a Q indifference threshold. Therefore, the linear preference function is selected for the four quantitative evaluation indices of distance to existing HCFs, accessibility to medical services, medical service equalization, and total distance to HCFs. The indice of construction land suitability has only two grades, and the alternatives with large values have absolute advantages, so the usual preference function is selected. Distance to industrial area is a qualitative indice and has multiple levels. The level preference function is better suited to qualitative criteria when the decision-maker wants to modulate the preference degree according to the deviation between evaluation levels. Hence, the level preference function is selected for the evaluation index of distance to industrial areas.

The indifference and preference thresholds of the linear preference functions are determined based on the average absolute deviation of the quantitative evaluation indices. The detailed equation is as follows:

1) Determine the mean absolute deviation S of index j.

$$S = \frac{\sum_{i=1}^{m} \left| a_{ij} - \bar{a}_{ij} \right|}{m} \tag{16}$$

where a_{ij} is the value of the jth evaluation index for alternative i, and m is the number of alternatives.

2) If the preference function requires only a single indifference threshold or preference threshold, the threshold equals 0.5S.
3) If the preference function requires both an indifference threshold and a preference threshold, the indifference threshold q equals 0.25S and the preference threshold p equals 0.75S.

The level preference function of the evaluation index of distance to industrial area defines the indifference threshold q as 0 and the preference threshold p as 1.

The quantitative evaluation indices for 12 alternatives are calculated using Eqs 11–15 and standardized. The higher the

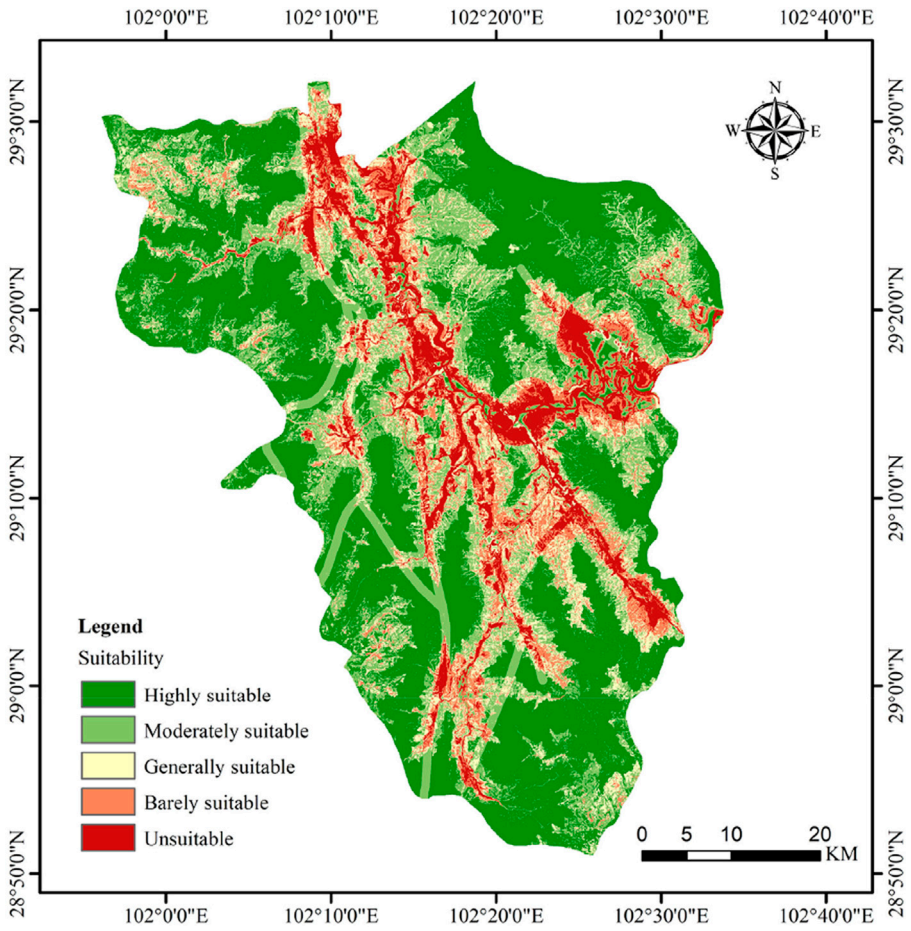

FIGURE 7
Results of the construction land suitability analysis.

value of these indices, the higher the degree of preference. According to the results of construction land suitability analysis, different grades of construction land suitability are assigned. The grades of unsuitable, barely suitable, generally suitable, moderately suitable and highly suitable are assigned 1, 2, 3, 4 and 5, respectively. The numerical results of the distance to industrial area are obtained by extracting the value of the distance to industrial area grading chart into the alternatives (Figure 7). The numerical results of the evaluation indices for 12 alternatives are shown in Table 6.

Based on the calculation results in Table 6, the indifferent and preference thresholds for each quantitative index are calculated using Eq. 16, as shown in Table 7.

The results in Tables 6 and 7 are input into Visual PROMETHEE software, and then the positive flow, negative flow, net flow and ranking results of 12 site alternatives for new healthcare facilities in geological hazard-prone areas are shown in Table 8.

The net flow values of the alternatives are S2, S3, S1, S4, S5, S12, S8, S9, S6, S7, S10 and S11 in descending order, as shown in Table 8. S2, with a net flow value of 0.5738, is the best site for a new healthcare facility. S11, with a net flow value of -0.6595, is the most unfavorable site for a new healthcare facility.

5 Discussion

5.1 Analysis of suitability results

As shown in Figure 7, the barely suitable and unsuitable construction land areas are distributed in the longitudinal central and central-eastern parts of Shimian County, which are mostly areas with high geological hazard susceptibility. The highly suitable and moderately suitable areas are mainly distributed in western, northeastern and southeastern Shimian County. Generally, suitable areas are mixed at the junction of suitable and unsuitable areas. There is a high consistency between the results of construction land suitability and geological hazard susceptibility. This situation occurs because the OWA operator is chosen for the suitability analysis with an "optimistic" attitude and the decision preference coefficient is small, which gives more weights to indices with a high degree of importance. Therefore, the geological hazard susceptibility indices have the greatest weights, and their influences on the suitability results are most significant. Comparing the results of the construction land suitability analysis with the land use type map of Shimian County (Figure 4), it can be found that almost all the construction land with the highest suitability rating in the land use type map is located in the highly suitable areas in Figure 7. This

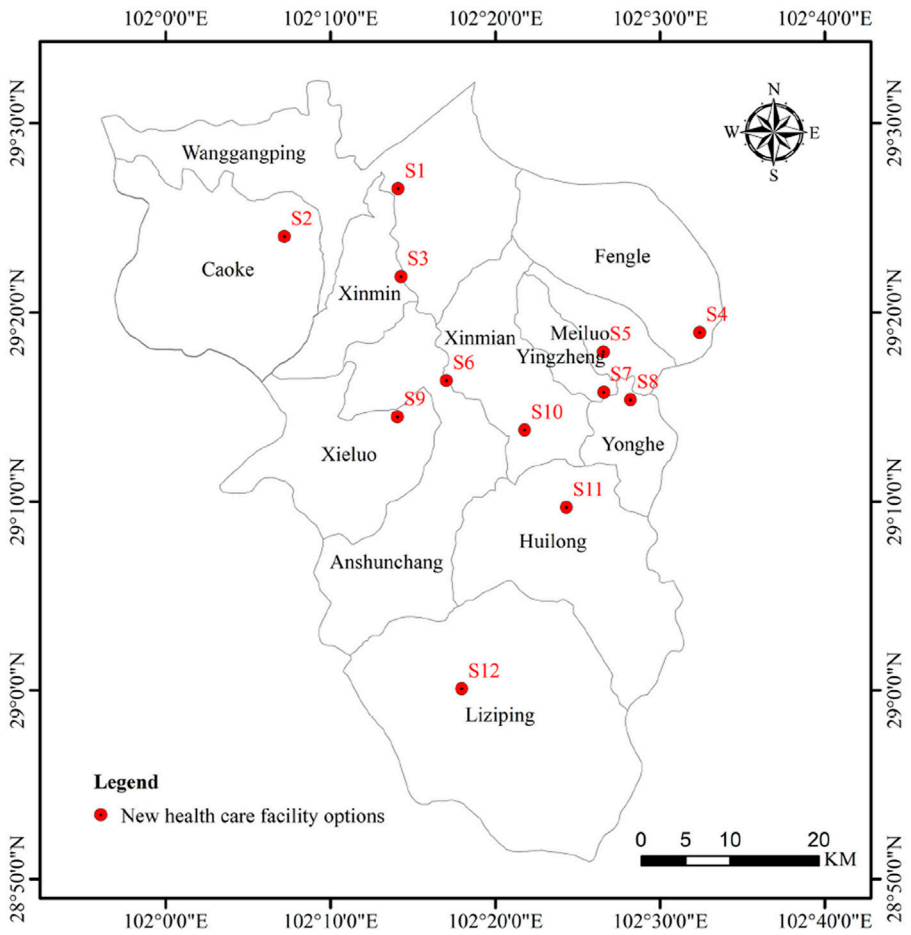

FIGURE 8
The site alternatives for new healthcare facilities.

TABLE 6 Results of evaluation indices for alternatives.

Alternatives	S1	S2	S3	S4	S5	S6	S7	S8	S9	S10	S11	S12
D1	0.735	1.000	0.592	0.683	0.426	0.227	0.226	0.333	0.383	0.000	0.253	0.741
D2	0.351	1.000	0.430	0.440	0.264	0.117	0.093	0.368	0.200	0.000	0.105	0.559
D3	0.735	1.000	0.806	0.792	0.672	0.403	0.315	0.733	0.566	0.000	0.355	0.879
D4	0.740	0.822	0.951	0.112	0.323	1.000	0.325	0.000	0.905	0.716	0.086	0.188
D5	5	4	5	5	5	5	4	4	4	4	4	4
D6	5	5	5	5	5	3	5	5	4	4	2	5

finding indicates that the suitability analysis of construction land is reasonable in this study.

5.2 Analysis of comprehensive evaluation results of site selection

After obtaining the ranking of site alternatives, the PROMETHEE Rainbow and Graphical Analysis for Interactive Aid (GAIA) functions in Visual PROMETHEE software are used to further analyze the comprehensive evaluation results of the site selection of new healthcare facilities.

1) Subindex analysis of site alternatives

The rainbow chart is generated by the function of PROMETHEE Rainbow, as shown in Figure 9. A bar chart is drawn for each site alternative, with different fragments representing different

TABLE 7 Preference functions and thresholds of evaluation indices.

Evaluation indices	Preference function	Indifference threshold *q*	Preference threshold *p*
D1	Linear	0.059	0.177
D2	Linear	0.049	0.148
D3	Linear	0.058	0.173
D4	Linear	0.085	0.256
D5	Usual	—	—
D6	Level	0	1

TABLE 8 Flow scores of site alternatives.

Alternatives	The positive flow	The negative flow	Net flow	Rank
S2	0.6617	0.0879	0.5738	1
S3	0.5927	0.0861	0.5066	2
S1	0.5470	0.1178	0.4293	3
S4	0.4790	0.1734	0.3056	4
S5	0.4202	0.2896	0.1305	5
S12	0.4224	0.3204	0.1020	6
S8	0.2653	0.3534	-0.0880	7
S9	0.2824	0.4476	-0.1652	8
S6	0.2962	0.4919	-0.1957	9
S7	0.1575	0.5164	-0.3589	10
S10	0.1212	0.7016	-0.5804	11
S11	0.0390	0.6985	-0.6595	12

evaluation indices. The size of the fragments is proportional to the net flow of the index and is ordered from top to bottom by the size of the net flow of the index. The names of evaluation indices corresponding to the sequence of fragments are marked on the upper and lower sides of the bar chart. The site alternatives are also ranked from left to right according to the numerical magnitude of their net flows. Figure 9 shows the subindex scores for the site alternatives. As an example, S2 scores higher on indices D1, D2, D3, D4, and D6 and lower on D5. The results show that compared to other alternatives, the new healthcare facility at S2 can be located as far away from existing healthcare facilities as possible, which can balance the layout of medical resources, increase accessibility to medical services, and improve the level of medical service equalization in the study area. Meanwhile, a new healthcare facility at S2 can also reduce the total distance to healthcare facilities for residents and be located away from industrial areas. However, the net flow value of the construction land suitability for S2 is negative, indicating that the construction land suitability rating of S2 is moderately suitable. Although the score of S2 is lower compared to other site alternatives, the site meets the requirements for construction suitability. The Rainbow figure can also be used to compare different alternatives. For example, compared with S3 and S2, the net flow of all indices in S3 is positive, but the fragments size of D1, D2, D3, and D6 indices is smaller than S2. It shows that the new healthcare facility at S3 can increase the accessibility to medical services and improve the level of medical service equalization to a certain extent. And it is far from the existing healthcare facilities and industrial areas, which can basically meet the requirements of balanced distribution and competitiveness of medical resources. However, the effect of the new healthcare facility at S3 is far worse than that at S2. In addition, it is better than S2 in terms of the total distance to healthcare facilities for residents and construction land suitability. Based on the above methods, the analysis of the subindexes of other site alternatives can also be obtained. The decision-maker can choose the site alternative according to his personal preference.

2) Graphical Analysis for Interactive Aid (GAIA)

GAIA is used to carry out an interaction-aided graphical analysis of the site alternatives. Three-dimensional space is used to visualize the proximity of evaluation indices and alternatives by GAIA, which is expressed in three planes: U-V, U-W and W-V (Figure 10). As shown in Figure 10, the red lines at the end of the

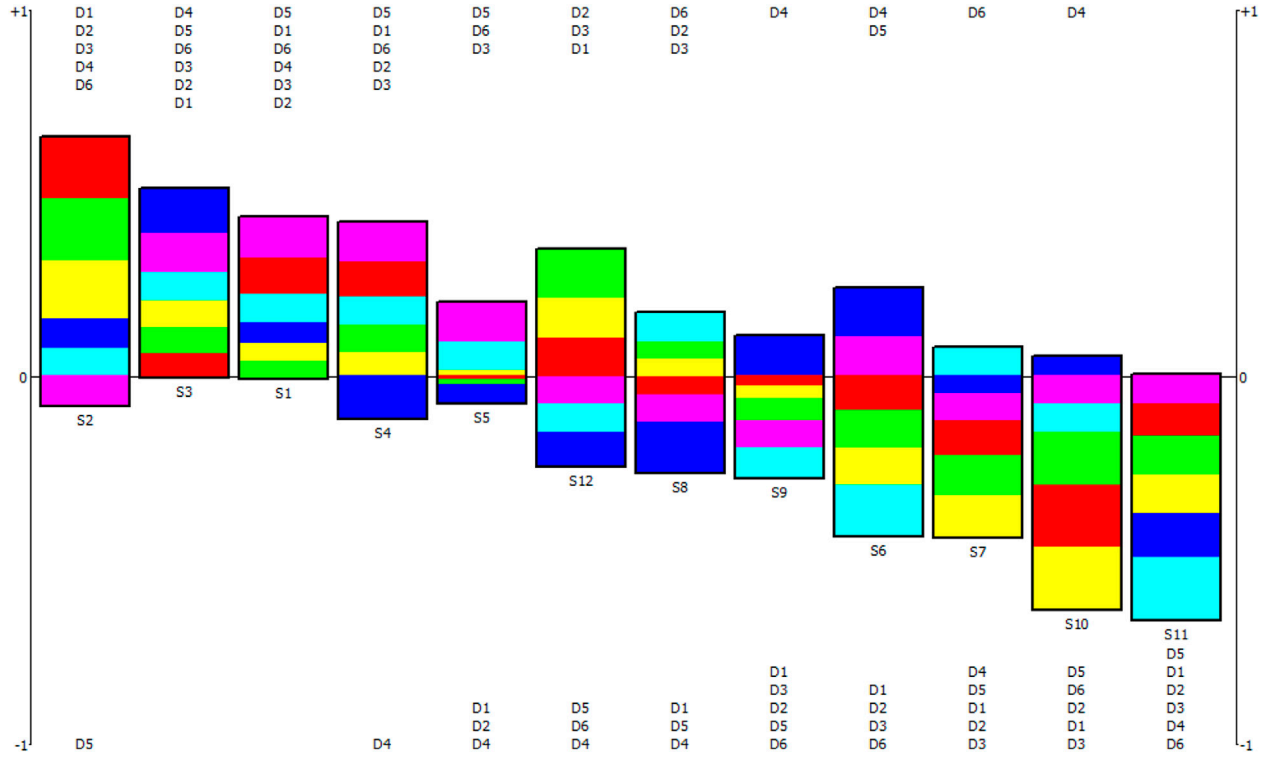

FIGURE 9
PROMETHEE Rainbow figure.

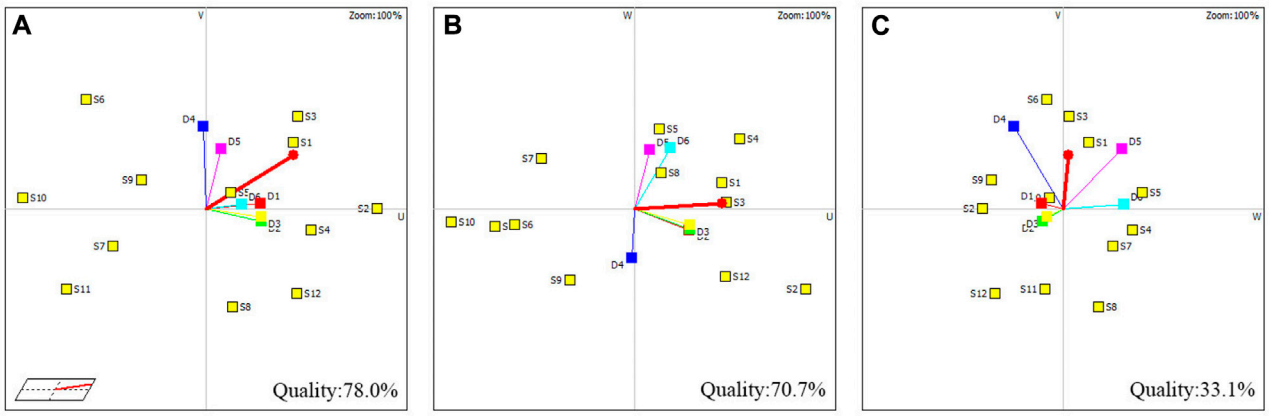

FIGURE 10
Interaction-assisted graphic: **(A)** U-V plane, **(B)** U-W plane, **(C)** W-V plane.

circles represent the decision axes; the longer the decision axis is, the more information the plane expresses and the more accurate the decision. Thus, Figures 10A expresses the most information, representing 78.0% of the 3D spatial information. In Figures 10A, when the decision-maker uses D1, D5, and D6 as the main evaluation indices, S1, S3, S4, and S2 will be the final decision targets. When D2 and D3 are defined as the main evaluation indices, S3, S2, S12, and S8 will be the optimal solutions. If an evaluation index is in the same or similar direction as the decision axis, then the index meets the current evaluation criteria. Therefore, all 6 evaluation indices meet the current evaluation criteria in Figures 10A–C can all be analyzed according to the above methods and will not be repeated here. The decision-maker can analyze whether the current results are

the same as their expectations using GAIA to make timely adjustments.

6 Conclusion

Healthcare is a matter of national economy and people's livelihood. This paper aims to reduce the losses caused by geological hazards and to achieve equalization of medical services and balanced allocation of medical resources in mountainous areas with heterogeneous population distribution and economic development. Thus, this paper proposes a GIS and PROMETHEE II-based method for determining the site selection of new healthcare facilities in geological hazard-prone areas. First, GIS and OWA operator are used to identify site alternatives for new healthcare facilities. Second, based on the identification of site alternatives, the PROMETHEE II method is used to conduct a comprehensive evaluation of the alternatives. This comprehensive evaluation method has the following advantages: 1) four criteria of geohazard, topography, geohydrology and socioeconomic are fully considered; 2) the importance of each index is measured using the α value set by the OWA operator; and 3) both qualitative and quantitative evaluation indices are considered, meeting the requirement of multiple criteria to be considered in the site selection study for new healthcare facilities. The paper fully measures the suitability of the site and the competition, accessibility, equalization, environment, and demand for new healthcare facilities, effectively ensuring the safety, suitability and development of the site and achieving a reasonable and scientific site selection for new healthcare facilities in geological hazard-prone areas. The results of the study show that the GIS and PROMETHEE II-based evaluation method has the ability and advantage of solving the site selection of new healthcare facilities in geological hazard-prone areas and other similar complex site selection problems, which can provide some references for similar studies.

In addition, the method allows the decision-making process for suitability analysis to be more flexible by setting the α value according to the decision-makers' attitudinal preferences. The α value can represent the mutual restriction relationship between geological hazards and construction land development. At the same time, decision-makers can assign weights to indices in Visual PROMETHEE software to intuitively obtain the changes in weights on ranking results. Decision-makers can also conduct detailed analysis on the relationship between the subindexes of the ranking results and the alternatives to improve the accuracy of decision-making according to rainbow graph and GAIA.

With the development of society and economy, other standards should be considered for the site selection of new healthcare facilities in geological hazard-prone areas to improve the comprehensiveness and accuracy of the indices, such as land cost, land expansion, green area, air pollution and so on. Other multicriteria decision-making methods or fuzzy multicriteria decision-making methods, such as ANP, ELECTRE, TOPSIS, Fuzzy-TOPSIS, VIKOR, Fuzzy-VIKOR, TODIM, Fuzzy-SAW, and EDAS, can also be used to study site selection. Follow-up research can use a variety of MCDM tools for comparative research. The transparency of the decision-making process and the robustness of the decision-making results can be improved by comparing the advantages and disadvantages of different decision-making methods. In addition, machine learning methods, such as LSSVM, MPA, PSO, GA, GWO, SVR, LSSVR, and RBFNN, can also be tried to solve the site selection problems in the future.

Data availability statement

The original contributions presented in the study are included in the article/Supplementary Material, further inquiries can be directed to the corresponding author.

Author contributions

MY, formal analysis, investigation, methodology, writing—original draft; S-YH, investigation, formal analysis, data curation; J-MC, investigation, resources; P-NG, investigation, software, formal analysis; H-BL, investigation, formal analysis, visualization; H-GX, conceptualization, funding acquisition, writing—review and editing.

Funding

This work was supported by the National Natural Science Foundation of China (U20A20111).

Conflict of interest

The authors declare that the research was conducted in the absence of any commercial or financial relationships that could be construed as a potential conflict of interest.

Publisher's note

Supplementary material

The Supplementary Material for this article can be found online at: https://www.frontiersin.org/articles/10.3389/feart.2023.1121690/full#supplementary-material

References

Adali, E. A., and Tus, A. (2021). Hospital site selection with distance-based multi-criteria decision-making methods. *Int. J. Healthc. Manag.* 14 (2), 534–544. doi:10.1080/20479700.2019.1674005

Aghmashhadi, A. H., Azizi, A., Zahedi, S., Hoseinkhani, M., and Cirella, G. T. (2022). Land suitability mapping using GIS-based ANP for residential zoning: Case research from central Iran. *Trans. GIS* 26 (2), 1017–1039. doi:10.1111/tgis.12896

Ajaj, Q. M., Shareef, M. A., Jasim, A. T., Hasan, S. F., Noori, A. M., and Hassan, N. D. (2019). "An AHP-based GIS for a new hospital site selection in the kirkuk governorate," in Proceedings of the 2nd International Conference on Electrical, Communication, Computer, Power and Control Engineering (ICECCPCE), Iraq, February 2019.

Bagheri, M., Sulaiman, W. N. A., and Vaghefi, N. (2013). Application of geographic information system technique and analytical hierarchy process model for land-use suitability analysis on coastal area. *J. Coast. Conservation* 17 (1), 1–10. doi:10.1007/s11852-012-0213-4

Bahadori, M., Hosseini, S. M., Teymourzadeh, E., Ravangard, R., Raadabadi, M., and Alimohammadzadeh, K. (2017). A supplier selection model for hospitals using a combination of artificial neural network and fuzzy VIKOR. *Int. J. Healthc. Manag.* 13 (4), 286–294. doi:10.1080/20479700.2017.1404730

Behzadian, M., Kazemzadeh, R. B., Albadvi, A., and Aghdasi, M. (2010). Promethee: A comprehensive literature review on methodologies and applications. *Eur. J. Operational Res.* 200 (1), 198–215. doi:10.1016/j.ejor.2009.01.021

Billaud, O., Soubeyrand, M., Luque, S., and Lenormand, M. (2020). Comprehensive decision-strategy space exploration for efficient territorial planning strategies. *Comput. Environ. Urban Syst.* 83, 101516. doi:10.1016/j.compenvurbsys.2020.101516

Boyaci, A. C., and Sisman, A. (2022). Pandemic hospital site selection: A GIS-based MCDM approach employing pythagorean fuzzy sets. *Environ. Sci. Pollut. Res.* 29 (2), 1985–1997. doi:10.1007/s11356-021-15703-7

Chai, J., Liu, J. N. K., and Ngai, E. W. T. (2013). Application of decision-making techniques in supplier selection: A systematic review of literature. *EXPERT Syst. Appl.* 40 (10), 3872–3885. doi:10.1016/j.eswa.2012.12.040

Cosimo, L. H. E., Martins, S. V., and Gleriani, J. M. (2021). Suggesting priority areas in the buffer zone of Serra do Brigadeiro State Park for forest restoration compensatory to bauxite mining in Southeast Brazil. *Ecol. Eng.* 170, 106322. doi:10.1016/j.ecoleng.2021.106322

Csiszar, O. (2021). Ordered weighted averaging operators: A short review. *IEEE Syst. Man, Cybern. Mag.* 7 (2), 4–12. doi:10.1109/msmc.2020.3036378

Dell'Ovo, M., Capolongo, S., and Oppio, A. (2018). Combining spatial analysis with MCDA for the siting of healthcare facilities. *Land Use Policy* 76, 634–644. doi:10.1016/j.landusepol.2018.02.044

Dell'Ovo, M., Frej, E. A., Oppio, A., Capolongo, S., Morais, D. C., and de Almeida, A. T. (2017). "Multicriteria decision making for healthcare facilities location with visualization based on FITradeoff method," in Proceedings Of The Decision Support Systems Vii: Data, Information And Knowledge Visualization In Decision Support Systems, Namur, Belgium, May 2017.

Dulin, M. F., Ludden, T. M., Tapp, H., Blackwell, J., de Hernandez, B. U., Smith, H. A., et al. (2010). Using geographic information systems (GIS) to understand a community's primary care needs. *J. Am. Board Fam. Med.* 23 (1), 13–21. doi:10.3122/jabfm.2010.01.090135

Eghtesadifard, M., Afkhami, P., and Bazyar, A. (2020). An integrated approach to the selection of municipal solid waste landfills through GIS, K-Means and multi-criteria decision analysis. *Environ. Res.* 185, 109348. doi:10.1016/j.envres.2020.109348

Eldemir, F., and Onden, I. (2016). Geographical information systems and multicriteria decisions integration approach for hospital location selection. *Int. J. Inf. Technol. Decis. Mak.* 15 (5), 975–997. doi:10.1142/s0219622016500218

Gul, M., and Guneri, A. F. (2021). Hospital location selection: A systematic literature review on methodologies and applications. *Math. Problems Eng.* 2021, 1–14. doi:10.1155/2021/6682958

Guo, F., Gao, J., Men, H., Fan, Y., and Liu, H. (2021). Large-scale group decision-making framework for the site selection of integrated floating photovoltaic-pumped storage power system. *J. Energy Storage* 43, 103125. doi:10.1016/j.est.2021.103125

Halder, B., Bandyopadhyay, J., and Banik, P. (2020). Assessment of hospital sites' suitability by spatial information technologies using AHP and GIS-based multi-criteria approach of Rajpur-Sonarpur Municipality. *Model. EARTH Syst. Environ.* 6 (4), 2581–2596. doi:10.1007/s40808-020-00852-4

Joseph, A. E., and Bantock, P. R. (1982). Measuring potential physical accessibility to general practitioners in rural areas: A method and case study. *Soc. Sci. Med.* 16 (1), 85–90. doi:10.1016/0277-9536(82)90428-2

Kapoor, N., and Bansal, V. K. (2021). Spatial suitability assessment for planning infrastructure facilities at site level in hill areas. *J. Urban Manag.* 10 (1), 27–45. doi:10.1016/j.jum.2021.02.003

Kumar, S., and Kumar, R. (2014). Site suitability analysis for urban development of a hill town using GIS based multicriteria evaluation technique: A case study of nahan town, Himachal Pradesh, India. *Int. J. Adv. Remote Sens. GIS* 3 (1), 516–524.

Lin, J., Chen, W., Qi, X., and Hou, H. (2021). Risk assessment and its influencing factors analysis of geological hazards in typical mountain environment. *J. Clean. Prod.* 309, 127077. doi:10.1016/j.jclepro.2021.127077

Liu, R., Zhang, K., Zhang, Z., and Borthwick, A. G. L. (2014a). Land-use suitability analysis for urban development in Beijing. *J. Environ. Manag.* 145, 170–179. doi:10.1016/j.jenvman.2014.06.020

Liu, Y., Peng, J., Han, Y., Wei, H., and Du, Y. (2014b). Suitability assessment for building land consolidation on gentle hillside based on OWA operator: A case in dali Bai nationality borough in yunnan, China. *Acta Ecol. Sin.* 34 (12), 3188–3197.

Luan, C., Liu, R., and Peng, S. (2021). Land-use suitability assessment for urban development using a GIS-based soft computing approach: A case study of ili valley, China. *Ecol. Indic.* 123, 107333. doi:10.1016/j.ecolind.2020.107333

Ma, Z., and Mei, G. (2021). Deep learning for geological hazards analysis: Data, models, applications, and opportunities. *Earth-Science Rev.* 223, 103858. doi:10.1016/j.earscirev.2021.103858

Sahin, T., Ocak, S., and Top, M. (2019). Analytic hierarchy process for hospital site selection. *HEALTH POLICY Technol.* 8 (1), 42–50. doi:10.1016/j.hlpt.2019.02.005

Sara, B., and Abbas, A. (2014). A multi-objective optimization approach for location-allocation of clinics. *Int. Trans. Operational Res.* 22 (2), 313–328. doi:10.1111/itor.12088

Sennaroglu, B., and Celebi, G. V. (2018). A military airport location selection by AHP integrated PROMETHEE and VIKOR methods. *Transp. Res. PART D-TRANSPORT Environ.* 59, 160–173. doi:10.1016/j.trd.2017.12.022

Senvar, O., Otay, I., and Bolturk, E. (2016). Hospital site selection via hesitant fuzzy TOPSIS. *IFAC Pap.* 49 (12), 1140. doi:10.1016/j.ifacol.2016.07.656

Tripathi, A. K., Agrawal, S., and Gupta, R. D. (2021). Comparison of GIS-based AHP and fuzzy AHP methods for hospital site selection: A case study for prayagraj city. *GeoJournal* 28. doi:10.1007/s10708-021-10445-y

Tyagi, A., and Singh, P. (2019). Hospital performance management: A multi-criteria decision-making approach. *Int. J. Healthc. Manag.* 12 (4), 286–291. doi:10.1080/20479700.2017.1337606

Wang, L., Shi, H., and Gan, L. (2018). Healthcare facility location-allocation optimization for China's developing cities utilizing a multi-objective decision support approach. *Sustainability* 10 (12), 4580. doi:10.3390/su10124580

Wu, Y., Liu, F., Huang, Y., Xu, C., Zhang, B., Ke, Y., et al. (2020a). A two-stage decision framework for inland nuclear power plant site selection based on GIS and type-2 fuzzy PROMETHEE II: Case study in China. *Energy Sci. Eng.* 8 (6), 1941–1961. doi:10.1002/ese3.640

Wu, Y., Tao, Y., Zhang, B., Wang, S., Xu, C., and Zhou, J. (2020b). A decision framework of offshore wind power station site selection using a PROMETHEE method under intuitionistic fuzzy environment: A case in China. *Ocean Coast. Manag.* 184, 105016. doi:10.1016/j.ocecoaman.2019.105016

Wu, Y., Zhang, B., Wu, C., Zhang, T., and Liu, F. (2019). Optimal site selection for parabolic trough concentrating solar power plant using extended PROMETHEE method: A case in China. *Renew. Energy* 143, 1910–1927. doi:10.1016/j.renene.2019.05.131

Yager, R. R. (1988). On ordered weighted averaging aggregation operators in multicriteria decisionmaking. *IEEE Trans. Syst. Man, Cybern.* 18 (1), 183–190. doi:10.1109/21.87068

Yager, R. R. (1996). Quantifier guided aggregation using OWA operators. *Int. J. Intelligent Syst.* 11 (1), 49–73. doi:10.1002/(SICI)1098-111X(199601)11:1<49:AID-INT3>3.0.CO;2-Z

Yang, Y., Tang, X-l., and Li, Z-h. (2021). Land use suitability analysis for town development planning in nanjing hilly areas: A case study of tangshan new town, China. *J. Mt. Sci.* 18 (2), 528–540. doi:10.1007/s11629-020-6037-z

Yilmaz, M., and Atan, T. (2021). Hospital site selection using fuzzy EDAS method: Case study application for districts of Istanbul. *J. INTELLIGENT FUZZY Syst.* 41 (2), 2591–2602. doi:10.3233/jifs-201757

Yu, M., Xing, H., and Hu, S. (2021). Debris flow susceptibility assessment based on information value and logistic regression coupled model: Case of shimian county, sichuan Province. *Yangtze River* 52 (12), 107–114.

Zhang, W., Cao, K., Liu, S., and Huang, B. (2016). A multi-objective optimization approach for health-care facility location-allocation problems in highly developed cities such as Hong Kong. *Comput. Environ. Urban Syst.* 59, 220–230. doi:10.1016/j.compenvurbsys.2016.07.001

Zolfani, S. H., Yazdani, M., Torkayesh, A. E., and Derakhti, A. (2020). Application of a gray-based decision support framework for location selection of a temporary hospital during COVID-19 pandemic. *SYMMETRY* 12 (6), 886. doi:10.3390/sym12060886

frontiers | Frontiers in Earth Science

TYPE Original Research
PUBLISHED 01 September 2023
DOI 10.3389/feart.2023.1223785

OPEN ACCESS

EDITED BY
Jia-wen Zhou,
Sichuan University, China

REVIEWED BY
Chong Xu,
Ministry of Emergency Management, China
Huazhe Jiao,
Henan Polytechnic University, China
Erol Yilmaz,
Recep Tayyip Erdoğan University, Türkiye
Xiaocheng Huang,
Hunan University of Science and Technology, China

*CORRESPONDENCE
Wei Sun,
kmustsw@kust.edu.cn

RECEIVED 16 May 2023
ACCEPTED 14 August 2023
PUBLISHED 01 September 2023

CITATION
Li Z-r, Jiang M-g, Feng X-l, Wang S-y, Zeng Q-t, Chen C, Liu W-l and Sun W (2023), Analysis of energy consumption characteristics and fracture characteristics of moraine grouting solidified body under uniaxial compression.
Front. Earth Sci. 11:1223785.
doi: 10.3389/feart.2023.1223785

Analysis of energy consumption characteristics and fracture characteristics of moraine grouting solidified body under uniaxial compression

Zheng-rong Li[1,2], Ming-gui Jiang[1], Xing-long Feng[2], Shao-yong Wang[3], Qing-tian Zeng[2], Chong Chen[3], Wen-lian Liu[4] and Wei Sun[1]*

[1]Faculty of Land and Resources Engineering, Kunming University of Science and Technology, Kunming, China, [2]Yunnan Diqing Non-Ferrous Metal Co, Ltd, Diqing, China, [3]School of Civil and Resources Engineering, University of Science and Technology Beijing, Beijing, China, [4]China Non-ferrous Metal Industry Kunming Exploration Design Research Institute, Kunming, China

Glacial movement causes massive accumulation of fine-grained moraine, which often induces slope instability, moraine debris flow, and other geological hazards due to the effects of rain and the ice-snow melting. This study used a modified phosphoric acid-water glass slurry for grouting and curing moraine, and analyzed the influencing law of water glass Baume degree and curing age on energy consumption characteristics as well as the fracture properties of the grout-cured body of moraine using the uniaxial compression test. The results showed that the gel time of phosphoric acid-water glass slurry increased with the increasing addition of phosphoric acid and that it had a mutation phenomenon. The gel time increased linearly with the increasing addition of phosphoric acid before the mutation. Moreover, the compressive strength, pre-peak total energy, pre-peak elastic energy, pre-peak dissipative energy, elastic energy density, dissipative energy density, and pre-peak fracture toughness of the moraine curing body at same curing age increased linearly with the increase of water glass Baume degree by 46%–218%. The compressive strength, pre-peak elastic energy, and pre-peak elastic energy density of the moraine curing body increased with the curing age but grew slowly from 3 days to 7 days and rapidly from 7 days to 14 days. Through regression analysis of the test results, the fracture toughness calculation formula was derived from an energy perspective. These research results have significant implications for the reinforcement of moraine strata grouting and glacial debris flow disaster prevention and control.

KEYWORDS

moraine, phosphoric acid-water glass, grouting reinforcement, energy dissipation, fracture toughness

1 Introduction

The Pulang copper deposit has relatively complete Quaternary glacial relics, meaning that the overlying strata have many glacial deposits. These glacial deposits are comprised of sediment and stones that have been deposited during glacial movement, mainly composed of clay, silt, gravel, pebbles, and boulders. The grain size distribution is vast, the structure is

different, and there is no stratification (Hart, 1998; Evans et al., 2021). The transport force of glaciers gradually decreases as they melt, resulting in the accumulation of large amounts of fine-grained moraines, which provide a rich source of material for forming glacial debris flows (Meng et al., 2023). With the increase of mining depth and the expansion of the surface collapse area, once the flood season arrives, the rainfall in the mining area, upstream surface runoff, and snow melt water in high mountains drive the surface moraine cover layer (tens of meters and weathered, broken rock debris) into the collapse area, which can easily cause underground mudflow accidents (Zaginaev et al., 2019; Gao et al., 2022). To date, research by both domestic and foreign scholars on glacial debris flow has mostly focused on the formation mechanisms, evolutionary process, risk evaluation and monitoring, and early warning (Marr et al., 2002; Li et al., 2016; Medeu et al., 2022), but research on the specific prevention and control measures for moraine debris flow disasters is needed. In response to the above problems, grouting reinforcement is used to change the moraine from powder to block, improve the integrity and stability of the loose accumulation, and improve the mechanical properties of the moraine as well as to preserve the surface vegetation to the maximum extent (Zhang et al., 2021; Fan et al., 2023). It is therefore important to study the mechanical properties and bearing mechanism of the moraine slurry curing body for both the prevention and control of downhole mudflow and the evaluation of the slurry effect. Coulter et al. (Coulter and Martin, 2006) and others have performed jet grouting in the boring tunnel process of moraine and analyzed the surface settlement of the grouting by numerical simulation in reverse, and the results showed that the narrow settlement trough was formed because of the local shear zone caused by high pressure during jet grouting. Luo et al. (Luo et al., 2019) and others have investigated the effects of different temperatures and envelope pressures on the strength of moraine permafrost by triaxial compression tests, and the results showed that the strength envelope is nonlinear when the average stress is less than the consolidation yield pressure defined as the strength envelope boundary stress, while it is approximately linear when the average stress is greater than the consolidation yield pressure. Li et al. (Li et al., 2022) investigated the effect of different ice forms, such as crushed ice and block ice, on the mechanical properties of moraine soils by triaxial constant strain rate (CSR) with coupled thermomechanical (CTM) tests. The test results show that moraine soils containing block ice have higher peak strength and moraine soils containing crushed ice are more sensitive to temperature changes. Begam et al. (Begam et al., 2018) showed that the height of the moraine dam and the volume of the lake upstream of the dam are the most sensitive parameters affecting the GLOF peak using coupled numerical simulations and indoor similar experimental simulations to verify the moraine dam overflow and erosion damage. Peng et al. (Peng et al., 2022) derived the flow discharge, erosion, entrainment, and deposition processes of glacial debris flows through field investigations and numerical simulations, revealing the origin mechanism and dynamic evolution process of the debris-ice landslide-debris flow hazard chain. Because there are few studies on moraine grouting and curing at home and abroad, the study was conducted with reference to the test and evaluation methods of the strength of fractured rock after grouting. Weng et al. (Weng et al., 2022) showed that the infiltration grouting tests on fractured sandstone samples analyzed the flow and diffusion mechanism of the slurry, and the results showed that the final injection volume of grouting decreased with the increase of temperature and surrounding pressure, and the effective grouting time was inversely proportional to the slurry flow rate, while it was positively correlated with temperature. Zhang et al. (Zhang et al., 2022) investigated the mechanical properties of compressed pre-cracked sandstone before and after grouting by triaxial compression tests with different surrounding pressures, and the results showed that the strength of grouted specimens mainly depended on the micromechanical properties of the contact surface between sandstone and cement paste, and the elastic modulus of grouted specimens was lower than that of uncracked sandstone. Liu et al. (Liu et al., 2022) proposed an NMM-HM grouting model based on the numerical flow form method (NMM) to study the flow of slurry, and the results showed that the fracture grouting pressure could increase the fracture aperture, which is beneficial to grouting efficiency. Salimian et al. (Salimian et al., 2017) performed direct shear tests on grout cracks by preparing specimens with three different surface roughnesses using dental silica gel, and the test results showed that the compressive grout strength increased with decreasing water-cement ratio, but not necessarily with increasing shear strength. Sui et al. (Sui et al., 2015) showed that the two largest factors affecting the sealing efficiency were the initial water flow velocity and the width of the hole diameter, with the former having a greater effect than the latter. Kumar et al. (Kumar et al., 2022) studied the mechanical properties of intact specimens, ungrouted joints, cement joint grout, and epoxy joint grout specimens under dynamic and static loads, and the test results showed that the strength of the epoxy grout joint samples was all greater than that of the cement grout samples.

In summary, research on grouting reinforcement for moraine strata is still in the exploration and development stage. The overlying moraines of the Purang copper mine are mostly composed of fine clay wrapped with stones that are randomly distributed, and the permeability of the soil body is extremely poor under the double extrusion of glacial accumulation and geological movement. Figure 1A shows that the traditional cement slurry cannot be injected permeably. The cement particles and the moraine soil have a noticeable percolation effect. Many cement particles are retained on the moraine's surface to obstruct the continuous injection of the slurry. Because of the above engineering problems, the modified phosphoric acid-water glass slurry with better injectability is chosen to grout and cure the moraine, and its grouting effect is shown in Figure 1B; under the same grouting conditions, the slurry can be fully diffused in the moraine, and the slurry is distributed along both sides of the splitting channel and forms a large volume of slurry-soil complex at the end of the splitting track. After the grouting is completed, the grouting effect of the reinforced soil needs to be evaluated to determine the feasibility and sustainability of the grouting project. Therefore, this paper investigates the influence law of water glass Baume degree and curing age on moraine slurry curing body through a uniaxial compression test and discusses and analyzes the mechanical properties and energy consumption characteristics of moraine slurry curing, further revealing the damage mechanism of moraine slurry curing body and slurry consolidation mechanism. Based on the regression fitting analysis method, our study

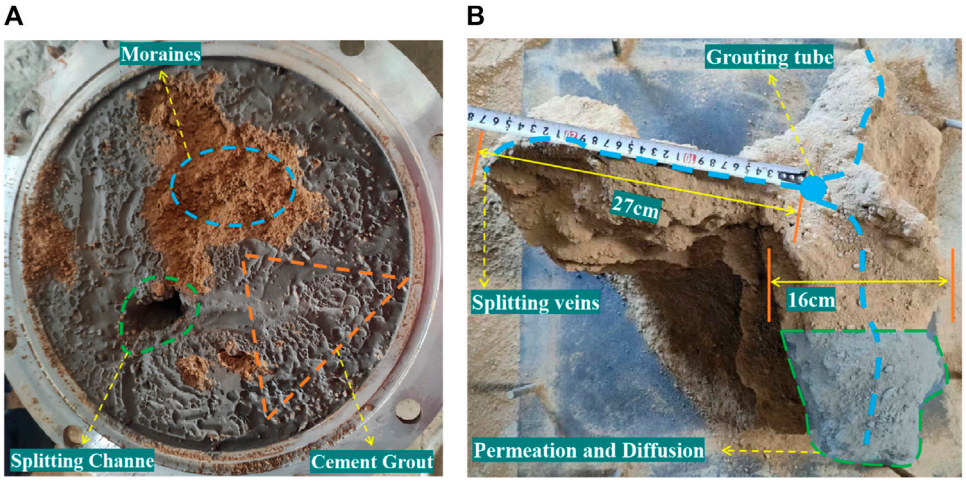

FIGURE 1
Dispersion distribution of different slurry injections: **(A)** cement slurry; **(B)** phosphoric acid-water glass slurry.

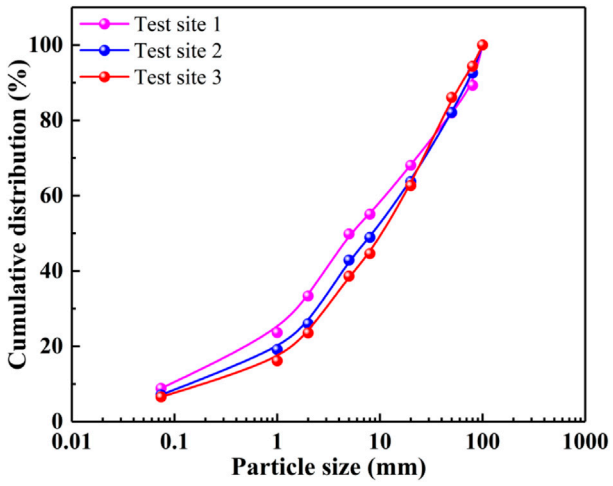

FIGURE 2
Moraine grain level composition curve.

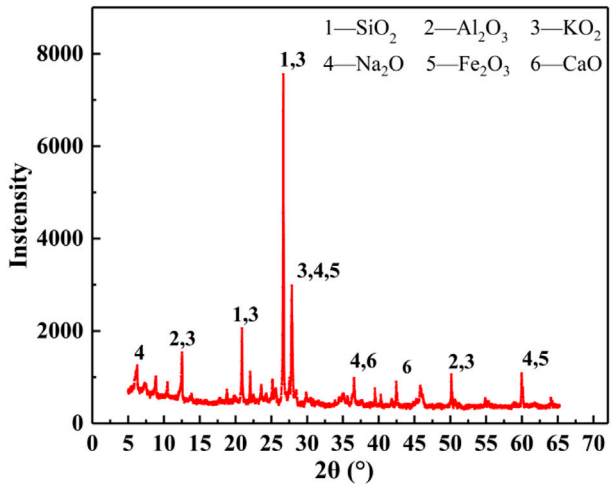

FIGURE 3
X-ray powder diffraction test spectra of moraines.

establishes a fracture toughness relationship model based on energy analysis and proposes an evaluation method for establishing slurry and the parameters and fracture toughness of the moraine slurry curing body. The results have great significance to engineering theories of moraine slurry reinforcement and the prevention and control of moraine debris flow disasters.

2 Experimental design

2.1 Test material

In this experiment, a modified phosphoric acid-water glass solution was chosen as the grouting material, and the water glass has a Baume degree of 35°B e' and a modulus of 3.05. The test water was ordinary tap water, and the moraine selected for the test was taken from the Pulang copper mine in Yunnan. According to the genesis of the formation, geotechnical type, and physical and mechanical properties, the soil within the 10 m exploration depth of the test site was divided into three layers, and the exploratory pit was excavated to take *in-situ* soil samples for each layer and carry out the test of physical and chemical indexes of the soil. According to the genesis of the stratum, geotechnical type, and physical and mechanical properties, the soil within the 10 m exploration depth of the test site was divided into three layers, pits were excavated, and *in-situ* soil samples were taken for each layer. The soil physicochemical index test was carried out, the grain-level composition and XRD patterns are shown in Figure 2 and Figure 3, respectively, and the chemical composition and basic properties of the original moraine formation are shown in Table 1 and Table 2, respectively. From

TABLE 1 X-ray powder diffraction analysis of moraines.

Quartz (%)	Albite (%)	Chlorite (%)	Mica (%)	Montmorillonite (%)	Illite (%)	Kaolinite (%)	Andesine (%)	Saspachite (%)	Pargasite (%)
28.8	24.8	14.9	16.1	0	0	0	6.9	3.3	5.2

TABLE 2 Basic properties of *in situ* stratigraphy.

Wet density/(kg/cm^3)	dry density (kg/cm^3)	Porosity/%	Permeability coefficient/(cm/s)	Plasticity limit/%	Liquid limit/%
2.29×10^3	2.21×10^3	17.21	8.95×10^{-5}	16	22

Figure 2, the moraine inhomogeneity coefficient is 113.43, and the curvature coefficient is 2.77, which indicates that the moraine is well-graded and dense. As can be seen from Table 1 and Figure 3, the main constituents of moraines are SiO_2, Na_2O-Al_2O_3-$6SiO_2$, and $KAl_2(AlSi_3O)$ $(OH)_2$, *etc.*, of which quartz and nannofeldspar account for about 53.6% of the total weight, feldspar and quartz are all stable minerals in nature and are widely found in nature, chlorite does not show special properties when exposed to water. It does not contain montmorillonite, illite, Kaolinite, and other water-sensitive minerals (Zhao et al., 2018; Yi et al., 2022). As can be seen from Table 2, the wet density of the moraine stratum is 2.29 g/cm^3, the dry density is 2.21 g/cm^3, the plastic limit of the soil is 16%, the liquid limit is 22% its low liquid limit powdery clay, the permeability coefficient of the soil is 8.95×10^{-5} cm/s for the weak permeability level.

2.2 Formulation of phosphoric acid-water glass slurry

The slurry gelation time in actual engineering grouting should be controlled from 30 to 60 min to ensure slurry penetration or diffusion in the grouted reinforced area (Cui et al., 2022). If the gel time is less than 30min, the slurry condenses prematurely, which blocks the grouting line, and if it is more than 60min, the slurry spreads too far in the formation and causes slurry loss. In this experiment, modified phosphoric acid-water glass chemical slurry was used as grouting material, and the suitable gel time of phosphoric acid-water glass slurry with different Baume degrees was explored. This test uses a water glass Baume degree of 35 and modulus of 3.05; phosphoric acid is selected as a medical phosphoric acid solution, with a concentration of 95%. The project examined two-liquid groutings and used diluted phosphoric acid and water glass solution with a volume ratio of 1:1 to carry out the test. First of all, according to the experimental design of water glass, the phosphoric acid solution is diluted with water to get the concentration of water glass solution and the phosphoric acid solution required for the test, and then the diluted, filtered water glass solution and the phosphoric acid solution is poured into the beaker according to the volume ratio of 1:1, and constantly stirred with a glass rod to make it fully react, using the inverted cup method to determine its gel time, the PH of the mixed slurry was measured to record the test data, to avoid test errors for each group tests were performed three times. The average value of gel time was taken after each test was undertaken three times.

2.3 Moraine solidified specimen preparation

In situ moraines have a wide range of particle gradation distribution, with fine to micron-level clay particles as coarse as tens of meters of boulders. Due to the consideration of size effect (Zhu et al., 2020; Zheng et al., 2023) in this experiment, the moraine retrieved from the field was milled, dried, and screened through a 10 mm screen for backup. Tests were undertaken before the drying moraine should be rehydrated to restore the field moisture content after 24 h maintenance. The prepared phosphoric acid-water glass slurry was poured into the mixing bucket and mixed with moraine material, and the slurry was poured into a standard mold measuring 70.7×70.7×70.7 mm. After resting for 24 h for demolding, the specimens were placed in a constant temperature and humidity curing box with a temperature of 20°C and humidity of 90% for 3 days, 7 days and 14 days, respectively. The uniaxial compression test was carried out on the specimens that reached the curing age. This test uses microcomputer-controlled EM3.305 servo single-axis compression equipment, the maximum axial force is 300kN, the displacement control is used to load at a rate of 2 mm/min, and the average value is taken after three parallel tests for each group. The test flow is shown in Figure 4.

2.4 Energy dissipation principle and analysis method

The essence of moraine solidification body deformation damage is the combined result of various dissipation and energy releases. Energy dissipation was used to induce internal damage to produce microcracks, leading to the deterioration of material properties and loss of strength. Energy release triggers sudden damage to the solidified body of the moraine (Huang et al., 2021; Li et al., 2021). Assuming that there is no heat energy dissipation during the deformation and damage of the specimen under load, it is known from the principle of energy conservation:

$$U = U^d + U^e = \int F_N d(l_N) \tag{1}$$

$$U^e = \frac{\sigma_i^2}{2E} = \frac{1}{2E_u}\left[\sigma_1^2 + \sigma_2^2 + \sigma_3^2 - 2\,\bar{\mu}\,(\sigma_1\sigma_2 + \sigma_2\sigma_3 + \sigma_1\sigma_3)\right] \tag{2}$$

$$U^d = U - U^e \tag{3}$$

In the formula: U is the total work done by the external force on the specimen, J; U^d is the energy dissipated inside the specimen due

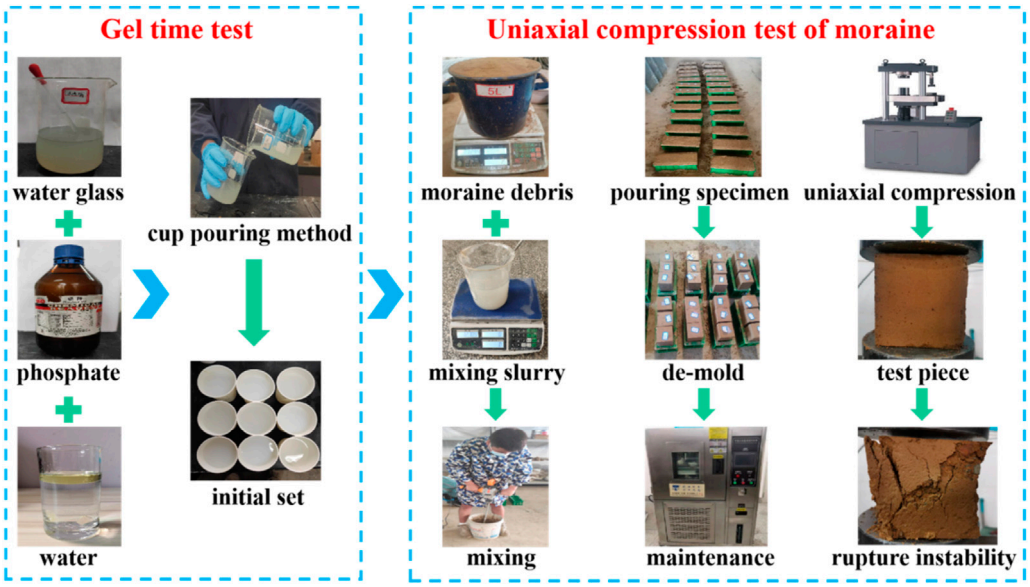

FIGURE 4
Flow chart of moraine solidified specimen preparation.

to the compaction of pores or microcracks and the connection and expansion of microcracks to form a macroscopic rupture surface, J; U^e is the elastic energy accumulated inside the specimen, J; F_N is the axial load, N; l_N is the displacement of the test piece machine indenter in the vertical direction, m; V is the volume of the specimen, m^3; σ and ε are the stress and strain of the specimen respectively; E and μ are the modulus of elasticity and Poisson's ratio of the specimens, respectively.

Dissipative energy density and elastic energy density are introduced to analyze the energy consumption characteristics of the specimen, which are calculated as shown in (4) to (5):

$$\rho_d = \frac{U_d}{V} \tag{4}$$

$$\rho_e = \int_0^{\varepsilon_1} \sigma d\varepsilon \tag{5}$$

The irreversible energy consumed by the pores and microcracks inside the specimen during the bearing process is compacted, or the microcracks expand and connect to form a new fracture surface, which leads to the dissipation of energy. That is, the fracture energy consumed during the deformation and damage of the specimen can be characterized as shown in Equation 6. The relation (7) holds in the linear elastic fracture mechanics when the crack is the stable quasi-static extension, i.e., when the dynamic effect is zero (Dong et al., 2018). At this point, the fracture toughness was introduced to characterize the ability of the specimen to prevent crack expansion, i.e., to reflect the ability of the material to resist brittle fracture (Guo et al., 2005). The expansion law of fracture toughness of moraine solidified specimens is shown in Equation 9:

$$U^d = G_F \tag{6}$$

$$G_F = G_{IC} \tag{7}$$

$$K_{IC}^2 = G_{IC} \times E \tag{8}$$

$$K_{IC} = \sqrt{G_{IC} \times E} = \sqrt{U^d \times E} \tag{9}$$

In the formula: U^d is dissipate energy, J; G_F is the fracture energy, J; G_{IC} is the energy release rate; K_{IC} is the fracture toughness, kPa $\cdot m^{0.5}$; E is the modulus of elasticity.

According to the mechanics of materials and current research (Kivi et al., 2018; Lin et al., 2022; Jiao et al., 2023a; Zou et al., 2023), the area enclosed by the force-displacement curve and the horizontal axis represents the total work done on the material. The area enclosed by the stress-strain curve and the horizontal axis indicates the ability of the material to absorb energy, also known as the strain energy density. The force-displacement curve and stress-strain curve of moraine-cured specimens with a curing age of 14 days and a Baume degree of 20°B e' are used to illustrate the total energy consumption and elastic energy density characterization method. As shown in Figures 5A is the peak load point, the area S_1 is enclosed by its pre-peak deformation phase OA, the x-axis is the total pre-peak energy consumption, and the area S_2 is enclosed by the post-peak deformation phase AB, and the x-axis is the total post-peak energy consumption. As shown in Figure 5B, Point A is the peak stress point, and the area S_1 enclosed by OA and x-axis in its pre-peak deformation phase is the pre-peak elastic energy density, and the area S_2 enclosed by AB and x-axis in the post-peak deformation phase is the post-peak elastic energy density. Since the curves of all post-peak deformation stages cannot be recorded during the actual test, to ensure the comparability of the test data, only the pre-peak change stages of the force-displacement curve and the stress-strain curve are studied in this paper.

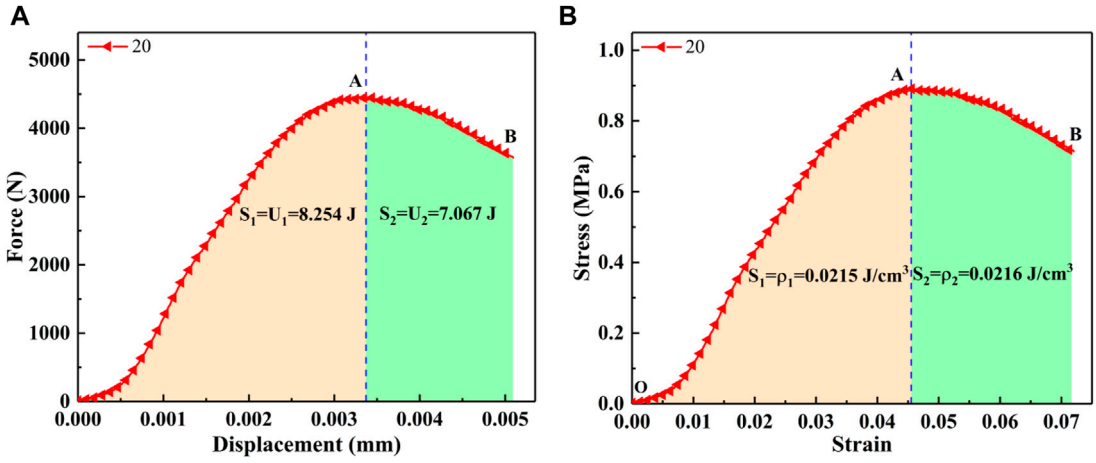

FIGURE 5
Schematic diagram of energy consumption and energy density characterization: **(A)** Schematic representation of energy consumption; **(B)** Schematic representation of elastic energy density.

3 Results and analysis

3.1 Phosphoric acid-water glass slurry gelation test

3.1.1 Mechanism of acidic water-glass gel

Acidic water glass can gel in a neutral or acidic environment, and the gel is not alkaline, so there is no toxicity because there is no alkali leaching, meaning it does not cause pollution to the environment. It is durable and cheaper than alkaline water glass, so it is widely used. The main anions in the water-glass solution are $H_2SiO_4^{2-}$and $H_3SiO_4^-$, and the phosphoric acid solution contains cations H^+. The phosphoric acid solution will be added to the water glass solution in the anion and cation reaction. The chemical reaction equation is as follows:

$$H_2SiO_4^{2-} + H^+ = H_3SiO_{4^-} \quad (10)$$

$$H_3SiO_{4^-} + H^+ = H_4SiO_4 \quad (11)$$

$$H_4SiO_4 + H^+ = H_5SiO_{4^+} \quad (12)$$

In an acidic water-glass solution, the coordination number of the silicic acid molecule is 6. The silicic acid molecule and positive monovalent silicic acid ion carry out a hydroxyl association reaction to form bisilicicic acid, and the specific chemical reaction equation is as follows:

$$H_4SiO_4 + H_5SiO_{4^+} + 2H_2O = H_{13}Si_2O_{10^+} \quad (13)$$

Bisilicicic acid will polymerize again to trisilicicic acid by hydroxyl linkage reaction, and then continue to polymerize to form polysilicicic acid until the formation of silica sol. As the reaction time continues, the SiO_2 particles in the silica sol continue to increase. When the content of SiO_2 particles in the sol exceeds a certain value, these particles condense with each other to form an open and continuous gel network structure. The particles in the gel can intermittently condense to form Si-O-Si bonds, eventually forming a silicon gel with a certain degree of stiffness (Koohestani et al., 2021).

3.1.2 Gel time of phosphate-water glass slurry

As shown in Table 3, the gelation time of phosphoric acid-water glass slurry is non-linearly related to the phosphoric acid addition, and there are mutation points. For example, when the water glass Baume degree is 22°B e', phosphoric acid addition from 10% to 14%, its gel time increased from 2min to 9min relative to each 1% phosphoric acid addition, and its average gel time increased by 1.75min. The gel time increased from 9min to 54min when the acid addition was increased from 14% to 14.5%, and the average gel time increased by 900min for every 1% phosphoric acid addition. The sensitivity of its water glass to the phosphoric acid gel reaction system increases sharply when the phosphoric acid addition exceeds a certain range. As shown in Figure 6, the gel time mutation points of the phosphoric acid-water glass slurry systems with different wavelengths are different. When the phosphoric acid addition amount is less than the phosphoric acid addition amount required for the gel time mutation point, its gel time increases linearly with the increase of the phosphoric acid addition amount. For example, when the water glass Baume degree is 24°B e' its gel time mutation point required phosphoric acid addition is 16.8%. When the phosphoric acid addition is from 10% to 14%, its gel time with phosphoric acid addition follows a linear function y=0.56x-5.07 increasing. This is because the cationic H^+ content in phosphoric acid at this stage is not enough to combine with all the anions $H_2SiO_4^{2-}$ and $H_3SiO_4^-$ ions in the water glass solution, and the H^+ in phosphoric acid at this stage is quickly consumed to form a chain hydroxyl linkage reaction, so the gel time is very short. As phosphoric acid increases, the H^+ ions required to reach the gel time mutation point are sufficient, and the ability of the anions $H_2SiO_4^{2-}$ and $H_3SiO_4^-$ ions in the water glass solution to consume H^+ is limited, resulting in a small pH of the solution, so the gel time increases sharply.

3.2 Moraine slurry curing test

3.2.1 Uniaxial compressive stress-strain curve of moraine curing body

To investigate the effect of phosphoric acid-water glass slurry with different wavelengths on the curing effect of moraines,

TABLE 3 Initial setting time of phosphoric acid-water glass slurry at different wavelengths.

Baume degree of water glass/°Be′	20	22	24	26	28	30
Phosphoric acid concentration/%	Initial setting time/min					
10	6	2	0.8	0.4	0.22	0.08
11	8	3	0.83	0.67	0.3	0.12
12	10	4	1.45	0.72	0.53	0.26
13	24	8	2	1.05	0.58	0.28
13.5	52					
14	>120	9	3	1.56	0.78	0.32
14.5	>120	54				
15	>120	>120	5	2	0.87	0.41
16.8			45			
18.5				35		
20.5					32	
23						37

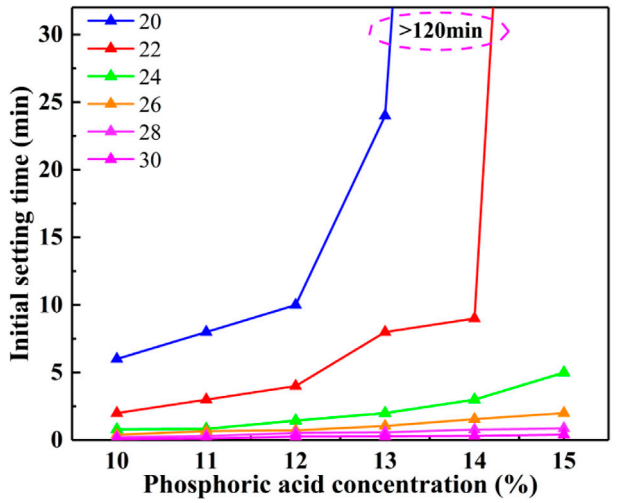

FIGURE 6
Relationship between phosphoric acid concentration and slurry initial setting time at different wavelengths.

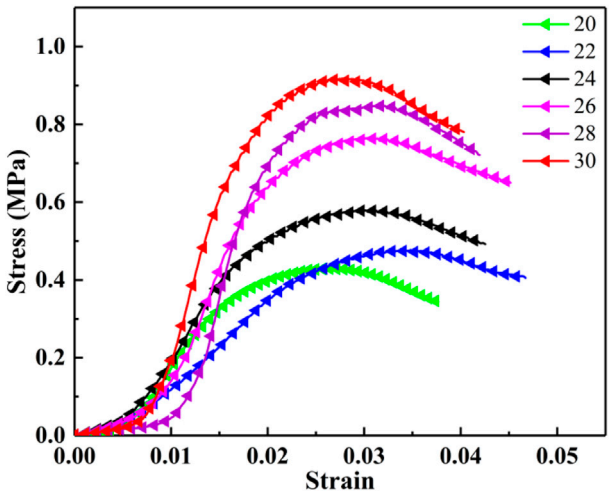

FIGURE 7
Stress-strain curves of solidified bodies of moraines with different baume degrees.

stress-strain curves with a maintenance age of 3 days were selected for analysis. As shown in Figure 7, the stress-strain curves of moraine curing bodies with different wavelengths have the same variation pattern. The stresses all increase slowly with the increase of axial strain and then increase approximately linearly to reach the peak stress point and decay rapidly after reaching the peak stress point. It is suggested that the load-bearing deformation damage of moraine curing bodies with different wavelengths under uniaxial loading are the same type of damage process. In addition, it can be seen from the changing pattern of the curve that the deformation and damage of the solidified body of moraine can all be divided into four stages: initial pressure density, linear elastic deformation, elastic-plastic deformation, and post-peak rupture destabilization. As shown in Figure 8, OA is the initial pressure-density stage. The stress-strain curve of the moraine curing body at the early loading stage is concave, mainly because the moraine curing body is a multi-phase composite damage material. The internal inevitably contains many micro-pores, micro-cracks and bubbles, and other structures. In the uniaxial compression of the moraine curing body, internal micro-pores, micro-cracks, and other structures experience gradual pressure-density closure. The pore volume inside the moraine curing body at this stage gradually decreases with the increase of stress, and the stress growth and radial expansion are smaller. AB is the linear elastic deformation stage. This stage of stress with the increase in strain is a linear growth

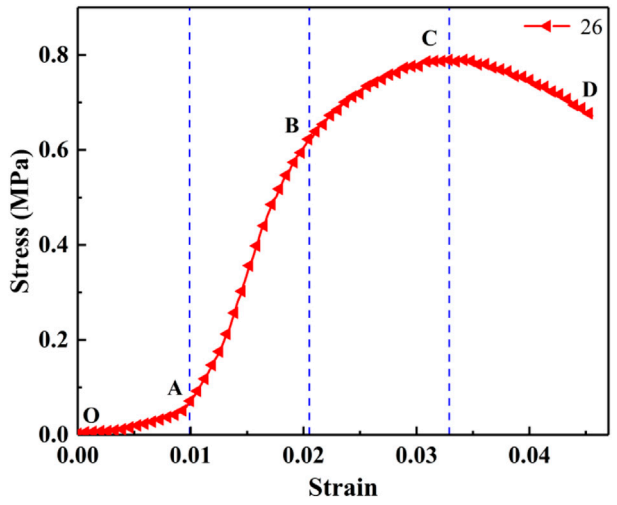

FIGURE 8
Stress-strain curve of moraine solidified specimen.

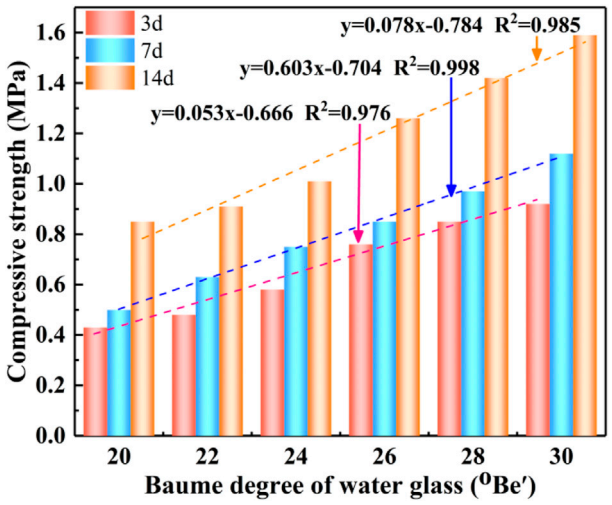

FIGURE 9
Relationship between compressive strength of moraine curing body and Baume degree.

law. It is mainly because a large number of microcracks and microporous structures previously existing inside the moraine curing body have closed, and the damage deformation of the moraine curing body has entered the elastic deformation stage. Its internal microcracks are in a stable development stage, and the damage is also growing, but it has not yet reached the inflection point of the crack damage stress. BC is the elastoplastic deformation stage. This stage curve shows that with the increase of strain, the stress has a small convexity, reaching the bearing limit C point of the specimen. At this time, the moraine solidification internal body undergoes new crack sprouting, crack interlocking, and crack expansion simultaneously. The internal crack grows rapidly during the non-stationary development stage and the evolution of the damage follows a non-stationary growth trend. The internal specimen has not yet generated a macroscopic crack. At the CD for the peak after rupture destabilization stage, the interconnection between the microcracks will form the moraine curing body in the macroscopic formation of a dominant crack after reaching the peak stress. Its direction is nearly parallel to the main stress direction. Damage takes place during the development of the dominant crack and its rupture (Jiao et al., 2023b). At this stage of the moraine curing body, the bearing capacity decreases sharply whilst retaining a certain strength, meaning the curve shows a gradual decrease in stress with the increase in strain law, and damage deformation shows accelerated evolution until the specimen damaged.

3.2.2 Relationship between the influence of water glass baume degree on compressive strength

Figure 9 shows the relationship between the compressive strength of the cured body of moraine under early curing age and different water-glass boehmites. The relevant data were fitted, and the results of the fitting showed that the compressive strength of the moraine curing body under the same curing age condition increased linearly with the increase of the water glass Baume degree, which followed the growth law of the unitary linear regression equation $y = kx - b$. As an example, in the moraine curing body with a curing age of 7 days, with the increase of water glass Baume degree, the compressive strength of the specimens were 0.5, 0.63, 0.75, 0.85, 0.97, and 1.12 MPa, which increased by 26%, 50%, 70%, 94%, and 124%, respectively. This is because the content of SiO_4^{2-} ions in its water-glass solution increases as the Baume degree increases. After mixing phosphoric acid with a water glass solution, PO_4^{3-} ions have a complementary net effect on SiO_4^{2-} ions (Noritake et al., 2022), forming a P-O-Si structure to reduce the degree of hydrolysis of water glass. With the gradual decomposition of the water glass structure, the number of SiO_4^{2-} and OH^- ions in the liquid phase increases, and the solution undergoes a condensation reaction to produce more $nSiO_2$ gel, which fills the pore structure between the moraine particles and plays a bridging role in making the specimen have a better load-bearing capacity. The compressive strength of the moraine-cured body increases with the age of curing under the same water glass Baume degree condition. As an example, the compressive strengths of the specimens were 0.76, 0.85, and 1.26 MPa, respectively, with the increase of the age of curing for the moraine-cured body with a water glass Baume degree of 26 °Be′. The compressive strength of the specimens increased by a factor of 1.1 when the age of moraine curing was increased from 3 days to 7 days. However, when the age of curing was increased from 7 days to 14 days, the strength of the moraine curing showed a sharp increase, and the compressive strength of the specimens increased by a factor of 1.7. This is because the age of curing is 3 days, and the early hydration reaction is not sufficient, the hydration products are relatively independent of each other without cross-linking phenomenon, resulting in the pores between the particles not being filled, so the mechanical strength of the specimen in the early curing is low. However, with the growth of the age of curing, the hydration reaction continues, and the free Ca^{2+} and SiO_4^{2-} undergo a condensation reaction to generate a large number of C-S-H gels (Feng et al., 2022), and the gels lap each other to form a solid, dense skeletal system, which enhances the mechanical strength of the specimens.

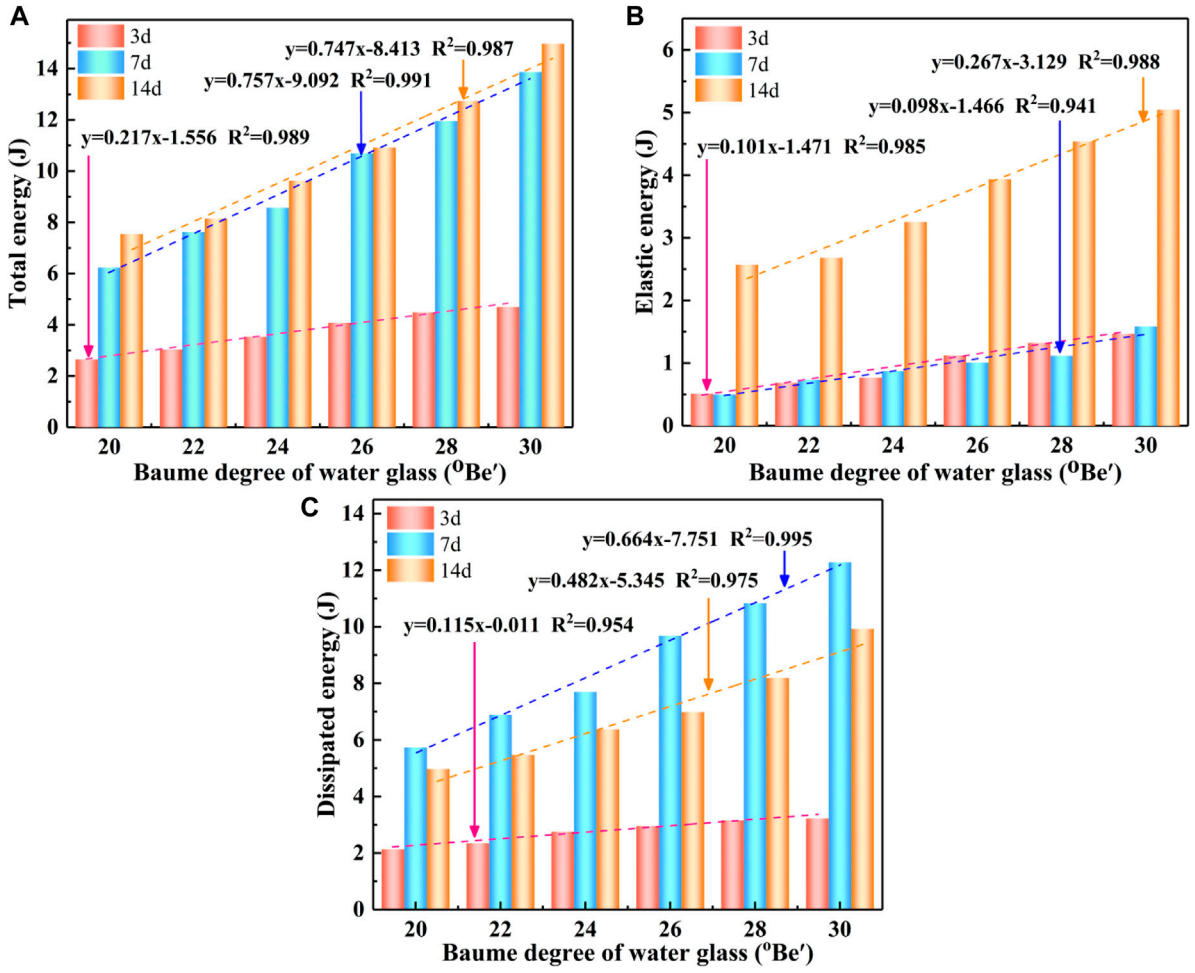

FIGURE 10
Relationship between total energy, elastic energy, dissipative energy, and Baume degree: **(A)** Total energy; **(B)** Elastic energy; **(C)** Dissipation energy.

3.3 Energy consumption characteristics before the peak of moraine solidification body

3.3.1 Relationship between total energy consumption, elastic energy and dissipation energy and water glass baume degree

Through the above energy dissipation principle, the energy of the moraine solidified body in different stages of the uniaxial loading process can be calculated, and the total energy before the peak, elastic energy before the peak, dissipation energy before the peak corresponding to the peak stress point of moraine solidified body under different Baume degree and curing age. The relevant data were fitted, as shown in Figure 9. As can be seen from Figure 10, under the same maintenance age conditions, the total energy before the peak, the elastic energy before the peak, and the dissipation energy before the peak linearly increases with the increase of the water glass Baume degree, which follows the one-dimensional linear regression equation $y = kx - b$ growth law. As shown in Figure 10A, the relationship between the total energy before peak for different curing age conditions is $U_{14d} > U_{7d} > U_{3d}$, but the total energy before peak for curing age 7 days and 14 days is similar and 1.5 times of curing age 3 days, and the total energy before peak increases sharply in phase with the increase of curing age from 3 days to 7 days. When the age of curing was 3 days, the total energy of the specimens with different Baume degree moraine curing bodies was 2.64, 3.04, 3.53, 4.08, 4.48, 4.69 J. As the age of curing increased to 7 days, the total energy before the peak of the specimen was 6.23, 7.63, 8.57, 10.69, 11.95, and 13.87 J. The relative 3 days strength increases were 136%, 151%, 143%, 162%, 167%, and 196%. As shown in Figure 10B, the relationship of peak pre-elastic energy for different curing age conditions is $U^e_{14d} > U^e_{7d} > U^e_{3d}$, and the peak pre-elastic energy of the moraine curing body is similar at the curing ages of 3 days and 7 days, but the elastic energy of the moraine curing body increases sharply as the curing age increases from 7 days to 14 days. As an example, the elastic energy of the specimens with the increase of the curing age was 1.47, 1.59, and 5.05 J. The increase was 8% and 218% respectively. As shown in Figure 10C, the relationship between the peak front dissipation energy for different curing age conditions is $U^d_{7d} > U^d_{14d} > U^d_{3d}$, and the dissipation energy of the specimen with the increase of curing age was 3.22, 12.28, and 9.92 J with increases of 281% and 208%, respectively, for the moraine solidified body with a wavelength of 30 °Be′

The essence of the deformation damage of the solidified body of the moraine is the result of the interaction of the energy of the

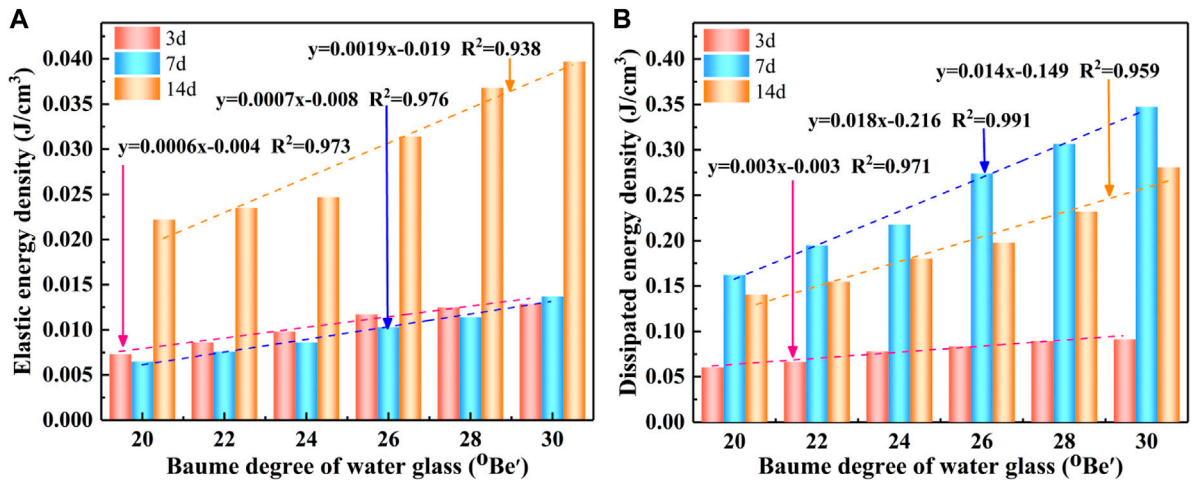

FIGURE 11
Relationship between elastic energy density, dissipative energy density, and Baume degree: **(A)** Elastic energy density; **(B)** Dissipation energy density.

components so that it can be described from the energy point of view: When the curing age is 3 days, the moraine curing body has viscoelastic characteristics, specimen internal hydration reaction is not entirely in the early stage, and at this stage the moraine curing body bearing limit and energy storage capacity are small, resulting in the absorption of smaller energy is sufficient to deformation damage, and at this stage, energy is mainly dissipated in the form of dissipation energy. Although the moraine curing body damage form is mainly manifested in the axial central crack expansion and penetration, the degree of the broken ring depends primarily on the internal microporosity and microfracture structure. Compared to the curing age of 3 days, when the curing age was 7 days, the moraine solidified body specimen's internal hydration reaction into the middle stage generated more C-S-H gel filled parts in the pore structure to improve the energy storage capacity of the specimen. The total energy before the peak of the moraine solidified body increased at this stage, but the number of hydration products inside the specimen was not enough to link the formation of the skeletal structure. This was because the adhesion between the particles was weak, meaning the bearing limit and energy absorption capacity of the moraine solidified body did not grow significantly, increasing the dissipation energy of the specimen. When the curing age was 14 days, the hydration reaction inside the specimen completely entered the final stage, the number of microcracks and microporosity inside the moraine curing body was obviously reduced, the denseness between the particles was better, and the hydration products are cross-linked to each other as the skeleton, meaning the moraine curing body in the later stage of curing has stronger bearing capacity.

3.3.2 Relationship between the effect of water glass baume degree on energy consumption density

Figure 11 shows the relationship between the moraine curing body and energy consumption density for different Baume degrees. As can be seen from Figure 11, the elastic energy density and dissipative energy density of the moraine curing body increase with the increase of water glass Baume degree under the same maintenance age condition, which follows the law of increasing unity linear function $y = kx - b$. Under the same water-glass Baume degree condition, the elastic energy density relationship of the moraine curing body at different curing ages was $\rho_e(14d) > \rho_e(3d) > \rho_e(7d)$, as can be seen from Figure 11A. For example, the elastic energy density of the moraine curing body with the age of curing is 0.0125, 0.0114, 0.0368 J/cm^3 with the increase of the age of maintenance of the moraine curing body with the Baume degree of 28 °Be′. The elastic energy density of the moraine curing body is similar between the curing age of 3 days and 7 days. The elastic energy density of the curing age of 14 days has increased by 2.94 times and 3.23 times relative to 3 days and 7 days, respectively, indicating that the energy absorption capacity of the moraine curing body grows slowly in the early stage of curing and shows a tendency of decreasing first before increasing sharply. From Figure 11B, it can be seen that the dissipative energy density relationship for moraine solidification bodies at different curing ages is $\rho_d(7d) > \rho_d(14d) > \rho_d(3d)$. As an example, the dissipated energy density of the moraine curing body with increasing age of curing is 0.0894, 0.3066, 0.2319 J/cm^3, respectively, with the age of maintenance of the moraine curing body with a Baume degree of 28 °Be′. The dissipation density at the curing age of 7 days was 3.43 and 2.59 times higher than those at 3 days and 14 days, respectively, indicating that the ability to dissipate energy was strongest at the curing age of 7 days.

3.4 Pre-peak fracture characteristics analysis of moraine solidified bodies

Figure 12 shows the peak front fracture toughness *versus* water glass Baume for moraine-cured bodies with different Baume degrees. To qualitatively analyze the variation law of fracture toughness and water glass Baume degree before the peak of the moraine curing body, the relevant data are linearly fitted to show that the pre-peak fracture toughness of the moraine curing body

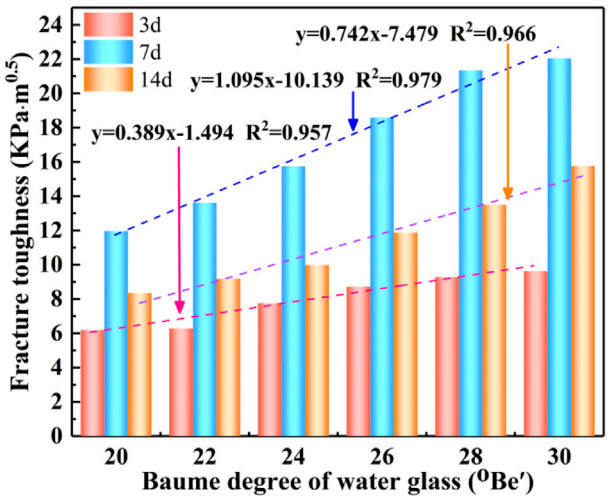

FIGURE 12
Relationship between water glass Baume degree and fracture toughness.

increases linearly with the increase of the water glass Baume degree under the same curing age condition, which follows a linear unity function $y = kx - b$ regular increasing. The pre-peak fracture toughness relationship for moraine cured bodies under the same water glass Baume degree is $K_{IC}(7d) > K_{IC}(14d) > K_{IC}(3d)$. As an example, the fracture toughness of the moraine-cured body specimens with a waviness of 30 °Be′ increased with the age of curing to 9.63, 22.04, and 15.77 kPa · $m^{0.5}$, which increased by 129% and 64%, respectively. This was due to the moraine curing body fracture toughness increasing with the increase of dissipation energy. The moraine curing body specimen is divided into many small units with an increase in dissipation energy. For the internal specimen pores, microcracks are compacted or microcracks expand through each other as energy increases, meaning the moraine curing body internal energy carried by each unit gradually increased, and this part of the energy is irreversible energy (Bi et al., 2020; Bi et al., 2022; Bi et al., 2023). The increased pore structure inside the moraine curing body resulted in the reduction of the force area on each unit and the unit area of the unstressed part increased. As a result, the consumption of irreversible energy gradually increased, meaning the curing body of the moraine was less able to resist fracturing and was at its weakest when the age of curing was 3 days.

4 Discussion

The moraine produced by melting glaciers includes accumulated sediment that is transported into the surrounding landscpae. Surface moraine and side moraine are mostly a mixture of fine particles including soil and stones. When combined with rainfall and ice and snow melt water, moraine soil water content very easily reaches saturation, resulting in the original soil stability structure being destroyed, which quickly collapses to form a debris flow. Moraine debris flow has the characteristics of long movement distance, fast movement speed, and grand scale washout. To effectively prevent and control the debris flow disaster of the moraine in the Pulang copper mine, grouting reinforcement is used to solidify the moraine stratum, solidify the moraine from independent powder fine particles into a whole, and reduce the hazard of debris flow by decreasing the material source of debris flow initiation. It is therefore of great engineering significance to carry out grouting and curing research on moraine soils rich in fine particles to prevent and control moraine debris flow hazards. In this experiment, modified phosphoric acid-water glass slurry was selected as the material used to grout and cure the moraine soil to evaluate the grouting effect by using uniaxial compression equipment. The study analyzed the influence law of water glass Baume degree and the curing age on the energy consumption characteristics and fracture toughness of the grouted fixed body. The calculation formula of the fracture toughness of the moraine was derived and constructed based on the energy consumption principle, the gelling mechanism of phosphoric acid-water glass slurry is revealed, and the suitable slurry ratio is

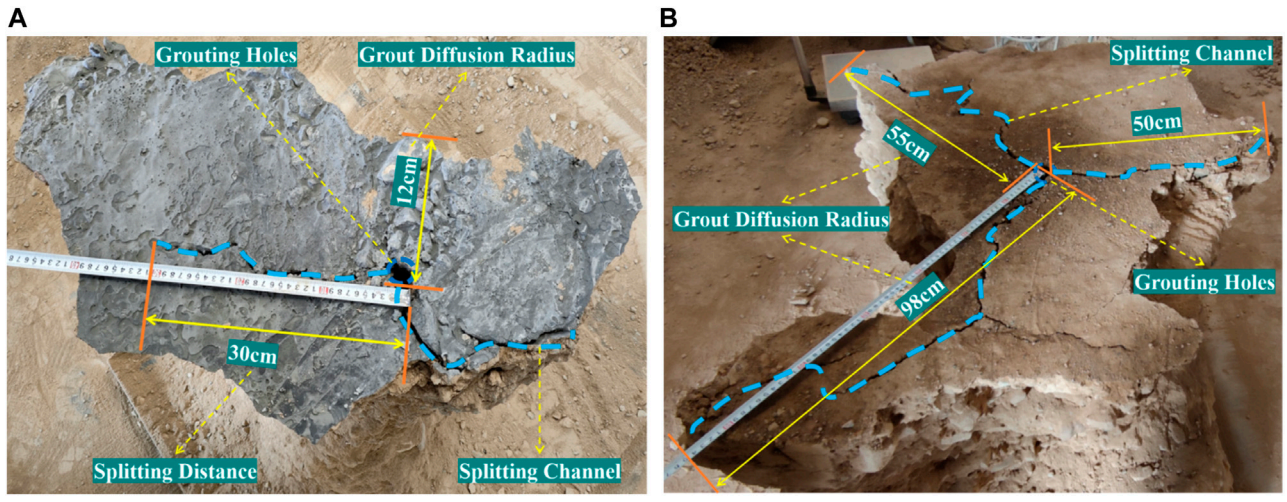

FIGURE 13
Morphology of the cured body of different slurry injections: **(A)** cement slurry; **(B)** phosphoric acid-water glass slurry.

preferred, which is of great significance for the theory of grouting and strengthening of moraine and the mitigation and prevention of glacial debris flow.

Scholars at home and abroad have yet to study the grouting and curing of moraine strata. Yang et al. (Yang et al., 2021) used cement slurry for grouting on moraine slopes with more overhead structures. The effective reinforcement radius was 20–55 cm, and the radius of the hard shell body was only 8–10 cm. In this test, cement slurry and modified phosphoric acid-water glass slurry were used for grouting with a high content of fine particles and poor permeability, and dense moraine formation, respectively, as shown in Figure 13. At the same grouting pressure, the cement slurry spreads in the moraine formation only by splitting, and the effective reinforcement radius is 12–30 cm. While the modified phosphoric acid-water glass grout spreads in the moraine formation by penetration and splitting together, the effective reinforcement radius of the slurry was 50–100cm, and the penetration distance was 20–45 cm. The curing volume was much larger than that of the cement slurry, which indicates that the grouting material has a better grouting effect on the moraine formation with abundant fine particles. This study was mainly based on the principle of energy consumption and evaluates the grouting effect of slurry. Results indicated that the slurry in the moraine stratum diffusion distribution law needs to be further improved, while the test found that the strength of the modified phosphoric acid-water glass slurry, which was used to cure the moraine, was less than 3 MPa. For moraine with a rich content of fine particles, further in-depth study of the poor permeability of the stratum should be undertaken, with the aim of developing a strong injectability and high curing strength of the material.

5 Conclusion

In order to study the curing effect of modified phosphoric acid-water glass slurry on moraine after grouting, the present study investigated initial setting times for phosphoric acid-water glass slurry for grouting and the gelation mechanism of the slurry through the slurry gelation test. The influence law of water glass Baume degree and maintenance age on the mechanical properties, energy consumption characteristics and fracture characteristics of the moraine curing body were analyzed with the help of uniaxial compression test. The research conclusions are as follows.

1) In the phosphoric acid-water glass slurry system, the gel time increases with the addition of phosphoric acid but has a mutation point. The gel time increases linearly with increasing phosphoric acid addition when the required phosphoric acid addition is not reached at the mutation site. After reaching the required phosphoric acid addition at the mutation point, the sensitivity of the water glass to phosphoric acid in the gelation reaction increases sharply, leading to a sharp increase in gelation time. The amount of phosphoric acid addition required for the abrupt gel time change point increases with increasing water glass Baume.
2) The axial stress of the moraine curing body under uniaxial compression is nonlinear with the increase of axial strain. Peak stress increases with increasing water glass Baume degree. The stress-strain curves of different wavelength moraine curing bodies have the same change pattern. Stress is related to the increase of axial strain, which, at first, slowly increases and then shows a near linear increase to reach the peak stress point. The peak stress point is reached after the rapid decay. Its damage evolution process can be divided into four stages the initial pressure density, linear elastic deformation, and elastoplastic deformation after the peak rupture instability.
3) The compressive strength, total pre-peak energy, pre-peak elastic energy, pre-peak dissipation energy, elastic energy density, dissipation energy density, and pre-peak fracture toughness of the moraine curing body under the same curing age conditions show a linear increasing law with the increase of water glass Baume degree. The compressive strength, pre-peak elastic energy, and pre-peak elastic energy density of the moraine curing body increased with the increase of the curing age under different curing age conditions. Despite this, the increase was not the same, and the curing age increased slowly from 3 days to 7 days and increased rapidly from 7 days to 14 days.
4) Moraine solidification body in the curing age of 7 days and 14 days occurs when the total energy before the peak is similar and 1.5 times the total energy before the height of the curing age of 3 days. The curing age from 3days to 7 days and the total energy before the peak increases sharply and in 7 days to 14 days as soon as the growth is slow. The pre-peak dissipation energy, dissipation energy density, and pre-peak fracture toughness of the moraine curing body were at their maximum at a curing age of 7 days and minimum at a curing age of 3 days.

Data availability statement

The original contributions presented in the study are included in the article/supplementary material, further inquiries can be directed to the corresponding author.

Author contributions

Investigation, Z-rL and S-yW; methodology, Z-rL; conceptualization, M-gJ and S-yW; writing—original draft preparation, Z-rL; funding acquisition, S-yW; writing—review and editing, Z-rL and M-gJ; supervision, Q-tZ and WS; visualization, X-lF; validation, CC; data curation, W-lL. All authors contributed to the article and approved the submitted version.

Funding

This research was financially supported by the National Natural Science Foundation of China (Grant No. 51964023), the Yunnan Major Scientific and Technological Projects (Grant No. 202202AG050014), and by Yunnan Fundamental Research Projects (Grant No. 202101BE070001-038; 202201AT070146).

Conflict of interest

Z-rL, X-lF, Q-tZ were employed by Yunnan Diqing Non-Ferrous Metal Co, Ltd.

The remaining authors declare that the research was conducted in the absence of any commercial or financial relationships that could be construed as a potential conflict of interest.

Publisher's note

References

Begam, S., Sen, D., and Dey, S. (2018). Moraine dam breach and glacial lake outburst flood generation by physical and numerical models. *J. Hydrol.* 563, 694–710. doi:10.1016/j.jhydrol.2018.06.038

Bi, J., Liu, P., and Gan, F. (2020). Effects of the cooling treatment on the dynamic behavior of ordinary concrete exposed to high temperatures. *Constr. Build. Mat.* 248, 118688. doi:10.1016/j.conbuildmat.2020.118688

Bi, J., Ning, L., Zhao, Y., Wu, Z., and Wang, C. (2023). Analysis of the microscopic evolution of rock damage based on real-time nuclear magnetic resonance. *Rock Mech. Rock Eng.* 56, 3399–3411. doi:10.1007/s00603-023-03238-x

Bi, J., Tang, J., Wang, C., Quan, D., and Teng, M. (2022). Crack coalescence behavior of rock-like specimens containing two circular embedded flaws. *Lithosphere* 11, 9498148. doi:10.2113/2022/9498148

Coulter, S., and Martin, C. (2006). Effect of jet-grouting on surface settlements above the Aeschertunnel, Switzerland. *Tunn. Undergr. Sp. Tech.* 21, 542–553. doi:10.1016/j.tust.2005.07.005

Cui, Y., Tan, Z., and An, C. (2022). Research and application of multi-functional acrylic resin grouting material. *Constr. Build. MATER* 359, 129381. doi:10.1016/j.conbuildmat.2022.129381

Dong, L., Jin, L., Xui, D., and Liu, J. (2018). A theoretical method to predict the mechanical properties of concrete considering of the size effect in material. *J. Hydraul. Eng.* 49, 464–473. doi:10.13243/j.cnki.slxb.20171162

Evans, D., Smith, I., Gosse, J., and Galloway, J. (2021). Glacial landforms and sediments (landsystem) of the smoking hills area, northwest territories, Canada: implications for regional pliocene – pleistocene laurentide ice sheet dynamics. *Quat. Sci. Rev.* 262, 106958. doi:10.1016/j.quascirev.2021.106958

Fan, H., Xu, Q., Lai, J., Liu, T., Zhu, Z., Zhu, Y., et al. (2023). Stability of the loess tunnel foundation reinforced by jet grouting piles and the influence of reinforcement parameters. *Transp. Geotech.* 40, 100965. doi:10.1016/j.trgeo.2023.100965

Feng, H., Liang, J., Pang, Y., Zhao, X., Wang, Y., and Sheikh, S. (2022). Effects of the fly ash and water glass on the mechanical properties and water stability of the high ductile magnesium phosphate cement-based composite. *Constr. Build. MATER* 333, 127395. doi:10.1016/j.conbuildmat.2022.127395

Gao, T., Sun, W., Liu, Z., and Cheng, H. (2022). Investigation on fracture characteristics and failure pattern of inclined layered cemented tailings backfill. *Constr. Build. Mater* 343, 128110. doi:10.1016/j.conbuildmat.2022.128110

Guo, X., Fang, K., and Leng, F. (2005). Analysis of the theory of fracture energy of concrete. *J. Harbin Inst. Technol.* 37, 1219–1222. doi:10.3321/j.issn:0367-6234.2005.09.017

Hart, J. (1998). The deforming bed/debris-rich basal ice continuum and its implications for the formation of glacial landforms (flutes) and sediments (melt-out till). *Quat. Sci. Rev.* 17, 737–754. doi:10.1016/S0277-3791(98)00065-6

Huang, Z., Yilmaz, E., and Cao, S. (2021). Analysis of strength and microstructural characteristics of mine backfills containing fly ash and desulfurized gypsum. *Minerals* 11, 409. doi:10.3390/min11040409

Jiao, H., Yang, W., Ruan, Z., Yu, J., Liu, J., and Yang, Y. (2023a). The micro-scale mechanism of tailings thickening processing from metal mines. *Int. J. Min. Metall. Mater* 2023, 2587. doi:10.1007/s12613-022-2587-0

Jiao, H., Zhang, W., Yang, Y., Chen, X., Yang, L., Shen, H., et al. (2023b). Static mechanical characteristics and meso-damage evolution characteristics of layered backfill under the condition of inclined interface. *Constr. Build. Mater* 366, 130113. doi:10.1016/j.conbuildmat.2022.130113

Kivi, I., Ameri, M., and Molladavoodi, H. (2018). Shale brittleness evaluation based on energy balance analysis of stress-strain curves. *J. Pet. Sci. Eng.* 167, 1–19. doi:10.1016/j.petrol.2018.03.061

Koohestani, B., Mokhtari, P., Yilmaz, E., Mahdipour, F., and Darban, A. (2021). Geopolymerization mechanism of binder-free mine tailings by sodium silicate. *Constr. Build. Mater* 268, 121217. doi:10.1016/j.conbuildmat.2020.121217

Kumar, S., Tiwari, G., Parameswaran, V., and Das, A. (2022). Rate-dependent mechanical behavior of jointed rock with an impersistent joint under different infill conditions. *J. Rock Mech. Geotech. Eng.* 14, 1380–1393. doi:10.1016/j.jrmge.2022.05.002

Li, C., Wang, R., Gu, D., Wang, J., Chen, X., Zhou, J., et al. (2022). Temperature and ice form effects on mechanical behaviors of ice-richmoraine soil of Tianmo valley nearby the Sichuan-Tibet Railway. *Eng. Geol.* 305, 106713. doi:10.1016/j.enggeo.2022.106713

Li, J., Yilmaz, E., and Cao, S. (2021). Influence of industrial solid waste as filling material on mechanical and microstructural characteristics of cementitious backfills. *Constr. Build. Mater* 299, 124288. doi:10.1016/j.conbuildmat.2021.124288

Li, L., Tu, W., Shi, S., Chen, J., and Zhang, Y. (2016). Mechanism of water inrush in tunnel construction in karst area. *Geomat. Nat. HAZ RISK* 7, 35–46. doi:10.1080/19475705.2016.1181342

Lin, H., Liu, J., Yang, J., Ran, L., Ding, G., Wu, Z., et al. (2022). Analysis of damage characteristics and energy evolution of salt rock under triaxial cyclic loading and unloading. *J. Energy Storage* 56, 106145. doi:10.1016/j.est.2022.106145

Liu, X., Chen, H., Liu, Q., Liu, B., and He, J. (2022). Modelling slurry flowing and analyzing grouting efficiency under hydro-mechanical coupling using numerical manifold method. *Eng. Anal. BOUND Elem.* 134, 66–78. doi:10.1016/j.enganabound.2021.09.030

Luo, F., Liu, E., and Zhu, Z. (2019). A strength criterion for frozen moraine soils. *COLD Reg. Sci. Technol.* 164, 102786. doi:10.1016/j.coldregions.2019.102786

Marr, J. G., Anders, E., Harbitz, C., Imran, J., and Harff, P. (2002). Numerical simulation of mud-rich subaqueous debris flows on the glacially active margins of the Svalbard–Barents Sea. *Mar. Geol.* 188, 351–364. doi:10.1016/S0025-3227(02)00310-9

Medeu, A., Popov, N., Blagovechshenskiy, V., Askarova, M., Medeu, A., Ranova, S., et al. (2022). Moraine-dammed glacial lakes and threat of glacial debris flows in South-East Kazakhstan. *Earth-Sci. Rev.* 229, 103999. doi:10.1016/j.earscirev.2022.103999

Meng, Z., Lyu, L., Xu, M., Yu, G., Ma, C., Wang, Z., et al. (2023). Effects of frequent debris flows on barrier lake formation, sedimentation and vegetation disturbance, Palongzangbo River, Tibetan Plateau. *CATENA* 220, 106697. doi:10.1016/j.catena.2022.106697

Noritake, F., Sato, T., Yamamoto, A., Wakabayashi, D., Urakawa, S., and Funamori, N. (2022). Structure of sodium silicate water glass—X-Ray scattering experiments and force-field molecular dynamics simulations. *J. NON-CRYST SOLIDS* 579, 121370. doi:10.1016/j.jnoncrysol.2021.121370

Peng, D., Zhang, L., Jiang, R., Zhang, S., Shen, P., Lu, W., et al. (2022). Initiation mechanisms and dynamics of a debris flow originated from debris-ice mixture slope failure in southeast Tibet, China. *Eng. Geol.* 307, 106783. doi:10.1016/j.enggeo.2022.106783

Salimian, M., Baghbanan, A., Hashemolhosseini, H., Dehghanipoodeh, M., and Norouzi, S. (2017). Effect of grouting on shear behavior of rock joint. *Int. J. ROCK Mech. Min.* 98, 159–166. doi:10.1016/j.ijrmms.2017.07.002

Sui, W., Liu, J., Hu, W., Qi, J., and Zhan, K. (2015). Experimental investigation on sealing efficiency of chemical grouting in rock fracture with flowing water. *Tunn. Undergr. Sp. Tech.* 50, 239–249. doi:10.1016/j.tust.2015.07.012

Weng, L., Wu, Z., Zhang, S., Liu, Q., and Chu, Z. (2022). Real-time characterization of the grouting diffusion process in fractured sandstone based on the low-field nuclear magnetic resonance technique. *Int. J. ROCK Mech. Min.* 152, 105060. doi:10.1016/j.ijrmms.2022.105060

Yang, D., Wang, J., Shi, S., and Yang, D. (2021). Reinforcement of the moraine slope with steel screen pipe grouting. *Drill. Eng.* 48, 89–95. doi:10.12143/j.ztgc.2021.08.014

Yi, Q., Pu, H., Preuße, A., Bian, Z., and Wu, J. (2022). Effect of dry-wet cycles on dynamic mechanic and microstructure of cemented broken mudstone. *Constr. Build. MATER* 357, 129347. doi:10.1016/j.conbuildmat.2022.129347

Zaginaev, V., Petrakov, D., Erokhin, S., Meleshko, A., Stoffel, M., and Ballesteros-Cánovas, J. (2019). Geomorphic control on regional glacier lake outburst flood and

debris flow activity over northern Tien Shan. *Glob. Planet. Change* 176, 50–59. doi:10.1016/j.gloplacha.2019.03.003

Zhang, C., Yang, J., Fu, J., Wang, S., Yin, J., Xie, Y., et al. (2021). Cement based eco-grouting composite for pre-reinforcement of shallow underground excavation in vegetation protection area. *Tunn. Undergr. Sp. Tech.* 118, 104188. doi:10.1016/j.tust.2021.104188

Zhang, G., Xiao, M., Zhang, Y., Liu, H., Zhuo, L., Xie, H., et al. (2022). Experimental and numerical study on the mechanical properties of compressively precracked sandstone repaired by grouting. *Constr. Build. MATER* 350, 12881. doi:10.1016/j.conbuildmat.2022.128816

Zhao, J., Lu, C., Deng, L., and Liu, G. (2018). Impacts of simulated acid solution on the disintegration and cation release of purple rock (mudstone) in Southwest China. *GEOMORPHOLOGY* 316, 35–43. doi:10.1016/j.geomorph.2018.05.009

Zheng, Y., Zhang, Y., Zhuo, J., Zhang, P., and Hu, S. (2023). Mesoscale synergistic effect mechanism of aggregate grading and specimen size on compressive strength of concrete with large aggregate size. *Constr. Build. MATER* 367, 130346. doi:10.1016/j.conbuildmat.2023.130346

Zhu, H., Alam, S., and Loukili, A. (2020). An experimental investigation on the correlation between the aggregate size effect and the structural size effect. *Eng. Fract. Mech.* 234, 107101. doi:10.1016/j.engfracmech.2020.107101

Zou, C., Li, J., Liu, K., and Zhao, X. (2023). Dynamic cracking process of rock interpreted by localized strain-rate, rate-dependent strength field and transition strain-rate. *Int. J. ROCK Mech. Min.* 163, 105340. doi:10.1016/j.ijrmms.2023.105340

frontiers | Frontiers in Earth Science

TYPE Original Research
PUBLISHED 21 September 2023
DOI 10.3389/feart.2023.1193824

OPEN ACCESS

EDITED BY
Tianshou Ma,
Southwest Petroleum University, China

REVIEWED BY
Paramate Horkaew,
Suranaree University of Technology, Thailand
Ruzhong Li,
Hefei University of Technology, China
Natalie Griffiths,
Oak Ridge National Laboratory (DOE), United States

*CORRESPONDENCE
Qihua Ran,
ranqihua@hhu.edu.cn

†PRESENT ADDRESS
Jiajia Pan,
Zhejiang Design Institute of Water Conservancy and Hydroelectric Power Co., Ltd., Hangzhou, Zhejiang, China

RECEIVED 25 March 2023
ACCEPTED 04 September 2023
PUBLISHED 21 September 2023

CITATION
Ye S, Pan J, Li J, Yu T and Ran Q (2023), The seasonal and spatial variability of ammonium uptake in a hilly watershed. *Front. Earth Sci.* 11:1193824. doi: 10.3389/feart.2023.1193824

The seasonal and spatial variability of ammonium uptake in a hilly watershed

Sheng Ye[1,2], Jiajia Pan[2†], Jiyu Li[2], Tianxue Yu[2] and Qihua Ran[1,2*]

[1]Key Laboratory of Hydrologic-Cycle and Hydrodynamic-System of Ministry of Water Resources, Hohai University, Nanjing, China, [2]Institute of Water Science and Engineering, Zhejiang University, Hangzhou, China

Elevated nutrient loading can cause deleterious impacts on aquatic ecosystems such as eutrophication. Seasonal variability and land use change often lead to varied nutrient uptake from streams. However, the impacts of seasonal and spatial variation on stream nutrient transport within the same watershed haven't been fully understood. Here, we conducted nutrient addition experiments using the Tracer Additions for Spiraling Curve Characterization (TASCC) approach within the Xiaogang Watershed, Zhejiang Province, China. Six of the experiments were conducted in one stream every other month and eight releases in eight different streams to quantify ammonium uptake kinetics across different seasons and land uses. Our findings suggest that the uptake capability increases with both discharge and ambient concentration (C_0): seasonal variability of discharge shows small impacts on uptake metrics, except the ambient uptake length ($S_{w\text{-}amb}$), which increases with discharge; while the change in C_0 could have more significant effects on both ambient areal uptake (U_{amb}) and maximum areal uptake rate parameter (U_{max}). Downstream the river network, the increase in discharge led to a significant increase in U_{amb}, ambient uptake velocity ($V_{f\text{-}amb}$), and U_{max}. On the other hand, the change in C_0 is less influential than discharge along the river network, which may be correlated with the hydraulic geometry. Additionally, there is an optimal temperature (T) for uptake in our study region around 17°C, which may be explained by the growth of chlorophyll *a*. The positive correlation between $V_{f\text{-}amb}$ and Q at the spatial scale may be attributed to the increase of dissolved organic carbon (DOC) and river chlorophyll *a* downstream with stream width. In addition, land use had an important effect on ion concentration in streams, and the proportion of agricultural land was positively correlated with nutrient concentration. Our findings could help provide scientific support for land use management and water quality regulation.

KEYWORDS

nutrients uptake, TASCC method, seasonal and spatial variation, hilly watershed, correlation analysis

1 Introduction

Nutrients such as nitrogen (N) and phosphorus (P), are critical to stream biotic activity (Mulholland and Webster, 2010) and often limit ecosystem productivity (Grimm and Fisher, 1986; Vitousek and Howarth, 1991). From the beginning of the 20th century, nutrient inputs to aquatic ecosystems have increased dramatically owing to expanded human activities globally such as urbanization and fertilizer applications related to agricultural land use

(Vitousek et al., 1997; Smil, 2000; Bouwman et al., 2005; Seitzinger et al., 2005). Excess N loading can have harmful impacts on water quality, leading to eutrophication and the loss of biological diversity (Webster, 1975; Bormann and Likens, 1979). While it's found that about 30% of the soluble phosphate and 37%–76% of the nitrogen nutrients entering the water body are intercepted by small rivers of grade 1 to 4 during the transport in the river basin, confirming that low-grade streams can play an important role in the process of nutrient uptake (Seitzinger et al., 2002; Mulholland, 2004). Therefore, giving full play to the uptake effect and reduction capacity of source streams on nitrogen and phosphorus nutrients can be practically essential to improve and regulate the quality of the water environment.

Nutrient spiraling is an important ecological process characterizing nutrient transport and uptake in a small river system (Newbold et al., 1981; Stream Solutes Workshop, 1990). According to [Webster (1975); Webster and Patten, 1979], nutrients in a stream do not cycle *in situ*; rather, they are continually pushed downstream as they complete a cycle. This combination of transport and cycling was characterized as "spiraling": the "tightness" of the spirals indicates how well a stream can use nutrients. The idea of spiraling was discussed by other scholars (Wallace et al., 1977; Meyer, 1979; Naiman and Sedell, 1979; Benke and Wallace, 1980) who also noted the significance of spatially dependent reutilization of nutrients (Ball et al., 1963; Short and Maslin, 1977).

Stream nutrient tracer additions and nutrient spiraling metrics are widely used to quantify lotic ecosystem behavior. Many studies have conducted constant and continuous added tracer experiments and used nutritive salt concentration and spiral indexes under a steady state for quantitative depiction and measurement of nutritive salt uptake abilities, mostly at small-scale water bodies like headwaters (Peterson et al., 2001; Saunders et al., 2006; Alexander et al., 2007). Tank et al. (2008) started to conduct tracer addition experiments in big rivers. Covino et al. (2010b) refined the pulse method, and developed the Tracer Additions for Spiraling Curve Characterization (TASCC) method, using the variable concentration of a highly concentrated pulse to estimate uptake kinetics.

Our current understanding of the processes that drive nutrient uptake in aquatic systems reflects the focus of early studies on understanding ecosystem limitation by macronutrients, particularly on the N or P limitation of biomass growth and production (Meyer and Likens, 1979; Mulholland et al., 2008; Gardner et al., 2011; Hall et al., 2013). Ammonium (NH_4^+-N) is easy to be adsorbed and used by aquatic plants and can be eliminated from water through nitrification and denitrification (Billen et al., 1991). It is an important index that influences the remediation and improvement of the water environment. Though it has been generally accepted that hydrological regimes and environmental conditions are important drivers for nutrient uptake in streams, there are still a lot of unknowns in nitrogen nutrient cycling due to the complexity and diversity of small river systems and sample number limitations such as the impacts of photosynthesis, heterotroph and so on (Arango et al., 2008; Hall R. O. et al., 2009).

Consequently, parameters such as the rate of biomass accumulation and magnitude of gross primary production at the ecosystem level have been identified as important drivers of nutrient uptake rates in streams (Grimm, 1987; Hall and Tank, 2003; Elser et al., 2007). Researchers have discovered that stream nitrogen (N) uptake kinetics vary with development. Land use/land cover change and fertilization effect were evident, which could lead to increased ash-free dry mass, chlorophyll *a*, and ambient and maximum uptake rates in developed compared with undeveloped streams. Ash-free dry mass (AFDM) of biofilm, chlorophyll *a*, and the number of structures in a sub-watershed were significantly correlated to nutrient spiraling and kinetic parameters, while ambient and average annual N concentrations were not (Covino et al., 2012). Seybold and McGlynn (2018) investigated the seasonality of nutrient uptake, detecting that seasonal decrease in dissolved organic carbon (DOC) and nitrate (NO_3^-) concentration reduced the biotic community's ability to take up nutrients, and seasonal uptake was consistent with the seasonal dynamics of ecosystem metabolism. During the growing season (from June to August), the biotic community shows its capability of nutrient retention and water quality regulation.

Numerous studies have investigated drivers of the nutrient uptake in streams and rivers (Webster et al., 2003; Ensign and Doyle, 2006; Hall R. O. et al., 2009) and the importance of these uptake processes for downstream water quality and ecosystem health, yet few were conducted to investigate the influence and mechanism of both seasonal and spatial variation on stream nutrient uptake in the same watershed. Seasonal alternation and land use change often lead to varied nutrient loading and uptake (Reisinger et al., 2015; Seybold and McGlynn, 2018). It is necessary to understand the uptake kinetics and their relationship to the physical and biological drivers to better understand the dynamics of nutrient transport and transformation at the watershed scale. To address this, we conducted 13 ammonium addition experiments for a whole year in a hilly watershed. Considering the time and cost, the TASCC method (Covino et al., 2010b; Piper et al., 2017) was applied in this study. Hydrologic and biological characteristics were collected and measured to examine their relationship with uptake metrics.

2 Materials and methods

2.1 Study area

This study was conducted in a hilly watershed, Xiaogang Watershed, in the southwest of Zhejiang Province, China (Figure 1). The dominant climate is subtropical monsoon climate, which is warm and humid, providing abundant rainfall. The mean temperature is 17.7°C. January is the coldest month with a mean temperature of 6.4°C. While the mean temperature in July is 28.4°C, the hottest month. The mean annual precipitation and evaporation in the area are 1,658.6 mm and 1,291 mm respectively. The rainy season is from March to September: 880.5 mm of rainfall comes between March and June, accounting for 53.1% of annual precipitation; while rainfall comes between July and September accounts for 25.6% of annual precipitation. The rainy season is prone to flooding and inducing geological disasters. Xiaogang Watershed drains through a hilly area of 500.3 km^2, with elevations ranging from 120 m to 1,493 m. The land use type of the Xiaogang Watershed is dominated by undeveloped natural land.

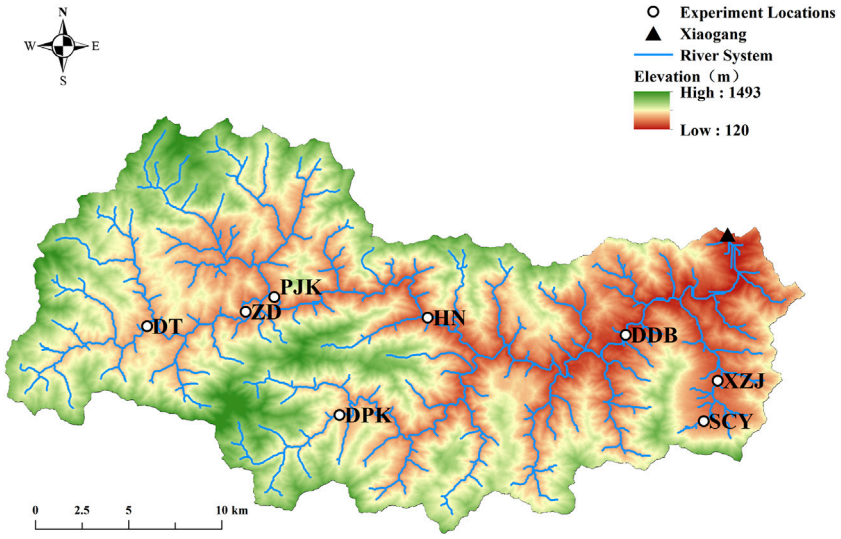

FIGURE 1
Map of the Xiaogang watershed with experimental sites and the Xiaogang Hydrological Station marked with a triangle.

TABLE 1 Characteristics and land use data of the eight experimental streams.

Experiment site	Watershed area (km^2)	Stream temperature (°C)	Discharge ($L\ s^{-1}$)	$[NH_4^+\text{-}N]_{amb}$ ($mg\ L^{-1}$)	Ambient m C:N	Proportion of agricultural land	Proportion of natural land	Proportion of other land
DDB	420	22.5	1,440	0.03	2.66	9.2%	85.9%	5.0%
HN	207	11.4	5,907	0.11	2.95	11.1%	83.1%	5.9%
PJK	170	16.0	7,224	0.11	1.72	14.9%	78.2%	6.9%
ZD	90	18.0	568.8	0.07	2.76	13.0%	80.7%	6.3%
DT	40	14.5	487.1	0.07	2.80	13.6%	80.4%	6.0%
DPK	23	14.5	41.76	0.03	6.95	4.8%	92.5%	2.8%
XZJ	17	13	849.2	0.07	0.89	/	/	/
SCY	4	8.2	204.5	0.07	1.30	24.5%	68.9%	6.6%

2.2 Experiment design

Our goal here was to measure NH_4^+-N uptake kinetics across seasonal and spatial scales. A total of six field experiments were conducted in a headwater named Shicangyuan (SCY) Stream every other month from May 2021 to March 2022 to examine the seasonal variation of ammonium uptake kinetics (Table 2). Besides, we conducted eight experiments across Xiaogang Watershed to investigate the spatial distribution of ammonium uptake between March 8 and 16, 2022 at Dadongba (DDB), Huangnan (HN), Paijukou (PJK), Zhudai (ZD), Doutan (DT), Dapankeng (DPK), Xiazhaijie (XZJ), and Shicangyuan (SCY) (Figure 1). The eight experiment sites were distributed along the upper and lower reaches of the watershed and the mainstream tributaries, with watershed areas ranging from 4 km^2 to 420 km^2 and discharge varying from 42 L s^{-1}–7,224 L s^{-1} (Table 1). The DDB, HN, PJK, DT, and ZD experimental sites are on the mainstream of Songyang River, and the rest are on the tributaries.

2.3 Watershed characteristic data

To understand the impact of land use on nutrient uptake efficiency, the land use distribution within the study area was collected from the government maps based on satellite images. The proportion of different land use types was estimated for the drainage area of the sampling sites. Topographic characteristics (i.e., topographic gradient) were extracted from the digital elevation model (DEM). Water samples from eight streams during the spatial experiment were collected, filtered, and stored on ice before being sent to the lab for water quality characteristics including DOC, Cl^-, TN, NH_4^+, NO_3^-, and chlorophyll *a* to further analyze the potentially influential factors. Two replicates were

collected for each sample. Samples were kept in a dark polyethylene bottle with ice and analyzed at the lab within 24 h. Epilithic material was collected from rocks at each stream reach for benthic chlorophyll *a* and AFDM. Chlorophyll *a* concentration was measured using the spectrophotometry method; AFDM was measured from samples that were oven-dried at 60°C, weighed, and burned in a muffle furnace. These watershed characteristics were used to assess their potential impacts on uptake kinetics spatially. Since the water samples were not collected during the seasonal experiments at SCY, monthly sampling data of water quality data records at the mouth of the DDB stream were collected from the local government to show the water quality condition at the seasonal scale. The Pearson correlation coefficient was calculated to examine the internal correlation between these characteristics. Linear correlation was applied to examine the relationship between the uptake metrics and watershed characteristics.

2.4 Field experiments

The TASCC approach (Tracer Additions for Spiraling Curve Characterization) uses a slug addition at a single enrichment level and collects samples on the rising and falling limbs to obtain a set uptake rate (Covino et al., 2010b). It provides a rapid and relatively easy technique for quantifying ambient-spiraling parameters, nutrient uptake kinetics and kinetic model parameterization, and assessment of stream proximity to saturation. It could be readily generalized to other catchments including big rivers.

At the beginning of our TASCC experiments, stream measurements (e.g., discharge, width, depth flow velocity, temperature, etc.) were measured and background concentration was sampled first. The velocity was measured by a current meter which was multiplied by cross section area for discharge estimation. Initial specific conductance and water temperature at the downstream endpoints of the 600 m-long stream reach would also be measured before tracer addition (i.e., ambient N and Cl). NaCl (conservative tracer) and $(NH_4)_2SO_4$ were weighted and dissolved to generate the solution to add to the stream as an instantaneous injection. Real-time specific conductance measurements were collected at the downstream endpoint at a 60 s time-step. The complete breakthrough curve was sampled with a conductivity meter according to specific conductance data. Stream water samples were taken at the downstream endpoint at intervals of 1–10 min depending on the variability of the conductivity curve; more frequent sampling was done when concentrations changed quickly. After the experiments, stream water samples were stored in high-density polyethylene bottles, cooled at 4°C, filtered, and examined in the lab within 24 h. For each sample, chloride (Cl^-) values were determined using Ion Chromatography and ammonium-nitrogen (NH_4^+-N) by Salicylic acid spectrophotometry.

Nutrient spiraling, which is characterized by uptake length (S_w), the cycle length of the typical dissolved molecule flowing downstream, has enhanced the study of stream nutrient dynamics (Newbold et al., 1981). By graphing the natural log of the NH_4^+-N: Cl ratio of the injectate and each background-corrected sample taken downstream against stream distance, we were able to determine the added nutrient dynamic longitudinal uptake rates ($k_{w-add-dyn}$) for each sample. The dynamic uptake length ($S_{w-add-dyn}$), uptake rates ($U_{add-dyn}$) and uptake velocities ($V_{f-add-dyn}$) for added nutrients were calculated as

$$S_{w-add-dyn} = -\frac{1}{k_{w-add-dyn}} \tag{1}$$

$$U_{add-dyn} = \frac{Q \times \left[NH_4^+ - N_{add-dyn}\right]}{w \times S_{w-add-dyn}} \tag{2}$$

$$V_{f-add-dyn} = \frac{U_{add-dyn}}{\left[NH_4^+ - N_{add-dyn}\right]} \tag{3}$$

where Q is the stream discharge ($L^3\ T^{-1}$), $[NH_4^+ - N_{add-dyn}]$ (Eq. 4, below) is the geometric mean of observed (background corrected) and conservative NH_4^+-N concentration ($M\ L^{-3}$), w is the stream width (L) of the experimental reach. In general, the water samples collected need to meet the following conditions: $[NH_4^+ - N_{ambcorr}]/[Cl_{ambcorr}] \leq [NH_4^+ - N_{add}]/[Cl_{add}]$ (Li et al., 2021). Conservative NH_4^+-N is the amount of NH_4^+-N that would have arrived at a sampling site if NH_4^+-N traveled conservatively (i.e., no uptake, maximum that could arrive), and we calculate this as the product of observed Cl values (background corrected) and the NH_4^+-N: Cl ratio of the injectate.

$$\left[NH_4^+ - N_{add-dyn}\right] = \sqrt{[NH_4^+ - N_{add-obs}] \times [NH_4^+ - N_{cons}]} \tag{4}$$

The ambient uptake length (S_{w-amb}) was calculated by regressing the $S_{w-add-dyn}$ values against in-stream concentration and extrapolating to ambient concentration to estimate S_{w-amb} (Payn et al., 2005; Covino et al., 2010a). Ambient areal uptake rates (U_{amb}) and uptake velocities (V_{f-amb}) were calculated as

$$U_{amb} = \frac{Q \times [NH_4^+ - N_{amb}]}{w \times S_{w-amb}} \tag{5}$$

$$V_{f-amb} = \frac{U_{amb}}{[NH_4^+ - N_{amb}]} \tag{6}$$

where Q is stream discharge ($L^3\ T^{-1}$), $[NH_4 - N_{amb}]$ is the ambient stream NH_4^+-N concentration ($M\ L^{-3}$), w is the average wetted stream width (L).

The sum of ambient (background) and added nutrient intake throughout the addition experiment represents total nutrient uptake. Total nutrient uptake ($U_{tot-dyn}$) was calculated as the sum of ambient and added nutrient spiraling values for TASCC techniques (Covino et al., 2010a):

$$U_{tot-dyn} = U_{amb} + U_{add-dyn} \tag{7}$$

where U_{amb} is the ambient uptake rate ($M\ L^{-2}\ T^{-1}$), $U_{add-dyn}$ is the dynamic areal uptake rate of added nutrient ($M\ L^{-2}\ T^{-1}$) for each sample. Total dynamic uptake velocity ($V_{f-tot-dyn}$) was calculated as

$$V_{f-tot-dyn} = \frac{U_{tot-dyn}}{\left[NH_4^+ - N_{tot-dyn}\right]} \tag{8}$$

where $[NH_4 - N_{tot-dyn}]$ is the geometric mean of the total observed and conservative NH_4^+-N concentration ($M\ L^{-3}$) in each sample:

$$\left[NH_4^+ - N_{tot-dyn}\right] = \sqrt{[NH_4^+ - N_{tot-obs}] \times ([NH_4^+ - N_{cons}] + [NH_4^+ - N_{amb}])} \tag{9}$$

where $[NH_4 - N_{tot-obs}]$ is the total observed NH_4^+-N concentration ($M\ L^{-3}$) in the samples collected throughout the BTC (note that this concentration is not background corrected).

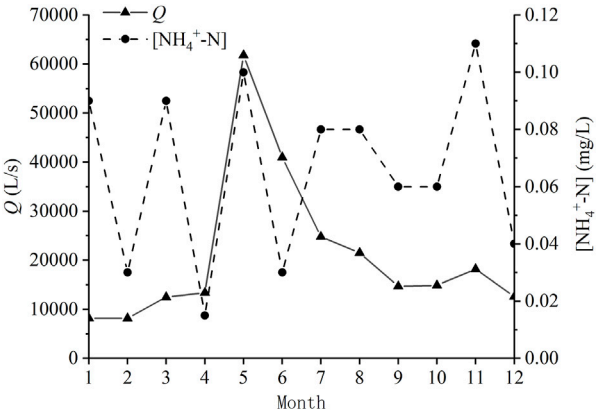

FIGURE 2
The mean monthly discharge (Q) of Xiaogang Hydrological Station in 2021 and the monthly NH_4^+-N concentrations at Dadongba in 2021.

2.5 Model fitting and uptake metrics estimating

The Michaelis-Menten (M-M) model was used to estimate the maximum areal uptake rate parameter (U_{max}) and half saturation concentration parameter (K_m) for each tracer test (Eq. 10), where $[NH_4^+ - N_{tot-dyn}]$ denotes the solute concentration of each sample or time point (mg L^{-1}) (Syebold and McGlynn, 2018).

$$U_{tot-dyn} = \frac{U_{max} \times \left[NH_4 - N_{tot-dyn}\right]}{K_m + \left[NH_4 - N_{tot-dyn}\right]} \quad (10)$$

We also estimated ambient uptake length for our experiments based on the discharge and ambient concentration following Eq. 11 derived in Ye et al. (2017) to compare our data with the literature.

$$log_{10}S_{w-amb} = 2.18 + 0.79log_{10}(Q/w) + 0.32log_{10}[NH_4^+ - N_{amb}] \quad (11)$$

3 Results

3.1 Stream characteristics

The monthly discharge data at Xiaogang Hydrometric Station exhibited great seasonality. From April through August, there was a flood period (consistent with the rainy season of the watershed). However, the ammonium-nitrogen concentration measured at Dadongba did not show clear seasonal variation (Figure 2).

Agricultural land includes arable land and plantation land. Natural land (unused) includes woodland, wetland, and grassland. Other land includes commercial service land, industrial and mining land, residential land, public administration and public service land, transportation land, special land, and water conservancy facilities. SCY had the highest share of agricultural land (24.5%) and the lowest share of natural land (68.9%) among the seven experimental sites, while DPK had the highest share of natural land (92.5%) and the smallest percentage of agricultural land (4.8%) (Table 1).

Meanwhile, water quality data including NH_4^+-N, pH, conductance, dissolved oxygen (DO), chemical oxygen demand (COD_{Mn}), biochemical oxygen demand (BOD), total nitrogen (TN), total phosphorus (TP), fluoride, and fecal coliform bacteria (FCB) were collected at Dadongba on a monthly basis from local government records, as well as the discharge (Q) and temperature (T) data. Pearson correlation coefficients were calculated between each variable (Figure 3). Results show that DO and T were negatively correlated ($p < 0.01$) probably due to oxygen solubility with temperature, while Q and FCB had a significantly positive correlation ($p < 0.01$). What's more, there was a significant positive correlation between Q and TP ($p < 0.05$), and a significant negative correlation between FCB and fluoride ($p < 0.05$). Both COD_{Mn} and Q had a positive correlation with T ($p < 0.1$). NH_4^+-N and conductance are also positively correlated ($p < 0.1$).

3.2 Seasonal variation of uptake kinetics

The uptake data were estimated by conducting TASCC experiments every other month at the SCY experimental site. It could be seen that the S_{w-amb} was larger in summer and winter, smaller in spring and autumn, bottomed in September, and peaked in November (Figure 4). Both ambient [NH_4^+-N] concentrations (C_0) and discharge (Q) peaked in November and Q also reached the lowest point in September (Table 2).

It is obvious from the chart that the changes in ambient uptake velocity (V_{f-amb}) and ambient areal uptake rate (U_{amb}) were consistent in different seasons of the same location. The seasonality of the uptake kinetics characteristics was clear: the uptake capability reached its maximum at the end of the growing season in the fall; it then gradually decreased in the winter, reaching its minimal in January; after which the uptake metrics began to increase during the growing season.

Figure 5 shows the fitted Michaelis-Menten kinetic model for the seasonal experiments. Maximum uptake values (U_{max}) ranged from 9.72 to 43.82 (μg m^{-2} s^{-1}). Half saturation constants (K_m) ranged from 0.08 to 0.43 (mg L^{-1}) (Table 2). As we can see, there were apparent differences between seasons in K_m. The maximum areal uptake rate (U_{max}) escalated from January to November (Figure 5A). This seasonal trend was also seen in the ambient areal uptake rate (U_{amb}) value in Figure 4, which was the smallest in January and kept rising until September. The response to nutrient addition was faster in September, presenting a steep rise to U_{max} (Table 2; Figure 5A). In comparison, K_m values from January to July were larger so the curve appeared flat. Curves in May and July were similar and almost overlapped. K_m value was larger in summer (May and July), smaller in autumn (September), and gradually recovered in winter and spring (January and March).

3.3 Spatial heterogeneity of uptake kinetics

Through our addition experiments, discharge (Q) varied from 123 L s^{-1}–5,370 L s^{-1} and ambient ammonium nitrogen concentration (C_0) varied from 0.056 mg L^{-1} to 0.234 mg L^{-1} among the eight streams (Tables 1, 3). Maximum uptake values (U_{max}) among the sites ranged

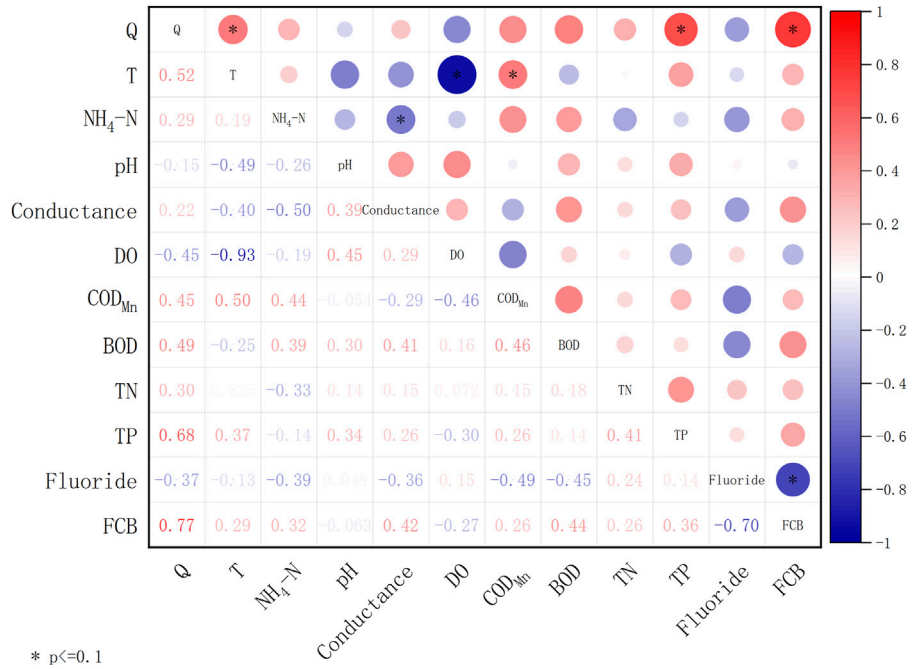

FIGURE 3
Matrix of Pearson correlation coefficients for Q, T and water quality factors at Xiaogang Station (* means $p < 0.1$).

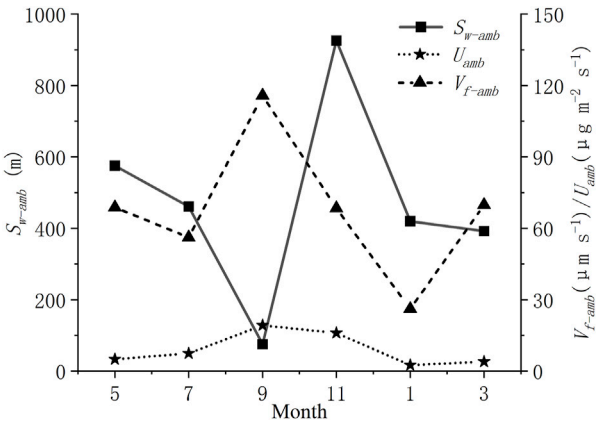

FIGURE 4
Ambient uptake length ($S_{w\text{-}amb}$), ambient areal uptake rate (U_{amb}), and ambient uptake velocity ($V_{f\text{-}amb}$) for ammonium nitrogen.

from 5.92 μg m^{-2} s^{-1}–237.84 μg m^{-2} s^{-1} (Table 3). Headwater SCY had the smallest value and PJK had the largest. In addition, half-saturation constants (K_m) ranged from 0.03 mg L^{-1}–4.39 mg L^{-1} spatially (Table 3). PJK on the mainstream had the lowest value, followed by DDB at the watershed outlet, and headwater XZJ had the highest value. U_{max} values generally increased with greater stream discharge, and PJK had a particularly high U_{max} value but the lowest K_m value, indicating rapid response to increasing nutrient concentration and a high upper limit in uptake.

For spatial scale, mainstream reaches (i.e., DDB, HN, and PJK) reacted more rapidly to increased nutrients, as can be seen in the smaller K_m values at DDB, HN, and PJK sites relative to other sites located in tributaries (Table 3; Figure 5B). U_{max} should also be taken into account when considering K_m. Although $U_{tot\text{-}dyn}$ at ZD responded more rapidly at lower concentrations, U_{max} at elevated concentrations was greater at DPK, XZJ, and DT (Figure 5B).

3.4 Relationship between uptake kinetics and watershed characteristics

Relationships between the uptake kinetics (ambient uptake length, ambient areal uptake rate, ambient uptake velocity, maximum uptake rate, half-saturation constant), and stream discharge Q, water temperature T, as well as ambient ammonium nitrogen concentration (i.e., in-stream concentration at the time of the experiment), were shown in Figures 6B,E,F,J–L,N,O. We found a positive correlation between U_{max} and stream discharge Q among 13 experiments, both seasonally and spatially (Figure 6D). That is, the correlation between uptake metrics and discharge at SCY was consistent both at seasonal and spatial heterogeneity scales. On the other hand, U_{amb} and $V_{f\text{-}amb}$ were only correlated with discharge downstream at the spatial scale; while the correlation between $S_{w\text{-}amb}$ and discharge was observed at the seasonal scale but not at the spatial scale downstream in the river network. There was a positive correlation between U_{amb}, U_{max}, and C_0 throughout the year; yet this correlation with C_0 was not seen across the watershed. The ambient concentration (C_0) was correlated with K_m at the spatial scale only (Figure 6M). These relationships were consistent with previously published research (e.g., Mulholland et al., 1990; Hart et al., 1992). Moreover, U_{amb}, $V_{f\text{-}amb}$, and U_{max} increased with temperature first and then decreased around 17°C, this rising and falling trend was more obvious spatially (Figures 6G–I).

TABLE 2 Nutrient uptake metrics for the seasonal experiments in the shicangyuan (SCY) experiment site.

Experiment date	Stream temperature (°C)	Ambient [NH_4^+-N] (mg L^{-1})	Discharge (L s^{-1})	$S_{w\text{-}amb}$ (m)	U_{amb} (μg m^{-2} s^{-1})	$V_{f\text{-}amb}$ (μm s^{-1})	U_{max} (μg m^{-2} s^{-1})	K_m (mg L^{-1})
2021/5/14	20.5	0.072	178	575.4	4.98	68.75	29.74	0.42
2021/7/6	23.7	0.132	114	461.1	7.44	56.19	30.20	0.43
2021/9/26	21.0	0.166	36.6	75.3	19.24	115.80	28.59	0.08
2021/11/23	11.0	0.234	285	925.9	16.01	68.41	43.82	0.37
2022/1/12	6.8	0.096	46.0	419.6	2.52	26.11	9.72	0.28
2022/3/8	8.5	0.056	123	392.3	3.94	69.84	19.40	0.25

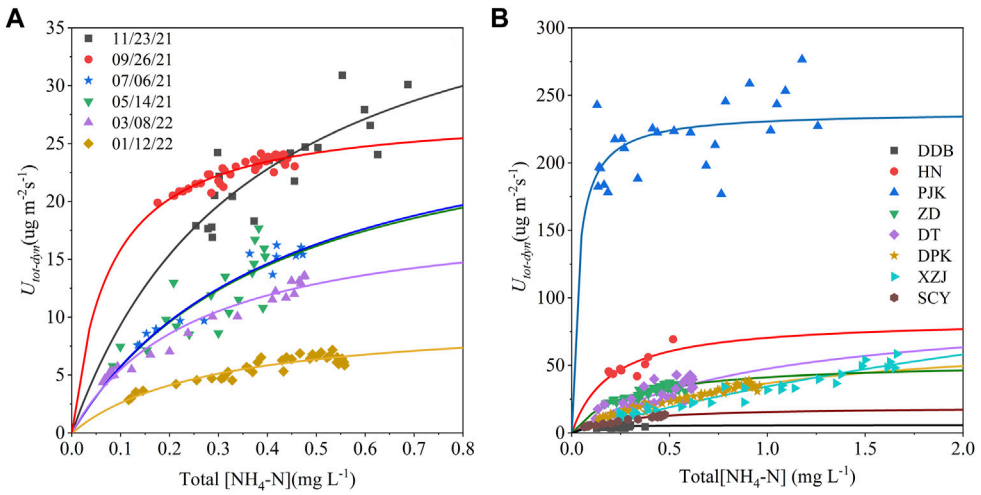

FIGURE 5
(A) Seasonal and **(B)** spatial variation in total areal uptake rates ($U_{tot\text{-}dyn}$) versus the geometric mean of total nitrate NH_4^+-N concentration in Xiaogang Watershed, respectively. The Michaelis–Menten model fits are indicated with solid lines.

TABLE 3 Nutrient uptake metrics for the spatial experiments in the shicangyuan experiment site.

Experiment site	Stream temperature (°C)	Ambient [NH_4^+-N] (mg L^{-1})	Discharge (L s^{-1})	$S_{w\text{-}amb}$ (m)	U_{amb} (μg m^{-2} s^{-1})	$V_{f\text{-}amb}$ (μm s^{-1})	U_{max} (μg m^{-2} s^{-1})	K_m (mg L^{-1})
DDB	22.5	0.126	553.5	1933.9	3.28	26.02	5.92	0.05
HN	11.4	0.181	2,625	1,281.7	41.15	227.60	84.48	0.20
PJK	16	0.117	5,370	481.2	163.21	1,394.95	237.84	0.03
ZD	18	0.144	280.8	439.8	18.39	127.69	52.70	0.28
DT	14.5	0.110	351.3	1984.3	9.76	88.52	95.17	1.00
DPK	14.5	0.103	149.5	489.5	7.65	74.49	75.71	1.06
XZJ	13	0.222	430.9	2,501.5	10.31	46.56	185.63	4.39
SCY	8.5	0.056	123.2	392.3	3.94	69.84	19.40	0.25

There is a positive correlation between $S_{w\text{-}amb}$ and Q in Figure 6A through the year in SCY, which is consistent with Figure 7A showing the fitted relationship according to Eq. 11. But this only existed in one site instead of being across the watershed. $V_{f\text{-}amb}$ and Q in Figure 6C are positively related significantly. While the fitted $V_{f\text{-}amb}$ value is relatively stable

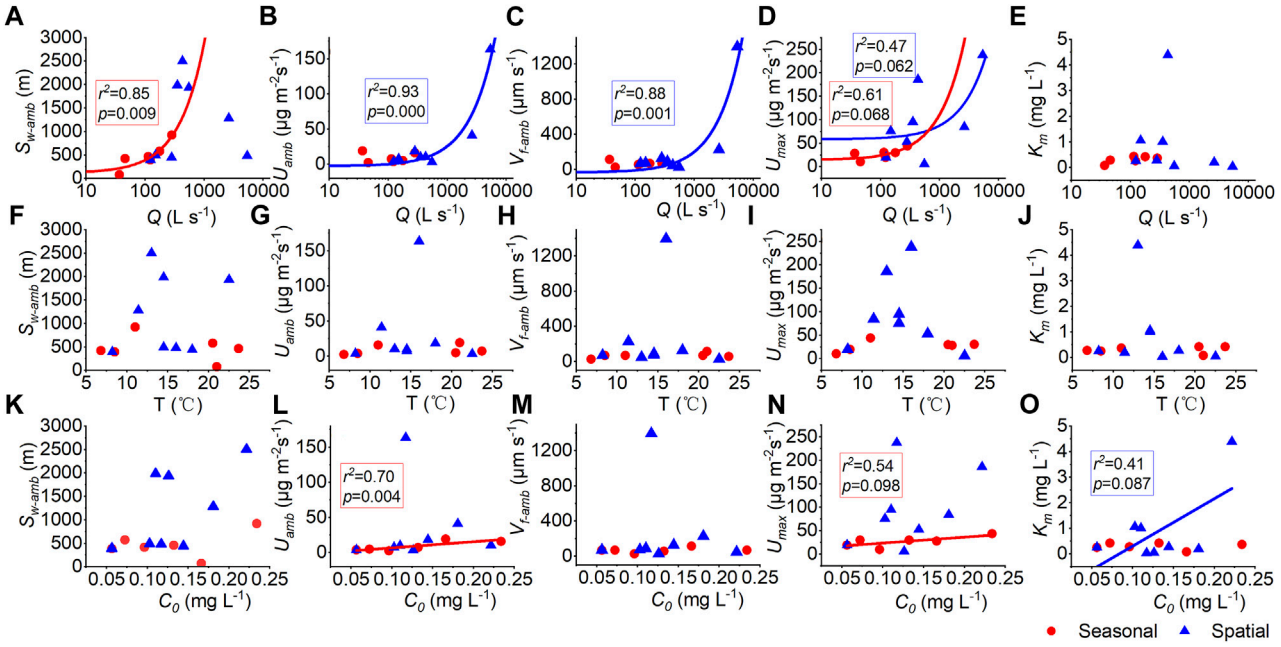

FIGURE 6
Relationships between uptake metrics (ambient uptake length, $S_{w\text{-}amb}$; ambient areal uptake rate, U_{amb}; ambient uptake velocity, $V_{f\text{-}amb}$; the maximum areal uptake rate, U_{max}; and half-saturation constant, K_m) and stream discharge Q **(A–E)**, water temperature T **(F–J)**, and ambient ammonium nitrogen concentration C_0 **(K–O)**. Red symbols indicate experiments at SCY through the year and blue symbols indicate experiments across the watershed. Solid lines indicate correlations at 0.1 level.

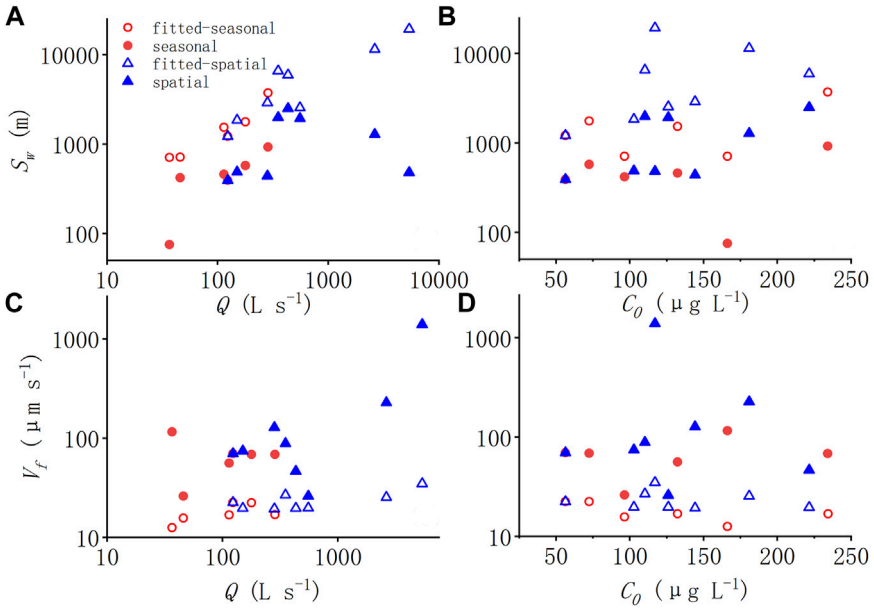

FIGURE 7
(A–D) Relationships between ambient uptake length ($S_{w\text{-}amb}$), ambient uptake velocity ($V_{f\text{-}amb}$) and the stream discharge **(A,C)** and ambient NH_4^+-N concentration **(B,D)**. Red symbols indicate seasonal experiments and blue symbols indicate spatial experiments. The hollow triangle represents the result of estimated uptake metrics using the regressed Eq. 11.

according to the regressed equation in Figure 7C. In fact, the $V_{f\text{-}amb}$ value rose with the increase of Q, whether seasonally or spatially in the study watershed rivers that didn't reach saturation. Besides, instead of the predicted uptake length which increased with discharge, the measured ambient uptake length ($S_{w\text{-}amb}$) increased and then decreased with Q (Figures 7B,D). The higher the discharge,

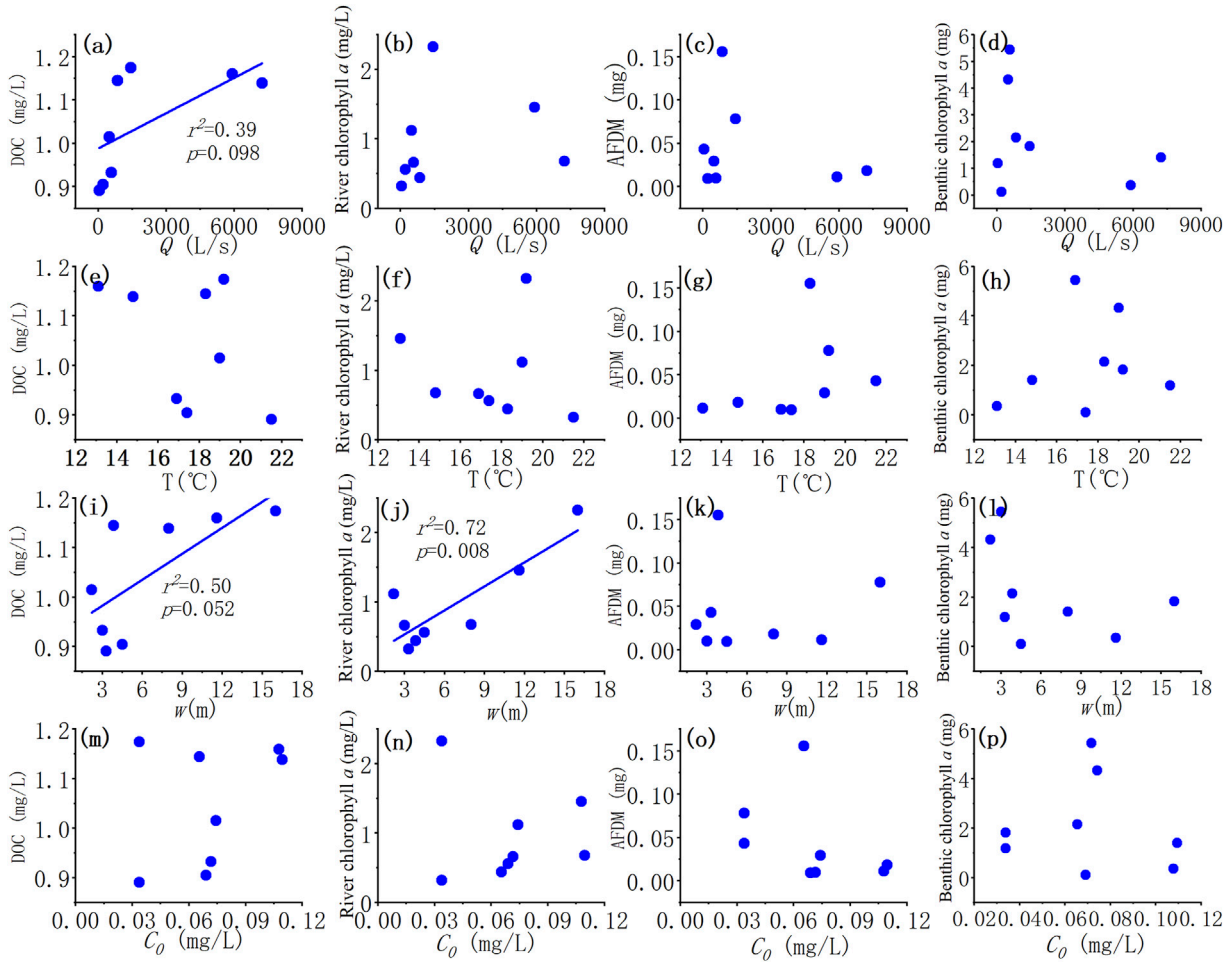

FIGURE 8
(A–P) Relationships between stream ecological characteristics: dissolved organic carbon (DOC), river chlorophyll *a*, ash-free dry mass (AFDM), benthic chlorophyll *a* and stream discharge, Q **(A–D)**, water temperature, T **(E–H)**; stream width w **(I–L)** and ambient ammonium nitrogen C_0 **(M–P)**. The solid line indicates a correlation at 0.1 level.

the larger the difference between measured and predicted $S_{w\text{-}amb}$. That is, the results fit from the regression equation underestimated the ability of uptake in the large flow condition downstream.

3.5 Influences of stream characteristics

We further examined the relationships between stream ecological characteristics: dissolved organic carbon, river chlorophyll *a*, AFDM, and benthic chlorophyll a with stream discharge *Q*, water temperature T, and ambient ammonium nitrogen C_0 among the eight reaches (Figures 8B–H,K–P). As we can see, DOC was positively correlated with discharge (*Q*) and river width (*w*) (Figures 8A,I). River chlorophyll *a* was also significantly positively correlated with river width (Figure 8J). The benthic chlorophyll *a* showed a rising and falling correlation with temperature, similar to the pattern between temperature and uptake metrics (U_{amb}, $V_{f\text{-}amb}$, U_{max}). Yet there was little correlation between these stream ecological characteristics and ambient concentration of ammonium.

We also collected land use data for the drainage area of seven experimental reaches (Figure 9). It was found that land use showed a positive correlation with the concentration of both nitrogen compounds: NH_4^+-N and NO_3^-N ($p < 0.05$). The larger the proportion of agricultural land, the higher the concentration of TN, NO_3^- and Cl^-. On the other hand, AFDM declined with the proportion of agricultural land.

4 Discussion

4.1 Seasonal variability

In this study, a high degree of seasonality in NH_4^+-N uptake kinetics in the SCY stream was seen. On the seasonal scale, we observed that the maximum ambient areal uptake rate (U_{amb}) and ambient uptake velocity ($V_{f\text{-}amb}$) were reached in September, at the end of the growing season, when stream discharge (*Q*) was the lowest and ambient concentration (C_0) was at a high level (Figure 4). $S_{w\text{-}amb}$ is also correlated with *Q* significantly, consistent with the

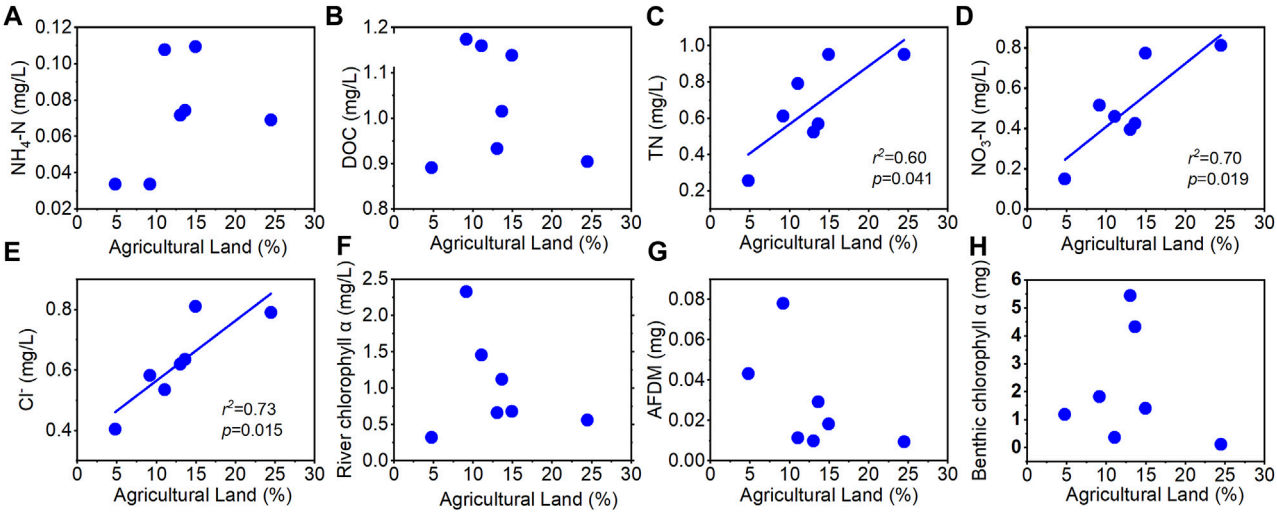

FIGURE 9
Relationships between the proportion of agricultural land and **(A)** NH_4^+-N concentration, **(B)** DOC, **(C)** total nitrogen (TN), **(D)** NO_3-N concentration, **(E)** Cl^- concentration, **(F)** river chlorophyll *a*, **(G)** ash-free dry mass, and **(H)** benthic chlorophyll *a*. The solid line indicates a significant correlation at 0.1 level.

prediction of the regression equation. Further plots suggested that three uptake metrics (U_{amb}, $V_{f\text{-}amb}$, U_{max}) correlated with Q at both seasonal and spatial scales. Besides, the rising and falling trend between the uptake metrics and temperature indicated that there might be an optimal temperature (T) for uptake in our study region around 17°C, usually after the growing season (Figure 6). Compared with discharge and ambient concentration, the correlation between temperature and uptake metrics was not that significant.

The uptake capacity varies with time which validates the conclusion of previous studies that the nutrient uptake capacity of rivers is dynamic, i.e., the shape and magnitude of the kinetic curve varies seasonally (Syebold and McGlynn, 2018). As our results show, considerable seasonality of nutrient uptake was captured in this work, which has been noted in earlier research (Marti and Sabater, 1996; Simon et al., 2005; Hoellein et al., 2007). This indicated that simulations using only the uptake metrics estimated at one time and one place may not be representative of the aquatic ecosystem's capability of nutrient retention across space and time. The seasonality of uptake capabilities may not be well captured by water quality models that scale uptake parameters with only temperature either. The overall quantity of ammonium nitrogen absorbed by the biotic community would have been significantly underestimated if we calculated seasonal uptake using just one set of kinetic parameters. The higher the discharge or concentration, the larger the divergence between the measured uptake metrics and the one predicted based on the regressed curves (Figure 7). That is, the uptake capability of the stream varies with discharge and concentration nonlinearly, the regression curves derived from traditional measurements at a single point/time were not able to capture this nonlinearity. This is crucial for water quality modeling, in that adopting a single set of removal rates from regression curves are accepted procedure when simulating the uptake of nutrients in stream networks. We suggest that more measurements are needed to better assess uptake variation at the seasonal scale, especially in dynamic systems that haven't reached saturation.

4.2 Scaling impact

Under the same seasonal and precipitation conditions, different environmental circumstances lead to distinct uptake rates but still along the M-M curve (Figure 5B). Downstream, the uptake metrics (U_{amb}, $V_{f\text{-}amb}$, U_{max}) increased with rising stream discharge Q and were significantly correlated with Q, while their correlation with ambient NH_4^+-N concentration (C_0) was more scattered (Figure 6). Among the uptake metrics, only the maximum areal uptake rate (U_{max}) showed a correlation with discharge both seasonally and spatially. On the other hand, though U_{amb} and $V_{f\text{-}amb}$ were correlated with discharge at the spatial scale, their response to the seasonal variation of discharge was not monotonically. Compared with the predicted uptake length which increased with Q, the measured ambient uptake length ($S_{w\text{-}amb}$) increased and then decreased with Q (Figure 7). The higher the discharge, the larger the difference between the measured and predicted ambient uptake length. This is different from the consistency at the seasonal scale. The correlation between ambient uptake velocity ($V_{f\text{-}amb}$) and Q further suggested that the $V_{f\text{-}amb}$ usually considered with little variation did show little correlation with ambient concentration but a relatively clear positive correlation with discharge downstream, which was not captured by the regression curve. That is, the uptake capability did not just change seasonally, but also varied spatially, increasing with discharge linearly downstream. With the increase in discharge/stream width, the biological activity increased even more.

4.3 Impacts of stream characteristics

The positive correlation between $V_{f\text{-}amb}$ and Q was observed seasonally and spatially, which might be attributed to the increasing DOC and river chlorophyll *a* downstream. When discharge increased downstream, river width increased rapidly, while the riparian vegetation density decreased downstream. Thus, the

streams were shadowed by riparian canopy at upstream sites. This light limitation was reduced downstream due to decreased riparian vegetation density and increased stream width. As a result, river chlorophyll *a* increased downstream (Figures 6, 8). Besides, according to the literature, the threshold ratio of molar DOC: NO_3^--N across global ecosystems was from 2.2 to 5.2 (Taylor and Townsend, 2010; Syebold and McGlynn, 2018). This resource stoichiometry was found to strongly influence N accumulation by regulating microbial processes in C and N cycling: lower than the threshold, the system would be energy-limited; higher than that, it would be nutrient-limited (Sterner and Elser, 2002; Sinsabaugh et al., 2016). The C:N ratio (DOC:NO_3^--N) in this study varied from 0.89 to 6.95 (Table 1), mostly smaller than the threshold except DPK. Therefore, most of our study streams were energy-limited. That is, the increase in DOC could further improve the uptake capability.

The optimal temperature shown in Figure 6 may be explained by chlorophyll *a* too, which also showed a similar rising and falling trend with temperature. This might be the suitable temperature for the aquatic ecosystem growth in our study watershed. The land use impacts on nitrogen concentration were also significant as expected. In particular, the concentrations of total nitrogen, nitrate, and chloride had a significant positive linear correlation with the proportion of agricultural land, thanks to the agricultural activities (Figure 9).

4.4 Uptake geometry

Our findings suggest that the uptake capability increased with Q and C_0, but the impact of Q and C_0 was different throughout the year and across the river network. We may hypothesize that, like hydraulic geometry, the uptake metrics also varied differently at-a-site and downstream.

The variation of discharge was much higher at spatial scale from upstream to downstream than the seasonal variation at certain sites; while the change of ambient concentration was similar seasonally and downstream. At-a-site (seasonally), the impacts of discharge on uptake metrics were relatively limited, while the change in C_0 could have more important effects. On the other hand, downstream change in C_0 is less influential than discharge variation when considering influences of hydrological conditions. This may be attributed to hydraulic geometry: stream width increased faster with discharge downstream, suggesting a larger wet perimeter, larger benthic area, less light limitation, and more growth space for benthic biota. The river chlorophyll *a* also increased with discharge downstream, that is, the pelagic biota (phytoplankton) also increased which might also help explain the increase of biota uptake ($V_{f\text{-}amb}$) downstream. Measurements of seasonal variation of biota were needed for further validation of our hypothesis.

As a result, we measured both seasonal and spatial uptake to capture the uptake geometry, which is different from the traditional assumption in numerical simulations. Our study emphasized the coupling relationship between hydrological and biological factors affecting uptake metrics and compared the differences between seasonal and spatial uptake factors, which could help improve the traditional assumptions of nitrogen uptake scaling in water quality models.

5 Conclusion

This study aimed to understand the impacts of seasonal and spatial scales on nutrient uptake efficiency. Nutrient addition experiments were conducted: six experiments at one upstream site throughout the year and eight experiments across the river network. The seasonality in our experiment is obvious. The nutrient uptake coefficient reached the highest value at the end of the growth season in September and decreased gradually afterwards. At our experimental site SCY, the correlation between the uptake metrics and the environmental concentration C_0 is stronger on the seasonal scale.

The correlation between uptake metrics and discharge was different at the seasonal scale and the spatial scale. The measured uptake length ($S_{w\text{-}amb}$) was correlated with discharge at the seasonal scale but not at the spatial scale; while U_{amb}, $V_{f\text{-}amb}$ were more correlated with discharge at the spatial scale with stream size. The uptake metrics that increase with Q at the spatial scale may be attributed to the positive correlation of DOC and river chlorophyll *a*, related to hydraulic geometry for the number of biological activities in the wet perimeter of different river channels. Generally speaking, as the Q increases downstream, the wider the river, the longer the wet perimeter, and the larger the area for biofilm and benthic biota growth, thus, the stronger the uptake capacity. In addition, K_m was positively correlated with C_0 at the spatial scale, indicating a faster response to the saturation of elevated C_0 in different river reaches.

Our research tested the characteristics of uptake efficiency in time and space concurrently, emphasized the coupling relationship between hydrological and biological factors affecting uptake metrics, and compared the differences between seasonal and spatial uptake factors. The divergence between the measured uptake metrics and the ones fitted from regression indicated the necessity to update the traditional assumptions in the simulation of water quality models. More seasonal experiments at all the other streams are needed to fully compare the spatial and seasonal patterns in our study watershed. Based on the measured relationship across the river network, numerical simulation could be implemented to reconstruct a nutrient uptake map across the watershed. This study expanded the assumption of influences for uptake capacity in previous studies, that is, the different emphasis of discharge and environmental concentration on the impact of spatial and temporal uptake scales. We also found that the proportion of agricultural land has a positive correlation with the concentration of nutrient elements in the river, which indirectly affects the solute content of the river environment, and thus leads to different uptake capacities. Therefore, revitalizing land use type and hydraulic geometry can be suggested as effective means to improve uptake capacity for the river ecological environment.

Data availability statement

The original contributions presented in the study are included in the article/Supplementary Material, further inquiries can be directed to the corresponding author.

Author contributions

QR and SY conceptualized the original idea and designed the work. JP, JL, and TY contributed to the data collection and preparation. JP also conducted the data analysis. QR, JP, and SY wrote the paper. All authors contributed to the article and approved the submitted version.

Funding

This research has been funded by the National Key Research and Development Program of China (grant no. 2019YFC1510701-01) and the National Natural Science Foundation of China (grant no. 51979243).

Acknowledgments

The Xiaogang Hydrometric Station and Songyang County Water Conservancy Bureau are thanked for permission to conduct our field experiments and release the data.

Conflict of interest

The authors declare that the research was conducted in the absence of any commercial or financial relationships that could be construed as a potential conflict of interest.

Publisher's note

All claims expressed in this article are solely those of the authors and do not necessarily represent those of their affiliated organizations, or those of the publisher, the editors and the reviewers. Any product that may be evaluated in this article, or claim that may be made by its manufacturer, is not guaranteed or endorsed by the publisher.

Supplementary material

The Supplementary Material for this article can be found online at: https://www.frontiersin.org/articles/10.3389/feart.2023.1193824/full#supplementary-material

References

Alexander, R. B., Boyer, E. W., Smith, R. A., Schwarz, G. E., and Moore, R. B. (2007). The role of headwater streams in downstream water quality. *J. Am. Water Resour. Assoc.* 43 (1), 41–59. doi:10.1111/j.1752-1688.2007.00005.x

Arango, C. P., Tank, J. L., Johnson, L. T., Hamilton, S. K., and Kellogg, W. K. (2008). Assimilatory uptake rather than nitrification and denitrification determines nitrogen removal patterns in streams of varying land use. *Limnol. Oceanogr.* 53 (6), 2558–2572. doi:10.4319/lo.2008.53.6.2558

Ball, R. C., and Hooper, F. F. (1963). "Translocation of phosphorus in a trout stream ecosystem," in *Radioecology*. Editors V. Schultz and A. W. Klement (New York, NY, USA: Reinhold hbl. Cop.), 217–228.

Benke, A. C., and Wallace, J. B. (1980). Trophic basis of production among net-spinning caddisflies in a southern Appalachian stream. *Ecology* 61, 108–118. doi:10.2307/1937161

Billen, G., Lancelot, C., and Meybeck, M. (1991). "N, P and Si retention along the aquatic continuum from land to ocean," in *Ocean margin processes in global change*. Editors R. F. C. Mantoura, J. M. Martin, and R. Wollast (Hoboken, NJ, USA: John Wiley), 19–44.

Bormann, F. H., and Likens, G. E. (1979). *Pattern and process in a forested ecosystem*. New York, NY, USA: Springer-Verlag, 253.

Bouwman, A. F., Van Drecht, G., Knoop, J. M., Beusen, A. H., and Meinardi, C. R. (2005). Exploring changes in river nitrogen export to the world's oceans. *Glob. Biogeochem. Cycles* 19, GB1002. doi:10.1029/2004GB002314

Covino, T. P., McGlynn, B. L., and Baker, M. A. (2010a). Separating physical and biological nutrient retention and quantifying uptake kinetics from ambient to saturation in successive mountain stream reaches. *J. Geophys.Res.* 115, G04010. doi:10.1029/2009JG001263

Covino, T. P., McGlynn, B. L., and McNamara, R. A. (2012). Land use/land cover and scale influences on in-stream nitrogen uptake kinetics. *J. Geophys Res.* 117, 1–13. doi:10.1029/2011JG001874

Covino, T. P., McGlynn, B. L., and McNamara, R. A. (2010b). Tracer additions for spiraling curve characterization (TASCC): quantifying stream nutrient uptake kinetics from ambient to saturation. *Limnol. Oceanogr.Methods* 8, 484–498. doi:10.4319/lom.2010.8.484

Earl, S. R., Valett, H. M., and Webster, J. R. (2006). Nitrogen saturation in stream ecosystems. *Ecology* 87 (12), 3140–3151. doi:10.1890/0012-9658(2006)87[3140:NSISE]2.0.CO;2

Elser, J. J., Bracken, M. E. S., Cleland, E. E., Gruner, D. S., Harpole, W. S., Hillebrand, H., et al. (2007). Global analysis of nitrogen and phosphorus limitation of primary producers in freshwater, marine and terrestrial ecosystems. *Ecol. Lett.* 10, 1135–1142. doi:10.1111/j.1461-0248.2007.01113.x

Ensign, S. H., and Doyle, M. W. (2006). Nutrient spiraling in streams and river networks. *J. Geophys. Res. Biogeosciences* 111, 1–13. doi:10.1029/2005JG000114

Gardner, K. K., McGlynn, B. L., and Marshall, L. A. (2011). Quantifying watershed sensitivity to spatially variable N loading and the relative importance of watershed N retention mechanisms. *Water Resour. Res.* 47, W08524. doi:10.1029/2010WR009738

Grimm, N. B., and Fisher, S. G. (1986). Nitrogen limitation in a Sonoran desert stream. *J. N. Am. Benthol. Soc.* 5 (1), 2–15. doi:10.2307/1467743

Grimm, N. B. (1987). Nitrogen dynamics during succession in a desert stream. *Ecology* 68, 1157–1170. doi:10.2307/1939200

Hall, R. O., Baker, M. A., Arp, C. D., and Koch, B. J. (2009a). Hydrologic control of nitrogen removal, storage, and export in a mountain stream. *Limnol. Oceanogr.* 54, 2128–2142. doi:10.4319/lo.2009.54.6.2128

Hall, R. O., Baker, M. A., Rosi-Marshall, E. J., Tank, J. L., and Newbold, J. D. (2013). Solute specific scaling of inorganic nitrogen and phosphorus uptake in streams. *Biogeosciences* 10, 7323–7331. doi:10.5194/bg-10-7323-2013

Hall, R. O., and Tank, J. L. (2003). Ecosystem metabolism controls nitrogen uptake in streams in Grand Teton National Park, Wyoming. *Limnol. Oceanogr.* 48, 1120–1128. doi:10.4319/lo.2003.48.3.1120

Hall, R. O., Tank, J. L., Sobota, D. J., Mulholland, P. J., O'Brien, J. M., Dodds, W. K., et al. (2009b). Nitrate removal in stream ecosystems measured by total uptake ^{15}N addition experiments: total uptake. *Limnol. Oceanogr.* 3, 653–665. doi:10.4319/lo.2009.54.3.0653

Hart, B. T., Freeman, P., and McKelvie, I. D. (1992). Whole-stream phosphorus release studies: variation in uptake length with initial phosphorus concentration. *Hydrobiologia* 235-236, 573–584. doi:10.1007/BF00026245

Hoellein, T. J., Tank, J. L., Rosi-Marshall, E. J., Entrekin, S. A., and Lamberti, G. A. (2007). Controls on spatial and temporal variation of nutrient uptake in three Michigan headwater streams. *Limnol. Oceanogr.* 52, 1964–1977. doi:10.4319/lo.2007.52.5.1964

Li, R. Z., Fu, Y., Xu, D. Q., Wang, X. H., and Jin, G. Q. (2021). Assessing the potential and kinetics of coupled nutrients uptake in mesotrophic streams in Chaohu Lake Basin, China. *Environ. Sci. Pollut. Res. Int.* 44, 62877–62890. doi:10.1007/S11356-021-15214-5

Marti, E., and Sabater, F. (1996). High variability in temporal and spatial nutrient retention in mediterranean streams. *Ecology* 77, 854–869. doi:10.2307/2265506

Meyer, J. L., and Likens, G. E. (1979). Transport and transformation of phosphorus in a forest stream ecosystem. *Ecology* 60, 1255. doi:10.2307/1936971

Meyer, J. L. (1979). The role of sediments and bryophytes in phosphorus dynamics in a headwater stream ecosystem. *Limnol. Oceanogr.* 24 (2), 365–375. doi:10.4319/lo.1979.24.2.0365

Mulholland, P. J., Helton, A. M., Poole, G. C., Hall, R. O., Hamilton, S. K., Peterson, B. J., et al. (2008). Stream denitrification across biomes and its response to anthropogenic nitrate loading. *Nature* 452 (7184), 202–205. doi:10.1038/nature06686

Mulholland, P. J., Steinman, A. D., and Elwood, J. W. (1990). Measurement of phosphorus uptake length in streams: comparison of radiotracer and stable PO_4 releases. *Can. J. Fish. Aquatic Sci.* 47 (12), 2351–2357. doi:10.1139/f90-261

Mulholland, P. J. (2004). The importance of in-stream uptake for regulating stream concentrations and outputs of N and P from a forested watershed: evidence from long-term chemistry records for walker branch watershed. *Biogeochemistry* 70 (3), 403–426. doi:10.1007/s10533-004-0364-y

Mulholland, P. J., and Webster, J. R. (2010). Nutrient dynamics in streams and the role of J-NABS. *J. N. Am. Benthol. Soc.* 29 (1), 100–117. doi:10.1899/08-035.1

Naiman, R. J., and Sedell, J. R. (1979). Characterization of particulate organic matter transported by some Cascade Mountain streams. *J. Fish. Res. Board Can.* 36, 17–31. doi:10.1139/f79-003

Newbold, J. D., Elwood, J. W., Oneill, R. V., and Winkle, W. V. (1981). Measuring nutrient spiralling in streams. *Can. J. Fish. Aquatic Sci.* 38 (7), 860–863. doi:10.1139/f81-114

Payn, R. A., Webster, J. R., Mulholland, P. J., Valett, H. M., and Dodds, W. K. (2005). Estimation of stream nutrient uptake from nutrient addition experiments. *Limnol. Oceanogr. Methods* 3, 174–182. doi:10.4319/lom.2005.3.174

Peterson, B. J., Wollheim, W. M., Mulholland, P. J., Webster, J. R., Meyer, J. L., Tank, J. L., et al. (2001). Control of nitrogen export from watersheds by headwater streams. *Sci. (New York, N.Y.)* 292 (5514), 86–90. doi:10.1126/science.1056874

Piper, L. R., Cross, W. F., and McGlynn, B. L. (2017). Colimitation and the coupling of N and P uptake kinetics in oligotrophic mountain streams. *Biogeochemistry* 132, 165–184. doi:10.1007/s10533-017-0294-0

Reisinger, A. J., Tank, J. L., Rosi-Marshall, E. J., Hall, R. O., Jr, and Baker, M. A. (2015). The varying role of water column nutrient uptake along river continua in contrasting landscapes. *Biogeochem.* 125 (1), 115–131. doi:10.1007/s10533-015-0118-z

Saunders, T. J., Mcclain, M. E., and Llerena, C. A. (2006). The biogeochemistry of dissolved nitrogen, phosphorus, and organic carbon along terrestrial-aquatic flowpaths of a montane headwater catchment in the peruvian amazon. *Hydrol. Process.* 20 (12), 2549–2562. doi:10.1002/hyp.6215

Seitzinger, S. P., Harrison, J. A., Dumont, E., Beusen, A. H. W., and Bouwman, A. F. (2005). Sources and delivery of carbon, nitrogen, and phosphorus to the coastal zone: an overview of global nutrient export from watersheds (NEWS) models and their application. *Glob. Biogeochem. Cycles* 19, GB4S01. doi:10.1029/2005GB002606

Seitzinger, S. P., Styles, R. V., Boyer, E. W., Alexander, R. B., Billen, G., Horwth, R. W., et al. (2002). Nitrogen retention in rivers: model development and application to water sheds in the north eastern USA. *Biogeochemistry* 57 (1), 199–237. doi:10.1023/a:1015745629794

Seybold, E., and McGlynn, B. (2018). Hydrologic and biogeochemical drivers of dissolved organic carbon and nitrate uptake in a headwater stream network. *Biogeochemistry* 1, 23–48. doi:10.1007/s10533-018-0426-1

Short, R. A., and Maslin, P. E. (1977). Processing of leaf litter by a stream detritivore: effect on nutrient availability to collectors. *Ecology* 58, 935–938. doi:10.2307/1936231

Simon, K. S., Townsend, C. R., Biggs, B. J. F., and Bowden, W. B. (2005). Temporal variation of N and P uptake in 2 New Zealand streams. *J. North Am. Benthol. Soc.* 24 (1), 1–18. doi:10.1899/0887-3593(2005)024<0001:TVONAP>2.0.CO;2

Sinsabaugh, R. L., Turner, B. L., Talbot, J. M., Waring, B. G., Powers, J. S., Kuske, C. R., et al. (2016). Stoichiometry of microbial carbon use efficiency in soils. *Ecol. Monogr.* 86, 172–189. doi:10.1890/15-2110.1

Smil, V. (2000). Phosphorus in the environment: natural flows and human interferences. *Annu. Rev. Energy Environ.* 23, 53–88. doi:10.1146/annurev.energy.25.1.53

Sterner, R. W., and Elser, J. J. (2002). *Ecological stoichiometry: The biology of elements from molecules to the biosphere*. Princeton, New Jersey, United States: Princeton University Press.

Stream Solute Workshop (1990). Concepts and methods for assessing solute dynamics in stream ecosystems. *J. North Am. Benthol. Soc.* 9, 95–119. doi:10.2307/1467445

Tank, J. L., Rosi-Marshall, E. J., Baker, M. A., and Hall, R. O., Jr. (2008). Are rivers just big streams? A pulse method to quantify nitrogen demand in a large river. *Ecology* 89 (10), 2935–2945. doi:10.1890/07-1315.1

Taylor, P., and Townsend, A. (2010). Stoichiometric control of organic carbon–nitrate relationships from soils to the sea. *Nature* 464, 1178–1181. doi:10.1038/nature08985

Vitousek, P. M., Aber, J. D., Howarth, R. W., Likens, G. E., Matson, P. A., Schindler, D. W., et al. (1997). Human alteration of the global nitrogen cycle: sources and consequences. *Ecol. Appl.* 7, 737–750. doi:10.1890/1051-0761(1997)007[0737:haotgn]2.0.co;2

Vitousek, P. M., and Howarth, R. W. (1991). Nitrogen limitation on land and in the sea: how can it occur? *Biogeochemistry* 13, 87–115. doi:10.1007/BF00002772

Wallace, J. B., Webster, J. R., and Woodall, W. R. (1977). The role of filter feeders in flowing waters. *Arch. Hydrobiol.* 79, 506–532.

Webster, J. R., Mulholland, P. J., Tank, J. L., Valett, H. M., Dodds, W. K., Peterson, B. J., et al. (2003). Factors affecting ammonium uptake in streams–an inter-biome perspective. *Freshw. Biol.* 48 (8), 1329–1352. doi:10.1046/j.1365-2427.2003.01094.x

Webster, J. R. (1975). *Analysis of potassium and calcium dynamics in stream ecosystems on three southern Appalachian watersheds of contrasting vegetation*. Doctoral dissertation. Athens. GA, USA: University Of Georgia, 232.

Webster, J. R., and Patten, B. C. (1979). Effects of watershed perturbation on stream potassium and calcium dynamics. *Ecol. Monogr.* 49, 51–72. doi:10.2307/1942572

Ye, S., Reisinger, A. J., Tank, J. L., Baker, M. A., Hall, R. O., Rosi, E. J., et al. (2017). Scaling dissolved nutrient removal in river networks: A comparative modeling investigation. *Water Resour. Res.* 11, 9623–9641. doi:10.1002/2017WR020858

frontiers | Frontiers in Earth Science

TYPE Methods
PUBLISHED 09 October 2023
DOI 10.3389/feart.2023.1254509

OPEN ACCESS

EDITED BY
Qihua Ran,
Hohai University, China

REVIEWED BY
Min Xiong,
Tongji University, China
Jixiong Zhang,
China University of Mining and Technology, China
Linqi Huang,
Central South University, China

*CORRESPONDENCE
Mengchao Xu,
2750690437@qq.com
Jiawen Wang,
2601437740@qq.com

RECEIVED 07 July 2023
ACCEPTED 22 September 2023
PUBLISHED 09 October 2023

CITATION
Hou D, Xu M, Li X, Wang J, Wang M and Li S (2023), Study on filling mining technology for gently inclined thin to medium thick phosphorus deposits. *Front. Earth Sci.* 11:1254509. doi: 10.3389/feart.2023.1254509

Study on filling mining technology for gently inclined thin to medium thick phosphorus deposits

Di Hou[1], Mengchao Xu[1,2,3]*, Xiaoshuang Li[2,4], Jiawen Wang[5]*, Menglai Wang[3] and Shujian Li[3]

[1]Guizhou Survey and Design Research Institute for Water Resources and Hydropower, Guiyang, China, [2]School of Civil Engineering, Shaoxing University, Shaoxing, China, [3]Yunnan Phosphating Group Co., LTD., Kunming, China, [4]College of Civil Engineering, Qilu Institute of Technology, Jinan, Shandong, China, [5]School of Resources and Environmental Engineering, Jiangxi University of Science and Technology, Ganzhou, China

This study is grounded in research conducted at the Kunyang Phosphate Mine No. 2, a Chinese open-pit phosphate mining enterprise owned by the Yunnan Phosphate Group Co., Ltd. Due to the small inclination angle and the presence of weak interlayers in the middle of the gently inclined thin to medium thick phosphate ore layer, mining such ore bodies cannot rely on self weight migration, making roof management difficult and mining costs high technical challenges. The methods utilized on-site research, engineering comparisons, and theoretical analysis experiments to address the gently inclined phosphorus deposits. Based on the actual technical and economic conditions of current phosphorus mines, the advantages, disadvantages, and practical conditions of upward horizontal layered filling mining method, upward horizontal layered drift filling mining method, and pseudo inclined segmented strip filling mining method are compared. Priority should be given to using the pseudo inclined segmented strip method as the main method for mining, supplemented by the upward horizontal layered filling method in the panel area. And theoretical calculation methods were applied to obtain various numerical values of the filling capacity of the 2 million t/a mine filling test section, providing technical support for the mining design and equipment selection of the filling test system. The relevant research results can provide guidance for the selection of mining methods for gently inclined thin to medium thick phosphate deposits with an average inclination angle of 15°. The theoretical calculation method used can provide technical guidance for the filling system and filling equipment.

KEYWORDS

gently inclined phosphate rock, filling technique, underground-mining, filling system, technical guidance

1 Introduction

Phosphate ore is a crucial strategic resource for China due to its diverse applications across various industries, including agriculture, energy, materials, chemical engineering, and national security. Phosphate ore is primarily produced in sedimentary rock, with phosphorite accounting for 85% of such rock. Smaller amounts of this ore can also be found in metamorphic and igneous rock formations. With few exceptions, phosphorus in minerals predominantly occurs as orthophosphate, with apatite as its primary mineral source. The phosphate rock layers in China generally have a state of "gently inclined,

medium to thin layers, and multiple interlayers". There are technical challenges such as high ore loss and dilution rate, layered mining, and stability of roof and pillar. Therefore, in order to solve the problems in underground mining of phosphorus mines, the research on underground mining methods and filling techniques is of great significance.

The characteristics of China's phosphate ore can be described as follows: firstly, the ore is predominantly middle to low-grade, with only a few rich ores available. The average grade of P_2O_5 in China's phosphate ore is approximately 17%. The second characteristic is relatively fewer easily processable ores and sedimentary rock boasts the highest proven reserves. However, most of the ores are of medium to low grade. As a result, most of the ores must be sorted to meet the high-concentration phosphorus compound fertilizer industry's production requirements, with only a select number of rich ores meeting these requirements. Thirdly, the mining of phosphorus ore presents several challenges. Due to the lengthy mineralization history, deep burial, strong rock formation, and densely packed cement, most phosphate mines are difficult to mine either through open-pit or underground methods, resulting in high loss and dilution rates and low mining rates.

In China, three main mining methods are employed for phosphate ore: single open-pit mining (Erdenv, 2022; Wei et al., 2022), underground mining (Gong, 2022; Li, 2022), and combined open-pit and underground mining (LI et al., 2019; Li et al., 2021; Jiang et al., 2022; Li et al., 2022; Li et al., 2023).

The selection of filling mining method and the study of filling mining technology have always been the focus of research as the main technical means of deep ore body mining. Qu Liping et al. Zhang Runda et al. (2021) (Qu and Wang, 2021) chose the staggered upward horizontal layered filling mining method, which achieved a production capacity of 2,745 t/d and increased the economic benefits of the mine. Bai Yang (2023) et al. (Zhang et al., 2021) optimized the traditional upward horizontal layered filling mining process to address the technical challenges encountered in the mining process of steeply inclined thin ore bodies, and proposed an upward horizontal layered graded tailings filling mining method suitable for steep and gently inclined thin ore bodies. Deng Gaoling et al. (2023) (Bai et al., 2023) conducted research on the mining method and process optimization of steeply inclined and fractured thin ore veins using the downward drift filling mining method. Yan Huifeng (2023) (Deng et al., 2023) introduced the basic concept, application advantages, and application strategies of different types of backfill mining technologies of paste filling technology. Hao Yingjie et al. Zeng Jialong (2022) et al. (Yan, 2023) used FLAC^{3D} and Midas GTS software to compare and analyze the stress disturbance and displacement changes under the pseudo inclined segmented strip filling mining method, providing a theoretical basis for selecting structural parameters of the same type of mining site, which has certain guiding significance.

Kunyang Phosphate Mine No. 2 is a large open-pit to underground phosphorus mine under Yunnan Phosphate Group. The research on underground mining technology and filling technology can provide important significance for the filling technology mining of gently inclined mines containing soft armor layers that are currently undergoing the process of open-pit to underground mining.

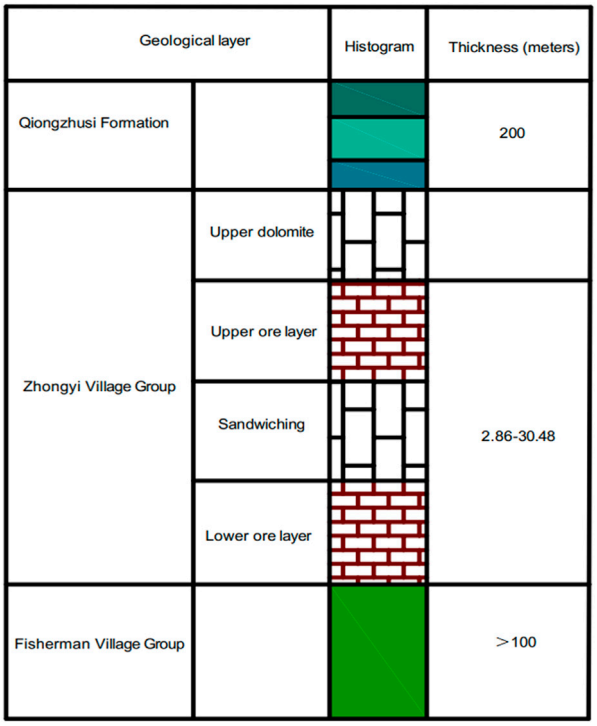

FIGURE 1
Stratigraphic histogram.

2 Project overview

2.1 Mine location and rock mass overview

The Kunyang Phosphate Mine No. 2 is located in the southwest region of the Dianchi Phosphate Accumulation Zone, adjacent to Kunyang Phosphate Mine in the east and Xiaojiaying Phosphate Mine in the west. The northern part of the region is Haikou Phosphate Mine, situated in Erjie Town, Jinning District. The mining area is 44.5 km away from Kunming City and 9 km away from Jinning City. The exploration line extends from Dawei Mountain in the east to Erming Road in Erjie Town in the west, between 56 and 74. Its east-west length is around 4.5 km, north-south width is around 1.7 km, and the total area is 7.66 km^2. The northern end of the mining area is near 320 National Highway, Kunming Kunyang Yuxi Railway and Highway, Gaohai Expressway, Anjin Expressway in the east, and the Bajie Erjie Haikou Highway in the south. The internal road network of the mining area spans approximately 13 km, and there are approximately 62 km to Kunming City and approximately 10 km to the nearest train station, Zhongyi Village Station, making transportation exceptionally convenient (Qu and Wang, 2021; Zhang et al., 2021).

2.2 Selection principles and scope of filling test area

As a permanent facility in mines, the selection of filling stations is one of the key factors affecting the investment, operating costs,

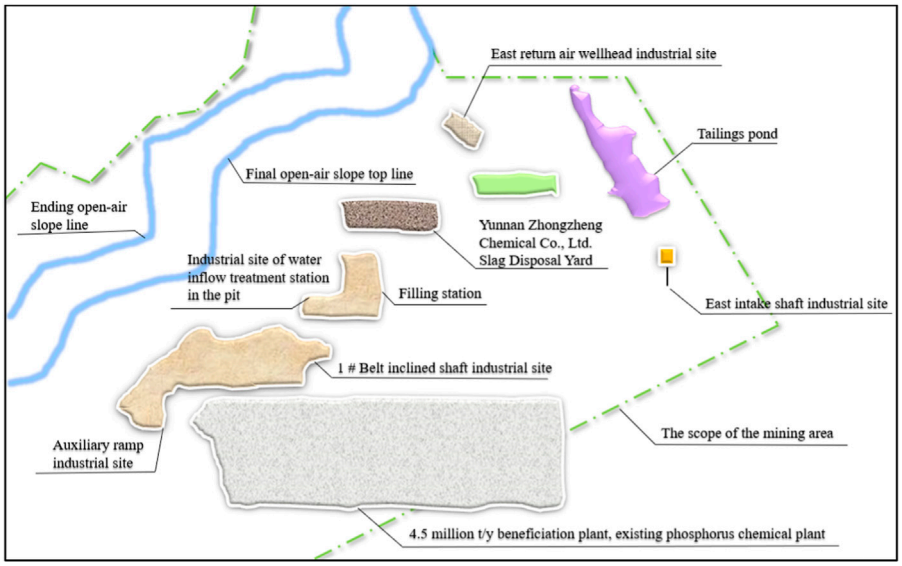

FIGURE 2
Site selection diagram of the filling station.

and reliability of the filling system (Ren Q., 2021). Therefore, the selection principles and scope of the filling test area should follow the following principles.

1) The station site is not affected by underground mining activities;
2) Having suitable filling lines;
3) Facilitate the transportation of materials from the beneficiation plant to the filling station;
4) Having sufficient industrial sites and stable water and electricity supply;
5) Try not to acquire new land;
6) There are tunnel projects in corresponding underground locations, which are convenient for filling and drilling construction, and reduce the number of new projects;
7) It meets the current filing requirements for the middle stage of production and the filling requirements for deep ore bodies.

The filling test is situated in the Kunyang Phosphate Mine No. 2, with an average inclination angle of 15°. It is typically gently sloping thin to medium-thick ore body with a soft protective layer, making it highly representative. The stratigraphic column is shown in Figure 1. The 63-67# exploration lines' outcrop area in Kunyang Phosphate Mine No. 2 and the northern side of the 62-59# exploration lines in the northern part of the mining rights are undergoing open-air terrace mining. The lowest step in the middle has been recovered to nearly 2,100 m. The western mining area has excavated 1.1600 million tons, with a local minimum altitude of 2,000 m. At 2,050 m in the eastern mining area, the maximum horizontal resistance is 38 times the maximum geometric filling line. By contrast, at 1,860 m in the western mining area, the horizontal resistance varies considerably and has a maximum geometric filling line of 16.1.

Based on the selection principles and scope for the filling test area mentioned earlier, a location near the high-level water tank has been chosen for the filling test area. The station is located on the south side of the east return air shaft, with a surface elevation of 2,161 m for the filling station. Two independent filling systems are installed at the filling station site. When the filling station is located there, the tailings from the 450 beneficiation plant are transported to the filling preparation station through a 2.1 km tailings conveying pipe, and then prepared into filling slurry through the filling station. It can be directly transported to various underground mining sites through the filling boreholes in the station, and then flow to each underground mining site through the filling boreholes, achieving the "self flow"

FIGURE 3
Filling the experimental area.

transportation of the filling slurry. The site selection of the filling station is shown in Figure 2.

2.3 Geological conditions of the filling test area

The test area is positioned in the center of Kunyang Phosphate Mine No. 2. The filling test area is shown in Figure 3. The mining area is generally a tilted structure that slopes from south to east, and due to the gentle production of the ore layer, the open-air shape is relatively complicated. The distribution is from the south to the north of the mountains. The sedimentary-type phosphorus rock bed was formed, resulting in the production status of the mine layer being relatively stable, remaining consistent with the upper layer. Typically, the mine's production status moves towards the northeast to the southwest and inclines at an angle ranging from 2° to 31°, tending towards the southeast.

The upper layer of ore is distributed between exploration lines 58~74, with an average thickness of 6.88 m and an average P_2O_5 content of 21.8%. The minimum thickness of the upper ore layer is 2.62 m, while the maximum thickness is 12.69 m. On average, the thickness measures 6.7 m, and the variation coefficient for thickness is 33%, indicating this layer is stable. Regarding its P_2O_5 content, the average grade is 22%, and the grade change coefficient is 17%, indicating that it is uniform. This layer contains I~III grade ores, distributed in a spatial pattern that gradually becomes richer from the upper poor to the middle lower. The ore layer is relatively continuous and stable along the strike and dip. The interlayer mainly occurs in the southwest of the mining area (between exploration lines 63–74), while it is scattered in the east. The lithology consists of gray, white, and yellow clay, with a thickness ranging from 0 to 3.08 m. The rock thickness varies between 0 and 3.15m, with an average thickness of 1.08 m. The lower ore layer is distributed between exploration lines 58–74. The average thickness of the ore layer is 5.65 m, and the average content of P_2O_5 is 27.66%. The minimum thickness of the lower ore layer is 0.34 m, the maximum thickness is 12.77 m, the average thickness is 5.67 m, and the thickness variation coefficient is 36%, belonging to the stable type. The average content of P_2O_5 is 26.9%, and the grade change coefficient is 15%, belonging to the uniform type. I~III grade ores are distributed in this layer and have a spatial distribution pattern of upper rich and bottom poor.

Based on the classification of ore products, the first-grade products (P_2O_5 content ≥25%) are located on the phosphorus ore's intermediate and upper mine layers. Second-grade products (P_2O_5 content between 15% and 25%) are mainly located in the upper mine layer with phosphorus-containing layers. Third-grade products (P_2O_5 content between 8% and 15%) are situated in the middle and lower portions of the phosphorus ore layer.

The phosphate rock deposit in the experimental area is continuously deposited between rich and poor ore layers, with gradual changes in material composition and gradual transition in ore grade. The ore layer in the experimental section has good stability with continuous and stable strike and dip, with an average dip angle of 15°, making it highly suitable for filling in the experimental area.

3 Implementation plan for underground mining engineering

3.1 Overall plan and mining scale

This experiment is an industrial test project focused on underground mining and mining methods. Its primary objective is to seek effective mining methods suitable for underground mining, optimize the mineral structure parameters of the mining method, analyze and determine the safety hazard factors associated with underground mining, and conduct mining testing calculations—Economic Indicators. The mining method test will use the field's production capacity as the assessment indicator. The mining production capacity is 2 million tonnes annually, with a filling capacity of 2.67 t/m³. As the mine scale is related to mining scope, methods, and equipment level (Bai et al., 2023), this trial will primarily evaluate the field's production capacity, transportation capacity, and economic indicators during the test period.

3.2 Optimization of mining methods

Green mining is an inevitable trend in mining development (Deng et al., 2023; Hao et al., 2023; Yan, 2023). The filling mining method can greatly improve the mining recovery rate while the dilution rate is minimal. Additionally, this method provides the ability to mine the ore body under the principles of "Three underminings." The filling mining method provides a high resource utilization rate and allows for effective control over ground pressure. Furthermore, this method significantly reduces water inflow into the mine and helps prevent geological disasters such as ground collapse, cracking, and mountain collapse. The filling mining method can fill the empty areas with waste rock and tailings. This eliminates the need for large waste rock dams and tailings ponds on the ground, which can significantly improve the surrounding environment of the mining areas and prevent potential conflicts between enterprises and local communities (Zeng et al., 2022a; Liu, 2022; Shen and Ning, 2022).

In this experiment, if the upward horizontal layered drift filling method is utilized by arranging ore rooms along the strike (Ren Q., 2021; Cui and Qi, 2023; Wu and Wang, 2023), it has good safety; Additionally, a larger number of ore rooms can be arranged in each panel, thereby improving production capacity. Nonetheless, the design does not deem this method suitable due to the complex process and poor ventilation environment. The upward horizontal layered filling method (with a vertically oriented layout of the ore house) can protect the roof via anchor bolts and reserve ore pillars and adjust to layered drift filling mining based on the ore body and surrounding rock conditions. When the panel slope is arranged outside of the vein, it exhibits good adaptability to the technical mining conditions of the ore body. However, it has a low recovery rate after reserving ore pillars and presents multiple constraints on the panel production capacity (Wang, 2023). The pseudo-inclined segmented strip-filling method (Zhang, 2014; Wang et al., 2022; Zeng, 2023) has the advantages of large panel production capacity, long service life, good safety, and good economy (Ren Y. D., 2021). The comparison of this experimental mining method is shown in Table 1.

TABLE 1 Advantages and disadvantages of mining plans.

Indicator name	Mining plan			
	Pseudo-inclined segmented strip-filling mining method	Upward horizontal slicing and filling mining method (vertically arranged mining rooms)		Upward horizontal slicing and filling mining method
		Extravenous sampling	Intravenous sampling	
Advantages	1.Arranging mining rooms along the inclined direction can more efficiently separate the upper and lower layers of ore	Used when the inclination angle of the ore body is greater than 15°	1.The mining room is arranged vertically along the direction of the ore body, with high equipment efficiency	1.Many mining rooms can be arranged in each panel
	2.The production capacity of the panel is large			
	3.High recovery rate			
Disadvantages	1.Poor ventilation environment in the mining area		1.High mining costs	1.Poor ventilation in the mining area
	2.The equipment operation efficiency is low		2.Low pillar recovery rate	2.There are many process steps
Conclusion	Recommend			

After analyzing and studying 88 boreholes within the designated mining area, the following conclusions can be drawn: Approximately 33.70% of individual projects have an upper ore bed thickness of ≤ 6 m, with an average thickness of 4.29 m. On the other hand, thicknesses greater than 6 m account for 66.30%, with an average thickness of 7.92 m. Additionally, individual projects with a thickness of ≤ 6 m in the lower seam represent 59.55%, with an average thickness of 4.39 m, while 40.45% are thicker than 6 m, with an average thickness of 7.56 m. A calculated approach has been implemented to enhance the recovery rate of the lower seam, mitigate inclusions, and maintain stable roof conditions in the upper seam. The pseudo-inclined segmented strip-filling mining method (I) is applied primarily to ore bodies with a thickness of ≤ 6 m, comprising 40% of the total, while the pseudo-inclined segmented strip-filling mining method (II) is utilized mostly for ore bodies with a thickness of>6 m, accounting for 50%. The remaining 10% of the mine is reserved for the upward horizontal layered filling method (Peng, 2022).

FIGURE 4
Filling test equipment.

3.3 Filling system design

The process flow of the filling station is to transport the tail mortar produced by the flotation plant to the thickener of the filling station (Wang, 2020; Zeng et al., 2022b; Xu, 2022) and then pump the thickener to the mixer of the filling station through a slurry pump. The internally purchased crushed stones are stored in the crushed stone pile shed. Materials are loaded into the feed bin using a scraper and transported to the mixer via the belt when filling. Cementitious material is delivered to the filling station by a cement tanker and discharged through a soot-blowing pipe into the cement silo. The screw feeder at the bottom of the silo feeds the mixture to the mixer according to the required filling strength. They enter the filling pump after fully mixing the tail mortar, crushed stone, and cementitious materials. They are transported along the surface through the filling pipeline to the borehole near the east return air shaft before reaching the goaf for filling. The filling test equipment and filling station process flow are shown in Figure 4, 5. The station has three sets of filling pumps, two for normal operation and one for standby. Accident waste slurry and production wastewater are collected in the sewage collection tank, while clarified water is discharged to the high-level water tank. The accumulated waste sand is regularly cleared out. Apart from receiving overflow water, the sand return tank can also discharge the tailings deposited in the thickener to the sand return tank in case of a system failure.

The designed mining production scale is 2 million t/a, with 330 working days per year. The specific gravity of ore is 2.67 t/m^3, and the filling system is also based on 330 working days per year. We need to meet the current production demand and consider that there should be a certain margin in filling system production capacity.

(1) Annual volume of empty space to be filled

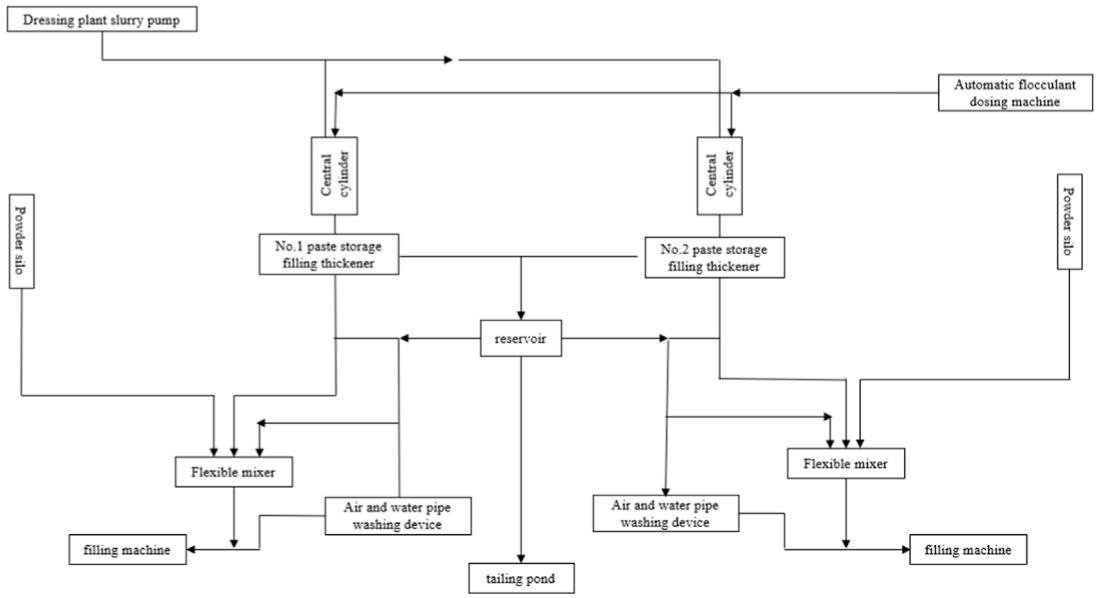

FIGURE 5
Filling station process flow.

$$V = \frac{T_y}{u} \times Z \times K_1 = 74.16\left(10000\mathrm{m}^3/a\right)$$

In the formula: T_y—Annual filling mining capacity
u—Ore weight
Z—Mining and filling ratio
K_1—Unbalance coefficient, taking $K_1 = 1.1$

(2) The annual consumption of full tailings cemented filling slurry volume is:

$$V_m = K_2K_3V = 1.02 \times 1.03 \times 74.16 \approx 78\left(10000\mathrm{m}^3/a\right)$$

In the formula: K_2—Compression settlement coefficient, taking $K_2 = 1.02$ K_3—Loss coefficient, taking $K_3 = 1.03$

(3) Average daily filling volume required

$$Q_d = \frac{V_m}{T} = \frac{780000m^3/a}{330} \approx 2360\left(\mathrm{m}^3/d\right)$$

In the formula: V_m—Annual average demand for filling slurry, m^3/aT—Filling workday, 330d/a

(4) Maximum daily filling volume

$$Q_{dmax} = KQ_r \approx 2830\left(\mathrm{m}^3/d\right)$$

In the formula: Q_m—Daily filling capacity of the mine, m^3/dK—Uneven coefficient of filling operation, $K = 1.2$

(5) Hourly slurry preparation capacity of filling station

$$Q_h = \frac{Q_d}{n_1t} = \frac{2360}{2 \times 6} \approx 200\left(\mathrm{m}^3/h\right)$$

$$Q_{hmax} = \frac{Q_{dmax}}{n_1t} = \frac{2830}{2 \times 6} \approx 240\left(m^3/h\right)$$

In the formula: Q_h—Hourly slurry preparation capacity of filling station, m^3/h

Q_{hmax}—Maximum hourly slurry preparation capacity of the filling station, m^3/h

n_1—Number of daily work shifts, taking $n_1 = 2$;

t—Filling time per shift, taking $t = 6h$

Design 2 sets of filling slurry with a separate preparation capacity of 100 m^3/The filling system of H, with two sets of systems operating in parallel (two shifts) or a separate filling system operating continuously for 24 h, can meet production needs. The filling capacity calculation is shown in Table 2.

We calculated that the maximum daily filling slurry volume in the experimental area was 2,830 m^3/d, and the average daily filling slurry volume was 2,360 m^3/d. The filling system has two sets of filling pumping systems, comprising filling pumps, feeding belts, tailings feed pumps, paddle mixers, screw mixers, cement slurry, filling pumps, off-site gravel storage yards, and tailings deep cone thickeners.

The filling station has an aggregate storage yard and cement warehouse to meet the daily filling material volume. For this experiment, tailings and crushed stones serve as the main filling aggregates, and bulk cement is stored in a 300 t cement silo, which can provide materials for filling buffer for approximately 3 days. The gravel filling dosage is between 70–80 tons/hour, and each shift dose ranges from 420 to 480 t. One shift per day is worked, calculated based on an eighth shift. The gravel pile shed stores 3 days' worth of filling materials, and the lattice screen on top of the feeding bin controls the size of the aggregate entering it. Three ZL50 loaders are configured for filling and loading. The filling system is equipped

TABLE 2 Calculated values of filling capacity.

Serial number	Parameter	Unit	Number
1	mine production capacity	10,000 t/a	200
2	Annual working days	d/a	330
3	Ore weight	t/m³	2.67
4	Annual production gap	10,000 m³/a	74.16
5	Annual filling of empty areas	10,000 m³/a	74.16
6	Annual preparation amount of filling slurry	10,000 m³/a	78
7	Annual filling operation days	d/a	330
8	Daily average filling slurry volume	m³/d	2,360
9	Imbalanced coefficient of filling		1.2
10	Maximum daily filling slurry volume	m³/d	2,830
11	Daily filling time of filling station	h/d	12
12	Hourly filling slurry volume	m³/h	200–240
13	Required number of filling coefficient sets	Cover	2
14	Filling capacity of a single system	m³/h	100

with two cement silos, and the storage capacity of each silo should be no less than the demand for 3 days. The maximum daily consumption of cement is 400 t, so the storage capacity of each cement silo should be no less than 300 t, with an effective volume of 250 m³, which can meet the cement consumption needs for 3 days. A transmission pipeline has been constructed from the concentrator to the tailings pond, with a branch pipe connected starting from pipeline stake No. PN11 leading to the filling station. The pipeline is utilized for filling purposes after concentration.

The horizontal mixing system used in this design boasts several advantages, such as low equipment and small building height requirements, mature equipment with high performance, and convenient installation and maintenance. For each system, we recommend using two stages of mixing: double shaft blade mixer and double screw mixer, with a mixing capacity of 100–120 m³. During mixing, the tail mortar is first diluted in a central barrel and then mixed evenly with the flocculant. It is then concentrated and settled before being metered and batched by the weighing system. Crushed stone is transported to the main material hopper by a belt conveyor, while bulk cement is stored in a weighing hopper through a cement weighing system. The water used for filling the slurry comes from the production water of the concentrator. A proper proportion of full-tail mortar, cement, and concentrated water is measured and added to the mixer to mix evenly. The filling material should be thoroughly stirred to create a slurry with a moderate concentration and excellent fluidity, ensuring that it can be easily supplied to the filling material delivery pump or the lower hopper of the filling borehole.

A concrete pump then transports the mixed filler slurry. Before feeding the concrete delivery pump, it is important to ensure even mixing of the concrete. During feeding, unloading should be carried out uniformly in conjunction with pumping while maintaining the concrete above the height mark line in the aggregate hopper. A mesh screen should also be placed on the concrete pump feed hopper, and someone should be assigned to monitor the feeding process carefully to prevent excessive particle size aggregate or foreign matter from entering the pump and causing a blockage.

In order to make the filling slurry transportation system adopt self flow transportation, it is necessary to calculate the pipe diameter and theoretical thickness of the self flow transportation system separately.

(1) Calculation of the pipe diameter of the self flow transportation system:

Many filling mines at home and abroad use seamless smooth pipes and pipeline steel as filling pipelines. This time, pipeline steel is used as filling pipelines. According to the flow rate of the filling slurry in the semi industrial test section, which is 1.4–18 m/s, the minimum inner diameter of the filling pipeline is:

$$D_T = \sqrt{\frac{4Q_h}{3600\pi v}} = 132.9mm$$

In the formula: Q_h is the hourly filling capacity requirement of the filling system, taking 100 m³/h; V is the working flow rate designed for the filling system, V=1.6 m/s=5,760 m/h

(2) Theoretical thickness calculation of pipeline:

$$\delta = \frac{P \cdot D}{2[\sigma]} + K$$

In the formula: P is the maximum pressure that the pipeline can withstand, MPa; The maximum weight of the slurry is 1.96 t/m³, The maximum pressure exerted on the pipeline is approximately 11 MPa $[\sigma]$ is the allowable tensile stress of the steel, with a value of 160 MPa for 16 Mn seamless steel pipes

TABLE 3 Main power equipment of the filling system.

Serial number	Name	Number	Technical parameter	Power and level
1	Filling industrial pump	3	100 m^3~120 m^3, Working pressure, 10 MPa, 10 KV	560
2	Feeding tape machine	2	B=800 × 3400, 380 V	11
3	Belt conveyor	2	B=1,000 m, L=60 m, V=2 m/s, 380 V	55
4	Double shaft paddle mixer	2	Φ680, V=3.5 m^3, Q=100 m^3/h	2 × 37
5	Double axis spiral mixer	2	Φ750, V=5.1 m^3, Q=100 m^3/h	2 × 45
6	Cement silo	4	300 t, Φ5.5 m, Cement silo height 8.9 m, Cone height 3 m	
7	Current stabilizing device	4	15–70 m^3/h, 1,000 m × 550 mm	2 × 7.5
8	Screw conveyor	4	Φ300 mm, L=4.5 m, Q=10–35 t/h	2 × 11
9	Deep cone thickener	1	Φ26 m	15
10	Slurry Pump	3	Q=100 m^3/h, H=20 m, 380 V	37
11	clean water pump	2		18.5
12	Underarm slurry pump	2		45
13	Underarm slurry pump	2		11

K is the amount of wear and corrosion, taken as 4 mm.

After calculation, $[\sigma]$ =12 mm, considering a certain margin, and using 16Mn steel, according to the steel pipe specifications, select a steel pipe with a wall thickness of no less than 14 mm for the high-pressure pipe section from the pump outlet to the vertical pipe area.

To improve the wear resistance of the filling pipeline, the main pipe adopts 16 Mn seamless steel pipes with strong wear resistance. Based on the above calculation results, the specifications of the main pipe are Φ 168 mm × 14 mm, actual effective inner diameter of pipeline DI=140 mm; Branch pipe, 8-4 MPa, steel pipe specification Φ 168 mm × 10 mm, effective inner diameter DI=148 mm; 4-0MPa, steel pipe specification Φ 168 mm × 8 mm, effective inner diameter DI=152 mm, and DN150 ultra-high molecular weight polyethylene pipes are used in the end segmented branch line and mining area.

When filling industrial pumps, it is essential to consider pipe plugging and outlet pressure fully. The pipes should be arranged in an S-shaped fashion to achieve optimal results. The flow rate for these industrial pumps should be set between 100 and 120 m^3/h. When the distance is relatively close, the high-volume filling can be utilized.

The selection of the location of the filling station and the filling pipe in the well is complementary, and the combination of the two directly determines the filling of multiple lines of the pipeline. The filling pipe needs to be transported 400 m across the ground to reach the borehole for filling. Considering both surface topography and subsurface development, the east vertical air shaft was filled by drilling in the early stage, providing service to the mined-out areas above 1,890 m in the east. In the later stage, it fills the east and west mined-out areas below 1890m through the central air intake shaft.

Through research on mining technology and theoretical numerical calculation of the filling test section of Kunyang Phosphate Mine No. 2, preliminary Table 3 shows the power equipment of the filling system:

According to the above filling experimental calculation requirements, the main power equipment for the filling system is selected as shown in Table 3.

4 Problems that still exist during the filling process

Slightly inclined thin to medium-thick ore bodies have typical characteristics, such as slow dip angles, large changes in ore body shape, and unclear ore-rock boundaries. These features pose technical difficulties for both open-pit and underground mining, resulting in high loss rates, high dilution rates, and low resource recovery rates. These difficulties seriously restrict the development of phosphorus ore mining technology in China. Currently, the main problems in mining gently inclined thin to medium-thick phosphorus ore bodies persist, including.

(1) The mechanical equipment, mining methods, and technology necessary for underground mining of these ore bodies have not been resolved yet.

(2) The stability of the filling system operation and the overall filling process is relatively complex. The stability of each subsystem is particularly critical to the overall system, and any problem in the filling process can lead to the stoppage of filling work.

(3) There are few studies on the underground mining of gently inclined thin to medium-thick phosphorous ore bodies, especially for fractured and unstable ones.

(4) The research on the preparation and process of filling slurry is still imperfect. The filling effect's core issue lies in the filling slurry's preparation effect. If the filling effect is not good, it can lead to problems such as side chipping or large area collapse, increasing safety risks.

(5) There are no significant breakthrough research results on the rock movement and surface subsidence caused by underground mining of phosphate mines, and the relevant theoretical system is far from mature and perfect. It is still in the preliminary research stage.

5 Conclusion

The gently inclined thin to medium thick ore body refers to an ore body with an inclination of 5°–30° and a 1.0–15 m thickness. The Kunyang Phosphate Mine No. 2 has an average inclination angle of 15°, typically a gently inclined thin to medium-thick deposit. Through research on phosphate mining and filling technology, the following conclusions are drawn.

(1) Gently inclined thin to medium-thick phosphate ore deposits are mainly mined using the pseudo-inclined segmented strip drift filling method arranged along the ore room, supplemented by the upward horizontal layered drift filling method. This approach can increase the production capacity of coiled coils, improve the recovery rate, and separate the mining of upper and lower layers of ore, ultimately increasing the mining efficiency of phosphorus mines and extending the service life of the mine.
(2) The selection of the filling station site for Kunyang Phosphate Mine No. 2 not only follows basic standards, but also meets the current filling requirements for the eastern part and the filling requirements for the western ore body. The filling slurry prepared by the filling station can be directly transported to various mining sites through the filling boreholes in the station, and then flows to various underground mining sites through the filling boreholes, achieving the "self flow" transportation of the filling slurry.
(3) Based on the designed production scale of 2 million tons/a, the annual volume of the filling area required for the filling station, the annual consumption of all tailings cemented filling slurry volume, the daily average filling volume, the daily maximum filling volume, the hourly preparation capacity of the filling station slurry, as well as the calculation of the diameter of the gravity conveying pipeline and the theoretical thickness of the pipeline, were calculated through theoretical values. This provides technical and theoretical support and equipment selection for mine filling experiments. This paper focuses on Kunyang Phosphate Mine No. 2, under Yunnan Phosphate Chemical Group, and studies the filling mining technology after underground mining. The relevant research results are significant in guiding the underground mining and construction of difficult-to-mine phosphorous ore bodies in the Yunnan Dianchi region.

Data availability statement

The original contributions presented in the study are included in the article/Supplementary Material, further inquiries can be directed to the corresponding authors.

Author contributions

DH: Conceptualization, Writing–original draft. MX: Validation, Writing–original draft, Writing–review and editing. XL: Investigation, Validation, Writing–review and editing. JW: Visualization, Validation, Writing–original draft. MW: Writing–original draft, Validation. SL: Validation, Writing–original draft.

Funding

The research work was funded by the Research Fund of National Natural Science Foundation of China (NSFC) (Grant No.42277154), the project of Slope safety control and disaster prevention technology innovation team of "Youth Innovation Talent Introduction and Education Plan" of Shandong Colleges and universities (Grant No. Lu Jiao Ke Han [2021] No. 51); Guizhou Province Science and Technology Planning Project (Grant No. Guizhou science and technology cooperation support [2022] common 229), National Natural Science Foundation of Shandong Province of China (NSFC) (Grant No. ZR2022ME188), Jinan City "new university 20" research leader studio project (Grant No. 20228108), The State Key Laboratory of Coal Resources and safe Mining, CUMT (SKLCRSM22KF009), and Open Fund of National Engineering and Technology Research Center for Development and Utilization of Phosphate Resources of China (Grant No. funded the research work NECP 2022-04) and the Open Fund of Key Laboratory of Geological Hazards on Three Gorges Reservoir Area (China Three Gorges University), Ministry of Education (Grant No. 2022KDZ07).

Conflict of interest

Authors MX, MW, and SL were employed by Yunnan Phosphating Group Co., LTD.

The remaining authors declare that the research was conducted in the absence of any commercial or financial relationships that could be construed as a potential conflict of interest.

Publisher's note

References

Bai, Y., Zhou, Y. B., and Cui, Y. (2023). Etc Research on the upward horizontal slicing and filling mining method for steep inclined thin ore bodies outside the vein. *Min. Res. Dev.* 43 (05), 1–6. doi:10.13827/j.cnki.kyyk

Bin, T. (2016). Application of pseudo-inclined arrangement in gently inclined thin ore body in mining method. *Eng. Constr.* 48 (03), 33–36+78. doi:10.13402/j.gcjs

Cui, Na., and Qi, J. J. (2023). Research trends and prospects of green mining in China. *Resour. Inf. Eng.* 38 (01), 60–64. doi:10.19534/j.cnki.zyxxygc

Deng, G. L., Zheng, B. K., and Li, X. D. (2023). Research on filling mining technology in qianhe gold mine. *Min. Technol.* 23 (04), 196–198. doi:10.13828/j.cnki.ckjs

Erdenv, (2022). Mining technology and safety of open-pit mining. *Inn. Mong. Coal Econ.* 357 (16), 115–117. doi:10.13487/j.cnki.imce

Gong, X. L. (2022). Main problems and countermeasures of deep mining in underground mining. *China Met. Bull.* 1064 (03), 16–18.

Hao, Y. J., Wang, C. L., Jiang, M. W., et al. (2023). Optimization of upward drift filling mining method and ground pressure control for gently inclined medium thick ore bodies. *Non Ferr. Met. Eng.* 13 (05), 114–121.

Huang, J., Li, S. J., Xia, G. Y., Wang, M. L., Zhang, B., and Liu, Y. H. (2022). Study underground mining method of gently inclined medium and thick ore body of Kunyang phosphate ore No. 2 ore. *Mod. Min.* 38 (07), 45–50+55.

Jiang, A. M., Dong, Y. C., Jiang, X. L., Xiong, Q. W., and Wang, F. F. (2022). Numerical simulation study on slope collapse caused by open-pit to underground mining. *Min. Metallurgical Eng.* 42 (03), 14–17.

Jin, J. R., Zhang, F. G., Tang, M. W., Yang, Z. B., Zheng, Z., Tang, T., et al. (2017). Experimental study and application of mechanized pseudo-tilted slitting mining method for disk area. *Gold* 38 (07), 33–39.

Lao, Y. X., Deng, G. L., Zheng, B. K., and Zhang, L. Y. (2022). Application of upward layered full tailings cementation filling mining method in cold-water copper nickel ore. *Min. Technol.* 22 (06), 161–162+165. doi:10.13828/j.cnki.ckjs

Li, G. Z. (2022). Progress and the prospect of exploration of underground mining technology in metal mines. *World Nonferrous Met.* 609 (21), 169–171. doi:10.19614/j.cnki.jsks

Li, Q. H., Song, D. Q., Yuan, C. M., and Nie, W. (2022). An image recognition method for the deformation area of open-pit rock slopes under variable rainfall. *Measurement* 188, 110544. doi:10.1016/j.measurement.2021.110544

Li, X. S., Li, Q. H., Wang, Y. M., Liu, W., Hou, D., Zheng, W. B., et al. (2023). Experimental study on instability mechanism and critical intensity of rainfall of high-steep rock slopes under unsaturated conditions. *Int. J. Min. Sci. Technol.* doi:10.1016/j.ijmst.2023.07.009

Li, X., Wang, Y. M., Zhao, K., and Yang, S. (2019). Research progress on key issues of open-pit to underground mining of metal mines. *Metal. Mine* (12), 12–20. doi:10.2478/AMNS

Li, X. S., Wang, Y. M., Yang, S., Xiong, J., and Zhao, K. (2021). Research progress in the mining technology of the slowly inclined, thin to medium-thick phosphate rock transition from open-pit to underground mine. *Appl. Math. Nonlinear Sci.* 6 (1), 319–334. doi:10.2478/amns.2021.2.00017

Liu, Y. H. (2022). Prediction of water inflow in underground mining pit of Kunyang phosphate ore No. 2 mine. *Chem. Mineral Geol.* 44 (01), 78–85.

Peng, J. (2022). Multi-objective optimization of stope structural parameters by upward horizontal layered filling method. *Mod. Min.* 38 (08), 68–72.

Qu, L. P., and Wang, Y. Q. (2021). The application of upward horizontal slicing and filling mining method in steeply inclined and fractured thin ore bodies. *Min. Res. Dev.* 41 (12), 1–4. doi:10.13827/j.cnki.kyyk

Ren, Q. (2021a). Application and related problems of fill-fill mining technology in mining. *Inn. Mong. Coal Econ.* 327 (10), 10–12.

Ren, Y. D. (2021b). Application of upward horizontal layered step-and-step fill mining method in Honghuagou gold mine. *Gold* 42 (10), 49–53+58.

Shen, D. Y., and Ning, G. J. (2022). Hydrogeological characteristics of Kunyang phosphate ore No. 2 ore and water prevention and control of inclined shaft engineering. *China Min. Eng.* 51 (01), 86–89. doi:10.19607/j.cnki.cn11-5068/tf

Wang, B. (2023). Analysis of the status quo and countermeasures of mine ecological restoration. *Surf. Min. Technol.* 38 (01), 125–128. doi:10.13235/j.cnki.ltcm

Wang, X. (2020). Application of upward horizontal layered approach filling method in Xiajiadian gold mine. *Mod. Min.* 36 (06), 83–86.

Wang, X. R., Zhao, B. S., Liang, J. L., and Gong, Y. C. (2022). Study the optimization of mining method by refilling and filling a copper mine. *Min. Technol.* 22 (06), 158–160. doi:10.13828/j.cnki.ckjs

Wei, G. D., Zhen, D. S., and Liu, Z. Y. (2022). Discussion on mining technology and safety of open-pit mining. *Inn. Mong. Coal Econ.* 345 (04), 97–99. doi:10.13487/j.cnki.imce

Wu, H. J., and Wang, L. (2023). Analysis of key points of green mine construction. *Min. Technol.* 23 (01), 202–204. doi:10.13828/j.cnki.ckjs

Xu, A. H. (2022). Analysis and study of upward horizontal approach filling method. *World Nonferrous Met.* 612 (24), 190–192.

Yan, H. F. (2023). Discussion on the application of strip paste filling mining technology in mining engineering. *Contemp. Chem. Res.* (14), 92–94. doi:10.20087/j.cnki.1672-8114

Zeng, J. L., Zhou, Y., and Gao, X. (2022a). Etc Stability analysis of the stope using pseudo inclined segmented strip filling mining method. *Min. Technol.* 22 (04), 107–111. doi:10.13828/j.cnki.ckjs

Zeng, J. L., Zhou, Y., Gao, X., He, B. L., Guo, H. Q., Liu, Q., et al. (2022b). Stability analysis of stope by pseudo-inclined segmented strip filling mining method. *Min. Technol.* 22 (04), 107–111. doi:10.13828/j.cnki.ckjs

Zeng, L. Y. (2023). Optimization of low-grade inclined medium-thick ore body filling mining method. *Gold* 44 (02), 22–26.

Zhang, R. D., Li, J., and Zhu, C. D. (2021). Panel staggered upward horizontal slicing and filling mining method. *Min. Technol.* 21 (02), 18–21. doi:10.13828/j.cnki.ckjs

Zhang, R. X., Wang, Q. Y., Wang, M. L., Wang, H. L., and Huang, J. (2022). Experimental study on cementation filling of phosphate ore flotation ultrafine whole tailings. *Min. Res. Dev.* 42 (09), 39–43. doi:10.13827/j.cnki.kyyk

Zhang, Y. J. (2014). Application and development of fill-and-fill mining method in mining process. *Heilongjiang Sci. Technol. Inf.* (19), 4.

Zhu, F., Liu, X. S., and Zhang, M. (2020). Experimental study on cementation filling of tailings in a lead-zinc mine in Gansu Province. *China Min. J.* 29 (S1), 502–505.

Zhu, X., Peng, L., Yin, X. Y., Wang, Z. W., Yao, W., and Yang, X. (2022). Experimental study and engineering application of total tailings cementation filling of Huangshaping polymetallic ore. *Min. Res. Dev.* 42 (08), 83–86. doi:10.13827/j.cnki.kyyk

frontiers | Frontiers in Earth Science

TYPE Original Research
PUBLISHED 27 December 2023
DOI 10.3389/feart.2023.1285766

OPEN ACCESS

EDITED BY
Chong Xu,
Ministry of Emergency Management, China

REVIEWED BY
Sangdan Kim,
Pukyong National University, Republic of Korea
Huiran Gao,
Ministry of Emergency Management, China

*CORRESPONDENCE
Sheng Ye,
0015927@zju.edu.cn

RECEIVED 30 August 2023
ACCEPTED 03 November 2023
PUBLISHED 27 December 2023

CITATION
Yu T, Ran Q, Pan H, Li J, Pan J and Ye S (2023), The impacts of rainfall and soil moisture to flood hazards in a humid mountainous catchment: a modeling investigation.
Front. Earth Sci. 11:1285766.
doi: 10.3389/feart.2023.1285766

The impacts of rainfall and soil moisture to flood hazards in a humid mountainous catchment: a modeling investigation

Tianxue Yu[1], Qihua Ran[2], Hailong Pan[1], Jiyu Li[1], Jiajia Pan[3] and Sheng Ye[1]*

[1]Institute of Water Science and Engineering, College of Civil Engineering and Architecture, Zhejiang University, Hangzhou, China, [2]Key Laboratory of Hydrologic-Cycle and Hydrodynamic-System of Ministry of Water Resources, Hohai University, Nanjing, China, [3]Zhejiang Design Institute of Water Conservancy and Hydroelectric Power Co., LTD., Hangzhou, China

Floods pose a significant threat to the safety of countries with severe societal, economic, and environmental consequences, especially the flash floods in mountainous regions. Previous studies have shown that many floods were caused by intense rainfall with highly saturated soil. In this study, we applied a physically-based distributed hydrological model (Integrated Hydrology Model, InHM) to a warm humid mountainous catchment in Southwest China, the Shouxi River. The main objective of our research is to investigate the relative importance of rainfall and antecedent soil moisture on flood generation in our study region. Our results show that an increase in rainfall return period and antecedent soil saturation ratio significantly increased peak flow and shortened peak time. There is a correlation between the ratio of antecedent soil saturation ratio to rainfall (SPR) and peak flow. When SPR <1, there is a positive correlation; when SPR >1, there is a negative correlation. Additionally, with the increase in drainage area, the relative importance of rainfall tends to decrease, while the relative contribution of soil saturation ratio tends to increase. The findings could provide support for the determination of the dominant factors influencing runoff generation in humid regions, offering scientific support for the timely and effective flood prevention and mitigation measures in mountainous regions.

KEYWORDS

flood generation, scale effect, antecedent soil saturation ratio, rainfall, mountainous catchment

1 Introduction

Floods are usually caused by sudden rainstorms or massive snowmelt and are one of the most common natural disasters in the world (Zhong et al., 2021). As the issue of climate change intensifies, flood risks have increased significantly in recent years, posing serious threats to public safety and property. This ultimately results in severe economic and social disruptions to countries (Soo et al., 2019). In mountainous catchments of a few hundred square kilometers or less, flash floods with short response time and heavy rain is tended to be aggravated due to natural and anthropogenic activities (Zhai et al., 2018). In China, the mortality caused by flash flood reached 4540, occupying 80% of that caused by floods from 2010 to 2014 (http://www.mwr.gov.cn/zzsc/tjgb/zgshzhgb/2014/mobile/index.html), according to the bulletin of flood and drought disaster in China of 2014. Flash flood,

along with water-induced hazards, geological and hydrological conditions, have become a global issue, particularly in the mountainous regions of southwest China (Gan et al., 2018).

Generally, the causes of floods are complex and include both anthropic and natural factor, such as climate change and landscape change. Climate change is highly likely to alter flood hazards (Arnell and Gosling, 2016). As the climate warms, occurrence of extreme rainfall events is likely to increase (Min et al., 2011), elevating the flood risk (Milly et al., 2002; Pall et al., 2011). Numerous studies have shown that extreme precipitation has intensified across continents, and extreme precipitation is a major cause of catastrophic flooding (Guha-Sapir et al., 2013; Guha-Sapir et al., 2014). Bertola *et al.* (2021) suggested that in northwestern Europe, extreme rainfall contributed significantly to positive changes in floods, with an increase of 2.8%–3.3% in flood frequency per decade of return period. However, some studies have also shown that the trend of increasing extreme precipitation does not directly translate into positive trends in large catchments (Madsen et al., 2014; Sharma et al., 2018). This suggests that there are other factors that modulate the flood response, such as antecedent soil moisture.

It has been observed that flood variability can poorly explained by rainfall characteristics alone (Berghuijs et al., 2016), and one of the most likely culprits is the antecedent soil moisture of the catchment (Pathiraja et al., 2012). Landscape change has a strong impact on floods because of the severe human alteration of the natural landscape. Deforestation can increase or decrease antecedent soil moisture and trigger erosion (Rogger et al., 2017). Event runoff coefficients tend to be higher when antecedent soil moisture reaches a high level, increasing flood peak in dry catchments (Borga et al., 2007; Vivoni et al., 2007). Grillakis *et al.* (2016) used the Kampus model to estimate the sensitivity of flood discharge to antecedent soil moisture and found that small-event floods show greater sensitivity to antecedent soil moisture than large-event magnitude. Sriwongsitanon and Taescombat (2011) found that for small events, the hydrological response in forest area was lower in the non-forested by comparing forested and non-forested areas. However, for large events, the hydrological response in forest area was greater.

Therefore, understanding the relative importance of rainfall and antecedent soil saturation ratio and their impacts on a range of catchment scales and event magnitudes plays an important role in flood forecasting. Pathiraja et al. (2012) used a continuous rainfall runoff model to calibrate 45 catchments in the Murray-Darling Basin, and found that correctly simulating antecedent soil moisture can greatly improve simulation accuracy. Flood frequency curve was steeper than rainfall frequency curve in dry catchments (Breinl et al., 2021). Antecedent soil moisture was also found with a significant effect on rainfall thresholds for flash flood warning (Zhai et al., 2018). Wasko and Nathan (2019) identified a tipping point in rainfall: beyond which watershed rainfall dominated flood response and below this point, flood discharge decreased as the soil moisture reduced. Although there are many researches about the joint role of rainfall and antecedent soil moisture, few of them focus on the relative contribution of rainfall and antecedent soil saturation ratio.

The formation mechanisms of floods are different on different scales (Blöschl, 2022). It is necessary to study the scale effects on flood generation. In large catchments (>1000 km^2), flood discharge is more influenced by antecedent soil moisture, whereas in smaller catchments (<1000 km^2), flood discharge is more likely to be caused by precipitation (Wasko and Sharma, 2017). Furthermore, Nikolopoulos et al. (2011) studied on three watershed (24, 165, and 329 km^2) and also found that flood responses were more sensitive to antecedent soil moisture for increasing catchment scale. Many studies have identified the importance of rainfall and antecedent soil moisture, yet not much specifically focused on the quantitative evaluation of the relative contribution of rainfall and antecedent soil moisture, and their variation with spatial scales, especially in humid China where floods have been one of the major natural hazards for centuries.

Here we conducted numerical analysis in a humid mountainous catchment in Southwest China (Shouxi River), the goals of this study are to: (1) examine the impact of rainfall and antecedent soil saturation ratio on runoff generation, and the potential mechanisms that cause these effects; (2) investigate the relative importance of rainfall and soil saturation ratio in different catchment scales; (3) explore scale effects on rainfall and soil saturation ratio.

2 Material and methods

2.1 Study area

The Shouxi River catchment (SXRC), located in the southwest mountainous area of China (103°02′-103°27′ E, 30°47′-31°02′ N) (Figure 1A), is a small tributary of the Minjiang River. SXRC is situated at the transitional zone between the Sichuan Basin and the Qinghai-Tibet Plateau. The elevation gradually decreases from southwest to northeast, ranging from approximately 5000 m in the Qinghai-Tibet Plateau to 900 m in the Sichuan Basin. The catchment covers an area of approximately 560 km^2 and presents a fan-shaped topography. The climate of the SXRC is subtropical humid climate, with significant vertical temperature differences. The average slope in the catchment is 32.5°, and the annual mean temperature is 15.2°C (Liu, 2022). Average annual precipitation is about 1134 mm, with most of it occurring between June and September (Liu et al., 2021). The geological structure of the catchment is complex, with developed folds and faults. The upstream valley has a “V" shape, while the middle and downstream valleys are slightly broader with a “U" shape. Some sections of the river have developed joints and fissures, with strong tectonic erosion and river cutting activities (Yuan et al., 2022).

The floods in the SXRC are mainly caused by heavy rainfall. Correspondingly, the flood season in the study area is from June to September. The annual maximum floods are particularly concentrated between July and August. The slopes within the river basin are steep, leading to rapid rise and fall of floods (Yin et al., 2022). For example, Wenchuan County experienced severe torrential rain in 20 August 2019, with the maximum cumulative rainfall reaching 65 mm within 1 hour. The discharge in Shouxi River reached 1840 m^3/s within 3 h. The whole flood event lasted for 5 days, causing large-scale flooding and geological disasters, and significant personnel and property losses (Yang et al., 2022). In addition, the SXRC is located near the epicenter of the 2008 Mw=7.8 Wenchuan earthquake. After the earthquake, there

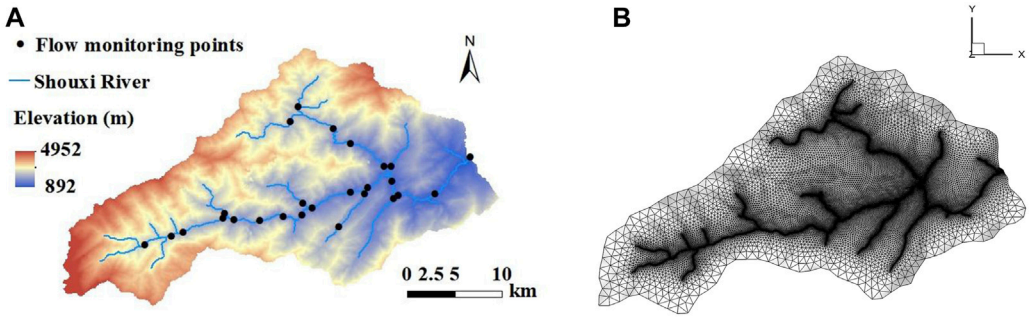

FIGURE 1
(A) Location of the study area; **(B)** the configuration of the numerical mesh used in this study.

are frequent occurrences of landslides, mudslides and other geological disasters, with serious damage to vegetation and loose sediments. As a result, the likelihood of mountain floods and debris flows increased.

2.2 Model structure

This study uses the physically-based distributed hydrological model InHM (Integrated Hydrology Model), which is originally developed by Vanderkwaak of Waterloo University (1999). InHM simulates water and solute in three-dimensional dual continua subsurface as well as two-dimensional surface and river flow.

The 3D variably saturated fluid motion and macroporous fluid motion in subsurface pore media are described by Richard's equation, which degenerates to Darcy's formula in the saturated state:

$$f^{v}\frac{\partial \varphi S_{w}}{\partial t} = \nabla \cdot f^{a}\vec{q} \pm q^{e} \pm q^{b} \tag{1}$$

Where $\vec{q}$ (m/s) is Darcy flux, q^{e} (s^{-1}) is the water rate between surface and subsurface soil, q^{b} (s^{-1}) is the input/output terms on the boundary, f^{v} (-) and f^{a} (-) are volume and area fraction associated with each continuum respectively, φ (-) is soil porosity, S_{w} (-) is water saturation, t (s) is time. The Darcy flux is given by:

$$\vec{q} = -k_{rw}\frac{\rho_{w}g}{\mu_{w}}\vec{k}\nabla(\psi + Z) \tag{2}$$

Where k_{rw} (-) is relative permeability, μ_{w} (kg/(m·s)) is viscosity of water, $\vec{k}$ (-) is intrinsic permeability vector, ψ (m)is pressure head , Z (m) is elevation head. The surface water flow motion (both open channel flow and slope flow) in InHM is described using the diffusive wave approximation of the two-dimensional shallow water equation. The surface water flow motion equation is defined as:

$$\frac{\partial\left(S_{w_s}h_s + \psi_s^{store}\right)}{\partial t} = \nabla \cdot \psi_s^{mobile}\vec{q}_s \pm a_s q^{b} \pm a_s q^{e} \tag{3}$$

Where S_{w_s} (-) is surface saturation, h_s (m) is the average height of surface microtopography, ψ_s^{store} (-) is stored surface water depth, ψ_s^{mobile} (-) is mobile surface water depth, $\vec{q}_s$ (m/s) is surface water velocity, a_s (m) is surface coupling length scale, and the surface water velocity in Eq. 3 can be given by:

$$\vec{q}_s = -\frac{\left(\psi_s^{mobile}\right)^{2/3}}{n\Phi^{1/2}}\nabla(\psi_s + z) \tag{4}$$

Where n ($s \cdot m^{-1/3}$) is the Manning's surface roughness tensor, Φ (-) is the energy slope.

InHM uses the Finite Volume Element (FVE) method to discretize the control equations and employs the Newton iteration method to solve the nonlinear equations in an implicit manner. More details about the governing equations can be found in VanderKwaak (1999) and Loague and VanderKwaak (2002). The model can provide hydrological information at any time and location within the entire drainage area (i.e., soil moisture, soil saturation ratio, water depth, cross-sectional runoff process line) or the dynamic changes in hydrological information during the operation of any node, making it suitable for this theoretical analysis (Su, 2012). It has been applied to different catchments and terraces, validated for runoff generation (Ran et al., 2019a; Ran et al., 2019b; Ran et al., 2020), as well as sediment movement simulation (Ran et al., 2012; Ran et al., 2018). It has also been applied to nearby watershed of similar characteristics, and proved its suitability on the study region (Liu et al., 2021).

2.3 Mesh configuration

The 2D surface mesh for the SXRC is shown in Figure 1B, and the 3D mesh was constructed by adding layers. Given that soil moisture fluctuates more strongly in the surface layer and most of the water eventually converges in the river channel, the resolution of the mesh was set to increase from the boundary to the river channel and from upper soil layers to lower soil layers. The mesh boundary resolution, channel resolution, and exit resolution of the SXRC are about 1000 m, 50 m, and 20 m, respectively. The vertical profile was generally divided into the surface layer (0–1 m), the middle layer (1–3 m), and the deep layer (3–13 m) with the nodal spacing of 0.2 m, 0.5 m and 2.5 m.

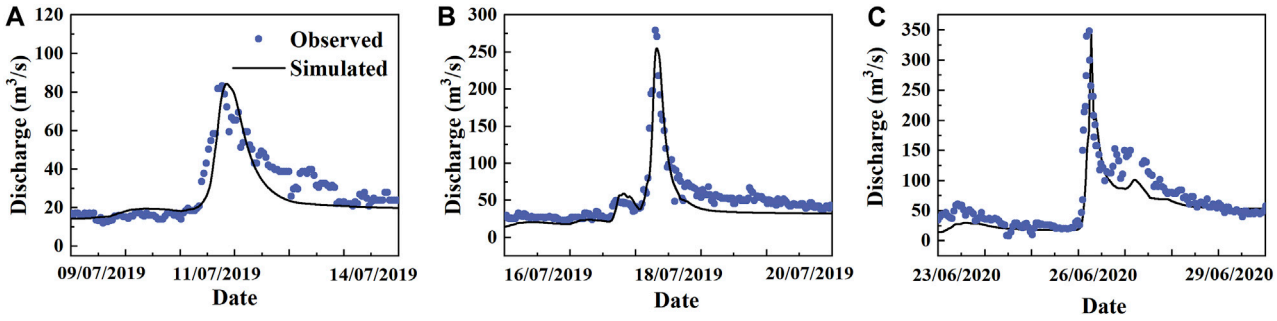

FIGURE 2
Comparison between observed and simulated discharge during the **(A)** calibrated event (July 9—14 July 2019) and two validated events **(B)** July 16—20, 2019), and **(C)** June 23–29, 2020. The black line represents the simulated hydrograph, and the blue points represent observed discharge.

2.4 Model set up

The objective of this study is to investigate how antecedent soil saturation ratio and rainfall return period affect runoff generation in humid mountainous catchment. The DEM data used in the study was from the Geospatial Data Cloud (https://www.gscloud.cn/sources/accessdata/310?pid=302), with a spatial resolution of 30 m. The rainfall and runoff data used for model calibration and validation were obtained from the measured hourly rainfall and runoff in the SXRC. Rainfall data was obtained from hourly measurements between 4 June 2019 and 5 August 2020. Runoff data was obtained from hourly measurements at the outlet of the catchment during the main flood season (June to September) in both 2019 and 2020. Since our study focused on event scale research, three relatively large events with complete rainfall and runoff data were selected for calibration and validation. The model was calibrated with event during July 9–14, 2019; while events from July 16–20, 2019 and June 23–29, 2020 were used for validation.

Figure 2 illustrates the comparison between the observed and simulated hydrograph used for model calibration and validation. As we can see from Figure 2, the model captured the flow event relatively well during both calibration and validation periods, especially during the high flow period, which is the focus of this study. The criterion used to measure model performance was Nash coefficient (NS) (Nash and Sutcliffe, 1970) and R^2. During the calibration period, the NS and R^2 values reached 0.65 and 0.76, respectively. During the validation period, the NS and R^2 values averaged 0.715 and 0.83, respectively. Given the goal of this study, we think the simulation results were acceptable for our theoretical analyses of the large flow events in this study.

2.5 Scenarios

To fully understand the influence of runoff generation in mountainous catchment, a series of scenarios were designed with varying return periods and antecedent soil saturation ratio. According to the Flood Manual in Small and Medium-sized Watersheds of Sichuan Province (Department of Water Resources of Sichuan Province, 1984), we applied 6 rainfall return periods ranging from 5 years to 1000 years (5, 10, 50, 100, 500, 1000 years), lasting for 6 hours with constant rainfall intensity. In addition, to examine the effects of antecedent soil moisture, the saturation ratio level was set at 40%, 50%, 60%, 70%, 80%, and 90%. Totally, there were 36 scenarios (i.e., 6 rainfall return periods × 6 antecedent soil saturation ratio) in this study.

Given the impact of scale effects, 27 flow monitoring points were set up in different sections of the SXRC. The drainage areas ranged from a few square kilometers to several hundred square kilometers, covering small catchments to large catchments. The mean topographic gradient varied from 29° to 37°, with a major concentration in the 33°–35° range. Results from these observation points were used to investigate the synergetic effects on runoff generation for different rainfall, antecedent soil saturation ratio and catchment scales.

We explored the relationship between rainfall return period and antecedent soil saturation ratio to peak flow under 36 scenarios (6 rainfall return periods × 6 antecedent soil saturation ratio) (Section 3.1). To investigate the scale effects (Section 3.2), we calculated the relationship between rainfall return period, antecedent soil saturation ratio and drainage area at 27 flow monitoring spots across the catchment, using 50% saturation ratio and 100-year-event rainfall return period as reference. To further explore the relative contribution of rainfall and antecedent soil saturation ratio (Section 3.3), we combined all drainage areas, rainfall return periods, and soil saturation ratio for investigation, that is, a total of 972 relationships (6 rainfall return periods × 6 antecedent soil saturation ratio × 27 drainage areas).

2.6 Quantification the relative contribution of soil saturation ratio and rainfall

To measure the effects of rainfall and soil saturation ratio on flood generation, we introduced the ratio of saturation ratio to event rainfall (SPR). We expressed the relative saturation of soil moisture by normalizing the antecedent soil saturation ratio (S′) with the maximum and the relative intensity of rainfall by normalizing the event rainfall (P′) with the maximum. The impact of soil moisture and rainfall is expressed through the ratio of these two normalizations, i.e., SPR = S'/P'.

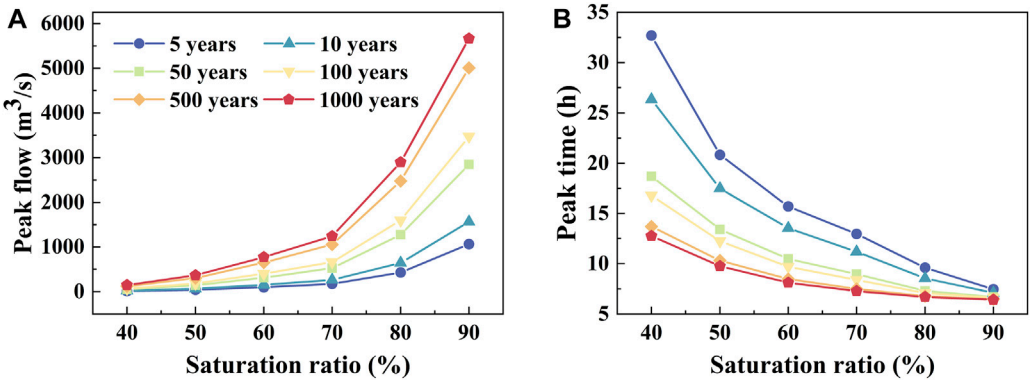

FIGURE 3
The **(A)** peak flow and **(B)** peak time at different antecedent soil saturation ratio and rainfall return periods. The color represents the rainfall return period.

To investigate the impacts of rainfall and antecedent soil saturation ratio for peak flow discharge, relative importance was defined as the proportional contribution to the determination coefficient (R^2) of the regression between peak flow and rainfall and soil saturation ratio. The method proposed by Lindeman, Merenda and Gold (LMG) (Sen et al., 1981) in the R package "reliaimpo" was used. This metric decomposes R^2 into non-negative contributions, summing up the total R^2, considering the unique contribution of the variable itself and the increased contribution when combined with other variables (Johnson and Lebreton, 2004). It is based on sequential R^2, which handles dependencies on ranking by taking an unweighted average over the rankings (Grömping, 2006). The R^2 of a model with regression in set S is:

$$R^2(S) = \frac{Model\ SS}{Total\ SS} \tag{5}$$

Where *Model SS* is the regression sum of squares that includes the regressors, *Total SS* is the total sum of squares. The order of regression variables is denoted by the permutation of regressors $x_1, \ldots, x_p$, with subscripts $r = (r_1, \ldots, r_p)$ in the form of a tuple. $S_k(r)$ represents the set of regression variables that enter the model at order r before x_k. The portion of R^2 assigned to x_k can be expressed as:

$$seqR^2(\{x_k\}|S_k(r)) = R^2(\{x_k\} \cup S_k(r)) - R^2(S_k(r)) \tag{6}$$

The metric LMG can be written as:

$$LMG(x_k) = \frac{1}{p!} \sum_{r\ permutation} seqR^2(\{x_k\}|r) \tag{7}$$

3 Results

3.1 Floods response to rainfall and antecedent soil saturation ratio

Figure 3A presents the peak flow under different antecedent soil saturation ratio and return period. As we can see, the peak flow under all six return periods increased with soil saturation ratio. The peak flow with high soil saturation ratio was much greater than the scenario with low saturation ratio. The increment in peak flow was gradual when the antecedent saturation ratio was low (40%–60%), and increased rapidly when the antecedent saturation ratio was higher (70%–90%). The change with antecedent saturation ratio was more significant in the 1000 years return periods. Although larger rainfall leads to larger peak flow, the variability of peak flow with different rainfall return periods was minimal at 40% soil saturation ratio. The peak flow increased with rainfall return period, and reached its highest point at 90% soil saturation ratio: the difference in peak flow between 5-year-event and 1000-year-event was 4100 m^3/s. This is due to the fact that when the antecedent soil saturation is low, soil water storage consumes the majority of the rainfall, with only a small portion of it actually generates runoff. It is evident from Supplementary Figure S1 that the peak flow increased with return period rapidly first and the increment slowed down afterwards.

Figure 3B illustrates the variation of peak time with antecedent soil saturation ratio and rainfall return period. As we can see, the peak time declined with antecedent soil saturation ratio and return period. Simultaneously, the peak time tended to stabilize, especially when the return period was large (100–1000 years). In contrast to the peak flow, which was more sensitive to large rainfall and higher saturation ratio, peak time was more sensitive at small return period and low antecedent soil saturation ratio. For 5-year-event and 1000-year-event, a half rise in soil saturation led to 4/5 and 1/2 decrease in peak time, respectively; while for the 40% and 90% soil saturation ratio scenario, peak time decreased by 0.6 and 0.15 as the return period raised from 5 years to 1000 years. Antecedent soil saturation ratio and rainfall return period affect runoff generation together. As shown in Figure 4A the peak flow was small regardless of the rainfall amount when the soil was relatively dry. When the soil saturation ratio exceeded 70%, even small return period could result in large peak flow. With the increase of rainfall return period, the impact of soil saturation ratio on peak flow gradually increased. The peak time was very large (up to 32 h) with low soil saturation ratio and small rainfall return period (Figure 4B), which may be due to the fact that the soil is not fully saturated at this time.

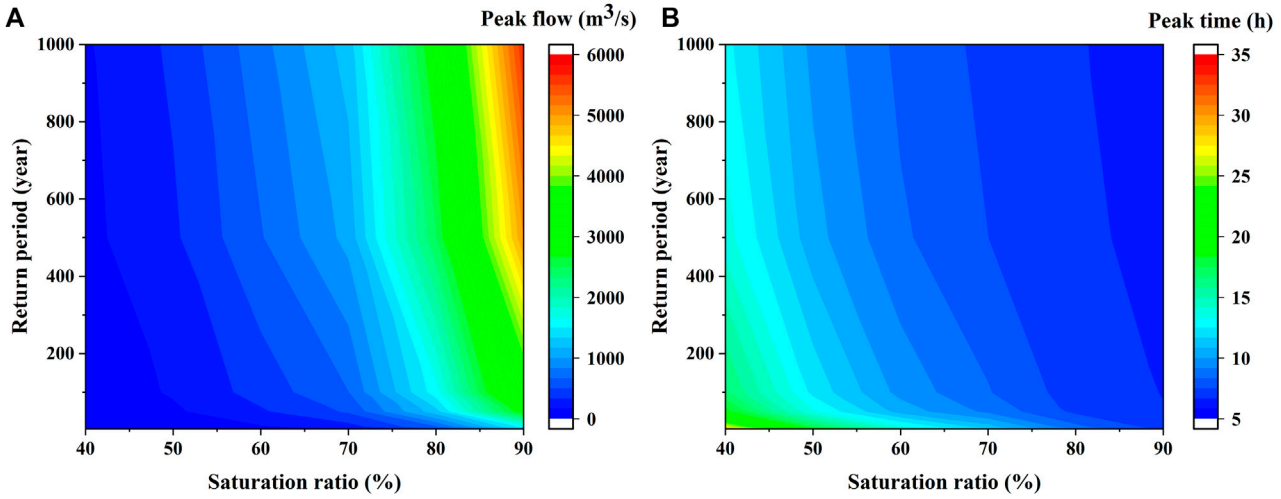

FIGURE 4
Contour map of antecedent soil saturation ratio and rainfall return period. **(A)** peak flow, **(B)** peak time.

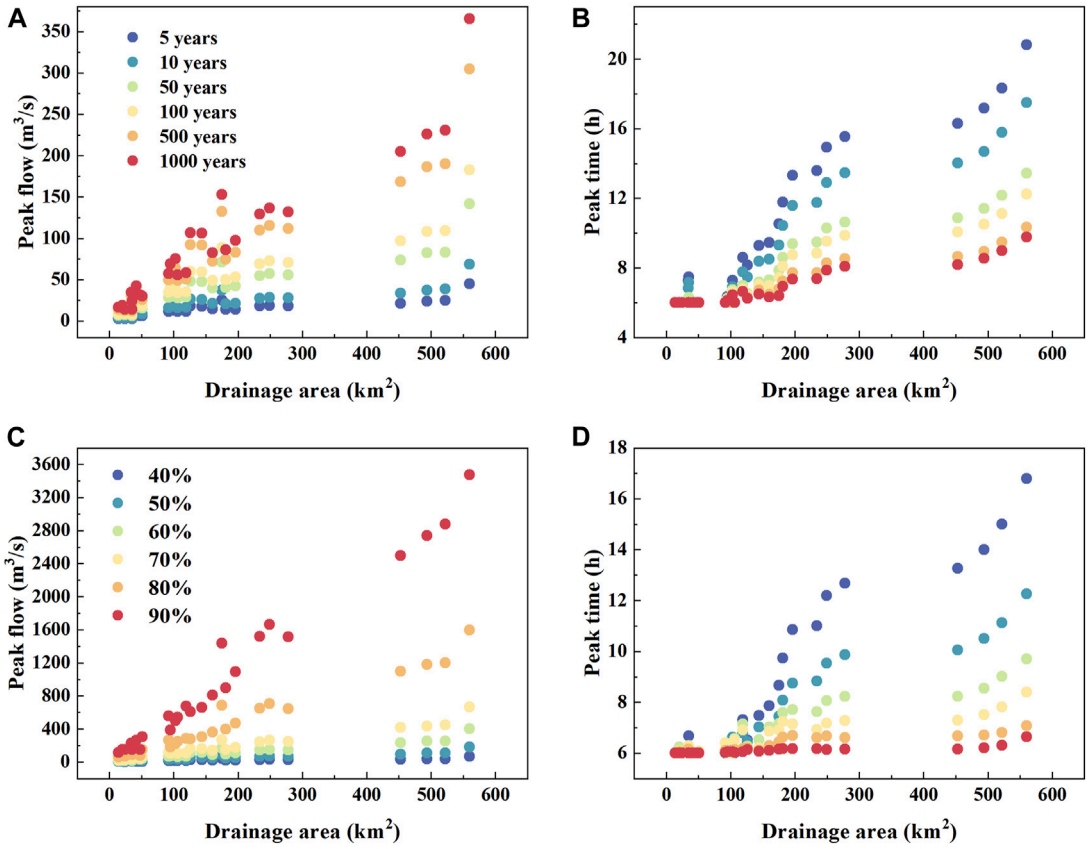

FIGURE 5
Scatter plots between peak flow and drainage area under different **(A)** rainfall return period, and **(C)** antecedent soil saturation ratio; and scatter plots between peak time and drainage area under different **(B)** rainfall return period and **(D)** antecedent soil saturation ratio.

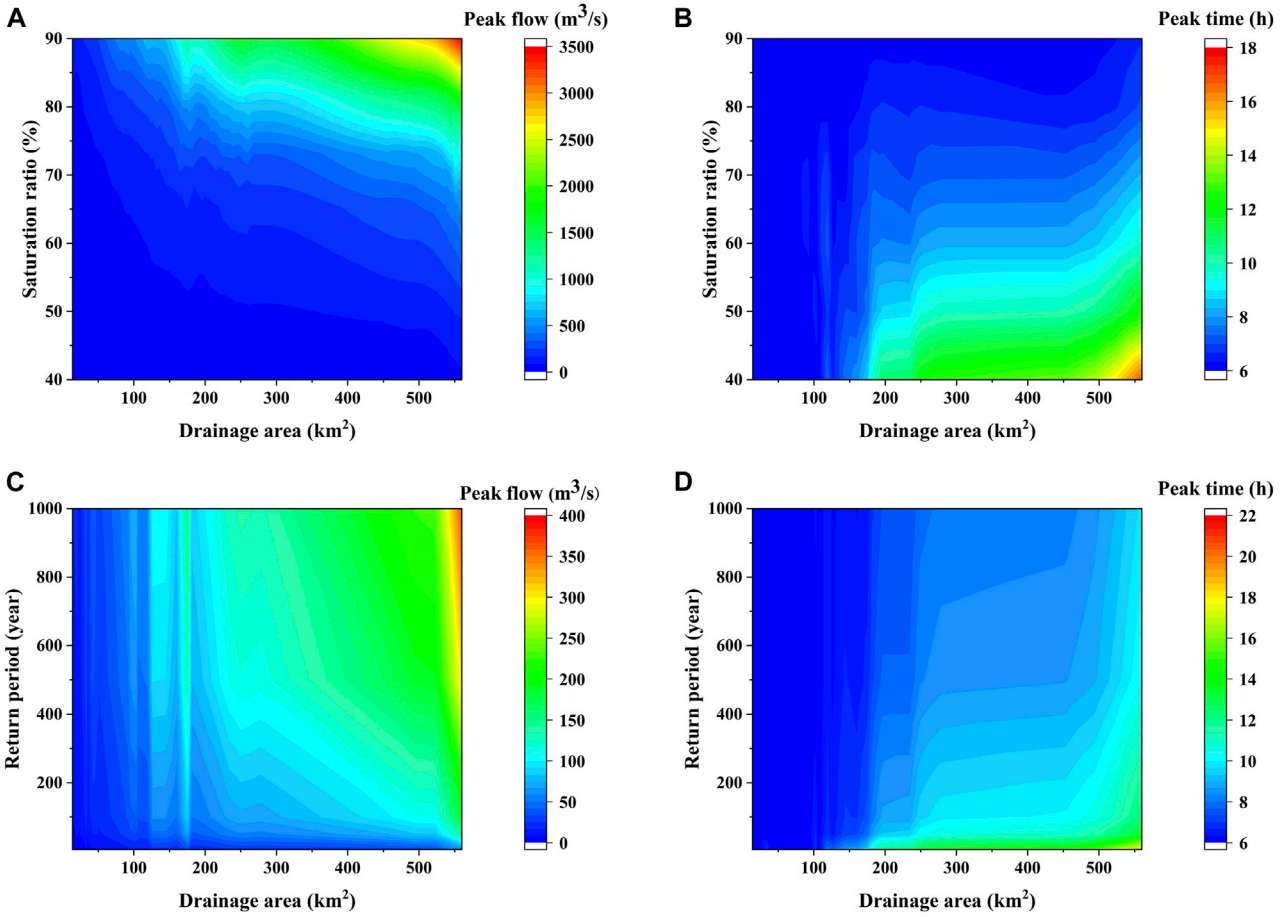

FIGURE 6
The scale effects of runoff on antecedent soil saturation ratio and rainfall return period. **(A)** Scale effect of peak flow on antecedent soil saturation ratio at 100-year-event; **(B)** scale effect of peak time on antecedent soil saturation ratio at 100-year-event; **(C)** scale effect of peak flow on return period at 50% soil saturation ratio; **(D)** scale effect of peak time on return period at 50% soil saturation ratio.

3.2 Scale effects on runoff generation

Scale effect has been identified in flood generation (Blöschl, 2022). Here we explored how the impacts of antecedent saturation ratio and rainfall magnitudes vary with scales by taking 50% antecedent soil saturation ratio and 100-year rainfall return period as base case. Figure 5 presents the peak flow and peak time under different rainfall return periods and antecedent soil saturation ratio with various drainage area. We can see that the peak flow and peak time were positively correlated with the drainage area, but there was great variation for small and medium catchments (100—300 km^2) (Figure 5A). The reason for this was that small and medium catchments were located at various tributaries and influenced by local topography (e.g., slopes), whereas large catchments (the last four points) were at the main steam of the catchment. The scale effect of peak flow was more significant under higher rainfall return period and antecedent soil saturation ratio. In contrast, with the increase of return period and antecedent soil saturation ratio, the variation in peak time gradually decreased with the change of drainage area.

To further clarify the effects of antecedent soil saturation ratio, rainfall return period and drainage area on runoff generation, we have plotted contour maps depicting these variables (Figure 6). From Figure 6A, it can be seen that peak flow increased with drainage area and antecedent soil saturation ratio, though the increase rate was not consistent. As soil saturation ratio exceeded 70%, there was significant variation in peak flow with changes in drainage area. On the contrary, noticeable changes were found in peak flow when rainfall return period was low, with a surge in the range of 100–200 km^2 (Figure 6C). This may be related to the topography of the sub-catchment. This shows that peak flow was not sensitive to low antecedent soil moisture, while small increase in rainfall would result in greater runoff in each catchment, which is consistent with Figure 4A.

The peak time increased from the upper left to the lower right, with larger drainage areas, lower soil saturation ratio, and smaller rainfall return periods (Figures 6C, D). When soil saturation ratio was above 80%, runoff occurred almost instantaneously after the end of the rainfall event. This is because all sub-catchments in the region were saturated before the end of the rainfall event. This indicates that the dominant runoff generation mechanism of SXRC is saturation excess. This is also matching the results of our previous findings in the southwest humid China (Liu et al., 2021). For catchments with an area less than 150 km^2, peak time was generally consistent with rainfall time due to the short length of the stream channel in the study catchments.

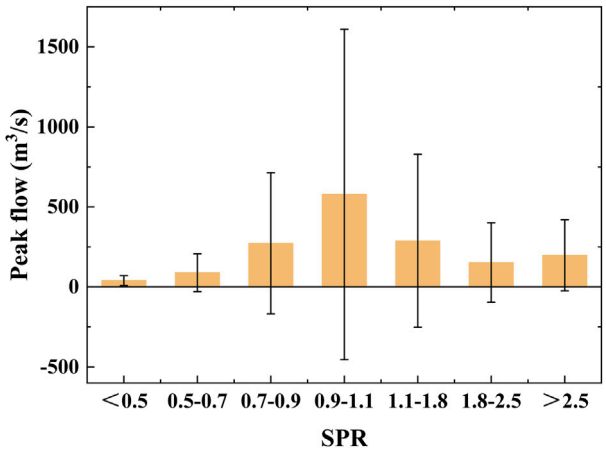

FIGURE 7
Bar plot of the peak flow under different SPR (ratio of antecedent soil saturation and precipitation). The error bars indicate variance among catchments and scenarios.

3.3 Relative contribution of rainfall and antecedent soil saturation ratio

To quantify the impact of soil moisture and rainfall on flood generation, we calculated the ratio of antecedent soil saturation ratio and rainfall (SPR) (Ran et al., 2022). Figure 7 compares the peak flow from different sub-catchments with various SPR values. When SPR was in the first four groups (SPR <1), the peak flow increased with SPR. When SPR was in the last four groups (SPR >1), there was a negative correlation between SPR and peak flow. That is, when the relative magnitude of soil moisture in the input data is greater, magnitude of floods decreased with the decrease of rainfall dominance. On the other hand, when the relative magnitude of rainfall was greater, this situation was reversed. The maximum flood peak flow occurred when SPR was around one. That is, the flood peak reached the maximum when the contribution of rainfall and antecedent soil saturation ratio was close, both rainfall and antecedent soil saturation ratio were relatively large. The peak flow was more sensitive to scenarios with larger rainfall and higher soil moisture saturation ratio. Note that the error in each group followed the same trend as the peak flow due to the larger variance in larger catchments (Supplementary Figure S2). While in small catchments, the change of flood peak flow with SPR was not obvious.

To further explore the relative contribution of rainfall and antecedent soil saturation ratio individually, we calculated the relative importance of rainfall and soil saturation ratio to flood peak. As can be seen from Figure 8, there were apparent trend in the contribution rates of both rainfall and soil saturation ratio. With the increase in catchment drainage area, the relative contribution rates of rainfall gradually decreased while the antecedent soil saturation ratio increased. In the main stream areas near the outlet (the last four points), the changes in these two indicators are particularly prominent. Note that in this algorithm, the value of antecedent soil moisture importance has always been greater. Similar importance has also been found in Vreugdenhil *et al.* (2022) on overland flow and tile drainage in a Hydrological Open Air Laboratory, Austria. Given the calculation of this method, this may be attributed to the relatively larger value and smaller variance of soil saturation ratio. Different methods could derive various values of the relative importance, yet their trends with drainage area are similar: with the increase in catchment size, the impact of antecedent soil moisture decreases and that of rainfall increases, which is consistent with the previous findings.

4 Discussion

4.1 Impact of antecedent soil moisture and rainfall on flood generation

Obviously, the peak flow increased with rainfall return period and antecedent soil saturation ratio, while the peak time decreased with them. Meanwhile, the growth rate of peak flow increased with soil moisture but decreased with rainfall return period. The increase

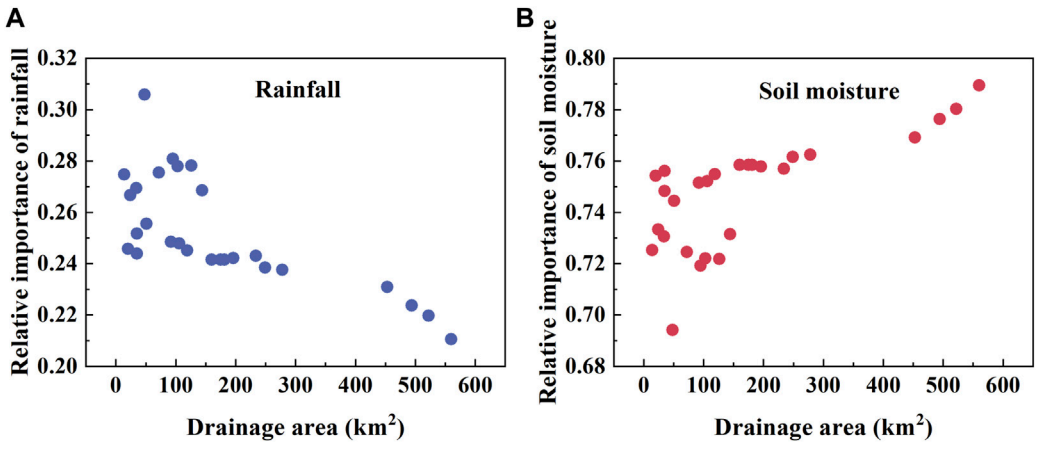

FIGURE 8
Scatter plot of the relative importance of rainfall **(A)** and soil moisture **(B)** to peak flow as the drainage area changes.

rate was steeper under heavy rainfall return periods and high soil saturation ratio. This result ties well with previous studies in Turkey River in the midwestern United States (Zhu et al., 2018). The rapid generation of surface runoff due to saturated soil can lead to greater sensitivity of the flow to changes in rainfall. Conversely, when the soil was dry, most of the rainfall would infiltrate into the soil, slowing the surface runoff (Viglione et al., 2016). This suggests that the dominant mode of runoff generation within the study catchment is Dunne overland flow, which is consistent with previous research findings (Ran et al., 2015).

Rainfall and antecedent soil saturation ratio level have been identified as being main driving factors of runoff generation, and they jointly influence flood (Berghuijs et al., 2016; Ye et al., 2017; Wasko and Nathan, 2019; Breinl et al., 2021). Extreme floods were found occurring under high return period and high antecedent soil saturation ratio in many catchments (Zhu et al., 2018; Zhong et al., 2021). As the rainfall increased, the response of peak flow to high soil saturation ratio become stronger (Figure 4A). Comparing our results with literature, it must be pointed out that some studies have suggested that dry catchments are more sensitive to changes in rainfall than wet ones (Yang and Yang, 2011; Tang et al., 2019). Our results do not necessarily contradict these findings. This may be due to the existence of a critical value for soil saturation. Above this threshold, changes in soil moisture do not significantly affect peak flow. However, when soil moisture is below the critical value, flood size decreases with soil moisture (Wasko and Nathan, 2019). Besides, runoff sensitivity to soil moisture is closely related to the dominant runoff generation mechanisms (Castillo et al., 2003). In arid regions where runoff mainly occurs as infiltration-excess, its sensitivity is expected to show lower than basins where subsurface mechanisms predominate (Cao et al., 2019). Moreover, the increase in rainfall may not necessarily result in higher peak flow due to the reduction of soil saturation ratio. The findings are in line with previous findings (Wasko and Sharma, 2017; Sharma et al., 2018).

We examined the influence of soil saturation ratio and rainfall by comparing their ratios. The results show that when SPR was less than one, there was a positive correlation between SPR and peak flow, while when it was greater than one, it was a negative correlation (Figure 7). That is, the maximum peak flow occurred when both rainfall and antecedent soil saturation ratio were relatively high and contributed to runoff generation. Previous study in the Yangtze River Basin has observed a negative correlation between the multi-year averaged SPR and flood peak flow (Ran et al., 2022). Our result further expanded the data set to event scale and found that there was a more complex relationship between SPR and peak flow at event scale. This finding that event flow peak was maximum when SPR was close to one is consistent with the findings in many humid catchments worldwide (Bennett et al., 2018; Bertola et al., 2021; Ran et al., 2022).

4.2 Impact of scale effects on flood generation

There was a clear correlation between peak flow and peak time with drainage area (Figure 5). When the catchment drainage area was small, there were fluctuations in peak flow and peak time, which could be attributed to the variation of the topography of these small catchments. Overall, it showed a positive correlation with drainage area. This helps quantify the impact of catchment drainage area on runoff generation in the existing work.

Furthermore, the impacts of influential factors on runoff generation may vary for catchments with different drainage areas. Soil saturation ratio condition of larger catchments played a more significant role in regulating flood response compared to smaller ones (Figure 8). Studies conducted in Australia also found that the correlation between peak flow and soil moisture was higher than that between rainfall (Wasko and Nathan, 2019). Additionally, Cao *et al.* (2019) also reported that the effect of antecedent soil moisture is stronger in larger catchments. These findings are consistent with our results. This may be attributed to the longer time for catchment drainage in larger catchments comparing to smaller ones, which also have greater spatial heterogeneity including geomorphological and topographic characteristics (Saharia et al., 2017). For example, catchments with steep slope and high drainage density will respond faster to rainfall (Saharia et al., 2017). Smith *et al.* suggested that the impact of antecedent soil moisture on river flow could be more significant in larger catchments (Smith et al., 2013). Our study further quantifies the relative importance of rainfall and antecedent soil conditions. With the increase of catchment area, the relative importance of rainfall decreases while the relative importance of antecedent soil moisture increases (Figure 8).

Given the scale effects of the relative importance of soil moisture and rainfall, this can be done by assimilating drainage area and soil moisture into hydrological forecasting system to mitigate flood hazards in mountainous areas.

The peak time is also an important indicator of runoff generation, which is of great significance to the early warning of flash flood. In small catchments (i.e., <100 km^2), the peak time was insensitive to both antecedent soil saturation ratio and rainfall magnitude. This is because the confluence distance is very short in the range of several to tens of square kilometers. On the other hand, even in large catchments, extremely short peak time can be observed when antecedent soil saturation ratio was high (Figure 6B). This means that the peak flow occurs immediately at the end of the rainfall. Events with high antecedent soil moisture were likely to convert more precipitation to discharge, and took a shorter time to reach peak flow (Thomas et al., 2021). Simulating the runoff generation process accurately is crucial for reliable flash flood warnings in mountainous catchments. For example, when the soil is close to saturation, the peak time will advance by approximately 300%. Moreover, this effect is more significant under rainfall of shorter return period. Therefore, attention also should be paid to the peak time for small rainfall events coming after series of previous events that have substantially saturated the soil (high soil saturation ratio).

4.3 Limitations and implications

In this study, the InHM model was used to simulate the process of runoff generation in a humid mountainous catchment, aiming to understand the impact and the relative importance of rainfall and antecedent soil saturation ratio on runoff generation. However, our research also has some limitations.

In this analysis, the rainfall was set as the mean maximum 6-h rainstorm from historical records with the homogeneous assumption. That is to say, the rainfall was uniform across the whole catchment. Studies have suggested that spatial rainfall structure has an important impact on river basin runoff in large scale (Zhu et al., 2018). But Lobligeois et al. (2014) found that the spatially uniform rainfall inputs in catchments smaller than 500 km^2 performed better by simulating 3620 flood events observed in 181 catchments. As nearly 95% of our catchments are smaller than 500 km^2, it is reasonable to adopt spatially uniform rainfall in our research.

This work is a theoretical analysis based on simulations from a physically-based distributed hydrological model InHM. Although the model has been successfully employed for many event-based rainfall-runoff simulations in different catchments (Mirus et al., 2007; Ebel et al., 2008), and calibrated in our study region, more accurate measured data on rainfall, soil moisture and runoff are needed to further validate our findings. In addition, studies are needed to be applied to catchments in more climate regions, which will further expand our findings and lead to more general conclusions about the impacts of rainfall and soil moisture.

Studies have shown that extreme precipitation has intensified globally (Do et al., 2017). The increase of rainfall intensity can lead to major floods, especially in humid regions (Milly et al., 2002; Sharma et al., 2018). Better understandings of the contribution of rainfall and antecedent soil moisture at catchments with different drainage area can be crucial for improving flood risk predictions. By investigating the impacts of dominant factors of runoff generation across scales, we can provide guidance on the causes of runoff generation at different scales.

5 Conclusion

In this paper, we apply the physically-based distributed hydrological model InHM to Shouxi River Catchment in Southwest China to analyze the relative contribution of rainfall return period and antecedent soil saturation ratio on runoff generation. By simulating runoff generation processes in different sub-catchments, we explored how rainfall and soil moisture influenced runoff at different scales.

Our results showed that both antecedent soil saturation ratio and rainfall return period had significant impacts on runoff generation. Increasing return period and soil saturation ratio can greatly increase peak flow and shorten peak time. When a high return period was matched with a high antecedent soil saturation ratio, rare extreme flood peak flow would occur rapidly. Our analysis further showed that there was a certain correlation between the antecedent soil saturation ratio to rainfall (SPR) and peak flow. When SPR <1, there was a positive correlation between SPR and peak flow; while when SPR >1, it shifted to a negative correlation. This indicated that the maximum floods usually occurred when rainfall was relatively large and soil water close to saturation; maximum rainfall falling on dry soil could not necessarily generate annual maximum floods.

Furthermore, we found that there were also scale effects on flood generation. Both peak flow and peak time increased linearly with the drainage area. The scale effect was more pronounced when there was high antecedent soil saturation ratio and rainfall return period. Based on the analysis in Shouxi River Catchment, we found that with the increase in catchment drainage area, the relative contribution of rainfall gradually decreased while the antecedent soil saturation ratio increased.

Data availability statement

The raw data supporting the conclusion of this article will be made available by the authors, without undue reservation.

Author contributions

TY: Formal Analysis, Writing–original draft. QR: Conceptualization, Writing–review and editing. HP: Data curation. JL: Investigation. JP: Investigation. SY: Conceptualization, Writing–review and editing.

Funding

The author(s) declare financial support was received for the research, authorship, and/or publication of this article. This research was funded by the National Key Research and Development Program of China (2019YFC1510701-01), and National Natural Science Foundation of China (51979243).

Conflict of interest

Author JP was employed by Zhejiang Design Institute of Water Conservancy and Hydroelectric Power Co., LTD.

The remaining authors declare that the research was conducted in the absence of any commercial or financial relationships that could be construed as a potential conflict of interest.

Publisher's note

Supplementary material

The Supplementary Material for this article can be found online at: https://www.frontiersin.org/articles/10.3389/feart.2023.1285766/full#supplementary-material

SUPPLEMENTARY FIGURE S1
The **(A)** peak flow and **(B)** peak time at different return period and soil saturation ratio. The color represents the antecedent soil saturation ratio.

SUPPLEMENTARY FIGURE S2
Scatter plot of the peak flow under different SPR. The color represents drainage area.

References

Arnell, N. W., and Gosling, S. N. (2016). The impacts of climate change on river flood risk at the global scale. *Clim. Change* 134 (3), 387–401. doi:10.1007/s10584-014-1084-5

Bennett, B., Leonard, M., Deng, Y., and Westra, S. (2018). An empirical investigation into the effect of antecedent precipitation on flood volume. *J. Hydrology* 567, 435–445. doi:10.1016/j.jhydrol.2018.10.025

Berghuijs, W. R., Woods, R. A., Hutton, C. J., and Sivapalan, M. (2016). Dominant flood generating mechanisms across the United States: flood Mechanisms across the U.S. *Geophys. Res. Lett.* 43 (9), 4382–4390. doi:10.1002/2016GL068070

Bertola, M., Viglione, A., Vorogushyn, S., Lun, D., Merz, B., and Blöschl, G. (2021). Do small and large floods have the same drivers of change? A regional attribution analysis in Europe. *Hydrology Earth Syst. Sci.* 25 (3), 1347–1364. doi:10.5194/hess-25-1347-2021

Blöschl, G. (2022). Three hypotheses on changing river flood hazards. *Hydrology Earth Syst. Sci.* 26 (19), 5015–5033. doi:10.5194/hess-26-5015-2022

Borga, M., Boscolo, P., Zanon, F., and Sangati, M. (2007). Hydrometeorological analysis of the 29 August 2003 flash flood in the eastern Italian alps. *J. Hydrometeorol.* 8 (5), 1049–1067. doi:10.1175/JHM593.1

Breinl, K., Lun, D., Müller-Thomy, H., and Blöschl, G. (2021). Understanding the relationship between rainfall and flood probabilities through combined intensity-duration-frequency analysis. *J. Hydrology* 602, 126759. doi:10.1016/j.jhydrol.2021.126759

Cao, Q., Mehran, A., Ralph, F. M., and Lettenmaier, D. P. (2019). The role of hydrological initial conditions on atmospheric river floods in the Russian River Basin. *J. Hydrometeorol.* 20 (8), 1667–1686. doi:10.1175/JHM-D-19-0030.1

Castillo, V., Gomezplaza, A., and Martinezmena, M. (2003). The role of antecedent soil water content in the runoff response of semiarid catchments: a simulation approach. *J. Hydrology* 284 (1–4), 114–130. doi:10.1016/S0022-1694(03)00264-6

Department of Water Resources of Sichuan Province (1984). *Flood manual in small and medium-sized watersheds of sichuan Province*. Chengdu: Complied by Department of Water Resources of Sichuan Province.

Do, H. X., Westra, S., and Leonard, M. (2017). A global-scale investigation of trends in annual maximum streamflow. *J. Hydrology* 552, 28–43. doi:10.1016/j.jhydrol.2017.06.015

Ebel, B. A., Loague, K., Montgomery, D. R., and Dietrich, W. E. (2008). Physics-based continuous simulation of long-term near-surface hydrologic response for the Coos Bay experimental catchment: simulation of Long-Term Hydrologic Response. *Water Resour. Res.* 44 (7). doi:10.1029/2007WR006442

Gan, B., Liu, X., Yang, X., Wang, X., and Zhou, J. (2018). The impact of human activities on the occurrence of mountain flood hazards: lessons from the 17 August 2015 flash flood/debris flow event in Xuyong County, south-western China. *Geomatics, Nat. Hazards Risk* 9 (1), 816–840. doi:10.1080/19475705.2018.1480539

Grillakis, M. G., Koutroulis, A. G., Komma, J., Tsanis, I. K., Wagner, W., and Blöschl, G. (2016). Initial soil moisture effects on flash flood generation – a comparison between basins of contrasting hydro-climatic conditions. *J. Hydrology* 541, 206–217. doi:10.1016/j.jhydrol.2016.03.007

Grömping, U. (2006). Relative importance for linear regression in R: the package relaimpo. *J. Stat. Softw.* 17 (1). doi:10.18637/jss.v017.i01

Guha-Sapir, D., Hoyois, P., and Below, R. (2013). *Annual disaster statistical review*. Brussels, Belgium: Université catholique de Louvain.

Guha-Sapir, D., Hoyois, P., and Below, R. (2014). *Annual disaster statistical review*. Brussels, Belgium: Université catholique de Louvain.

Johnson, J. W., and Lebreton, J. M. (2004). History and use of relative importance indices in organizational research. *Organ. Res. Methods* 7 (3), 238–257. doi:10.1177/1094428104266510

Liu, L. (2022). "Soil moisture movement and its influence on rainstorm and flash flood in Southwest mountainous area," (China: Zhejiang University). Ph.D. Thesis.

Liu, L., Ye, S., Chen, C., Pan, H., and Ran, Q. (2021). Nonsequential response in mountainous areas of southwest China. *Front. Earth Sci.* 9, 660244. doi:10.3389/feart.2021.660244

Loague, K., and VanderKwaak, J. E. (2002). Simulating hydrological response for the R-5 catchment: comparison of two models and the impact of the roads. *Hydrol. Process.* 16 (5), 1015–1032. doi:10.1002/hyp.316

Lobligeois, F., Andréassian, V., Perrin, C., Tabary, P., and Loumagne, C. (2014). When does higher spatial resolution rainfall information improve streamflow simulation? An evaluation using 3620 flood events. *Hydrology Earth Syst. Sci.* 18 (2), 575–594. doi:10.5194/hess-18-575-2014

Madsen, H., Lawrence, D., Lang, M., Martinkova, M., and Kjeldsen, T. R. (2014). Review of trend analysis and climate change projections of extreme precipitation and floods in Europe. *J. Hydrol.* 519, 3634–3650. doi:10.1016/j.jhydrol.2014.11.003

Milly, P. C. D., Wetherald, R. T., Dunne, K. A., and Delworth, T. L. (2002). Increasing risk of great floods in a changing climate. *Nature* 415 (6871), 514–517. doi:10.1038/415514a

Min, S.-K., Zhang, X., Zwiers, F. W., and Hegerl, G. C. (2011). Human contribution to more-intense precipitation extremes. *Nature* 470 (7334), 378–381. doi:10.1038/nature09763

Mirus, B. B., Ebel, B. A., Loague, K., and Wemple, B. C. (2007). Simulated effect of a forest road on near-surface hydrologic response: redux. *Earth Surf. Process. Landforms* 32 (1), 126–142. doi:10.1002/esp.1387

Nash, J. E., and Sutcliffe, J. V. (1970). River flow forecasting through conceptual models, part I-a discussion of principles. *J. Hydrology* 10 (3), 282–290. doi:10.1016/0022-1694(70)90255-6

Nikolopoulos, E. I., Anagnostou, E. N., Borga, M., Vivoni, E. R., and Papadopoulos, A. (2011). Sensitivity of a mountain basin flash flood to initial wetness condition and rainfall variability. *J. Hydrology* 402 (3–4), 165–178. doi:10.1016/j.jhydrol.2010.12.020

Pall, P., Aina, T., Stone, D. A., Stott, P. A., Nozawa, T., Hilberts, A. G. J., et al. (2011). Anthropogenic greenhouse gas contribution to flood risk in England and Wales in autumn 2000. *Nature* 470 (7334), 382–385. doi:10.1038/nature09762

Pathiraja, S., Westra, S., and Sharma, A. (2012). Why continuous simulation? The role of antecedent moisture in design flood estimation. *Water Resour. Res.* 48 (6). doi:10.1029/2011WR010997

Ran, Q., Chen, X., Hong, Y., Ye, S., and Gao, J. (2020). Impacts of terracing on hydrological processes: a case study from the Loess Plateau of China. *J. Hydrology* 588, 125045. doi:10.1016/j.jhydrol.2020.125045

Ran, Q., Hong, Y., Chen, X., Gao, J., and Ye, S. (2019a). Impact of soil properties on water and sediment transport: a case study at a small catchment in the Loess Plateau. *J. Hydrology* 574, 211–225. doi:10.1016/j.jhydrol.2019.04.040

Ran, Q., Hong, Y., Li, W., and Gao, J. (2018). A modelling study of rainfall-induced shallow landslide mechanisms under different rainfall characteristics. *J. Hydrology* 563, 790–801. doi:10.1016/j.jhydrol.2018.06.040

Ran, Q., Qian, Q., Li, W., Fu, X., Yu, X., and Xu, Y. (2015). Impact of earthquake-induced-landslides on hydrologic response of a steep mountainous catchment: a case study of the Wenchuan earthquake zone. *J. Zhejiang University-SCIENCE A* 16 (2), 131–142. doi:10.1631/jzus.A1400039

Ran, Q., Su, D., Qian, Q., Fu, X., Wang, G., and He, Z. (2012). Physically-based approach to analyze rainfall-triggered landslide using hydraulic gradient as slide direction. *J. Zhejiang Univ. Sci. A* 13 (12), 943–957. doi:10.1631/jzus.A1200054

Ran, Q., Wang, F., and Gao, J. (2019b). Modelling effects of rainfall patterns on runoff generation and soil erosion processes on slopes. *Water* 11 (11), 2221. doi:10.3390/w11112221

Ran, Q., Wang, J., Chen, X., Liu, L., Li, J., and Ye, S. (2022). The relative importance of antecedent soil moisture and precipitation in flood generation in the middle and lower Yangtze River basin. *Hydrology Earth Syst. Sci.* 26 (19), 4919–4931. doi:10.5194/hess-26-4919-2022

Rogger, M., Agnoletti, M., Alaoui, A., Bathurst, J. C., Bodner, G., Borga, M., et al. (2017). Land use change impacts on floods at the catchment scale: challenges and opportunities for future research. *Water Resour. Res.* 53 (7), 5209–5219. doi:10.1002/2017WR020723

Saharia, M., Kirstetter, P.-E., Vergara, H., Gourley, J. J., and Hong, Y. (2017). Characterization of floods in the United States. *J. Hydrology* 548, 524–535. doi:10.1016/j.jhydrol.2017.03.010

Sen, P. K., Lindeman, R. H., Merenda, P. F., and Gold, R. Z. (1981). Introduction to bivariate and multivariate analysis. *J. Am. Stat. Assoc.* 76 (375), 752. doi:10.2307/2287559

Sharma, A., Wasko, C., and Lettenmaier, D. P. (2018). If precipitation extremes are increasing, why aren't floods? *Water Resour. Res.* 54 (11), 8545–8551. doi:10.1029/2018WR023749

Smith, J. A., Baeck, M. L., Villarini, G., Wright, D. B., and Krajewski, W. (2013). Extreme flood response: the June 2008 flooding in Iowa. *J. Hydrometeorol.* 14 (6), 1810–1825. doi:10.1175/JHM-D-12-0191.1

Soo, E. Z. X., Jaafar, W. Z. W., Lai, S. H., Islam, T., and Srivastava, P. (2019). Evaluation of satellite precipitation products for extreme flood events: case study in Peninsular Malaysia. *J. Water Clim. Change* 10 (4), 871–892. doi:10.2166/wcc.2018.159

Sriwongsitanon, N., and Taesombat, W. (2011). Effects of land cover on runoff coefficient. *J. Hydrology* 410 (3–4), 226–238. doi:10.1016/j.jhydrol.2011.09.021

Su, D. (2012). "Study on the parallelization of a physics-based hydrologic model InHM utilizing computer cluster," (China: Zhejiang University). Ph.D. Thesis.

Tang, Y., Tang, Q., Wang, Z., Chiew, F. H. S., Zhang, X., and Xiao, H. (2019). Different precipitation elasticity of runoff for precipitation increase and decrease at watershed scale. *J. Geophys. Res. Atmos.* 124 (22), 11932–11943. doi:10.1029/2018JD030129

Thomas, N. W., Ayalew, T. B., Arenas, A. A., Schilling, K. E., Weber, L. J., and Krajewski, W. F. (2021). Characterizing the effects of dry antecedent soil moisture conditions, channel transmission losses, and variable precipitation on peak flow scaling. *Adv. Water Resour.* 158, 104061. doi:10.1016/j.advwatres.2021.104061

Vanderkwaak, J. E. (1999). "Numerical simulation of flow and chemical transport in integrated surface-subsurface hydrologic systems," (Canada: University of Waterloo). Ph.D. Thesis.

Viglione, A., Merz, B., Viet Dung, N., Parajka, J., Nester, T., and Blöschl, G. (2016). Attribution of regional flood changes based on scaling fingerprints. *Water Resour. Res.* 52 (7), 5322–5340. doi:10.1002/2016WR019036

Vivoni, E. R., Entekhabi, D., Bras, R. L., and Ivanov, V. Y. (2007). Controls on runoff generation and scale-dependence in a distributed hydrologic model. *Hydrol. Earth Syst. Sci.* 11 (5), 1683–1701. doi:10.5194/hess-11-1683-2007

Vreugdenhil, M., Széles, B., Salinas, J. L., Strauß, P., Oismueller, M., Hogan, P., et al. (2022). Non-linearity in event runoff generation in a small agricultural catchment. *Hydrol. Process.* 36 (8), e14667. doi:10.1002/hyp.14667

Wasko, C., and Nathan, R. (2019). Influence of changes in rainfall and soil moisture on trends in flooding. *J. Hydrology* 575, 432–441. doi:10.1016/j.jhydrol.2019.05.054

Wasko, C., and Sharma, A. (2017). Global assessment of flood and storm extremes with increased temperatures. *Sci. Rep.* 7 (1), 7945. doi:10.1038/s41598-017-08481-1

Yang, H., and Yang, D. (2011). Derivation of climate elasticity of runoff to assess the effects of climate change on annual runoff. *Water Resour. Res.* 47 (7). doi:10.1029/2010WR009287

Yang, Z., Jin, E., Zhou, X., Gao, J., and Wang, X. (2022). "Simulation study on "8.20" rainstorm flash flood process in Shouxi River, Wenchuan." in Proceedings of the 16th National Hydrodynamics Conference and the 32nd National Symposium on Hydrodynamics. 1985-1990. (in Chinese)

Ye, S., Li, H.-Y., Leung, L. R., Guo, J., Ran, Q., Demissie, Y., et al. (2017). Understanding flood seasonality and its temporal shifts within the contiguous United States. *J. Hydrometeorol.* 18 (7), 1997–2009. doi:10.1175/JHM-D-16-0207.1

Yin, Z., Li, H., Tang, X., and Gong, Z. (2022). Flash flood forecasting of Shouxi River in southwestern region based on deep learning. *Water Resour. Power* 40 (2), 88–91. (in Chinese).

Yuan, X., Liu, C., Lu, H., Nie, R., Chen, C., Liu, T., et al. (2022). Analysing evolution characteristics of landslide deposits in Shouxi River Basin in the wenchuan earthquake zone. *Adv. Eng. Sci.* 54 (6), 32–42. (in Chinese). doi:10.15961/j.jsuese.202200732

Zhai, X., Guo, L., Liu, R., and Zhang, Y. (2018). Rainfall threshold determination for flash flood warning in mountainous catchments with consideration of antecedent soil moisture and rainfall pattern. *Nat. Hazards* 94 (2), 605–625. doi:10.1007/s11069-018-3404-y

Zhong, M., Zeng, T., Jiang, T., Wu, H., Chen, X., and Hong, Y. (2021). A copula-based multivariate probability analysis for flash flood risk under the compound effect of soil moisture and rainfall. *Water Resour. Manag.* 35 (1), 83–98. doi:10.1007/s11269-020-02709-y

Zhu, Z., Wright, D. B., and Yu, G. (2018). The impact of rainfall space-time structure in flood frequency analysis. *Water Resour. Res.* 54 (11), 8983–8998. doi:10.1029/2018WR023550

Frontiers in Earth Science

Investigates the processes operating within the major spheres of our planet

Advances our understanding across the earth sciences, providing a theoretical background for better use of our planet's resources and equipping us to face major environmental challenges.

Discover the latest Research Topics

See more →

Frontiers

Avenue du Tribunal-Fédéral 34
1005 Lausanne, Switzerland
frontiersin.org

Contact us

+41 (0)21 510 17 00
frontiersin.org/about/contact